TRAJECTORY DESIGN STRATEGIES FROM GEOSYNCHRONOUS TRANSFER ORBITS TO LAGRANGE POINT ORBITS IN THE SUN EARTH SYSTEM

by

Juan A. Ojeda Romero

A Dissertation

Submitted to the Faculty of Purdue University

In Partial Fulfillment of the Requirements for the Degree of

Doctor of Philosophy

School of Aeronautics and Astronautics

West Lafayette, Indiana

December 2021

THE PURDUE UNIVERSITY GRADUATE SCHOOL
STATEMENT OF COMMITTEE APPROVAL

Dr. Kathleen C. Howell, Chair

School of Aeronautics and Astronautics

Dr. Carolin E. Freuh

School of Aeronautics and Astronautics

Dr. James M. Longuski

School of Aeronautics and Astronautics

Dr. Karen Marais

School of Aeronautics and Astronautics

Approved by:

Dr. Gregory A. Blaisdell

Para mi familia

ACKNOWLEDGMENTS

First, I want to thank my family: Rocky, Juan Fernando, Juan Diego, Maria Fernanda, Coca, Joey. Additionally, I want to thank my extended family, both in the US and in Perú. Thank you for your support throughout my journey at Grad school.

I would like to extend my thanks to the past and current members of the Multibody Dynamics Research Group. Your advice, encouragement, friendship, and tough questions during our meetings have made the four years at Purdue memorable. A special thanks to Kenza, Steven, Maaninee, Vivek, Bonnie, Ash, Ted, Paige, Chris, Emily, Nick, Andrew, Robert, Collin, David, RJ, Fouad, and Brian.

Next, I want to extend my gratitude to Professor Kathleen Howell. Thank you for your support, for your advice, for your tough questions, for teaching me to think like a researcher and question everything. Also, thank you for facilitating so many amazing research and work opportunities outside Purdue. I would also like to thank my committee members: Prof. James Longuski, Prof. Carolin Frueh and Prof. Karen Marais. Your insightful questions, advice, and feedback have been invaluable on this journey.

I would also like to thank Mr. Mike Mesarch from NASA Goddard Space Flight Center (GSFC) for his mentorship during my summer internship and for his introduction to this research topic. Additionally, I want to thank Dr. Wayne Schlei and Mr. Sean Phillips for their mentorship and advice during my internship at John Hopkins Applied Research Laboratory (APL).

Furthermore, I would like to thank the Purdue Department of Mathematics for funding my first semester at Purdue. Additionally, I want to extend my gratitude to the National Science Foundation Research Fellowship Program (Grant No. DGE-1333468) for funding me for the last three years.

Finalmente, este mensaje es para mis padres. Gracias por tu sacrificio, tu coraje, y tu amor. Sé que no soy un hijo perfecto, pero los quiero agradecer por tu paciencia y tu amor. Para mi mama Lita, papa Beto, mama Paula, y mi papa Lucio, los quiero y los extraño.

TABLE OF CONTENTS

LIST OF TABLES

LIST OF FIGURES

ABSTRACT

Over the past twenty years, ridesharing opportunities for smallsats, i.e., secondary payloads, has increased with the introduction of Evolved Expendable Launch Vehicle (EELV) Secondary Payload Adapter (ESPA) rings. However, the orbits available for these secondary payloads is limited to Low Earth Orbits (LEO) or Geostationary Orbits (GEO). By incorporating a propulsion system, propulsive ESPA rings offer the capability to transport a secondary payload, or a collection of payloads, to regions beyond GEO. In this investigation, the ridesharing scenario includes a secondary payload in a dropped-off Geosynchronous Transfer Orbit (GTO) and the region of interest is the vicinity near the Sun-Earth Lagrange points. However, mission design for secondary payloads faces certain challenges. A significant mission constraint for a secondary payload is the drop-off orbit orientation, as it is dependent on the primary mission. To address this mission constraint, strategies leveraging dynamical structures within the Circular Restricted Three-Body Problem (CRTBP) are implemented to construct efficient and flexible transfers from GTO to orbits near Sun-Earth Lagrange points. First, single-maneuver ballistic transfers are constructed from a range of GTO departure orientations. The ballistic transfer utilize trajectories within the stable manifold structure associated with periodic and quasi-periodic orbits near the Sun-Earth L_1 and L_2 points. Numerical differential corrections and continuation methods are leveraged to create families of ballistic transfers. A collection of direct ballistic transfers are generated that correspond to a region of GTO departure locations. Additional communications constraints, based on the Solar Exclusion Zone and the Earth's penumbra shadow region, are included in the catalog of ballistic transfers. An integral-type path condition is derived and included throughout the differential corrections process to maintain transfers outside the required communications restrictions. The ballistic transfers computed in the CRTBP are easily transitioned to the higher-fidelity ephemeris model and validated, i.e., their geometries persist in the ephemeris model. To construct transfers to specific orbits near Sun-Earth L_1 or L_2, families of two-maneuver transfers are generated over a range of GTO departure locations. The two-maneuver transfers consist of a maneuver at the GTO

departure location and a Deep Space Maneuver (DSM) along the trajectory. Families of two-maneuver transfers are created via a multiple-shooting differential corrections method and a continuation process. The generated families of transfers aid in the rapid generation of initial guesses for optimized transfer solutions over a range of GTO departure locations. Optimized multiple-maneuver transfers into halo and Lissajous orbits near Sun-Earth L_1 and L_2 are included in this analysis in both the CRTBP model and the higher-fidelity ephemeris model. Furthermore, the two-maneuver transfer strategy employed in this analysis are easily extended to other Three-Body systems.

1. INTRODUCTION

Over the past 60 years, thousands of satellites have been successfully launched into Low Earth Orbit (LEO) and beyond. The cost to launch a satellite to Low Earth Orbit (LEO) typically ranges from $5,000/kg to $30,000/kg. Additionally, the cost for a launch to Geostationary Orbit (GEO) is approximately $30,000/kg. For a small satellites, usually less than 500 kg, the launch costs are often significantly higher than the cost to build the satellite bus [1]. Over the last two decades, launching groups of small satellites simultaneously to LEO and GEO have decreased overall mission costs. This ridesharing scenario accommodates multiple small satellites into a single launch. Recent advances into novel propulsive systems coupled with ridesharing vehicles allow multiple satellites to reach regions beyond GEO and necessitates a strategic methodology to construct efficient transfers to specific regions of interest.

1.1 Motivation

Rideshare launches are now more frequent as they offer opportunities to expand mission capabilities. For example, the Lunar Crater and Observation and Sensing Satellite (LCROSS) mission was launched as a secondary payload with the Lunar Reconnaissance Orbiter (LRO) in 2009 to study the polar regions of the Moon [2]. This strategy decreased mission cost for LCROSS and increased the science potential for the combined venture. In the past ten years, an increasing number of CubeSats have launched as secondary payloads into LEO and beyond. The two MarCO CubeSats were launched from the Insight lander in 2018 en route to Mars. Additionally, thirteen CubeSats will be launched aboard the Artemis-1 mission to destinations in heliocentric space and the low lunar vicinity [3]. These CubeSats and smallsats, i.e., small satellites, are secondary payloads that benefit from the excess capacity available from launches to LEO and GEO. However, these secondary payloads face several challenges, such as significantly varying orbital geometries, shifting launch dates and the impact of launch vehicle performance [4]. Shifting launch dates, in particular, are dictated by constraints on the primary payload, i.e., the primary mission, and signifi-

cantly influence the orbital geometry available for secondary payloads. Generally, a single satellite is launched en route to an intermediate orbit before entering into its operational orbit. In a ridesharing scenario, a secondary payload is dropped off at the intermediate orbit used by the primary spacecraft. For example, a general mission scenario for a single satellite en route to GEO consists of the following steps:

- Launch of satellite.
- The satellite is placed in an intermediate Geosynchronous Transfer Orbit (GTO) via a propulsive maneuver performed by an upper stage of the launch vehicle.
- The satellite enters the operational orbit at GEO by performing an insertion maneuver at GTO apogee.

In this scenario, any secondary payloads are dropped off at the GTO, i.e., the intermediate orbit. With roughly twenty-five yearly launches to GEO [5], see a ten-year history of worldwide launches in Figure 1.1, that ridesharing smallsats have adequate opportunities to leverage. An increasing number of CubeSats have been launched from GTO as secondary

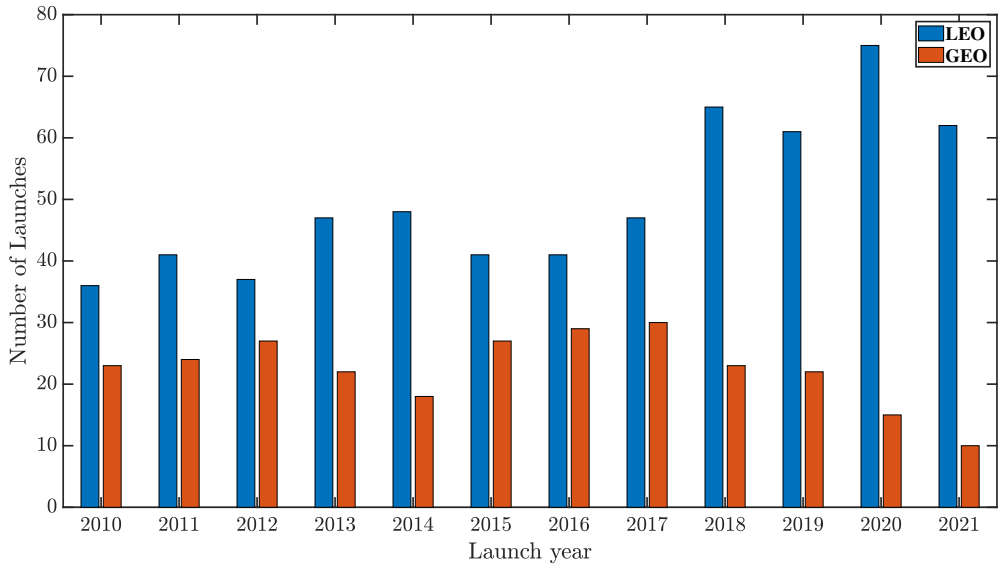

Figure 1.1. : Worldwide launches to LEO and GEO in the past 10 years. Data retrieved from [6], [7]

payloads into LEO, in fact, the launch cost for a CubeSat starts at \$10,000/kg [8]. Additionally, interest in launching CubeSats with low-thrust engines from GTO to regions beyond GEO has surged. Some low-thrust concepts from GTO include interplanetary transfers to Mars [9]. Additionally, SMART-1 was launched in 2003 on a GTO with a low-thrust engine and eventually impacted the lunar surface in 2006 [10]. Note that additional maneuvers by the secondary payloads, e.g., smallsats and CubeSats, is provided by any on-board propulsion system. However, due to the compact size of the secondary payloads, the on-board propulsive capabilities are limited, especially if the desired destination is beyond GEO. Therefore, secondary payloads with chemical engines must have the propulsive capability to reach regions beyond GEO. However, this may limit the mission lifetime as more spacecraft mass is directed towards energy raising maneuvers. Recently, propulsive Evolved Expendable Launch Vehicle (EELV) Secondary Payload Adapter (ESPA) rings have been proposed to increase the range of available orbits for secondary payloads. A propulsive ESPA ring offers the capability to mitigate restrictive ΔV requirements imposed on the spacecraft as the system is independent of the secondary payload bus. The LCROSS mission demonstrated the use of these propulsive system enhancements[4].

Some regions of interest beyond GEO are the collinear Lagrange points in the Sun-Earth system. The Sun-Earth L_1 Lagrange point region is an ideal location to explore the solar environment while also offering favorable thermal conditions, eclipse avoidance, and continuous communications. However, preliminary transfer design must incorporate the avoidance of communications interference caused by the Sun [11]. The location of the L_2 Lagrange point offers convenient thermal conditions for any observatory mission but is constrained by Earth eclipse conditions. The first orbiter placed in the vicinity of the Sun-Earth L_1 collinear Lagrange point was the successful International Sun-Earth Explorer-3 (ISEE-3), renamed the International Cometary Explorer (ICE) as the mission later evolved. The objective involved observations of the solar environment; the spacecraft successfully completed four revolutions in its Sun-Earth halo orbit before departing toward a comet via a lunar gravity assist [12]. The ISEE-3 mission was a catalyst for future long-term missions to Lagrange point orbits. Within the L_1 region, the Advanced Composition Explorer (ACE),

Solar Heliospheric Observatory (SOHO), and the International Physics Laboratory (WIND) are additional examples of orbiters launched in the past twenty years [11]. The addition of smallsats near the Sun-Earth L_1 Lagrange point increases our understanding of solar environment. Alternatively, several European Space Agency (ESA) missions have leveraged the favorable thermal and radiation conditions provided by the Sun-Earth L_2 point. The Planck and Gaia missions were placed in Lissajous orbits near L_2 to study cosmic background radiation and construct a skymap of the universe, respectively [13]. Additionally, the Sun-Earth L_2 point is the selected destination for the Nancy Grace Roman Space Telescope and the James Webb Space Telescope.

Insights from Dynamical Systems Theory (DST) are frequently leveraged to investigate potential transfers to Sun-Earth Lagrange points. While transfers are frequently constructed via numerical searches in a higher-fidelity model, fundamental understanding of the dynamical regime gained through DST in a simplified model offers efficiency and flexibility for the search effort. Periodic orbits and their invariant manifolds are frequently implemented in a search for low cost transfers [14]–[16]. Although periodic motion exists in the Circular Restricted Three Body Model (CRTBP), periodicity is not maintained when the orbit is transferred to a higher-fidelity model. In the CRTBP model, quasi-periodic behavior is also available near the vicinity of specific reference periodic orbits and the geometry of the final trajectory is significantly altered as a result of the orbit selection. Thus, quasi-periodic motion near periodic orbits are viable design options to construct alternative initial guesses. Manipulating hyperbolic invariant manifolds from periodic and quasi-periodic orbits expands the search for transfers from established departure orbits [17]–[19]. These structures have been investigated previously in the Earth-Moon system and serve to construct transfers from locations near LEO [20]. Additionally, the existence of quasi-periodic motion is extendable for motion near irregularly shaped bodies [21] as well as formation flying [22]. Leveraging previous designs, as well as fundamental behaviors, enable trajectory options for secondary payloads towards regions beyond GEO.

1.2 Summary of Previous Contributions

Periodic orbits in the CRTBP are frequently manipulated to construct feasible transfers in a complex multibody regime. Families of planar Lyapunov and out-of-plane halo orbits have been computed and utilized for missions in the Sun-Earth and Earth-Moon systems [23]–[25]. Grebow outlines numerical strategies for evaluating periodic orbits in the Earth-Moon system and categorizes several periodic orbit families [26]. The numerical strategies provided by Grebow are straightforwardly extended to the Sun-Earth system. Additionally, existing dynamical structures in the CRTBP, such as hyperbolic invariant manifolds associated with periodic orbits, are regularly implemented in a guided search for feasible transfers [14], [20], [27]. Incorporating periodic orbits and their associated hyperbolic manifold structures facilitates the construction of preliminary design transfer to orbits near the Sun-Earth Lagrange points. The GENESIS orbiter was launched in 2001 en route to a halo orbit near Sun-Earth L_1 with a subsequent excursion towards L_2 and leveraged hyperbolic manifolds from halo orbits [15]. In 2004, the International Physics Laboratory (WIND) arrived near L_1 after a series of transfers through the Sun-Earth system that involved Distant Retrograde Orbits (DROs), close approaches near L_1 and L_2, and 38 targeted lunar flybys [28]. Additionally, several preliminary mission design strategies to Sun-Earth L_1 and L_2 incorporate periodic orbits including SOHO (L_1) [11], WIND (L_1) [11], the Wilkinson Microwave Anisotropy Probe (L_2), the Nancy Roman Space Telescope (expected L_2) [14], and the James Web Space Telescope [29] (expected L_2).

Bounded quasi-periodic motion observed in the CRTBP provides mission designers with added insight about the complex dynamical model. Analytical methods, such as the Lindstedt-Poincaré method, for generating quasi-periodic orbits typically implement higher-order expansions to express a quasi-periodic orbit near a Lagrange point as a function of time. However, analytical methods usually require additional numerical effort to evaluate an adequate representation of a quasi-periodic orbit. Furthermore, Akiyama et al. produced quasi-periodic orbits in the Sun-Earth system using a semi-analytical approach by leveraging the center manifold associated with periodic orbits [30]. Kolemen et al. devel-

oped a methodology to construct quasi-periodic orbits from a set of Poincaré sections [31]. Numerical methods of generating quasi-periodic orbits in the Sun-Earth and Earth-Moon systems have also been successfully implemented by previous authors [18], [21], [32], [33]. These methods represent periodic and quasi-periodic orbits as invariant tori in a numerical corrections process [32], [34]. The numerical corrections process is easily extended to the Bicircular Four-Body Problem and the Elliptical Restricted Three-Body Problem [17], [35]. Using this numerical technique, Bosanac generated quasi-periodic orbits from resonant orbits in the Sun-Earth and Earth-Moon systems [36]. Dynamical structures from quasi-periodic orbits, such as hyperbolic invariant manifolds, exist and are frequently utilized in early mission design. McCarthy leveraged dynamical structures from quasi-periodic orbit to construct transfers to Sun-Earth L_1 Lissajous orbits from circular low Earth orbits [20]. Missions focused on the observation of the solar environment have effectively utilized quasi-periodic orbits to establish long-term presence near the Sun-Earth L_1 Lagrange point. Howell et al. investigated Lissajous orbits near the Sun-Earth L_1 region that avoid the Solar Exclusion Zone (SEZ) [27]. An optimal trajectory to Sun-Earth L_1 for the ACE spacecraft with imposed SEZ restrictions is offered by Sharer et al. [37]. The operational orbit of the SOHO spacecraft is essentially a quasi-periodic orbit around Sun-Earth L_1 that maintains a long-term presence in the L_1 region to observe the heliosphere and the solar wind [11], [38]. A recent addition to the L_1 regime is the Deep Space Climate Observatory (DSCOVR), launched in 2015. The mission objectives include real-time solar wind dynamics and space weather forecasts while in a Lissajous orbit [39], [40]. A future addition to Sun-Earth L_1 includes the Interstellar Mapping and Acceleration Probe (IMAP) mission, expected launch in 2025, which will be placed in a Lissajous orbit and will investigate the interaction of energetic particles and the solar wind [41]. Near Sun-Earth L_2 , the Gaia mission, launched in 2013, is in a Lissajous orbit and performs maneuvers to avoid Earth eclipsing events [13]. Quasi-periodic motion offers alternative design options for orbiters near the Sun-Earth Lagrange points.

Access to regions beyond GEO is facilitated with propulsive ESPA rings for ridesharing satellites in a GTO. Small satellites face limited access into space as the launch costs

usually exceed the production costs. However, ESPA rings, designed and built by Moog Space and Defense, offer the possibility to increase the number of satellites launched from a single launch with minimal impact to the primary mission. The Department of Defense (DoD) Space Test Program (STP-1) mission was the first mission to implement the ESPA ring configuration on an Atlas V launch in 2007 [42]. Additionally, the LCROSS mission and the ESPA Augmented Geostationary Laboratory Experiment (EAGLE) were the first missions to fly on-board a propulsive ESPA ring. Recently, a number of concept designs for propulsive EPSA rings, which integrate either chemical or electrical propulsion, have been proposed to transport a smallsat or a group of smallsats into GEO or beyond [43]. The Moog developed Orbital Maneuvering Vehicle (OMV) is a propulsive ESPA ring capable of transporting a series of smallsats into orbits beyond GEO. Some examples of the OMV include the Small Launch Orbital Maneuvering Vehicle (SL-OMV), the Maneuverable ESPA Tug for Extended Orbital Range (METEOR), ASTRO Plus, and the JUPITER concept [42]. Additionally, ESPAStar (Northrop Grumman) and Sherpa 2200 (Spaceflight Inc.) implement a Moog ESPA ring to build a mechanical interface to accommodate multiple smallsats [44], [45]. Table 1.1 summarizes the capabilities of these propulsive ESPA ring concepts. In this investigation, transfers for secondary payloads are constructed from a departure location along a GTO. Pearson et al. proposed the use of a Moog OMV to facilitate transfers from GTO to Sun-Earth Lagrange points and lunar orbits [5], [46]. Structures in the Sun-Earth system were leveraged to construct a transfer for the Dark Ages Radio Explorer (DARE) spacecraft which utilized a GTO rideshare option [47]. The DARE spacecraft will be launched as a secondary payload en route to a low lunar orbit. Additionally, Penzo et al. utilized GTOs to investigate impulsive transfers to Mars and Venus with lunar flybys using a Two-Body approximation [48]. Kéchichian et al. proposed two strategies that implemented DST to place a group of microsatellites in DROs and L_1 halo orbits in the Sun-Earth system from GTO [49]. Eismont et al. investigated transfers to Sun-Earth L_1 halos from GTO at varying launch epochs and orientations [50]. Di Salvo identified 'free' transfers to large amplitude quasi-periodic orbits near Sun-Earth L_2 [51]. These 'free' transfers required one maneuver from GTO and leveraged the natural dynamics in the system to enter large amplitude quasi-periodic orbits.

Table 1.1. : Comparison of propulsive ESPA modules

Name	Manufacturer	ΔV [m/s]	Payload Mass [kg]
METEOR	Moog Inc.	500	<1,000
Astro Plus	Moog Inc.	<3,000	<500
JUPITER	Moog Inc.	<6,000	<5,000
ESPAStar	Northrop Grumman	>400	>1,920
Sherpa 2200	Spaceflight Inc.	<2,200	<1,500

1.3 Current Work

Propulsive ESPA rings offer secondary payloads, i.e., smallsats or CubeSats, access to regions beyond GEO. However, in a ridesharing scenario, secondary payloads are restricted by the drop-off orbit orientation which is dictated by the primary mission. Therefore, there is a need for mission designers to anticipate the transfer geometries available from any drop-off orbit orientation. In this investigation, the focus is transfers from a GTO drop-off orbit into an orbit near the Sun-Earth L_1 and L_2 vicinity. For secondary payloads, a highly efficient transfer implements a single maneuver, that is, a maneuver is performed at a departure location along the GTO and the satellite approaches and enters an orbit near the Sun-Earth L_1 and L_2 Lagrange points. This type of transfer, termed a ballistic transfer, leverages the natural motion observed in the Sun-Earth system in the simplified CRTBP model. Additionally, multiple-maneuver transfers are also considered, especially when targeting operational orbits with specific amplitudes for secondary payloads. To provide insight into transfers from GTO in the Sun-Earth system, the following research objectives are addressed:

1. Understand ballistic transfers to Sun-Earth Lagrange point orbits.

   The objective is to identify ballistic transfers from a range of near-Earth departure locations to the Sun-Earth L_1 and L_2 regions. Identification of direct and indirect pathways to orbits near Sun-Earth Lagrange points is obtained through this analysis. Direct ballistic transfers are constructed from a range of near-Earth locations to periodic and quasi-periodic motion near the Sun-Earth L_1 and L_2 points.

2. Catalog direct prograde ballistic transfers from GTO to Sun-Earth Lagrange point orbits.

   Ballistic transfers leverage the natural dynamics in the system to enter bounded motion, either a periodic or quasi-periodic orbit, near a Lagrange point. The guide provides insight into direct ballistic transfers available from prograde GTOs for a range of orientations near the Earth. The guide also presents an initial estimate of maneuver ΔV requirements and final orbit geometries near Sun-Earth L_1 and L_2 Lagrange points.

3. Investigate multiple-maneuver transfers to periodic and quasi-periodic orbits

   Ballistic transfers are not available for all orbits in the Sun-Earth system, therefore, an additional maneuver is appended to construct two-maneuver transfers over a range of GTO departure locations near the Earth. To construct efficient transfers into a desired orbit near the Sun-Earth Lagrange points, trajectories along the hyperbolic stable manifold and a Deep Space Maneuver are included in the design scenario. Multiple-maneuver transfers over a range of GTO orientations into select periodic and quasi-periodic orbits are investigated through this methodology.

These objectives will yield an understanding of pathways available from a GTO of any orientation near the Earth and offer insight on the exploration of the Sun-Earth system. The results of the current investigation are organized as follows:

- Chapter 2: Dynamical Models

  In this chapter, the dynamical models for the CRTBP and the ephemeris model, i.e., a higher-fidelity model, are introduced. Equations of motion associated with the dynamical models are derived and any assumptions implemented are stated. Additionally, the method of transitioning a satellite state between an inertial reference frame and a rotating frame consistent with the CRTBP is outlined.

- Chapter 3: Dynamical Structures

  The existence of equilibrium solutions, periodic orbits, quasi-periodic orbits associ-

ated with the CRTBP model are discussed in this chapter. The free-variable and constraint numerical technique coupled with a multidimensional Newton's method are introduced. This numerical method is implemented in the construction of periodic and quasi-periodic orbits and examples in the Sun-Earth system are provided. Additionally, a linear stability analysis of the equilibrium points, periodic, and quasi-periodic orbits is summarized and invariant hyperbolic manifolds associated with these dynamical structure are identified.

- Chapter 4: Rideshare Mission Overview

  This chapter begins with a description of the rideshare scenario for a secondary payload on a drop-off orbit, i.e., a GTO, in the Sun-Earth system. A discussion regarding the GTO orientation expressed in the J2000 inertial reference frame and the Sun-Earth rotating frame is provided.

- Chapter 5: Ballistic Transfers to Collinear Lagrange Points

  Ballistic transfers into periodic and quasi-periodic orbits near Sun-Earth L_1 and L_2 are constructed by leveraging hyperbolic invariant manifolds in this section. A collection of direct ballistic transfers to quasi-periodic orbits are identified in a region near the Earth. An integral-type path constraint is derived and applied to transfers constrained by additional communications requirements. Additionally, the direct ballistic transfers observed in the Sun-Earth CRTBP model are transitioned into the higher-fidelity ephemeris model.

- Chapter 6: Multiple Maneuver Transfers in Sun-Earth System

  In this chapter, transfers utilizing a Deep Space Maneuver, i.e., two-maneuver transfers, that enter select quasi-periodic and periodic orbits near the Sun-Earth L_1 and L_2 Lagrange points are generated. The transfers are designed with trajectories along the stable manifold of quasi-periodic and periodic orbits and a bridging arc. In the CRTBP, two-maneuver transfers exist as families of transfers from a range of GTO departure locations near the Earth. Locally optimal transfers are constructed by carefully

selecting a solution from the families of two-maneuver transfers. Finally, the transfers are transitioned into the higher-fidelity ephemeris model.

- Chapter 7: Conclusion

  Finally, in this chapter, a summary of the proposed methodology and results from the applications is provided. Recommendations for future work are outlined as a response to the conclusions of this investigation.

2. DYNAMICAL MODELS

Dynamical models describe the motion of a spacecraft under the gravitational influence of multiple celestial bodies. A dynamical model can be formulated as a basic Two-Body system or a more complex $\mathfrak{N}$-Body system. An understanding of any simplifying assumptions in the formulation of a model reveals important dynamical insights. For example, A Two-Body model describes the motion of a spacecraft under the gravitational influence of a celestial body, e.g., a spacecraft in a Low Earth Orbit. A basic Two-Body model assumes that both bodies are point-masses and that the celestial body is significantly larger than the spacecraft. The Two-Body model is usually the first dynamical model implemented in early design stages, while more complex higher-fidelity models are incorporated in later stages and, eventually, during post-launch operations. For a spacecraft in LEO, a higher-fidelity Two-Body model based on a non-spherical Earth with added atmospheric drag and solar radiation pressure effects is utilized during operations. Although mission designers implement complex models to describe the motion of a spacecraft, it is often difficult to derive any insightful information from these complex models. However, dynamical behavior observed in lower-fidelity models may provide important insights about the motion of a spacecraft. Additionally, desirable characteristics of a spacecraft trajectory, such as geometry, in the lower-fidelity model may persist upon transitioning to a higher-fidelity model. In this investigation, insights obtained from the Circular Restricted Three-Body Problem (CRTBP), i.e., a lower-fidelity model, are leveraged to, eventually, generate cost efficient and flexible transfers in a higher-fidelity ephemeris model.

2.1 $\mathfrak{N}$-Body Problem

The motion of a spacecraft under the gravitational influence of $\mathfrak{N}$ bodies is described by Newton's Universal Law of Gravitation and Newton's 2$^{\text{nd}}$ Law [52]. Newton's Law of Gravitation describes the force on a particle with point mass under the gravitational influence of a group of bodies, also modeled as point masses. For example, in a Three-Body system,

e.g., a system consisting of the Earth, Moon, and a spacecraft, all three bodies are modeled as point masses, see Figure 2.1. By combining the universal law of gravitation and Newton's 2nd Law, a vector equation describing the motion of a spacecraft under the influence of $\mathfrak{N}$ bodies, P_{j}, is written as,

$$M_{\mathrm{j}}\ddot{\bar{\mathfrak{R}}}_{\mathrm{j}} = \tilde{G}\sum_{\substack{k=1\\k\neq \mathrm{j}}}^{\mathfrak{N}} \frac{M_k M_{\mathrm{j}}\bar{\mathfrak{R}}_{\mathrm{j}k}}{\mathfrak{R}_{\mathrm{j}k}^3}, \tag{2.1}$$

where $\tilde{G}$ is the universal gravitational constant and M is the mass of a body, i.e., a celestial body or the spacecraft. Note that, in Equation (2.1), overbars represent column vectors and $[\dot{\ }]$ is a time derivative. The position vector of the spacecraft, P_{j}, is defined as $\bar{\mathfrak{R}}_{\mathrm{j}}$ with respect to an inertial origin and $\bar{\mathfrak{R}}_{\mathrm{j}k}$ is the position vector from P_{j} to P_k. The motion of the spacecraft, $\bar{\mathfrak{R}}_{\mathrm{j}}$, in Equation (2.1) is defined in an inertial frame, however, a vector equation relative to a body P_q is derived from Equation (2.1) as,

$$\ddot{\bar{\mathfrak{R}}}_{q\mathrm{j}} = \underbrace{-\tilde{G}\frac{(M_{\mathrm{j}}+M_q)}{\mathfrak{R}_{q\mathrm{j}}^3}\bar{\mathfrak{R}}_{q\mathrm{j}}}_{\text{Direct}} + \underbrace{\tilde{G}\sum_{\substack{k=1\\k\neq \mathrm{j},q}}^{\mathfrak{N}} M_k\left(\frac{\bar{\mathfrak{R}}_{\mathrm{j}k}}{\mathfrak{R}_{\mathrm{j}k}^3} - \frac{\bar{\mathfrak{R}}_{qk}}{\mathfrak{R}_{qk}^3}\right)}_{\text{Indirect}}. \tag{2.2}$$

Note that, in Equation (2.2), the direct term is the effect of the body P_q on the spacecraft P_{j} and the indirect terms are due to the additional $\mathfrak{N}-2$ bodies. Throughout this investigation, Equation (2.2) is termed as the ephemeris equation of motion (EOM). The position and velocity vectors for the celestial bodies included in the ephemeris EOM, i.e., $\bar{\mathfrak{R}}_{\mathrm{j}}$ and $\bar{\mathfrak{V}}_{\mathrm{j}}$], respectively, are retrieved from the SPICE ephemerides files provided by the NASA Jet Propulsion Laboratory (JPL) Navigation and Ancillary Information Facility (NAIF) in Pasadena, California [53]. The SPICE files contain approximate states for celestial bodies in the solar system based on observational data. There is no closed-form analytical solution to the ephemeris EOM in Equation (2.2), which poses challenges for mission designers. However, a Two-Body system, i.e., Equation (2.2) with the indirect terms omitted, has a closed-form analytical solution. In most preliminary design phases, insights from a Two-Body approximation are adequate to identify initial transfers or feasible orbits that are subsequently transitioned into the higher-fidelity ephemeris model. By leveraging fundamental behaviors observed in lower-fidelity models, such as the Two-Body model or the Three-Body model,

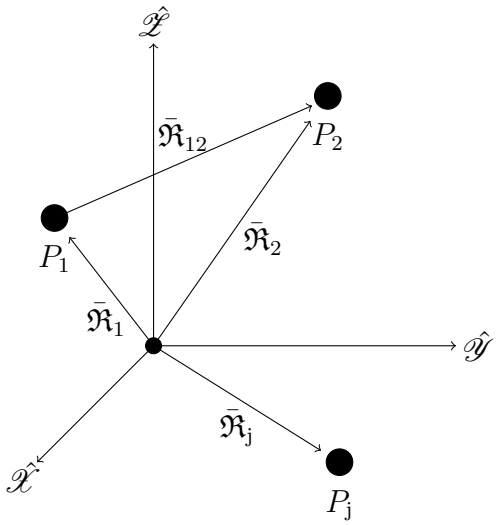

Figure 2.1. : $\mathfrak{N}$ bodies in an inertial reference frame. The basis vectors for the inertial frame is the set $\{\hat{\mathscr{X}}, \hat{\mathscr{Y}}, \hat{\mathscr{Z}}\}$

cost efficient transfers are constructed that are transitioned into a higher-fidelity ephemeris model.

2.2 Circular Restricted Three-Body Problem

Insights from the Circular Restricted Three-Body Problem are leveraged to construct flexible transfer itineraries that are straightforwardly transitioned to a higher-fidelity model. A general Three-Body model, i.e., a model corresponding to Equation (2.1) with $\mathfrak{N} = 3$, has no closed-form analytical solution. Note that, in this investigation, a Three-Body model, i.e., the Three-Body problem (3BP), consists of a spacecraft and two additional bodies, e.g., the Sun-Earth-spacecraft system. Although no closed-form analytical solution exists for the 3BP, by carefully incorporating simplifying assumptions and by implementing techniques from Dynamical Systems Theory (DST), significant insights are observed that aid in the mission design process.

2.2.1 Formulation

Preliminary transfer design in a simplified Three-Body model is facilitated by leveraging the motion within the CRTBP [24]. The reformulation of the Two-Body problem (2BP), i.e., Equation (2.1) with $\mathfrak{N} = 2$, in terms of relative motion about a primary body, presented in Equation (2.2), afforded significant insightful information. The relative formulation of the 2BP has a closed-form analytical solution, but the 3BP does not have a closed-form analytical solution. However, implementing simplifying assumptions to the 3BP, reformulating the equations of motion, and applying techniques from DST allows mission designers to observe important dynamical behavior. The simplifying assumptions applied to the 3BP are summarized as follows [24]:

1. The mass of the spacecraft, M_3, is infinitesimally smaller than the two primary bodies, M_1 and M_2, i.e., $M_3 << M_1, M_2$.

2. The mass of the spacecraft, M_3, does not influence the motion of the other two primary bodies, P_1 and P_2. Additionally, the motion of the primaries, P_1 and P_2, is represented by a Two-Body system, i.e., 2BP.

3. The motion of the two primaries, P_1 and P_2, is a circular orbit about the center of mass of the Two-Body system.

Additionally, the motion of the spacecraft is observed in a rotating reference frame with the origin at the barycenter of the Two-Body system created by the primaries, i.e., P_1 and P_2, see Figure 2.2. The basis for the rotating frame is the unit vectors $\left\{\hat{X}, \hat{Y}, \hat{Z}\right\}$, where $\hat{X}$ is measured from the barycenter in the direction of P_2, $\hat{Z}$ is in the direction of the angular momentum vector of the P_1-P_2 system, and $\hat{Y}$ completes the dextral triad; the basis vectors are plotted in Figure 2.2. The basis vectors for the inertial frame, presented in Figure 2.2, is $\left\{\hat{X}', \hat{Y}', \hat{Z}'\right\}$; note that $[\,\hat{\cdot}\,]$ denotes a unit vector. In this analysis, an underscript denotes the reference frame associated with the vector or matrix, e.g., $\underset{\mathfrak{i}'}{\bar{R}}$ is the position of the spacecraft, P_3, in the inertial frame, $\mathfrak{i}'$, plotted in Figure 2.2 and defined with basis vectors $\left\{\hat{X}', \hat{Y}', \hat{Z}'\right\}$.

However, no underscript denotes a vector or matrix in the rotating frame associated with the CRTBP model. The EOM associated with the CRTBP model are formulated from the general 3BP by incorporating the set of simplifying assumptions and by observing the motion in a rotating reference frame.

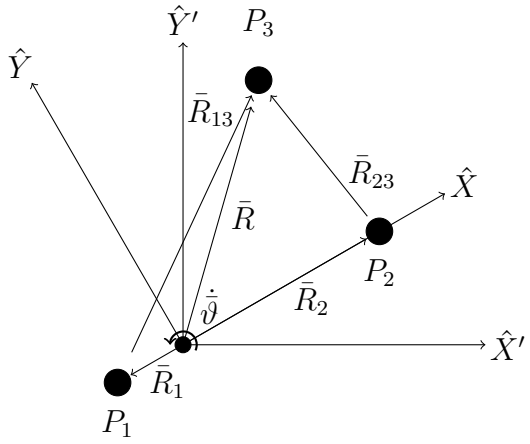

Figure 2.2. : A schematic of the rotating frame, with basis vectors $\left\{\hat{X}, \hat{Y}, \hat{Z}\right\}$, associated with the CRTBP model and an arbitrary inertial reference frame with basis vectors $\left\{\hat{X}', \hat{Y}', \hat{Z}'\right\}$

In this investigation, the Equations of Motion for the CRTBP are derived via the Euler-Lagrange Equation, i.e., an energy method. The Lagrangian, $\mathcal{L}$, for the spacecraft in the Three-Body system in Figure 2.2, is stated as:

$$\mathcal{L} = \underbrace{\frac{1}{2} M_3 V_{\mathrm{i}'}^2}_{\substack{\text{Kinetic Energy} \\ \text{(s/c)}}} + \underbrace{\frac{\tilde{G} M_1 M_3}{R_{13_{\mathrm{i}'}}} + \frac{\tilde{G} M_2 M_3}{R_{23_{\mathrm{i}'}}}}_{\text{Gravitational Potential}} . \tag{2.3}$$

The objective is to derive the EOM for the spacecraft, therefore the kinetic energy terms corresponding to the primary bodies, i.e., P_1 and P_2, in Equation (2.3), are ignored. Note that the Lagrangian in Equation (2.3) is a function of the inertial position, $\underset{\mathrm{i}'}{\bar{R}}$, and velocity, $\underset{\mathrm{i}'}{\bar{V}}$, of the spacecraft. However, the Equations of Motion for the CRTBP are defined in the

rotating reference frame with basis vectors $\left\{\hat{X}, \hat{Y}, \hat{Z}\right\}$. The relationship between the inertial position, $\underset{\text{i}'}{\bar{R}}$, and rotating position, $\bar{R}$, vectors of the spacecraft is defined as,

$$\begin{bmatrix} X \\ Y \\ Z \end{bmatrix} = \begin{bmatrix} \cos(\vartheta) & \sin(\vartheta) & 0 \\ -\sin(\vartheta) & \cos(\vartheta) & 0 \\ 0 & 0 & 1 \end{bmatrix} \begin{bmatrix} X' \\ Y' \\ Z' \end{bmatrix}, \tag{2.4}$$

where the angle, ϑ, is

$$\vartheta = \dot{\vartheta}\mathscr{T}, \tag{2.5}$$

and $\dot{\vartheta}$ is defined as the constant angular velocity of the rotating frame in Figure 2.2 with dimensional time, $\mathscr{T}$. Recall that the angular velocity is essentially the mean motion of the Two-Body system, i.e., P_1-P_2. The Lagrangian in the rotating frame is now written as,

$$\mathcal{L} = \frac{1}{2}M_3\left(\bar{V} + \dot{\bar{\vartheta}} \times \bar{R}\right)^T\left(\bar{V} + \dot{\bar{\vartheta}} \times \bar{R}\right) + \frac{\tilde{G}M_1M_3}{R_{13}} + \frac{\tilde{G}M_2M_3}{R_{23}}, \tag{2.6}$$

where the angular velocity vector, $\dot{\bar{\vartheta}}$, is defined as $\dot{\bar{\vartheta}} = [0, 0, \dot{\vartheta}]^T$; Recall that all vectors in this investigation are column vectors. The position vectors from the primaries, P_1 and P_2, to the spacecraft, P_3, are defined as $\bar{R}_{13}$ and $\bar{R}_{23}$, respectively, where $\bar{R}_{13} = \bar{R} - \bar{R}_1$ and $\bar{R}_{23} = \bar{R} - \bar{R}_2$, see Figure 2.2. Note that in Equations (2.3) and (2.6), the magnitude of the position vectors in the inertial frame and the rotating frame, $\underset{\text{i}'}{\bar{R}}$ and $\bar{R}$, respectively, are equal. Additionally, the magnitudes of the position vectors are expanded as,

$$R = \sqrt{\bar{R}^T\bar{R}}, \tag{2.7}$$

where ^{T} is the matrix transpose. The derivatives of the Lagrangian with respect to $\bar{R}$, $\dot{\bar{R}}$, and $\mathscr{T}$ are computed as:

$$\frac{\partial \mathcal{L}}{\partial \bar{R}} = M_3 \left(\bar{V} + \dot{\bar{\vartheta}} \times \bar{R} \right)^T \left[\dot{\bar{\vartheta}} \right]_x - \frac{\tilde{G} M_1 M_3 \left(\bar{R} - \bar{R}_1 \right)^T}{R_{13}^3} - \frac{\tilde{G} M_2 M_3 \left(\bar{R} - \bar{R}_2 \right)^T}{R_{23}^3}, \quad (2.8)$$

$$\frac{\partial \mathcal{L}}{\partial \dot{\bar{R}}} = M_3 \left(\bar{V} + \dot{\bar{\vartheta}} \times \bar{R} \right)^T, \quad (2.9)$$

$$\frac{d}{d\mathscr{T}} \left(\frac{\partial \mathcal{L}}{\partial \dot{\bar{R}}} \right) = M_3 \left(\bar{A} + \dot{\bar{\vartheta}} \times \bar{V} \right)^T, \quad (2.10)$$

where $\bar{A}$ is the acceleration of the spacecraft and the cross product of two vectors, i.e., $\dot{\bar{\vartheta}} \times \bar{R}$, is written as,

$$\dot{\bar{\vartheta}} \times \bar{R} = \left[\dot{\bar{\vartheta}} \right]_x \bar{R}. \quad (2.11)$$

Note that a skew-symmetric matrix, $[\bar{\mathfrak{a}}]_x$, is defined as,

$$[\bar{\mathfrak{a}}]_x = \begin{bmatrix} 0 & -\mathfrak{a}_3 & \mathfrak{a}_2 \\ \mathfrak{a}_3 & 0 & -\mathfrak{a}_1 \\ -\mathfrak{a}_2 & \mathfrak{a}_1 & 0 \end{bmatrix}, \quad (2.12)$$

where $\bar{\mathfrak{a}} = [\mathfrak{a}_1, \mathfrak{a}_2, \mathfrak{a}_3]^T$. Additionally, the derivative of the cross product with respect to a vector is given by the properties:

$$\frac{\partial}{\partial \dot{\bar{\vartheta}}} \left(\dot{\bar{\vartheta}} \times \bar{R} \right) = - \left[\bar{R} \right]_x, \quad (2.13)$$

$$\frac{\partial}{\partial \bar{R}} \left(\dot{\bar{\vartheta}} \times \bar{R} \right) = \left[\dot{\bar{\vartheta}} \right]_x. \quad (2.14)$$

The EOM for the spacecraft are then derived in vector form via the Standard Form of Lagrange's Equation, i.e.,

$$\frac{d}{d\mathscr{T}} \left(\frac{\partial L}{\partial \dot{\bar{R}}} \right) = \frac{\partial L}{\partial \bar{R}}. \quad (2.15)$$

Note that there are no non-conservative forces acting on the system, therefore the Standard Form of Lagrange's Equation is applicable. The Equations of Motion for the CRTBP, in vector form, are given as,

$$\left(\bar{A}+\dot{\bar{\vartheta}}\times\bar{V}\right)^T=\left(\bar{V}+\dot{\bar{\vartheta}}\times\bar{R}\right)^T\left[\dot{\bar{\vartheta}}\right]_x-\frac{\tilde{G}M_1\left(\bar{R}-\bar{R}_1\right)^T}{R_{13}^3}-\frac{\tilde{G}M_2\left(\bar{R}-\bar{R}_2\right)^T}{R_{23}^3}. \tag{2.16}$$

Note that the mass of the spacecraft, M_3, is removed from both sides of Equation (2.16) and the acceleration vector for the spacecraft in the rotating frame is $\bar{A}=[\ddot{X},\ddot{Y},\ddot{Z}]^T$. The following property is derived from Equation (2.11),

$$-\left(\dot{\bar{\vartheta}}\times\bar{R}\right)^T=\bar{R}^T\left[\dot{\bar{\vartheta}}\right]_x, \tag{2.17}$$

such that, Equation (2.16) simplifies to:

$$\bar{A}+\underbrace{2\dot{\bar{\vartheta}}\times\bar{V}}_{\text{Coriolis force}}+\underbrace{\dot{\bar{\vartheta}}\times\left(\dot{\bar{\vartheta}}\times\bar{R}\right)}_{\text{Centrifugal force}}=-\frac{\tilde{G}M_1\left(\bar{R}-\bar{R}_1\right)}{R_{13}^3}-\frac{\tilde{G}M_2\left(\bar{R}-\bar{R}_2\right)}{R_{23}^3}. \tag{2.18}$$

In Equation (2.18), the terms corresponding to the fictitous Coriolis force and the centrifugal force are identified; note that these forces are by-products of the rotating frame. The scalar EOM are derived from the vector form presented in Equation (2.18) such that,

$$\begin{aligned}
\ddot{X}-2\dot{\vartheta}\dot{Y}-\dot{\vartheta}^2X&=-\frac{\tilde{G}M_1\left(X-X_1\right)}{R_{13}^3}-\frac{\tilde{G}M_2\left(X-X_2\right)}{R_{23}^3},\\
\ddot{Y}+2\dot{\vartheta}\dot{X}-\dot{\vartheta}^2Y&=-\frac{\tilde{G}M_1\left(Y-Y_1\right)}{R_{13}^3}-\frac{\tilde{G}M_2\left(Y-Y_2\right)}{R_{23}^3},\\
\ddot{Z}&=-\frac{\tilde{G}M_1\left(Z-Z_1\right)}{R_{13}^3}-\frac{\tilde{G}M_2\left(Z-Z_2\right)}{R_{23}^3}.
\end{aligned} \tag{2.19}$$

The Equations of Motion presented in Equation (2.19) are written in terms of dimensional units, e.g., $\tilde{G}=6.67384\text{e}^{-20}\,\frac{\text{km}^3}{\text{kg-s}^2}$. There is no closed-form analytical solution of the CRTBP and any solution, i.e., trajectory state information, is obtained through numerical integration of the differential equations in Equation (2.19). However, to minimize round-off and truncation errors associated with the numerical integration of the dimensional CRTBP equa-

tions of motion, a nondimensional form of the Equations of Motion is derived. Generally, nondimensionalizing a dynamical system by a set of characteristic values identifies intrinsic properties of the general system. The characteristic length and mass associated with the dimensional CRTBP EOM are defined as,

$$l^* = R_2 + R_1, \tag{2.20}$$

$$m^* = M_1 + M_2, \tag{2.21}$$

where, it is recalled that, R_1 and R_2 are measured from the system barycenter and a mass parameter value is denoted as,

$$\mu = \frac{M_2}{m^*}. \tag{2.22}$$

A characteristic time is derived by observing the mean motion of the Two-Body system consisting of the primaries, i.e., P_1-P_2. The mean motion for the Two-Body system, in terms of the characteristic length, l^*, and characteristic mass, m^*, is given as,

$$\mathscr{N} = \left(\frac{\tilde{G}m^*}{{l^*}^3}\right)^{\frac{1}{2}}. \tag{2.23}$$

Note that the mean motion, $\mathscr{N}$, is equal to the angular velocity, $\dot{\vartheta}$, of the CRTBP rotating frame. The characteristic time is defined such that the nondimensional mean motion, $\mathbb{m} = \mathscr{N}t^*$, is unity and is stated as:

$$t^* = \left(\frac{{l^*}^3}{\tilde{G}m^*}\right)^{\frac{1}{2}}, \tag{2.24}$$

where the nondimensional position and velocity vectors, i.e., $\bar{r}$ and $\bar{v}$, respectively, and a nondimensional time, t, are written as,

$$\bar{r} = \frac{\bar{R}}{l^*}, \tag{2.25}$$

$$\bar{v} = \frac{\bar{V}t^*}{l^*}, \tag{2.26}$$

$$t = \frac{\mathscr{T}}{t^*}. \tag{2.27}$$

The derivation of the nondimensional equations are provided in Appendix A. The nondimensional Equations of Motion for the CRTBP are written as,

$$\begin{aligned}
\ddot{x} &= 2\dot{y} + x - \frac{(1-\mu)(x+\mu)}{r_{13}^3} - \frac{\mu(x-1+\mu)}{r_{23}^3}, \\
\ddot{y} &= -2\dot{x} + y - \frac{y(1-\mu)}{r_{13}^3} - \frac{y\mu}{r_{23}^3}, \\
\ddot{z} &= -\frac{z(1-\mu)}{r_{13}^3} - \frac{z\mu}{r_{23}^3},
\end{aligned} \tag{2.28}$$

where the distances from the primaries, P_1 and P_2, are defined as: $\bar{r}_{13} = [x+\mu, y, z]^T$ and $\bar{r}_{23} = [x-1+\mu, y, z]^T$. In this investigation, the CRTBP nondimensional EOM, presented in Equation (2.28), are analyzed to identify important insights about the simplified Three-Body system.

2.2.2 Pseudo-Potential in the CRTBP model

The Lagrangian associated with the CRTBP is leveraged to observe important dynamical insight. The Lagrangian for a dynamical system is not unique, that is, a Lagrangian, $\mathcal{L}$, can be multiplied by a constant, a, such the new Lagrangian $\mathcal{L}_a$ and $\mathcal{L}$ provide the same Equations of Motion. This property is frequently implemented to cancel out cumbersome fictitious forces associated with complex dynamical models, if possible. The dimensional Lagrangian for the spacecraft in the CRTBP, in the rotating frame, is stated in Equation (2.6). The Lagrangian is more compactly denoted, with the characteristic values in Equations (2.20),(2.21) and (2.24), as:

$$\mathcal{L} = M_3 \left(\frac{l^*}{t^*}\right)^2 \left[\frac{1}{2}\left(\bar{v} + \hat{z} \times \bar{r}\right)^T \left(\bar{v} + \hat{z} \times \bar{r}\right) + \frac{(1-\mu)}{r_{13}} + \frac{\mu}{r_{23}}\right]. \tag{2.29}$$

Recall that $\dot{\bar{\vartheta}}$ can be written as: $\dot{\bar{\vartheta}} = \dot{\vartheta} \cdot [0,0,1]^T = \dot{\vartheta}\hat{z}$. Note that the units of the Lagrangian, $\mathcal{L}$, are $\frac{\text{kg}\cdot\text{m}^2}{\text{s}^2}$. A nondimensional Lagrangian is now defined:

$$\mathcal{L}' = \frac{1}{2}\left(\bar{v} + \hat{z} \times \bar{r}\right)^T \left(\bar{v} + \hat{z} \times \bar{r}\right) + \frac{(1-\mu)}{r_{13}} + \frac{\mu}{r_{23}}, \tag{2.30}$$

and is expanded to:

$$\mathcal{L}' = \underbrace{\frac{1}{2}\bar{v}^T\bar{v}}_{\mathcal{L}'_A} + \underbrace{\bar{v}^T\left(\hat{z}\times\bar{r}\right)}_{\mathcal{L}'_B} + \underbrace{\frac{1}{2}\left(\hat{z}\times\bar{r}\right)^T\left(\hat{z}\times\bar{r}\right)}_{\mathcal{L}'_C} + \underbrace{\frac{(1-\mu)}{r_{13}} + \frac{\mu}{r_{23}}}_{\mathcal{L}'_D}. \tag{2.31}$$

In Equation (2.31), $\mathcal{L}'_B$ and $\mathcal{L}'_C$ are products of the rotating frame; recall that the Lagrangian for a system is not unique. Note that the gravitational potential terms, $\mathcal{L}'_D$ in Equation (2.31), are functions of the position of the spacecraft, i.e., $\bar{r}$. However, $\mathcal{L}'_C$ is also a function of the spacecraft position and represents the centrifugal force present in the rotating frame. $\mathcal{L}'_C$ is termed as the centrifugal potential and contour plots of the gravitational potential energy, $\mathcal{L}'_D$, and the centrifugal potential, $\mathcal{L}'_C$, are displayed in Figure 2.3. Note that the contours presented in Figure 2.3 are magnitudes of the centrifugal and gravitational potential in the Earth-Moon system. In Figure 2.3(a), the magnitude of the centrifugal potential is zero at the origin of the rotating frame and increases quadratically, that is, the magnitude is the squared distance of the spacecraft from the origin. The region inside the red box in Figure 2.3(b) corresponds to a local minimum of the gravitational potential; observing that the minimum is located along the $\hat{x}$-axis of the Earth-Moon rotating frame. The inverse-square relationship, corresponding to the gravitational potential, of the spacecraft distance with respect to the primary bodies is displayed in Figure 2.3(b), where the potential energy is significantly higher near the primaries. For the CRTBP, a pseudo-potential energy magnitude is defined as the summation of potential energies, $\mathcal{L}'_C$ and $\mathcal{L}'_D$, and simplified as:

$$\mathcal{U}^* = \frac{1}{2}\left(x^2+y^2\right) + \frac{(1-\mu)}{r_{13}} + \frac{\mu}{r_{23}}. \tag{2.32}$$

The pseudo-potential magnitude for the Earth-Moon system is plotted as contours lines in Figure 2.4. Five regions are highlighted in the contour map, see Figure 2.4, which represent regions corresponding to local minima of the pseudo-potential magnitude. Three collinear minima and two non-collinear minima are observed in Figure 2.4. In Figure 2.4, the magnitudes of the centrifugal potential, the gravitational potential, and the pseudo-potential are contained in the $\hat{x}$-$\hat{y}$ plane, i.e., the plane that also contains the motion of the primary

bodies, P_1 and P_2. The Equations of Motion for the CRTBP, presented in Equation (2.28),

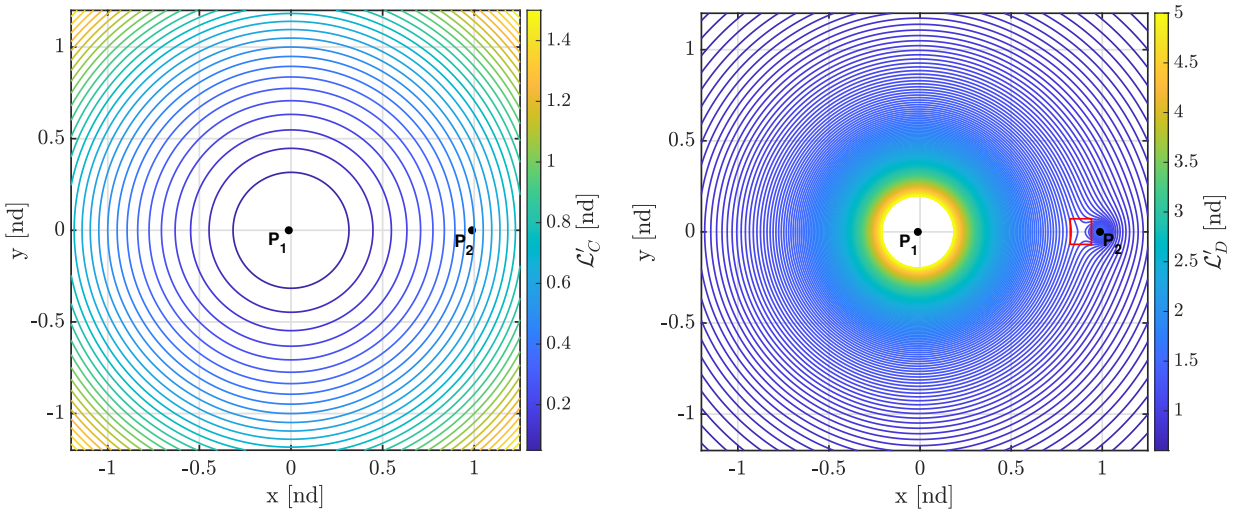

Figure 2.3. : (a) Centrifugal and (b) gravitational potential in the Earth-Moon CRTBP model. The boxed region contains a local minimum for the gravitational potential, $\mathcal{L}'_D$

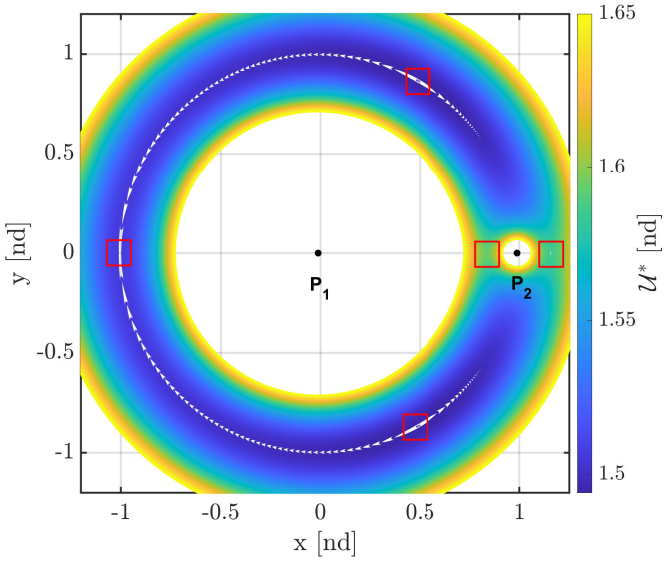

Figure 2.4. : Pseudo-potential associated with the Earth-Moon CRTBP model. Five local minima are identified inside the region boxed in red

are also written more compactly with the pseudo-potential, $\mathcal{U}^*$, as:

$$\begin{aligned} \ddot{x} - 2\dot{y} &= \frac{\partial \mathcal{U}^*}{\partial x}, \\ \ddot{y} + 2\dot{x} &= \frac{\partial \mathcal{U}^*}{\partial y}, \\ \ddot{z} &= \frac{\partial \mathcal{U}^*}{\partial z}. \end{aligned} \tag{2.33}$$

A notable insight from Equation (2.33) is that equilibrium points, defined as $\dot{x} = \dot{y} = \dot{z} = \ddot{x} = \ddot{y} = \ddot{z} = 0$, are identified as the local minima of the pseudo-potential, i.e., situations when the partial derivative of the pseudo-potential is zero. The existence and numerical computation of equilibrium points are discussed in more detail in Section 3.1. Additionally, important dynamical behavior extracted from observing the flow information near equilibrium points in the rotating frame of the CRTBP model aid in the design of feasible transfer options

2.2.3 Integral of Motion

Integrals of motion are implicit solutions to dynamical systems which offer important insights about the particle behavior. Solutions of a dynamical system are either explicit, e.g., analytical integrations of the CRTBP coordinates $\{x, y, z, \dot{x}, \dot{y}, \dot{z}\}$, or implicit, such as functions of the CRTBP coordinates. The desirable solution is an explicit solution, however, there is no analytical solution to the CRTBP or the general 3BP. For comparison, the 2BP has an analytical solution and three integrals of motion, i.e., implicit solutions which are constant in time, which provide ten constants of motion. The integrals of motion for the conservative system of the 2BP are: the mechanical energy, the linear momentum, and the angular momentum. In the CRTBP, one integral of motion is derived by utilizing Jacobi's Integral, i.e.,

Theorem 2.2.1. ***Jacobi's Integral*** *[54] If all forces in a system are conservative, and if the resulting Lagrangian is explicitly independent of time, then the following function*

$$\mathfrak{h}\left(\bar{\mathfrak{q}}, \dot{\bar{\mathfrak{q}}}\right) = \frac{\partial \mathcal{L}}{\partial \dot{\bar{\mathfrak{q}}}} \dot{\bar{\mathfrak{q}}} - \mathcal{L} \tag{2.34}$$

is conservative.

The derivation in Theorem 2.2.1 utilizes the generalized coordinate vector, $\bar{\mathfrak{q}}$, and the time derivative of the generalized coordinate vector, $\dot{\bar{\mathfrak{q}}}$. In this analysis, the generalized coodinate vector is defined as: $\bar{\mathfrak{q}} = [x, y, z]^T$, i.e., the position vector in the CRTBP rotating frame. The derivative required for Jacobi's Integral is denoted as,

$$\frac{\partial \mathcal{L}'}{\partial \dot{\bar{\mathfrak{q}}}} = \frac{\partial \mathcal{L}'}{\partial \dot{\bar{v}}} = \bar{v}^T + (\hat{z} \times \bar{r})^T, \tag{2.35}$$

where the nondimensional form of the Lagrangian, $\mathcal{L}'$, is utilized. Then, from Theorem 2.2.1, Jacobi's Integral is expanded to:

$$\mathfrak{h} = \frac{1}{2}\bar{v}^T\bar{v} - \frac{1}{2}\left(x^2 + y^2\right) - \frac{(1-\mu)}{r_{13}} - \frac{\mu}{r_{23}}. \tag{2.36}$$

The Jacobi Integral is a time-independent energy-like quantity. A more common form of the Jacobi Integral is written by substituting the definition of the pseudo-potential, $\mathcal{U}^*$, from Equation (2.32),

$$\mathcal{C} = 2\mathcal{U}^* - v^2, \tag{2.37}$$

where $\mathcal{C}$ is termed as the Jacobi Constant and is defined as $\mathcal{C} = -2\mathfrak{h}$. The Jacobi constant, i.e., an integral of motion of the CRTBP, is a function of the position and velocity of the spacecraft, P_3. The existence of the Jacobi constant also decreases the dimensionality of the phase-space of the system. The motion of the spacecraft particle, in the CRTBP, is contained in a phase-space with dimension, $\mathfrak{n} = 6$. The Jacobi constant, an implicit solution to the CRTBP, decreases the dimension by one. The reduction in dimensionality of the phase-space is an important insight utilized for observing important dynamical behavior in the CRTBP model.

2.3 Coordinate Transformation

Coordinate transformations are important functions often implemented to observe and compare insightful dynamical properties of a particle in different reference frames. For example, important dynamical behavior, such as the existence of periodic orbits, is extracted from a rotating frame in the CRTBP as opposed to an inertial frame. However, a comparison of the spacecraft trajectory in the rotating frame of the CRTBP and an inertial frame reveals important trajectory characteristics, such as geometry. In this investigation, coordinate transformations between rotating and inertial reference frames are leveraged to investigate specific dynamical and geometric properties of a spacecraft transfer.

2.3.1 Transformation between the CRTBP model and an arbitrary Inertial Frame

A coordinate transformation between the rotating frame of the CRTBP model and an arbitrary inertial frame is realized via a rotation matrix. Recall that the dimensional coordinate system for the rotating frame, $\{\hat{X}, \hat{Y}, \hat{Z}\}$, and an arbitrary inertial system, $\{\hat{X}', \hat{Y}', \hat{Z}'\}$, are illustrated in Figure 2.2. However, a nondimensional coordinate systems $\{\hat{x}, \hat{y}, \hat{z}\}$ and $\{\hat{x}', \hat{y}', \hat{z}'\}$ corresponding to the rotating and inertial frame, respectively, are implemented in this investigation, as illustrated in Figure 2.5. A state for the spacecraft, $\bar{\mathcal{X}}$, in the rotating frame is defined as $\bar{\mathcal{X}} = [x, y, z, \dot{x}, \dot{y}, \dot{z}]^T$, and a state in an arbitrary inertial frame is written with $\underset{\text{i}'}{\bar{\mathcal{X}}} = [x', y', z', \dot{x}', \dot{y}', \dot{z}']^T$. Note that $\underset{\text{i}'}{[\bar{\cdot}]}$ represents a vector expressed in the nondimensional arbitrary inertial frame and, in this investigation, a vector in the nondimensional rotating frame is written with no underscript. The change of basis transformation for a position vector expressed in an arbitrary inertial frame, $\underset{\text{i}'}{\bar{r}}$, to a CRTBP rotating frame is expressed as,

$$\begin{bmatrix} x \\ y \\ z \end{bmatrix} = \begin{bmatrix} \mathcal{P}_x \\ \mathcal{P}_y \\ \mathcal{P}_z \end{bmatrix} + \begin{bmatrix} \cos(t) & \sin(t) & 0 \\ -\sin(t) & \cos(t) & 0 \\ 0 & 0 & 1 \end{bmatrix} \begin{bmatrix} x' \\ y' \\ z' \end{bmatrix}, \tag{2.38}$$

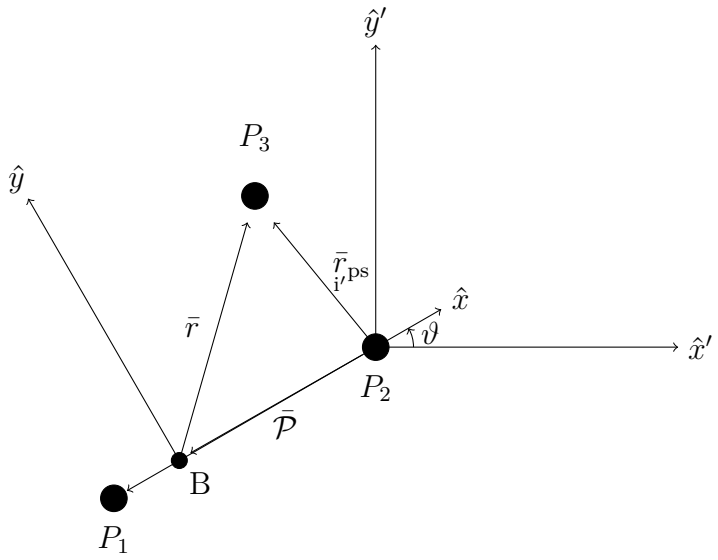

Figure 2.5. : Relationship between the nondimensional coordinate system of the rotating frame ($\{\hat{x}, \hat{y}, \hat{z}\}$) and an arbitrary inertial frame ($\{\hat{x}', \hat{y}', \hat{z}'\}$)

where $\bar{\mathcal{P}} = [\mathcal{P}_x, \mathcal{P}_y, \mathcal{P}_z]^T$ is the position of the CRTBP barycenter, B in Figure 2.5, measured from the inertial frame origin and expressed in the rotating frame. Equation (2.38) is a general formula for a change of basis from an inertial frame to a rotating frame with a stationary barycenter. A rotation matrix, ${}^{r}\mathbf{L}^{\mathrm{i}'}$, is defined as,

$$ {}^{r}\mathbf{L}^{\mathrm{i}'} = \begin{bmatrix} \cos(t) & \sin(t) & 0 \\ -\sin(t) & \cos(t) & 0 \\ 0 & 0 & 1 \end{bmatrix}, \tag{2.39} $$

where a position vector, written as a column vector, is rotated from an arbitrary inertial frame to a rotating frame. In this investigation, a matrix is denoted in bold font, unless otherwise stated. Note that the rotation matrix in Equation (2.39) is the nondimensional analog to the dimensional rotation matrix in Equation (2.4). By substituting Equation (2.27) and the definition of the angular velocity, i.e., $\dot{\vartheta} = \mathscr{N} = \frac{1}{t^*}$, into Equation (2.5), the angle ϑ is defined as the nondimensional time, $\vartheta = t$. Let the origin of the arbitrary inertial frame be

one of the primary bodies, as illustrated in Figure 2.5, such that Equation (2.38) is written more compactly as:

$$\bar{r} = \bar{\mathcal{P}} + {}^{r}\mathbf{L}^{\mathrm{i}'}\, \underset{\mathrm{i}'}{\bar{r}_{ps}}, \tag{2.40}$$

where $\underset{\mathrm{i}'}{\bar{r}_{ps}}$ is the position in the inertial frame with respect to one of the primaries and $\bar{\mathcal{P}}$ is the position of the CRTBP barycenter written with respect to the rotating frame. Conversely, $\bar{r}$ is transformed to the inertial frame via,

$$\underset{\mathrm{i}'}{\bar{r}_{ps}} = {}^{\mathrm{i}'}\mathbf{L}^{r}\, \left(\bar{r} - \bar{\mathcal{P}}\right). \tag{2.41}$$

The nondimensional inertial velocity is the time derivative of the position vector, i.e., $\underset{\mathrm{i}'}{\bar{v}_{ps}}$, and is computed from Equation (2.41) as,

$$\underset{\mathrm{i}'}{\bar{v}_{ps}} = {}^{\mathrm{i}'}\dot{\mathbf{L}}^{r}\, \bar{r}_{ps} + {}^{\mathrm{i}'}\mathbf{L}^{r}\, \bar{v}_{ps}, \tag{2.42}$$

where $\bar{r}_{ps}$ and $\bar{v}_{ps}$ are the position and velocity vectors of the satellite in the rotating frame measured from one of the primaries and defined as: $\bar{r}_{ps} = \bar{r} - \bar{\mathcal{P}}$ and $\bar{v}_{ps} = \bar{v}$. The derivative of the rotation matrix, ${}^{\mathrm{i}'}\dot{\mathbf{L}}^{r}$, is denoted as,

$${}^{\mathrm{i}'}\dot{\mathbf{L}}^{r} = \begin{bmatrix} -\sin(t) & -\cos(t) & 0 \\ \cos(t) & -\sin(t) & 0 \\ 0 & 0 & 0 \end{bmatrix}. \tag{2.43}$$

The full state relationship between the rotating and arbitrary inertial frame, $\bar{\mathcal{X}}_{ps}$ and $\underset{\mathrm{i}'}{\bar{\mathcal{X}}_{ps}}$, respectively, is given by:

$$\begin{bmatrix} x'_{ps} \\ y'_{ps} \\ z'_{ps} \\ \dot{x}'_{ps} \\ \dot{y}'_{ps} \\ \dot{z}'_{ps} \end{bmatrix} = \begin{bmatrix} \cos(t) & -\sin(t) & 0 & 0 & 0 & 0 \\ \sin(t) & \cos(t) & 0 & 0 & 0 & 0 \\ 0 & 0 & 1 & 0 & 0 & 0 \\ -\sin(t) & -\cos(t) & 0 & \cos(t) & -\sin(t) & 0 \\ \cos(t) & -\sin(t) & 0 & \sin(t) & \cos(t) & 0 \\ 0 & 0 & 0 & 0 & 0 & 1 \end{bmatrix} \begin{bmatrix} x_{ps} \\ y_{ps} \\ z_{ps} \\ \dot{x}_{ps} \\ \dot{y}_{ps} \\ \dot{z}_{ps} \end{bmatrix}. \tag{2.44}$$

The transformation matrix that relates the inertial and the rotating frame is defined as:

$$\mathscr{L} = \begin{bmatrix} \cos(t) & -\sin(t) & 0 & 0 & 0 & 0 \\ \sin(t) & \cos(t) & 0 & 0 & 0 & 0 \\ 0 & 0 & 1 & 0 & 0 & 0 \\ -\sin(t) & -\cos(t) & 0 & \cos(t) & -\sin(t) & 0 \\ \cos(t) & -\sin(t) & 0 & \sin(t) & \cos(t) & 0 \\ 0 & 0 & 0 & 0 & 0 & 1 \end{bmatrix}. \tag{2.45}$$

A state in the rotating frame is rotated into an arbitrary inertial frame through the equation,

$$\underset{\mathrm{i}'}{\bar{\mathcal{X}}_{ps}} = \mathscr{L}\, \bar{\mathcal{X}}_{ps}. \tag{2.46}$$

and the inverse rotation is performed with,

$$\bar{\mathcal{X}}_{ps} = \mathscr{L}^{-1}\, \underset{\mathrm{i}'}{\bar{\mathcal{X}}_{ps}}, \tag{2.47}$$

A comparison of the dynamical behavior of a spacecraft in the rotating and inertial frame reveals qualitative information about the geometry of the spacecraft trajectory.

2.3.2 Transformation between the CRTBP model and the J2000 Inertial Frame

The relationship between the rotating frame associated with the CRTBP model and the J2000 inertial reference frame is evaluated with approximated ephemeris data. Ephemeris data, which includes the state information, i.e., position and velocity vectors, for celestial bodies in the solar system, is collected from the Jet Propulsion laboratory in Pasadena, California [53]. In this investigation, the ephemeris information is retrieved from the DE430 ephemerides SPICE file. Many inertial and non-inertial frames are implemented in mission design and navigation, and each has advantages based on the mission objectives. The J2000 Earth Mean Equatorial inertial reference frame (EME) is an inertial frame frequently used in navigation and mission design. The basis unit vectors for the EME frame, $\{\hat{\underline{X}}, \hat{\underline{Y}}, \hat{\underline{Z}}\}$,

form a dextral triad, where $\hat{\underline{X}}$ is in the direction of the vernal equinox, $\hat{\underline{Z}}$ is normal to the Earth mean equator, and $\hat{\underline{Y}} = \hat{\underline{Z}} \times \hat{\underline{X}}$. Note that the direction of the vernal equinox is also the intersection of the equatorial and ecliptic planes; note that the ecliptic plane contains the motion of the sun. The dimensional position and velocity vectors in the EME frame are defined as,

$$\bar{R}_{\mathrm{i}} = \left[\underline{X}, \underline{Y}, \underline{Z}\right], \tag{2.48}$$

$$\bar{V}_{\mathrm{i}} = \left[\dot{\underline{X}}, \dot{\underline{Y}}, \dot{\underline{Z}}\right], \tag{2.49}$$

and the nondimensional position and velocity vectors are written as,

$$\bar{r}_{\mathrm{i}} = \left[\underline{x}, \underline{y}, \underline{z}\right], \tag{2.50}$$

$$\bar{v}_{\mathrm{i}} = \left[\dot{\underline{x}}, \dot{\underline{y}}, \dot{\underline{z}}\right]. \tag{2.51}$$

The relationship between the EME frame and the CRTBP rotation frame, implemented as a series of steps in this analysis, is based on a methodology defined by Ocampo [55]. The methodology implements a transformation between the inertial and rotating frames by including the instantaneous oscillating distance between the primary bodies, P_1 and P_2. Recall that a fixed distance between the primary bodies, P_1 and P_2, is a simplifying assumption of the CRTBP formulation. However, the actual distance, based on ephemeris data, between the primary bodies is not fixed and is oscillatory in nature. In the EME frame, the position and velocity of the spacecraft are often written with respect to one of the two primary bodies in the Three-Body system. Throughout the transformation procedure, it is necessary to define the position of the system barycenter measured from one of the primary bodies, i.e., $\bar{R}_{pb}$; recalling that the position is dependent on the instantaneous distance between the primaries. The position of the barycenter is denoted as,

$$P_1 \text{ is the central body: } \bar{R}_{\mathrm{i}pB} = \mu \bar{R}_{\mathrm{i}12}, \tag{2.52}$$

$$P_2 \text{ is the central body: } \bar{R}_{\mathrm{i}pB} = -(1-\mu)\bar{R}_{\mathrm{i}12}, \tag{2.53}$$

where $\bar{R}_{12}$ is the dimensional position vector from P_1 to P_2 and μ is the mass parameter associated with the CRTBP model. Additionally, the velocity of the barycenter with respect to the primary bodies is evaluated by differentiating Equations (2.52) and (2.53) with respect to the dimensional time, $\mathscr{T}$. The velocity of the barycenter is computed as,

$$P_1 \text{ is the central body: } {}^{\mathrm{i}}\bar{V}_{pB} = \mu \, {}^{\mathrm{i}}\bar{V}_{12}, \tag{2.54}$$

$$P_2 \text{ is the central body: } {}^{\mathrm{i}}\bar{V}_{pB} = -(1-\mu) \, {}^{\mathrm{i}}\bar{V}_{12}, \tag{2.55}$$

where time derivative in the inertial frame is indicated by left superscripts, e.g., ${}^{\mathrm{i}}\bar{V}$. In this investigation, the transformation between the rotating frame and the inertial EME frame includes the instantaneous distance between the primary bodies.

2.3.2.1 Rotating Frame to Inertial EME Frame

The transformation process from the rotating frame into the inertial EME frame is computed with the ephemeris information and includes the contribution of the instantaneous distance between the primary bodies. In this investigation, the spacecraft position and velocity is expressed in the inertial EME frame during a trajectory corrections process using a higher-fidelity ephemeris model. A rotation matrix from the CRTBP rotating frame to the EME frame is defined as:

$${}^{\mathrm{i}}\boldsymbol{\mathcal{R}}^{\mathrm{r}} = \left[\hat{x} \;\; \hat{y} \;\; \hat{z} \right], \tag{2.56}$$

where the unit basis vectors of the rotating frame, expressed in the EME frame, are given as,

$$\underset{\mathrm{i}}{\hat{x}} = \frac{\underset{\mathrm{i}}{\bar{R}_{12}}}{\|\underset{\mathrm{i}}{\bar{R}_{12}}\|}, \tag{2.57}$$

$$\underset{\mathrm{i}}{\hat{z}} = \frac{\underset{\mathrm{i}}{\bar{H}}}{\|\underset{\mathrm{i}}{\bar{H}}\|}, \tag{2.58}$$

$$\underset{\mathrm{i}}{\hat{y}} = \frac{\underset{\mathrm{i}}{\hat{z}} \times \underset{\mathrm{i}}{\hat{x}}}{\|\underset{\mathrm{i}}{\hat{z}} \times \underset{\mathrm{i}}{\hat{x}}\|}, \tag{2.59}$$

with the angular momentum vector, $\underset{\mathrm{i}}{\bar{H}}$, denoted as,

$$\underset{\mathrm{i}}{\bar{H}} = \underset{\mathrm{i}}{\bar{R}_{12}} \times \underset{\mathrm{i}}{\bar{V}_{12}}. \tag{2.60}$$

Recall that $\underset{\mathrm{i}}{\bar{R}_{12}}$ is the dimensional position vector from P_1 and P_2, as plotted in Figure 2.2, expressed in the inertial frame, and $\underset{\mathrm{i}}{\bar{V}_{12}}$ is the corresponding inertial velocity. The position and velocity information of the primaries, P_1 and P_2, are collected from the planetary ephemeris data file DE430 provided by JPL. The nondimensional position in the inertial frame is given as:

$$\underset{\mathrm{i}}{\bar{r}} = \frac{\tilde{l}^*}{l^*} \, {}^{\mathrm{i}}\boldsymbol{\mathcal{R}}^{\mathrm{r}} \, \bar{r}, \tag{2.61}$$

where the instantaneous characteristic length is defined as: $\tilde{l}^* = \|\underset{\mathrm{i}}{\bar{R}_{12}}\|$. In this process, the nondimensional position in the CRTBP, $\bar{r}$, is first dimensionalized with the instantaneous distance between the primaries, $\tilde{l}^*$, then nondimensionalized with a characteristic length, l^*, corresponding to the EME inertial frame. The nondimensionalized position in the EME frame offers the same advantages as the nondimensional position in the CRTBP rotating frame. In this analysis, the characteristic length selected to nondimensionalize in the inertial EME frame is the CRTBP characteristic length stated in Equation (2.20) and corresponds

to a fixed distance, l^*, between the two primaries. In the CRTBP rotating frame, for this coordinate transformation process, the time is nondimensionalized via:

$$t = \frac{\mathscr{T}}{\tilde{t}^*}, \tag{2.62}$$

where $\tilde{t}^*$ is the instantaneous characteristic time corresponding to the instantaneous characteristic length, $\tilde{l}^*$, and defined with Equation (2.24). Recall that $\mathscr{T}$ is the dimensional time. In the inertial EME frame, the time is nondimensionalized with the following relationship,

$$t' = \frac{\mathscr{T}}{t^*}, \tag{2.63}$$

where t' is the nondimensional time in the EME frame and the characteristic time, t^*, is defined via Equation (2.24) with the fixed characteristic length, l^*. The nondimensional velocity in the inertial EME frame is evaluated by differentiating Equation (2.61) by the nondimensional time t' such as,

$$\frac{{}^{\mathrm{i}}d\bar{r}}{dt'} = \frac{\tilde{l}^*}{l^*}\,{}^{\mathrm{i}}\boldsymbol{\mathcal{R}}^{\mathfrak{r}}\,\frac{{}^{r}d\bar{r}}{dt}\frac{dt}{dt'} + \frac{\tilde{l}^*}{l^*}\,\frac{d\,{}^{\mathrm{i}}\boldsymbol{\mathcal{R}}^{\mathfrak{r}}}{dt'}\,\bar{r} + \frac{d\tilde{l}^*}{dt'}\frac{1}{l^*}\,{}^{\mathrm{i}}\boldsymbol{\mathcal{R}}^{\mathfrak{r}}\,\bar{r}, \tag{2.64}$$

where the time derivative in the inertial frame and the rotating frame are indicated by left superscripts, e.g., $\frac{{}^{\mathrm{i}}d(\cdot)}{dt}$. Note that the instantaneous characteristic length is a function of the dimensional time, $\mathscr{T}$, i.e, $\tilde{l}^*(\mathscr{T}) = \|\bar{R}_{12}(\mathscr{T})\|$, and may be written in the following form:

$$\tilde{l}^*(\mathscr{T}) = \sqrt{\bar{R}_{12}^T\,\bar{R}_{12}}, \tag{2.65}$$

such that the time derivative, with respect to the nondimensional time, t', is computed as,

$$\frac{d\tilde{l}^*}{dt'} = \frac{\bar{R}_{12}^T\,\bar{V}_{12}}{\|\bar{R}_{12}\|}\frac{d\mathscr{T}}{dt'} = \frac{\bar{R}_{12}^T\,\bar{V}_{12}}{\tilde{l}^*}t^*, \tag{2.66}$$

recalling that t^* is the characteristic length for the CRTBP system defined in Equation (2.24). The derivative of the rotation matrix, ${}^{\mathrm{i}}\boldsymbol{\mathcal{R}}^{\mathrm{r}}$, is given by:

$$\frac{d\,{}^{\mathrm{i}}\boldsymbol{\mathcal{R}}^{\mathrm{r}}}{dt'} = \frac{d\,{}^{\mathrm{i}}\boldsymbol{\mathcal{R}}^{\mathrm{r}}}{d\mathscr{T}}\frac{d\mathscr{T}}{dt'} = \left[\bar{\Gamma}_{\mathrm{i}}\right]_{\mathrm{x}} {}^{\mathrm{i}}\boldsymbol{\mathcal{R}}^{\mathrm{r}}\, t^*, \tag{2.67}$$

where $\bar{\Gamma}_{\mathrm{i}}$ is the instantaneous angular velocity vector of the P_1-P_2 system in the inertial frame. Recall that $[\,\cdot\,]_{\mathrm{x}}$ is a skew symmetric matric defined via Equation (2.12). For a point mass, the angular velocity vector is denoted as,

$$\bar{\Gamma}_{\mathrm{i}} = \frac{\bar{H}_{\mathrm{i}}}{\tilde{l}^{*2}}, \tag{2.68}$$

where the angular momentum vector is defined in Equation (2.60) such that,

$$\frac{d\,{}^{\mathrm{i}}\boldsymbol{\mathcal{R}}^{\mathrm{r}}}{dt'} = \left(\frac{t^*}{\tilde{l}^{*2}}\right)\left[\bar{H}_{\mathrm{i}}\right]_{\mathrm{x}} {}^{\mathrm{i}}\boldsymbol{\mathcal{R}}^{\mathrm{r}}. \tag{2.69}$$

Then, Equation (2.64) is, by substituting Equations (2.66) and (2.69), more compactly written as:

$$\frac{{}^{\mathrm{i}}d\bar{r}_{\mathrm{i}}}{dt'} = \frac{t^*}{l^*}\left(\frac{\tilde{l}^*}{\tilde{t}^*}{}^{\mathrm{i}}\boldsymbol{\mathcal{R}}^{\mathrm{r}}\,\bar{v} + \frac{1}{\tilde{l}^*}\left[\bar{H}_{\mathrm{i}}\right]_{\mathrm{x}} {}^{\mathrm{i}}\boldsymbol{\mathcal{R}}^{\mathrm{r}}\,\bar{r} + \frac{1}{\tilde{l}^*}\left(\bar{R}^T_{12_{\mathrm{i}}}\bar{V}_{12_{\mathrm{i}}}\right) {}^{\mathrm{i}}\boldsymbol{\mathcal{R}}^{\mathrm{r}}\,\bar{r}\right), \tag{2.70}$$

with the nondimensional position and velocity in the rotating frame denoted as, $\bar{r}$ and $\bar{v}$, respectively. The transformation process from the rotating frame to the inertial EME frame is outlined as follows:

- Let $\bar{r}$ and $\bar{v}$ be the nondimensional position and velocity vectors in the CRTBP rotating frame measured from the system barycenter.
- Collect the dimensional vectors $\bar{R}_{12_{\mathrm{i}}}$ and $\bar{V}_{12_{\mathrm{i}}}$ from the DE430 ephemeris file.
- Calculate the rotation matrix, ${}^{\mathrm{i}}\boldsymbol{\mathcal{R}}^{\mathrm{r}}$, from Equations (2.56)-(2.59).
- Evaluate the nondimensional position, $\bar{r}_{\mathrm{i}}$, in the inertial EME frame via Equation (2.61).

- Compute the nondimensional velocity, ${}^{\mathrm{i}}\bar{v}_{\mathrm{i}}$, with Equation (2.70).

- Translate the nondimensional inertial position from the barycenter to the desired central primary body, i.e.,

$$\bar{r}_{ps_{\mathrm{i}}} = \bar{r}_{\mathrm{i}} + \left(\frac{1}{l^*}\right) \bar{R}_{pB_{\mathrm{i}}}, \tag{2.71}$$

  where $\bar{r}_{ps_{\mathrm{i}}}$ is the nondimensional position of the spacecraft measured from one of the primaries via Equations (2.52)-(2.53).

- Translate the nondimensional velocity via the following expression,

$${}^{\mathrm{i}}\bar{v}_{ps_{\mathrm{i}}} = {}^{\mathrm{i}}\bar{v}_{\mathrm{i}} + \left(\frac{t^*}{l^*}\right) \bar{V}_{\mathrm{i}\,pB}, \tag{2.72}$$

  where ${}^{\mathrm{i}}\bar{v}_{ps_{\mathrm{i}}}$ is the nondimensional velocity of the spacecraft measured from one of the primaries via Equations (2.54)-(2.55).

In this process, the nondimensional position and velocity vectors are evaluated with respect to one of the primaries. The state formulated by these nondimensional position and velocity vectors is input into an ephemeris propagator based on the relative ephemeris equation.

2.3.2.2 EME Frame to Rotating Frame

The transformation process from the inertial EME frame to the CRTBP rotating frame is computed via the transformation process defined by Ocampo [55]. In this investigation, a state in the inertial EME frame is propagated in the higher-fidelity model, but it is advantageous to observe the geometry of the trajectory in the CRTBP rotating frame. The transformation process from the inertial EME frame to the rotating frame is outlined as follows:

- Let $\bar{r}_{ps_{\mathrm{i}}}$ and ${}^{\mathrm{i}}\bar{v}_{ps_{\mathrm{i}}}$ be the nondimensional position and velocity vectors in the inertial EME frame measured from the central primary body.

- Collect the dimensional vectors $\bar{R}_{\mathrm{i}_{12}}$ and $\bar{V}_{\mathrm{i}_{12}}$ from the DE430 ephemeris file.
- Calculate the rotation matrix, ${}^{\mathrm{r}}\boldsymbol{\mathcal{R}}^{\mathrm{i}}$, from Equations (2.56)-(2.59). Recall the rotation matrix property: ${}^{\mathrm{r}}\boldsymbol{\mathcal{R}}^{\mathrm{i}} = {}^{\mathrm{i}}\boldsymbol{\mathcal{R}}^{\mathrm{r}^T}$.
- Translate the nondimensional inertial position from the current central primary body to the system barycenter, i.e.,

$$\bar{r}_{\mathrm{i}} = \bar{r}_{\mathrm{i}_{ps}} - \left(\frac{1}{l^*}\right)\bar{R}_{\mathrm{i}_{pB}}, \tag{2.73}$$

  where $\bar{R}_{\mathrm{i}_{pB}}$ is the dimensional position of the barycenter measured from one of the primaries via Equations (2.52)-(2.53). Recall that $\bar{r}_{\mathrm{i}}$ is the position of the spacecraft in the inertial EME frame with respect to the CRTBP barycenter.
- Translate the nondimensional velocity via the following expression,

$${}^{\mathrm{i}}\bar{v}_{\mathrm{i}} = {}^{\mathrm{i}}\bar{v}_{\mathrm{i}_{ps}} - \left(\frac{t^*}{l^*}\right)\bar{V}_{\mathrm{i}_{pB}}, \tag{2.74}$$

  where ${}^{\mathrm{i}}\bar{v}_{\mathrm{i}_{pB}}$ is the dimensional velocity of the barycenter measured from one of the primaries via Equations (2.54)-(2.55).
- Evaluate the nondimensional position, $\bar{r}$, in the CRTBP rotating frame via Equation (2.61), i.e.,

$$\bar{r} = \frac{l^*}{\tilde{l}^*}\,{}^{\mathrm{r}}\boldsymbol{\mathcal{R}}^{\mathrm{i}}\,\bar{r}_{\mathrm{i}}, \tag{2.75}$$

- Compute the nondimensional velocity, $\bar{v}$, by multiplying Equation (2.70) by the rotation matrix ${}^{\mathrm{r}}\boldsymbol{\mathcal{R}}^{\mathrm{i}}$ such that,

$$\bar{v} = \frac{\tilde{t}^*}{\tilde{l}^*}\left(\frac{l^*}{t^*}\,{}^{\mathrm{r}}\boldsymbol{\mathcal{R}}^{\mathrm{i}}\,{}^{\mathrm{i}}\bar{v}_{\mathrm{i}} - \frac{1}{\tilde{l}^*}\left[\bar{H}_{\mathrm{r}}\right]_{\mathrm{x}}\bar{r} - \frac{1}{\tilde{l}^*}\left(\bar{R}_{\mathrm{i}_{12}}^T\bar{V}_{\mathrm{i}_{12}}\right)\bar{r}\right), \tag{2.76}$$

  where $\bar{H}_{\mathrm{r}}$ is the angular momentum expressed in the rotating frame, i.e., multiplying Equation (2.60) by the rotation matrix ${}^{\mathrm{r}}\boldsymbol{\mathcal{R}}^{\mathrm{i}}$.

In this investigation, the orientation of the spacecraft is expressed in the rotating frame consistent with the CRTBP and the EME inertial frame. Additionally, a transitioning method between these two coordinate frames is required when moving feasible transfers from the CRTBP model into the higher-fidelity ephemeris model.

3. DYNAMICAL STRUCTURES

The study of predictable long-term behavior of complex dynamical models is essential in the absence of a closed-form analytical solution. The motion in a general dynamical system can be categorized into four types: equilibrium solutions, periodic solutions, quasi-periodic solutions, and chaotic. Additionally, dynamical structures may exist that fall into one of these categories. Recalling that the CRTBP has no closed-form analytical solution, an analysis of long-term dynamical structures such as equilibrium points, periodic orbits, quasi-periodic orbits and their associated hyperbolic invariant manifolds offers insight into the complex motion in the model. Dynamical structures are also manipulated to construct efficient and flexible transfers that are straightforwardly transitioned into a higher-fidelity model.

3.1 Equilibrium Solutions

Equilibrium solutions are one of the basic long-term dynamical structures identified in a dynamical system. The search for equilibrium solutions is one of the first fundamental processes necessary for learning important insights about the dynamical behavior in a general system. The equilibrium solutions have a range of names such as: stationary points, equilibrium points, and, in the CRTBP, Lagrange points or libration points. In this investigation, equilibrium solutions associated with the CRTBP are termed Lagrange points. The equations of motion for the CRTBP, written in Equation (2.28), are compactly expressed as the vector function:

$$\dot{\bar{\mathcal{X}}} = \bar{\mathfrak{f}}\left(\bar{\mathcal{X}}\right), \tag{3.1}$$

where $\bar{\mathfrak{f}}$ defines a differentiable vector field and $\bar{\mathcal{X}} \in \mathbb{R}^6$, or a six-dimensional state vector, is defined as,

$$\bar{\mathcal{X}} = \begin{bmatrix} x \\ y \\ z \\ \dot{x} \\ \dot{y} \\ \dot{z} \end{bmatrix}. \tag{3.2}$$

The vector form of the equations of motion are expanded such that,

$$\bar{\mathfrak{f}}\left(\bar{\mathcal{X}}\right) = \begin{bmatrix} \dot{x} \\ \dot{y} \\ \dot{z} \\ 2\dot{y} + \frac{\partial \mathcal{U}^*}{\partial x} \\ -2\dot{x} + \frac{\partial \mathcal{U}^*}{\partial y} \\ \frac{\partial \mathcal{U}^*}{\partial z} \end{bmatrix}. \tag{3.3}$$

A trajectory in the CRTBP is a solution to Equation (3.3), i.e., the state space form of the equations of motion. With no analytical solution to the CRTBP, a trajectory is computed via numerical integration from an initial state, $\bar{\mathcal{X}}_0$, after a propagation time t. In this investigation, and in the literature, the trajectory is also termed as the flow of the system. The flow, $\bar{\phi}$, is a function of an initial state and propagation time, i.e., $\bar{\phi} = \bar{\mathcal{X}}(\bar{\mathcal{X}}_0, t)$. A Lagrange point, i.e., an equilibrium solution, $\widetilde{\mathcal{X}}$, is defined via:

$$\bar{\mathfrak{f}}\left(\widetilde{\mathcal{X}}\right) = \bar{0}, \tag{3.4}$$

or expanded, via substitution of the CRTBP equations, to,

$$\begin{bmatrix} \dot{x} \\ \dot{y} \\ \dot{z} \\ 2\dot{y} + \frac{\partial \mathcal{U}^*}{\partial x} \\ -2\dot{x} + \frac{\partial \mathcal{U}^*}{\partial y} \\ \frac{\partial \mathcal{U}^*}{\partial z} \end{bmatrix} = \begin{bmatrix} 0 \\ 0 \\ 0 \\ 0 \\ 0 \\ 0 \end{bmatrix}. \tag{3.5}$$

The partial derivatives of the pseudo-potential are computed from Equation (2.32) and any Lagrange points are identified as solutions to the following system of equations:

$$0 = x - \frac{(1-\mu)(x+\mu)}{r_{13}^3} - \frac{\mu(x-1+\mu)}{r_{23}^3}, \tag{3.6}$$

$$0 = y - \frac{y(1-\mu)}{r_{13}^3} - \frac{y\mu}{r_{23}^3}, \tag{3.7}$$

$$0 = -\frac{z(1-\mu)}{r_{13}^3} - \frac{z\mu}{r_{23}^3}, \tag{3.8}$$

where, it is recalled that, $\bar{r}_{13} = [x+\mu, y, z]^T$ and $\bar{r}_{23} = [x-1+\mu, y, z]^T$. From Equation (3.8), it is observed that all Lagrange points exist on the $\hat{x}-\hat{y}$ plane, i.e., the plane of motion of the primary bodies. Note that there are three collinear Lagrange points, i.e., locations on the $\hat{x}$-axis, computed by solving for all solutions of Equation (3.6), and two triangular Lagrange points, computed by solving Equations (3.6)-(3.7). The collinear Lagrange points are calculated by solving the following equations:

$$\mathrm{L}_1: \quad f_{L_1}(x) = x - \frac{(1-\mu)}{(x+\mu)^2} + \frac{\mu}{(x-1+\mu)^2} = 0, \tag{3.9}$$

$$\mathrm{L}_2: \quad f_{L_2}(x) = x - \frac{(1-\mu)}{(x+\mu)^2} - \frac{\mu}{(x-1+\mu)^2} = 0, \tag{3.10}$$

$$\mathrm{L}_3: \quad f_{L_3}(x) = x + \frac{(1-\mu)}{(x+\mu)^2} + \frac{\mu}{(x-1+\mu)^2} = 0. \tag{3.11}$$

The solutions to Equations (3.9)-(3.11) usually require a numerical technique. Newton's method is implemented to numerically solve for the location of the collinear Lagrange points.

An algorithm consistent with Newton's method is constructed such that an initial guess, x_{j}, is updated via,

$$x_{\mathrm{j+1}} = x_{\mathrm{j}} - \frac{f_{L_k}(x_{\mathrm{j}})}{Df_{L_k}(x_{\mathrm{j}})}, \tag{3.12}$$

where $x_{\mathrm{j+1}}$ is the updated guess, f_{L_k} is the function associated with the k^{th} Lagrange point, i.e., Equations (3.9)-(3.11), and Df_{L_k} is the derivative of f_{L_k} with respect to x such that, $Df_{L_k} = \frac{df_{L_k}}{dx}$. Note that the value of f_{L_k} and its derivative, Df_{L_k}, is evaluated at the initial guess, x_{j}. In this application, the stop criteria for Newton's method is defined as: $|f_{L_k}(x_{\mathrm{j+1}})| < \mathfrak{E}$, where $|\cdot|$ is absolute value and $\mathfrak{E}$ is a user specified tolerance value. To search for Lagrange points, the value of the error tolerance, $\mathfrak{E}$, is set to 1×10^{-11}. If the value of the function, f_{L_k}, at the updated guess, $x_{\mathrm{j+1}}$, is higher than the user specified tolerance, then a new iteration is required and a new updated guess, $x_{\mathrm{j+2}}$, is evaluated via Equation (3.12) with $x_{\mathrm{j+1}}$ as the initial guess. Remember that Newton's method is a numerical method and the value of the tolerance dictates the accuracy of the solution. Szehebely [24] provides initial guesses to start the iteration process for the collinear Lagrange points. The triangular Lagrange points are the solutions of Equations (3.6)-(3.7) and are denoted by L_4 and L_5. The L_4 and L_5 points are defined as:

$$\mathrm{L}_4: \quad x = \frac{1}{2} - \mu, \quad y = \frac{\sqrt{3}}{2}, \tag{3.13}$$

$$\mathrm{L}_5: \quad x = \frac{1}{2} - \mu, \quad y = -\frac{\sqrt{3}}{2}. \tag{3.14}$$

Equilibrium solutions of the CRTBP model provide insightful flow information about the dynamical system. A notable observation is the existence and location of the Lagrange points in the $\hat{x}$ -$\hat{y}$ plane. Analysis into the dynamical behavior near the vicinity of the Lagrange points facilitates the design process of desirable transfers into and away from the Lagrange points.

3.1.1 Stability of Lagrange Points

Stability analysis near equilibrium solutions, i.e., Lagrange points, provides information regarding the local behavior. Recalling that the Lagrange points are stationary points in the phase-space, i.e., $\mathbb{R}^6$ in the CRTBP, then important dynamical insights are derived near the vicinity of these equilibrium solutions. In this investigation, stability of dynamical structures is based on Lyapunov stability, which analyzes the isochronous correspondence of two points, i.e., the distance of two points measured at a specified time t [24]. To understand the local behavior near a point, $\bar{\mathcal{X}}^*$, a small variation is introduced such that,

$$\bar{\mathcal{X}} = \bar{\mathcal{X}}^* + \Delta\bar{\mathcal{X}}, \tag{3.15}$$

where $\Delta\bar{\mathcal{X}}$ is defined as a variation. Equation (3.15) is input into Equation (3.1) and expanded, via a Taylor series expansion, as:

$$\dot{\bar{\mathcal{X}}} = \dot{\bar{\mathcal{X}}}^* + \Delta\dot{\bar{\mathcal{X}}} = \bar{\mathfrak{f}}(\bar{\mathcal{X}}^*) + \left.\frac{D\bar{\mathfrak{f}}}{D\bar{\mathcal{X}}}\right|_{\bar{\mathcal{X}}^*} \Delta\bar{\mathcal{X}} + \text{H.O.T.s}, \tag{3.16}$$

where H.O.T.s represents the higher-order terms in the expansion. The linear approximation of this expansion is expressed as,

$$\Delta\dot{\bar{\mathcal{X}}} = \left.\frac{D\bar{\mathfrak{f}}}{D\bar{\mathcal{X}}}\right|_{\bar{\mathcal{X}}^*} \Delta\bar{\mathcal{X}}, \tag{3.17}$$

with the derivative of the vector field, $\bar{\mathfrak{f}}$, written as:

$$\frac{D\bar{\mathfrak{f}}}{D\bar{\mathcal{X}}} = \mathbf{A}(t) = \begin{bmatrix} 0 & 0 & 0 & 1 & 0 & 0 \\ 0 & 0 & 0 & 0 & 1 & 0 \\ 0 & 0 & 0 & 0 & 0 & 1 \\ \mathcal{U}_{xx}(t) & \mathcal{U}_{xy}(t) & \mathcal{U}_{xz}(t) & 0 & 2 & 0 \\ \mathcal{U}_{yx}(t) & \mathcal{U}_{yy}(t) & \mathcal{U}_{yz}(t) & -2 & 0 & 0 \\ \mathcal{U}_{zx}(t) & \mathcal{U}_{zy}(t) & \mathcal{U}_{zz}(t) & 0 & 0 & 0 \end{bmatrix}, \tag{3.18}$$

where $\mathcal{U}_{ij}$ is the second derivative of the pseudo-potential function, $\mathcal{U}$, such that: $\frac{\partial^2 \mathcal{U}}{\partial i \partial j}$. For the linear stability analysis near a Lagrange point, the $\mathbf{A}(t)$ matrix has constant entries, i.e., its entries are time-independent, and is written as $\mathbf{A}$. A general solution to the system in Equation (3.17), with a constant $\mathbf{A}$ matrix, is denoted as,

$$\Delta\bar{\mathcal{X}}(t) = \mathrm{e}^{\mathbf{A}t}\Delta\bar{\mathcal{X}}(t_0). \tag{3.19}$$

Thus, from Szebehely, the Lyapunov stability of each Lagrange point is observed through the eigenvalue decomposition of the matrix $\mathbf{A}$. Let $\{{}^{E}\Lambda_1, {}^{E}\Lambda_2, \ldots, {}^{E}\Lambda_6\}$ be the set of eigenvalues corresponding to the real matrix $\mathbf{A}$ with complementary eigenvectors: $\{{}^{E}\bar{\Psi}_1, {}^{E}\bar{\Psi}_2, \ldots, {}^{E}\bar{\Psi}_6\}$. Szebehely categorizes the stability properties of the linearized system in Equation (3.17) at the Lagrange points through the eigenvalues associated with $\mathbf{A}$ as [24],

- Asymptotically stable:
  - All complex eigenvalues with negative real components
  - All negative real eigenvalues
- Stable:
  - All complex eigenvalues with imaginary components
- Unstable:
  - All complex eigenvalues and some eigenvalues have positive real components
  - All real eigenvalues and some eigenvalues are positive

Insightful flow information near the vicinity of the Lagrange points is revealed through linear stability analysis.

3.1.2 Invariant Subspaces near Lagrange Points

Invariant subspaces observed through a linear stability analysis near the Lagrange points offer important flow information that is leveraged in the construction of transfers in the CRTBP model. Equation (3.19) is the general solution to the linear variational equation, i.e., Equation (3.17), such that the matrix $e^{\mathbf{A}t}$ provides important flow information regarding all possible solutions to the variational equation. Linear stability properties are derived from an analysis of the associated eigenvalues and eigenvectors of the $\mathbf{A}$ matrix in Equation (3.19). Additionally, the existence and the dimension of invariant subspaces are indicated via an investigation into the eigenstructure of the $\mathbf{A}$ matrix. Guckenheimer categorizes the invariant subspaces as [56]:

- Stable subspace, $\mathcal{E}^S = \text{span}\{{}^E\bar{\Psi}_1^S, \ldots, {}^E\bar{\Psi}_{n_s}^S\}$
- Unstable subspace, $\mathcal{E}^U = \text{span}\{{}^E\bar{\Psi}_1^U, \ldots, {}^E\bar{\Psi}_{n_u}^U\}$
- Center subspace, $\mathcal{E}^C = \text{span}\{{}^E\bar{\Psi}_1^C, \ldots, {}^E\bar{\Psi}_{n_c}^C\}$

The dimensions of the stable, unstable, and center subspaces are denoted with: n_s, n_u, and n_c, respectively, and the sum of these invariant subspaces spans the entire phase-space of the dynamical system, that is, $n_s + n_u + n_c = 6$. Eigenvectors corresponding to eigenvalues with negative real parts, $\{{}^E\bar{\Psi}_1^S, \ldots, {}^E\bar{\Psi}_{n_s}^S\}$, span the stable subspace and the unstable subspace is spanned via a set of eigenvectors, $\{{}^E\bar{\Psi}_1^U, \ldots, {}^E\bar{\Psi}_{n_u}^U\}$, corresponding to eigenvalues with positive real parts. These statements are summarized by the following theorem [56]:

Theorem 3.1.1. ***Stable Manifold Theorem*** *Suppose that* $\dot{\bar{\mathcal{X}}} = \bar{\mathfrak{f}}\left(\bar{\mathcal{X}}\right)$ *has a hyperbolic equilibrium solution* $\widetilde{\mathcal{X}}$*. Then there exists local stable,* W_{loc}^s*, and unstable manifolds,* W_{loc}^u*, of the same dimensions* n_s *and* n_u*, respectively. These local manifolds,* W_{loc}^s *and* W_{loc}^u*, correspond to the invariant subspaces* $\mathcal{E}^S$ *and* $\mathcal{E}^U$ *of the linearized system, and are tangent to* $\mathcal{E}^S$ *and* $\mathcal{E}^U$ *at* $\bar{\mathcal{X}}^*$*.* W_{loc}^s *and* W_{loc}^u *are also as smooth as the function* $\bar{\mathfrak{f}}$*.*

If all eigenvalues associated with an equilibrium solution, i.e., from the eigenstructure of the **A** matrix, have nonzero real parts, then the equilibrium solution is termed as hyperbolic. The asymptotic behavior of solutions near the equilibrium point is derived from the linearixation in Equation (3.19). A state along the local stable manifold, W^s_{loc}, asymptotically approaches the equilibrium point, $\widetilde{\mathcal{X}}$, for $t \to \infty$, whereas a state along the local unstable manifold, W^u_{loc} asymptotically approaches $\widetilde{\mathcal{X}}$ for $t \to -\infty$. Global analogs of the local stable and unstable manifolds exist and are generated by propagating a state within the local manifolds, near the equilibrium point, in reverse time and forward time, respectively. The center manifold associated with an equilibrium point is described by Guckenheimer via the following theorem[56]:

Theorem 3.1.2. ***Center Manifold Theorem*** *Let $\bar{\mathfrak{f}}$ be a vector field in $\mathbb{R}^n$ vanishing at an equilibrium point $\widetilde{\mathcal{X}}$ defined in Equation (3.4). Let* **A** *be defined with Equation (3.18) and divide the spectrum of* **A** *into three parts, such that,*

$$\mathrm{Re}\left[{}^{E}\Lambda\right] \begin{cases} < 0 \ \text{ if } {}^{E}\Lambda \in \sigma_s \\ = 0 \ \text{ if } {}^{E}\Lambda \in \sigma_c \\ > 0 \ \text{ if } {}^{E}\Lambda \in \sigma_u \end{cases}, \tag{3.20}$$

where the eigenspaces of the sets σ_s, σ_c, and σ_u are $\mathcal{E}^s$, $\mathcal{E}^c$, and $\mathcal{E}^u$, respectively. Then, there exists stable, unstable, and center invariant manifolds (W^s_{loc}, W^u_{loc}, and W^c_{loc}) tangent to their respective eigenspaces, $\mathcal{E}^s$, $\mathcal{E}^u$, and $\mathcal{E}^c$, at the equilibrium point $\widetilde{\mathcal{X}}$. The local manifolds W^s_{loc}, W^u_{loc}, and W^c_{loc} are all invariant to the flow. The stable and unstable manifolds are unique, but the center manifold need not be.

Further discussion into invariant manifold structures for dynamical systems is provided in Guckenheimer [56]. Structured flow, such as periodic orbits and quasi-periodic orbits, exist within the center manifold and, in this investigation, periodic and quasi-periodic orbits near the Sun-Earth L_1 and L_2 points are generated via numerical methods.

3.2 Numerical Methods

In the absence of an analytical solution to the CRTBP, solutions, i.e., trajectories, are evaluated via numerical methods. Within the context of the CRTBP, a trajectory is computed via numerical propagation from an initial six-dimensional state. Anticipation of numerical errors, such as truncation and round-off errors associated with numerical propagation techniques, offers opportunities to construct feasible solutions. Additionally, there are challenges associated with constructing a feasible trajectory near a dynamically complex region, such as near a primary body in the CRTBP model. An understanding of the global dynamical behaviors and the implementation of numerical shooting techniques facilitates the construction of periodic and quasi-periodic orbits in the CRTBP model as well as more complex geometries.

3.2.1 State Transition Matrix

The construction of feasible transfers in a dynamical system with no analytical solution requires numerical corrections techniques. The numerical method to construct a continuous trajectory with user-specified characteristics, e.g., orbit geometry or time-of-flight, is an iterative process. The iterative process is more commonly termed as a numerical "shooting method". In this investigation, single-shooting and multiple-shooting methods are implemented to construct transfers with specified attributes. Note that in the simplest case for a single-shooter, an initial state, $\bar{\mathcal{X}}_0$, is propagated by a time, T_0, to a final state, $\bar{\mathcal{X}}_f$. Additional constraints are placed at the boundaries of the transfer, i.e., the initial or final state, or along the path of the transfer. However, this iterative process requires knowledge about the evolution of the variations associated with a propagated state, i.e., the relationship between the initial and final variation. Equation (3.17) describes the linear approximation

of the variation near a fixed point, $\bar{\mathcal{X}}^*$, where the derivative of the vector field is given in Equation (3.18). The equation is re-written below as,

$$\Delta\dot{\bar{\mathcal{X}}} = \mathbf{A}(t)\Delta\bar{\mathcal{X}}, \tag{3.21}$$

where, it is recalled that, $\Delta\bar{\mathcal{X}}$ is the variation from a state, $\bar{\mathcal{X}}^*$. Note that Equation (3.21) is written as a linear state equation and a solution is given, from Rugh [57], as,

$$\Delta\bar{\mathcal{X}}(t_f) = \mathbf{\Phi}(t_f, t_0)\Delta\bar{\mathcal{X}}(t_0), \tag{3.22}$$

with $\mathbf{\Phi}(t_f, t_0)$ termed as the State Transition Matrix (STM). The STM is a linear representation of the change of an initial variation, $\Delta\bar{\mathcal{X}}(t_0)$, and a final variation, $\Delta\bar{\mathcal{X}}(t_f)$. Additionally, the STM can be expanded as,

$$\mathbf{\Phi}(t_f, t_0) = \begin{bmatrix} \frac{\partial x(t_f)}{\partial x(t_0)} & \frac{\partial x(t_f)}{\partial y(t_0)} & \frac{\partial x(t_f)}{\partial z(t_0)} & \frac{\partial x(t_f)}{\partial \dot{x}(t_0)} & \frac{\partial x(t_f)}{\partial \dot{y}(t_0)} & \frac{\partial x(t_f)}{\partial \dot{z}(t_0)} \\ \frac{\partial y(t_f)}{\partial x(t_0)} & \frac{\partial y(t_f)}{\partial y(t_0)} & \frac{\partial y(t_f)}{\partial z(t_0)} & \frac{\partial y(t_f)}{\partial \dot{x}(t_0)} & \frac{\partial y(t_f)}{\partial \dot{y}(t_0)} & \frac{\partial y(t_f)}{\partial \dot{z}(t_0)} \\ \frac{\partial z(t_f)}{\partial x(t_0)} & \frac{\partial z(t_f)}{\partial y(t_0)} & \frac{\partial z(t_f)}{\partial z(t_0)} & \frac{\partial z(t_f)}{\partial \dot{x}(t_0)} & \frac{\partial z(t_f)}{\partial \dot{y}(t_0)} & \frac{\partial z(t_f)}{\partial \dot{z}(t_0)} \\ \frac{\partial \dot{x}(t_f)}{\partial x(t_0)} & \frac{\partial \dot{x}(t_f)}{\partial y(t_0)} & \frac{\partial \dot{x}(t_f)}{\partial z(t_0)} & \frac{\partial \dot{x}(t_f)}{\partial \dot{x}(t_0)} & \frac{\partial \dot{x}(t_f)}{\partial \dot{y}(t_0)} & \frac{\partial \dot{x}(t_f)}{\partial \dot{z}(t_0)} \\ \frac{\partial \dot{y}(t_f)}{\partial x(t_0)} & \frac{\partial \dot{y}(t_f)}{\partial y(t_0)} & \frac{\partial \dot{y}(t_f)}{\partial z(t_0)} & \frac{\partial \dot{y}(t_f)}{\partial \dot{x}(t_0)} & \frac{\partial \dot{y}(t_f)}{\partial \dot{y}(t_0)} & \frac{\partial \dot{y}(t_f)}{\partial \dot{z}(t_0)} \\ \frac{\partial \dot{z}(t_f)}{\partial x(t_0)} & \frac{\partial \dot{z}(t_f)}{\partial y(t_0)} & \frac{\partial \dot{z}(t_f)}{\partial z(t_0)} & \frac{\partial \dot{z}(t_f)}{\partial \dot{x}(t_0)} & \frac{\partial \dot{z}(t_f)}{\partial \dot{y}(t_0)} & \frac{\partial \dot{z}(t_f)}{\partial \dot{z}(t_0)} \end{bmatrix}, \tag{3.23}$$

or written more compactly as,

$$\mathbf{\Phi}(t_f, t_0) = \begin{bmatrix} \mathbf{\Phi}_{rr}(t_f, t_0) & \mathbf{\Phi}_{rv}(t_f, t_0) \\ \mathbf{\Phi}_{vr}(t_f, t_0) & \mathbf{\Phi}_{vv}(t_f, t_0) \end{bmatrix}, \tag{3.24}$$

where the linearized variation of the final position, $\Delta\bar{r}(t_f)$, with respect to the initial position and velocity variation is stated as $\mathbf{\Phi}_{rr}$ and $\mathbf{\Phi}_{rv}$, respectively. The matrices $\mathbf{\Phi}_{vr}$ and $\mathbf{\Phi}_{vV}$ correspond to the variation of the final velocity with respect to the initial position and velocity variation, respectively. Note that the components in Equation (3.24), i.e.,

$\{\mathbf{\Phi}_{rr}, \mathbf{\Phi}_{rv}, \mathbf{\Phi}_{vr}, \mathbf{\Phi}_{vv}\}$, are 3×3 matrices. Some properties associated with the STM are summarized below [57]:

$$\mathbf{\Phi}(t_f, t_0) = \mathbf{\Phi}(t_f, t_1)\mathbf{\Phi}(t_1, t_0), \tag{3.25}$$

$$\mathbf{\Phi}^{-1}(t_f, t_0) = \mathbf{\Phi}(t_0, t_f), \tag{3.26}$$

$$\frac{d\mathbf{\Phi}(t_f, t_0)}{dt} = \mathbf{A}(t)\mathbf{\Phi}(t_f, t_0). \tag{3.27}$$

A more complete discussion about the STM and its properties is provided by Rugh [57]. Equation (3.27) is implemented in the computation of the STM along a propagated trajectory. Note that Equation (3.27) is a matrix function, such that, each individual entry is solved via numerical integration at different times along the propagated trajectory; a common practice is to group the integration of the state, via Equation (3.2), and the STM together. Knowledge about the evolution of a state variation associated with a trajectory arc facilitates the corrections process for a shooting method.

3.2.2 Single-Shooting Method

The construction of trajectories with desirable characteristics, e.g., geometry, is facilitated via numerical single-shooting methods. In this formulation, the trajectory construction process is essentially a Boundary Value Problem (BVP). A simple-shooting method example is illustrated in Figure 3.1. The trajectory arc in Figure 3.1 is created by propagating an initial state, $\bar{\mathcal{X}}(t_0)$, by time T_0, such that the final state is written as: $\bar{\mathcal{X}}(t_f)$, where the final time, t_f, is denoted as: $t_f = t_0 + T_0$. In Figure 3.1, a desired state, i.e., $\bar{\mathcal{X}}_d$, is "targeted", that is the single-shooter method is essentially a targeting problem. A set of independent variables, termed as free-variables, explicitly describe the transfer characteristics. A set of target conditions, termed as constraints, describe any desired transfer characteristics, e.g., initial or final state components. The free-variables are written as a column vector, $\bar{\mathfrak{X}}$, such that $\bar{\mathfrak{X}} \in \mathbb{R}^{n_t}$, where n_t is the number of free-variables. The constraints are also expressed as a column vector, $\bar{F}$, with $\bar{F} \in \mathbb{R}^{n_f}$, where n_f is the number of constraint conditions, i.e.,

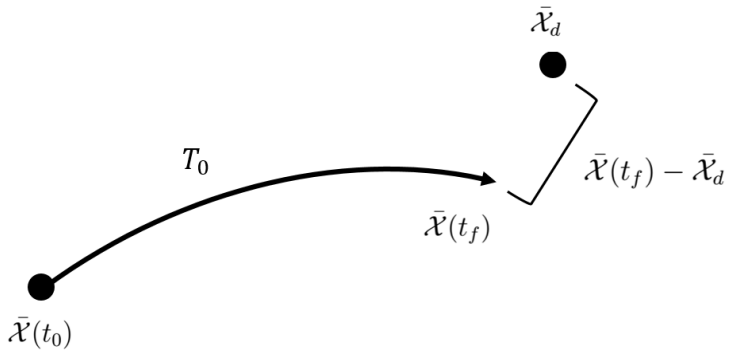

Figure 3.1. : A single trajectory arc for a single-shooter example

the targeting conditions. The targeting problem is formulated such that the solution is a free-variable vector, $\bar{\mathfrak{X}}$, that solves the following function,

$$\bar{F}(\bar{\mathfrak{X}}) = \bar{0}, \tag{3.28}$$

where $\bar{F}$ is a constraint vector function and the targeting conditions are satisfied when all components of $\bar{F}$ are zero. A single-shooter example is constructed, similar to Figure 3.1, such that a maneuver is performed at the initial state, i.e., $\bar{\mathcal{X}}_0$, and a final position is targeted, $\bar{r}_d$. The free-variable vector is written as,

$$\bar{\mathfrak{X}} = \begin{bmatrix} \bar{v}_0 \\ T_0 \end{bmatrix}, \tag{3.29}$$

where it is recalled that $\bar{v}_0$ is the velocity of the initial state and T_0 is the propagation time. Note that, in this example, the initial position, $\bar{r}_0$, is fixed such that the dimension of the free-variable vector is written as: $n_t = 4$. The target is a desired final position, $\bar{r}_d$, with the constraint vector function denoted as,

$$\bar{F} = \left[\bar{r}_0(t_f) - \bar{r}_d\right] = \bar{0}. \tag{3.30}$$

The dimension of the constraint vector is Equation (3.30) is: $n_f = 3$. In this simplified example, the initial velocity, $\bar{v}_0$, and the propagation time, T_0, are free, that is, they may

change throughout the corrections process. A straightforward way to solve a single-shooting problem is via a numerical multidimensional Newton method algorithm.

3.2.3 Multidimensional Newton Method

The multidimensional Newton's method facilitates the numerical corrections process associated with trajectories formulated as a single- or multiple-shooting problem. Newton's method is an iterative method often implemented to calculate the zeros of a function, that is, compute the solutions to the following arbitrary function: $f(t) = 0$. An appropriate initial guess, i.e., a guess close to the desired solution, is required to mitigate any convergence challenges, however, identifying an appropriate guess necessitates prior knowledge about the function. A one-dimensional Newton method is implemented to locate the collinear Lagrange points in the CRTBP model with the update equation stated in Equation (3.12) . A multidimensional analog to the one-dimensional Newton method is derived to solve the single-shooting targeting problem. In a targeting problem, the objective is to find a solution, i.e., a vector $\mathfrak{X}_c$, that satisfies Equation (3.28). Let $\bar{\mathfrak{X}}_{\mathrm{j}}$ be an initial guess and let the solution vector, $\bar{\mathfrak{X}}_c$, be written as: $\bar{\mathfrak{X}}_c = \bar{\mathfrak{X}}_{\mathrm{j}+1}$. A small perturbation, $\delta\bar{\mathfrak{X}}$, is defined as, $\delta\bar{\mathfrak{X}} = \bar{\mathfrak{X}}_{\mathrm{j}+1} - \bar{\mathfrak{X}}_{\mathrm{j}}$, that is, the initial guess is assumed to be close to the solution. Next, a Taylor expansion of the constraint function is denoted as,

$$\bar{F}(\bar{\mathfrak{X}}_{\mathrm{j}} + \delta\bar{\mathfrak{X}}) \approx \bar{F}(\bar{\mathfrak{X}}_{\mathrm{j}}) + \mathbf{D}\bar{\mathbf{F}}(\bar{\mathfrak{X}}_{\mathrm{j}})(\delta\bar{\mathfrak{X}}) + \mathrm{H.O.T.s}, \tag{3.31}$$

where $\mathbf{D}\bar{\mathbf{F}}(\bar{\mathfrak{X}}_{\mathrm{j}})$ is defined as the Jacobian of the system of constraint equations. For simplicity, higher order terms are ignored, i.e., the perturbation is assumed to be small. The Jacobian in Equation (3.31) is expanded such that,

$$\mathbf{D}\bar{\mathbf{F}} = \frac{D\bar{F}}{D\bar{\mathfrak{X}}} = \begin{bmatrix} \frac{DF_1}{D\mathfrak{X}_1} & \frac{DF_1}{D\mathfrak{X}_2} & \cdots & \frac{DF_1}{D\mathfrak{X}_{n_t}} \\ \frac{DF_2}{D\mathfrak{X}_1} & \frac{DF_2}{D\mathfrak{X}_2} & \cdots & \frac{DF_2}{D\mathfrak{X}_{n_t}} \\ \vdots & \vdots & \ddots & \vdots \\ \frac{DF_{n_f}}{D\mathfrak{X}_1} & \frac{DF_{n_f}}{D\mathfrak{X}_2} & \cdots & \frac{DF_{n_f}}{D\mathfrak{X}_{n_t}} \end{bmatrix}, \tag{3.32}$$

with the constraint vector denoted as: $\bar{F} = [F_1, F_2, \ldots, F_{n_f}]^T$, and the free-variable vector defined as: $\bar{\mathfrak{X}} = [\mathfrak{X}_1, \mathfrak{X}_2, \ldots, \mathfrak{X}_{n_t}]^T$. Recalling that, the left side of Equation (3.31) is equal to zero, $\bar{F}(\mathfrak{X}_\mathrm{j} + \delta\mathfrak{X}) = \bar{0}$, Equation (3.31) is rewritten such that,

$$-\bar{F}(\bar{\mathfrak{X}}_\mathrm{j}) = \mathbf{D}\bar{\mathbf{F}}(\bar{\mathfrak{X}}_\mathrm{j})(\bar{\mathfrak{X}}_{\mathrm{j}+1} - \bar{\mathfrak{X}}_\mathrm{j}). \tag{3.33}$$

This is a linear system of equation in the form of, $\mathfrak{B} = \mathfrak{A}\mathfrak{x}$, where $\mathfrak{B}$ is a column vector with dimension n_f, i.e., the dimension of the constraint vector, $\mathfrak{x}$ is a column vector of dimension n_t, that is, the same size as the free-variable vector, $\bar{\mathfrak{X}}$, and $\mathfrak{A}$ is an $n_f \times n_t$ matrix. The linear system of equations described has three scenarios with the corresponding update equations given as:

- Overconstrained ($n_f > n_t$): Least-Square Solution

$$\bar{\mathfrak{X}}_{\mathrm{j}+1} = \bar{\mathfrak{X}}_\mathrm{j} - \left(\mathbf{D}\bar{\mathbf{F}}(\bar{\mathfrak{X}}_\mathrm{j})^T\mathbf{D}\bar{\mathbf{F}}(\bar{\mathfrak{X}}_\mathrm{j})\right)^{-1}\mathbf{D}\bar{\mathbf{F}}(\bar{\mathfrak{X}}_\mathrm{j})^T\bar{F}(\bar{\mathfrak{X}}_\mathrm{j}). \tag{3.34}$$

- Underconstrained ($n_f < n_t$): Minimum-Norm Solution

$$\bar{\mathfrak{X}}_{\mathrm{j}+1} = \bar{\mathfrak{X}}_\mathrm{j} - \mathbf{D}\bar{\mathbf{F}}(\bar{\mathfrak{X}}_\mathrm{j})^T\left(\mathbf{D}\bar{\mathbf{F}}(\bar{\mathfrak{X}}_\mathrm{j})\mathbf{D}\bar{\mathbf{F}}(\bar{\mathfrak{X}}_\mathrm{j})^T\right)^{-1}\mathbf{D}\bar{\mathbf{F}}(\bar{\mathfrak{X}}_\mathrm{j}). \tag{3.35}$$

- Constraints equal to number of free-variables ($n_f = n_t$): Unique Solution

$$\bar{\mathfrak{X}}_{\mathrm{j}+1} = \bar{\mathfrak{X}}_\mathrm{j} - \mathbf{D}\bar{\mathbf{F}}(\bar{\mathfrak{X}}_\mathrm{j})^{-1}\bar{F}(\bar{\mathfrak{X}}_\mathrm{j}). \tag{3.36}$$

The update function utilized in Newton's method is dependent on the scenario. Recall that Newton's method is an iterative method such that the objective is: $\bar{F}(\bar{\mathfrak{X}}_{\mathrm{j}+1}) = \bar{0}$. However, due to computational challenges, an error tolerance, $\mathfrak{E}$, is selected such that the objective of the corrections process, i.e., the multidimensional Newton's Method, is defined as: $\|\bar{F}(\bar{\mathfrak{X}}_{\mathrm{j}+1})\|_2 \leq \bar{\mathfrak{E}}$, where $\|\cdot\|_2$ is the Eucledian norm of the vector. The update equation corresponding to a unique solution, i.e., Equation (3.36), is the multidimensional analog to a one-dimensional Newton's method. There exists an infinite number of solutions in the

underconstrained scenario, and, in this investigation, the minimum norm solution is selected to identify transfers with similar geometries to an initial guess. Further discussion about the scenario for a linear system is provided in [58].

A multidimensional Newton's method is implemented to correct a single-shooting problem. Recall the example illustrated in Figure 3.1 and expressed by the free-variable and constraint vectors in Equations (3.29) and (3.30), respectively. In the example, the dimension corresponding to the free-variable vector and the constraint vector are denoted as: $n_t = 4$ and $n_f = 3$, respectively, such that, the single-shooting problem is underconstrained. The update equation corresponding to an underconstrained scenario is presented in Equation (3.35). The Jacobian associated with the constraint vector in Equation (3.30) is denoted as,

$$\mathbf{D}\bar{\mathbf{F}} = \begin{bmatrix} \frac{\partial \bar{r}(t_f)}{\partial \bar{v}_0(t_0)} & \frac{\partial \bar{r}}{\partial t}\Big|_{T_0} \end{bmatrix}, \tag{3.37}$$

where, it is recalled from Equation (3.22), $\frac{\partial \bar{r}(t_f)}{\partial \bar{v}_0(t_0)}$ is final position variation with respect to the initial velocity variation, i.e., the matrix $\mathbf{\Phi}_{rv}$ in Equation (3.24). Additionally, $\frac{\partial \bar{r}}{\partial t}$ is the velocity of the propagated arc at the end of the segment, $t = T_0$. Constructing the Jacobian matrix requires knowledge of the dependencies of the problem, i.e., the constraint vector. Similar to its one-dimensional analog, the multidimensional Newton method has a quadratic convergence rate. In this investigation, this numerical technique is implemented to construct dynamical structures in the CRTBP model, such as periodic and quasi-periodic orbits, as well as trajectories with complex geometries.

3.2.4 Multiple-Shooting Method

In dynamically complex regions, a multiple-shooting strategy is implemented to identify solutions with desirable geometries. The multiple-shooting scheme simultaneously corrects a series of single-shooting problems, recalling that, in a single-shooting scheme, a single trajectory arc is propagated from a single state. In a multiple-shooting scheme, a single trajectory is subdivided into a set of N nodes. Each node has a corresponding initial state,

$\bar{\mathcal{X}}$, and propagation time, T. A simple multiple-shooting example is illustrated in Figure 3.2. The objective, similar to the single-shooting scenario, is to target a specific position, i.e., $\bar{r}_d$,

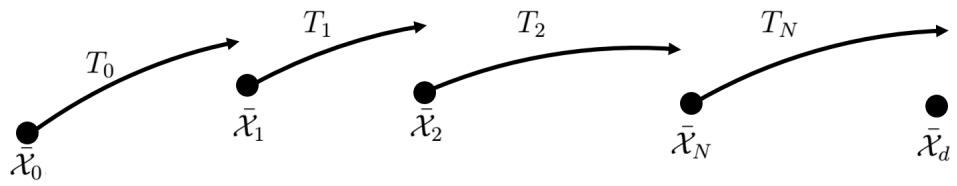

Figure 3.2. : Simple multiple-shooting example. The series of arcs are simultaneously corrected to produce a continuous trajectory

from a stationary position, $\bar{r}_0$. Note that in this example, the initial position, $\bar{r}_0$, is fixed, and therefore excluded from the free-variable vector. The free-variable vector is stated as:

$$\bar{\mathfrak{X}} = \begin{bmatrix} \bar{v}_0 \\ \bar{\mathcal{X}}_1 \\ \bar{\mathcal{X}}_2 \\ \bar{\mathcal{X}}_N \\ T_0 \\ T_1 \\ T_2 \\ T_N \end{bmatrix}, \tag{3.38}$$

where $\bar{v}_0$ is the velocity corresponding to the first node. The constraint vector for the multiple-shooting example is denoted as,

$$\bar{F} = \begin{bmatrix} \bar{\mathcal{X}}_0(T_0) - \bar{\mathcal{X}}_1(0) \\ \bar{\mathcal{X}}_1(T_1) - \bar{\mathcal{X}}_2(0) \\ \bar{\mathcal{X}}_2(T_2) - \bar{\mathcal{X}}_N(0) \\ \bar{r}_N(T_N) - \bar{r}_d \end{bmatrix}. \tag{3.39}$$

In this example, the dimension of the free-variable and the constraint vectors are: $n_t = 25$ and $n_f = 21$, respectively. This represents an underconstrained scenario and a minimum norm

solution, consistent with implementing Equation (3.35) with Newton's method, is desired. The Jacobian associated with the constraint vector is defined as,

$$\mathbf{D}\bar{\mathbf{F}} = \begin{bmatrix} \frac{\partial \bar{\mathcal{X}}_0(T_0)}{\partial \bar{v}_0(0)} & -\mathbf{I}_{6,6} & \mathbf{0}_{6,6} & \mathbf{0}_{6,6} & \left.\frac{\partial \bar{\mathcal{X}}_0}{\partial t}\right|_{T_0} & \mathbf{0}_{6,1} & \mathbf{0}_{6,1} & \mathbf{0}_{6,1} \\ \mathbf{0}_{6,3} & \frac{\partial \bar{\mathcal{X}}_1(T_1)}{\partial \bar{\mathcal{X}}_1(0)} & -\mathbf{I}_{6,6} & \mathbf{0}_{6,6} & \mathbf{0}_{6,1} & \left.\frac{\partial \bar{\mathcal{X}}_1}{\partial t}\right|_{T_1} & \mathbf{0}_{6,1} & \mathbf{0}_{6,1} \\ \mathbf{0}_{6,3} & \mathbf{0}_{6,6} & \frac{\partial \bar{\mathcal{X}}_2(T_2)}{\partial \bar{\mathcal{X}}_2(0)} & -\mathbf{I}_{6,6} & \mathbf{0}_{6,1} & \mathbf{0}_{6,1} & \left.\frac{\partial \bar{\mathcal{X}}_2}{\partial t}\right|_{T_2} & \mathbf{0}_{6,1} \\ \mathbf{0}_{3,3} & \mathbf{0}_{3,6} & \mathbf{0}_{3,6} & \frac{\partial \bar{r}_N(T_N)}{\partial \bar{\mathcal{X}}_N(0)} & \mathbf{0}_{3,1} & \mathbf{0}_{3,1} & \mathbf{0}_{3,1} & \left.\frac{\partial \bar{r}_N}{\partial t}\right|_{T_N} \end{bmatrix}, \tag{3.40}$$

with dimension: $n_f \times n_t$. Recall that the minimum norm solution produces a trajectory with shared characteristics as the initial guess, e.g., similar geometry. Multiple-shooting methods are implemented in the construction of trajectories in complex dynamical regimes, e.g., near a primary body, and a feasible trajectory is identified with a combination of Newton's method.

3.2.5 Continuation Methods

Continuation methods are powerful techniques frequently leveraged to observe the behavior of solutions associated with a dynamical system. Continuation methods, also termed embedding or homotopy methods [59], are often implemented to find solutions to a system of equations in the form of Equation (3.4). Recall that solutions to Equation (3.4) require a priori knowledge to generate a "good" initial guess, however in the absence of any system intuition, Equation (3.4) may be rewritten as,

$$\dot{\bar{\mathcal{X}}} = \bar{\mathfrak{f}}\left(\bar{\mathcal{X}}, \mathfrak{g}\right) = \bar{0}, \tag{3.41}$$

where $\mathfrak{g}$ is a system parameter, i.e., also termed a natural parameter. Note that if $\mathfrak{g} = 0$, then Equation 3.41 reduces to Equation 3.4. Let $\bar{\mathcal{X}}^c$ be a known solution of Equation 3.41 with $\mathfrak{g} = \mathfrak{g}^c$ and $\bar{\mathcal{X}}^*$ be the desired solution with $\mathfrak{g} = 0$. The assumption is there exists a curve of solutions to Equation 3.41 for a range of $0 \leq \mathfrak{g} \leq \mathfrak{g}^c$. A numerical corrections process, such as Newton's method, is implemented in conjunction with the continuation method to identify

the desired solution. Further discussion regarding continuation and homotopy methods is provided by Allgower and Georg [59]. A solution to Equation (3.1) is an equilibrium solution to the dynamical system, however, families of periodic orbits, quasi-periodic orbits, and transfers are computed via continuation methods. For a general case, the targeting problem, stated in Equation (3.28), is rewritten as:

$$\bar{F}(\bar{\mathfrak{x}}, \mathfrak{g}) = \bar{0}, \tag{3.42}$$

where $\mathfrak{g}$ is labeled as a natural parameter, e.g., time-of-Flight (TOF) or ΔV, and $\bar{\mathfrak{x}}$ is a free-variable vector. Note that the free-variable vector, $\bar{\mathfrak{X}}$, in Equation (3.28), is also written as, $\bar{\mathfrak{X}} = [\bar{\mathfrak{x}}; \mathfrak{g}]$, where $[;]$ represents vertical vector concatenation. In this analysis, natural parameter and pseudo-arclength continuation, utilizing Newton's method, are implemented to compute families of solutions with the form stated in Equation (3.42).

3.2.5.1 Natural Parameter Continuation

Natural parameter continuation is a numerical technique that builds a set of solutions associated with a TPBVP from an initial solution. In this investigation, a solution to a TPBVP is a transfer, a periodic orbit, or a quasi-periodic orbit within the context of the CRTBP model. Natural parameter continuation begins with an initial solution defined at $\{\bar{\mathfrak{x}}_0, \mathfrak{g}_0\}$, plotted in Figure 3.3. A new solution is computed by shifting the natural parameter by a small variation, or step size, $\Delta\mathfrak{g}$, such that, $\mathfrak{g}_1 = \Delta\mathfrak{g} + \mathfrak{g}_0$. Newton's method is implemented to solve Equation (3.42) with an initial guess, $\{\bar{\mathfrak{x}}_0, \mathfrak{g}_1\}$, plotted as an open blue circle in Figure 3.3, and the new solution is defined as: $\{\bar{\mathfrak{x}}_1, \mathfrak{g}_1\}$. Implementing a small step size $\Delta\mathfrak{g}$ aids in the convergence process, that is, if a solution exists. In Figure 3.3, natural parameter continuation is leveraged to compute select points along the curve in blue. Observe that natural parameter continuation in $\mathfrak{g}$ fails to converge near a turning point, i.e., the region in the red box in Figure 3.3, for the step size selected. In the turning point example illustrated in Figure 3.3, the corrections process fails to converge for the

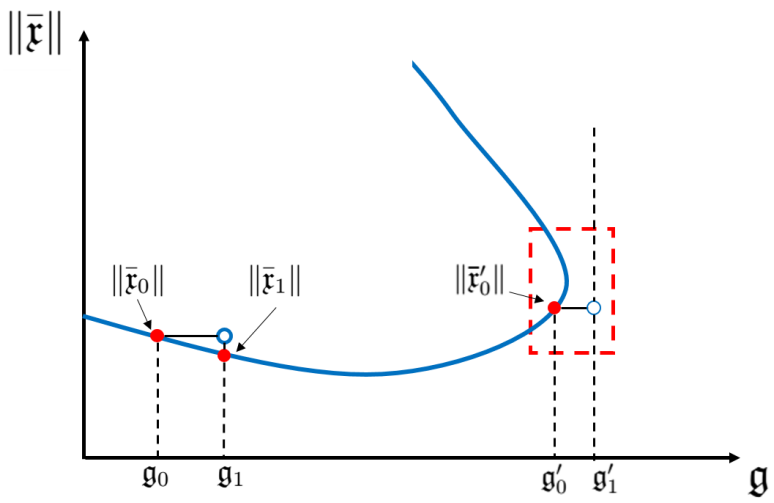

Figure 3.3. : Natural Parameter continuation along $\mathfrak{g}$. The turning point region, defined by a dashed red box, presents challenges for natural parameter continuation. Figure adapted from [60]

initial guess, defined as $\{\bar{\mathfrak{x}}'_0, \mathfrak{g}'_1\}$; recalling that $\mathfrak{g}'_1$ remains fixed throughout the corrections process. Convergence near turning points is an inherent challenge associated with natural parameter continuation. Some mitigation strategies include, but are not limited to, using an attenuation factor in the corrections process or decreasing the step size of the natural parameter, $\Delta\mathfrak{g}$. Additional insight regarding the TPBVP or the dynamical system offers opportunities to mitigate the associated challenges with natural parameter continuation.

3.2.5.2 Pseudo-Arclength Continuation

Pseudo-arclength continuation is a more sophisticated method that offers improved convergence performance near turning points along a curve. Proposed by Keller in 1977 [61], pseudo-arclength continuation utilizes the tangent space of a curve to closely approximate its geometry. An example is illustrated in Figure 3.4. The free-variable vector, $\bar{\mathfrak{x}}$, and a natural parameter, $\mathfrak{g}$, are parameterized via an arclength parameter, s, and defined such that: $\bar{\mathfrak{x}}(s)$

and $\mathfrak{g}(s)$. Equation (3.42) is rewritten as: $\bar{F}(\bar{\mathfrak{x}}(s), \mathfrak{g}(s)) = \bar{0}$ and the tangent space is defined as the derivative with respect to the arclength parameter, s, such that,

$$\frac{\partial \bar{F}}{\partial \bar{\mathfrak{x}}(s)} \frac{\partial \bar{\mathfrak{x}}(s)}{\partial s} + \frac{\partial \bar{F}}{\partial \mathfrak{g}(s)} \frac{\partial \mathfrak{g}(s)}{\partial s} = \bar{0}, \tag{3.43}$$

where the tangent space is defined via: $\left[\frac{\partial \bar{\mathfrak{x}}(s)}{\partial s}; \frac{\partial \mathfrak{g}(s)}{\partial s}\right]$; recalling that $[;]$ represent vertical vector concatenation. Note that Equation (3.43) is also written in matrix form as,

$$\begin{bmatrix} \frac{\partial \bar{F}}{\partial \bar{\mathfrak{x}}(s)} & \frac{\partial \bar{F}}{\partial \mathfrak{g}(s)} \end{bmatrix} \begin{bmatrix} \frac{\partial \bar{\mathfrak{x}}(s)}{\partial s} \\ \frac{\partial \mathfrak{g}(s)}{\partial s} \end{bmatrix} = \bar{0}, \tag{3.44}$$

where, it is observed, that the tangent space of the curve is in the null space of the Jacobian of the targeting problem. Recall that a general free-variable vector, $\bar{\mathfrak{X}}$, is defined as: $\bar{\mathfrak{X}} = [\bar{\mathfrak{x}}; \mathfrak{g}]$, and the Jacobian is denoted as: $\mathbf{D}\bar{\mathbf{F}} = \frac{\partial \bar{F}}{\partial \bar{\mathfrak{X}}}$ from Equation (3.28). The dimension of the tangent space associated with an $n_f \times n_t$ Jacobian matrix is computed through the rank-nullity theorem [58],

$$\text{rank}\left(\mathbf{D}\bar{\mathbf{F}}\right) + \text{nullity}\left(\mathbf{D}\bar{\mathbf{F}}\right) = n_t, \tag{3.45}$$

where n_t is the dimension of the free-variable vector, $n_t = \dim\left(\bar{\mathfrak{X}}\right)$. An additional pseudo-arclength condition is included in the constraint vector [60],

$$\bar{F}_{\text{pseudo}} = \frac{\partial \bar{\mathfrak{x}}}{\partial s}\bigg|_{s_0}^{T} (\bar{\mathfrak{x}}_1 - \bar{\mathfrak{x}}_0) + \frac{\partial \mathfrak{g}}{\partial s}\bigg|_{s_0} (\mathfrak{g}_1 - \mathfrak{g}_0) - (s_1 - s_0) = 0, \tag{3.46}$$

where the derivatives $\frac{\partial \bar{\mathfrak{x}}}{\partial s}$ and $\frac{\partial \mathfrak{g}}{\partial s}$ correspond to the free-variable vector and the natural parameter, respectively, and are evaluated at the initial solution corresponding to $s = s_0$. The step size associated with the continuation scheme is denoted as: $\Delta s = s_1 - s_0$. An expanded constraint vector is given as,

$$\bar{F}_c = \begin{bmatrix} \bar{F} \\ \bar{F}_{\text{pseudo}} \end{bmatrix}. \tag{3.47}$$

Pseudo-arclength continuation is best implemented with a $n_f \times n_t$ Jacobian where $n_f = n_t - 1$, that is, the Jacobian has a one-dimensional null space. In this scenario, an expanded Jacobian is formulated such that,

$$\mathbf{D\bar{F}_c} = \begin{bmatrix} \mathbf{D\bar{F}} \\ \left.\frac{\partial \bar{\mathfrak{x}}}{\partial s}\right|_{s_0}^{T} \quad \left.\frac{\partial \mathfrak{g}}{\partial s}\right|_{s_0} \end{bmatrix} \tag{3.48}$$

where the last row is the derivative of the pseudo-arclength constraint in Equation (3.46). Note that this expanded Jacobian is a square matrix so that a unique solution exists and Newton's method is solved via Equation (3.36). One example, illustrated in Figure 3.4, presents an initial solution, $\{\bar{\mathfrak{x}}_0, \mathfrak{g}_0\}$, and its associated the tangent line, plotted as a dashed red line. A surface normal to the tangent surface is parameterized via s, and a new solution, corresponding to $\{\bar{\mathfrak{x}}_1, \mathfrak{g}_1\}$, lies on the normal surface at a distance Δs from the initial solution. One of the benefits of pseudo-arclength continuation is improved convergence through

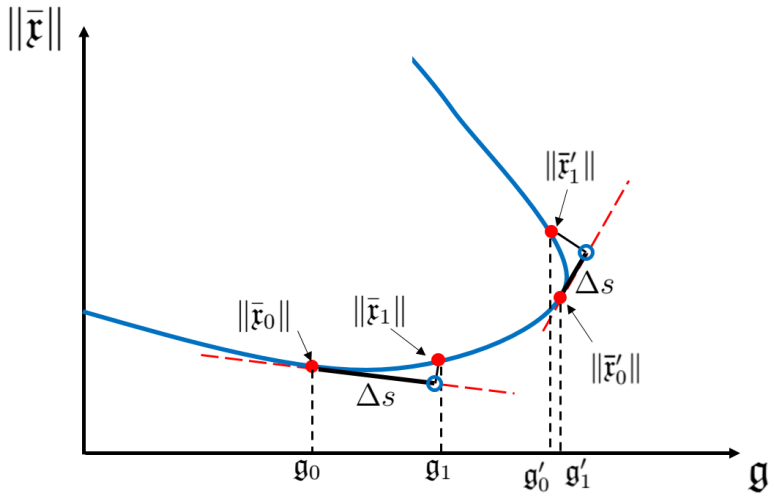

Figure 3.4. : Pseudoarclength continuation schematic. Pseudo-arclength continuation has improved convergence through turning points. Figure adapted from [60]

turning points as depicted via the initial solution, $\{\bar{\mathfrak{x}}_0', \mathfrak{g}_0'\}$, and the final solution, $\{\bar{\mathfrak{x}}_1', \mathfrak{g}_1'\}$, in Figure 3.4. Convergence challenges associated with the continuation scheme are mitigated by changing the step size, Δs, or by introducing an attenuation factor to the corrections process, i.e., Newton's method. Note that the step size is a parameter along the tangent surface of the curve and, depending on the targeting problem, it is difficult to have insightful

information on selecting an appropriate step size that aids convergence. In this investigation, pseudo-arclength and natural parameter continuation are implemented in the construction of periodic orbits, quasi-periodic orbits, and feasible transfers in the Sun-Earth system.

3.3 Periodic Orbits

Periodic orbits provide insightful information about predictable long-term behavior in a dynamical system. There is no closed-form analytical solution to the CRTBP, therefore trajectories are often numerically propagated. These trajectories are solutions to the equations of motion corresponding to the CRTBP, but they don't offer insightful information about the overall system. Periodic orbits are trajectories with repeatable flow such that: $\bar{\phi}(\bar{\mathcal{X}}_0, T_p) = \bar{\phi}(\bar{\mathcal{X}}_0, 0)$, where T_p is the corresponding period of the orbit. The existence of periodic orbits in time-invariant systems and systems that are periodic in time is further explored in Szebehely [24]. In this investigation, transfers are generated near the collinear Lagrange points L_1 and L_2. Linear stability analysis of the collinear Lagrange points in the CRTBP classifies them as center $\times$ center $\times$ saddle. Periodic motion, and quasi-periodic motion, exists within the center subspace associated with a collinear Lagrange point. Recalling that there is no closed-form analytical solution to the CRTBP, numerical methods are employed to compute periodic orbits. Happala provides a discussion about correcting for periodicity via the Mirror Theorem with a single-shooter [62]. In this investigation, periodic orbits are computed via a multiple-shooting method, see Figure 3.5 for an illustration. The objective is to enforce periodicity at the boundaries and state continuity along the trajectory. A multidimensional Newton's method is implemented to correct for a solution with the constraint vector written as,

$$\bar{F} = \begin{bmatrix} \bar{\mathcal{X}}_0(T_a) - \bar{\mathcal{X}}_1(0) \\ \bar{\mathcal{X}}_1(T_a) - \bar{\mathcal{X}}_2(0) \\ \bar{F}_{\text{period}} \end{bmatrix}, \tag{3.49}$$

where T_a is the propagation time for each trajectory segment such that: $T_a = \frac{T_p}{n_o}$, and $\bar{F}_{\text{period}}$ is the periodicity constraint defined as,

$$\bar{F}_{\text{period}} = \begin{bmatrix} x_2(T_a) - x_0(0) \\ y_2(T_a) - y_0(0) \\ z_2(T_a) - z_0(0) \\ \dot{x}_2(T_a) - \dot{x}_0(0) \\ \dot{z}_2(T_a) - \dot{z}_0(0) \end{bmatrix}. \tag{3.50}$$

For this corrector setup, the trajectory is divided into n_o arc segments. The existence of an integral of motion is an implicit constraint in the corrections process. Recall that the existence of an integral of motion reduces the dimension of the phase-space of a system by one and the phase-space in the CRTBP is six-dimensional, such that, at a fixed Jacobi Constant, the phase-space observed is five-dimensional. To constrain for periodicity, the components of the final state, $\bar{\mathcal{X}}_2(T_a)$, and the initial state, $\bar{\mathcal{X}}_0(0)$, must match and have the same Jacobi Constant value. Therefore, at a fixed Jacobi constant value, only five components of the final and initial states along the trajectory need to match. The free-variable vector is stated as,

$$\bar{\mathfrak{X}} = \begin{bmatrix} \bar{\mathcal{X}}_0(0) \\ \bar{\mathcal{X}}_1(0) \\ \bar{\mathcal{X}}_2(0) \\ T_a \end{bmatrix}. \tag{3.51}$$

The dimension of the constraint and free-variable vector are given as: $n_t = 19$ and $n_f = 17$, respectively. In the example illustrated by Figure 3.5, the orbit trajectory is subdivided into three segments where each segment has the same propagation time, T_a. A general case is derived for an orbit trajectory subdivided into n_0 segments, each sharing a propagation time of T_a, such that the dimensions of the constraint and free-variable vectors have defined dimensions: $n_f = 6n_o - 1$ and $n_t = 6n_o + 1$, respectively. In a general periodic orbit corrections process implementing a multiple-shooting method, the problem is underconstrained, that is, $n_f < n_t$. Therefore, a corrected periodic orbit is a minimum-norm solution to the multiple-

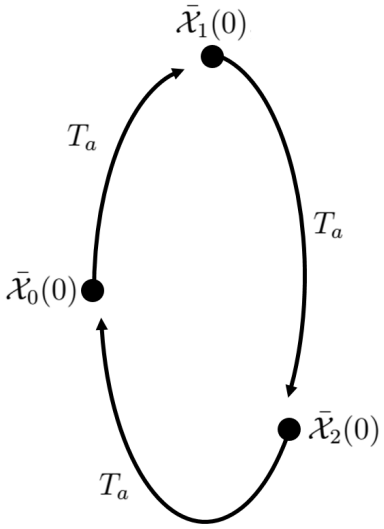

Figure 3.5. : Multiple-shooter setup to compute for periodicity in the CRTBP model

shooting problem described, leveraging Equation (3.35). The Jacobian associated with the constraint and free-variable vector in Equations (3.49) and (3.51), respectively, is denoted as,

$$\mathbf{D}\bar{\mathbf{F}} = \begin{bmatrix} \frac{\partial \bar{\mathcal{X}}_0(T_a)}{\partial \bar{\mathcal{X}}_0(0)} & -\mathbf{I}_{6,6} & \mathbf{0}_{6,6} & \frac{\partial \bar{\mathcal{X}}_0}{\partial t}\Big|_{T_a} \\ \mathbf{0}_{6,6} & \frac{\partial \bar{\mathcal{X}}_1(T_a)}{\partial \bar{\mathcal{X}}_1(0)} & -\mathbf{I}_{6,6} & \frac{\partial \bar{\mathcal{X}}_1}{\partial t}\Big|_{T_a} \\ \frac{\partial \bar{F}_{\text{period}}}{\partial \bar{\mathcal{X}}_0(0)} & \mathbf{0}_{5,6} & \frac{\partial \bar{F}_{\text{period}}}{\partial \bar{\mathcal{X}}_2(0)} & \frac{\partial \bar{F}_{\text{period}}}{\partial t}\Big|_{T_a} \end{bmatrix}, \tag{3.52}$$

where the partial derivative for the periodicity constraint vector are,

$$\frac{\partial \bar{F}_{\text{period}}}{\partial \bar{\mathcal{X}}_0(0)} = \begin{bmatrix} -1 & 0 & 0 & 0 & 0 & 0 \\ 0 & -1 & 0 & 0 & 0 & 0 \\ 0 & 0 & -1 & 0 & 0 & 0 \\ 0 & 0 & 0 & -1 & 0 & 0 \\ 0 & 0 & 0 & 0 & 0 & -1 \end{bmatrix}, \tag{3.53}$$

$$\frac{\partial \bar{F}_{\text{period}}}{\partial \bar{\mathcal{X}}_2(0)} = \begin{bmatrix} \frac{\partial x_2(T_a)}{\partial x_2(0)} & \frac{\partial x_2(T_a)}{\partial y_2(0)} & \frac{\partial x_2(T_a)}{\partial z_2(0)} & \frac{\partial x_2(T_a)}{\partial \dot{x}_2(0)} & \frac{\partial x_2(T_a)}{\partial \dot{y}_2(0)} & \frac{\partial x_2(T_a)}{\partial \dot{z}_2(0)} \\ \frac{\partial y_2(T_a)}{\partial x_2(0)} & \frac{\partial y_2(T_a)}{\partial y_2(0)} & \frac{\partial y_2(T_a)}{\partial z_2(0)} & \frac{\partial y_2(T_a)}{\partial \dot{x}_2(0)} & \frac{\partial y_2(T_a)}{\partial \dot{y}_2(0)} & \frac{\partial y_2(T_a)}{\partial \dot{z}_2(0)} \\ \frac{\partial z_2(T_a)}{\partial x_2(0)} & \frac{\partial z_2(T_a)}{\partial y_2(0)} & \frac{\partial z_2(T_a)}{\partial z_2(0)} & \frac{\partial z_2(T_a)}{\partial \dot{x}_2(0)} & \frac{\partial z_2(T_a)}{\partial \dot{y}_2(0)} & \frac{\partial z_2(T_a)}{\partial \dot{z}_2(0)} \\ \frac{\partial \dot{x}_2(T_a)}{\partial x_2(0)} & \frac{\partial \dot{x}_2(T_a)}{\partial \dot{x}_2(0)} & \frac{\partial \dot{x}_2(T_a)}{\partial z_2(0)} & \frac{\partial \dot{x}_2(T_a)}{\partial \dot{x}_2(0)} & \frac{\partial \dot{x}_2(T_a)}{\partial \dot{y}_2(0)} & \frac{\partial \dot{x}_2(T_a)}{\partial \dot{z}_2(0)} \\ \frac{\partial \dot{z}_2(T_a)}{\partial x_2(0)} & \frac{\partial \dot{z}_2(T_a)}{\partial y_2(0)} & \frac{\partial \dot{z}_2(T_a)}{\partial z_2(0)} & \frac{\partial \dot{z}_2(T_a)}{\partial \dot{x}_2(0)} & \frac{\partial \dot{z}_2(T_a)}{\partial \dot{y}_2(0)} & \frac{\partial \dot{z}_2(T_a)}{\partial \dot{z}_2(0)} \end{bmatrix}, \tag{3.54}$$

$$\left.\frac{\partial \bar{F}_{\text{period}}}{\partial t}\right|_{T_a} = \begin{bmatrix} \dot{x}_2(T_a) \\ \dot{y}_2(T_a) \\ \dot{z}_2(T_a) \\ \ddot{x}_2(T_a) \\ \ddot{z}_2(T_a) \end{bmatrix}, \tag{3.55}$$

where, it is recognized that, the components of $\frac{\partial \bar{F}_{\text{period}}}{\partial \bar{\mathcal{X}}_2(0)}$ are the components of the STM defined in Equation (3.23). Szehebely presents methods to generate initial guesses for periodic orbits near the collinear Lagrange points via linearization [24]. Additionally, periodic orbits are constructed near the primary bodies by leveraging Two-Body approximations as initial guesses [63]. The corrections process generates periodic orbits in the CRTBP model and is expanded to construct families of periodic orbits.

Periodic orbits in the CRTBP model exist as one-parameter orbit families. A numerical corrections process is derived to compute periodic orbits in the CRTBP via a multiple-shooting strategy. However, from Szehebely, one-parameter families of periodic orbits exist in the CRTBP model [24]. Numerical continuation techniques are leveraged to construct families of periodic orbits in the CRTBP model. The multiple-shooting method for periodicity,

illustrated in Figure 3.5, does not uniquely identify a periodic orbit. For example, a corrected periodic orbit from Figure 3.5 has associated corrected states, $\{\bar{\mathcal{X}}_0^c(0), \bar{\mathcal{X}}_1^c(0), \bar{\mathcal{X}}_2^c(0)\}$, with a defined period: $T_p = 3T_a$; however the following set of states, $\{\bar{\mathcal{X}}_0^c(T_s), \bar{\mathcal{X}}_1^c(T_s), \bar{\mathcal{X}}_2^c(T_s)\}$, also correspond to the same periodic orbit where T_s is defined as: $T_s \in \mathbb{R}$. The alternative states, i.e., $\{\bar{\mathcal{X}}_{\mathrm{j}}^c(T_s)\}$, are the propagated corrected states of $\{\bar{\mathcal{X}}_{\mathrm{j}}^c(0)\}$ by a time T_s. Note that the period of the orbit does not change, but the states in the corrections process are changed. A phasing constraint is included during the periodic orbit continuation process to mitigate any corrections challenges due to nonuniqueness. A simple phasing constraint is implemented by fixing certain components of a state, $\bar{\mathcal{X}}_{\mathrm{j}}(0)$, throughout the corrections process. For example, the y-component of the initial state, $\bar{\mathcal{X}}_0(0)$, is set to zero and the x-component is fixed so that the constraint vector in Equation (3.49) is expanded, such that,

$$\bar{F} = \begin{bmatrix} \bar{\mathcal{X}}_0(T_a) - \bar{\mathcal{X}}_1(0) \\ \bar{\mathcal{X}}_1(T_a) - \bar{\mathcal{X}}_2(0) \\ \bar{F}_{\text{period}} \\ x_0(0) - x_d \\ y_0(0) \end{bmatrix}, \tag{3.56}$$

where x_d is the desired value for the x-component of the initial state. Note that the free-variable vector, stated in Equation (3.51), is appended with the variable x_d. Now, the Jacobian is written as,

$$\mathbf{D}\bar{\mathbf{F}} = \begin{bmatrix} \frac{\partial \bar{\mathcal{X}}_0(T_a)}{\partial \bar{\mathcal{X}}_0(0)} & -\mathbf{I}_{6,6} & \mathbf{0}_{6,6} & \frac{\partial \bar{\mathcal{X}}_0}{\partial t}\Big|_{T_a} & 0 \\ \mathbf{0}_{6,6} & \frac{\partial \bar{\mathcal{X}}_1(T_a)}{\partial \bar{\mathcal{X}}_1(0)} & -\mathbf{I}_{6,6} & \frac{\partial \bar{\mathcal{X}}_1}{\partial t}\Big|_{T_a} & 0 \\ \frac{\partial \bar{F}_{\text{period}}}{\partial \bar{\mathcal{X}}_0(0)} & \mathbf{0}_{5,6} & \frac{\partial \bar{F}_{\text{period}}}{\partial \bar{\mathcal{X}}_2(0)} & \frac{\partial \bar{F}_{\text{period}}}{\partial t}\Big|_{T_a} & 0 \\ [1,0,0,0,0,0] & \mathbf{0}_{1,6} & \mathbf{0}_{1,6} & 0 & -1 \\ [0,1,0,0,0,0] & \mathbf{0}_{1,6} & \mathbf{0}_{1,6} & 0 & 0 \end{bmatrix}. \tag{3.57}$$

Observe that, in this formulation, the position of the first node, $\bar{\mathcal{X}}_0(0)$, is located along the $\hat{x}$-axis. Natural parameter continuation is implemented to generate a family of periodic orbits by varying a component of the free-variable vector, e.g., x_d, and by using Equation (3.51).

Alternatively, pseudo-arclength continuation is applied by introducing the pseudo-arclength constraint condition, stated in Equation (3.46), and rewritten as,

$$\bar{F}_{\text{pseudo}} = D\tilde{\mathfrak{X}}^T \left(\bar{\mathfrak{X}} - \tilde{\mathfrak{X}}\right) - \Delta s = 0, \tag{3.58}$$

where $\tilde{\mathfrak{X}}$ is the free-variable vector corresponding the previously corrected periodic orbit and $D\tilde{\mathfrak{X}}$ is the basis vector corresponding to the null space of the Jacobian in Equation (3.57). Recalling that for a periodic orbit multiple-shooting scheme, with n_o segments, the rank of the Jacobian in Equation (3.57) is $6n_o+1$, and, via the Rank-Nullity Theorem, the nullity of the Jacobian is unity. Therefore, the null space, i.e., the tangent space associated with the formulated problem, is one-dimensional. Additionally, the partial of the pseudo-arclength constraint is,

$$\frac{D\bar{F}_{\text{pseudo}}}{D\tilde{\mathfrak{X}}} = D\tilde{\mathfrak{X}}^T. \tag{3.59}$$

The pseudo-arclength constraint in Equation (3.58) and its associated Jacobian, i.e., Equation (3.59), are appended to the constraint vector in Equation (3.56) and the Jacobian matrix in Equation (3.57), respectively. The inclusion of the phasing constraint into the continuation process facilitates the generation of periodic orbit families.

The Poincaré orthogonality phasing condition is an alternative to fixing a state component on a periodic orbit [64]. Let $\bar{\mathfrak{U}}_0$ be defined as a vector containing the states corresponding to an initially corrected periodic orbit, generated via a multiple-shooting formulation illustrated in Figure 3.5, such that,

$$\bar{\mathfrak{U}}_0 = \begin{bmatrix} \bar{\mathcal{X}}_0^0(0) \\ \bar{\mathcal{X}}_1^0(0) \\ \bar{\mathcal{X}}_2^0(0) \\ \vdots \\ \bar{\mathcal{X}}_{n_o}^0(0) \end{bmatrix}, \tag{3.60}$$

then the Poincaré orthogonality phasing condition is expressed as the constraint,

$$\bar{F}_{\text{phasing}} = (\bar{\mathfrak{U}}_1 - \bar{\mathfrak{U}}_0)^T \dot{\bar{\mathfrak{U}}}_0, \tag{3.61}$$

where $\bar{\mathfrak{U}}_0$ and $\bar{\mathfrak{U}}_1$ are the collection of states associated with an initially corrected and the current periodic orbit, respectively, and $\dot{\bar{\mathfrak{U}}}_0$ is defined as,

$$\dot{\bar{\mathfrak{U}}}_0 = \begin{bmatrix} \bar{\mathfrak{f}}\left(\bar{\mathcal{X}}_0^0(0)\right) \\ \bar{\mathfrak{f}}\left(\bar{\mathcal{X}}_1^0(0)\right) \\ \bar{\mathfrak{f}}\left(\bar{\mathcal{X}}_2^0(0)\right) \\ \vdots \\ \bar{\mathfrak{f}}\left(\bar{\mathcal{X}}_{n_o}^0(0)\right) \end{bmatrix}, \tag{3.62}$$

with $\bar{\mathfrak{f}}$ defined as the vector field equation corresponding to the CRBTP model, see Equation (3.1). The orthogonality constraint is illustrated in Figure 3.6 for an initial periodic orbit consisting of states, $\{\bar{\mathcal{X}}_{\text{j}}^0\}$, and a current periodic orbit consisting of the collection of states, $\{\bar{\mathcal{X}}_{\text{j}}^1\}$. Note that in this investigation, a multiple-shooting formulation is implemented to cor-

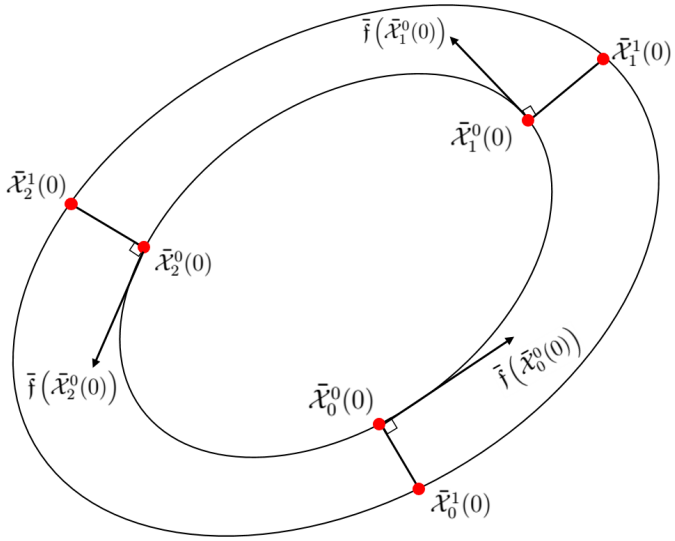

Figure 3.6. : Poincaré orthogonality constraint. Initial periodic orbit is given, via a multiple-shooting scheme, by $\{\bar{\mathcal{X}}_{\text{j}}^0\}$ and the current solution is described by the collection of states, $\{\bar{\mathcal{X}}_{\text{j}}^1\}$. Figure is adapted from [64].

rect for periodic orbits and to construct the families of periodic orbits, but the orthogonality constraint is easily modified for a single-shooting formulation. Returning to the example in Figure 3.5, a new constraint vector, $\bar{F}$, and Jacobian is formulated with the included orthogonality constraint. The free constraint vector is denoted as,

$$\bar{F} = \begin{bmatrix} \bar{\mathcal{X}}_0(T_a) - \bar{\mathcal{X}}_1(0) \\ \bar{\mathcal{X}}_1(T_a) - \bar{\mathcal{X}}_2(0) \\ \bar{F}_{\text{period}} \\ (\bar{\mathfrak{U}} - \bar{\mathfrak{U}}_0)^T \dot{\bar{\mathfrak{U}}}_0 \end{bmatrix}, \tag{3.63}$$

where the vector of the current states, $\bar{\mathfrak{U}}$, defined as,

$$\bar{\mathfrak{U}} = \begin{bmatrix} \bar{\mathcal{X}}_0(0) \\ \bar{\mathcal{X}}_1(0) \\ \bar{\mathcal{X}}_2(0) \end{bmatrix}, \tag{3.64}$$

and a previously corrected periodic orbit has associated states, $\bar{\mathfrak{U}}_0$ and $\dot{\bar{\mathfrak{U}}}_0$, stated as,

$$\bar{\mathfrak{U}}_0 = \begin{bmatrix} \bar{\mathcal{X}}_0^0(0) \\ \bar{\mathcal{X}}_1^0(0) \\ \bar{\mathcal{X}}_2^0(0) \end{bmatrix}, \tag{3.65}$$

$$\dot{\bar{\mathfrak{U}}}_0 = \begin{bmatrix} \bar{\mathfrak{f}}\left(\bar{\mathcal{X}}_0^0(0)\right) \\ \bar{\mathfrak{f}}\left(\bar{\mathcal{X}}_1^0(0)\right) \\ \bar{\mathfrak{f}}\left(\bar{\mathcal{X}}_2^0(0)\right) \end{bmatrix}. \tag{3.66}$$

The corresponding Jacobian matrix is written as,

$$\mathbf{D}\bar{\mathbf{F}} = \left[\begin{array}{ccc|c} \frac{\partial \bar{\mathcal{X}}_0(T_a)}{\partial \bar{\mathcal{X}}_0(0)} & -\mathbf{I}_{6,6} & \mathbf{0}_{6,6} & \frac{\partial \bar{\mathcal{X}}_0}{\partial t}\Big|_{T_a} \\ \mathbf{0}_{6,6} & \frac{\partial \bar{\mathcal{X}}_1(T_a)}{\partial \bar{\mathcal{X}}_1(0)} & -\mathbf{I}_{6,6} & \frac{\partial \bar{\mathcal{X}}_1}{\partial t}\Big|_{T_a} \\ \frac{\partial \bar{F}_{\text{period}}}{\partial \bar{\mathcal{X}}_0(0)} & \mathbf{0}_{5,6} & \frac{\partial \bar{F}_{\text{period}}}{\partial \bar{\mathcal{X}}_2(0)} & \frac{\partial \bar{F}_{\text{period}}}{\partial t}\Big|_{T_a} \\ \hline \multicolumn{3}{c|}{\dot{\bar{\mathfrak{U}}}_0^T} & 0 \end{array}\right]. \tag{3.67}$$

The periodicity targeting problem formulated with a phasing constraint, i.e., expressed via Equations (3.56) and (3.63), are applicable for the example illustrated in Figure 3.5. Families of periodic orbits are constructed via natural parameter or pseudo-arclength continuation. For natural parameter continuation, the natural parameter selected is $x_0(0)$, i.e., the x-component of the initial state in the free-variable vector stated in Equation (3.51). Additionally, a pseudo-arclength continuation scheme is implemented by including Equations (3.58) and (3.59) into Equations (3.63) and (3.67), respectively. Families of periodic orbits in the CRTBP model are constructed with these continuation strategies.

Families of periodic orbits are constructed in the Sun-Earth CRTBP model. In this investigation, families of Lyapunov, vertical, and halo periodic orbits are generated near the Sun-Earth collinear L_1 and L_2 Lagrange points. The planar Lyapunov orbit family is constructed via a multiple-shooter strategy with an initial guess from the planar linearization near the L_1 and L_2 points [24]. The planar Lyapunov orbit families near the L_1 and L_2 vicinity are plotted in Figure 3.7(a)-(b). The periodic orbits in Figure 3.7 represent a subset of the entire Lyapunov orbit family in the Sun-Earth system. The out-of-plane vertical orbits near the L_1 and L_2 Lagrange points in the Sun-Earth system are plotted in Figures 3.8(a)-(b), respectively. The spatial halo family near L_1 and L_2, plotted in Figures 3.9 and 3.10, respectively, emanate from the planar Lyapunov orbit family. Note that families of periodic orbits in Figures 3.7-3.10 are plotted via a color range corresponding to the associated Jacobi Constant value. Additional discussion regarding bifurcation from periodic orbits is provided by Zimovan [65] and Campbell [66].

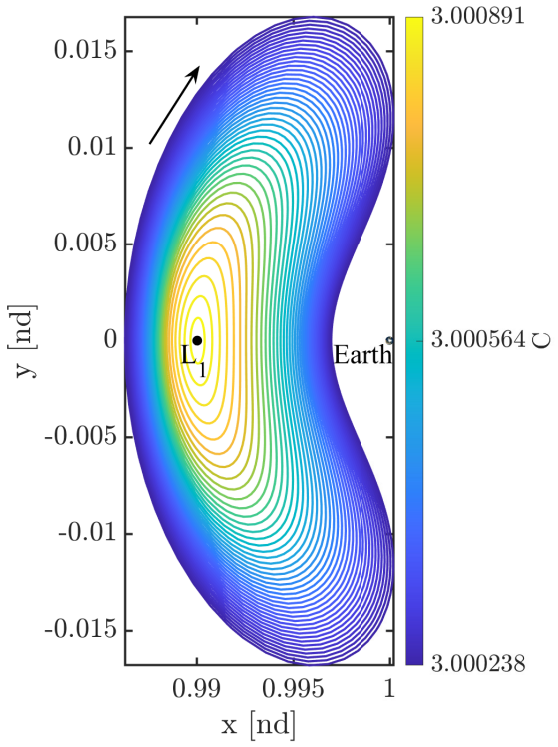

(a)

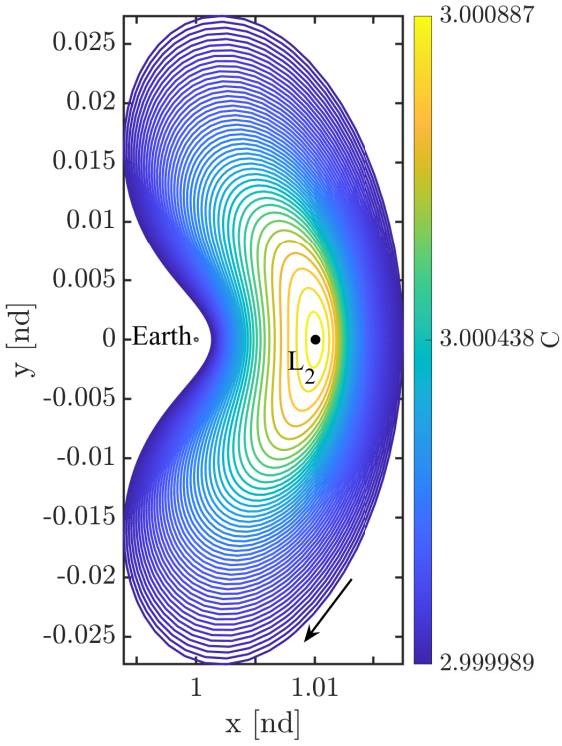

(b)

Figure 3.7. : Sun-Earth (a) L_1 Lyapunov orbit family and (b) L_2 Lyapunov orbit family

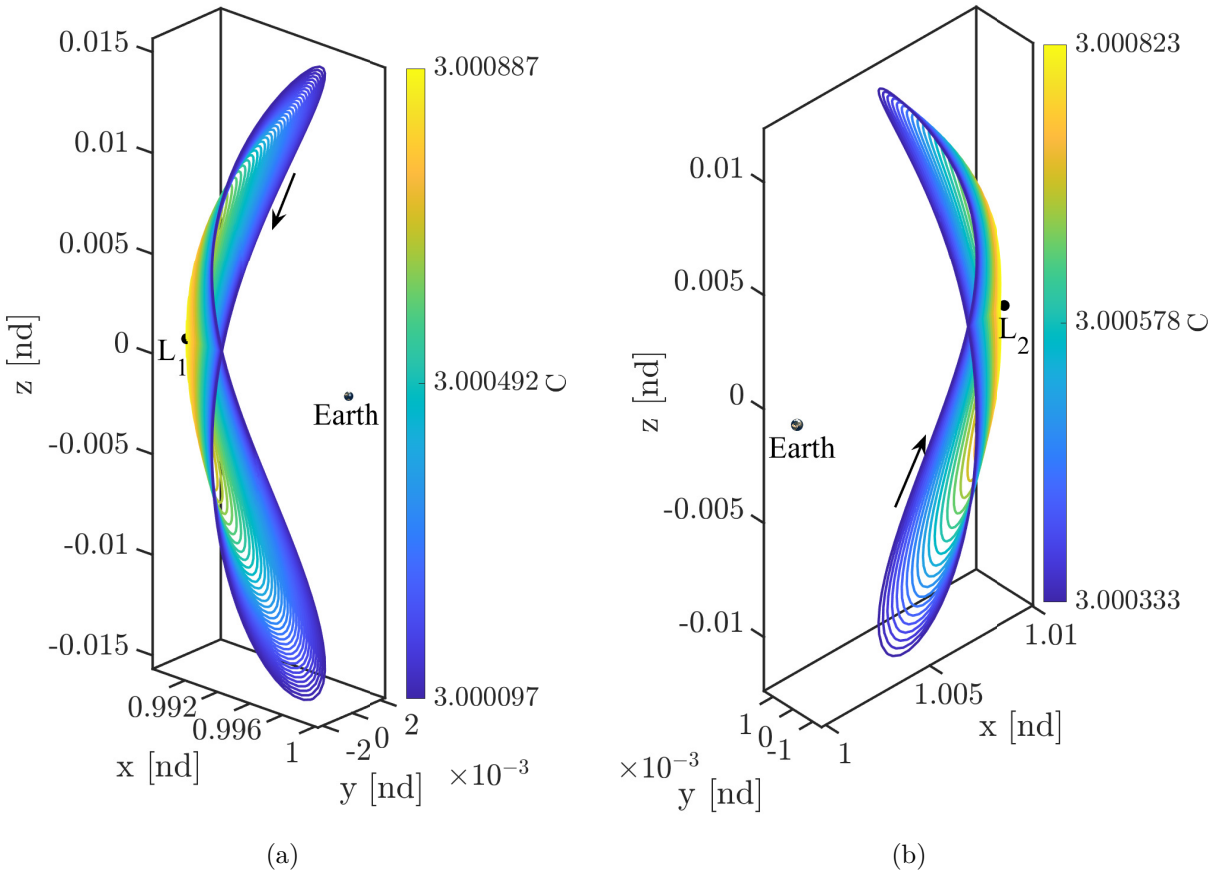

Figure 3.8. : Sun-Earth (a) L_1 vertical orbit family and (b) L_2 vertical orbit family

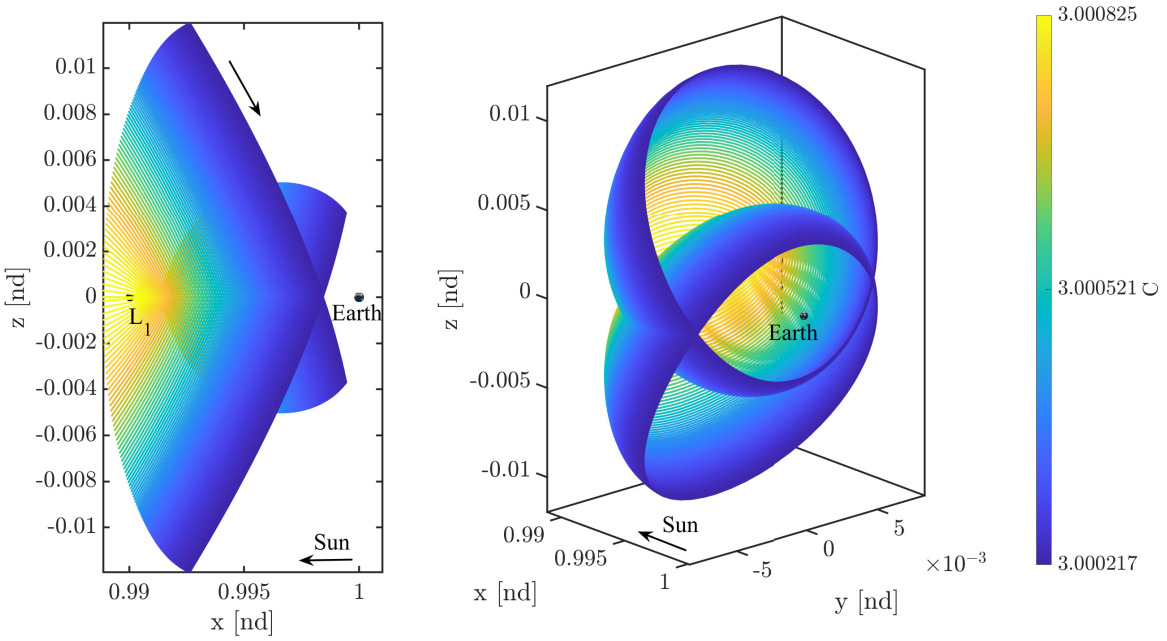

Figure 3.9. : Sun-Earth halo orbits near the L_1 Lagrange point. This subset of the halo orbit family contains both southern and northern members of the family

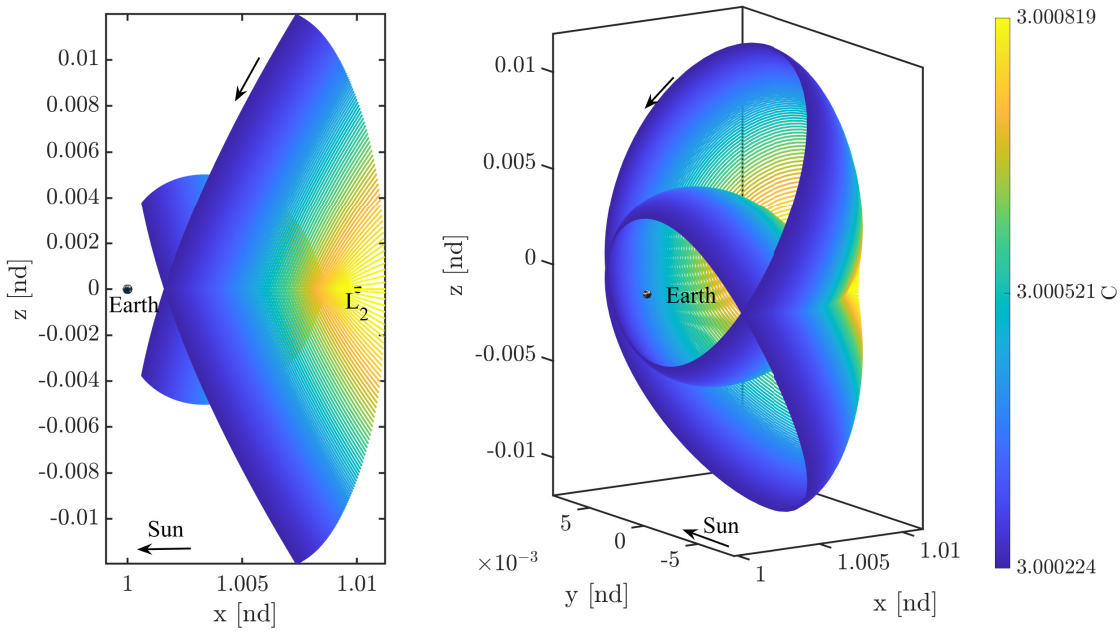

Figure 3.10. : Sun-Earth halo orbits near the L_2 Lagrange point. This represents only one subset of the entire halo orbit family

3.3.1 Stability

Lyapunov stability analysis offers insightful understanding into the local flow behavior near a periodic orbit. Periodic orbits are solutions to the vector field, i.e., the equations of motion, corresponding to the CRTBP model and represent long-term repeatable behavior. The geometries offered by families of periodic orbits, in the CRTBP, are often leveraged to construct efficient transfers in a simplified Three-Body model, which are straightforwardly corrected in a higher-fidelity model. Additionally, an analysis of the flow near the vicinity of a periodic orbit exposes important dynamical behavior. Recall that the flow near equilibrium points, i.e., Lagrange points, is analyzed through Lyapunov stability and the linear approximation near a point, $\bar{\mathcal{X}}^*$, is provided in Equations (3.17) and (3.18). Note that the matrix, $\mathbf{A}(t)$, has constant entries when observing equilibrium points, however, $\mathbf{A}(t)$ is time-varying and periodic for periodic orbits. For periodic orbits, maps are constructed to investigate stability properties associated with the local flow behavior. Maps are introduced into a dynamical system to convert a continuous time system into a discrete time system and offer insightful observations of the global flow of a dynamical system. Stroboscopic maps are implemented to observe the local flow behavior near periodic orbits. Stroboscopic maps are constructed by collecting the states, $\bar{\mathcal{X}}_{\text{map}}$, of a flow, $\bar{\phi}(\bar{\mathcal{X}}_0, t)$, at discrete time intervals, $n_{\text{map}}T_{\text{map}}$, where n_{map} is the number of crossings to the map, defined as $n_{\text{map}} = \{0, 1, 2, \ldots, \infty\}$, and T_{map} is the mapping time. Let the Poincaré map for a periodic orbit be defined as $\mathfrak{P}(\bar{\mathcal{X}}^*) = \bar{\phi}(\bar{\mathcal{X}}^*, T_p)$, where T_p is the orbital period and $\bar{\mathcal{X}}^*$ is termed a fixed point, such that the linearized state variation of the flow, i.e., $\bar{\phi}(\bar{\mathcal{X}}^*, T_p)$, associated with this fixed point is written as,

$$\Delta\bar{\mathcal{X}}(n_{\text{map}}T_p) = \mathbf{\Phi}(n_{\text{map}}T_p, 0)\Delta\bar{\mathcal{X}}(0), \tag{3.68}$$

where T_p is the orbital period, $\mathbf{\Phi}(n_{\text{map}}T_p, 0)$ is the state transition matrix after time $n_{\text{map}}T_p$, and n_{map} is the number of crossings onto the stroboscopic map. Note that the state transition matrix $\mathbf{\Phi}(n_{\text{map}}T_p, 0)$ is simplified to,

$$\mathbf{\Phi}(n_{\text{map}}T_p, 0) = \mathbf{\Phi}(T_p, 0)^{n_{\text{map}}}. \tag{3.69}$$

The state transition matrix after one revolution, one full period, is termed the monodromy matrix and defined as: $\mathbf{\Phi}(T_p, 0)$. The monodromy is also the linearization of the Poincaré map, $\mathfrak{P}$, at the fixed point of the periodic orbit. Floquet theory is implemented to determine the stability characteristic near the vicinity of a periodic orbit by analyzing the eigenstructure of its corresponding monodromy matrix. The eigenvalues, ${}^{P}\Lambda_{\text{j}}$, of the monodromy matrix, also termed the characteristic multipliers, expose the stability information near a fixed point. For a periodic orbit, there is one characteristic multiplier associated with the periodicity of the orbit and, thus, is equal to unity. The remaining characteristic multipliers determine the linear stability near the fixed point [56]. A characteristic multiplier with a value less than unity, $|{}^{P}\Lambda_{\text{j}}| < 1$, represents asymptotic linear stability near a fixed point, whereas a value greater than unity, $|{}^{P}\Lambda_{\text{j}}| > 1$, signifies unstable behavior. Characteristic multipliers with a magnitude equal to unity, $|{}^{P}\Lambda_{\text{j}}| = 1$, indicate marginal stability in a linear sense. An important property of the characteristic multipliers of a monodromy matrix in a time-invariant system, e.g., the CRTBP model, is provided by Lyapunov's Theorem:

Theorem 3.3.1. ***Lyapunov's Theorem*** *[54] If ${}^{P}\Lambda$ is an eigenvalue of the monodromy matrix, $\Phi(T, 0)$, in a time-invariant system, then ${}^{P}\Lambda^{-1}$ is also an eigenvalue.*

Eigenvalues of the monodromy matrix, i.e., characteristic multipliers, appear in reciprocal pairs. Additionally, the monodromy matrix contains real elements, so that any complex eigenvalue, ${}^{P}\Lambda$, also has an accompanying complex conjugate, ${}^{P}\Lambda^{\dagger}$, where † is a complex conjugate operator [58]. In summary, periodic orbits in the CRTBP model have at least one pair of characteristic multipliers equal to unity and two pairs of characteristic multipliers which determine the stability characteristics of the fixed point associated with the orbit.

3.3.2 Invariant Subspaces Near Periodic Orbits

Linear stability analysis near periodic orbits reveal insightful dynamical behavior that is leveraged to construct efficient transfers in the CRTBP model. Similar to the invariant subspaces for Lagrange points, invariant subspaces associated with a periodic orbit are identified via the linearized Poincaré map, i.e., the monodromy matrix, near the fixed point of the periodic orbit. Guckenheimer categorizes the hyperbolic invariant subspaces via the following theorem [56]:

Theorem 3.3.2. ***Stable Manifold Theorem for Fixed Points*** *Let $\mathfrak{P}$ be a diffeomorphism with a hyperbolic fixed point $\bar{\mathcal{X}}^*$. Then, there are local stable and unstable manifolds $\mathfrak{W}^S_{\text{loc}}$ and $\mathfrak{W}^U_{\text{loc}}$, tangent to the eigenspaces $P^S_{\bar{\mathcal{X}}^*}$ and $P^U_{\bar{\mathcal{X}}^*}$, respectively, of the linearized map $\mathbf{D}\mathfrak{P}(\bar{\mathcal{X}}^*)$ and of corresponding dimensions.*

The local eigenspaces are identified via eigenstructure of the linearized mapping $\mathbf{D}\mathfrak{P}(\bar{\mathcal{X}}^*)$, i.e., the monodromy matrix, as:

- Stable eigenspace is associated with $\|{}^P\lambda_{\text{j}}\| < 1$ where $\text{j} \in \{1, \ldots, n_s\}$. The local subspace is defined as $\mathcal{E}^S_{\bar{\mathcal{X}}^*} = \text{span}\{{}^P\bar{\Psi}^S_1, \ldots, {}^P\bar{\Psi}^S_{n_s}\}$ and has dimension n_s.
- Unstable eigenspace is associated with $\|{}^P\lambda_{\text{j}}\| > 1$ where $\text{j} \in \{1, \ldots, n_u\}$. The local subspace is defined as $\mathcal{E}^U_{\bar{\mathcal{X}}^*} = \text{span}\{{}^P\bar{\Psi}^S_1, \ldots, {}^P\bar{\Psi}^S_{n_u}\}$ and has dimension n_u.
- Center eigenspace is associated with $\|{}^P\lambda_{\text{j}}\| = 1$ where $\text{j} \in \{1, \ldots, n_c\}$. The local subspace is defined as $\mathcal{E}^C_{\bar{\mathcal{X}}^*} = \text{span}\{{}^P\bar{\Psi}^S_1, \ldots, {}^P\bar{\Psi}^S_{n_c}\}$ and has dimension n_c.

The dimensions of the eigenspaces span the phase-space of the dynamical system, i.e., CRTBP model, such that: $n_s + n_u + n_c = 6$. A state along the local stable manifold, $\mathfrak{W}^S_{\text{loc}}$, asymptocially approaches a fixed point, $\bar{\mathcal{X}}^*$, associated with a periodic orbit as $t \to \infty$.

Conversely, a propagated state along the local unstable manifold $\mathfrak{W}^U_{\text{loc}}$ approaches the fixed point as $t \to -\infty$. A state along the local stable manifold is approximated via,

$$\bar{\mathcal{X}}^S = \bar{\mathcal{X}}^* \pm \eta \frac{{}^P\bar{\Psi}^S_{\text{j}}}{\|{}^P\bar{\Psi}^S_{\text{j},r}\|}, \tag{3.70}$$

where ${}^P\bar{\Psi}^S_{\text{j}}$ is a vector in the direction of the local stable manifold, i.e., ${}^P\bar{\Psi}^S_{\text{j}} \in \mathfrak{W}^S_{\text{loc}}$. A step-off parameter, η, is introduced to transition from a fixed point $\bar{\mathcal{X}}^*$ to a point in the direction of the stable manifold, where the direction is dictated by the eigenvector ${}^P\bar{\Psi}^S_{\text{j}}$. The value of the step-off parameter η is important in the approximation of the local manifold state. If η is large, then the state $\bar{\mathcal{X}}^S$ may not be on the local stable manifold, likewise, if η is too small then it may require more propagation time to approach the fixed point. Note that ${}^P\bar{\Psi}^S_{\text{j}}$ is normalized by the magnitude of its positional components, ${}^P\bar{\Psi}^S_{\text{j},r}$. An eigenvector ${}^P\bar{\Psi}$ is also composed as: ${}^P\bar{\Psi} = [{}^P\bar{\Psi}_r; {}^P\bar{\Psi}_v]$, where ${}^P\bar{\Psi}_r$ is a three-dimensional vector that contains the position components and ${}^P\bar{\Psi}_v$ contains the corresponding velocity components. In Equation (3.70), the sign value, $\pm$, indicates that the state $\bar{\mathcal{X}}^S$ is on one of the half-manifolds that compose the entire manifold structure. The state along the local unstable manifold is evaluated in a similar process. Global analogs of the local hyperbolic manifolds are constructed via propagation of the local stable and unstable manifold states in reverse and forward time, respectively. So far, states along the local manifolds are approximated at a specified fixed point along a periodic orbit. However, the eigenvectors along the periodic orbit, i.e., along different locations of the orbit, are transitioned via the STM, e.g., let ${}^P\bar{\Psi}(0)$ be an eigenvector computed at the fixed point, $\bar{\mathcal{X}}^*(0)$, then,

$${}^P\bar{\Psi}(t) = \mathbf{\Phi}(t,0)^P\ \bar{\Psi}(0), \tag{3.71}$$

where $\mathbf{\Phi}(t,0)$ is the state transition matrix from the fixed point $\bar{\mathcal{X}}^*(0)$. Care should be taken to normalize a transitioned eigenvector, i.e, ${}^P\bar{\Psi}(t)$, before evaluating the local manifold state via Equation (3.70). From Guckenhemier [56], the dimensions of local stable and unstable manifolds are always one degree higher than the dimension of their respective subspaces, $\mathcal{E}^S_{\bar{\mathcal{X}}^*}$ and $\mathcal{E}^U_{\bar{\mathcal{X}}^*}$, respectively. The center subspace associated with periodic orbits

is more complex and, as opposed to the stable and unstable subspaces, can be nonunique. Further discussion regarding the stable manifold is provided by Guckenheimer [56]. In this investigation, the existence of quasi-periodic motion within the center subspace associated with periodic orbits is leveraged to generate quasi-periodic orbits near the collinear L_1 and L_2 Lagrange points. Quasi-periodic motion offers opportunities to construct trajectories with more complex geometries.

3.4 Quasi-Periodic Orbits

Quasi-periodic motion observed near the CRTBP Lagrange points offers complex geometries that facilitate the construction of efficient transfers for a range of mission design objectives. Several authors have generated quasi-periodic orbits within the context of the CRTBP model. Pernika constructed feasible quasi-periodic orbits in the Sun-Earth system for the ACE mission. McCarthy et al. generated quasi-periodic orbits in the Sun-Earth and Earth-Moon system and constructed transfers between periodic orbits via an intermediate quasi-periodic orbit [20]. Bosanac et al. cataloged families of quasi-periodic in the Sun-Earth system to facilitate mission design parameters [67]. Olikara implemented a numerical method to generate families of quasi-periodic orbits and to identify heteroclinic transfers between Earth-Moon L_1 and L_2 Lagrange points [17]. Recall that, Lagrange points, periodic orbits, and quasi-periodic orbits are dynamical structures frequently observed in the CRTBP model; these structures may also be described as invariant sets. In the context of this investigation, an invariant set is a dynamical structure in which a trajectory may flow into but not out of and may be described via a basic invariant object. A formal definition of an invariant set and invariant objects is provided by Wiggins [68]. An example of a basic invariant object is an p-dimensional Torus, $\mathfrak{T}$. Note that the dynamical structures previously discussed, i.e., the Lagrange points and periodic orbits are now defined as tori with dimensions denoted as,

- Lagrange points (Equilibrium Points) (p=0)
- Periodic orbits (p=1)

- Quasi-periodic orbits ($p \geq 2$)

A general schematic of the dynamical structures discussed as tori are plotted in Figure 3.11. The orbit along Lagrange points, periodic orbits, and quasi-periodic orbits densely cover the

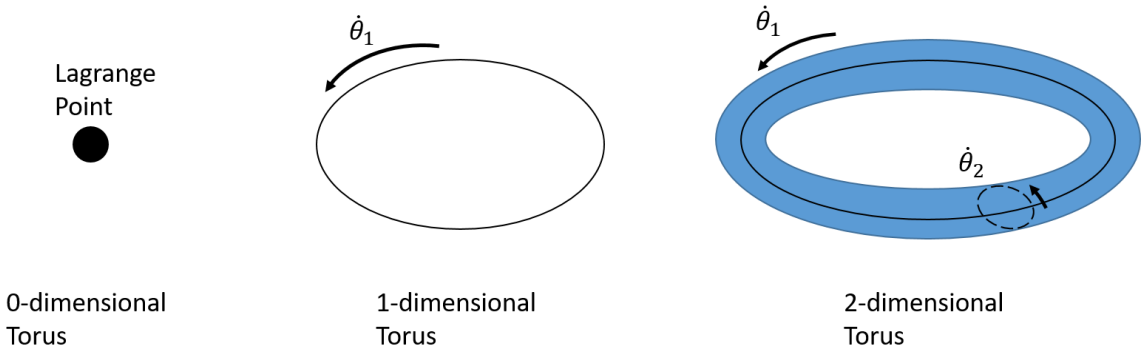

Figure 3.11. : Dynamical structures described as p-dimensional invariant tori

surface of their respective invariant tori, however an infinite amount of time is needed for tori with dimensions of $p \geq 2$, i.e., quasi-periodic orbits. A formal definition of an invariant torus, provided by Olikara [17], is denoted as,

$$\mathfrak{T} = cl\{\bar{\phi}(\bar{\mathcal{X}}_0, t) |\ t \in \mathbb{R}\}, \tag{3.72}$$

which defines the torus as the closure of the flow, $\bar{\phi}(\bar{\mathcal{X}}_0, t)$, from an initial state, $\bar{\mathcal{X}}_0$. For the stationary Lagrange points, the flow is fixed to the initial state, $\bar{\mathcal{X}}_0$, i.e., the equilibrium point. The closure of the flow corresponding to periodic orbits is defined by a finite period, T_p. In this investigation, quasi-periodic orbits are constructed from two-dimensional tori in the CRTBP model. A general p-dimensional torus, $\mathfrak{T}$, has p corresponding fundamental frequencies, $\left\{\dot{\theta}_1, \dot{\theta}_2, \ldots, \dot{\theta}_{p-1}, \dot{\theta}_p\right\}$. In the case of a two-dimensional torus, the fundamental frequencies, $\dot{\theta}_1$ and $\dot{\theta}_2$, are termed as the longitudinal and latitudinal frequencies, respectively, and are plotted in Figure 3.11. A numerical process that implements a multiple-shooting scheme is leveraged to compute quasi-periodic from a two-dimensional torus. Additionally, numerical continuation facilitates the construction of quasi-periodic families near the collinear Lagrange points.

3.4.1 Numerical Computation of Quasi-Periodic Orbits

Quasi-periodic orbits in the CRTBP are constructed via a numerical algorithm that leverages a multiple-shooting scheme. In this analysis, the method for generating families of quasi-periodic orbits originates with Gómez and Mondelo and includes enhancements by Olikara and Scheeres [32], [33]. Recalling that a two-dimensional torus is characterized via two fundamental frequencies, $\dot{\theta}_1$ and $\dot{\theta}_2$, plotted in Figure 3.11; define a state on the surface of the torus, termed the torus state, as $\bar{u}$. The torus state is parameterized by the angles, θ_1 and θ_2, such that $\bar{u}\left(\theta_1, \theta_2\right)$. Note that $\bar{u}$ is a six-dimensional state, i.e., the dimension of the phase-space associated with the CRTBP. The angles, θ_{j}, are defined such that $\theta_{\mathrm{j}}(t) = \dot{\theta}_{\mathrm{j}} t$, where t is the propagation time along the torus. A complete revolution is illustrated in Figure 3.12(a) where an initial state, $\bar{u}\left(\theta_1(0), \theta_2(0)\right)$, is propagated with longitudinal time T_1. Additionally, two and fifteen revolutions are plotted in Figures 3.12(b) and 3.12(c), respectively. Observe that if a state is collected after each successive revolution in Figure 3.12(c), i.e., a black point in the plot, a black curve along the surface of the torus is identified. The black curve formed in Figure 3.12(c) is termed as the invariant curve. From the invariant tori definition, quasi-periodic motion is observed for tori with irrational frequency ratios, that is $\mathfrak{r} = \frac{\dot{\theta}_1}{\dot{\theta}_2}$, and periodic motion is observed for tori with rational frequency ratios. This behavior is observed in Figure 3.12(c), where a propagated state, $\bar{u}\left(\theta_1(t), \theta_2(t)\right)$, does not return to the initial state and will densely cover the surface of the torus as $t \to \infty$.

To numerically produce a quasi-periodic orbit, the foundation of this method is a periodic orbit in the CRTBP represented in terms of a fixed point, $\bar{\mathcal{X}}^*$. A stroboscopic map, generated with the longitudinal time T_1, is leveraged to reduce the construction of the two-dimensional torus, one that characterizes the quasi-periodic orbit, to a search for an invariant curve. The periodic time for the stroboscopic map, i.e., T_1, is associated with the period of the longitudinal frequency, $\dot{\theta}_1$, defined as $\dot{\theta}_1 = \frac{2\pi}{T_1}$ and plotted in Figure 3.11. The invariant curve is revealed through the implementation of the stroboscopic mapping as illustrated in Figure 3.12. An initial state, defined as $\bar{u}(\theta_1(0), \theta_2(0))$, is propagated along the torus and the returns to the stroboscopic map represent the invariant curve associated with

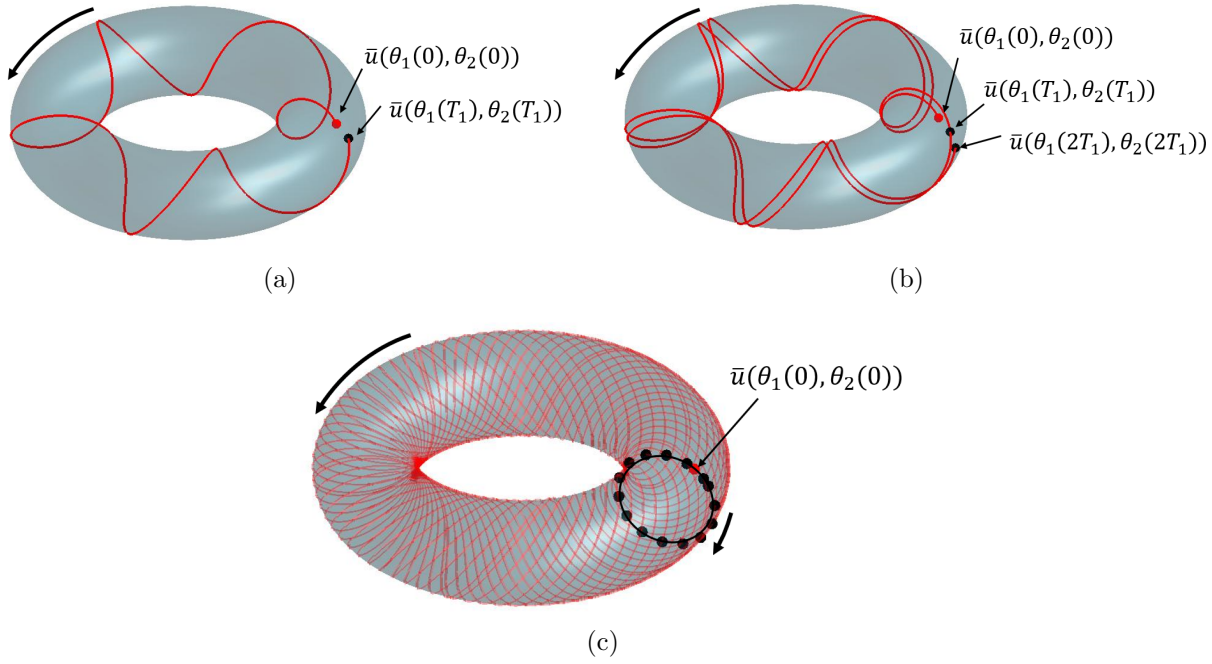

Figure 3.12. : (a) First revolution along the surface of two-dimensional torus. Initial state, $\bar{u}\,(\theta_1(0), \theta_2(0))$, is propagated with time T_1. (b) Two complete revolutions along the surface of the two-dimensional torus. (c) 15 revolutions along the surface of the torus. Invariant curve, black line, is described via a set of points collected every revolution.

a specific quasi-periodic orbit. Additionally, a state on the surface of the two-dimensional torus, in the rotating frame of the CRTBP, is defined with $\bar{\mathcal{X}}_{\text{qpo}} = \bar{u}(\theta_1, \theta_2) + \bar{\mathcal{X}}^*$, where, it is recalled that, $\bar{\mathcal{X}}^*$ is a fixed point associated with a periodic orbit. The geometry of the invariant curve associated with a specific torus is approximated via a set of n_q torus states $\bar{u}_{\text{j}}$ with $\text{j} = [1, ..., n_q]$ by using a truncated Fourier series. The number of torus states, n_q, used to approximate the invariant curve affects the accuracy of the numerical algorithm for quasi-periodic orbits. The search for an invariant curve is mathematically described by an invariance condition, such that a rotation matrix, $\mathbf{R}(-\rho)$, rotates the final state, $\bar{u}(\theta_1(T_1), \theta_2(T_1))$, on the torus back to its initial state, i.e.,

$$\mathbf{R}(-\rho)\Big[\bar{u}\Big(\theta_1(T_1), \theta_2(T_1)\Big)\Big] - \Big[\bar{u}\Big(\theta_1(0), \theta_2(0)\Big)\Big] = \mathbf{0}, \tag{3.73}$$

where $\mathbf{0}$ is a $n_q \times 6$ zero matrix and $\left[\bar{u}\right]$ represents the torus states that discretize the invariant curve such that,

$$\left[\bar{u}\Big(\theta_1(t), \theta_2(t)\Big)\right] = [\bar{u}]_t = \begin{bmatrix} \bar{u}_1^T\Big(\theta_1(t), \theta_2^1(t)\Big) \\ \bar{u}_2^T\Big(\theta_1(t), \theta_2^2(t)\Big) \\ \vdots \\ \bar{u}_{\mathrm{j}}^T\Big(\theta_1(t), \theta_2^{\mathrm{j}}(t)\Big) \end{bmatrix}, \tag{3.74}$$

where each torus state is written as a row vector and the latitudinal angle, θ_2, along the invariant curve is defined as $\theta_2^{\mathrm{j}}(0) \in [0, 2\boldsymbol{\pi}]$. The matrix, $[\bar{u}]_t$, representing the invariant curve has dimensions: $n_q \times 6$; recalling that the phase-space of the CRTBP is six-dimensional. For the stroboscopic map, $\theta_1(0) = \theta_1(T_1)$, therefore, the first return to the map occurs at $\theta_1(0)$ and the state of the first return onto the stroboscopic map, i.e., the final state in Equation (3.73), is parametrized as $\bar{u}(\theta_1(0), \theta_2(0) + \rho)$, where ρ represents a rotation angle along the invariant curve. Note that the torus states, $\bar{u}_{\mathrm{j}}$, are six-dimensional vectors and the rotation matrix, $\mathbf{R}(-\rho)$, is a $n_q \times n_q$ real matrix evaluated with elements of the Fourier series and the rotation angle $(-\rho)$[33].

Quasi-periodic orbits are numerically constructed by implementing a multiple-shooting strategy along with the invariance condition stated in Equation (3.73) [33]. In a multiple-shooting strategy, a single trajectory is divided into a series of smaller arcs which, in a numerical corrections process, facilitate the construction of a trajectory in a complex dynamical regime. Recalling that the stroboscopic map that identifies the invariant curve is constructed at times, T_1. In a multiple-shooting scheme, the propagated trajectory of a torus state along the invariant curve, i.e., $\bar{u}_{\mathrm{j}}(\theta_1(0), \theta_2^{\mathrm{j}}(0))$, is subdivided into q segments, each with an associated propagation time $\frac{T_1}{q}$. The quasi-periodic orbit, represented by a two-dimensional torus, is now characterized by torus states, $\bar{u}_{\mathrm{j}}^k$, where $k = [1, ..., q]$. A schematic of the multiple-shooting algorithm is illustrated in Figure 3.13 with the invariant curve indicated by a solid black curve. In Figure 3.13, the torus is divided into three sections, such that $q = 3$, and the invariant curve is discretized via the three torus states $\{\bar{u}_1^1, \bar{u}_2^1, \bar{u}_3^1\}$. Within the numerical corrections process, the invariant curve is termed as the first torus curve. The second and third torus curves are constructed with the set of torus

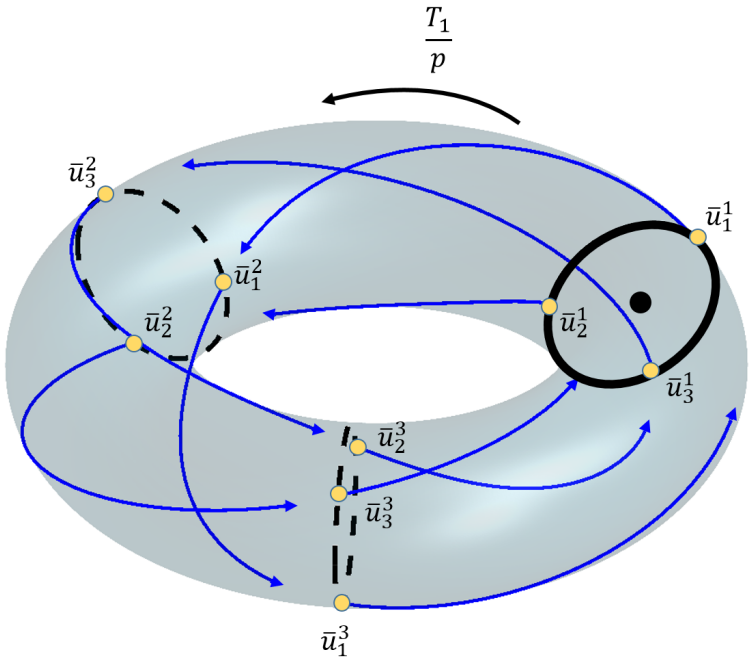

Figure 3.13. : Multiple-shooting schematic for two-dimensional torus

states $\{\bar{u}_1^2, \bar{u}_2^2, \bar{u}_3^2\}$ and $\{\bar{u}_1^3, \bar{u}_2^3, \bar{u}_3^3\}$. The propagation time for each trajectory arc, i.e., indicated by a solid blue line in Figure 3.13, is $\frac{T_1}{3}$. The invariance condition, Equation (3.73), is evaluated at the initial states along the invariant curve, $\bar{u}_{\mathrm{j}}^1(0, \theta_2^{\mathrm{j}}(0))$, and the final propagated states, $\bar{u}_{\mathrm{j}}^q(\theta_1(\frac{T_1}{q}), \theta_2^{\mathrm{j}}(0))$ with full state continuity enforced at the intermediate torus curves. Additionally, a torus state along the invariant curve, $\bar{u}_{\mathrm{j}}^1$, is expressed in the phase-space consistent with the CRTBP via $\bar{\mathcal{X}}_{\mathrm{j}}^1 = \bar{u}_{\mathrm{j}}^1 + \bar{\mathcal{X}}^*$, where, it is recalled that, $\bar{\mathcal{X}}^*$ is a fixed point associated with a periodic orbit. The invariant curve is approximated via a Discrete Fourier Transform (DFT) expressed as,

$$\mathfrak{C}_K = \frac{1}{n_q} \sum_{\mathrm{j}=1}^{n_q} \bar{u}(\theta_2^{\mathrm{j}}) \mathrm{e}^{\frac{-2\pi \mathrm{i}}{n_q} K(\mathrm{j}-1)}, \tag{3.75}$$

where a general torus state $\bar{u}(\theta_2^{\mathrm{j}})$ along the invariant curve is associated with evenly distributed angles θ_2^{j} defined as $\theta_2^{\mathrm{j}} = \frac{2\pi \mathrm{j}}{n_q}$ with $\mathrm{j} \in [0, \ldots, n_q - 1]$. Let W be a variable such that

$W = \mathrm{e}^{\frac{-2\pi\mathbb{i}}{n_q}}$, where $\mathbb{i} = \sqrt{-1}$, then Equation (3.75) is expanded into matrix form such that the Fourier coefficient matrix, $\mathfrak{C}$, is denoted as,

$$\mathfrak{C} = \frac{1}{n_q}\begin{bmatrix} W^{K(1)(0)} & W^{K(1)(1)} & W^{K(1)(2)} & \dots & W^{K(1)(n_q-1)} \\ W^{K(2)(0)} & W^{K(2)(1)} & W^{K(2)(2)} & \dots & W^{K(2)(n_q-1)} \\ \vdots & \vdots & \vdots & \ddots & \vdots \\ W^{K(n_q)(0)} & W^{K(n_q)(1)} & W^{K(n_q)(2)} & \dots & W^{K(n_q)(n_q-1)} \end{bmatrix}[\bar{u}]_t, \tag{3.76}$$

with $[\bar{u}]_t$ defined from Equation (3.74) and the vector $\bar{K}$ defined as $\bar{K} = [K(1), K(2), ..., K(n_q)]$. The vector $\bar{K}$ is selected based on the number of points used to approximate the invariant curve, i.e., n_q, such that:

$$\text{Odd number of points}: \ \bar{K} = \left[\frac{-(n_q-1)}{2}, \dots, -1, 0, 1, \dots, \frac{(n_q-1)}{2}\right] \tag{3.77}$$

$$\text{Even number of points}: \ \bar{K} = \left[\frac{-n_q}{2}, \dots, -1, 0, 1, \dots, \frac{n_q}{2} - 1\right] \tag{3.78}$$

Note that there are various choices for the $\bar{K}$ vector. The Fourier coefficient matrix in Equation (3.76) has dimensions $n_q \times 6$. Additionally, a matrix $\mathfrak{D}$ is defined as,

$$\mathfrak{D} = \frac{1}{n_q}\begin{bmatrix} W^{K(1)(0)} & W^{K(1)(1)} & W^{K(1)(2)} & \dots & W^{K(1)(n_q-1)} \\ W^{K(2)(0)} & W^{K(2)(1)} & W^{K(2)(2)} & \dots & W^{K(2)(n_q-1)} \\ \vdots & \vdots & \vdots & \ddots & \vdots \\ W^{K(n_q)(0)} & W^{K(n_q)(1)} & W^{K(n_q)(2)} & \dots & W^{K(n_q)(n_q-1)} \end{bmatrix}, \tag{3.79}$$

with the inverse denoted as,

$$\mathfrak{D}^{-1} = \begin{bmatrix} W^{-K(1)(0)} & W^{-K(2)(0)} & W^{-K(3)(0)} & \dots & W^{-K(n_q)(0)} \\ W^{-K(1)(1)} & W^{-K(2)(1)} & W^{-K(3)(1)} & \dots & W^{-K(n_q)(1)} \\ \vdots & \vdots & \vdots & \ddots & \vdots \\ W^{-K(1)(n_q-1)} & W^{-K(2)(n_q-1)} & W^{-K(3)(n_q-1)} & \dots & W^{-K(n_q)(n_q-1)} \end{bmatrix}. \tag{3.80}$$

Recognize the special property of the Fourier coefficient matrix [58],

$$\mathfrak{D}^{-1} = \mathfrak{D}^{H}, \tag{3.81}$$

where $[\,\cdot\,]^H$ is the conjugate transpose of the $\mathfrak{D}$ matrix. Equation (3.76) and the states along the invariant curve, $[\bar{u}]_t$, can be compactly written as,

$$\mathfrak{C} = \mathfrak{D}[\bar{u}]_t \tag{3.82}$$

$$[\bar{u}]_t = \mathfrak{D}^{-1}\mathfrak{C} \tag{3.83}$$

The information from the Fourier coefficient matrix, $\mathfrak{C}$, is used to approximate an arbitrary torus state along the invariant curve, $\bar{u}(\theta_2)$, associated with an angle, θ_2, with the following expression:

$$\bar{u}(\theta_2) = \begin{bmatrix} \mathrm{e}^{\mathbb{i}\theta_2 K(1)} & \mathrm{e}^{\mathbb{i}\theta_2 K(2)} & \dots & \mathrm{e}^{\mathbb{i}\theta_2 K(n_q)} \end{bmatrix} \mathfrak{C}, \tag{3.84}$$

where the angle θ_2 is defined in the interval $[0, 2\boldsymbol{\pi}]$. Next, the rotation matrix, $\mathbf{R}$, from the invariance condition is derived via the DFT. Let $\bar{u}(\theta_2 + \Delta\theta)$ be a torus state along the invariant curve that is rotated by an angle $\Delta\theta$ from an initial torus state $\bar{u}(\theta_2)$ and written as,

$$\bar{u}(\theta_2 + \Delta\theta) = \begin{bmatrix} \mathrm{e}^{\mathbb{i}(\theta_2+\Delta\theta) K(1)} & \mathrm{e}^{\mathbb{i}(\theta_2+\Delta\theta) K(2)} & \dots & \mathrm{e}^{\mathbb{i}(\theta_2+\Delta\theta) K(n_q)} \end{bmatrix} \mathfrak{C}, \tag{3.85}$$

with the Fourier coefficient matrix, $\mathfrak{C}$, and a $\bar{K}$ vector defined via Equations (3.77) and (3.78). The torus state $\bar{u}(\theta_2 + \Delta\theta)$ is also denoted in matrix form as,

$$\bar{u}(\theta_2 + \Delta\theta) = \begin{bmatrix} \mathrm{e}^{\mathbb{i}\theta_2 K(1)} & \mathrm{e}^{\mathbb{i}\theta_2 K(2)} & \dots & \mathrm{e}^{\mathbb{i}\theta_2 K(n_q)} \end{bmatrix} \mathbf{Q}(\Delta\theta)\mathfrak{C}, \tag{3.86}$$

where $\mathbf{Q}$ is a $n_q \times n_q$ matrix defined as,

$$\mathbf{Q}(\Delta\theta) = \begin{bmatrix} \mathrm{e}^{\mathbb{i}\Delta\theta K(1)} & 0 & \dots & 0 \\ 0 & \mathrm{e}^{\mathbb{i}\Delta\theta K(2)} & \dots & 0 \\ \vdots & \vdots & \ddots & \vdots \\ 0 & 0 & \dots & \mathrm{e}^{\mathbb{i}\Delta\theta K(n_q)} \end{bmatrix}. \tag{3.87}$$

Now, let $\mathfrak{C}$ be the Fourier coefficient matrix corresponding to a set of torus states $[\bar{u}]_0$ with an associated set of angles $[0, \frac{2\pi}{n_q}, ..., \frac{2\pi(n_q-1)}{n_q}]$. Then, let the set of torus states $[\bar{u}]_{T_1}$ be a rotation of the initial torus states $[\bar{u}]_0$ by some angle ρ, i.e., associated with angles $[\rho, \frac{2\pi}{n_q} + \rho, ..., \frac{2\pi(n_q-1)}{n_q} + \rho]$, such that,

$$[\bar{u}]_{T_1} = \begin{bmatrix} e^{\mathbb{i}(\frac{2\pi(0)}{n_q}+\rho)K(1)} & e^{\mathbb{i}(\frac{2\pi(0)}{n_q}+\rho)K(2)} & \dots & e^{\mathbb{i}(\frac{2\pi(0)}{n_q}+\rho)K(n_q)} \\ e^{\mathbb{i}(\frac{2\pi(1)}{n_q}+\rho)K(1)} & e^{\mathbb{i}(\frac{2\pi(1)}{n_q}+\rho)K(2)} & \dots & e^{\mathbb{i}(\frac{2\pi(1)}{n_q}+\rho)K(n_q)} \\ e^{\mathbb{i}(\frac{2\pi(2)}{n_q}+\rho)K(1)} & e^{\mathbb{i}(\frac{2\pi(2)}{n_q}+\rho)K(2)} & \dots & e^{\mathbb{i}(\frac{2\pi(2)}{n_q}+\rho)K(n_q)} \\ \vdots & \vdots & \ddots & \vdots \\ e^{\mathbb{i}(\frac{2\pi(n_q-1)}{n_q}+\rho)K(1)} & e^{\mathbb{i}(\frac{2\pi(n_q-1)}{n_q}+\rho)K(2)} & \dots & e^{\mathbb{i}(\frac{2\pi(n_q-1)}{n_q}+\rho)K(n_q)} \end{bmatrix} \mathfrak{C}. \tag{3.88}$$

Observe that Equation (3.88) is more compactly written as,

$$[\bar{u}]_{T_1} = \mathfrak{D}^{-1}\mathbf{Q}(\rho)\mathfrak{C}, \tag{3.89}$$

then substitute the definition of the Fourier coefficient matrix from Equation (3.82), i.e.,

$$[\bar{u}]_{T_1} = \mathfrak{D}^{-1}\mathbf{Q}(\rho)\mathfrak{D}[\bar{u}]_0. \tag{3.90}$$

Finally, the rotation matrix, $\mathbf{R}$, is identified as,

$$\mathbf{R}(\rho) = \mathfrak{D}^{-1}\mathbf{Q}(\rho)\mathfrak{D}. \tag{3.91}$$

To summarize, the rotation matrix $\mathbf{R}(\rho)$ rotates a set of states, approximated via an evenly distributed DFT, by an angle ρ. For the invariance condition stated in Equation (3.73), the propagated states are rotated back through the rotation angle, ρ.

The numerical algorithm implemented in the construction of quasi-periodic orbits is consistent with a TPBVP with a multidimensional Newton's method. The free-variable vector for a general algorithm is denoted as,

$$\bar{\mathfrak{x}} = \begin{bmatrix} \bar{\mathcal{X}}_1^1 \\ \bar{\mathcal{X}}_2^1 \\ \vdots \\ \bar{\mathcal{X}}_{n_q}^1 \\ \bar{\mathcal{X}}_1^2 \\ \bar{\mathcal{X}}_2^2 \\ \vdots \\ \bar{\mathcal{X}}_{n_q}^2 \\ \vdots \\ \bar{\mathcal{X}}_1^q \\ \bar{\mathcal{X}}_2^q \\ \vdots \\ \bar{\mathcal{X}}_{n_q}^q \\ T_1 \\ \rho \end{bmatrix} \tag{3.92}$$

where the invariance curve is approximated via the set of states $\{\bar{\mathcal{X}}_1^1, \bar{\mathcal{X}}_2^1, \ldots, \bar{\mathcal{X}}_{n_q}^1\}$ in the phase-space of the CRTBP. To construct the invariance condition constraint as a column vector, Equation (3.73) is rewritten via the following property,

$$\text{vec}\left(\mathbb{ABC}\right) = \left(\mathbb{C}^T \otimes \mathbb{A}\right) \text{vec}\left(\mathbb{B}\right), \tag{3.93}$$

where $\otimes$ is the kronecker product and $\text{vec}(\cdot)$ is the vectorization function. Vectorization is a linear transformation that converts a matrix into a column vector. For example, let $\mathbb{A}$ be a matrix such that $\mathbb{A} = \begin{bmatrix} a & b \\ c & d \end{bmatrix}$, then the vectorization is stated as,

$$\text{vec}(\mathbb{A}) = \begin{bmatrix} a \\ c \\ b \\ d \end{bmatrix}. \tag{3.94}$$

The transpose of the invariance condition, Equation (3.73), is given as,

$$\left[\bar{u}\right]_{T_1}^T \mathbf{R}^T(-\rho) - \left[\bar{u}\right]_0^T = [0], \tag{3.95}$$

where $[^T]$ represents the matrix transpose. Then, the invariance condition is rewritten via the vectorization property in Equation (3.93), i.e.,

$$\bar{F}_{\text{inv}} = (\mathbf{R}(-\rho) \otimes \mathbf{I}_{6,6}) \,\text{vec}\left(\left[\bar{u}\right]_{T_1}^T\right) - \text{vec}\left(\left[\bar{u}\right]_0^T\right) = \bar{0}, \tag{3.96}$$

where $\mathbf{I}_{6,6}$ is a 6×6 identity matrix. Recall that $\left[\bar{u}\right]_0$ contains initial torus states along the invariant curve and $\left[\bar{u}\right]_{T_1}$ contains the propagated torus states after time T_1, i.e., a first return to the stroboscopic map. In this analysis, families of quasi-periodic orbits with a fixed Jacobi Constant are constructed via the numerical algorithm presented. The constraint function associated with fixing the Jacobi Constant is stated as,

$$F_{\text{QPO,C}} = \mathcal{C}_{\text{des}} - \frac{1}{n_q}\sum_{\text{j}=1}^{n_q} \mathcal{C}\left(\bar{\mathcal{X}}_{\text{j}}^1\right), \tag{3.97}$$

where $\mathcal{C}$ is the function for the Jacobi Constant defined via Equation (2.37), $\bar{\mathcal{X}}_{\text{j}}^1$ is a state along the invariant curve associated with the quasi-periodic orbit, and $\mathcal{C}_{\text{des}}$ is the desired Jacobi Constant value. The fixed Jacobi Constant constraint is enforcing an average $\mathcal{C}$ value equal to the desired value $\mathcal{C}_{\text{des}}$ for all states along the invariant curve. Additionally, families of quasi-periodic orbits corresponding to a fixed mapping time, T_1, and rotation angle, ρ, exist,

but are not implemented in this analysis. Further discussion about families of quasi-periodic orbits with a fixed mapping time and rotation angle is provided by McCarthy [20]. The constraint vector implemented in the quasi-periodic orbit correction process with a desired $\mathcal{C}_{\text{des}}$ is written as,

$$\bar{F}_{\text{QPO}} = \begin{bmatrix} \bar{\mathcal{X}}_1^1\left(\frac{T_1}{q}\right) - \bar{\mathcal{X}}_1^2(0) \\ \bar{\mathcal{X}}_2^1\left(\frac{T_1}{q}\right) - \bar{\mathcal{X}}_2^2(0) \\ \vdots \\ \bar{\mathcal{X}}_{n_q}^1\left(\frac{T_1}{q}\right) - \bar{\mathcal{X}}_{n_q}^2(0) \\ \vdots \\ \bar{\mathcal{X}}_1^{p-1}\left(\frac{T_1}{q}\right) - \bar{\mathcal{X}}_1^q(0) \\ \bar{\mathcal{X}}_2^{p-1}\left(\frac{T_1}{q}\right) - \bar{\mathcal{X}}_2^q(0) \\ \vdots \\ \bar{\mathcal{X}}_{n_q}^{p-1}\left(\frac{T_1}{q}\right) - \bar{\mathcal{X}}_{n_q}^q(0) \\ (\mathbf{R}(-\rho) \otimes I_{6,6}) \operatorname{vec}\left(\left[\bar{u}\right]_{T_1}^T\right) - \operatorname{vec}\left(\left[\bar{u}\right]_0^T\right) \\ F_{\text{QPO,C}} \end{bmatrix}. \tag{3.98}$$

The vectorization of the torus states, from Equation (3.74), at the stroboscopic map are defined as,

$$\operatorname{vec}\left(\left[\bar{u}\right]_0^T\right) = \begin{bmatrix} \bar{\mathcal{X}}_1^1(0) - \bar{\mathcal{X}}^* \\ \bar{\mathcal{X}}_2^1(0) - \bar{\mathcal{X}}^* \\ \vdots \\ \bar{\mathcal{X}}_{n_q}^1(0) - \bar{\mathcal{X}}^* \end{bmatrix} \tag{3.99}$$

$$\operatorname{vec}\left(\left[\bar{u}\right]_{T_1}^T\right) = \begin{bmatrix} \bar{\mathcal{X}}_1^q(\frac{T_1}{q}) - \bar{\mathcal{X}}^* \\ \bar{\mathcal{X}}_2^q(\frac{T_1}{q}) - \bar{\mathcal{X}}^* \\ \vdots \\ \bar{\mathcal{X}}_{n_q}^q(\frac{T_1}{q}) - \bar{\mathcal{X}}^* \end{bmatrix}, \tag{3.100}$$

where $\left[\bar{u}\right]_0$ and $\left[\bar{u}\right]_{T_1}$ are $6n_q \times 1$ column vectors; recalling that $\bar{\mathcal{X}}$ is a 6×1 state vector. The Jacobian for the constraint vector is denoted as,

$$\mathbf{D}\bar{\mathbf{F}}_{\text{QPO}} = \begin{bmatrix} \bar{\mathbf{\Phi}}_1 & -\mathbf{I} & \mathbf{0} & \dots & \mathbf{0} & \frac{\partial[\bar{\mathcal{X}}]_1}{\partial T} & 0 \\ \mathbf{0} & \bar{\mathbf{\Phi}}_2 & -\mathbf{I} & \dots & \mathbf{0} & \frac{\partial[\bar{\mathcal{X}}]_2}{\partial T} & 0 \\ \vdots & \ddots & \ddots & \ddots & \vdots & \vdots & \vdots \\ \mathbf{0} & \mathbf{0} & \dots & \bar{\mathbf{\Phi}}_{p-1} & -\mathbf{I} & \frac{\partial[\bar{\mathcal{X}}]_{q-1}}{\partial T} & 0 \\ -\mathbf{I} & \mathbf{0} & \dots & \mathbf{0} & \mathbf{D_x\bar{F}_{QPO}} & D_{T_1}\bar{F}_{QPO} & D_\rho \bar{F}_{QPO} \\ D_x F_{\text{QPO,C}} & \mathbf{0}_{1,6n_q} & \dots & \mathbf{0}_{1,6n_q} & \mathbf{0}_{1,6n_q} & 0 & 0 \end{bmatrix}, \tag{3.101}$$

where $\mathbf{I}$ and $\mathbf{0}$ are $6n_q \times 6n_q$ identity and zero matrices, respectively. The matrix $\bar{\mathbf{\Phi}}_{\text{j}}$ is a collection of STMs that correspond to the states along an j^{th} intermediate curve, plotted in Figure 3.13, i.e.,

$$\bar{\mathbf{\Phi}}_{\text{j}} = \begin{bmatrix} \frac{\bar{\mathcal{X}}_1^{\text{j}}(\frac{T_1}{q})}{\bar{\mathcal{X}}_1^{\text{j}}(0)} & 0_{6,6} & \dots & 0_{6,6} \\ 0_{6,6} & \frac{\bar{\mathcal{X}}_2^{\text{j}}(\frac{T_1}{q})}{\bar{\mathcal{X}}_2^{\text{j}}(0)} & \dots & 0_{6,6} \\ \vdots & \vdots & \ddots & \vdots \\ 0_{6,6} & 0_{6,6} & \dots & \frac{\bar{\mathcal{X}}_{n_q}^{\text{j}}(\frac{T_1}{q})}{\bar{\mathcal{X}}_{n_q}^{\text{j}}(0)} \end{bmatrix}, \tag{3.102}$$

recalling the definition of the STM in Equation (3.22). The vector $\frac{\partial[\bar{\mathcal{X}}]_{\text{j}}}{\partial T_1}$ is a collection of acceleration states associated with,

$$\frac{\partial[\bar{\mathcal{X}}]_{\text{j}}}{\partial T} = \begin{bmatrix} \left(\frac{1}{q}\right)\dot{\bar{\mathcal{X}}}_1^{\text{j}}\Big|_{\frac{T_1}{q}} \\ \left(\frac{1}{q}\right)\dot{\bar{\mathcal{X}}}_2^{\text{j}}\Big|_{\frac{T_1}{q}} \\ \vdots \\ \left(\frac{1}{q}\right)\dot{\bar{\mathcal{X}}}_{n_q}^{\text{j}}\Big|_{\frac{T_1}{q}} \end{bmatrix}. \tag{3.103}$$

where the acceleration, computed via the CRTBP equations of motion, is evaluated at time $\frac{T_1}{q}$, i.e., the end of the propagation. Then, the partials of the invariance conditions with

respect to the states along the q^{th} torus curve, the propagation time T_1, and the rotation angle ρ, are denoted as,

$$\mathbf{D_x}\bar{\mathbf{F}}_{\mathbf{QPO}} = (\mathbf{R}(-\rho) \otimes \mathbf{I}_{6,6})\, \bar{\mathbf{\Phi}}_q, \tag{3.104}$$

$$D_{T_1}\bar{F}_{QPO} = (\mathbf{R}(-\rho) \otimes \mathbf{I}_{6,6})\, \frac{\partial[\bar{\mathcal{X}}]_q}{\partial t}\Big|_{\frac{T_1}{q}} \begin{pmatrix} 1 \\ \overline{q} \end{pmatrix}, \tag{3.105}$$

$$D_{\rho}\bar{F}_{QPO} = (\mathbf{DR}(-\rho) \otimes \mathbf{I}_{6,6})\, \mathrm{vec}\left(\left[\bar{u}\right]_{T_1}^{T} \right), \tag{3.106}$$

where the derivative of the rotation matrix $\mathbf{R}$ is,

$$\mathbf{DR}(-\rho) = \mathfrak{D}^{-1} \begin{bmatrix} -\mathbb{i}k(1)\mathrm{e}^{-\mathbb{i}\rho K(1)} & 0 & \dots & 0 \\ 0 & -\mathbb{i}k(2)\mathrm{e}^{-\mathbb{i}\rho K(2)} & \dots & 0 \\ \vdots & \vdots & \ddots & \vdots \\ 0 & 0 & \dots & -\mathbb{i}k(n_q)\mathrm{e}^{-\mathbb{i}\rho K(n_q)} \end{bmatrix} \mathfrak{D}, \tag{3.107}$$

with $\mathfrak{D}$ defined in Equation (3.79). The partial of the Jacobi Constant constraint, Equation (3.97), is given with the vector,

$$D_x F_{\mathrm{QPO,C}} = \frac{-1}{n_q} \begin{bmatrix} \frac{\partial \mathcal{C}(\bar{\mathcal{X}}_1^1)}{\partial \bar{\mathcal{X}}_1^1} & \dots & \frac{\partial \mathcal{C}(\bar{\mathcal{X}}_{n_q}^1)}{\partial \bar{\mathcal{X}}_{n_q}^1} \end{bmatrix}, \tag{3.108}$$

with the following property,

$$\frac{\partial \mathcal{C}\left(\bar{\mathcal{X}}\right)}{\partial \bar{\mathcal{X}}} = 2 \begin{bmatrix} \frac{\partial \mathcal{U}^*}{\partial x} & \frac{\partial \mathcal{U}^*}{\partial y} & \frac{\partial \mathcal{U}^*}{\partial z} & \dot{x} & \dot{y} & \dot{z} \end{bmatrix}, \tag{3.109}$$

where the partials of the pseudo-potential $\mathcal{U}^*$ are from Equation (2.33).

The initial conditions for the numerical corrections process are retrieved from information derived from the center manifold structure of the associated periodic orbit. The states along the invariant curve, i.e., $[\bar{u}]_0$, are initialized with the components of a six-dimensional eigenvector in the center subspace of the reference periodic orbit. Recall that the monodromy matrix of a reference periodic orbit contains two eigenvectors, ${}^{P}\bar{\Psi}_1^C$ and ${}^{P}\bar{\Psi}_2^C$, that are associated with the two eigenvalues equal to unity. Additionally, two additional eigenvectors in

the center subspace, ${}^{P}\bar{\Psi}_3^C$ and ${}^{P}\bar{\Psi}_4^C$, correspond to the eigenvalues with $|{}^{P}\Lambda| = 1$, assuming that they exist. The states in $[\bar{u}]_0$, defined in Equation (3.74), are initialized as follows [17],

$$\bar{u}_{\mathrm{j}}^1 = \epsilon \left[\mathbf{Re}\left[{}^{P}\bar{\Psi}_3^C \right] \cos\left(\frac{2\pi(\mathrm{j}-1)}{n_q} \right) - \mathbf{Im}\left[{}^{P}\bar{\Psi}_3^C \right] \sin\left(\frac{2\pi(\mathrm{j}-1)}{n_q} \right) \right], \tag{3.110}$$

where ϵ is a step-off distance in the direction of the eigenvector, $\mathbf{Re}[\,\cdot\,]$ is an operator that isolates the real components of a vector, and $\mathbf{Im}[\,\cdot\,]$ isolates the imaginary components of a vector. In Equation (3.110), components of the eigenvector ${}^{P}\bar{\Psi}_3^C$ are used, however, recall that, in the CRTBP model, ${}^{P}\bar{\Psi}_4^C$ is the complex conjugate of ${}^{P}\bar{\Psi}_3^C$. The rotation angle ρ is initialized with the angle of the eigenvalue associated with the periodic orbit in the center subspace, i.e.,

$$\rho = \mathbf{Re}\left[-\mathbb{i} \log\left[{}^{P}\Lambda_3^C \right] \right]. \tag{3.111}$$

The longitudinal time T_1 is initialize via the period of the reference periodic orbit. An example of a Lissajous orbit near the Sun-Earth L_1 vicinity is plotted in Figure 3.14. In Figure 3.14, a trajectory along the Lissajous is plotted in black and the point along the invariant curve are provided in red and the reference vertical orbit is in magenta. The multiple-shooting strategy helps mitigate any numerical challenges associated with highly complex dynamical regimes.

Families of quasi-periodic orbits are constructed by enforcing constraints on Jacobi Constant, $\mathcal{C}$, the rotation angle, ρ, or the mapping time associated with the stroboscopic map, T_1. In the CRTBP, quasi-periodic orbits exist as two-parameter families [17], however, one-parameter families of quasi-periodic orbits are constructed by fixing a parameter. The fixed parameter is one of the following choices: the Jacobi Constant $\mathcal{C}$, the rotation angle ρ, or the mapping time T_1. The construction process to generate families of quasi-periodic orbits is initialized with a quasi-periodic orbit corrected via a multidimensional Newton's method with the constraint conditions outlined in Equation (3.98). For a corrected quasi-periodic orbit, the approximation of the invariant curve via the DFT is not unique, that is, the states that approximate the geometry of the corrected invariant curve, i.e., $[\bar{u}]_0^1$, is not unique. In fact, the corrections process does not uniquely identify a corrected quasi-periodic

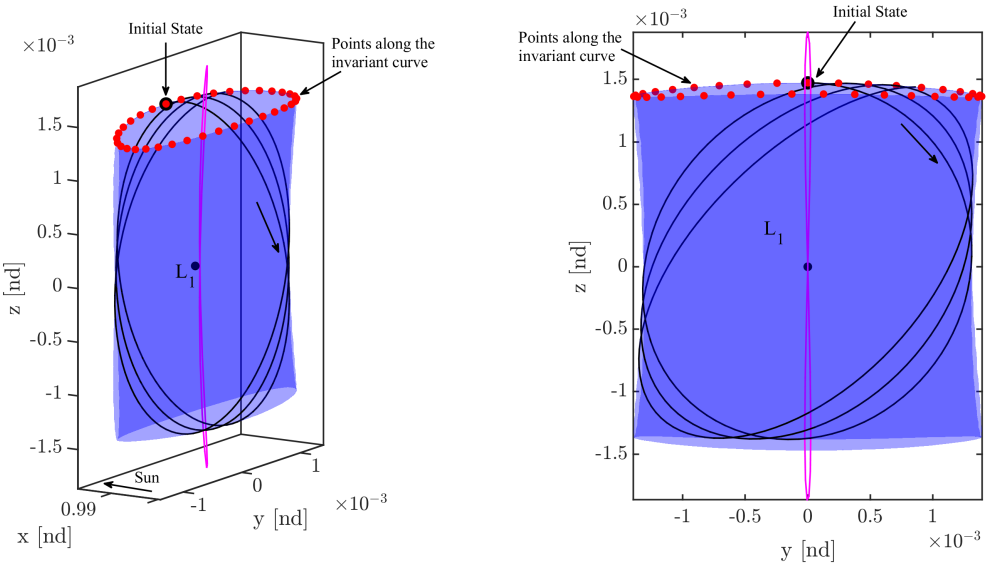

Figure 3.14. : (a) L_1 Lissajous orbit with a Jacobi Constant $\mathcal{C} = 3.0008763979870$ in the Sun-Earth system. Points along the invariant curve are in red. The initial state of a propagated trajectory along the Lissajous is in black. Note that this Lissajous orbit is constructed from a vertical orbit, plotted in magenta. (b) $\hat{y} - \hat{z}$ projection of the Lissajous orbit.

orbit. For example, let a corrected invariant curve, approximated by states $[\widetilde{\bar{u}}]_0^1$, correspond to a torus $\mathfrak{T}^2$, i.e., a two-dimensional torus. Then, a set of states rotated by an angle $\Delta\theta_2$ along the invariant curve is defined as $[\bar{u}]_0^{1'} = \mathbf{R}(\Delta\theta_2)[\widetilde{\bar{u}}]_0^1$. The rotated set of states along the invariant curve, $[\bar{u}]_0^{1'}$, also belong to the same torus $\mathfrak{T}^2$. The example implies that the states along the invariant curve are rotated along the latitudinal direction of the torus. A similar process is implemented by propagating all the states in the invariant curve, i.e., $[\bar{u}]_0^1$, by a time $T_{1'}$, in a process that describes the rotation of the invariant curve along the longitudinal direction. Note that the set of propagated states also correspond to the same torus $\mathfrak{T}^2$. To mitigate any issues encountered due to the nonuniqueness, a set of phasing constraints are included in the corrections process during the quasi-periodic orbit family generation. The phasing constraints implemented in this analysis are consistent with those in Olikara [33] and are applicable for a general torus. Let $[\widetilde{\bar{u}}]_0^1$ be a corrected invariant curve corresponding

to a two-dimensional torus $\widetilde{\mathfrak{T}}^2$ and $[\bar{u}]_0^1$ be the current approximation of the invariant curve associated with torus $\mathfrak{T}^2$. Then, the phasing constraints are denoted as [33],

$$F_{\theta_1} =< [\bar{u}]_0^1, \frac{\partial [\widetilde{\bar{u}}]_0^1}{\partial \theta_1} >, \tag{3.112}$$

$$F_{\theta_2} =< [\bar{u}]_0^1, \frac{\partial [\widetilde{\bar{u}}]_0^1}{\partial \theta_2} >, \tag{3.113}$$

where $< \cdot >$ is the dot product. To derive the partial derivatives of the corrected invariant curve with respect to the longitudinal angle, i.e., θ_1, let the corrected invariant curve be written as: $[\widetilde{\bar{u}}]_0^1(\theta_1, \theta_2)$. Then, the time derivative is computed via the chain rule, i.e.,

$$\frac{D[\widetilde{\bar{u}}]_0^1(\theta_1, \theta_2)}{Dt} = \frac{\partial [\widetilde{\bar{u}}]_0^1(\theta_1, \theta_2)}{\partial \theta_1} \frac{\partial \theta_1}{\partial t} + \frac{\partial [\widetilde{\bar{u}}]_0^1(\theta_1, \theta_2)}{\partial \theta_2} \frac{\partial \theta_2}{\partial t}, \tag{3.114}$$

such that $\frac{\partial \theta_1}{\partial t}$ and $\frac{\partial \theta_2}{\partial t}$ are the longitudinal and latitudinal frequencies associated with the torus, respectively. Recall that each vector in $[\widetilde{\bar{u}}]_0^1(\theta_1, \theta_2)$ is a torus state that is parameterized via the angles θ_1 and θ_2, see Equation (3.74). Now the partial derivative with respect to the longitudinal frequency is defined as,

$$\frac{\partial [\widetilde{\bar{u}}]_0^1(\theta_1, \theta_2)}{\partial \theta_1} = \frac{1}{\dot{\theta}_1} \left(\frac{D[\widetilde{\bar{u}}]_0^1(\theta_1, \theta_2)}{Dt} - \frac{\partial [\widetilde{\bar{u}}]_0^1(\theta_1, \theta_2)}{\partial \theta_2} \dot{\theta}_2 \right), \tag{3.115}$$

where the fundamental frequencies for the corrected invariant curve are defined as,

$$\dot{\theta}_1 = \frac{2\pi}{\widetilde{T}_1}, \tag{3.116}$$

$$\dot{\theta}_2 = \frac{\widetilde{\rho}}{\widetilde{T}_1}, \tag{3.117}$$

with $\widetilde{\rho}$ and $\widetilde{T_1}$ as the rotation angle and mapping time corresponding to the corrected invariant curve. The time derivative of the invariant curve is evaluated via the equations of motion associated with the CRTBP, Equation (3.3), i.e.,

$$\frac{D[\widetilde{\bar{u}}]_0^1(\theta_1,\theta_2)}{Dt} = \begin{bmatrix} \dot{\bar{u}}_1^{1^T} \\ \dot{\bar{u}}_2^{1^T} \\ \vdots \\ \dot{\bar{u}}_{\mathrm{j}}^{1^T} \end{bmatrix}, \tag{3.118}$$

where $\dot{\bar{u}}_{\mathrm{j}}^1$ is defined as $\dot{\bar{u}}_{\mathrm{j}}^1 = \bar{\mathfrak{f}}\left(\bar{\mathcal{X}}_{\mathrm{j}}^1\right)$; recall the definition of a torus state: $\bar{\mathcal{X}}_{\mathrm{j}}^1 = \bar{u}_{\mathrm{j}}^1 + \bar{\mathcal{X}}^*$. The time derivative of the torus states has a matrix dimension of $n_q \times 6$. Now, the partial derivative with respect to the latitudinal frequency is derived from the DFT approximation of the invariant curve. The corrected invariant curve is approximated via the DFT in Equation (3.83) such that, $[\widetilde{\bar{u}}]_0^1 = \boldsymbol{D}^{-1}\widetilde{\mathfrak{C}}$. Then,

$$\frac{\partial[\widetilde{\bar{u}}]_0^1(\theta_1,\theta_2)}{\partial\theta_2} = \frac{\partial\mathfrak{D}^{-1}}{\partial\theta_2}\widetilde{\mathfrak{C}}, \tag{3.119}$$

with $\widetilde{\mathfrak{C}}$ as the Fourier coefficient matrix associated with the corrected invariant curve and $\mathfrak{D}^{-1}$ is defined with Equation (3.80). Equation (3.119) is expanded to,

$$\frac{\partial[\widetilde{\bar{u}}]_0^1(\theta_1,\theta_2)}{\partial\theta_2} = \mathfrak{D}^{-1}\begin{bmatrix} \mathbb{i}K(1) & 0 & \dots & 0 \\ 0 & \mathbb{i}K(2) & \dots & 0 \\ \vdots & \vdots & \ddots & \vdots \\ 0 & 0 & \dots & \mathbb{i}K(n_q) \end{bmatrix}\widetilde{\mathfrak{C}}, \tag{3.120}$$

where $K(\mathrm{j})$ are components of the $\bar{K}$ vector defined via Equation (3.77) or (3.78). The phasing constraints in Equations (3.112) and (3.113) are rewritten with the vectorization function and denoted as,

$$F_{\theta_1} = \mathrm{vec}\left([\bar{u}]_0^{1^T}\right)^T \mathrm{vec}\left(\frac{\partial [\widetilde{\bar{u}}]_0^{1^T}}{\partial \theta_1}\right), \tag{3.121}$$

$$F_{\theta_2} = \mathrm{vec}\left([\bar{u}]_0^{1^T}\right)^T \mathrm{vec}\left(\frac{\partial [\widetilde{\bar{u}}]_0^{1^T}}{\partial \theta_2}\right), \tag{3.122}$$

where, it is recalled, that $[^T]$ is the vector transpose. The phasing constraints expressed in Equations (3.121) and (3.122) are evaluated via a dot product and, therefore, are scalar values. Phasing constraint are included in the corrections process to construct distinct members of a quasi-periodic orbit family. Families of quasi-periodic orbits occur in two-parameter families in the CRTBP model, but one-parameter families are constructed by fixing the following variables: Jacobi Constant $\mathcal{C}$, mapping time T_1, rotation angle ρ. The constraint vector implemented in the construction of a quasi-periodic orbit family with a fixed Jacobi Constant is denoted as,

$$\bar{F}_{\mathrm{QPO,phase}} = \begin{bmatrix} \bar{F}_{\mathrm{QPO}} \\ \bar{F}_{\mathrm{phase}\ \theta_1} \\ \bar{F}_{\mathrm{phase}\ \theta_2} \end{bmatrix}, \tag{3.123}$$

Where $\bar{F}_{\text{QPO}}$ is given via Equation (3.98). The Jacobian associated with the constraint vector and the free-variable vector, stated in Equation (3.92), is written with,

$$\mathbf{D}\bar{\mathbf{F}}_{\text{QPO,phase}} = \begin{bmatrix} \bar{\mathbf{\Phi}}_1 & -\mathbf{I} & \mathbf{0} & \dots & \mathbf{0} & \frac{\partial[\vec{\mathcal{X}}]_1}{\partial T_1} & 0 \\ \mathbf{0} & \bar{\mathbf{\Phi}}_2 & -\mathbf{I} & \dots & \mathbf{0} & \frac{\partial[\vec{\mathcal{X}}]_2}{\partial T_1} & 0 \\ \vdots & \ddots & \ddots & \ddots & \vdots & \vdots & \vdots \\ \mathbf{0} & \mathbf{0} & \dots & \bar{\mathbf{\Phi}}_{p-1} & -\mathbf{I} & \frac{\partial[\vec{\mathcal{X}}]_{p-1}}{\partial T_1} & 0 \\ -\mathbf{I} & \mathbf{0} & \dots & \mathbf{0} & \mathbf{D_x\bar{F}_{inv}} & D_{T_1}\bar{F}_{inv} & D_\rho \bar{F}_{inv} \\ D_x F_{\text{Q},\mathcal{C}} & \mathbf{0}_{1,6n_q} & \dots & \mathbf{0}_{1,6n_q} & \mathbf{0}_{1,6n_q} & 0 & 0 \\ D_x F_{\theta_1} & \mathbf{0}_{1,6n_q} & \dots & \mathbf{0}_{1,6n_q} & \mathbf{0}_{1,6n_q} & D_{T_1} F_{\theta_1} & D_\rho F_{\theta_1} \\ D_x F_{\theta_2} & \mathbf{0}_{1,6n_q} & \dots & \mathbf{0}_{1,6n_q} & \mathbf{0}_{1,6n_q} & D_{T_1} F_{\theta_2} & D_\rho F_{\theta_2} \end{bmatrix}, \tag{3.124}$$

with the partials of the phasing constraints, i.e., Equations (3.121) and (3.122), expressed with,

$$D_x F_{\theta_1} = \text{vec}\left(\frac{\partial[\widetilde{\bar{u}}]_0^1{}^T}{\partial \theta_1}\right)^T, \tag{3.125}$$

$$D_{T_1} F_{\theta_1} = 0, \tag{3.126}$$

$$D_\rho F_{\theta_1} = 0, \tag{3.127}$$

$$D_x F_{\theta_2} = \text{vec}\left(\frac{\partial[\widetilde{\bar{u}}]_0^1{}^T}{\partial \theta_2}\right)^T, \tag{3.128}$$

$$D_{T_1} F_{\theta_2} = 0, \tag{3.129}$$

$$D_\rho F_{\theta_2} = 0. \tag{3.130}$$

The dimension of the free-variable vector, written in Equation (3.92), is $(6\,q\,n_q + 2)$, and the dimension of the constraint vector in Equation (3.123) is $(6\,q\,n_q + 3)$. However, it is observed that there is some dependencies between the rows, such that the rank of the $\mathbf{D}\bar{\mathbf{F}}_{\text{QPO,phase}}$ matrix in Equation (3.124) is $6qn_q + 1$. The Jacobian stated in Equation (3.124) has a one-dimensional nullspace. Pseudo-arclength continuation is implemented by appending the

pseudo-arclength constraint into the constraint vector in Equation (3.123) and the Jacobian in Equation (3.124), i.e.,

$$\bar{F}_{\text{QPO,fam}} = \begin{bmatrix} \bar{F}_{\text{QPO,phase}} \\ \bar{F}_{\text{pseudo}} \end{bmatrix}, \tag{3.131}$$

$$\mathbf{D}\bar{\mathbf{F}}_{\text{QPO,fam}} = \begin{bmatrix} \mathbf{D}\bar{\mathbf{F}}_{\text{QPO,phase}} \\ D\tilde{\mathfrak{X}}^T \end{bmatrix}, \tag{3.132}$$

$$\tag{3.133}$$

where $\bar{F}_{\text{pseudo}}$ is the pseudo-arclength constraint from Equation (3.58) and $D\tilde{\mathfrak{X}}$ is defined in Equation (3.59). In this analysis, families of quasi-periodic orbits with a fixed $\mathcal{C}$ value are constructed in the Sun-Earth system of the CRTBP model near the L_1 and L_2 Lagrange points. A family of quasi-halo orbits at a fixed Jacobi Constant is constructed from a northern halo orbit near L_1. The family of quasi-halo orbits is plotted in Figure 3.15 and the ratio associated with the quasi-periodic family is presented in Figure 3.16. A family of Lissajous orbits that corresponds to a Jacobi Constant of $\mathcal{C} = 3.00087639$ is plotted in Figure 3.17(a). The family of Lissajous orbits in Figure 3.17(a) emanates from the vertical orbit, identified in magenta, and meets a planar Lyapunov orbit at the desired Jacobi Constant value.

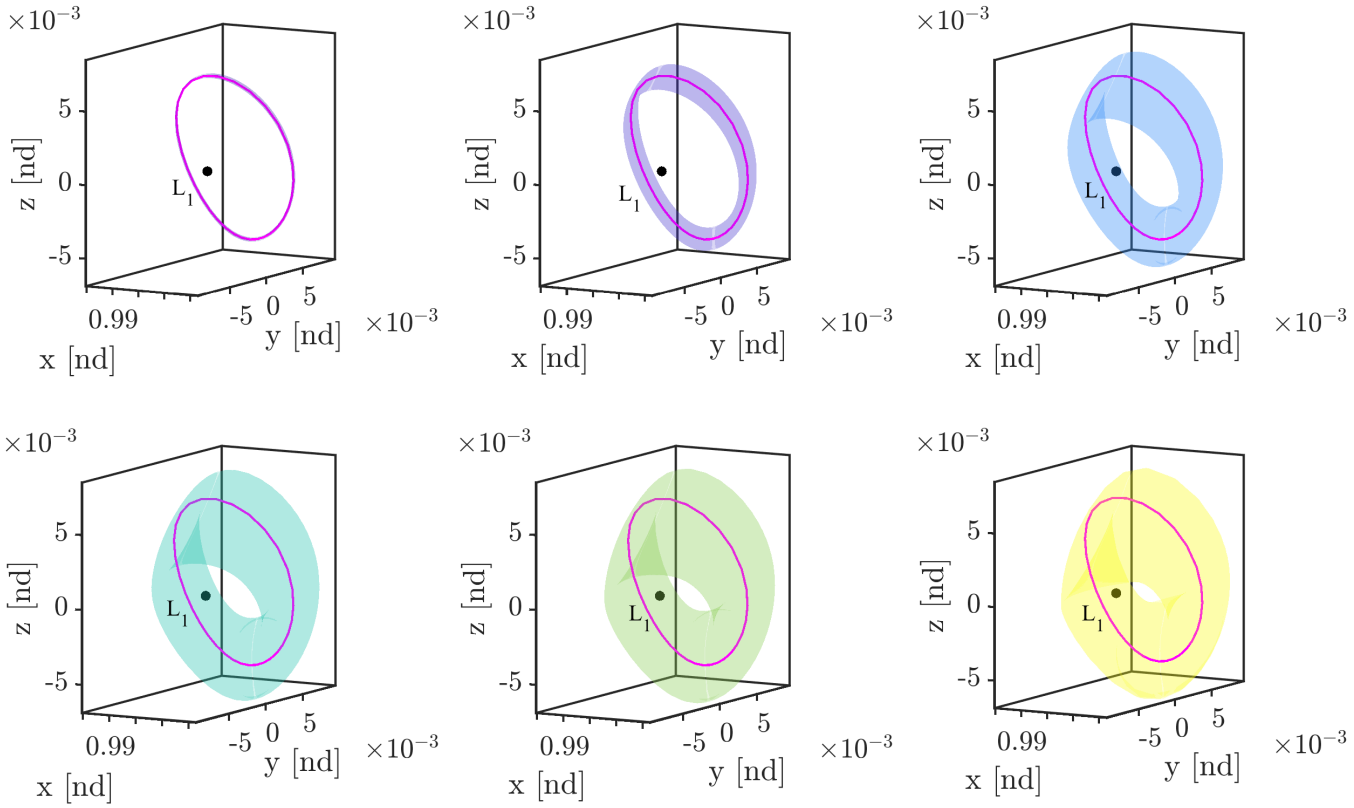

Figure 3.15. : Family of quasi-halo orbits near L_1 at a Jacobi Constant $\mathcal{C} = 3.00060309$. The originating halo orbit is in magenta

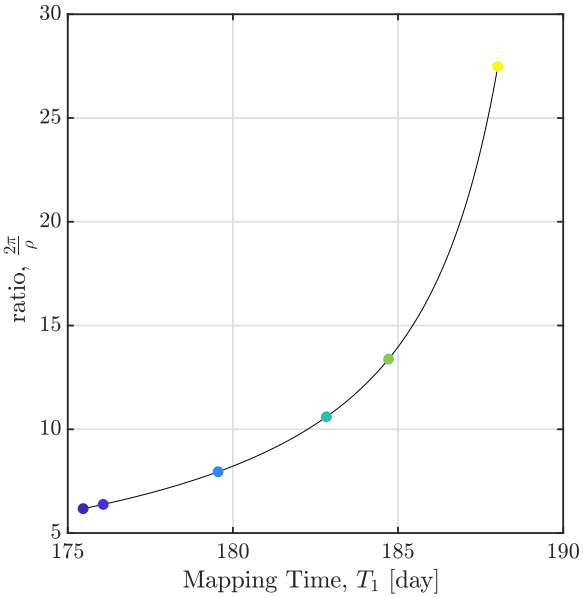

Figure 3.16. : Ratio and mapping time for quasi-halo family corresponding to $\mathcal{C} = 3.00060309$. Colors along the line correspond to the quasi-halos in Figure 3.15

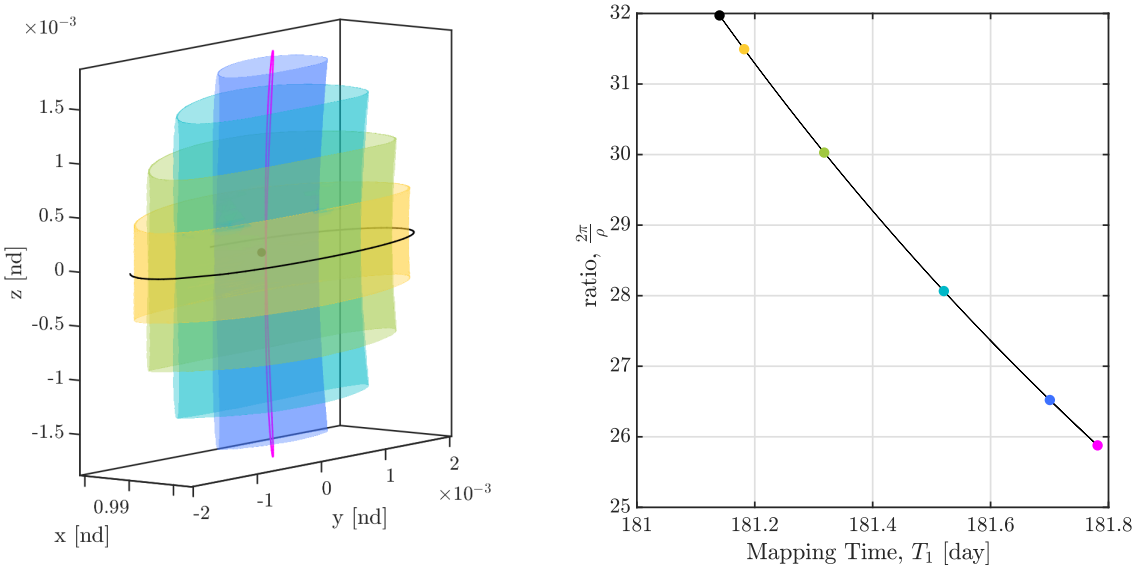

(a) (b)

Figure 3.17. : (a) Select orbits in the Lissajous orbit family near L_1 corresponding to a Jacobi Constant, $\mathcal{C} = 3.00087639$. (b) Lissajous orbit ratio and the mapping time T_1. The selected orbits in (a) are plotted with their respective colors. The originating orbit is a vertical orbit in magenta

Regions with large resonances may challenge the convergence of the multiple-shooting algorithm, especially when generating families with a fixed $\mathcal{C}$ value, but anticipating these regions mitigates the difficulties associated with this numerical algorithm.

3.4.2 Stability of Quasi-Periodic Orbits

Linear stability analysis is implemented to observe the local behavior of the flow in the vicinity of a quasi-periodic orbit. The stability properties investigated near a fixed point associated with a periodic orbit describe the local dynamical flow. Essentially, a stroboscopic map is constructed with the period corresponding to the periodic orbit. The linearization of the map reveals insightful local flow behavior near a fixed point associated with a periodic orbit. Similarly, the stability properties for quasi-periodic orbits are observed via a linearized stroboscopic map for the invariant curve [33]. For periodic orbits, the flow near a fixed point is observed; however, for quasi-periodic orbits, the flow near the vicinity of an invariant curve is now explored. Let a stroboscopic mapping with time T_1, i.e., the longitudinal period, be defined as

$$\bar{u}(\theta_2 + \rho) = \mathfrak{F}(\bar{u}(\theta_2)), \tag{3.134}$$

where a torus state is now parameterized with the latitudinal angle, θ_2, and ρ is the torus rotation angle. Recall that, for a two-dimensional torus, a torus state is parameterized with longitudinal and latitudinal angles, $\theta_1(t)$ and $\theta_2(t)$, respectively. However, as a consequence of the stroboscopic map, $\theta_1(0) = \theta_1(T_1)$, that is, the map is constructed at every revolution around the longitudinal direction of the torus, refer to the illustration in Figure 3.12. Therefore, a torus state on the map is parameterized via the latitudinal angle, θ_2, and these states are along an invariant curve associated with a two-dimensional torus. A linearized form of the mapping represented in Equation (3.134) is written as,

$$\delta\bar{u}(\theta_2 + \rho) = \mathfrak{F}_x(\bar{u}(\theta_2))\delta\bar{u}(\theta_2), \tag{3.135}$$

where the matrix $\mathfrak{F}_x(\bar{u}(\theta_2))$ is a derivative with respect to the initial torus state and $\delta\bar{u}$ is a small variation of the torus state. Note that the matrix $\mathfrak{F}_x(\bar{u}(\theta_2))$ is a function of the angle θ_2, that is, corresponding to different points along the invariant curve; no stability properties are derived from this matrix. However, from Jorba [34], if the torus is assumed to be reducible, then a change of coordinates is introduced such that $\bar{w} = C(\theta_2)\bar{u}$, and a linearized system is now written as,

$$\delta\bar{w}(\theta_2 + \rho) = \mathfrak{B}\delta\bar{w}(\theta_2), \tag{3.136}$$

where the constant matrix $\mathfrak{B}$ is defined as: $\mathfrak{B} = C(\theta_2 + \rho)^{-1}\mathfrak{F}_x(\bar{u}(\theta_2))C(\theta_2)$. Now, the stability properties of the invariant curve are observed through the eigenstructure of the constant $\mathfrak{B}$ matrix. Identifying an appropriate change of coordinate matrix, C, is not a trivial task, but for the quasi-periodic numerical algorithm implemented in this analysis, the eigenvalues of the constant $\mathfrak{B}$ matrix are evaluated through the eigenvalues of [34],

$$\mathfrak{G} = \Big(\mathbf{R}\big(-\rho\big) \otimes \mathbf{I}_{6,6}\Big)\bar{\mathbf{\Phi}}, \tag{3.137}$$

where $\mathbf{I}_{6,6}$ is a 6×6 identity matrix, $\otimes$ is the kronecker product, and $\bar{\mathbf{\Phi}}$ is a matrix, of size $6n_q \times 6n_q$, that includes the STMs from the states, $\bar{\mathcal{X}}^1_{\mathrm{j}}$, along the invariant curve, such that,

$$\bar{\mathbf{\Phi}} = \begin{bmatrix} \frac{\bar{\mathcal{X}}^1_1(T_1)}{\bar{\mathcal{X}}^1_1(0)} & \mathbf{0}_{6,6} & \dots & \mathbf{0}_{6,6} \\ \mathbf{0}_{6,6} & \frac{\bar{\mathcal{X}}^1_2(T_1)}{\bar{\mathcal{X}}^1_2(0)} & \dots & \mathbf{0}_{6,6} \\ \vdots & \vdots & \ddots & \vdots \\ \mathbf{0}_{6,6} & \mathbf{0}_{6,6} & \dots & \frac{\bar{\mathcal{X}}^1_{n_q}(T_1)}{\bar{\mathcal{X}}^1_{n_q}(0)} \end{bmatrix}, \tag{3.138}$$

with $\mathbf{0}_{6,6}$ as a 6×6 zero matrix. The details regarding reducibility of invariant tori is beyond the scope of this analysis and further discussion is provided by Jorba [34], [69]. The $\mathfrak{G}$ matrix plays a similar role as the monodromy matrix for a periodic orbit and its eigenvalues and eigenvectors reveal insightful stability information near the vicinity of the invariant curve associated with a quasi-periodic orbit.

The eigenvalues of the linearized map, $\mathfrak{G}$, provide the stability characteristic of the local behavior in the vicinity of a quasi-periodic orbit. The eigenvalues of a quasi-periodic orbit, corresponding to a reducible two-dimensional torus, have the following properties [34]:

- If Λ is an eigenvalue of $\mathfrak{G}$, then so is $e^{\mathbb{i}j\rho}\Lambda$ with $j \in \mathbb{Z}$ and $\mathbb{i} = \sqrt{-1}$. Note that $\mathbb{Z}$ represents all integers. All eigenvalues of the matrix $\mathfrak{G}$ densely fill concentric circles centered at the origin of the complex plane.

- If the system is autonomous, then there is one eigenvalue with modulus equal to unity, that is, there is at least one concentric circle of eigenvalues with radii, $\|\Lambda\|$, equal to unity, i.e., the unit circle.

- If Λ and $\bar{\psi}$ are an eigenvalue and eigenvector pair, then so is $e^{\mathbb{i}j\rho}\Lambda$ and $e^{-\mathbb{i}j\rho}\bar{\psi}$ with $j \in \mathbb{Z}$.

- For a stroboscopic map, i.e., a symplectic map used in the invariance condition, if $\Lambda \in \mathbb{C}$, then $\frac{1}{\Lambda}$, $\Lambda^{\dagger}$, and $\frac{1}{\Lambda^{\dagger}}$ are also eigenvalues of the system [70]. Note that $\mathbb{C}$ represents the set of complex numbers and $[^{\dagger}]$ is a complex conjugate. As a consequence of this symplectic property, a quasi-periodic orbit in an autonomous system has at least two concentric circles with $\|\Lambda\| = 1$.

In this numerical algorithm, an invariant curve is approximated via a DFT with n_q six-dimensional states, i.e., the phase-space of the CRTBP model. Therefore, the matrix in Equation (3.137) has $6n_q$ eigenvalues that form concentric circles in the complex plane. Similar to periodic orbits, the hyperbolicity of the invariant curve is observed through the modulus of the eigenvalues, i.e., $\|\Lambda_j\|$. The existence of a stable manifold subspace is defined via eigenvalues with modulus less than unity, i.e., $\|\Lambda\| < 1$, and the existence of an unstable manifold subspace is expressed via $\|\Lambda\| > 1$. The eigenvalues of each invariant subspace, either stable or unstable, occur in concentric circles in the complex plane [17]. The flow characterized by the stable and unstable subspaces provide opportunities to construct efficient transfers that approach and depart desired quasi-periodic orbits.

3.4.3 Invariant Subspaces Near Quasi-Periodic Orbits

Trajectories that exist within the stable and unstable subspaces associated with a quasi-periodic orbit offer opportunities to construct low-cost transfers in the CRTBP model. An infinite number of trajectories densely fill the surface of the hyperbolic, i.e., stable and unstable, manifolds and, by nature, these trajectories asymptotically approach the quasi-periodic orbit. The eigenvectors associated with the stable and unstable manifolds are locally tangent to the invariant curve, however, the global representation of the hyperbolic manifolds are constructed via propagation from the local eigenvectors. Let $\{\Lambda_{\mathrm{j}}^S\}$ be the collection of eigenvalues with modulus less than unity, $\|\Lambda_{\mathrm{j}}^S\| < 1$, i.e., the stable subspace, with corresponding eigenvectors defined as $\{\bar{\Psi}_{\mathrm{j}}^S\}$. Additionally, $\{\Lambda_{\mathrm{j}}^U\}$ is the collection of eigenvalues with modulus greater than unity, $\|\Lambda_{\mathrm{j}}^S\| > 1$, i.e., the unstable subspace, with corresponding eigenvectors defined as $\{\bar{\Psi}_{\mathrm{j}}^U\}$. The local representation of the stable manifold surface associated with a quasi-periodic orbit leverages an eigenvector, $\bar{\Psi}_1^S$, which corresponds to an eigenvalue, Λ_1^S, with a zero imaginary element, such that, $\mathrm{Im}[\Lambda_1^S] = 0$. Recalling that eigenvalues occur in concentric circles, an eigenvalue, Λ_1^S, with only real parts will have a corresponding eigenvector, $\bar{\Psi}_1^S$, with real components. The eigenvector, $\bar{\Psi}_1^S$, is a vector of size $6n_q$ and is divided into a set of sub-eigenvectors $\{\bar{\psi}_{1,\mathrm{j}}^S\}$ that correspond to torus states $\bar{u}_{\mathrm{j}}$ along the invariant curve, such that,

$$\{\bar{\Psi}_1^S\} = \begin{bmatrix} \bar{\psi}_{1,1}^S \\ \bar{\psi}_{1,2}^S \\ \vdots \\ \bar{\psi}_{1,n_q}^S \end{bmatrix}. \tag{3.139}$$

A state on the stable manifold, $\bar{\mathcal{X}}_{\mathrm{j}}^S$, is approximated as,

$$\bar{\mathcal{X}}_{\mathrm{j}}^S = \bar{\mathcal{X}}_{\mathrm{j}}^Q \pm \eta \frac{\bar{\psi}_{1,\mathrm{j}}^S}{\|\bar{\psi}_{1,\mathrm{j},r}^S\|}, \tag{3.140}$$

where η is a step-off magnitude, $\bar{\psi}^S_{1,\mathrm{j}}$ is the associated six-dimensional stable eigenvector for $\bar{u}_\mathrm{j}$ which is also written as, $\bar{\psi}^S_{1,\mathrm{j}} = [\bar{\psi}^S_{1,\mathrm{j},r}; \bar{\psi}^S_{1,\mathrm{j},v}]$ and $\bar{\mathcal{X}}^Q_\mathrm{j} = \bar{u}_\mathrm{j} + \bar{\mathcal{X}}^*$. Recall that $\bar{\mathcal{X}}^*$ is the fixed point of an associated periodic orbit. The three-dimensional vectors $\bar{\psi}^S_{1,\mathrm{j},r}$ and $\bar{\psi}^S_{1,\mathrm{j},v}$ are defined such that $\bar{\psi}^S_{1,\mathrm{j},r}$ corresponds to the elements associated with position and $\bar{\psi}^S_{1,\mathrm{j},v}$ isolate the velocity elements. The value of η is implemented as a step-off distance in the direction of the eigenvector direction. The global representation of the stable manifold is evaluated via propagation of the states on the local stable manifolds, $\bar{\mathcal{X}}^S_\mathrm{j}$, in reverse time, i.e., $t \to -\infty$. So far, only the stable manifold has been discussed, however, the same process is implemented to compute the state, $\bar{\mathcal{X}}^U_\mathrm{j}$, along the local unstable manifold. The global representation of the unstable manifold is then evaluated by forward time propagation.

A state on the local stable (or unstable) manifold is computed via Equation (3.140) along the invariant curve. To represent the states on the local hyperbolic manifolds from the full torus, i.e., all locations along the two-dimensional torus, the STM is implemented [33]. Let $\bar{\psi}^S_{1,\mathrm{j}}$ be an eigenvector in the stable subspace corresponding to a state along the invariant curve, $\bar{\mathcal{X}}^Q_\mathrm{j}(0)$. Then the eigenvector to corresponding to a state along the torus, $\bar{\mathcal{X}}^Q_\mathrm{j}(t)$, is evaluated as,

$$\bar{\psi}^S_{1,\mathrm{j}}(t) = \frac{\partial \bar{\mathcal{X}}^Q_\mathrm{j}(t)}{\partial \bar{\mathcal{X}}^Q_\mathrm{j}(0)} \bar{\psi}^S_{1,\mathrm{j}}, \tag{3.141}$$

where $\frac{\partial \bar{\mathcal{X}}^Q_\mathrm{j}(t)}{\partial \bar{\mathcal{X}}^Q_\mathrm{j}(0)}$ is the STM after the propagation time t. The information from the hyperbolic invariant manifolds associated with quasi-periodic orbits offers opportunities to construct efficient transfers that approach and depart quasi-periodic orbits. Quasi-periodic orbits provide more complex geometries for mission design objectives.

4. RIDESHARE MISSION OVERVIEW

The ridesharing scenario in this investigation includes two satellites, a primary and secondary payload, launched concurrently into a Geosynchronous Transfer Orbit. In this ridesharing scenario, the objective of the primary mission is to situate a satellite, i.e., a primary payload, into Geostationary Orbit. After launch, the primary payload is inserted into a GTO en route to the desired GEO altitude, a transfer strategy frequently implemented to place satellites in GEO; note that additional strategies to place a satellite in GEO are discussed in the United Launch Alliance (ULA) Atlas V Guide[71]. The ridesharing mission in this analysis is focused on the transfer options available for a secondary payload launched simultaneously with the primary payload from an intermediate GTO. The ridesharing mission scenario is illustrated in Figure 4.1 and is consistent with the following steps:

1. Launch of primary and secondary payloads.
2. Enter primary payload intermediate orbit.
    - Geosynchronous Transfer Orbit.
3. Primary payload separation.
    - Primary payload performs an insertion maneuver at GTO apoapsis and enters into a Geostationary Orbit. Secondary payload remains in GTO.
4. Secondary payload performs Transfer Insertion Maneuver (TIM) at GTO periapsis en route to destination in the Sun-Earth system.

The ridesharing strategy reduces the launch costs for secondary payloads; especially important for small satellites as launch costs may significantly exceed the production costs. However, secondary payloads face many challenges, such as:

- No control over launch epoch.

- No control over selected launch vehicle.
- No control over drop-off orbit.
- No abort option once the secondary payload is integrated into launch vehicle.

Preliminary design for secondary payloads must incorporate these constraints. In this analysis, transfers from an intermediate GTO are constructed considering a range of departure epochs and orbit orientations. Note that the departure epoch and launch epoch are different;

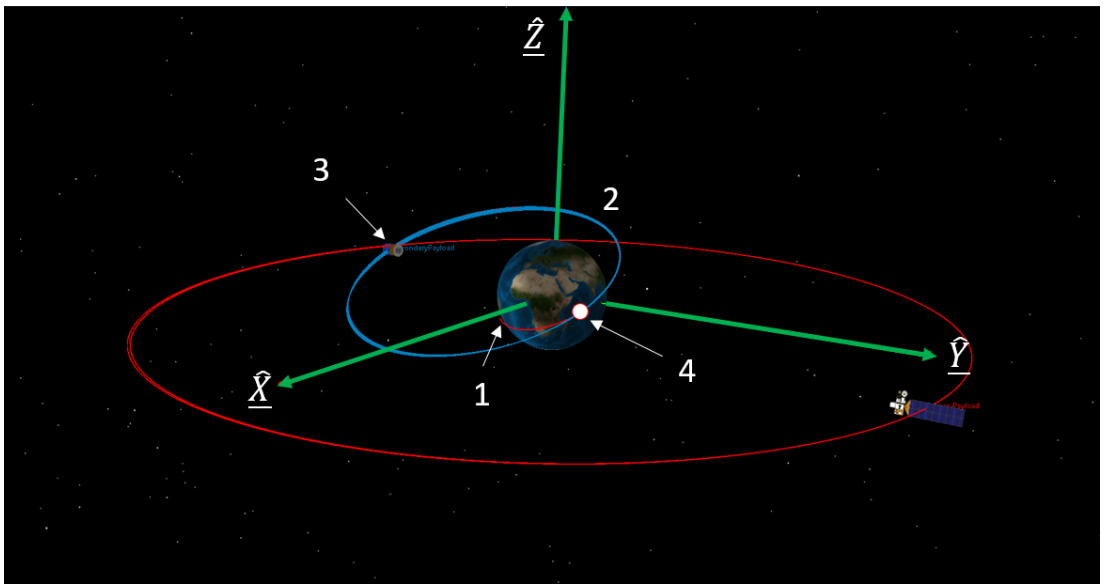

Figure 4.1. : Ridesharing mission scenario for primary and secondary payloads plotted in an inertial EME reference frame. The intermediate GTO orbit is in cyan and the primary Geostationary Orbit is in red

the departure epoch is defined as a time after the primary payload has detached, i.e., step 4 in Figure 4.1. Assuming no additional maneuvers are performed, i.e, the drop-off GTO remains unaltered, after the primary payload has detached, the GTO orientation is dependent on the primary mission launch constraints. With no a priori information regarding the primary mission launch epoch or the drop-off GTO orientation, strategies leveraging dynamical structures in the CRTBP model are formulated to construct flexible and efficient transfers to orbits near the Sun-Earth Lagrange points from a range of departure GTO orientations.

4.1 Geosynchronous Transfer Orbit in the CRTBP Rotating Frame

A Geosynchronous Transfer Orbit is a Keplerian elliptical orbit, defined within the context of the Two-Body problem, and is rotated into the CRTBP rotating frame. A GTO has a defined apogee altitude equal to the geosynchronous orbit altitude, i.e., $h_a = 35,786$ km, while the perigee altitude, h_p, is dependent on the performance and size of the launch vehicle and may vary from 185-1200 km. A GTO is a closed orbit defined via a Two-Body approximation, however, in the rotating frame consistent with the CRTBP model, the GTO is not a closed orbit. Actually, in this analysis, a GTO in the CRTBP model is a propagated arc from a rotated GTO state; note that the GTO state is rotated from an inertial frame. An arbitrary inertial frame and rotating frame associated with the CRTBP model is illustrated in Figure 2.5. The dimensional GTO position and velocity vectors in the inertial frame, $\underset{\mathrm{i}'}{\bar{R}}_{\mathrm{ps}}$ and $\underset{\mathrm{i}'}{\bar{V}}_{\mathrm{ps}}$, respectively, is defined as,

$$\underset{\mathrm{i}'}{\bar{R}}_{\mathrm{ps}} = \mathbf{C}^T(\Omega, {}^{\mathrm{i}'}\mathrm{i}, \omega) \begin{bmatrix} \frac{a(1-\mathrm{e}^2)}{(1+\mathrm{e}\cos(\nu))}\cos(\nu) \\ \frac{a(1-\mathrm{e}^2)}{(1+\mathrm{e}\cos(\nu))}\sin(\nu) \\ 0 \end{bmatrix}, \tag{4.1}$$

$$\underset{\mathrm{i}'}{\bar{V}}_{\mathrm{ps}} = \mathbf{C}^T(\Omega, {}^{\mathrm{i}'}\mathrm{i}, \omega) \begin{bmatrix} \sqrt{\frac{\tilde{G}M_2}{r_p(1+\mathrm{e})}}(-\sin(\nu)) \\ \sqrt{\frac{\tilde{G}M_2}{r_p(1+\mathrm{e})}}(\mathrm{e}+\cos(\nu)) \\ 0 \end{bmatrix}, \tag{4.2}$$

where a is the semimajor axis, e is the orbit eccentricity, ν is the true anomaly, $\tilde{G}$ is the gravitational constant, and M_2 is the mass of the Earth. Note that Equations (4.1) and (4.2) are consistent with a Two-Body approximation and, in this investigation, the position and velocity vectors, $\underset{\mathrm{i}'}{\bar{R}}_{\mathrm{ps}}$ and $\underset{\mathrm{i}'}{\bar{V}}_{\mathrm{ps}}$, are measured with respect to the Earth, i.e., P_2 in the

Sun-Earth system [72]. The rotation matrix, $\mathbf{C}$ in Equations (4.1)-(4.2), is consistent with a 3-1-3 body rotation matrix, i.e.,

$$\mathbf{C}(\Omega, {}^{\mathrm{i}'}\mathrm{i}, \omega) = \begin{bmatrix} \cos(\omega) & \sin(\omega) & 0 \\ -\sin(\omega) & \cos(\omega) & 0 \\ 0 & 0 & 1 \end{bmatrix} \begin{bmatrix} 1 & 0 & 0 \\ 0 & \cos({}^{\mathrm{i}'}\mathrm{i}) & \sin({}^{\mathrm{i}'}\mathrm{i}) \\ 0 & -\sin({}^{\mathrm{i}'}\mathrm{i}) & \cos({}^{\mathrm{i}'}\mathrm{i}) \end{bmatrix} \begin{bmatrix} \cos(\Omega) & \sin(\Omega) & 0 \\ -\sin(\Omega) & \cos(\Omega) & 0 \\ 0 & 0 & 1 \end{bmatrix} \tag{4.3}$$

where Ω, ω, and ${}^{\mathrm{i}'}\mathrm{i}$ are Keplerian orbital elements corresponding to the Right Ascension of the Ascending Node (RAAN), Argument of Periapsis, and inclination, respectively, in the inertial frame illustrated in Figure 2.5. The inertial position and velocity are nondimensionalized via Equations (2.25)-(2.26) and rotated to the CRTBP rotating frame with Equation (2.46); note that the rotation is performed at the initial time $t = 0$. In this investigation, the orientation of the GTO, i.e., the drop-off orbit in the rideshare scenario, is described via the GTO departure state. The location of the GTO departure state in the inertial frame and the CRTBP rotating frame is illustrated via a green point in Figure 4.2. The size of

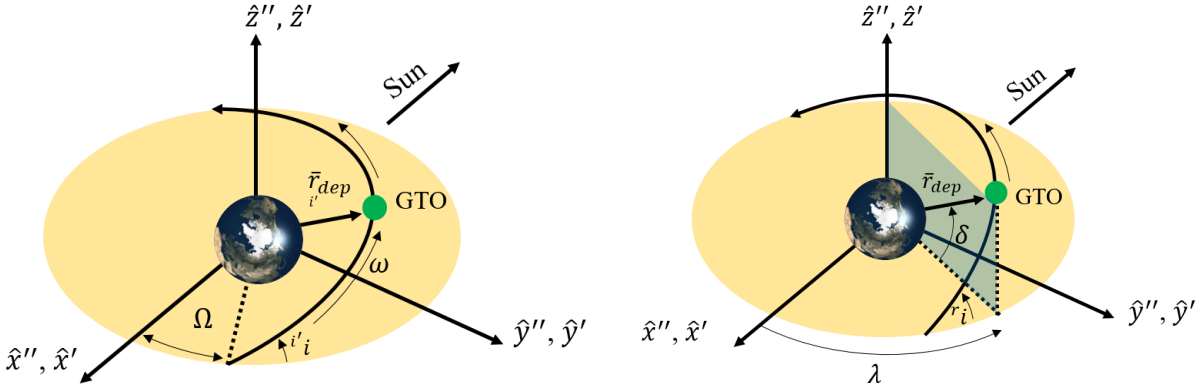

Figure 4.2. : (a) GTO departure state in an arbitrary inertial frame (b) GTO departure state in a shifted CRTBP rotating frame. In both illustrations, the shifted rotating frame basis vector $\{\hat{x}'', \hat{y}'', \hat{z}''\}$ coincide with the arbitrary inertial frame basis vectors $\{\hat{x}', \hat{y}', \hat{z}'\}$ at time $t = 0$. Note that, for both frames, the origin is at one of the primaries, e.g., the Earth

the GTO is fixed, i.e., the perigee and apogee altitudes are constant, such that the GTO departure position in the inertial frame, $\bar{r}_{\mathrm{i}'\mathrm{dep}}$, is parameterized as: $\bar{r}_{\mathrm{i}'\mathrm{dep}} = \bar{r}_{\mathrm{i}'\mathrm{ps}}(\Omega, \omega, {}^{\mathrm{i}'}\mathrm{i})$, see

Figure 4.2(a). In a shifted rotating frame, the GTO departure position is parameterized via the following variables: λ,δ, and ${}^{r}\mathrm{i}$ and is illustrated in Figure 4.2(b). Note that the shifted rotating frame, defined by the basis vectors $\{\hat{x}'', \hat{y}'', \hat{z}''\}$, is centered at the Earth, whereas the CRTBP rotating frame has an origin at the P_1-P_2 barycenter, see Figure 2.5. In the CRTBP rotating frame, the departure position is parameterized as: $\bar{r}_{\text{dep}} = \bar{r}_{\text{ps}}(\lambda, \delta, {}^{r}\mathrm{i})$. Additionally, in this analysis, the departure GTO state is consistent with the GTO perigee. Recall that the position and velocity vectors in the arbitrary inertial frame, $\underset{\mathrm{i}'}{\bar{r}}_{\text{dep}}$ and $\underset{\mathrm{i}'}{\bar{v}}_{\text{dep}}$, are written with respect to the Earth, i.e., P_2. Note that the inertial departure state, as illustrated in Figure 4.2(a), is a function of: Ω, ω, and ${}^{\mathrm{i}'}\mathrm{i}$; whereas the CRTBP departure state vector is a function of the angles: λ, δ, ${}^{r}\mathrm{i}$. The λ and δ angles are consistent with right ascension and declination angles, respectively, in the CRTBP rotating frame of the departure position. In Figure 4.2, the inclination values in the inertial and rotating frame are not equal, i.e., ${}^{\mathrm{i}'}\mathrm{i} \neq {}^{r}\mathrm{i}$. Although the inertial basis vectors $\{\hat{x}', \hat{y}', \hat{z}'\}$ are equal to the shifted rotating frame basis vectors $\{\hat{x}'', \hat{y}'', \hat{z}''\}$, the velocity vectors, used in computing the inclination value, are not equal along both frames. A comparison of the inertial, ${}^{\mathrm{i}'}\mathrm{i}$, and rotating, ${}^{r}\mathrm{i}$, inclination values is plotted in Figure 4.3. The inclination difference presented in Figure 4.3 is consistent with a GTO departure state with $\Omega = \omega = 0°$. Note that the inclination difference is zero at ${}^{\mathrm{i}'}\mathrm{i} = 0°$, i.e., when the GTO velocity vector is in the $\hat{x}$ -$\hat{y}$ or the ecliptic. Additionally, the inclination difference along a range of Ω values is within the range presented in Figure 4.3. In this investigation, the inclination values in both frames are utilized to identify prograde and retrograde orbits and to construct GTO departure states for a range of inclinations; note that the focus of the subsequent chapters is the construction of transfers from prograde GTOs.

The orientation of a GTO is dependent on the primary launch window and the launch vehicle performance metrics and is described via a GTO departure state. A GTO, i.e., a Keplerian elliptical orbit in the Two-Body Problem, with periapsis altitude of 185 km is plotted in the rotating reference frame consistent with the Sun-Earth CRTBP in Figure 4.4. In the rotating frame, the GTO is not a closed periodic orbit and its line of apsides shifts as demonstrated in Figure 4.4. A precession angle γ is defined to depict the shift in the GTO

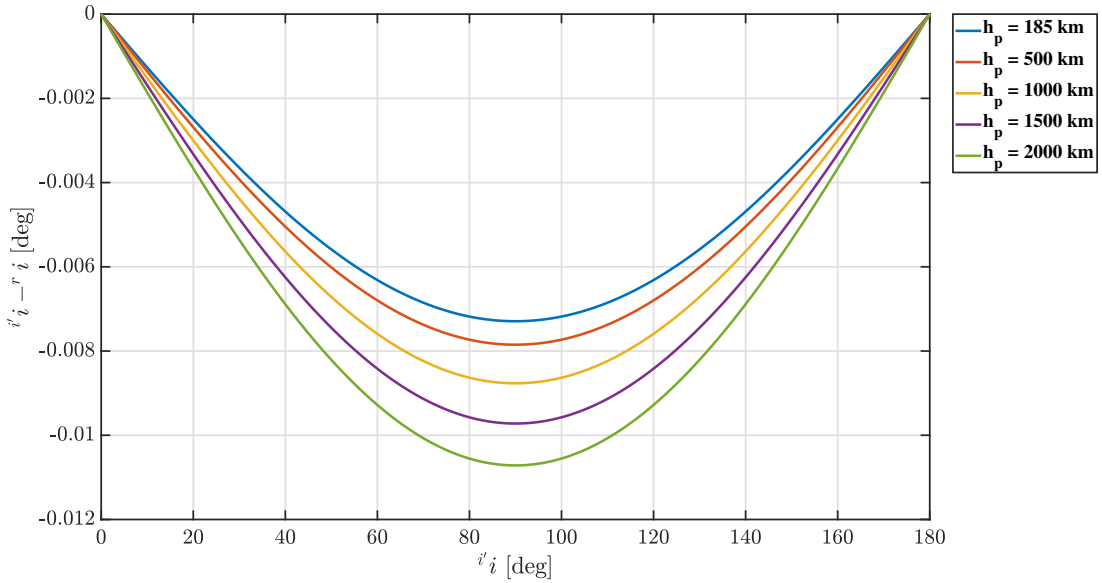

Figure 4.3. : Difference between the inertial and rotating inclination at different GTO departure state altitudes, h_p. This example corresponds to an inertial departure state consistent with $\Omega = \omega = 0°$

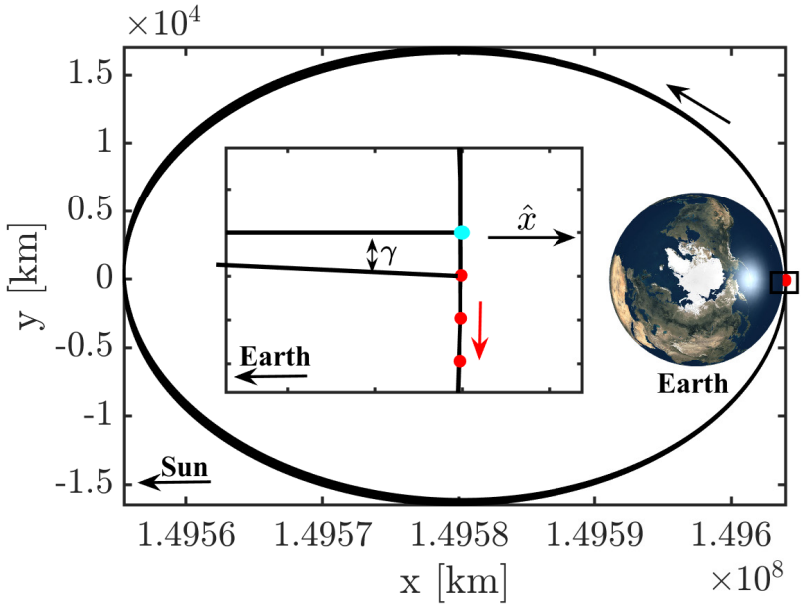

Figure 4.4. : Geometry of a GTO in the rotating frame of the CRTBP. The GTO departure state is in cyan and the subsequent perigee points are in red. Note that the motion of the GTO is counter-clockwise, but the perigee location moves clockwise

perigee (i.e., the shift in the line of apsides) after a number of revolutions in the rotating frame consistent with the CRTBP model. The angle γ is evaluated as the angle measured from the $\hat{x}$ axis, in the rotating frame, and the GTO perigee direction, defined with respect to the Earth. As an example, the precession angle for the GTO, plotted in Figure 4.4, after one revolution is $\gamma = 0.42°$ in the direction indicated. Note that the line of apsides rotates clockwise and opposite to the motion of the prograde satellite. A GTO perigee is defined such that $\bar{v}_{2s} \cdot \bar{r}_{2s} = 0$ with the condition that $v_{2s}^2 + \bar{r}_{2s} \cdot \ddot{\bar{r}}_{2s} \geq 0$, where $\bar{v}_{2s}$ is the velocity vector of the satellite in the rotating frame, $r_{2s} = r - [1-\mu, 0, 0]^T$ is the position vector with respect to the Earth, $\dot{\bar{r}}_{2s} = \bar{v}_{2s}$, and $\ddot{r}_{2s} = [\ddot{x}, \ddot{y}, \ddot{z}]^T$. The Keplerian GTO as observed in Figure 4.4 possesses a perigee altitude of 185 km, the standard GTO altitude as defined by the United Launch Alliance [71] and serves as the baseline geometry for this investigation. The orientation in Figure 4.4, defined as the midnight orientation, includes the initial perigee on the $\hat{x}$-axis opposite the Sun and Earth directions. If the initial drop-off orientation is considered unfavorable for a transfer towards the Sun-Earth Lagrange points, there is an option to wait an additional number of revolutions on the GTO. Waiting allows for a periapsis shift to rotate the GTO into an orientation associated with more efficient transfers to orbits near the Lagrange points. However, waiting may require weeks or months to achieve a specific desired orientation as necessary for an efficient transfer. For the 185 km GTO, with a period of 10.4 hrs, a desired shift in γ of 45° requires a wait time of 47 days. This wait time creates additional operational constraints for the satellite, such as additional maneuvers to maintain altitude and avoid possible conjunction events, therefore, waiting along a GTO is not considered as an option in this investigation. However, launch conditions or priorities for a primary payload may dictate a range of precession angles that must be accommodated.

4.2 GTO Departure State in the Inertial EME Frame and the CRTBP Rotating Frame

The drop-off orbit orientation presents a significant design challenge for secondary payloads. In this analysis, the GTO, i.e., the drop-off orbit, is the departure orbit for a secondary payload in a ridesharing scenario and the arrival orbit is a desired periodic or quasi-periodic orbit near the Sun-Earth Lagrange points. The size of the GTO is fixed, that is, the apoapsis altitude is fixed at the GEO altitude of $35,786$ km, and the periapsis altitude is 185 km. Note that the periapsis altitude for this analysis is a standard GTO periapsis altitude defined by the United Launch Alliance [71], although, higher altitudes can be assessed within the same framework. The orientation of the GTO is defined via the Keplerian orbital elements: Ω, ω, and ${}^{\mathrm{i}}\mathrm{i}$, defined in McClain [72] and the departure location is the GTO periapsis. Recall that the Keplerian orbital elements are defined in an inertial frame and ${}^{\mathrm{i}}\mathrm{i}$ is the inclination in the inertial EME frame, see Section 2.3.2. In a ridesharing scenario, the drop-off orbit orientation is dictated by the primary mission constraints, therefore, in this analysis, it is assumed that there is no a priori information about the orientation of the GTO, i.e., the drop-off orbit. In this investigation, a change in GTO orientation is described as a change in the position of the GTO periapsis, i.e., the departure location. The position of the GTO periapsis is described with Keplerian orbital elements associated with the J2000 Earth Mean Equatorial, or EME, inertial reference frame, but the target periodic and quasi-periodic orbits exist in the rotating frame of the Sun-Earth CRTBP model. The GTO departure position in the EME frame, $\bar{r}_{\mathrm{dep}}$, is parameterized via the traditional Keplerian orbital elements, Ω, ω, and ${}^{\mathrm{i}}\mathrm{i}$, see McClain [72] and Equation (4.1); note that ${}^{\mathrm{i}}\mathrm{i}$ is the inclination of the orbit in the EME frame. In the Sun-Earth rotating frame, the GTO departure position, $\bar{r}_{\mathrm{dep}}$, is parameterized via the angles, λ and δ, as illustrated in Figure 4.5(b), such that the departure position, at a fixed altitude, is represented as $\bar{r}_{\mathrm{dep}}(\lambda, \delta)$. Note that in Figure 4.5(b), the basis vectors $\{\hat{x}'', \hat{y}'', \hat{z}''\}$ represent a shifted rotating frame with an origin at P_2, i.e., the Earth. Additionally, the inclination of the ecliptic plane is illustrated in Figure 4.5(a), i.e., the yellow shaded region. Observe that, in Figure 4.6(b), the inclination of the ecliptic, i.e., the inclination of the Sun's orbital

plane with respect to the Earth's equatorial plane consistent with the EME frame, has an oscillatory component. In Figure 4.6(a), the instantaneous distance between the Sun and the Earth for a range of epochs is plotted; note that this information is retrieved from the DE430 ephemeris file provided by NASA JPL Navigation and Ancillary Information Facility. The peak-to-peak amplitude of the oscillatory behavior of the ecliptic plane inclination is small, approximately 0.004°, for an epoch range of ten years. Contrary to the significant variation of the instantaneous Sun-Earth distance with an approximate peak-to-peak amplitude of 5×10^6 km, see Figure 4.6(a).

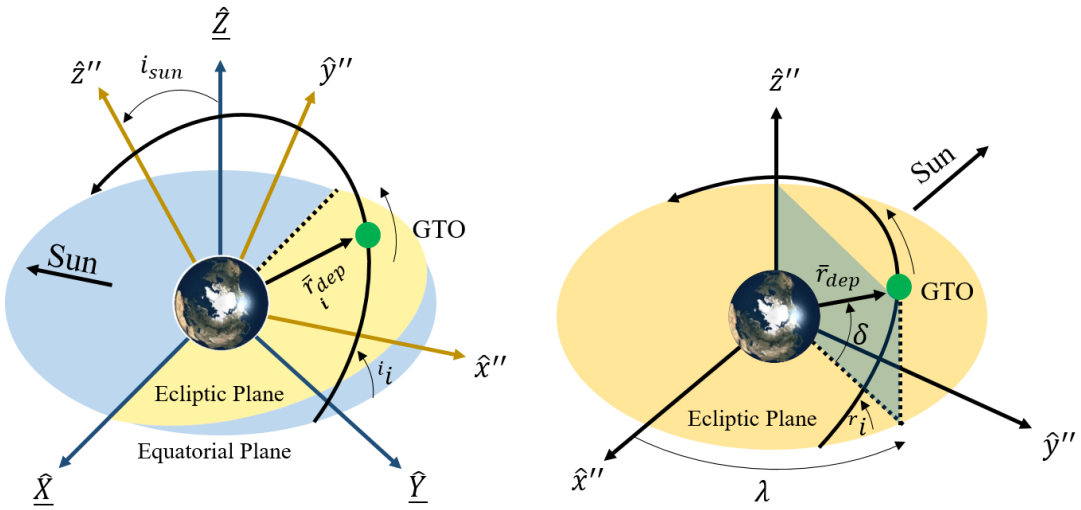

Figure 4.5. : (a) J2000 Earth Mean Equatorial inertial reference frame, denoted with $\{\hat{X},\hat{Y},\hat{Z}\}$, and a shifted Sun-Earth rotating frame, with basis vectors $\{\hat{x}'',\hat{y}'',\hat{z}''\}$ (b) GTO periapsis departure position, expressed in the Sun-Earth rotating frame, parameterized by angles: λ and δ

For a range of departure epochs, the GTO departure position, $\bar{r}_{\text{dep}}$, varies in the Sun-Earth rotating frame as $\bar{r}_{\text{dep}}$ remains constant in the EME frame. In this investigation, one of the objectives is the construction of transfers at a fixed departure epoch from a range of GTO orientations. The range of orientations is described via a changing Ω angle in the EME frame with a fixed inclination, $^{\text{i}}$i, and ω (refer to Table 4.1). The plots in Figures 4.7-4.8 present the instantaneous change in the rotating frame inclination, ^{r}i, over a ten year

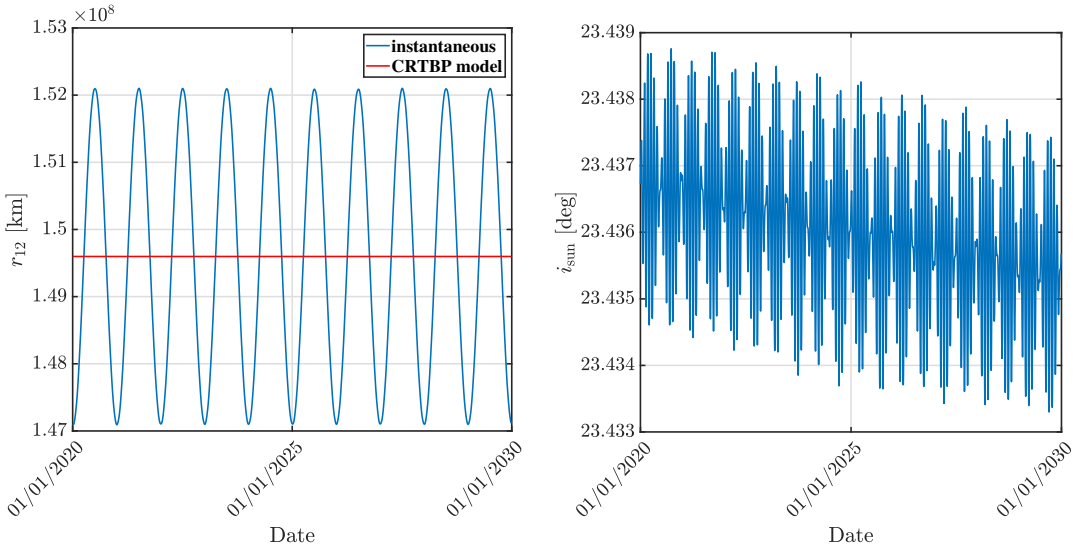

Figure 4.6. : Ten year time history of (a) the instantaneous distance between the Earth and the Sun and (b) the inclination of the ecliptic plane with respect to the Earth's equatorial plane. The constant Sun-Earth distance, implemented in the CRTBP model, is plotted as a red line

period. The rotating inclination, ${}^{r}\mathrm{i}$, values plotted in Figure 4.7 possess a range: $|{}^{i}\mathrm{i} - \mathrm{i}_{\mathrm{sun}}| < {}^{r}\mathrm{i} < |{}^{i}\mathrm{i} + \mathrm{i}_{\mathrm{sun}}|$, where $\mathrm{i}_{\mathrm{sun}}$ is the inclination of the ecliptic in the EME frame, as illustrated in Figure 4.5(a). Recall that the instantaneous inclination of the ecliptic, $\mathrm{i}_{\mathrm{sun}}$, varies with epoch, however, the variation is small such that, in this investigation, the inclination is defined as: $\mathrm{i}_{\mathrm{sun}} = 23.43°$. The range of ${}^{r}\mathrm{i}$ observed in Figure 4.7 corresponds to a value of $\omega = 0°$. Now, if the RAAN, Ω, is fixed to values of $\Omega = 0°$ and $\Omega = 90°$, the variation of the rotating inclination is plotted in Figure 4.8. The variation of ${}^{r}\mathrm{i}$ due to ω is small, approximately less than 0.01°, for period between 2020-2030. Recalling that the GTO departure location is parameterized via λ and δ in Figure 4.5(b), the variation of these angles is depicted in Figures 4.9-4.10. The variation of δ for a fixed epoch of Jun 2, 2022 over a range of Ω and ω is plotted in Figure 4.9. In Figure 4.9(a), the associated inclination, ${}^{i}\mathrm{i}$, is equal to 27°, i.e., the standard inclination for a GTO as defined by ULA. Based on the contour plot presented, the range for δ is observed to be $-\mathrm{i}_{\mathrm{sun}} - {}^{i}\mathrm{i} < \delta < \mathrm{i}_{\mathrm{sun}} + {}^{i}\mathrm{i}$, i.e., is a function of the inclination of the ecliptic plane and ${}^{i}\mathrm{i}$. A change of GTO inclination to ${}^{i}\mathrm{i} = 5°$ reveals a smaller range of δ, as plotted in Figure 4.9(b). Note that for smaller GTO inclinations,

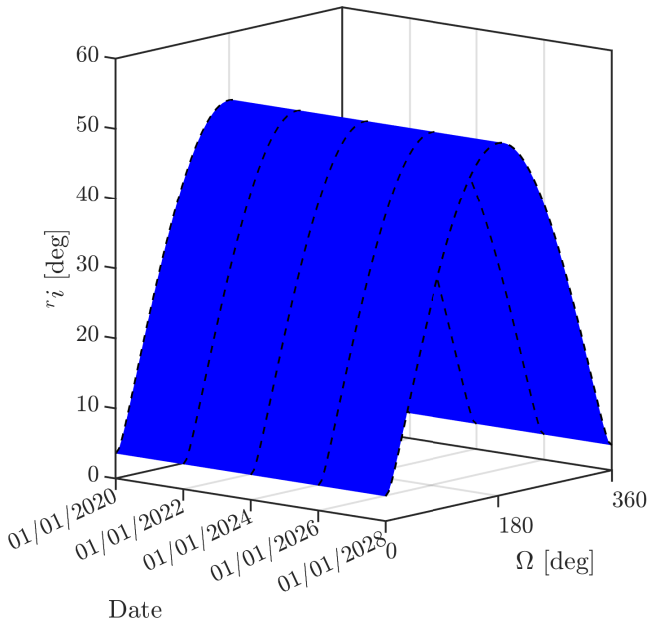

Figure 4.7. : Variation in rotating frame inclination, ^{r}i, over a ten year period for a range of RAAN angles, Ω. The dashed lines correspond to years: 2020, 2022, 2024, and 2026 and show the shape of the surface

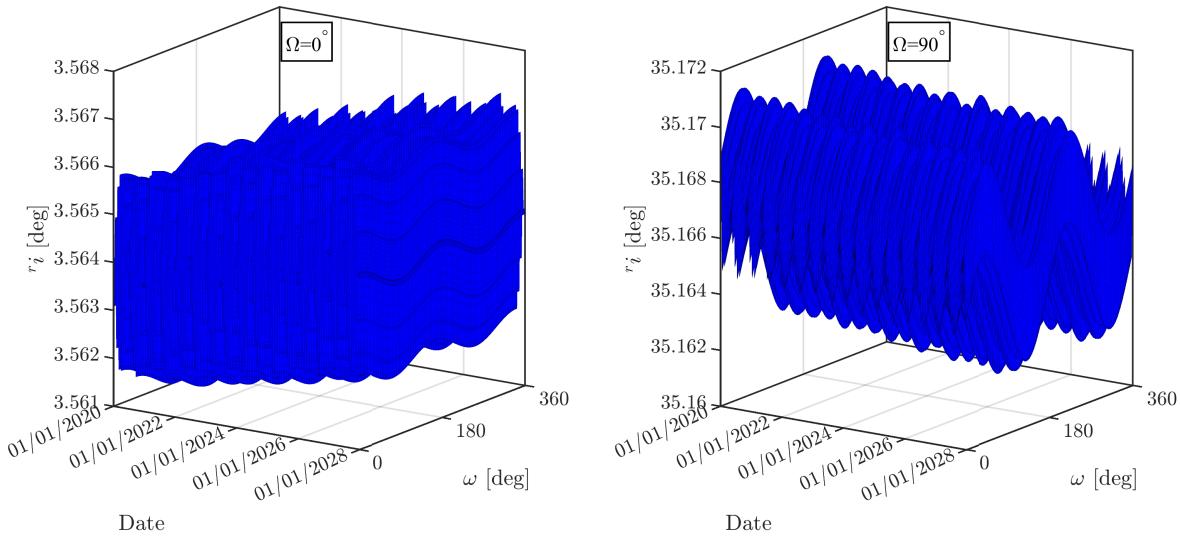

(a) (b)

Figure 4.8. : Rotating frame inclination, ^{r}i, variation for a range of ω values at fixed values of (a) $\Omega = 0°$ and (b) $\Omega = 90°$. The variation of the inclination is small in both plots

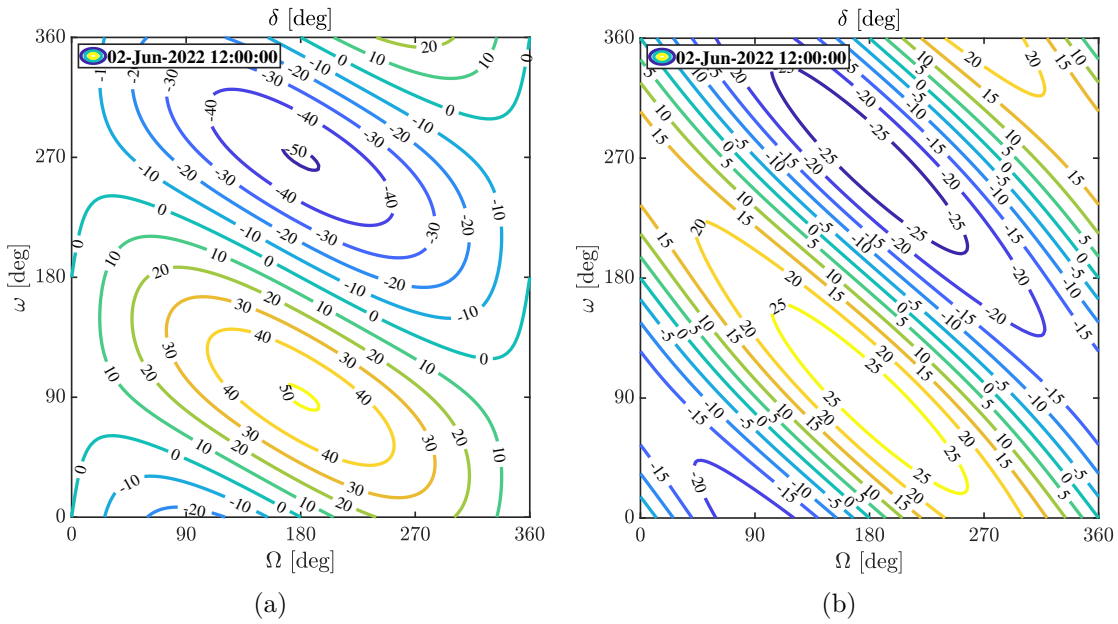

Figure 4.9. : Variation in δ angle over a range of Ω and ω corresponding to two different inclinations: (a) ${}^{i}\mathrm{i} = 27°$ and (b) ${}^{i}\mathrm{i} = 5°$. Note that the overall range of δ is defined as $-\mathrm{i}_{\mathrm{sun}} - {}^{i}\mathrm{i} < \delta < \mathrm{i}_{\mathrm{sun}} + {}^{i}\mathrm{i}$

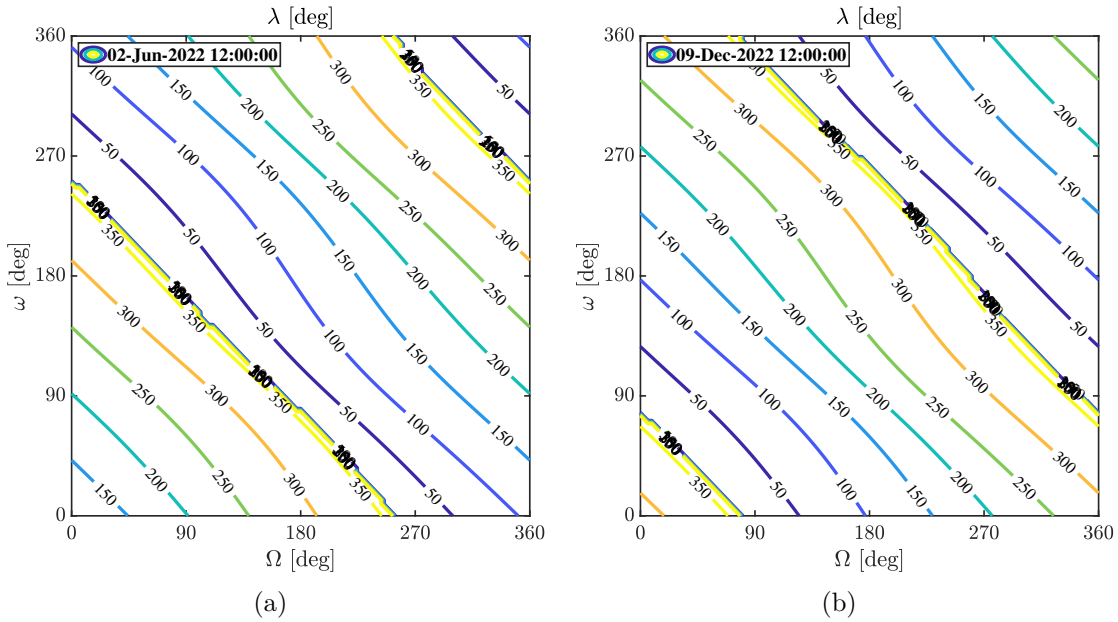

Figure 4.10. : Variation of λ over a range of Ω and ω corresponding to two different epochs: (a) Jun 2, 2022 and (b) Dec 9, 2022. Observe that the range of λ is $0° \leq \lambda \leq 360°$. The change in epoch shifts the contour lines corresponding to the λ values

the contour lines of δ appear more elongated. The range of δ as a function of i_{sun} and ${}^{i}i$ is consistent throughout a range of GTO inclinations. The contours in Figure 4.10 represent the variation in the λ angles corresponding to two different epochs. The range of λ plotted in Figure 4.10 is $-180^{\circ} \leq \lambda \leq 180^{\circ}$ and observe that changing the epoch shifts the contour lines of λ. The variation of λ and δ presented in Figures 4.9-4.10 conveys the changing GTO departure location in the rotating frame; recalling that transfers into the desired CRTBP Lagrange points are constructed in the Sun-Earth rotating frame. In this investigation, optimal ΔV transfers are constructed over a range of orientations from a fixed departure epoch. A summary of Keplerian orbital elements corresponding to the selected GTO in the inertial EME frame and the range of rotating frame λ and δ values is provided in Table 4.1. An understanding of the variable GTO departure positions, i.e., the varying orientations, facilitates the search and construction of efficient transfers to the vicinity of the Sun-Earth Lagrange points.

Table 4.1. : Comparison of variables that parameterize the GTO periapsis position in the J2000 EME inertial and Sun-Earth rotating frame

Inertial Frame	Rotating Frame
$r_a = 35,786$ km	$r_a = 35,786$ km
$r_p = 185$ km	$r_p = 185$ km
${}^{i}i = 27^{\circ}$	$\lvert {}^{i}i - i_{sun} \rvert < {}^{r}i < \lvert {}^{i}i + i_{sun} \rvert$
$0^{\circ} < \Omega < 360^{\circ}$	$-i_{sun} - {}^{i}i < \delta < i_{sun} + {}^{i}i$
$\omega = 0^{\circ}$	$0^{\circ} < \lambda < 360^{\circ}$

5. BALLISTIC TRANSFERS TO COLLINEAR LAGRANGE POINTS

Ballistic pathways into orbits near the Sun-Earth Lagrange points offer important dynamical insights and are implemented in a preliminary trajectory design strategy from a Geosynchronous Transfer Orbit. A ballistic transfer, in the context of this investigation, is defined as a single maneuver transfer from a GTO departure state onto a trajectory that enters into periodic or quasi-periodic motion near a Sun-Earth Lagrange point. The selected destinations in this analysis are the Sun-Earth L_1 and L_2 points. Recall that, in the rideshare scenario for the secondary payload discussed in Chapter 4, launch conditions and the drop-off GTO Keplerian orbital elements are not known a priori. The departure state for a smallsat secondary payload is from a GTO periapsis location, but the position of the departure state near the Earth vicinity is not known. One of the objectives of this analysis is the identification of regions near the Earth vicinity with access to ballistic transfers towards orbits near Sun-Earth L_1 or L_2 from a GTO departure state. In this section, ballistic transfers are constructed by leveraging information from the stable manifold structures associated with periodic and quasi-periodic orbits near the Lagrange points. Additionally, a group of direct ballistic transfers are generated for unconstrained, i.e., no enforced constraints along the trajectory, and constrained transfers to Sun-Earth L_1 and L_2. Then, these ballistic transfers are verified in the higher-fidelity ephemeris model. Knowledge of ballistic transfers informs mission designers with favorable GTO departure locations near the Earth vicinity that aid in the search effort for flexible and efficient transfer options for secondary payloads.

5.1 Ballistic Transfers into Periodic Orbits

Trajectories along the stable manifold structures associated with periodic orbits are frequently leveraged to generate efficient ballistic transfers to orbits near the Sun-Earth Lagrange points. These trajectories asymptotically approach a periodic orbit and are desirable for the delivery of single maneuver transfers from GTO. In this investigation, ballistic

transfers from Lagrange point orbits that are accessible from near the Earth are identified assuming a GTO departure altitude of 185 km. The objective of this analysis is the identification of regions near the Earth vicinity with access to ballistic transfers towards the Sun-Earth L_1 or L_2 points. Recall that a ballistic transfer is defined as a single maneuver transfer from a GTO departure state, i.e., a periapsis state, onto a trajectory along the stable manifold associated with a periodic orbit. To identify ballistic transfers, trajectories on the stable manifold of a periodic orbit are propagated in reverse time towards the Earth. Before ballistic transfers to periodic orbit are constructed, a precursory survey of ΔV magnitudes from departure locations along a GTO is completed by introducing a theoretical minimum ΔV parameter. The theoretical minimum ΔV, denoted as ΔV_{theo}, is computed with,

$$\Delta V_{\text{theo}} = \sqrt{2\mathcal{U}^*_{\text{dep}} - \mathcal{C}_{\text{arr}}} - V_{\text{dep}}, \tag{5.1}$$

where the GTO departure state has a corresponding pseudo-potential, $\mathcal{U}^*_{\text{dep}}$, and velocity, V_{dep}; recall that the pseudo-potential of the CRTBP is from Equation (2.32) and is a function of the position vector. The formulation in Equation (5.1) uses the energy, i.e., Jacobi Constant value $\mathcal{C}$, difference between the GTO departure state and an arrival orbit on the desired periodic orbit. The pseudo-potential, $\mathcal{U}^*_{\text{dep}}$, and the velocity, V_{dep}, are defined at a departure location along the GTO and the energy value for the arrival orbit is $\mathcal{C}_{\text{arr}}$. From Equation (5.1), for a fixed $\mathcal{C}_{\text{arr}}$, ΔV_{theo} varies as the departure location varies along the GTO. The theoretical minimum ΔV is a metric that offers a lower bound on ΔV that is dependent on the energy difference between the departure location and the arrival orbit. In practice, this minimum value simply assumes tangential maneuvers at departure and arrival locations, and essentially measures the cost to bridge the energy gap. A precursory survey of ΔV_{theo} magnitudes corresponding to the planar L_1 Lyapunov and out-of-plane L_1 halo orbit families in the Sun-Earth system at GTO periapsis and apoapsis is summarized in Table 5.1. Table 5.1 displays the lowest ΔV_{theo} magnitudes at the periapsis departure locations with the highest ΔV_{theo} values for apoapsis departures. Therefore, in this investigation, access to the ballistic transfers is only examined from GTO periapsis. However, there may also

exist accessibility regions along the GTO away from the periapsis, but such options are not explored in this analysis.

Table 5.1. : Theoretical minimum ΔV, ΔV_{theo}, requirements from GTO periapsis and apoapsis to periodic orbit families near Sun-Earth L_1

	$\mathcal{C}$	ΔV_{peri} (m/s)	ΔV_{apo} (m/s)
Lyapunov	3.00089069 - 3.00023778	736.35 - 762.67	2671.32 - 2738.71
halo	3.00082452 - 3.00020840	736.41 - 763.85	2661.45 - 2741.72

The construction of ballistic transfers leverages information from the stable manifold associated with periodic orbits in the CRTBP. A schematic for a general ballistic transfer into a periodic orbit is illustrated in Figure 5.1. In Figure 5.1, a ballistic transfer is initialized from an injection point on the periodic orbit. At the injection point, $\bar{\mathcal{X}}_{\text{inj}}$, the spacecraft steps in the direction of the local stable manifold, then the spacecraft is propagated in reverse time to the departure point, $\bar{\mathcal{X}}_f$, near the Earth vicinity. The departure point for the ballistic transfer is an apsis at a fixed altitude because the departure point for the rideshare scenario is a GTO periapsis from a desired altitude. The ballistic transfer is formulated as a Two

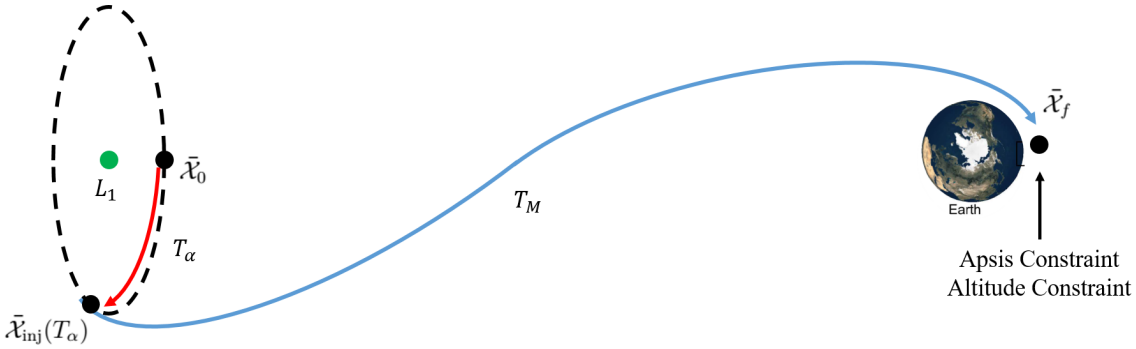

Figure 5.1. : Schematic for ballistic transfer into a periodic orbit. In this investigation, a ballistic transfer is a trajectory on the stable manifold of a periodic orbit and constructed via reverse propagation

Point Boundary Value Problem and corrected via a free-variable and constraint numerical method. The free-variable vector for the ballistic transfer illustrated in Figure 5.1 is,

$$\bar{\mathfrak{X}} = \begin{bmatrix} T_\alpha \\ T_M \end{bmatrix}, \tag{5.2}$$

where the injection point, $\bar{\mathcal{X}}_{\text{inj}}$, is evaluated after an initial state, $\bar{\mathcal{X}}_0$, on the periodic orbit is propagated by time T_α. The time T_M is the propagation time on a trajectory along the stable manifold associated with the periodic orbit. Recall that a periodic orbit is a dynamical structure with repeatable flow, such that, from an initial point on the periodic orbit, $\bar{\mathcal{X}}_0$, an arbitrary state, $\bar{\mathcal{X}}_1$, along the periodic orbit is computed by propagation from the initial point. Although, a long propagation time, i.e., if $T_\alpha > T_p$, may result in deviations from the periodic orbit as numerical error is accumulated during the propagation process; note that T_p is the period of the orbit. Additionally, a periodic orbit is also described by a one-dimensional torus with a fundamental frequency $\dot{\theta}_1$. In summary, a point on a periodic orbit is parameterized by a single variable and, in this application, the variable is a propagation time T_α. The dimension of the hyperbolic invariant manifolds is always one degree higher than the dimension of their respective subspaces, recall Theorem 3.3.2. For the ballistic transfers into periodic orbits, it is assumed that the periodic orbit possesses a one-dimensional stable subspace, therefore the stable manifold is a two-dimensional structure. In this application, a state along a global analog of the local stable manifold is parameterized via two variables, T_α and T_M. The apsis and altitudes constraints for the ballistic transfer are described via the following vector,

$$\bar{F} = \begin{bmatrix} (\bar{r}_f - \bar{r}_{\text{e}})^T \bar{v}_f \\ (\bar{r}_f - \bar{r}_{\text{e}})^T (\bar{r}_f - \bar{r}_{\text{e}}) - h_f^2 \end{bmatrix}, \tag{5.3}$$

where $\bar{r}_{\text{e}}$ is the position of the Earth in the rotating frame, h_f is the desired GTO altitude, and the final propagated state, $\bar{\mathcal{X}}_f$, in Figure 5.1 is written as $\bar{\mathcal{X}}_f = [\bar{r}_f; \bar{v}_f]$; recall that [;] represents vertical vector concatenation. The final propagated state, $\bar{\mathcal{X}}_f$, is a function of the

free variables in Equation (5.2), such that, $\bar{\mathcal{X}}_f(\bar{\mathcal{X}}_M(T_\alpha), T_M)$. The state on the local stable manifold, $\bar{\mathcal{X}}_M$, is written, from Equation (3.70), as:

$$\bar{\mathcal{X}}_M = \bar{\mathcal{X}}_{\text{inj}}(T_\alpha) \pm \eta \frac{\mathbf{\Phi}(T_\alpha, 0)\ {}^P\bar{\Psi}^S}{\sqrt{\left(\mathbf{\Phi}_r(T_\alpha, 0)\ {}^P\bar{\Psi}^S\right)^T \left(\mathbf{\Phi}_r(T_\alpha, 0)\ {}^P\bar{\Psi}^S\right)}}, \tag{5.4}$$

where ${}^P\bar{\Psi}^S$ is the eigenvector in the local stable manifold near the fixed point, $\bar{\mathcal{X}}_0$, of the periodic orbit and η is the step-off magnitude (nondimensional) from the injection point in the direction of the eigenvector. The eigenvector is transitioned via the STM, $\mathbf{\Phi}(T_\alpha, 0)$, from the fixed point, $\bar{\mathcal{X}}_0$, to the injection point, $\bar{\mathcal{X}}_{\text{inj}}$, via Equation (3.71). Note that $\mathbf{\Phi}_r$ represents the positional variation with respect to the state, i.e.,

$$\mathbf{\Phi}_r = \begin{bmatrix} \mathbf{\Phi}_{rr} & \mathbf{\Phi}_{rv}, \end{bmatrix}, \tag{5.5}$$

from Equation (3.24). The Jacobian consistent with the constraint vector in Equation (5.3) is denoted as,

$$\mathbf{D}\bar{\mathbf{F}} = \begin{bmatrix} (\bar{r}_f - \bar{r}_e)^T \frac{d\bar{v}_f}{dT_\alpha} + \bar{v}_f^T \frac{d\bar{r}_f}{dT_\alpha} & (\bar{r}_f - \bar{r}_e)^T \frac{d\bar{v}_f}{dT_M} + \bar{v}_f^T \frac{d\bar{r}_f}{dT_M} \\ 2(\bar{r}_f - \bar{r}_e)^T \frac{d\bar{r}_f}{dT_\alpha} & 2(\bar{r}_f - \bar{r}_e)^T \frac{d\bar{r}_f}{dT_M} \end{bmatrix}. \tag{5.6}$$

The derivatives with respect to the propagation time T_α are expanded as,

$$\frac{\partial \bar{v}_f}{\partial T_\alpha} = \frac{\partial \bar{v}_f}{\partial \bar{\mathcal{X}}_M} \frac{\partial \bar{\mathcal{X}}_M}{\partial T_\alpha}, \tag{5.7}$$

$$\frac{\partial \bar{r}_f}{\partial T_\alpha} = \frac{\partial \bar{r}_f}{\partial \bar{\mathcal{X}}_M} \frac{\partial \bar{\mathcal{X}}_M}{\partial T_\alpha}, \tag{5.8}$$

where the partial derivative of the manifold state, $\bar{\mathcal{X}}_M$ from Equation (5.4), with respect to the time T_α is written as,

$$\frac{\partial \bar{\mathcal{X}}_M}{\partial T_\alpha} = \dot{\bar{\mathcal{X}}}_{\text{inj}}(T_\alpha) \pm \eta \left(\frac{\mathbf{A}(\bar{\mathcal{X}}_{\text{inj}}) \mathbf{\Phi}(T_\alpha, 0)\ {}^P\bar{\Psi}^S}{\mathfrak{m}} - \frac{\mathbf{\Phi}(T_\alpha, 0)\ {}^P\bar{\Psi}^S}{\mathfrak{m}^2} \frac{\partial \mathfrak{m}}{\partial T_\alpha} \right), \tag{5.9}$$

where the variable $\mathfrak{m}$ is defined as: $\mathfrak{m} = \sqrt{\left(\mathbf{\Phi}_r(T_\alpha, 0)\ {}^P\bar{\Psi}^S\right)^T \left(\mathbf{\Phi}_r(T_\alpha, 0)\ {}^P\bar{\Psi}^S\right)}$. The value of $\mathbf{A}(\bar{\mathcal{X}}_{\text{inj}})$ is the derivative of the vector field associated with the CRTBP and defined via Equation (3.18). The partial derivative of the variable $\mathfrak{m}$ is now derived as,

$$\frac{\partial \mathfrak{m}}{\partial T_\alpha} = \frac{1}{2\mathfrak{m}} \left({}^P\bar{\Psi}^{S^T} \left(\mathbf{\Phi}^T(T_\alpha, 0) \begin{bmatrix} \mathbf{0} \\ \mathbf{I} \end{bmatrix} \mathbf{\Phi}_r(T_\alpha, 0) + \mathbf{\Phi}_r^T(T_\alpha, 0) \begin{bmatrix} \mathbf{0} & \mathbf{I} \end{bmatrix} \mathbf{\Phi}(T_\alpha, 0) \right)\ {}^P\bar{\Psi}^S \right), \tag{5.10}$$

with $\mathbf{0}$ and $\mathbf{I}$ as 3×3 zero and identity matrices, respectively, and $[^T]$ is a matrix transpose. The partial derivatives of the final position and velocity, $\bar{r}_f$ and $\bar{v}_f$, with respect to the manifold state, $\bar{\mathcal{X}}_M$, are,

$$\frac{\partial \bar{r}_f}{\partial \bar{\mathcal{X}}_M} = \frac{\partial \bar{r}_M(T_M)}{\partial \bar{\mathcal{X}}_M(0)} = \mathbf{\Phi}_r(T_M, 0), \tag{5.11}$$

$$\frac{\partial \bar{v}_f}{\partial \bar{\mathcal{X}}_M} = \frac{\partial \bar{v}_M(T_M)}{\partial \bar{\mathcal{X}}_M(0)} = \mathbf{\Phi}_v(T_M, 0), \tag{5.12}$$

where, it is recalled that, $\bar{\mathcal{X}}_f$ is the propagated state from the manifold state, $\bar{\mathcal{X}}_M$, by time T_M. The partial derivatives with respect to the manifold time are denoted as,

$$\frac{\partial \bar{r}_f}{\partial T_M} = \dot{\bar{r}}_M(T_M), \tag{5.13}$$

$$\frac{\partial \bar{v}_f}{\partial T_M} = \dot{\bar{v}}_M(T_M), \tag{5.14}$$

where the velocity and acceleration vectors are computed at the end of the reverse time propagation, i.e., $t = T_M$. The 2×2 Jacobian matrix in Equation (5.6) corresponds to a ballistic transfer into a specific periodic orbit. The constraint vector in Equation (5.3) and free-variable vector in Equation (5.2) are of equal dimesion size, i.e., $\dim(\bar{\mathfrak{X}}) = \dim(\bar{F}) = 2$. The formulated TPBVP is corrected via a multidimensional Netwon's method with an update equation that corresponds to a unique solution, Equation (3.36). Ballistic transfers into a specific periodic orbit occur as isolated solutions. However, if the periodic orbit is allowed to vary along its corresponding periodic orbit family, then a curve of solutions, that is, a family of ballistic transfers are constructed. To construct families of ballistic transfers that flow into members of a family of periodic orbits, a multiple-shooting approach is implemented.

In Figure 5.2, a ballistic transfer is illustrated with the trajectory of the periodic orbit, the dashed black line, and the manifold trajectory, the blue line, subdivided into a series of $n_p + 1$ and $n_M + 1$ nodes, respectively. In this multiple-shooting formulation, the periodic

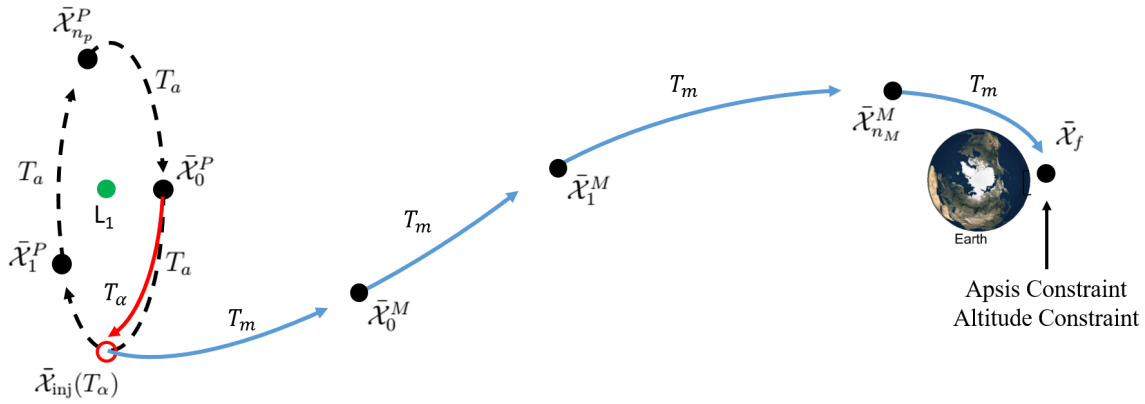

Figure 5.2. : Schematic for ballistic transfer into a periodic orbit constructed via reverse propagation

orbit trajectory is corrected for periodicity and the manifold trajectory is corrected for full state continuity. Recall that, the ballistic transfer is presented via reverse time propagation and that the final state, $\bar{\mathcal{X}}_f$, is defined as: $\bar{\mathcal{X}}_f = \bar{\mathcal{X}}^M_{n_M}(T_m)$. The free-variable vector consistent with the multiple-shooting formulation illustrated in Figure 5.2 is written as,

$$\bar{\mathfrak{X}} = \begin{bmatrix} \bar{\mathcal{X}}^P_0 \\ \bar{\mathcal{X}}^P_1 \\ \vdots \\ \bar{\mathcal{X}}^P_{n_p} \\ \bar{\mathcal{X}}^M_0 \\ \bar{\mathcal{X}}^M_1 \\ \vdots \\ \bar{\mathcal{X}}^M_{n_M} \\ T_a \\ T_m \\ T_\alpha \end{bmatrix}, \tag{5.15}$$

where $\{\bar{\mathcal{X}}_{\mathrm{j}}^{P}\}$ are state nodes corresponding to the periodic orbit and $\{\bar{\mathcal{X}}_{\mathrm{j}}^{M}\}$ are state nodes associated with the stable manifold trajectory. Each periodic orbit node, $\{\bar{\mathcal{X}}_{\mathrm{j}}^{P}\}$, has an associated propagation time, T_a, such that the period of the periodic orbit is defined as: $T_p = (n_p + 1)\, T_a$. Each node along the stable manifold trajectory, $\{\bar{\mathcal{X}}_{\mathrm{j}}^{M}\}$, possesses a propagation time T_m; recall that the ballistic transfer is constructed in reverse time such that $T_m < 0$. The constraint vector for the multiple-shooting formulation is denoted as,

$$\bar{F} = \begin{bmatrix} \bar{F}_{\text{periodic}} \\ \bar{F}_{\text{manifold}} \\ F_{\text{apsis}} \\ F_{\text{alt}} \end{bmatrix}, \tag{5.16}$$

where the constraint vectors associated with periodicity of the periodic orbit, continuity along the stable manifold, apsis, and altitude are,

$$\bar{F}_{\text{periodic}} = \begin{bmatrix} \bar{\mathcal{X}}_0^P(T_a) - \bar{\mathcal{X}}_1^P(0) \\ \vdots \\ \bar{\mathcal{X}}_{n_p-1}^P(T_a) - \bar{\mathcal{X}}_{n_p}^P(0) \\ x_{n_p}^P(T_a) - x_0^P(0) \\ y_{n_p}^P(T_a) - y_0^P(0) \\ z_{n_p}^P(T_a) - z_0^P(0) \\ \dot{x}_{n_p}^P(T_a) - \dot{x}_0^P(0) \\ \dot{z}_{n_p}^P(T_a) - \dot{z}_0^P(0) \\ y_0^P \end{bmatrix}, \tag{5.17}$$

$$\bar{F}_{\text{manifold}} = \begin{bmatrix} \bar{\mathcal{X}}_M(T_m, T_\alpha, \{\bar{\mathcal{X}}_{\mathrm{j}}^P\}, T_a) - \bar{\mathcal{X}}_0^M(0) \\ \bar{\mathcal{X}}_0^M(T_m) - \bar{\mathcal{X}}_1^M(0) \\ \vdots \\ \bar{\mathcal{X}}_{n_M-1}^M(T_m) - \bar{\mathcal{X}}_{n_M}^M(0) \end{bmatrix}, \tag{5.18}$$

$$F_{\text{apsis}} = (\bar{r}_f - \bar{r}_{\text{e}})^T \bar{v}_f, \tag{5.19}$$

$$F_{\text{alt}} = (\bar{r}_f - \bar{r}_{\text{e}})^T (\bar{r}_f - \bar{r}_{\text{e}}) - h_f^2. \tag{5.20}$$

In the formulation of a ballistic transfer into a specific periodic orbit, the dimension of the constraint vector and the free-variable vector is equal. For the multiple-shooting formulation, the dimension of the free-variable vector in Equation (5.15) is: $\dim(\bar{\mathfrak{X}}) = 6(n_p + n_M + 2) + 3$ and the dimension of the constraint vector from Equation (5.16) is: $\dim(\bar{F}) = 6(n_p + n_M + 2) + 2$. The multiple-shooting ballistic formulation is underconstrained, that is, the dimension of the free-variable vector is greater than the dimension of the constraint vector, i.e., $\dim(\bar{\mathfrak{X}}) > \dim(\bar{F})$. The associated Jacobian is constructed as,

$$\mathbf{D}\bar{\mathbf{F}} = \begin{bmatrix} \mathbf{D}_{\mathbf{x_p}}\bar{\mathbf{F}}_{\text{periodic}} & \mathbf{0} & D_{T_a}\bar{F}_{\text{periodic}} & \bar{0} & \bar{0} \\ \mathbf{D}_{\mathbf{x_p}}\bar{\mathbf{F}}_{\text{manifold}} & \mathbf{D}_{\mathbf{x_M}}\bar{\mathbf{F}}_{\text{manifold}} & D_{T_a}\bar{F}_{\text{manifold}} & D_{T_m}\bar{F}_{\text{manifold}} & D_{T_\alpha}\bar{F}_{\text{manifold}} \\ \bar{0} & D_{x_M}F_{\text{apsis}} & \bar{0} & D_{T_m}F_{\text{apsis}} & \bar{0} \\ \bar{0} & D_{x_M}F_{\text{alt}} & \bar{0} & D_{T_m}F_{\text{alt}} & \bar{0} \end{bmatrix}, \tag{5.21}$$

where $\mathbf{0}$ and $\bar{0}$ are zero matrices and vectors of appropriate sizes. The partial derivatives inside the Jacobian in Equation (5.21) are provided in Appendix B. For this underconstrained formulation, the Jacobian in Equation (5.21) has a one-dimensional null space, that is, all the solutions, i.e., ballistic transfers, are contained in a one-dimensional curve of solutions. A multidimensional Newton's method is implemented to correct for a feasible ballistic transfer into a family of periodic orbits; this formulation implements the update function in Equation (3.35). The solution space of the multiple-shooting ballistic formulation is not a consequence of subdividing the stable manifold trajectory into a series of nodes, but rather a factor of allowing the periodic orbit to vary along its respective orbit family. Multiple-shooting mitigates potential numerical challenges encountered in dynamically complex regimes, but does not change the solution space of the TPBVP. To construct the one-dimensional curve of ballistic transfers, pseudo-arclength continuation is implemented by appending the pseudo-arclength constraint in Equation (3.46). In this investigation, the formulation illustrated in Figure 5.2 is implemented to construct ballistic transfers into periodic orbits in the Sun-Earth system.

5.1.1 Ballistic Transfers to Lyapunov Orbits near Sun-Earth L_1 and L_2

Ballistic transfers to a subset of orbits in the planar Lyapunov orbit family near the L_1 and L_2 points is examined in the Sun-Earth system. Recall that, in the rideshare scenario for the secondary payload, the drop-off GTO orientation is not known a priori, although the GTO size is fixed, i.e., the semimajor axis and eccentricity. The objective is the identification of regions, i.e., departure locations near the Earth, such that a ballistic transfer from GTO periapsis delivers a secondary payload to a Sun-Earth Lagrange point orbit. The location of departure is a GTO periapsis near the Earth at a pre-determined altitude, 185 km. The departure location, with a fixed altitude, is described by two angles, λ and δ, as illustrated in Figure 4.5(b). From this originating location, ballistic transfers to the planar Lyapunov orbit families near L_1 and L_2 in the Sun-Earth system are explored. A ballistic transfer is a solution to the TPBVP illustrated in Figure 5.2 and expressed via a free-variable vector and constraint vector corresponding to Equations (5.15) and (5.16), respectively. The formulation in Figure 5.2 serves to investigate families of ballistic transfers along a periodic orbit family.

Initial guesses for ballistic transfers are identified via Poincaré maps in the rotating frame of the CRTBP model. Trajectories in the stable manifold associated with members of the Lyapunov periodic orbit family are propagated in reverse time. An event finding function is implemented to identify states that intersect the desired 185 km GTO altitude, measured with respect to the Earth, i.e., P_2 in the Sun-Earth system; note that this process is applied in the CRTBP rotating frame. Additionally, the propagation is stopped when a trajectory crashes into the Earth, defined by a radius of 6371 km. The manifold state for the stable manifold trajectories is defined via Equation (5.4) with a nondimensional η, i.e., step-off nondimensional distance, value of 6.68×10^{-7} (100 km dimensional). The captured event states from the stable manifold trajectories corresponding to a family of planar L_1 Lyapunov orbits are plotted in Figure 5.3 where the color indicates the approximate ΔV necessary to enter a ballistic transfer from a 185 km periapsis altitude GTO. Note that for ballistic transfers to planar Lyapunov orbits, the transfer is contained on the $\hat{x} - \hat{y}$ plane, i.e., $\delta = 0°$, see Figure 4.5(b). Additionally, the plot in Figure 5.3 corresponds to ballistic

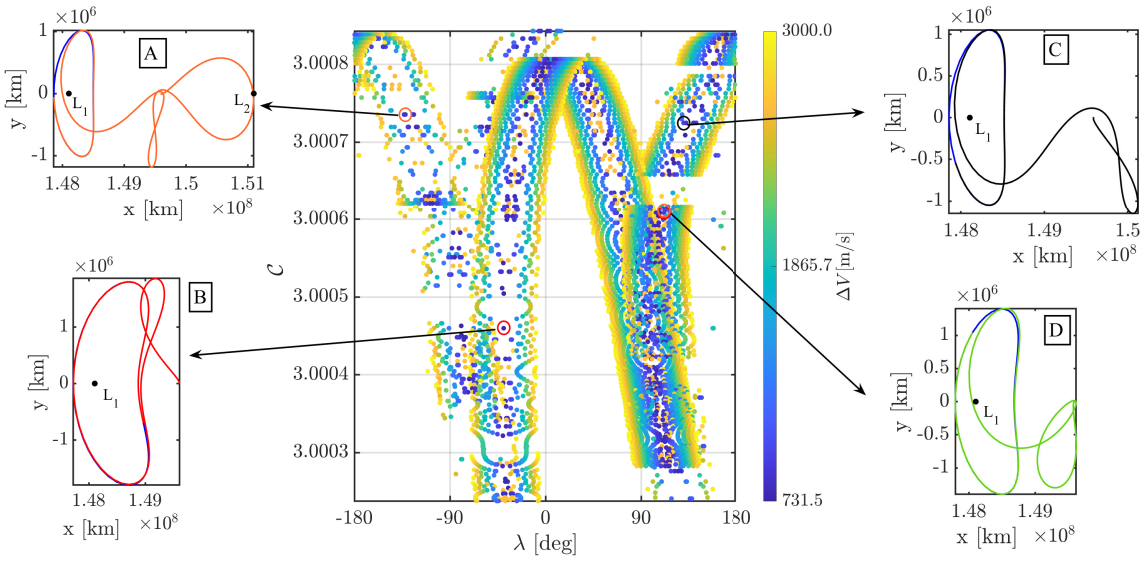

Figure 5.3. : Initial Conditions for event states from Sun-Earth L_1 Lyapunov orbits to an Earth altitude of 185 km. Selected orbits, highlighted with circles, have varying geometries

transfers from prograde GTOs. Selected transfer options A, C, and D highlighted in Figure 5.3 correspond to indirect ballistic transfers to L_1, note the excursion towards L_2 and the Earth flyby. Transfer option B is a defined as a direct ballistic transfer to L_1. The transfer options A-D in Figure 5.3 are selected as initial guesses for the multiple-shooting scheme illustrated in Figure 5.2.

Ballistic transfers into members of the Sun-Earth L_1 and L_2 Lyapunov orbit families are plotted in Figures 5.4-5.5 and 5.9-5.10 where, it is recalled that, $\delta = 0°$ for planar orbits. The ballistic transfers plotted in Figure 5.4 correspond to prograde GTO departure states; recall that the satellite departs from GTO periapsis. Observe that ballistic transfers into members of a periodic orbit family lie on a one-dimensional curve of solutions, isolated curves in Figure 5.4 are identified in terms of a family name and the targeted Lagrange point. For example, the family APL1 in Figure 5.4 is defined as the A family for prograde (P) transfers to Sun-Earth L_1. Additionally, these families of transfers, as plotted in Figures 5.4-5.5 and 5.9-5.10, are termed as Near-Earth Access (NEA) curves that correspond to ballistic transfers from a GTO with a periapsis altitude of 185 km. Each point on a NEA curve is a single ballistic transfer from a GTO periapsis situated at a location defined by λ and δ, recall

Figure 4.5(b). A similar analysis is computed for retrograde GTO departure states with a different set of NEA curves generated and plotted in Figure 5.5. The ΔV magnitude

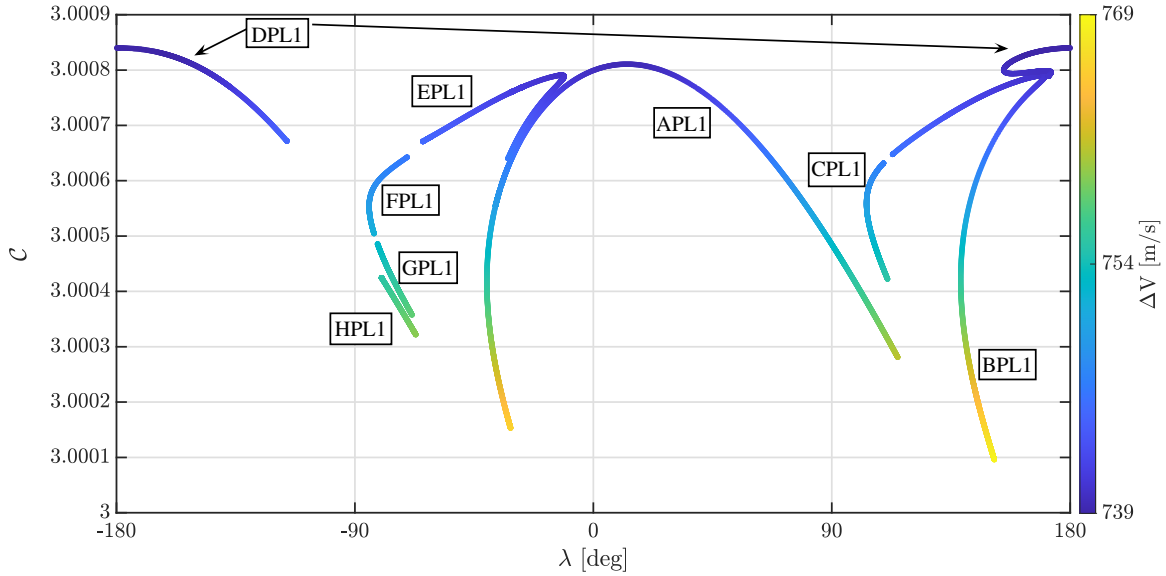

Figure 5.4. : Near-Earth Access Curves corresponding to ballistic transfers to planar Sun-Earth L_1 Lyapunov orbits from prograde GTOs with a periapsis altitude of 185 km

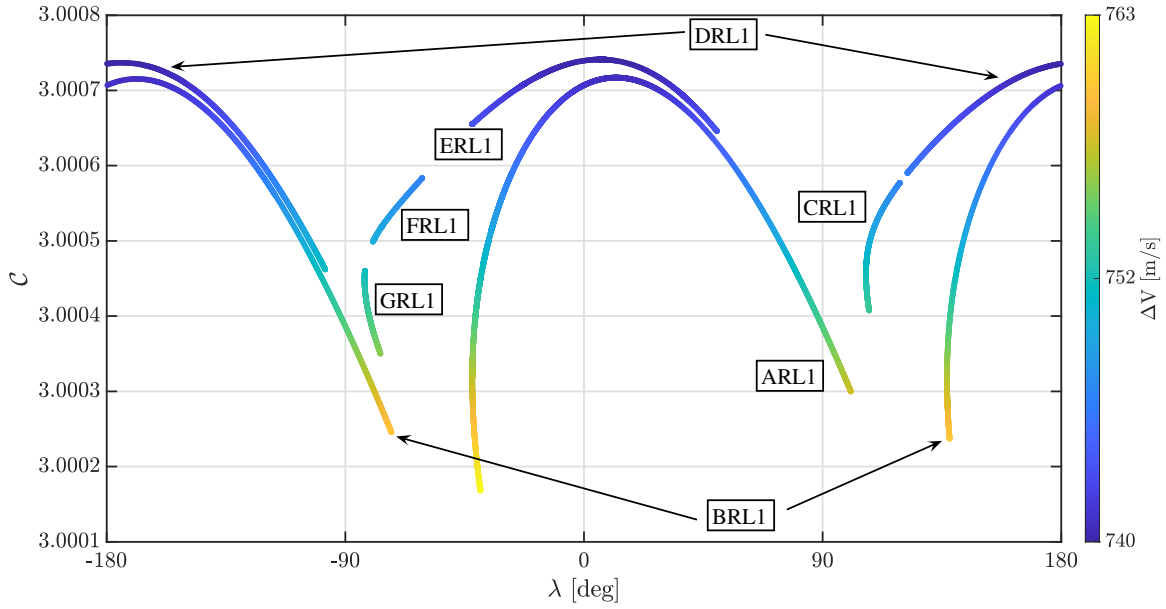

Figure 5.5. : Near-Earth Access Curves corresponding to ballistic transfers to planar Sun-Earth L_1 Lyapunov orbits from retrograde GTOs with a periapsis altitude of 185 km

in Figures 5.4-5.5 corresponds to the magnitude of the vector difference between the final

state of the ballistic transfer, $\bar{v}_f$ from Figure 5.2, and the GTO departure state at the λ angle. Note that in Figure 5.4, there is a region near-Earth, $-115° \leq \lambda \leq -85°$, where no transfers from prograde GTOs are available to planar L_1 Lyapunov orbits. The region with no available ballistic transfers to periodic orbits is labeled as the Periodic Orbit Ballistic Transfer Gap (POBTG). The POBTG range corresponding to transfers from retrograde GTOs is $-61° \leq \lambda \leq -42°$ and $101° \leq \lambda \leq 106°$. Additionally, in Figure 5.5, the region near $\lambda = 120°$ corresponds to transfers that approach significantly close to the Earth, and present numerical challenges during the continuation and corrections process. The geometries of the ballistic transfer corresponding to the NEA curves in Figures 5.4-5.5 are plotted in Figures 5.7-5.8. The families APL1 and ARL1, from Figures 5.7 and 5.8, respectively, correspond to direct ballistic transfers into planar Lyapunov orbits near L_1. The remaining ballistic transfer families are defined as indirect transfers, note that an L_2 excursion is included and one or more Earth flybys. The NEA curves for both prograde and retrograde transfers and the corresponding Lyapunov y-amplitude information is plotted in Figure 5.6.

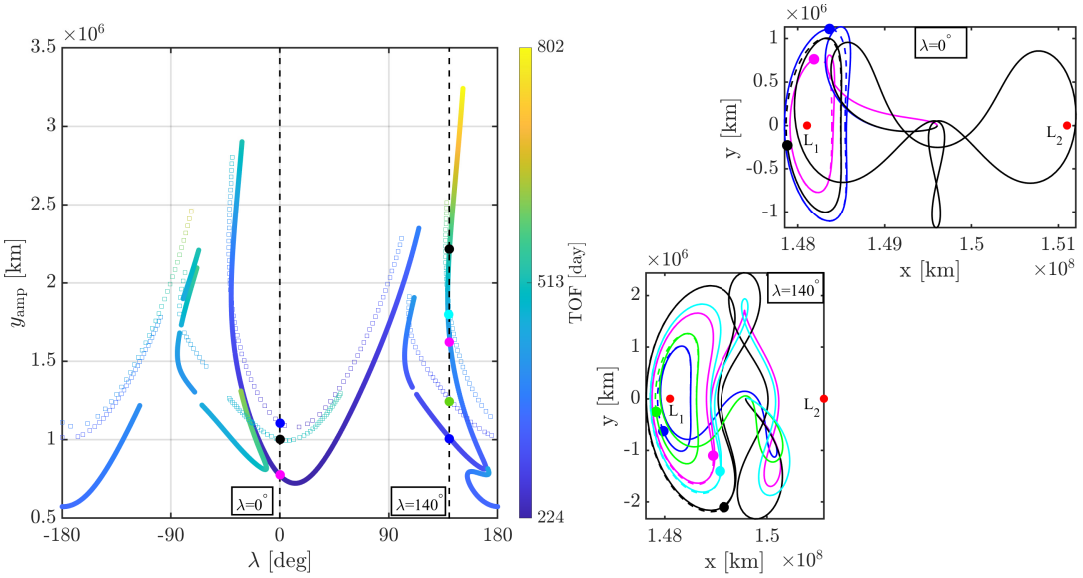

Figure 5.6. : Ballistic transfer NEA curves with corresponding Lyapunov orbit y-amplitude for both prograde and retrograde GTO departure states. The prograde transfer are solid lines and prograde transfer are open circles. Transfer geometries available from two selected GTO departure locations, i.e., λ values, are displayed

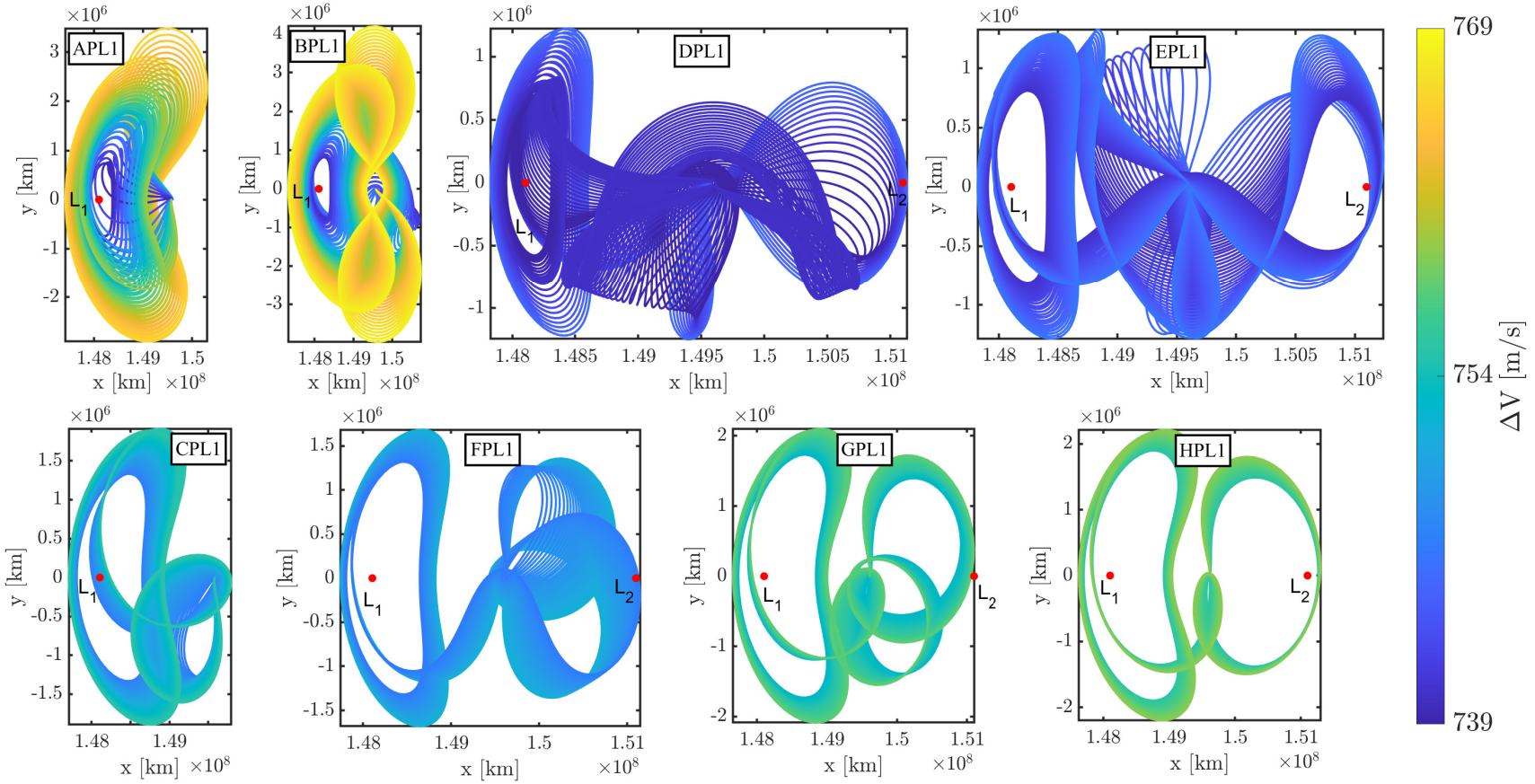

Figure 5.7. : Families of ballistic transfers from prograde GTOs to L_1 Lyapunov orbits

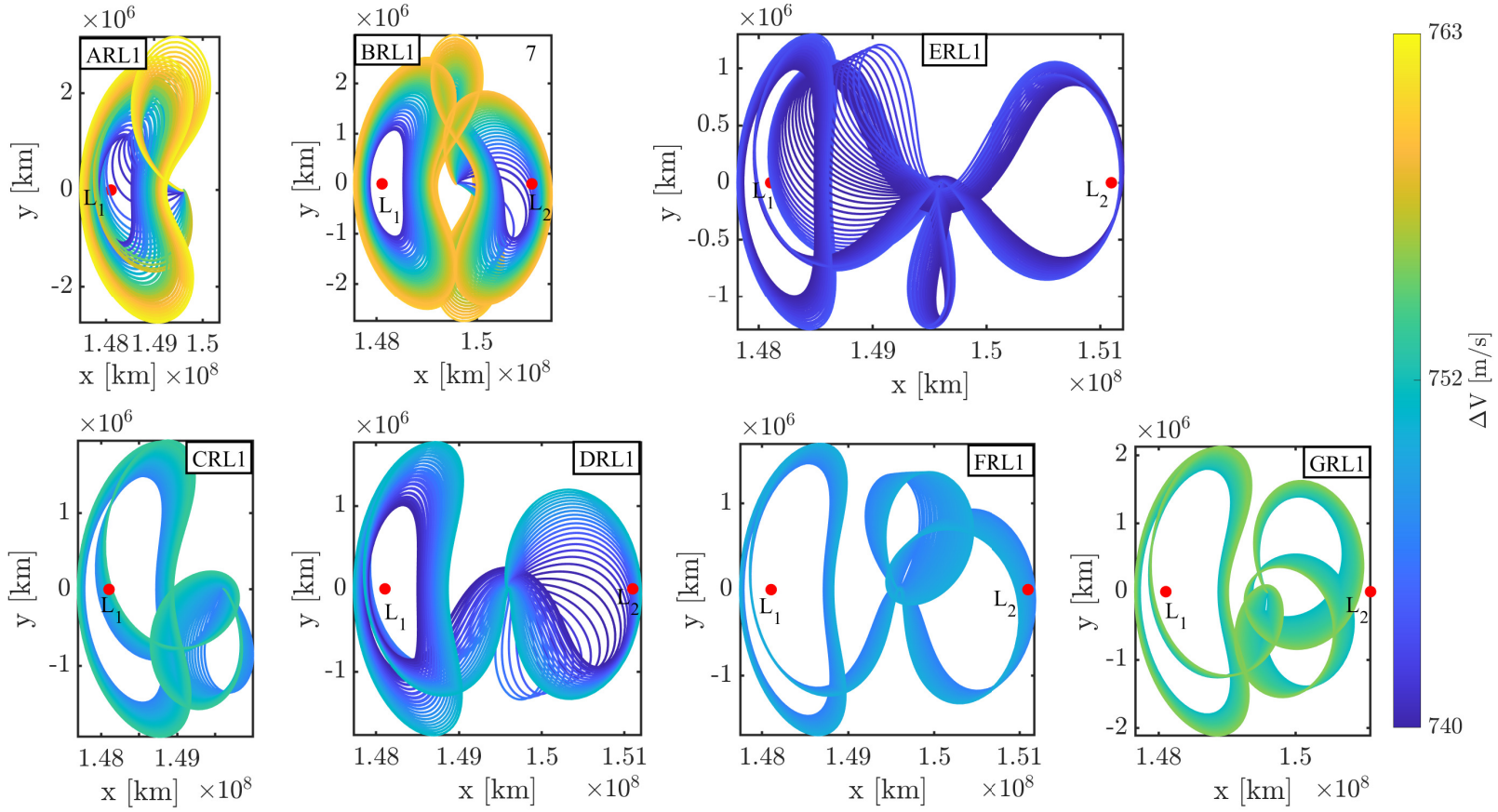

Figure 5.8. : Families of ballistic transfers from retrograde GTOs to L_1 Lyapunov orbits

The colormap in Figure 5.6 represents the Time-Of-Flight (TOF) for each ballistic transfer, i.e., each point on the map. Note that ballistic transfers into Lyapunov orbits with lower y-amplitudes are associated with lower TOF. In Figure 5.6, transfers from prograde GTOs are solid lines and transfers from retrograde GTOs are lines with open circle markers. Observe that the TOF values range from $224 - 802$ days, which is a consequence of including a stable manifold trajectory in the ballistic transfer formulation. Stable and unstable manifold structures associated with periodic orbits contain transfers that asymptotically approach and depart, respectively, the orbit and a ballistic transfer is essentially a trajectory within the stable manifold structure. Inherently, the ballistic transfer asymptotically approaches an injection point along a periodic orbit, which, in addition to the longer orbital periods associated with Sun-Earth periodic orbits, signifies that a ballistic transfer has longer TOF values. Transfers from two distinct GTO departure locations, i.e., λ values, are displayed in Figure 5.6. By including ballistic transfers from prograde and retrograde GTOs, the NEA curves in Figure 5.6 indicate that all GTO departure locations have at least one ballistic transfer option to L_1 Lyapunov orbits.

The NEA curves, representing families of ballistic transfers, into Sun-Earth L_2 Lyapunov orbits are collected in Figures 5.9-5.10. The naming convention implemented for the L_2 transfers is similar to Figures 5.4-5.5. Observe that, in Figures 5.9-5.10, ballistic transfers into periodic orbits at higher Jacobi Constant values require lower ΔV magnitudes. Additionally, the range of the POBTG for transfers from prograde GTOs is $-11^\circ < \lambda < 35^\circ$, and for retrograde GTOs, the POBTG range is $82^\circ < \lambda < 97^\circ$. In Figure 5.10, the departure location of $\lambda = -60^\circ$ is associated with a gap between families BRL2 and CRL2; this gap is associated with a ballistic curve that approaches near the center of the Earth, i.e., a discontinuity in the CRTBP model. The pseudo-arclength continuation strategy implemented to generate the NEA curves in Figures 5.9-5.10 encounters numerical challenges due to the close proximity of the trajecttory near the Earth primary body. The geometry of the ballistic transfers to L_2 Lyapunov orbits corresponding to the NEA curves in Figures 5.9-5.10 is catalogued in Figures 5.12-5.13. The families APL2 AND ARL2 are associated with direct ballistic transfers, i.e., the trajectory contains no excursions to L_1 or Earth fly-

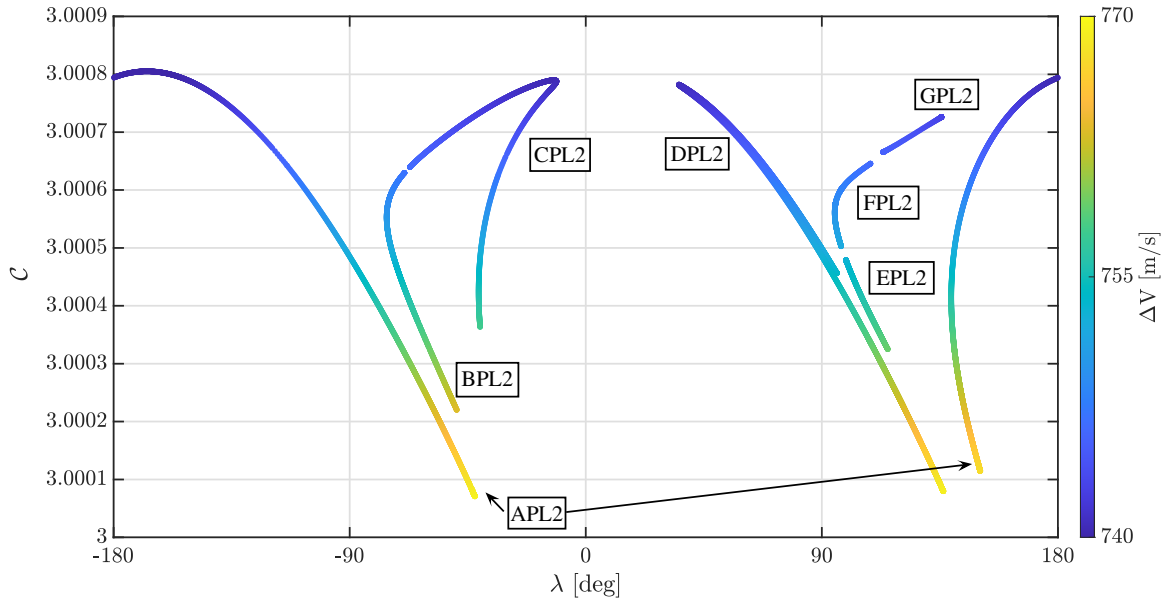

Figure 5.9. : Near-Earth Access curves corresponding to planar ballistic transfers to L_2 Lyapunov orbits from prograde GTOs

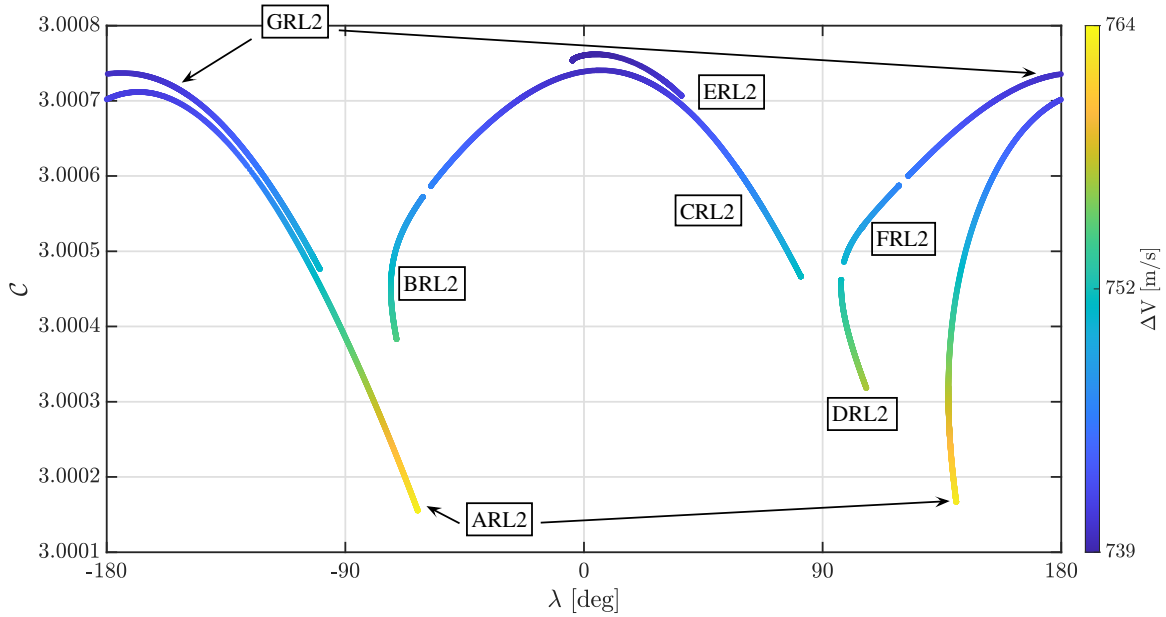

Figure 5.10. : Near-Earth Access curves corresponding to planar ballistic transfers to L_2 Lyapunov orbits from retrograde GTOs

bys. The TOF and y-amplitude information associated with the collected ballistic transfer families in Figures 5.9-5.10 is plotted in Figure 5.11. Ballistic transfers from prograde GTOs are presented as solid lines and transfers from retrograde GTOs are displayed with open

circle markers. By including transfers from both prograde and retrograde GTOs, a ballistic transfer is available along the entire span of the departure locations, $-180° \leq \lambda \leq 180°$; recalling that the departure location is a GTO periapsis with altitude of 185 km. Two GTO departure locations are highlighted in Figure 5.11, $\lambda = -180°$ and $\lambda = 70°$. From Figure 5.11, direct and indirect ballistic transfers are available for the departure location associated with $\lambda = -180°$, note that the direct transfers are in magenta and black and the indirect transfer is in blue. However, for a GTO departure location of $\lambda = 70°$, only indirect ballistic transfers to L_2 Lyapunov orbits are available. For transfers into Sun-Earth L_2 Lyapunov orbits, implementing a stable manifold trajectory, at least one ballistic transfer option is available for all departure locations.

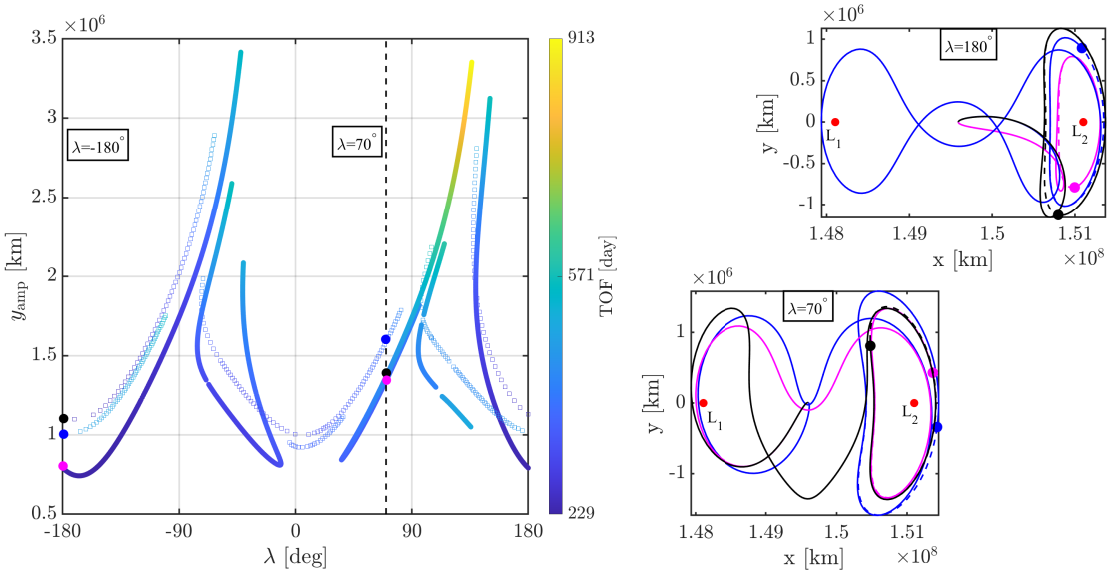

Figure 5.11. : Ballistic transfer NEA curves with corresponding L_2 Lyapunov orbit y-amplitude for both prograde and retrograde GTO departure states. The prograde transfer are solid lines and prograde transfer are open circles. Transfer geometries available from two selected GTO departure locations, i.e., λ, values are displayed

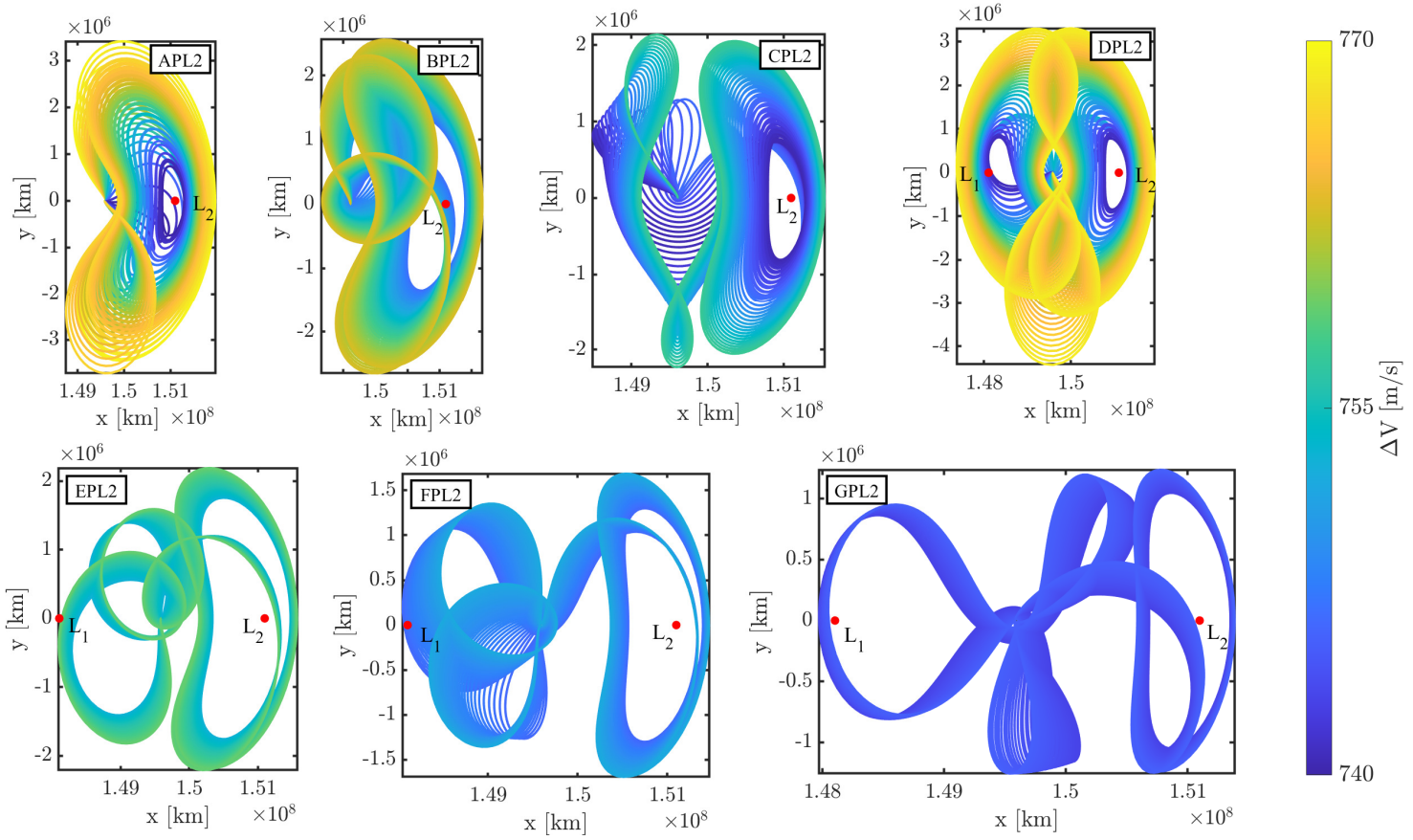

Figure 5.12. : Families of ballistic transfers from prograde GTOs to L_2 Lyapunov orbits

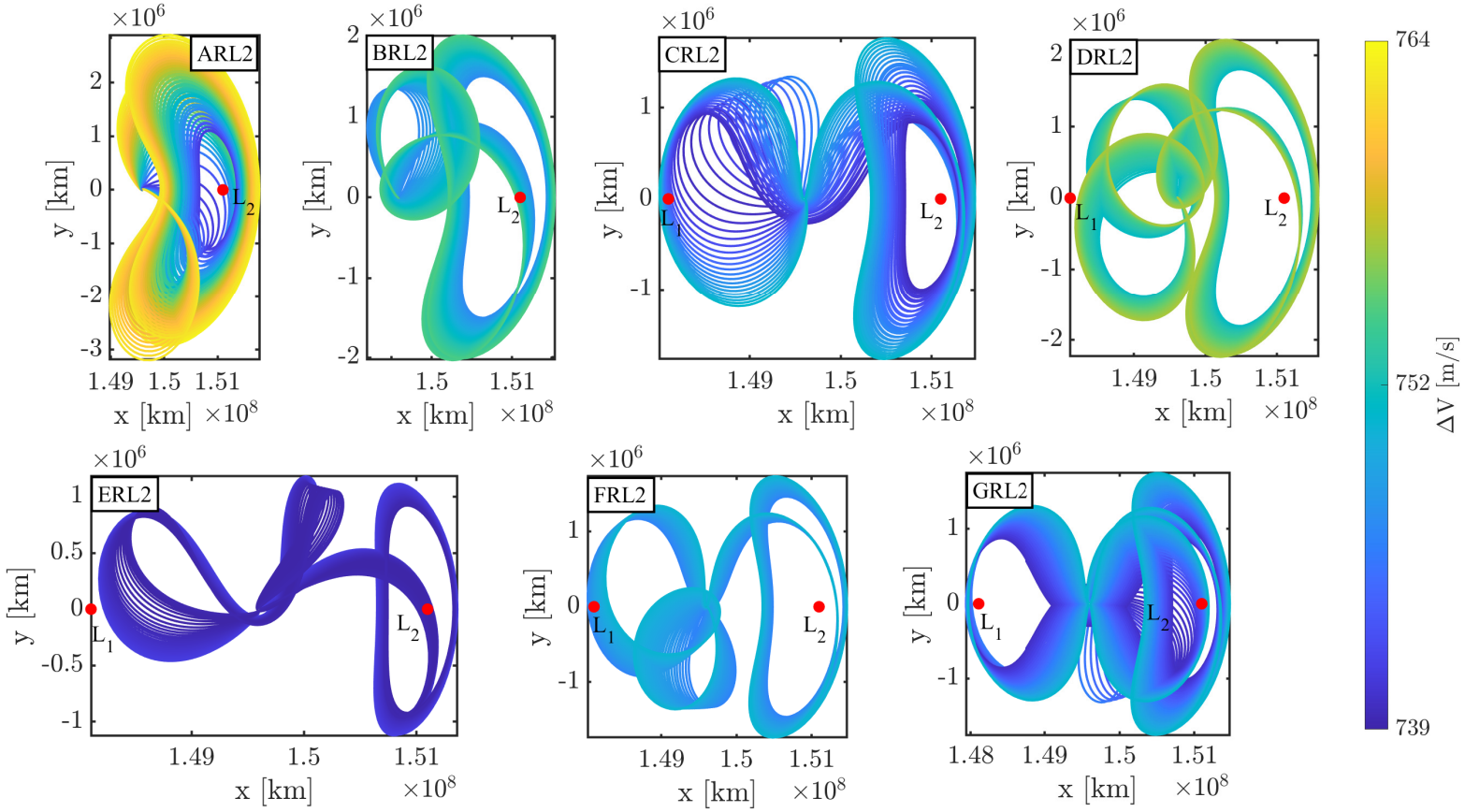

Figure 5.13. : Families of ballistic transfers from retrograde GTOs to L_2 Lyapunov orbits

Ballistic transfers to Sun-Earth L_1 and L_2 are constructed via a multiple-shooting algorithm with pseudo-arclength continuation and catalogued as families of transfers. Families of transfers, represented as NEA curves, are plotted in Figures 5.4-5.5 and 5.9-5.10 for a range of GTO departure locations, λ, near the Earth. The families presented in this analysis are only a subset of the available ballistic options to L_1 and L_2 Lyapunovs; if longer TOFs are considered, then additional families of indirect ballistic transfers become available. In summary, by including both prograde and retrograde GTO options, a ballistic transfer to L_1 or L_2 is available from any GTO departure location in the $\hat{x}$-$\hat{y}$ plane. The computed families of ballistic transfers offer preliminary design information for available transfers to the Sun-Earth Lagrange points when a drop-off GTO periapsis is located along the Sun-Earth ecliptic plane.

5.1.1.1 Altitude Variation for Transfers to Lyapunov Orbits

Ballistic transfers to planar Sun-Earth Lyapunov orbits from a range of GTO periapsis altitudes are constructed via a multiple-shooting strategy. In Figures 5.4-5.5 and 5.9-5.10, the families of ballistic transfers correspond to a GTO departure altitude of 185 km. Families of ballistic transfers over a range of GTO departure altitudes are also constructed via the same multiple-shooting algorithm and continuation strategy. In this investigation, transfers are constructed for a smallsat, i.e., a secondary payload, dropped off into a GTO, refer to Section 4, with no a priori information regarding the GTO orientation. However, the size of the drop-off GTO is dependent on the performance of the upper-stage of the launch vehicle, see Step 2 in Figure 4.1, such that the periapsis altitude is varied as, by definition, the GTO apoapsis altitude is the standard GEO altitude. The plots displayed in Figures 5.14-5.15 correspond to the NEA curves for ballistic transfers to L_1 and L_2 from GTOs with a variable periapsis altitude. The color variation along each NEA curve in Figures 5.14-5.15 is the ΔV magnitude for the single-maneuver ballistic transfers. For increasing GTO periapsis altitudes, h_f, the NEA curves are shifted both vertically and horizontally. For example, in Figure 5.14, the curves corresponding to transfers near the GTO departure location range

of $0 \leq \lambda \leq 20$ are shifted upward with increasing h_f. However, in the departure range of $\lambda \leq -39$, the curve is shifted downwards with an increasing h_f altitude. The shift in the

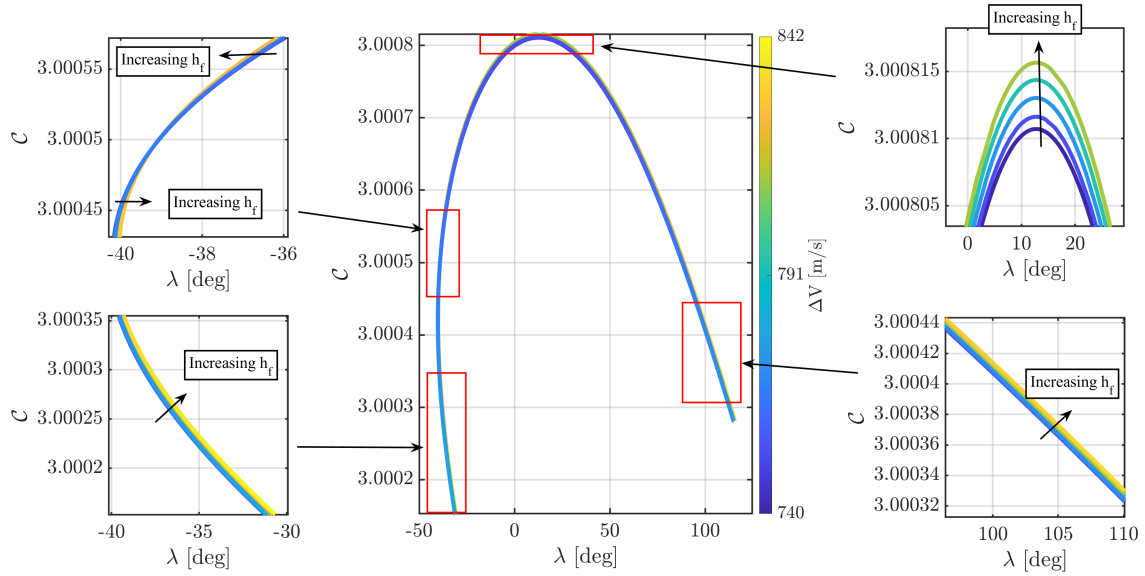

Figure 5.14. : NEA curves for direct ballistic transfers to Sun-Earth L_1 from prograde GTOs with varying periapsis altitudes

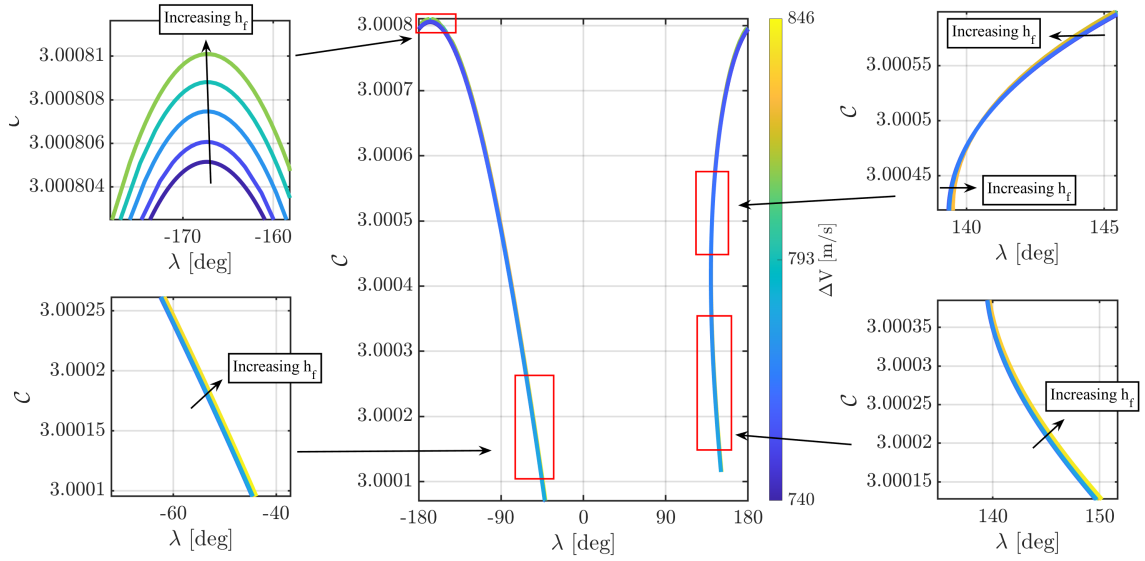

Figure 5.15. : NEA curves for direct ballistic transfers to Sun-Earth L_2 from prograde GTOs with varying periapsis altitudes

NEA curve is also interpreted as a change in the Lyapunov orbit that is available from a

specific GTO departure location. As a demonstration, assume the GTO departure location is set to $\lambda = 10^\circ$ in Figure 5.14. The L_1 Lyapunov orbit that corresponds to the ballistic transfer for an altitude of 185 km has a Jacobi Constant equal to $\mathcal{C} = 3.00081$, however, for a GTO with a higher altitude, i.e., $h_f = 2000$ km, the corresponding Lyapunov has an associated Jacobi Constant value of: $\mathcal{C} = 3.000815$. Similar behavior is observed for the NEA curves towards Sun-Earth L_2 in Figure 5.15. In Figures 5.14-5.15, the effects of GTO altitude variation for the NEA curves that correspond to direct ballistic transfers are plotted. In this investigation, only direct ballistic transfers, i.e., trajectories with no Earth flybys, are considered as they are associated with lower TOF values. Knowledge of the ΔV and geometry differences due to a variation in the GTO departure altitude aids in the prediction of single-maneuver direct transfers over a range of departure locations near the Earth.

5.1.2 Ballistic Transfers to Spatial Periodic Orbits near Sun-Earth L_1 and L_2

Ballistic transfers to orbits that are members of the spatial Sun-Earth L_1 and L_2 halo orbit families are explored by leveraging the trajectories on the stable manifolds associated with halo orbits. Ballistic transfers to spatial orbits are not restricted to the $\hat{x}$-$\hat{y}$ plane of the rotating Sun-Earth system, i.e., the ecliptic plane. In Figure 5.16, the angles λ and δ represent the near-Earth departure locations for ballistic transfers from a GTO with a 185 km periapsis altitude. Recall that angles λ and δ are defined in Figure 4.5(b) in the Sun-Earth rotating frame. Figures 5.16 and 5.18 display the NEA curves to members of the spatial halo orbit families near the L_1 and L_2 points. Note that Figures 5.16 and 5.18 represent the NEA curves via a range of color, corresponding to the ΔV required, with the retrograde ballistic transfers enclosed in a red box. For example, for the AL1-S family, a family of ballistic transfers to the L_1 southern halo orbits, the region enclosed by the red box, i.e., the region defined via the ranges of $0^\circ \leq \lambda \leq 26^\circ$ and $34^\circ \leq \delta \leq 45^\circ$ contains the retrograde ballistic transfers. Alternatively, the NEA curves are plotted in Figures 5.17 and 5.19 via a color range corresponding to the TOF, that is, the transfer time from the GTO departure location to an injection point on the halo orbit. The naming convention for

the spatial access curves are updated, where AL1-N is labeled the A group of transfers to L_1 northern (N) halo orbits. An important observation from Figures 5.16 and 5.18 is the limited region, i.e., space covered by NEA curves, that corresponds to ballistic transfers. An insightful comparison between the transfers to planar Lyapunov orbits and the transfers to spatial halo orbits is the behavior of the NEA curves. Spatial ballistic transfers, Figures 5.16 and 5.18, form closed NEA curves whereas the curves corresponding to planar ballistic transfers are not closed. Note that ballistic transfers to orbits with higher Jacobi Constant

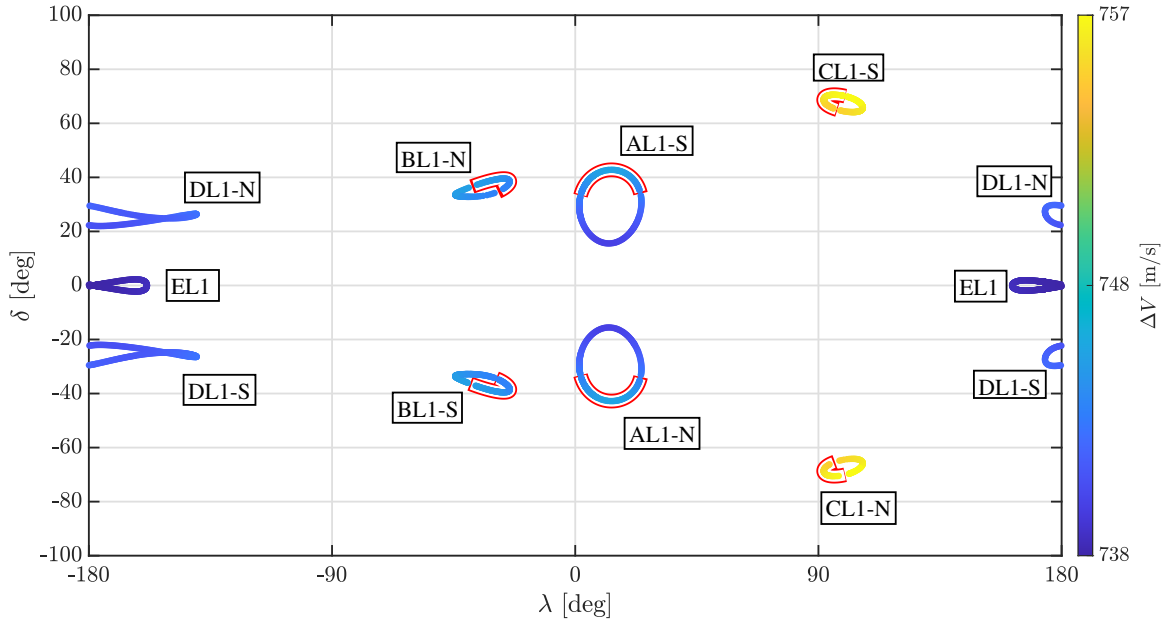

Figure 5.16. : Near-Earth Access curves to Sun-Earth L_1 halo orbits, the colors represent the ΔV magnitude of the single maneuver. Retrograde transfers are enclosed by a red box

values, $\mathcal{C}$, are available near the ecliptic, i.e., near $\delta = 0°$. Additionally, the ballistic transfers to halo orbits with higher $\mathcal{C}$ values also require the lowest ΔV magnitudes, recalling that the ballistic transfers involve a single maneuver. Direct ballistic transfers into the spatial halo orbits are identified as the curves corresponding to AL1-N, AL1-S, AL2-N, and AL2-S in Figures 5.16 and 5.18. Additionally, from Figures 5.17 and 5.19, the family of direct ballistic transfers have the smallest associated TOF values. Observe that the closed NEA curves plotted in Figures 5.16 and 5.18 are scattered throughout the near-Earth vicinity, i.e., if a halo orbit is desired, the GTO departure location is limited to the closed curves. The NEA curves plotted in Figures 5.16-5.18 only represent a subset of the ballistic curves available

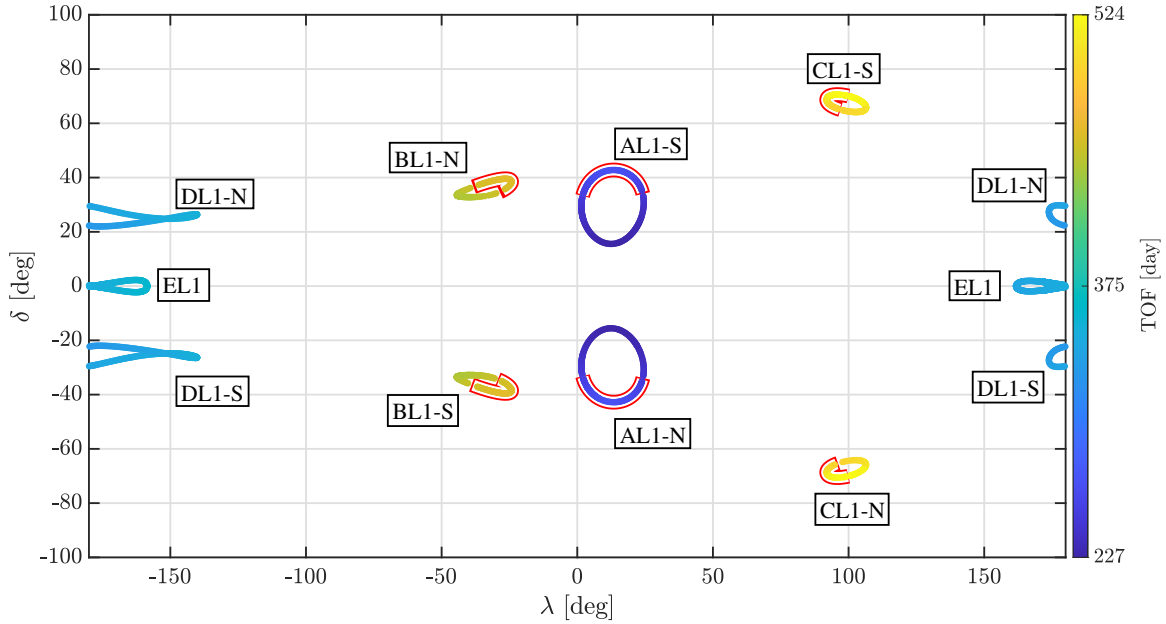

Figure 5.17. : Near-Earth Access curves to Sun-Earth L_1 halo orbits, the colors represent the TOF values for the transfer. Retrograde transfers are enclosed by a red box

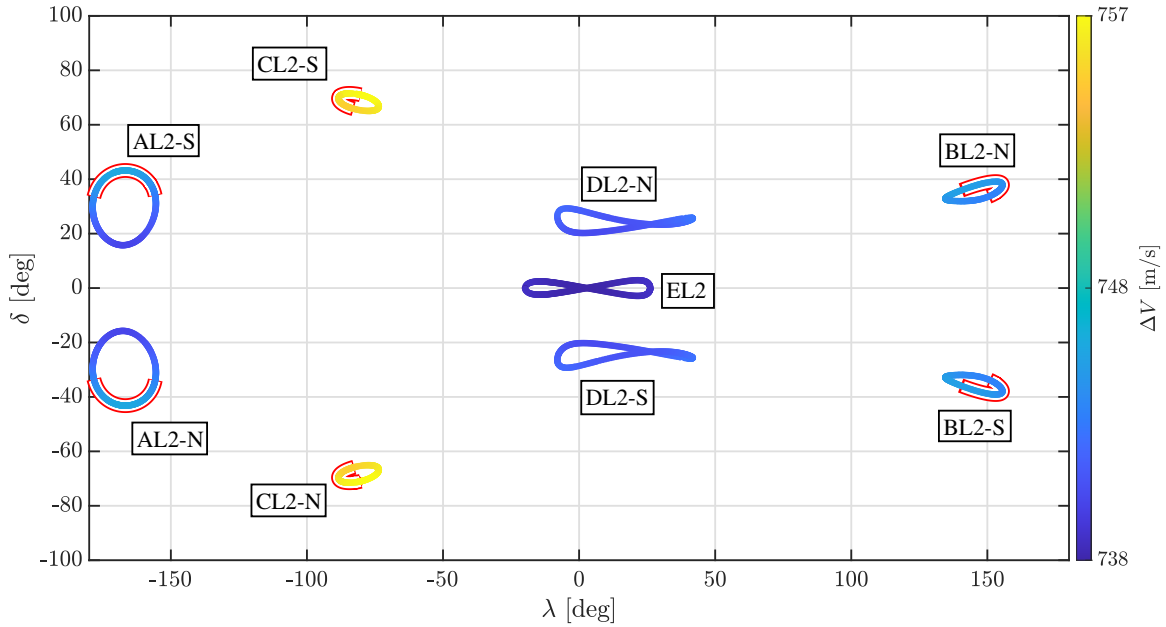

Figure 5.18. : Near-Earth Access curves to Sun-Earth L_2 halo orbits, the colors represent the ΔV magnitude of the single maneuver. Retrograde transfers are enclosed by a red box

to spatial halo orbits in the Sun-Earth system and, by considering a longer TOF, additional families of ballistic transfer can be constructed. The geometry of the transfers displayed in

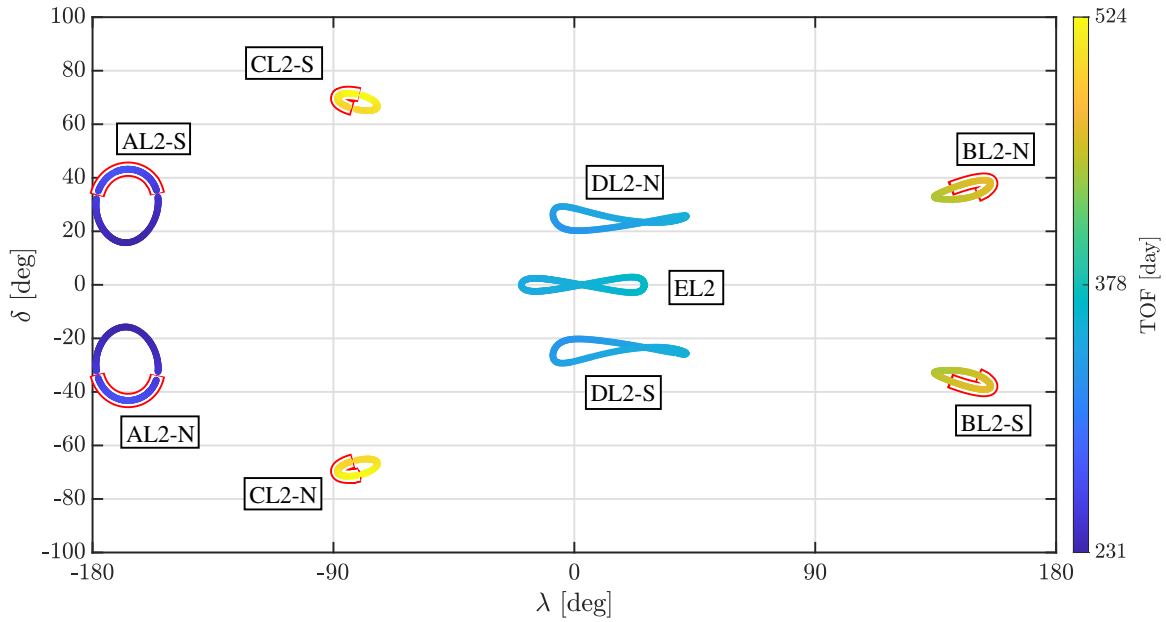

Figure 5.19. : Near-Earth Access curves to Sun-Earth L_2 halo orbits, the colors represent the TOF values for the transfer. Retrograde transfers are enclosed by a red box

the NEA curves in Figures 5.16 and 5.18 are plotted in Appendix C. In this investigation, direct transfers towards spatial orbits are desirable, but access from this altitude, the 185 km GTO periapsis altitude, using ballistic transfers is limited to a specific region near the Earth, see curves AL1-S, AL1-N, AL2-S, and AL2-N. While ballistic transfers to planar Lyapunov orbits near Sun-Earth L_1 and L_2 are available for all possible GTO departure locations, the NEA curves to spatial halo orbits are limited to specific regions.

5.1.2.1 Altitude Variation for Transfers to Spatial Halo Orbits

The Near-Earth Access curves corresponding to direct ballistic transfers into halo orbits near the Sun-Earth Lagrange points are explored for a range of GTO departure altitudes. Recall that the baseline GTO for this investigation possesses a periapsis altitude of 185 km; note that the departure location for the secondary payload is at the GTO periapsis. The NEA curves for halo orbits near L_1 and L_2 are plotted in Figures 5.16 and 5.18, however, NEA curves for variable GTO departure altitudes are created via the same multiple-shooting

algorithm and continuation scheme. In Figures 5.20-5.21, the NEA curves for direct ballistic transfers to the southern and northern halo orbit families are plotted for GTO departure altitudes ranging from 185 km to 2000 km. The altitude variation analysis is focused on direct ballistic transfers because direct transfers offer lower TOF values compared to the indirect trajectories. For ballistic transfers into Sun-Earth L_1 and L_2 , an increase in the

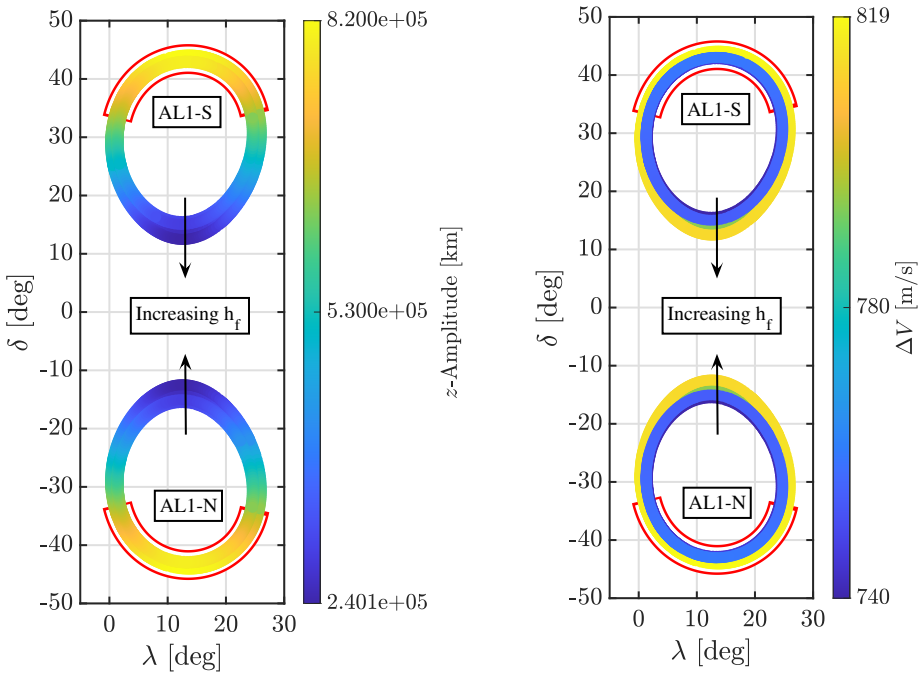

Figure 5.20. : Direct ballistic transfers to spatial halo orbits near Sun-Earth L_1 for a range of GTO departure altitudes between 185 km and 2000 km

GTO periapsis altitude creates a NEA curve with a larger circumference, see family AL1-S in Figure 5.20 for an example. Additionally, ballistic transfers from higher GTO departure altitudes require larger ΔV magnitudes; recalling that ballistic transfers are single maneuver transfers. The z-amplitude of the corresponding halo orbit for each ballistic transfer is also represented via color in Figures 5.20-5.21. As a demonstration of the effects of the GTO departure altitude, let the GTO departure location be written with $\lambda = 10°$. Observe that, in Figure 5.20, there are two scenarios which offer access to a ballistic transfer to a northern L_1 halo orbit: $\delta = -17°$ and $\delta = -41°$; note that these δ options are consistent with a GTO periapsis altitude of 185 km. For the same GTO departure location along the ecliptic, i.e., $\lambda = 10°$, an increase in the GTO periapsis altitude moves the required δ values

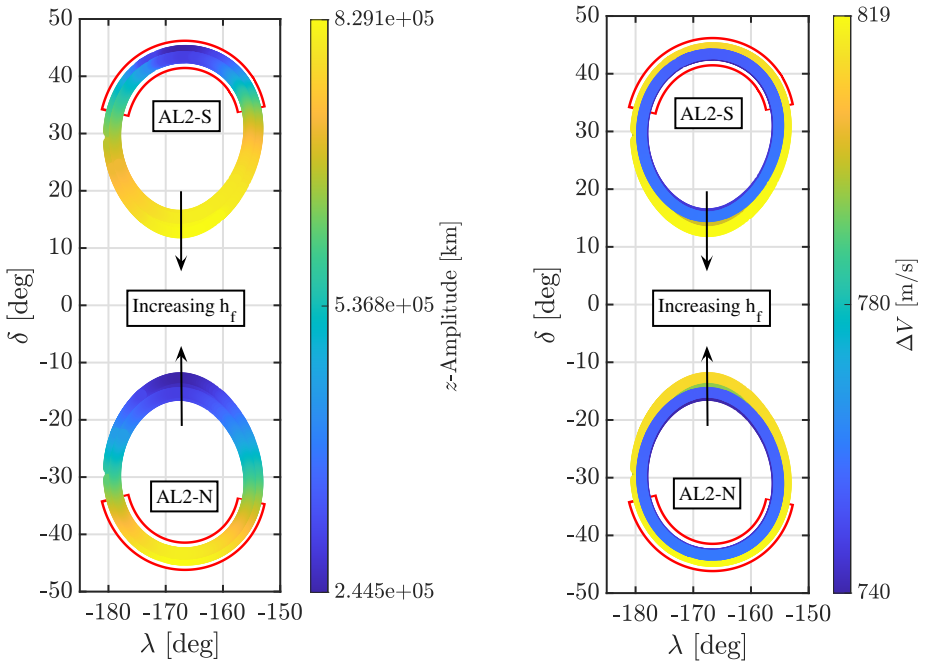

Figure 5.21. : Direct ballistic transfers to spatial halo orbits near Sun-Earth L_2 for a range of GTO departure altitudes between 185 km and 2000 km

in a direction away from an estimated center of the curve. For example, if a GTO periapsis altitude of $h_f = 2000$ km is considered, then the following δ values are required: $\delta = -12°$ and $\delta = -45°$. Observe that in this example, the required ΔV has increased as h_f increases, but the amplitude of the corresponding northern L_1 halo has not changed. In Summary, for direct ballistic transfers to Sun-Earth halo orbits, an increase in the GTO departure altitude increases the ΔV magnitude and grows the NEA curves.

5.2 Ballistic Transfers into Quasi-Periodic Orbits

Ballistic transfers to quasi-halo orbits are constructed with trajectories within the stable manifold structures associated with the quasi-periodic orbit. The closed NEA curves plotted in Figures 5.16 and 5.18 represent the regions where a GTO departure state may enter a ballistic transfer to a periodic halo orbit near Sun-Earth L_1 or L_2; recall that a single point along the curve corresponds to one ballistic transfer. However, this region is limited, i.e., contained along the curve, but bounded motion near the Lagrange points is not limited

to periodic orbits, as quasi-periodic orbits also offer additional opportunities for ballistic transfers. In this analysis, ballistic transfers are constructed into a family of quasi-halo orbits, that is, quasi-periodic orbits generated from an originating periodic halo orbit near Sun-Earth L_1. Families of quasi-halo orbits with a fixed Jacobi constant, $\mathcal{C}$, are generated via the numerical technique described in Section 3.4. A multiple shooting method is formulated, and is illustrated in Figure 5.22, to construct ballistic transfers into quasi-periodic orbits. The ballistic transfer is constructed via reverse propagation with an injection point along

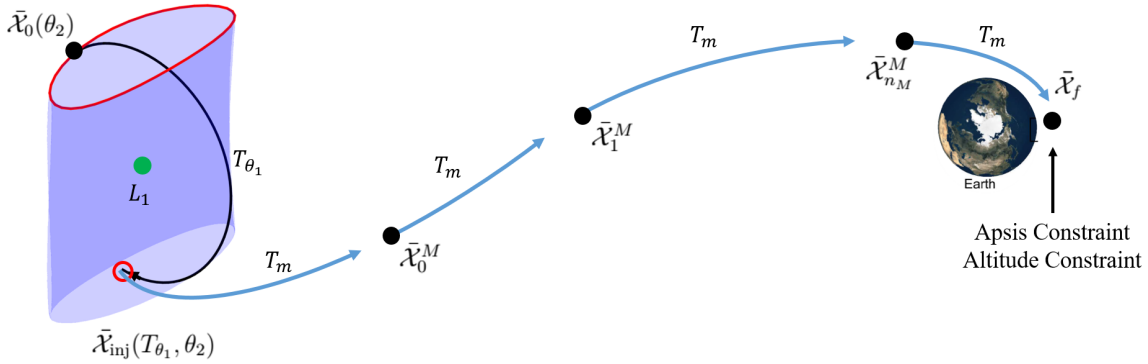

Figure 5.22. : Schematic for ballistic transfer into a quasi-periodic orbit constructed via reverse propagation

the quasi-periodic orbit defined as $\bar{\mathcal{X}}_{\text{inj}}$. The injection point $\bar{\mathcal{X}}_{\text{inj}}$ is generated by propagating an initial state along the invariant curve, i.e., $\bar{\mathcal{X}}_0(\theta_2)$, by time T_{θ_1}. The state on the local stable manifold, $\bar{\mathcal{X}}_M$, is written, from Equation (3.140), as:

$$\bar{\mathcal{X}}_M = \bar{\mathcal{X}}_{\text{inj}}(T_{\theta_1}, \theta_2) \pm \eta \frac{\boldsymbol{\Phi}(T_{\theta_1}, 0)\ \bar{\psi}^S(\theta_2)}{\sqrt{\left(\boldsymbol{\Phi}_r(T_{\theta_1}, 0)\ \bar{\psi}^S(\theta_2)\right)^T\ \boldsymbol{\Phi}_r(T_{\theta_1}, 0)\ \bar{\psi}^S(\theta_2)}}, \tag{5.22}$$

where $\boldsymbol{\Phi}(T_{\theta_1}, 0)$ is the STM from the initial state along the invariant curve, $\bar{\mathcal{X}}_0(\theta_2)$, after a propagation time T_{θ_1}. Recall that η represents a step-off distance in the direction of the

stable manifold and $\pm$ dictates direction of stable half-manifold. The free-variable vector consistent with the formulation in Figure 5.22 is denoted as,

$$\bar{\mathfrak{X}} = \begin{bmatrix} \bar{\mathcal{X}}_0^M \\ \bar{\mathcal{X}}_1^M \\ \vdots \\ \bar{\mathcal{X}}_{n_M}^M \\ T_{\theta_1} \\ \theta_2 \\ T_m \end{bmatrix}, \tag{5.23}$$

with a constraint vector defined as,

$$\bar{F} = \begin{bmatrix} \bar{F}_{\text{manifold}} \\ F_{\text{apsis}} \\ F_{\text{alt}} \end{bmatrix}. \tag{5.24}$$

The constraint functions corresponding to the state continuity along the ballistic transfer, $\bar{F}_{\text{manifold}}$, GTO periapsis, F_{apsis}, and the GTO departure altitude, F_{alt}, are described via,

$$\bar{F}_{\text{manifold}} = \begin{bmatrix} \bar{\mathcal{X}}\left(T_m, \bar{\mathcal{X}}_M(T_{\theta_1}, \theta_2)\right) - \bar{\mathcal{X}}_0^M(0) \\ \bar{\mathcal{X}}_0^M(T_m) - \bar{\mathcal{X}}_1^M(0) \\ \vdots \\ \bar{\mathcal{X}}_{n_M-1}^M(T_m) - \bar{\mathcal{X}}_{n_M}^M(0) \end{bmatrix}, \tag{5.25}$$

$$F_{\text{apsis}} = (\bar{r}_f - \bar{r}_{\text{e}})^T \bar{v}_f, \tag{5.26}$$

$$F_{\text{alt}} = (\bar{r}_f - \bar{r}_{\text{e}})^T (\bar{r}_f - \bar{r}_{\text{e}}) - h_f^2, \tag{5.27}$$

where $\bar{r}_f$ and $\bar{v}_f$ are the final position and velocity vectors at the end of reverse time propagation and $\bar{r}_{\text{e}}$ is the position of the Earth, i.e., $[1-\mu, 0, 0]^T$ in the rotating frame of the CRTBP model. The GTO departure altitude, h_f, is fixed to 185 km. A ballistic transfer is constructed via the multiple-shooting formulation with Equations (5.23) and (5.24) and

corrected with a multidimensional Newton method algorithm. The Jacobian corresponding to the constraint vector in Equation (5.24) is derived as,

$$\mathbf{D}\bar{\mathbf{F}} = \begin{bmatrix} \mathbf{D_x}\bar{\mathbf{F}}_{\text{manifold}} & D_{T_{\theta_1}}\bar{F}_{\text{manifold}} & D_{\theta_2}\bar{F}_{\text{manifold}} & D_{T_m}\bar{F}_{\text{manifold}} \\ D_x F_{\text{apsis}} & 0 & 0 & D_{T_m}F_{\text{apsis}} \\ D_x F_{\text{alt}} & 0 & 0 & D_{T_m}F_{\text{alt}} \end{bmatrix}, \tag{5.28}$$

where the partial derivatives of the stable manifold trajectory section, $\bar{F}_{\text{manifold}}$, in Equation (5.28) are defined as,

$$\mathbf{D_x}\bar{\mathbf{F}}_{\text{manifold}} = \begin{bmatrix} -\mathbf{I}_{6,6} & \mathbf{0}_{6,6} & \mathbf{0}_{6,6} & \dots & \mathbf{0}_{6,6} \\ \mathbf{\Phi}_0^M & -\mathbf{I}_{6,6} & \mathbf{0}_{6,6} & \dots & \mathbf{0}_{6,6} \\ \mathbf{0}_{6,6} & \mathbf{\Phi}_1^M & -\mathbf{I}_{6,6} & \dots & \mathbf{0}_{6,6} \\ \vdots & \vdots & \ddots & \ddots & \vdots \\ \mathbf{0}_{6,6} & \mathbf{0}_{6,6} & \mathbf{0}_{6,6} & \mathbf{\Phi}_{n_M}^M & -\mathbf{I}_{6,6} \end{bmatrix}, \tag{5.29}$$

$$D_{T_{\theta_1}}\bar{F}_{\text{manifold}} = \begin{bmatrix} \mathbf{\Phi}(T_m, 0)\frac{\partial \bar{\mathcal{X}}_M}{\partial T_{\theta_1}} \\ \bar{0} \\ \vdots \\ \bar{0} \end{bmatrix}, \tag{5.30}$$

$$D_{\theta_2}\bar{F}_{\text{manifold}} = \begin{bmatrix} \frac{\partial \bar{\mathcal{X}}\left(T_m, \bar{\mathcal{X}}_M(T_{\theta_1}, \theta_2)\right)}{\partial \theta_2} \\ \bar{0} \\ \vdots \\ \bar{0} \end{bmatrix}, \tag{5.31}$$

$$D_{T_m}\bar{F}_{\text{manifold}} = \begin{bmatrix} \frac{\partial \bar{\mathcal{X}}\left(T_m, \bar{\mathcal{X}}_M(T_{\theta_1}, \theta_2)\right)}{\partial T_m} \\ \dot{\bar{\mathcal{X}}}_0^M(T_m) \\ \vdots \\ \dot{\bar{\mathcal{X}}}_{n_M-1}^M(T_m) \end{bmatrix}. \tag{5.32}$$

where the STM is defined as $\Phi_{\text{j}}^M = \frac{\partial \bar{\mathcal{X}}_{\text{j}}^M(T_m)}{\partial \bar{\mathcal{X}}_{\text{j}}^M(0)}$. Note that $\mathbf{\Phi}$ represents the STM derived from propagation of the state along the invariant curve, $\bar{\mathcal{X}}_{\text{inv}}$, to the injection point, $\bar{\mathcal{X}}_{\text{inj}}$.

The partial derivative of the stable manifold state, $\bar{\mathcal{X}}_M$, with respect to the angle along the invariant curve, i.e., $\frac{\partial \bar{\mathcal{X}}\left(T_m, \bar{\mathcal{X}}_M(T_{\theta_1}, \theta_2)\right)}{\partial \theta_2}$, is evaluated via a numerical finite difference method; recall that the invariant curve is approximated via a discrete Fourier series. Note that, the state, $\bar{\mathcal{X}}\left(T_m, \bar{\mathcal{X}}_M(T_{\theta_1}, \theta_2)\right)$, is a propagated state from the stable manifold state in Equation (5.22) and the partial derivative of $\bar{\mathcal{X}}_M$ with respect to the longitudinal time, T_{θ_1}, is defined as,

$$\frac{\partial \bar{\mathcal{X}}_M(T_{\theta_1}, \theta_2)}{\partial T_{\theta_1}} = \dot{\bar{\mathcal{X}}}_{\text{inj}}(T_{\theta_1}, \theta_2) \pm \eta \left(\frac{A(\bar{\mathcal{X}}_{\text{inj}}) \mathbf{\Phi}(T_{\theta_1}, 0)\, \bar{\psi}^S(\theta_2)}{\mathfrak{m}_q} - \frac{\mathbf{\Phi}(T_{\theta_1}, 0)\, \bar{\psi}^S(\theta_2)}{\mathfrak{m}_q^2} \frac{\partial \mathfrak{m}_q}{\partial T_{\theta_1}} \right), \quad (5.33)$$

where the variable $\mathfrak{m}_q$ is defined as: $\mathfrak{m}_q = \sqrt{\left(\mathbf{\Phi}_r(T_{\theta_1}, 0)\, \bar{\psi}^S(\theta_2)\right)^T \left(\mathbf{\Phi}_r(T_{\theta_1}, 0)\, \bar{\psi}^S(\theta_2)\right)}$. The partial of the variable $\mathfrak{m}_q$ is now derived as,

$$\frac{\partial \mathfrak{m}_q}{\partial T_{\theta_1}} = \frac{1}{2\mathfrak{m}_q} \left(\bar{\psi}^{S^T}(\theta_2) \left(\mathbf{\Phi}^T(T_{\theta_1}, 0) \begin{bmatrix} \mathbf{0} \\ \mathbf{I} \end{bmatrix} \mathbf{\Phi}_r(T_{\theta_1}, 0) + \mathbf{\Phi}_r^T(T_{\theta_1}, 0) \begin{bmatrix} \mathbf{0} & \mathbf{I} \end{bmatrix} \mathbf{\Phi}(T_{\theta_1}, 0) \right) \bar{\psi}^S(\theta_2) \right), \quad (5.34)$$

with $\mathbf{0}$ and $\mathbf{I}$ as 3×3 zero and identity matrices, respectively, and $[^T]$ is a matrix transpose. The partial derivatives corresponding to the apsis and altitude constraints, i.e., F_{apsis} and F_{alt}, respectively, are given as,

$$D_x F_{\text{apsis}} = \left[\bar{0} \quad \dots \quad \bar{0} \quad \left((\bar{r}_f - \bar{r}_{\text{e}})^T \begin{bmatrix} \mathbf{0} & \mathbf{I} \end{bmatrix} + \bar{v}_f^T \begin{bmatrix} \mathbf{I} & \mathbf{0} \end{bmatrix} \right) \frac{\partial \bar{\mathcal{X}}_{n_M}^M(T_m)}{\partial \bar{\mathcal{X}}_{n_M}^M(0)} \right], \quad (5.35)$$

$$D_x F_{\text{alt}} = \left[\bar{0} \quad \dots \quad \bar{0} \quad 2 (\bar{r}_f - \bar{r}_{\text{e}})^T \begin{bmatrix} \mathbf{I} & \mathbf{0} \end{bmatrix} \frac{\partial \bar{\mathcal{X}}_{n_M}^M(T_m)}{\partial \bar{\mathcal{X}}_{n_M}^M(0)} \right], \quad (5.36)$$

$$D_{T_m} F_{\text{apsis}} = \left((\bar{r}_f - \bar{r}_{\text{e}})^T \begin{bmatrix} \mathbf{0} & \mathbf{I} \end{bmatrix} + \bar{v}_f^T \begin{bmatrix} \mathbf{I} & \mathbf{0} \end{bmatrix} \right) \dot{\bar{\mathcal{X}}}_{n_M}^M(T_m), \quad (5.37)$$

$$D_{T_m} F_{\text{alt}} = 2 (\bar{r}_f - \bar{r}_{\text{e}})^T \begin{bmatrix} \mathbf{I} & \mathbf{0} \end{bmatrix} \dot{\bar{\mathcal{X}}}_{n_M}^M(T_m). \quad (5.38)$$

where, it is recalled that, $\bar{r}_f$ and $\bar{v}_f$ are the final propagated position and velocity vectors, respectively, from $\bar{\mathcal{X}}_{n_M}^M$ as illustrated in Figure 5.22.

The multiple-shooting formulation derived is consistent with a ballistic transfer into any quasi-periodic orbit in the CRTBP that leverages manifold structures. In this analysis, the scenario includes a ballistic transfer from a point near the Earth to a quasi-periodic orbit that employs trajectories within the stable manifold. However, the same formulation is implemented to construct ballistic transfers from a quasi-periodic orbit to near-Earth locations via trajectories along the unstable manifold structures. In Figures 5.16 and 5.18, the ballistic transfers into a subset of a family of periodic orbits are contained within a curve of solutions, i.e., a one-dimensional curve. The dimensionality of the solution curve is also observed by comparing the dimension of the free-variable and constraint vectors, i.e. Equations (5.15) and (5.16), respectively. For ballistic transfers into a single quasi-periodic orbit, as formulated from Figure 5.22, the dimensions of the free-variable and constraint vectors, Equations (5.23) and (5.24), are: $\dim(\bar{\mathfrak{X}}) = 6(n_M+1)+3$ and $\dim(\bar{F}) = 6(n_M+1)+2$, respectively. The Jacobian, $\mathbf{D}\bar{\mathbf{F}}$, defined in Equation (5.28) has a null space of dimension: $\text{null}(\mathbf{D}\bar{\mathbf{F}}) = 1$, such that, all solutions lie on a one-dimensional curve. Note that, this observation is only applicable for ballistic transfers into quasi-periodic orbits constructed from a two-dimensional torus. Insight into the dimension of the formulated problem aides in the search for ballistic transfer into quasi-periodic orbits.

5.2.1 Ballistic Transfers into Quasi-Halo Orbits near L_1

Ballistic transfers into quasi-halo orbits near Sun-Earth L_1 are constructed by leveraging stable manifold structures associated with quasi-periodic orbits. In this analysis, families of quasi-halo orbits near Sun-Earth L_1 with a fixed Jacobi Constant, $\mathcal{C}$, are constructed via a numerical corrections method. Additionally, only direct ballistic transfers are considered, such that, the NEA curves corresponding to AL1-N, AL1-S, AL2-N, and AL2-S plotted in Figures 5.16 and 5.18 are investigated. The halo orbits corresponding to curves AL1-N, AL1-S, AL2-N, and AL2-S plotted in Figures 5.16 and 5.18 possess a center subspace that is consistent with quasi-periodic motion. For example, the range of Jacobi Constant in curve AL1-S is evaluated as: $3.000603 \leq \mathcal{C} \leq 3.000794$. A family of quasi-halo orbits built from a

halo orbit with $\mathcal{C} = 3.000794$ is plotted in Figure 5.23. Recall that ρ is the rotation angle associated with a single quasi-periodic orbit, T_1 is the longitudinal time, and the ratio, $\frac{2\pi}{\rho}$, is a value that parameterizes a quasi-periodic orbit. For the quasi-halo family in Figure 5.23, as the ratio increases, the size of the quasi-periodic orbit, i.e., the z-amplitude, increases. Additionally, quasi-halo orbits with higher ratios possess trajectories near the $\hat{x} - \hat{y}$ plane, i.e., the ecliptic. The ballistic transfers into the family of Sun-Earth L_1 quasi-halo orbits

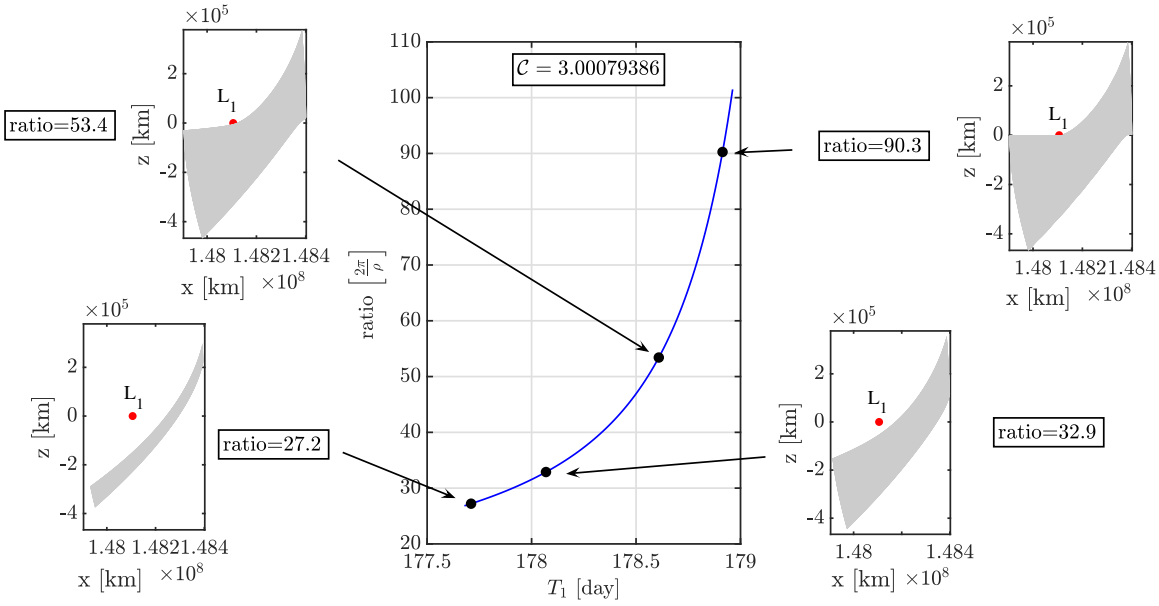

Figure 5.23. : Family of quasi-halo orbits near Sun-Earth L_1 with a fixed Jacobi Constant, $\mathcal{C} = 3.000794$

consistent with $\mathcal{C} = 3.000794$ are plotted as a family of NEA curves in Figure 5.24, with the NEA curves corresponding to five families of quasi-halo orbits with different fixed Jacobi Constants displayed in Figure 5.25. In Figure 5.24, the red point in the λ-δ plot corresponds to a ballistic transfer to the reference halo orbit, note that the family of quasi-halo orbits originate from this periodic orbit, and the NEA curves represented via a range of colors, corresponding to the quasi-periodic orbit ratio, are ballistic transfers to quasi-halo orbits. Recall, that a single point along each NEA curve is a ballistic transfer. The evolution of the NEA curves that correspond to the family of quasi-periodic orbits plotted in Figure 5.23 begins with the ballistic transfer to the reference halo orbit, i.e., the red point in Figure 5.24.

Next, as the quasi-halo orbits grow along the family of orbits, the ratio, see Figure 5.23,

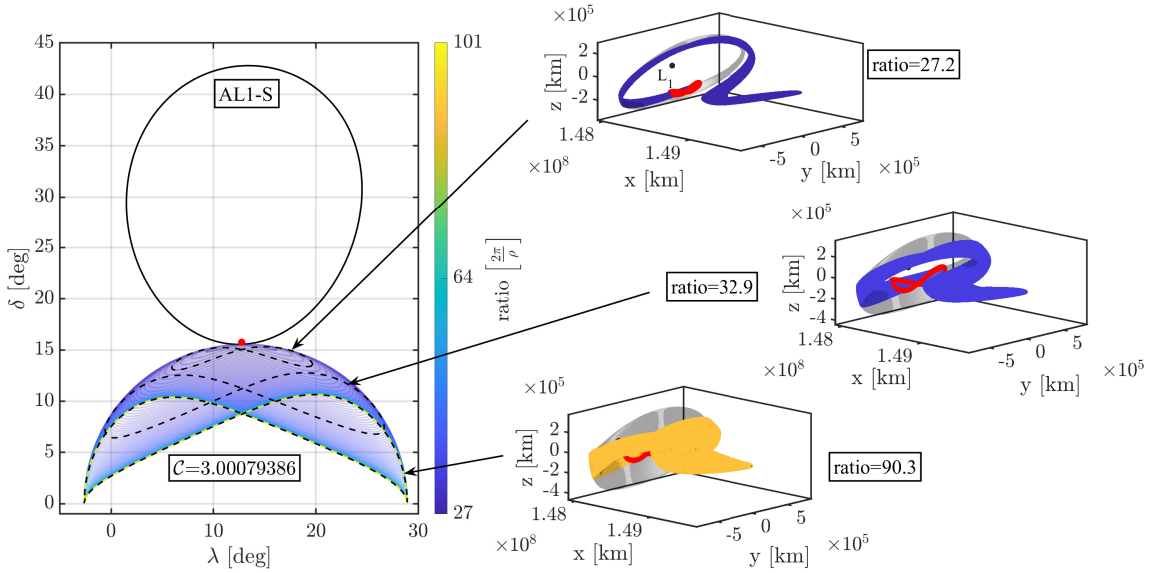

Figure 5.24. : Near-Earth Access curves corresponding to quasi-halo family with $\mathcal{C} = 3.000794$. The ballistic transfers for selected NEA curves are plotted in the right

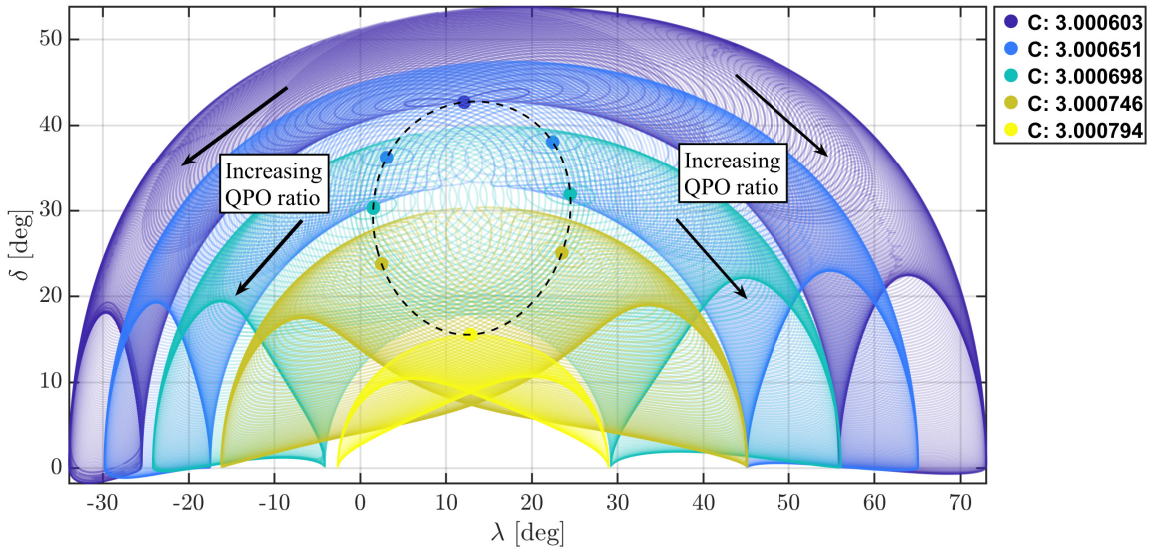

Figure 5.25. : Near-Earth Access curves for five quasi-halo orbit families. Note that each family is constructed with a fixed Jacobi Constant, $\mathcal{C}$. Observe that as the quasi-periodic ratio increases, the NEA curves move closer to the $\delta = 0°$ line

and the size of the NEA curve increases. The direction of the evolution of the NEA curves is toward the $\delta = 0^\circ$ line, i.e., the ecliptic plane in the Sun-Earth system. This observation reveals that, for this family of quasi-periodic orbits, quasi-halo orbits with higher ratios, but with a fixed Jacobi Constant, have ballistic transfer options from a GTO departure location near the ecliptic. Similar behavior is produced for different families of quasi-halo orbit constructed with fixed Jacobi Constants, see Figure 5.25. The geometry of three selected NEA curves are presented in Figure 5.24. Observe that the injection points into the quasi-halo orbits are marked in red and quasi-halo orbits with higher ratios contain larger z-amplitudes. The NEA curves in Figure 5.25 are plotted in Figure 5.26 with the accompanying inclination, ${}^r\mathrm{i}$, information. The colormap in Figure 5.26 corresponds to the quasi-periodic ratios and the black lines correspond to retrograde orbits. Recall that, in this investigation, direct ballistic transfers are preferred, such that, any ballistic transfer with ${}^r\mathrm{i} > 90^\circ$ is considered as a transfer from a retrograde GTO. Observe that the NEA curves corresponding to the quasi-halo family with a Jacobi Constant of $\mathcal{C} = 3.000794$ is associated with all prograde ballistic transfers. Alternatively, in the quasi-halo family with $\mathcal{C} = 3.000603$, some quasi-halo orbits have ballistic transfers from both prograde and retrograde GTOs.

Families of quasi-halo orbits offer additional ballistic transfer opportunities for a wider range of GTO departure locations. In this analysis, the families of quasi-halo orbits are constructed within the range of Jacobi Constants consistent with direct ballistic transfers to southern halo orbits in Figure 5.16. The NEA curves observed in Figures 5.24-5.26 correspond to families of quasi-halo orbits with fixed Jacobi Constants. However, families of quasi-halo orbits with fixed rotating angle, ρ, and mapping time, T_1, are feasible alternatives. Additionally, the NEA curves in Figure 5.25 are consistent with southern quasi-halo orbit families. Recall that in Figures 5.16 and 5.18, the NEA curves for southern and northern halo orbits are symmetric over the $\delta = 0^\circ$ line, i.e., the ecliptic. The same behavior is expected for the NEA curves corresponding to the families of southern and northern quasi-halo orbits. Based on this observation, the use of quasi-periodic halo orbits increases the number of opportunities available from regions near-Earth. Access curves for the spatial

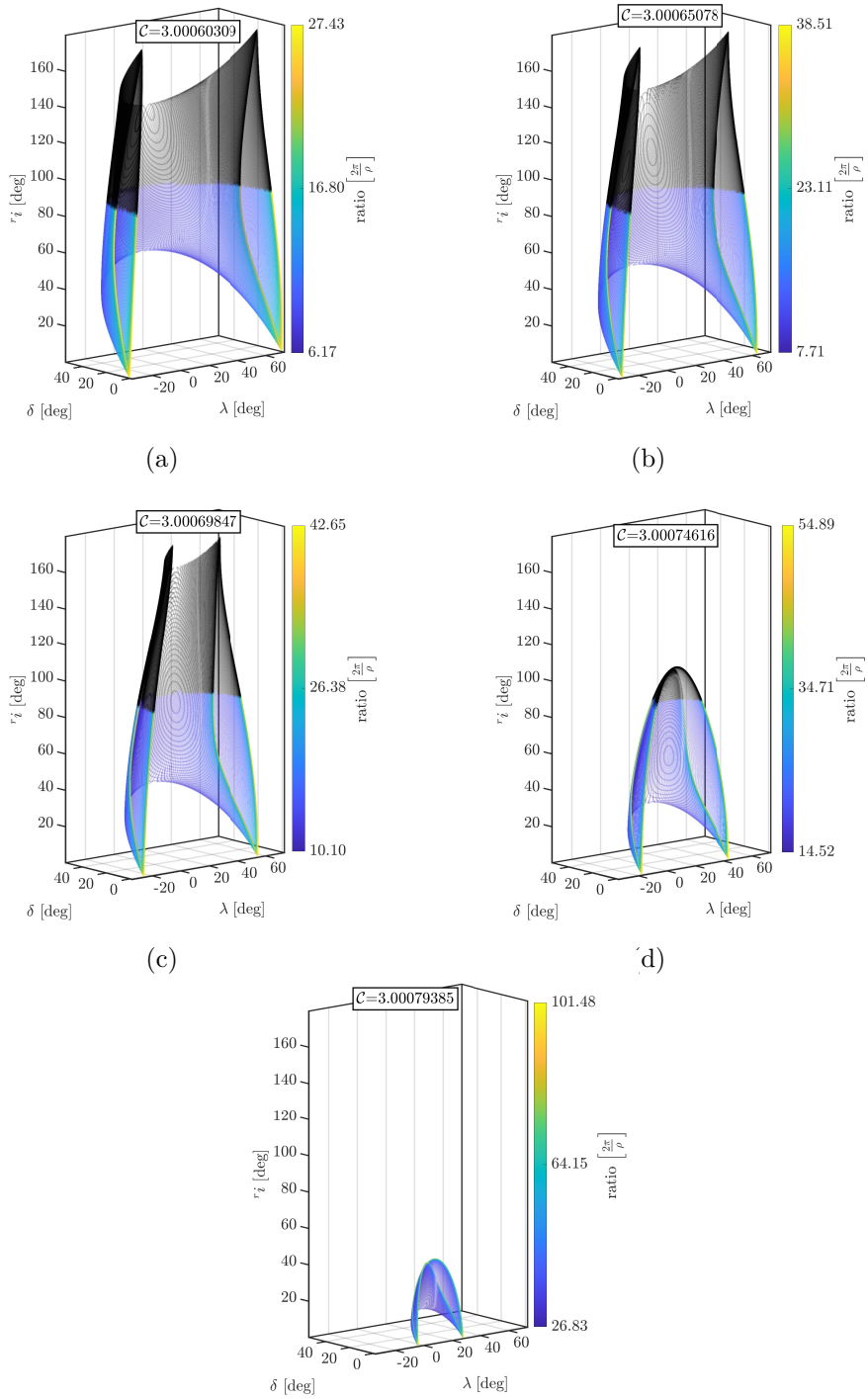

Figure 5.26. : Near-Earth Access curves for five quasi-halo orbit families constructed with fixed Jacobi Constants. Section in black represent transfers from retrograde GTOs

periodic and quasi-periodic orbits offer mission designers greater insight for the transfers available to secondary payloads from an out-of-plane GTO periapsis.

5.3 Guide of Ballistic Transfers from Geosynchronous Transfer Orbit

A ballistic transfer guide serves as a preliminary framework for direct transfers from a GTO to Sun-Earth Lagrange point orbits. The construction of such a guide is directed from the investigation of ballistic transfers to periodic orbits near L_1 and L_2. Recall that ballistic transfers are defined, in this investigation, as transfers to Sun-Earth L_1 or L_2 requiring a single maneuver performed at a GTO departure location, i.e., GTO periapsis, near the Earth. Only a collection of direct transfers are incorporated into a guide of solutions due to their lower TOF; recall that some ballistic transfers have geometries that include indirect excursions or Earth flybys. Transfers to orbits near Sun-Earth L_1 are also constrained by communications requirements due to the solar environment while transfers to L_2 are constrained by the Earth eclipsing conditions. In this investigation, unconstrained as well as constrained direct transfers are compiled in a ballistic guide to orbits near the Sun-Earth L_1 and L_2 points.

5.3.1 Constructing Ballistic Transfers From a GTO

A guide for unconstrained direct transfers to Sun-Earth Lagrange points requires a methodology to generate transfers from GTO to any quasi-periodic orbit. Ballistic transfers to quasi-periodic orbits are desired due to the increased opportunities available from low Earth altitudes. This methodology leverages trajectories within the stable manifold associated with quasi-periodic orbits, e.g., quasi-halo orbits, to connect to departure locations along a GTO with the use of a map. The following steps are consistent in developing feasible reference trajectories:

1. Generate a GTO trajectory in Sun-Earth CRTBP model. A candidate 'GTO initiating state' along the GTO is propagated in the Sun-Earth CRTBP and observed in the rotating frame.

2. Identify a candidate halo orbit to generate a family of fixed Jacobi Constant, $\mathcal{C}$, quasi-halo orbits. Note that families generated with fixed rotation angle, ρ, or constant mapping time, T_1, are alternative options.

3. Identify a candidate quasi-halo orbit. For constrained transfers in the Sun-Earth system, a candidate orbit avoids any communications contraints near L_1 or Earth eclipse conditions near L_2.

4. Generate trajectories along the hyperbolic stable manifold associated with candidate quasi-halo orbit. In this investigation, trajectories within the stable manifold surface that approach near to the Earth are employed to identify direct transfers.

5. Create mappings with trajectories from the stable manifold structure and potential departure locations along the GTO. Velocity magnitudes and directions are also available on the map.

6. Construct a reference trajectory from the selected arcs on the map. Correct a feasible reference trajectory to construct a viable transfer.

The focus of this investigation is the construction of ballistic transfers from a departure location along a GTO; the transfer is assumed to include only one deterministic maneuver. The design strategy involves departure into a ballistic transfer that leverages the natural dynamics and injects into quasi-periodic motion near a Lagrange point. Links involving departure locations along a generic GTO and stable manifold trajectories associated with quasi-periodic arrival orbits are identified via a new type of mapping strategy. In a ridesharing scenario, the secondary payload is restricted to the GTO orientation leveraged by the primary payload, as illustrated in Figure 4.1. Departure locations along planar GTOs are straightforwardly investigated with a Poincaré map formulated in an $\hat{x}$-$\hat{y}$, in the Sun-Earth rotating frame, plane. However, GTOs with non-zero inclinations, i.e., $^{i'}$i in Figure 4.2(a), are not defined

in terms of a consistent orbital plane in the context of the CRTBP model. Therefore, a new mapping approach is implemented to determine connections from locations along inclined GTOs. For example, the new mapping strategy is utilized to locate intersections between a GTO with inclination of ${}^{\mathrm{i}'}\mathrm{i} = 20°$ and the stable manifold trajectories of a southern quasi-halo orbit near the Sun-Earth L_1 point with $\mathcal{C} = 3.000808$. Note that the GTO inclinations, ${}^{\mathrm{i}'}\mathrm{i}$, are defined in an arbitrary inertial frame in Figure 4.2(a). The GTO departure position and velocity is evaluated with Equations (4.1)-(4.2) and rotated to the Sun-Earth CRTBP rotating frame via Equation (2.46). To identify potential departure locations that link with the stable manifold trajectories, the propagated states along the GTO are noted and a local region in their vicinity is defined. The scheme, illustrated in Figure 5.27, demonstrates a set of cylinders that are constructed surrounding the GTO; each cylinder is sized to deliver a feasible connection between the GTO and a trajectory within the quasi-halo stable manifold. A stable manifold intersection is described as a state $\bar{\mathcal{X}}^{ST} = [\bar{r}^{ST}; \bar{v}^{ST}]$, where $\bar{\mathcal{X}}^{ST}$ is the propagated state from the manifold state $\bar{\mathcal{X}}_M$ defined in Equation (5.22) by a time T_M; recall that $[;]$ represents vertical vector concatenation. The GTO departure locations are propagated states from an initial GTO periapsis and written as: $\bar{\mathcal{X}}_{\mathrm{j}}^{\mathrm{GTO}} = [\bar{r}^{\mathrm{GTO}}(t_{\mathrm{j}}); \bar{v}^{\mathrm{GTO}}(t_{\mathrm{j}})]$, where t_{j} is the propagation time from periapsis. The length of the j^{th} cylinder along the GTO trajectory, illustrated in Figure 5.27, is evaluated as $\mathbb{h}_{\mathrm{j}} = \left|\bar{r}^{\mathrm{GTO}}(t_{\mathrm{j}+1}) - \bar{r}^{\mathrm{GTO}}(t_{\mathrm{j}})\right|$ with GTO positions $\bar{r}^{\mathrm{GTO}}(t_{\mathrm{j}})$ and $\bar{r}^{\mathrm{GTO}}(t_{\mathrm{j}+1})$. The position of a k^{th} stable manifold intersection location along a j^{th} cylinder is defined with $\mathbb{p}_k^{\mathrm{j}}$, the distance along a line from $\bar{r}^{\mathrm{GTO}}(t_{\mathrm{j}})$ to $\bar{r}^{\mathrm{GTO}}(t_{\mathrm{j}+1})$ for the j^{th} cylinder, and $\mathbb{l}_k$, measured perpendicularly from $\mathbb{p}_k^{\mathrm{j}}$. For example, values of $\mathbb{p}$ and $\mathbb{l}$ for a stable manifold intersection point, $\bar{r}_k^{ST}$, with respect to the first cylinder ($\mathrm{j} = 0$), are evaluated as,

$$\mathbb{p}_k^0 = \frac{\left(\bar{r}^{\mathrm{GTO}}(t_1) - \bar{r}^{\mathrm{GTO}}(t_0)\right)}{\left|\bar{r}^{\mathrm{GTO}}(t_1) - \bar{r}^{\mathrm{GTO}}(t_0)\right|} \cdot \bar{r}_k^{ST}, \tag{5.39}$$

$$\mathbb{l}_k = \sqrt{\left|\bar{r}_k^{ST} - \bar{r}^{\mathrm{GTO}}(t_0)\right|^2 - (\mathbb{p}_k^0)^2}. \tag{5.40}$$

The maps in Figure 5.28 demonstrate a series of potential connections at departure locations along the GTO. Values for distances $\mathbb{P}_k^{ST} = \mathbb{p}_k^{\mathrm{j}} + \sum_{m=0}^{\mathrm{j}-1} \mathbb{h}_m$ and $\mathbb{P}_{\mathrm{j}}^{G} = \sum_{m=0}^{\mathrm{j}} \mathbb{h}_m$ represent

a k^{th} stable manifold intersection and a GTO departure location on the map, respectively. Thus, the horizontal axis in Figure 5.28 identifies locations where $\mathbb{P}_k^{ST}$ and $\mathbb{P}_{\mathrm{j}}^{G}$ overlap and is denoted as $\mathbb{P}$. The map is constructed with cylinders of radius $\mathbb{l}$ equal to 500 km and stable manifold intersections lie on the surface of a cylinder, i.e., $\mathbb{l} = 500$ km, or lie inside a cylinder, $\mathbb{l} < 500$ km. Additionally, a stable manifold intersection may only belong to one cylinder and is constrained by $\mathbb{p}_k^{\mathrm{j}} \leq \mathbb{h}_{\mathrm{j}}$. The distance $\mathbb{l}$ is then denoted on the vertical axis in Figure 5.28. Potential near-connections from the stable manifold in Figure 5.28(a) are depicted in blue and the GTO departure locations are in white. When a departure location along the GTO, a white point in Figure 5.28(a), is selected, the ΔV information is added to the plot in Figure 5.28(b). Note that Figure 5.28(b) is a zoomed view of the specified region boxed

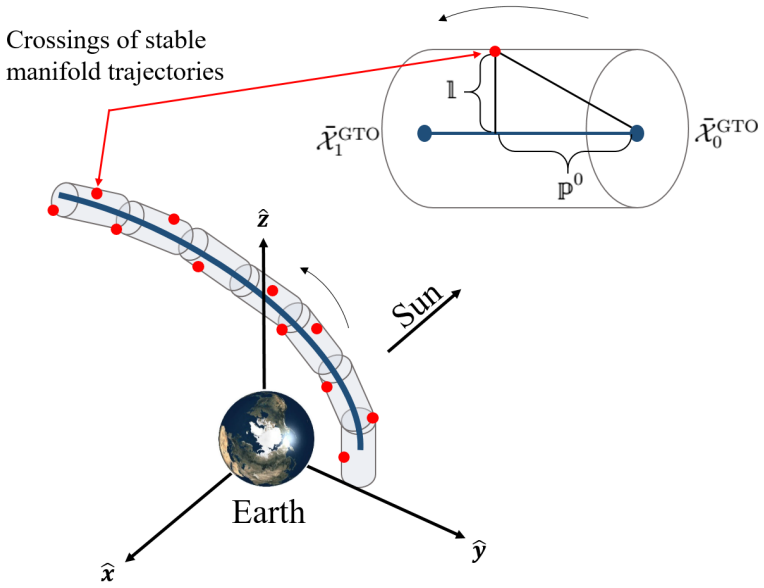

Figure 5.27. : Crossings from various stable manifold trajectories are captured inside cylinders defined with a length $\mathbb{p}^0$ and a constant radius $\mathbb{l}$

in red and illustrated in Figure 5.28(a). Additionally, in Figure 5.28(b), the direction of the line associated with a stable manifold trajectory point, $\bar{\mathcal{X}}_k^{ST}$, or a departure location, $\bar{\mathcal{X}}_{\mathrm{j}}^{\mathrm{GTO}}$, is constructed with the velocity components, $\dot{y}$ and $\dot{z}$, for the respective state. For example, a departure location in white with state $\bar{\mathcal{X}}^{\mathrm{GTO}}(t_1) = [x_1^{\mathrm{GTO}}, y_1^{\mathrm{GTO}}, z_1^{\mathrm{GTO}}, \dot{x}_1^{\mathrm{GTO}}, \dot{y}_1^{\mathrm{GTO}}, \dot{z}_1^{\mathrm{GTO}}]^T$ is plotted at $(\mathbb{P}_1^G, \mathbb{l} = 0)$ and includes a dashed line defined with an angle $\varphi = \tan^{-1}\left(\frac{\dot{z}_1^{\mathrm{GTO}}}{\dot{y}_1^{\mathrm{GTO}}}\right)$ measured from $\hat{x}$. The blue locations, i.e., $\bar{\mathcal{X}}^{ST}(\mathbb{p}^{ST})$, indicate velocity direction with the

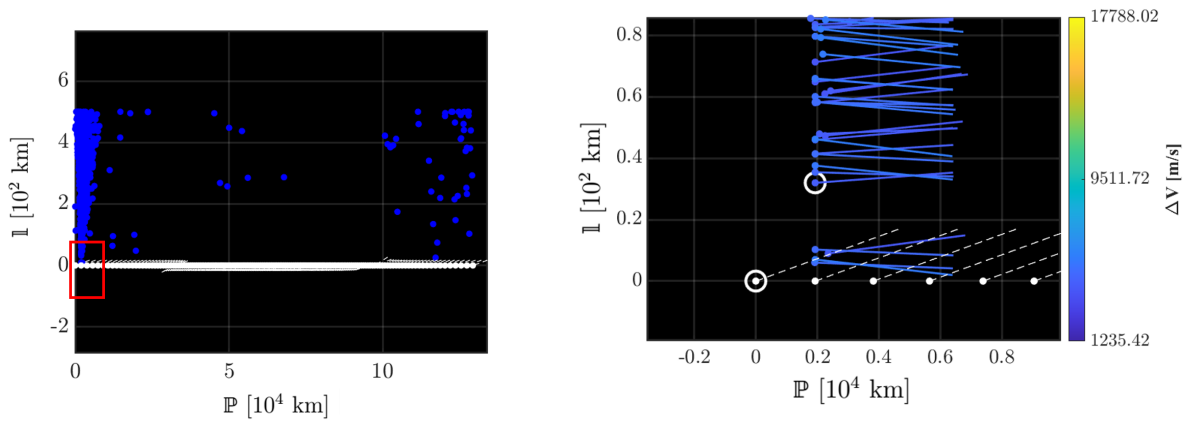

(a) (b)

Figure 5.28. : (a) Map leveraged to identify near crossings into the cylinder created from a GTO. (b) Potential crossings are highlighted in white

blue lines. A potential transfer opportunity is selected in Figure 5.28(b), depicted via a white circle, and an initial guess is constructed from the map information. The mapping in Figure 5.28(b) offers connections with the approximate ΔV information, indicated via a range of colors, and offers the capability of selecting GTO departure locations, white points on the x-axis of the plot, and the near-connections corresponding to the trajectories within the stable manifold of the associated target quasi-periodic orbit.

A reference trajectory is constructed from the near-link highlighted on the map, i.e., the two white circles in Figure 5.28(b). Note that a reference trajectory is constructed with a GTO segment and a stable manifold trajectory segment. In Figure 5.28(b), the GTO segment is represented by a white point and a white dashed line and a stable manifold trajectory segment is represented by a point and solid line with a color corresponding to the approximate ΔV required. The GTO segment arc is created via propagation in forward time from the GTO departure location, indicated by a white point in Figure 5.28(b), and stable manifold trajectory segment is constructed with reverse time propagation along the surface of the stable manifold from the pre-specified quasi-halo orbit. A multiple-shooting strategy that

incorporates a multidimensional Newton's method for updates in a differential corrections scheme is leveraged to construct feasible solutions [73] and is illustrated in Figure 5.29. In

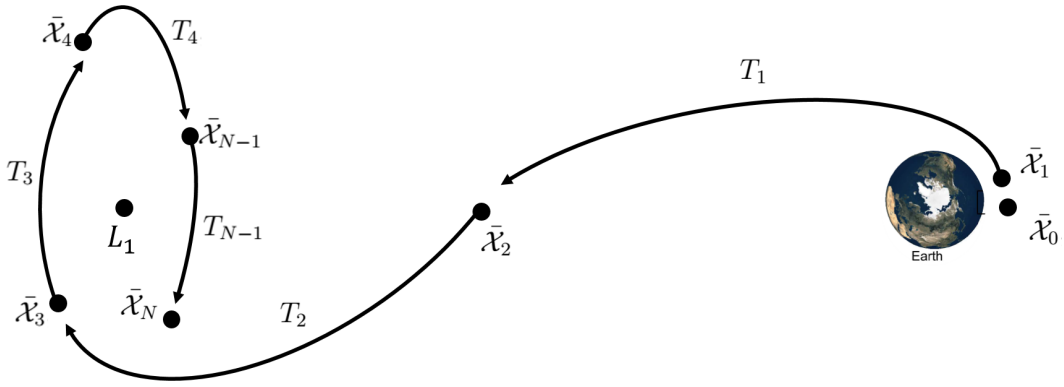

Figure 5.29. : Multiple-shooting scheme to construct ballistic transfers into orbits in the Sun-Earth CRTBP model

this investigation, a reference trajectory is defined as the superposition of trajectory arcs selected from the mapping in Figure 5.28 and a specified number of revolutions of a quasi-periodic orbit. Reference trajectories are introduced with state discontinuities and input as initial guesses for the differential corrections process to produce a continuous solution with similar characteristics. The reference trajectory is constructed with three sections: a GTO arc, a stable manifold trajectory arc, and a quasi-periodic arc. The GTO arc is a propagated trajectory from the GTO perigee to a departure location. The perigee state is fixed to constrain departures from a single GTO specified orientation. The stable manifold trajectory arc, associated with a quasi-periodic orbit near the Sun-Earth L_1 or L_2 points, is a trajectory selected from a crossing identified in Figure 5.28(b) and propagated forward in time, essentially replicating the arc originally constructed in reverse time. The quasi-periodic arc is generated by stacking a number of revolutions along the quasi-periodic orbit. The multiple-shooting strategy is implemented by decomposing each transfer segment along the reference solution into a series of N nodes along the arc, $\bar{\mathcal{X}}_{\mathrm{j}} = [x_{\mathrm{j}}, y_{\mathrm{j}}, z_{\mathrm{j}}, \dot{x}_{\mathrm{j}}, \dot{y}_{\mathrm{j}}, \dot{z}_{\mathrm{j}}]^T$, with $\mathrm{j} = [0, ..., N]$ [74]. All nodes are defined in terms of a full state with a corresponding arc time T_{j}. The final solution possesses full state continuity except for a velocity discontinuity at

the GTO departure location. The free-variable vector consistent with the ballistic transfer multiple-shooting scheme in Figure 5.29 is denoted as,

$$\bar{\mathfrak{X}} = \begin{bmatrix} \bar{\mathcal{X}}_1 \\ \vdots \\ \bar{\mathcal{X}}_N \\ T_0 \\ T_1 \\ \vdots \\ T_{N-1} \end{bmatrix}. \tag{5.41}$$

Note that the first node, i.e., $\bar{\mathcal{X}}_0$, is omitted from the free-variable vector in Equation (5.41) because the ballistic transfer is constructed from a fixed GTO departure location described via the first node $\bar{\mathcal{X}}_0$. The multiple-shooting scheme is implemented within the context of the CRTBP model. The constraint vector corresponding to a ballistic transfer from a GTO departure location is,

$$\bar{F} = \begin{bmatrix} \bar{r}_0(T_0) - \bar{r}_1(0) \\ \bar{\mathcal{X}}_1(T_1) - \bar{\mathcal{X}}_2(0) \\ \vdots \\ \bar{\mathcal{X}}_{N-1}(T_{N-1}) - \bar{\mathcal{X}}_N(0) \end{bmatrix}, \tag{5.42}$$

where the position continuity is only enforced at the intersection between the propagated position from the GTO departure state, $r_0(T_0)$, and the second node on the ballistic transfer, $\bar{\mathcal{X}}_1$. A maneuver is implied by omitting a velocity continuity constraint at the intersection between nodes $\bar{\mathcal{X}}_0$ and $\bar{\mathcal{X}}_1$. In this formulation, the impulsive maneuver performed can be

prograde, in the direction of motion, or retrograde, in the opposite direction of motion. The Jacobian associated with the constraint vector in Equation (5.42) is stated as,

$$\mathbf{D}\bar{\mathbf{F}} = \begin{bmatrix} [-\mathbf{I}_{3,3}, \mathbf{0}_{3,3}] & \mathbf{0}_{3,6} & \cdots & \mathbf{0}_{3,6} & \mathbf{0}_{3,6} & \bar{v}_0(T_0) & \bar{0}_{3,1} & \cdots & \bar{0}_{3,1} & \bar{0}_{3,1} \\ \mathbf{\Phi}_1 & -\mathbf{I}_{6,6} & \cdots & \mathbf{0}_{6,6} & \mathbf{0}_{6,6} & \bar{0}_{6,1} & \dot{\bar{\mathcal{X}}}_1 & \cdots & \bar{0}_{6,1} & \bar{0}_{6,1} \\ \vdots & \vdots & \ddots & \vdots & \vdots & \vdots & \vdots & \ddots & \vdots & \vdots \\ \mathbf{0}_{6,6} & \mathbf{0}_{6,6} & \cdots & -\mathbf{I}_{6,6} & \mathbf{0}_{6,6} & \bar{0}_{6,1} & \bar{0}_{6,1} & \cdots & \dot{\bar{\mathcal{X}}}_{N-2} & \bar{0}_{6,1} \\ \mathbf{0}_{6,6} & \mathbf{0}_{6,6} & \cdots & \mathbf{\Phi}_{N-1} & -\mathbf{I}_{6,6} & \bar{0}_{6,1} & \bar{0}_{6,1} & \cdots & \bar{0}_{6,1} & \dot{\bar{\mathcal{X}}}_{N-1} \end{bmatrix}, \tag{5.43}$$

where the STM is defined as: $\mathbf{\Phi}_{\mathrm{j}} = \frac{\partial \bar{\mathcal{X}}_{\mathrm{j}}(T_{\mathrm{j}})}{\partial \bar{\mathcal{X}}_{\mathrm{j}}(0)}$ and the acceleration vector, $\dot{\bar{\mathcal{X}}}_{\mathrm{j}}$, is evaluated via the equations of motion corresponding to the CRTBP at the end of the propagation arc, i.e., $\dot{\bar{\mathcal{X}}}_{\mathrm{j}}(T_{\mathrm{j}})$. The feasible transfer constructed from the multiple-shooting algorithm is the initial solution for a continuation scheme that reduces the total ΔV of a single maneuver ballistic transfer. The continuation scheme is essentially a natural parameter continuation algorithm with a maximum ΔV magnitude, $\Delta V_{\max}$, defined as the natural parameter. An inequality constraint is introduced to enforce a maximum ΔV magnitude for the single maneuver in the ballistic transfer. A slack variale, $\beta_{\Delta V}$, is included in the formulation of an inequality constraint, i.e.,

$$F_{\Delta V_{\max}} = \|\bar{v}_0(T_0) - \bar{v}_1(0)\| - \Delta V_{\max} + \beta_{\Delta V}^2, \tag{5.44}$$

where $\|\cdot\|$ is the vector norm. The inequality constraint in Equation (5.44) is appended to the constraint vector in Equation (5.42). The partial derivatives of the inequality constraint are denoted as,

$$\frac{DF_{\Delta V_{\max}}}{D\bar{\mathcal{X}}_1(0)} = \frac{\left(\bar{v}_0(T_0) - \bar{v}_1(0)\right)^T}{\|\bar{v}_0(T_0) - \bar{v}_1(0)\|} \begin{bmatrix} \mathbf{0}_{3,3} & -\mathbf{I}_{3,3} \end{bmatrix}, \tag{5.45}$$

$$\frac{DF_{\Delta V_{\max}}}{DT_0} = \frac{\left(\bar{v}_0(T_0) - \bar{v}_1(0)\right)^T}{\|\bar{v}_0(T_0) - \bar{v}_1(0)\|} \dot{\bar{v}}_0(T_0), \tag{5.46}$$

$$\frac{DF_{\Delta V_{\max}}}{D\beta_{\Delta V}} = 2\beta_{\Delta V}. \tag{5.47}$$

Each solution from the continuaton scheme delivers a transfer with an associated ΔV below the user input $\Delta V_{\max}$ magnitude. The continuation process continues with the previously corrected transfer as an input and by decreasing the $\Delta V_{\max}$ magnitude. A final solution is identified when the correction process, i.e., the multiple-shooting algorithm that corrects for state continuity along the transfer nodes, fails to converge after 50 iterations. Note that this continuation process is a pseudo-optimization process and that the final solution is a single maneuver transfer with an associated ΔV_{low} magnitude. Figure 5.30 illustrates

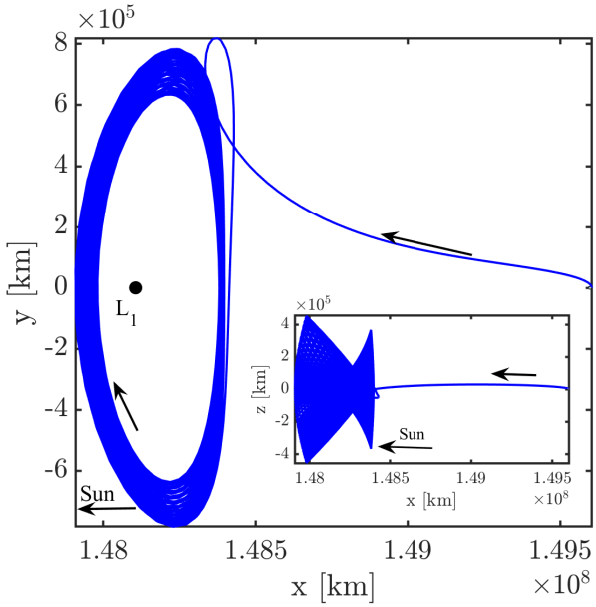

Figure 5.30. : Transfer solution with single maneuver magnitude of 740.0 m/s in the CRTBP model

a transfer with a ΔV_{low} magnitude of 740.0 m/s, which emerged from the initial transfer identified in Figure 5.28(b) and thirty revolutions along the quasi-halo orbit. The transfer in Figure 5.30 departs from GTO periapsis with an inclination equal to ${}^{\text{i}'}\text{i} = 20°$, recalling the definition in Figure 4.2(a), and enters a Lissajous orbit with a large z-amplitude. Note that the initial guess leverages a southern quasi-halo orbit, but the continuation scheme lowered the total ΔV for the single maneuver that initiates the ballistic transfer, and altered the geometry of the target quasi-periodic orbit. In this continuation strategy, the geometry and Jacobi Constant, $\mathcal{C}$, associated with the quasi-periodic orbit are unconstrained, that is, a specified transfer trajectory is not targeted. Although the mapping presented in Figure 5.28

is not as intuitive as a Poincaré map with a planar cross-section, it can be applied to expose near-connections from any trajectory.

5.3.2 Unconstrained Transfers into Orbits near L_1 and L_2

A collection of unconstrained direct ballistic transfers is generated by employing the previous mapping strategy and a natural parameter continuation scheme. The mapping strategy identifies feasible initial guess information, see the maps in Figure 5.28 for an example, for ballistic transfers to the Sun-Earth L_1 and L_2 points. The initial guess, i.e., the stable manifold trajectory corresponding to a quasi-periodic orbit and a set of revolutions around the quasi-periodic orbit, is corrected via a multiple-shooting numerical algorithm utilizing Equations (5.41)-(5.43). Natural parameter continuation is implemented to construct a pseudo-optimal ballistic transfer by introducing the inequality constraint in Equation (5.44). Recall that natural parameter continuation on $\Delta V_{\max}$ identifies efficient transfers while continuation with other parameters, i.e., inertial frame inclination ${}^{i'}i$, explores transfers from a range of GTO orientations, see Figure 4.2(a). From Figures 4.5 and 4.2, the Sun-Earth rotating frame inclination, ${}^{r}i$, and the inertial inclination, ${}^{i'}i$, are not equal to the inertial EME frame inclination, ${}^{i}i$; and, in this section, a collection of ballistic transfers is constructed from a GTO with a range of the inertial inclinations, ${}^{i'}i$. A GTO departure state is constructed via Equations (4.1) and (4.2) with a selected inclination (${}^{i'}i$), RAAN (Ω), and argument of periapsis (ω) angle; recall that the GTO has a fixed periapsis altitude of 185 km and an apogee altitude of 35,786 km, i.e., geosynchronous altitude. The GTO departure position and velocity vectors are nondimensionalized and rotated to the Sun-Earth rotating frame via Equation (2.46); note that the rotation from the arbitrary inertial frame in Figure 4.2 is performed with $t = 0$. In Figure 5.4, the locations near the Earth that are consistent with direct ballistic transfers to Sun-Earth L_1 Lyapunov orbits are restricted to a range of $-40^\circ < \lambda < 110^\circ$, i.e., the range along the APL1 access curve. Therefore, for ballistic transfers to L_1, the range explored in this investigation is $-40^\circ < \lambda < 110^\circ$ along the Sun-Earth ecliptic plane, i.e., $\delta = 0^\circ$ in Figure 4.5(b). Additionally, transfers from inclined GTOs with

prograde motion are produced by continuation along the GTO inclination, $^{i'}$i. The polar plots in Figure 5.31 summarize the ballistic transfer ΔV and the final quasi-periodic orbit z-amplitudes via a range of colors from a fixed GTO periapsis altitude, 185 km. In Figure

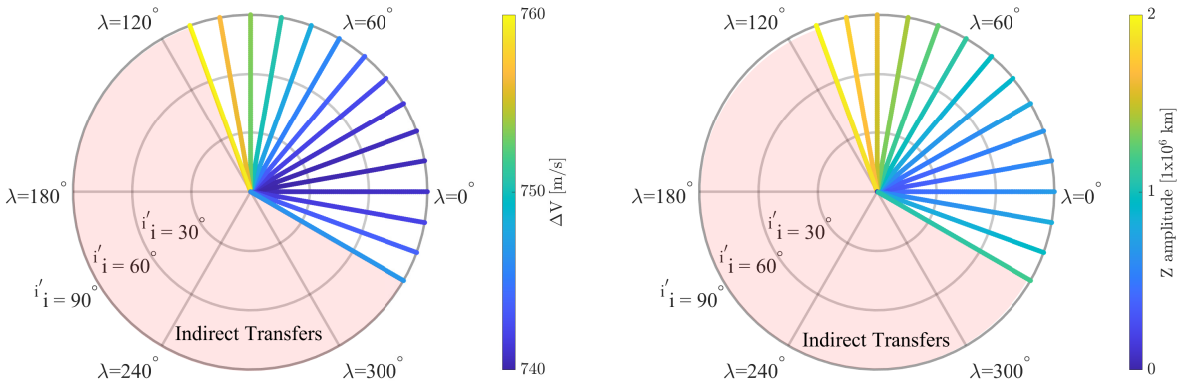

(a) (b)

Figure 5.31. : (a) Maneuver magnitudes for direct unconstrained transfers to Sun-Earth L_1 around the Earth. (b) $z-$amplitudes for unconstrained transfers to L_1

5.31, the angular direction corresponds to λ, from Figure 4.5(b), and the radial direction is the GTO inclination, $^{i'}$i, for a given transfer. The transfers presented in Figure 5.31 corresponds to ballistic transfer with optimized ΔV magnitude, i.e., ΔV_{low}, that is, transfers after the pseudo-optimization via natural parameter continuation with ΔV_{max}. The shaded region in Figure 5.31 corresponds to indirect transfers to L_1 which are not explored in this investigaton. Additionally, the transfer ΔV, in Figure 5.31(a), is within the theoretical minimum values associated with periodic Lyapunov and halo orbits in Table 5.1, although the ballistic transfers in the polar plot approach quasi-periodic orbits. The region near-Earth with a GTO periapsis altitude of 185 km between $10° < \lambda < 20°$ is associated with lower ballistic ΔV magnitudes and with lower quasi-periodic z-amplitudes. The geometries of select ballistic transfers are plotted in Figures 5.32 and 5.33. The view in Figures 5.32 and 5.33 corresponds to an observer in the Earth towards the Sun-Earth L_1 point. The ballistic

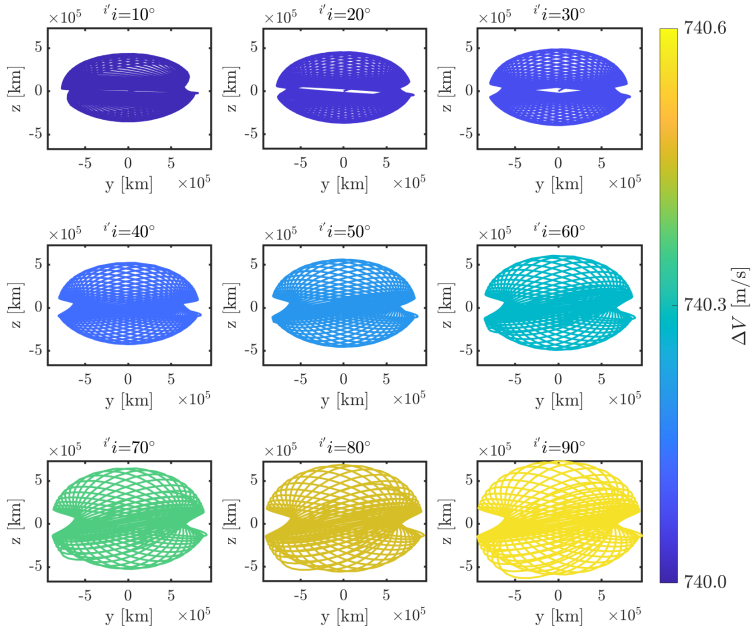

Figure 5.32. : Unconstrained ballistic transfers into Sun-Earth L_1 quasi-periodic orbits from a GTO departure state with $\lambda = 0°$ and $\delta = 0°$

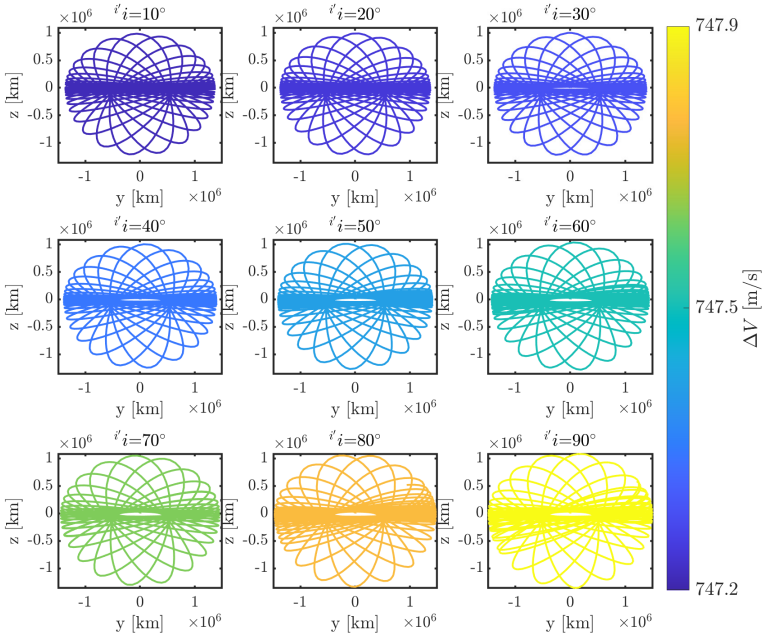

Figure 5.33. : Unconstrained ballistic transfers into Sun-Earth L_1 quasi-periodic orbits from a GTO departure state with $\lambda = 70°$ and $\delta = 0°$

transfers correspond to a GTO departure location of $\lambda = 0°$, in Figure 5.32, and $\lambda = 70°$, in Figure 5.33. The geometry plotted for a GTO departure location at $\lambda = 0°$ is consistent with very large Lissajous orbits while the ballistic transfer from $\lambda = 70°$ resemble very large quasi-halo orbits. Recall that the direct ballistic transfers require a single maneuver from the GTO periapsis toward a quasi-periodic orbit near the Sun-Earth Lagrange points. The unconstrained ballistic transfers summarized in Figure 5.31 require low ΔV magnitudes, compared to the theoretical values in Table 5.1, and offer access to very large Lissajous and quasi-halo orbits near Sun-Earth L_1

A continuation scheme in both $\Delta V_{\max}$ and inclination is leveraged to construct efficient direct unconstrained ballistic transfers to Sun-Earth L_2. For ballistic transfers towards L_2, the range of direct transfers is $150° < \lambda < 290°$, refer to Figure 5.9. Figure 5.34 displays the ΔV and z-amplitude information for the efficient ballistic transfers in a polar plot; note that the shaded region corresponds to indirect transfers to L_2. Observe the region associated lower ΔV and lower z-amplitudes is $190° < \lambda < 200°$. Select ballistic transfer geometries of Sun-Earth L_2 from Figure 5.34 are plotted in Figures 5.35 and 5.36. The ballistic transfers

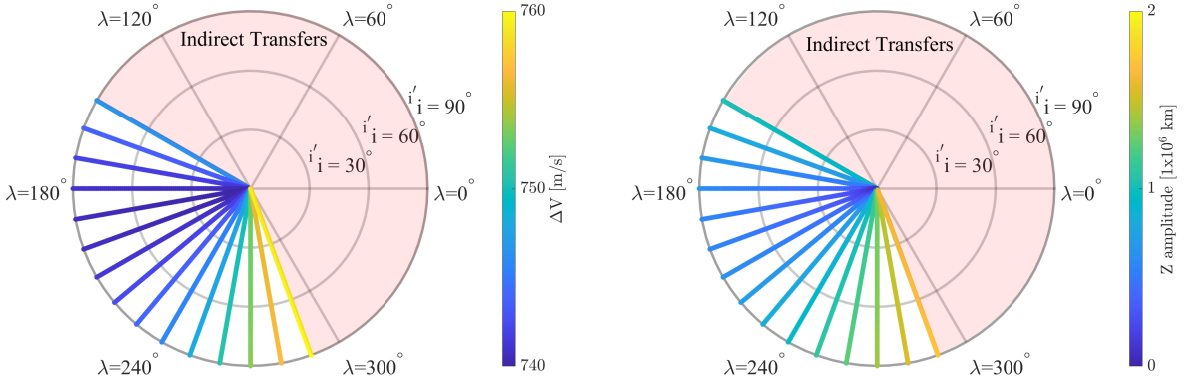

(a) (b)

Figure 5.34. : (a) Maneuver magnitudes for direct unconstrained transfers to L_2 around the Earth. (b) $z-$amplitudes for unconstrained transfers to L_2

corresponding to $\lambda = 180°$ and $\delta = 0°$, in Figure 5.35, approach Lissajous orbits with increasing z-amplitudes for increasing inclinations, $^{i'}$i. The transfers plotted in Figure 5.36 enter large quasi-halo orbits. Observe that the transfers presented in Figures 5.35 and 5.36 cross the x-axis in the Sun-Earth system. The continuation strategy leveraged to determine the ballistic transfers in Figures 5.31 and 5.34 can be leveraged for GTOs with a periapsis location above or below the ecliptic, i.e., $\delta \neq 0°$, and for a range of GTO departure altitudes.

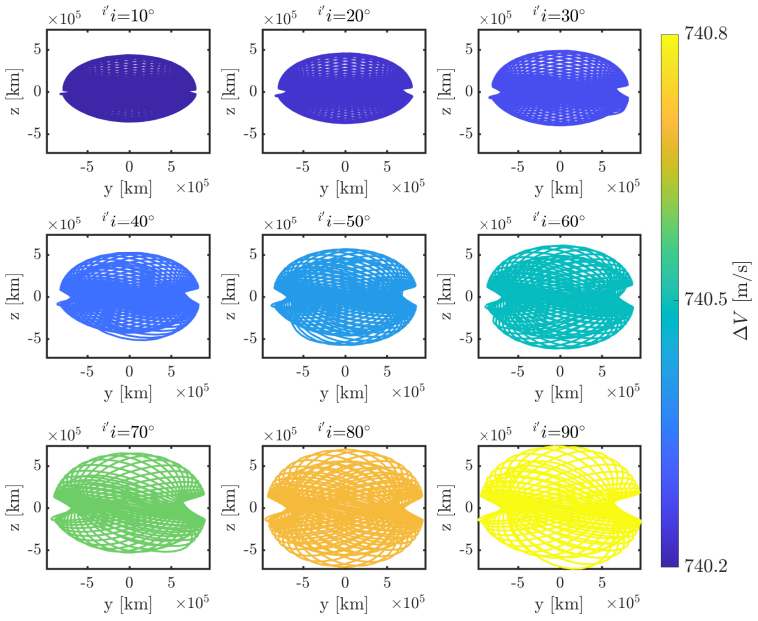

Figure 5.35. : Unconstrained ballistic transfers into Sun-Earth L_1 quasi-periodic orbits from a GTO departure state with $\lambda = 180°$ and $\delta = 0°$

Unconstrained direct ballistic transfers to Sun-Earth L_1 for GTO departure states above or below the ecliptic are constructed via a multiple-shooting strategy. Figures 5.31 and 5.34 include maneuver information for unconstrained ballistic transfers from a GTO depature state along the ecliptic, i.e., $\delta = 0°$, from a fixed GTO departure altitude of 185 km. However, ballistic transfers from regions above or below the ecliptic offer additional insight into the geometry of available ballistic transfers to Sun-Earth L_1. A GTO departure state is constructed via Equations (4.1) and (4.2). In the preceding analysis, ω was fixed

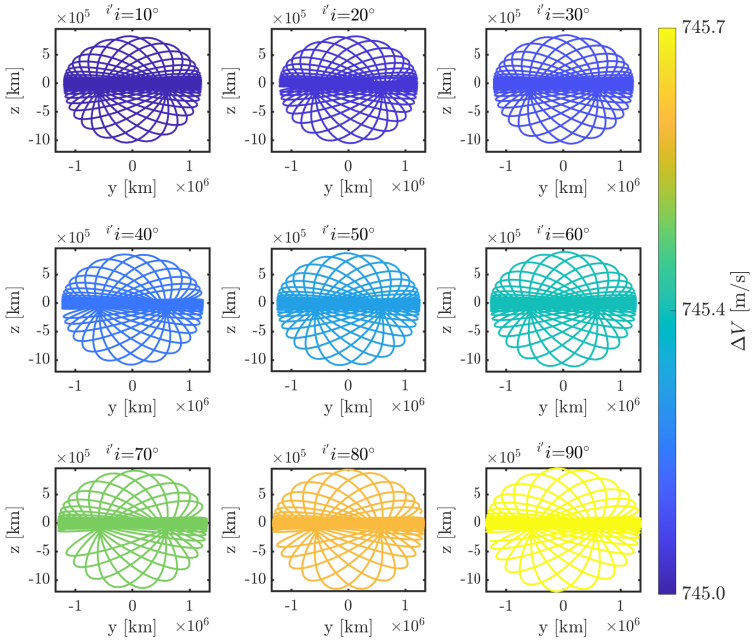

Figure 5.36. : Unconstrained ballistic transfers into Sun-Earth L_1 quasi-periodic orbits from a GTO departure state with $\lambda = 240°$ and $\delta = 0°$

at: $\omega = 0°$ and Ω was essentially equal to $\Omega = \lambda$. To construct ballistic transfers from any departure location, the relationships between the inertial keplerian elements and the rotating frame elements are summarized by leveraging the properties of a right spherical triangle, i.e.,

$$\sin({}^{i'}\mathrm{i}) = \frac{\sin(\delta)}{\sin(\omega)}, \tag{5.48}$$

$$\tan({}^{i'}\mathrm{i}) = \frac{\tan(\delta)}{\sin(\Delta\Omega)}, \tag{5.49}$$

$$\tan(\Delta\omega) = \cos({}^{i'}\mathrm{i})\tan(\omega), \tag{5.50}$$

$$\sin(\omega) = \frac{\sin(\delta)}{\sin({}^{i'}\mathrm{i})}, \tag{5.51}$$

$$\cos(\omega) = \cos(\Delta\Omega)\cos(\delta), \tag{5.52}$$

$$\tan(\omega) = \frac{\tan(\delta)}{\sin({}^{i'}\mathrm{i})\cos(\Delta\Omega)}, \tag{5.53}$$

where $\Delta\Omega = \lambda - \Omega$. The angles corresponding to Ω, ω, ${}^{i'}\mathrm{i}$, λ, and δ are illustrated in Figure 5.37. For a specified δ angle, a range of values corresponding to ${}^{i'}\mathrm{i}$ and ω are derived as,

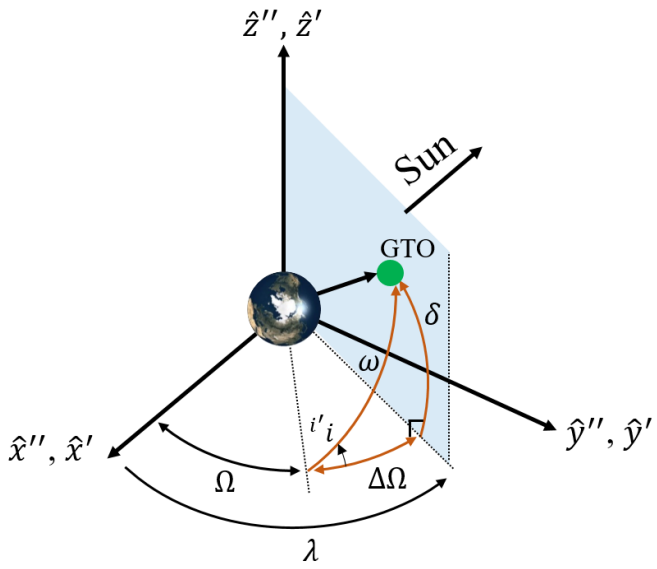

Figure 5.37. : Relationship between the inertial keplerian elements, $\{\Omega, {}^{i'}\mathrm{i}, \omega\}$, and the rotating frame elements, $\{\lambda, \delta\}$. Recall that the basis vectors $\{\hat{x}'', \hat{y}'', \hat{z}''\}$ correspond to a shifted rotating frame with an origin at P_2, i.e., the Earth

$$\text{If } \delta > 0: \quad \delta \leq \omega, {}^{i'}\mathrm{i} \leq \boldsymbol{\pi} - \delta, \tag{5.54}$$

$$\text{If } \delta < 0: \quad \delta \leq \omega, {}^{i'}\mathrm{i} \leq -\boldsymbol{\pi} - \delta. \tag{5.55}$$

The ranges for ω and ${}^{i'}\mathrm{i}$ described are also plotted in Figure 5.38. In Figure 5.38, prograde GTO departure states correspond to a range of $\Delta\Omega$ values of $0° \leq \Delta\Omega \leq 180°$ and the retrograde departure states are in the range of $180° \leq \Delta\Omega \leq 360°$. For a GTO departure state with $\delta = 0°$, an inclination, i.e., ${}^{i'}\mathrm{i}$, is only defined at $\Delta\Omega = 0°, 180°$. Additionally, observe that, for $\delta = 0°$, $\omega = \Delta\Omega$. In this analysis, ballistic transfers from prograde GTOS are constructed, such that, only one region in Figure 5.38 is implemented. GTO departure states are constructed with a set of δ values, i.e., $\delta = \{-50°, -40°, \cdots, 0°, \cdots, 40°, 50°\}$. The range of δ values was selected based on the assumption that a GTO in the inertial EME frame has an inclination of ${}^{i}\mathrm{i} = 27°$ and, from Figure 4.9, the range of δ is approximately $-50° \leq \delta \leq 50°$. The unconstrained direct ballistic transfers corresponding to $\delta = 10°$ are highlighted in Figure 5.39. The surface in Figure 5.39 is plotted along the λ, ω, and ΔV values and the colors for the surface correspond to the inclination, ${}^{i'}\mathrm{i}$. Observe that the higher inclinations ballistic transfers in the curve appear near the boundaries of the ω

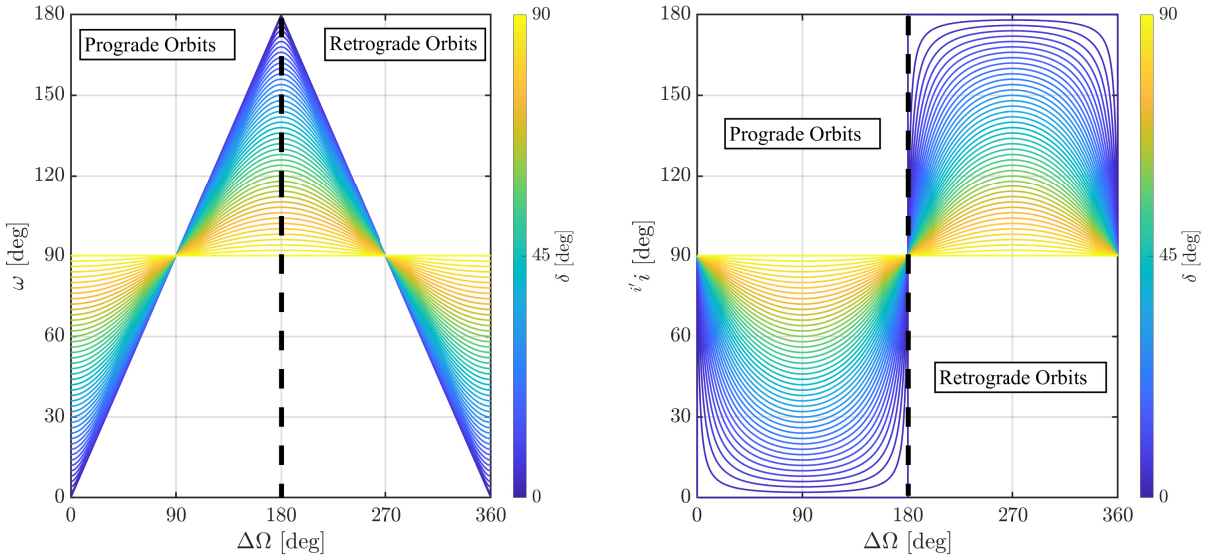

Figure 5.38. : (a) Argument of periapsis angle, ω, and (b) inertial inclination, ${}^{i'}i$, at a range of $\Delta\Omega$ angles. Note that $\Delta\Omega = \lambda - \Omega$

angle range. The range of λ values corresponds to the range for direct ballistic transfer to Sun-Earth L_1, i.e., $-40^\circ \leq \lambda \leq 120^\circ$, and the GTO departure states are constructed for a range of ω equal to $10^\circ \leq \omega \leq 170^\circ$. Selected transfers are highlighted via a black asterisk and represent ballistic transfer from a location $\lambda = 10^\circ$ near the Earth. From Figure 5.39, for increasing ω values, the geometry of the ballistic transfer transitions from a Lissajous to a quasi-halo orbit; note that the plots of the geometry are in a $\hat{y}$-$\hat{z}$ projection. The surface plotted in Figure 5.40 represents the unconstrained direct ballistic transfers for a range of δ values. For positive δ values, i.e., $\delta > 0$, the ballistic transfer surfaces are contained within a region of the ω values of $0^\circ \leq \omega \leq 180^\circ$; and the ballistic transfers for negative δ values correspond to a range of $180^\circ \leq \omega \leq 360^\circ$. Recall that the range for the inertial inclination, i.e., ${}^{i'}i$, is defined via the ranges in Equations (5.54)-(5.55) and are dependent on the δ values. Additionally, curves of unconstrained ballistic transfer corresponding to a GTO departure location of $\lambda = 0^\circ$ and $\delta = 0^\circ$ are plotted in Figure 5.41. For increasing δ values, i.e., $|\delta|$, the ΔV magnitude required for the single maneuver ballistic transfers increases, see Figure 5.41.

The geometry of select ballistic transfer, depicted as black points, from the information in Figure 5.41 are plotted in Figures 5.42-5.51.

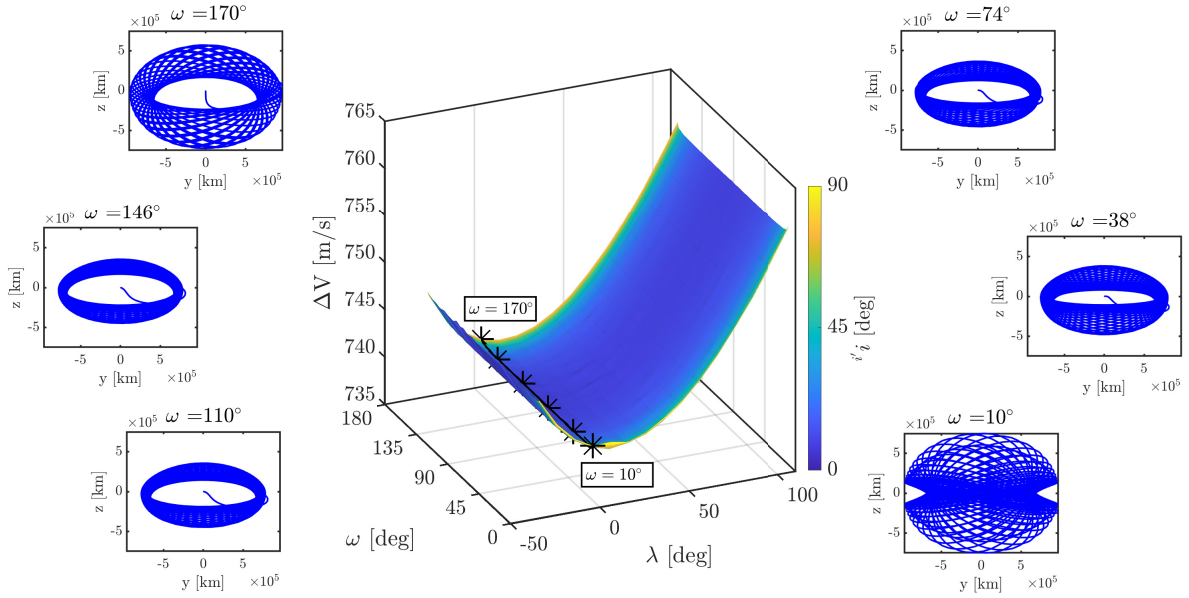

Figure 5.39. : Surface of unconstrained ballistic transfers to Sun-Earth L_1 corresponding to $\delta = 10°$

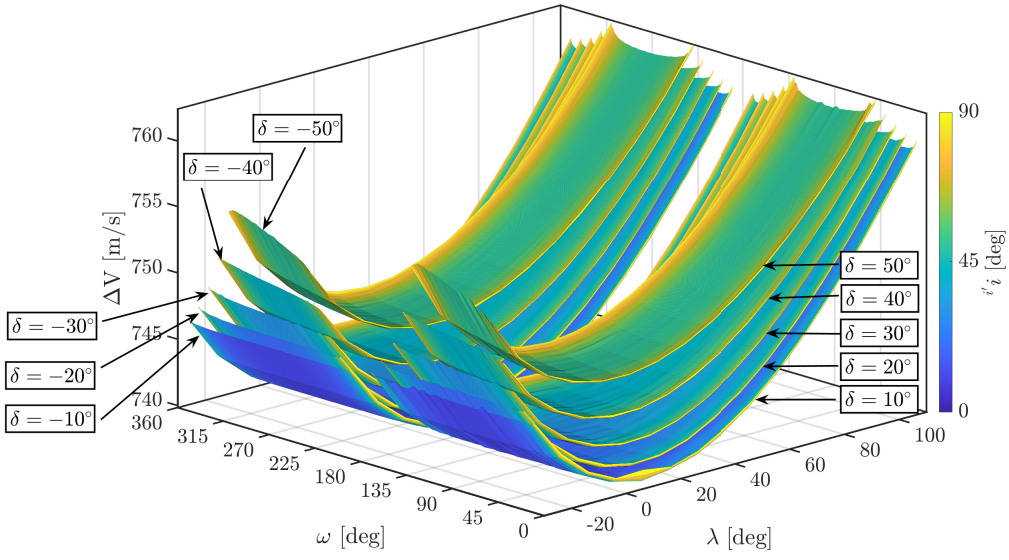

Figure 5.40. : Surface of unconstrained ballistic transfers to Sun-Earth L_1 corresponding to a range of δ values of $-50° \leq \delta \leq 50°$

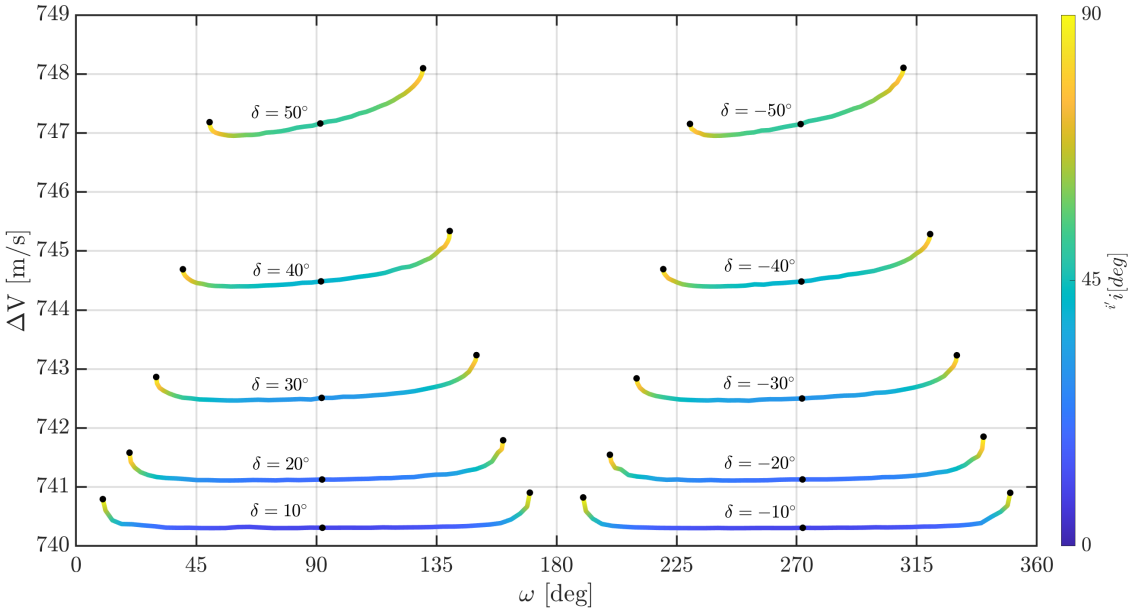

Figure 5.41. : Unconstrained direct ballistic transfers to Sun-Earth L_1 corresponding to a range of δ values of $-50° \leq \delta \leq 50°$ from a GTO departure state of $\lambda = 0°$

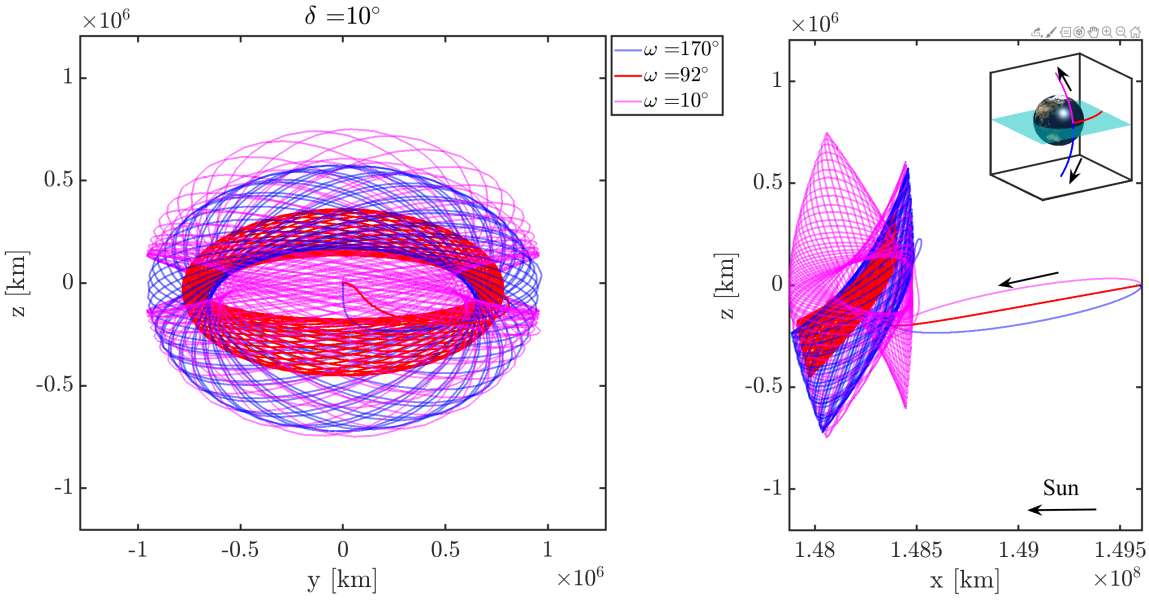

Figure 5.42. : Selected unconstrained direct ballistic transfers to Sun-Earth L_1 corresponding to $\delta = 10°$ and $\lambda = 0°$

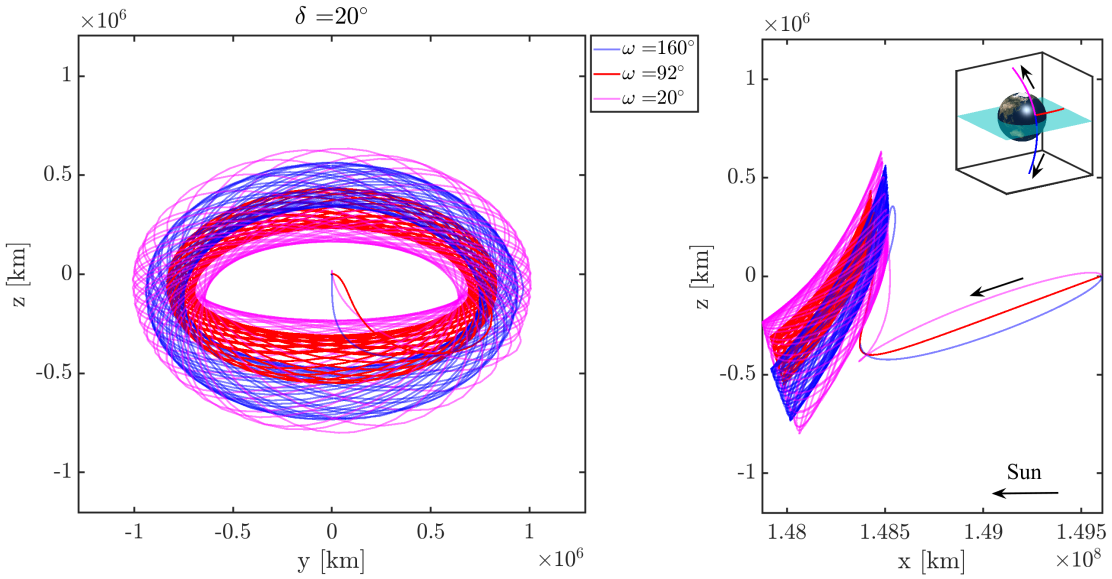

Figure 5.43. : Selected unconstrained direct ballistic transfers to Sun-Earth L_1 corresponding to $\delta = 20°$ and $\lambda = 0°$

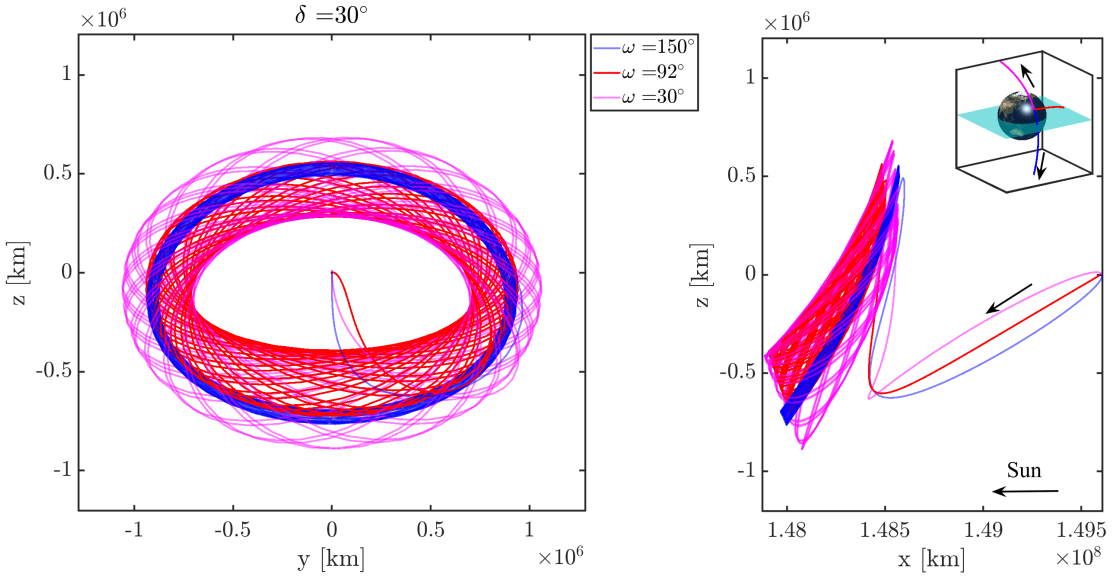

Figure 5.44. : Selected unconstrained direct ballistic transfers to Sun-Earth L_1 corresponding to $\delta = 30°$ and $\lambda = 0°$

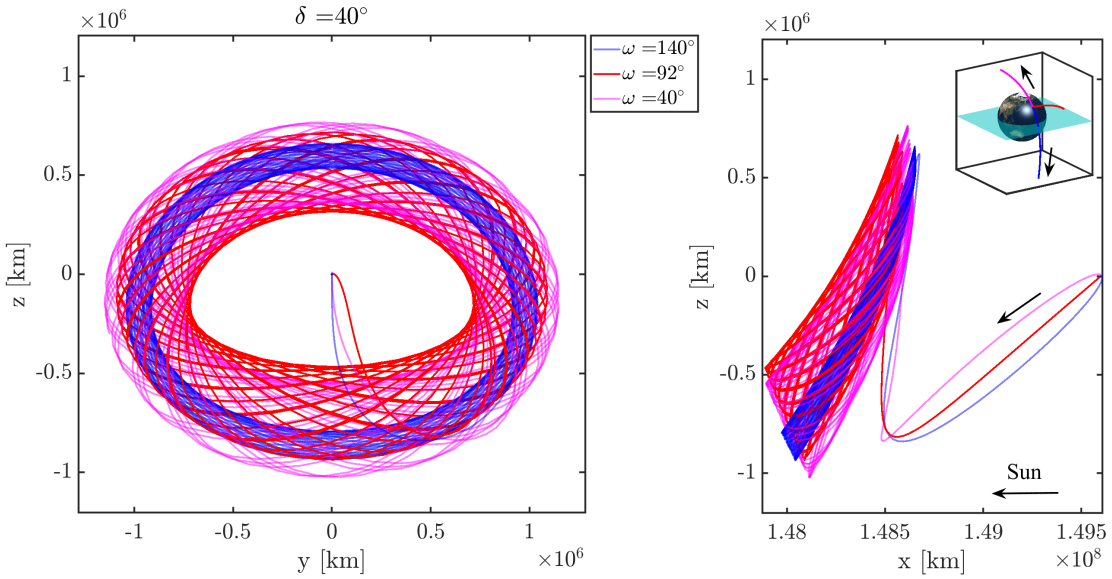

Figure 5.45. : Selected unconstrained direct ballistic transfers to Sun-Earth L_1 corresponding to $\delta = 40°$ and $\lambda = 0°$

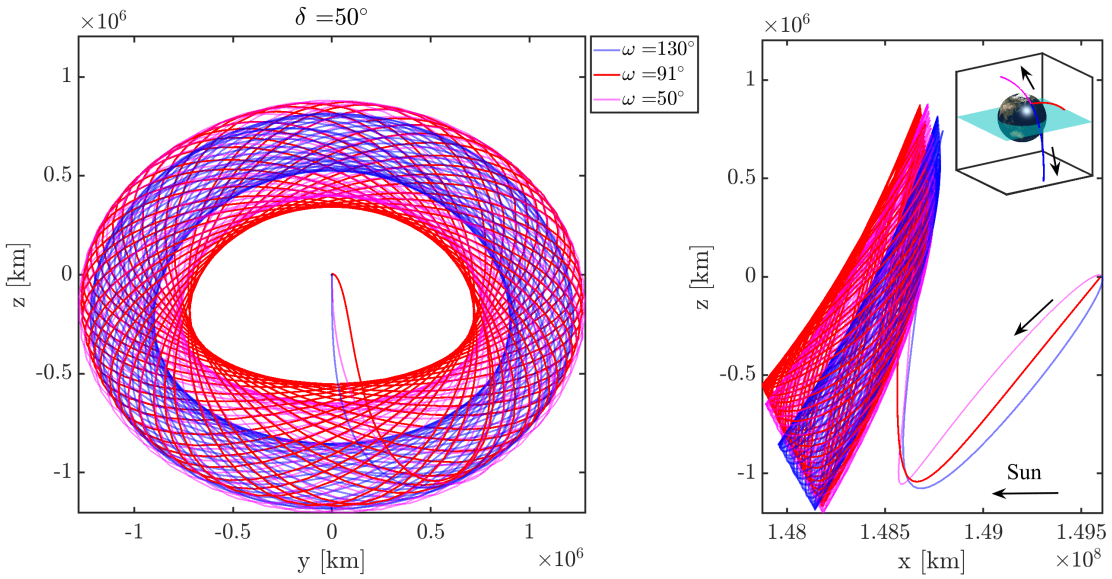

Figure 5.46. : Selected unconstrained direct ballistic transfers to Sun-Earth L_1 corresponding to $\delta = 50°$ and $\lambda = 0°$

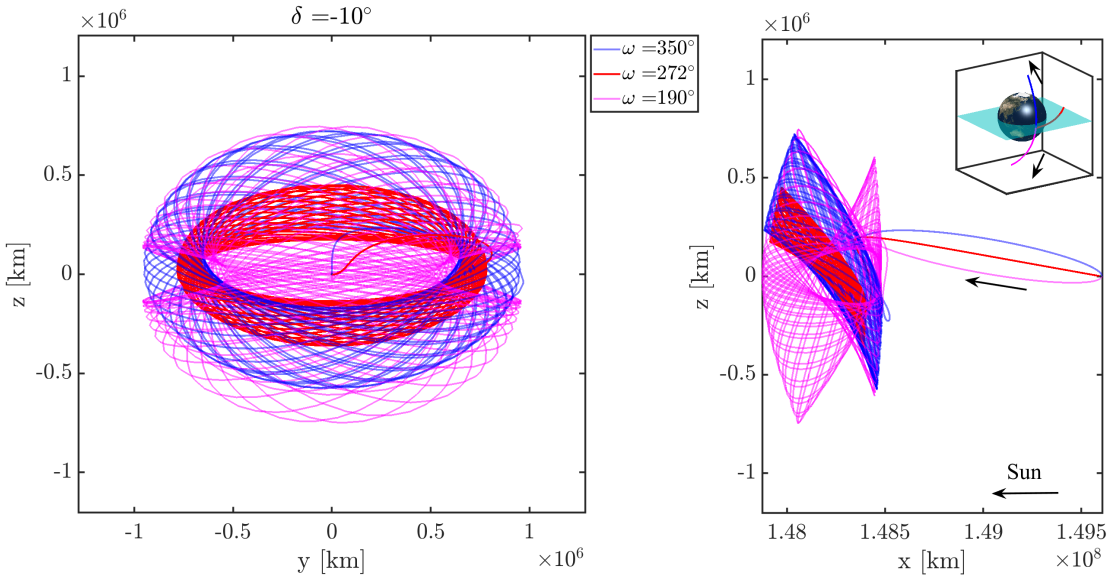

Figure 5.47. : Selected unconstrained direct ballistic transfers to Sun-Earth L_1 corresponding to $\delta = -10°$ and $\lambda = 0°$

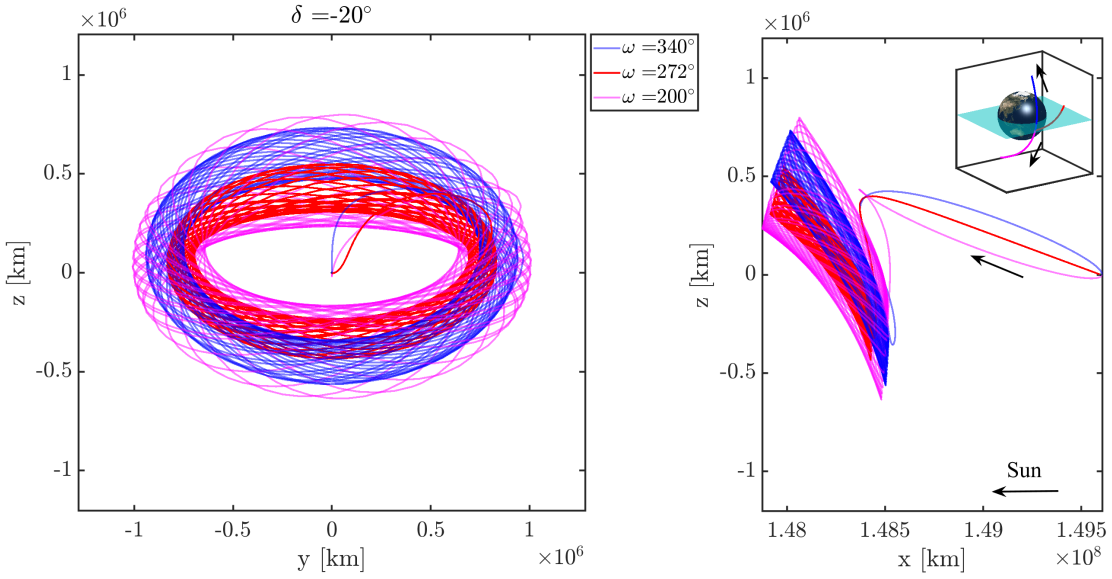

Figure 5.48. : Selected unconstrained direct ballistic transfers to Sun-Earth L_1 corresponding to $\delta = -20°$ and $\lambda = 0°$

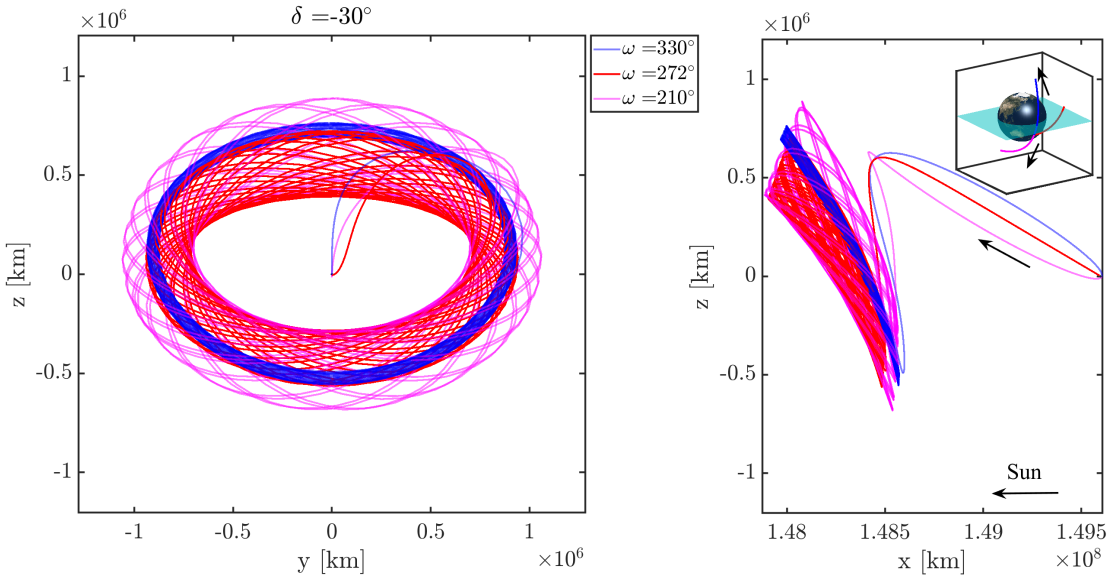

Figure 5.49. : Selected unconstrained direct ballistic transfers to Sun-Earth L_1 corresponding to $\delta = -30°$ and $\lambda = 0°$

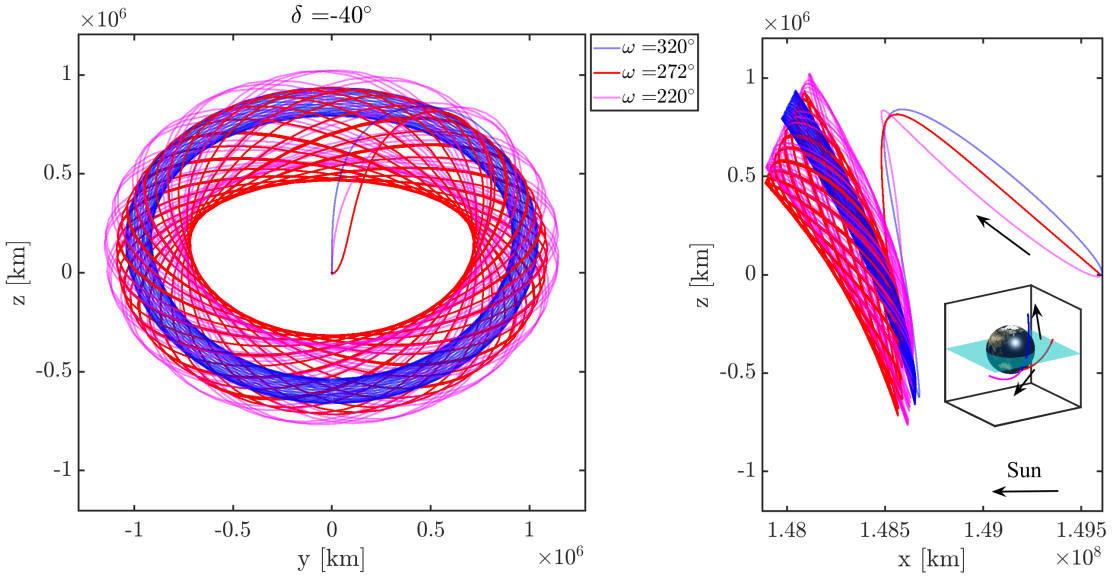

Figure 5.50. : Selected unconstrained direct ballistic transfers to Sun-Earth L_1 corresponding to $\delta = -40°$ and $\lambda = 0°$

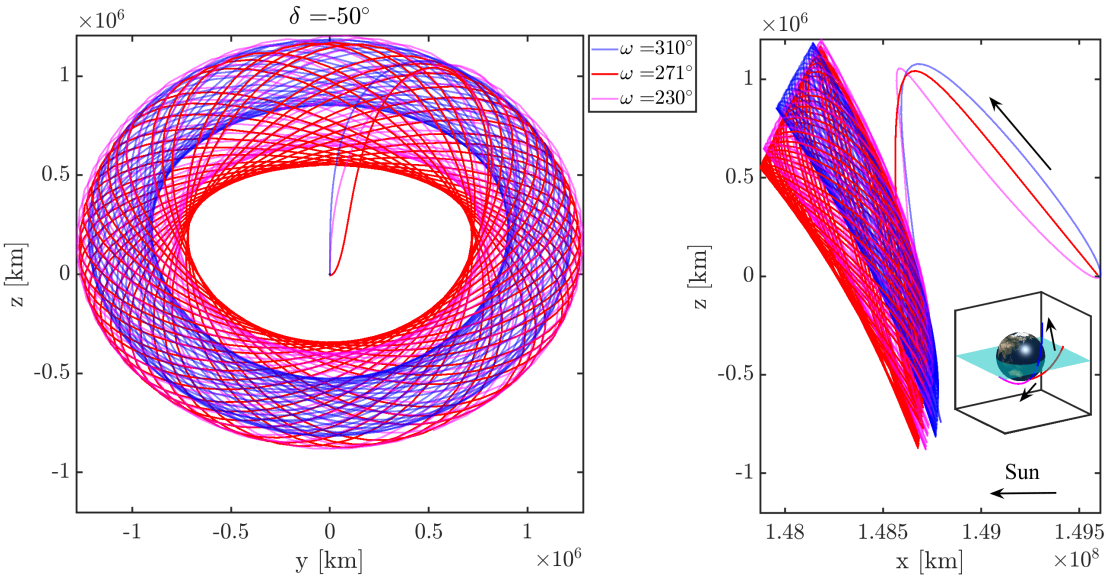

Figure 5.51. : Selected unconstrained direct ballistic transfers to Sun-Earth L_1 corresponding to $\delta = -50°$ and $\lambda = 0°$

GTO departure states at near-Earth locations above or below the ecliptic, i.e., $|\delta| > 0°$, are often associated with ballistic transfers into quasi-halo orbits. From Figures 5.42-5.51, unconstrained direct ballistic transfers into Sun-Earth L_1 southern quasi-halo orbits are observed for $\delta > 0°$ and transfers into northern quasi-halos correspond to $\delta < 0$. Observe that this is consistent with the ballistic Near-Earth Access curve analysis for southern and northern quasi-halo orbits in Section 5.2. The collection of unconstrained ballistic transfers over a range of inclinations provides initial ΔV magnitude estimates and a range of locations near-Earth for transfers from GTO periapsis to Sun-Earth L_1 and L_2 points. In this investigation, only direct ballistic transfers are observed as potential options from a GTO departure state, with the range of GTO departure locations parameterized via λ and δ angles in the near Earth vicinity. Additionally, for the rideshare scenario including a secondary payload satellite, it is assumed that there is no a priori information concerning the GTO Keplerian elements, i.e., no information on the location of the GTO periapsis in the Sun-Earth rotating frame. Although transfers from a GTO with a 185 km periapsis altitude are included, continuation on the periapsis altitude can expose transfer opportunities for GTOs

of variable orbit size. Only unconstrained ballistic transfers are constructed, but, depending on the destination, additional constraints must be incorporated into the trajectory design process.

5.3.3 Path Constraint for Sun-Earth L_1 Transfers

A collection of constrained ballistic transfers to Sun-Earth L_1 quasi-periodic orbits is constructed with the ballistic transfer information from the unconstrainted results and a mathematically defined path constraint. Communications constraints during an Earth-to-L_1 transfer and in a Sun-Earth L_1 Lagrange point orbit require that the spacecraft avoid crossing in front of the solar disk when viewed from the Earth [11]. In the rotating frame, a Sun-Earth-Vehicle (SEV) angle α is defined as the angle between $\bar{r}_{23}$ and -$\hat{x}$ as illustrated in Figure 5.52. The vector $\bar{r}_{23}$ is the satellite position with respect to the Earth and is defined as: $\bar{r}_{23} = \bar{r} - \bar{r}_{\mathrm{e}}$, where $\bar{r}$ and $\bar{r}_{\mathrm{e}}$ are the positions of the satellite and the Earth, respectively, measured from the Sun-Earth barycenter. The SEV angle is defined with:

$$\alpha = \cos^{-1}\left(\frac{\bar{r}_{23} \cdot -\hat{x}}{\|\bar{r}_{23}\|}\right), \tag{5.56}$$

where -$\hat{x} = [-1, 0, 0]^T$ and $\bar{\mathfrak{A}} \cdot \bar{\mathfrak{B}}$ is the vector dot product in this formulation. The Solar Exclusion Zone (SEZ) is a region, illustrated in Figure 5.52 via a red dashed line, defined by a right circular cone with the vertex at the Earth and a constant SEV angle. A communications constraint is enforced along the transfer and a mathematical definition for the path constraint is necessary. A general scalar path constraint is formulated as a line integral, i.e.,

$$F_{\mathrm{path}} = \sum_{\mathrm{j}}^{N} \int_0^{T_{\mathrm{j}}} F_p^2\left(\bar{\mathcal{X}}_{\mathrm{j}}(t)\right) - \left|F_p\left(\bar{\mathcal{X}}_{\mathrm{j}}(t)\right)\right| F_p\left(\bar{\mathcal{X}}_{\mathrm{j}}(t)\right) dt = 0. \tag{5.57}$$

In this formulation, $|\cdot|$ implies an absolute value, N is the number of nodes along the trajectory, and T_{j} is the propagation time for a j^{th} arc. Equation (5.57) is a summation of line integrals evaluated for every trajectory arc, consistent with a multiple-shooting scheme,

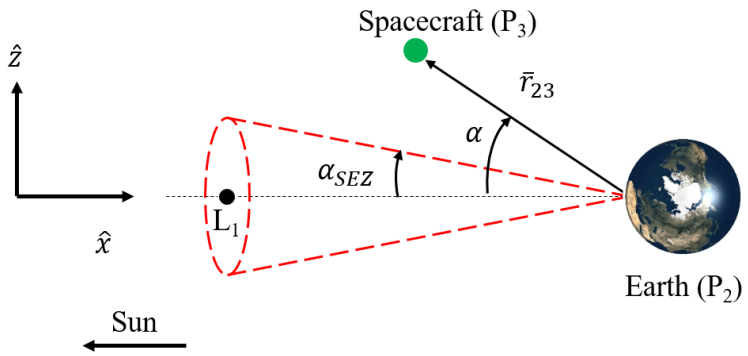

Figure 5.52. : Solar Exclusion Zone defined in the Sun-Earth rotating frame (red). The angle α_{SEZ} defines the size of this region

in the constructed ballistic transfer, see Figure 5.29 for the multiple-shooting schematic. However, the scalar path constraint may be modified to only enforce the path condition, i.e., the SEZ cone constraint in this example, along a designated set of propagated trajectory arcs. Additionally, Equation (5.57) is written for a multiple-shooting formulation of the trajectory, but is easily adapted for a single-shooting problem. The integrand in Equation (5.57) is evaluated for every state in the transfer, i.e., every state computed via the propagation process, and is either a negative value (violates path condition) or equal to zero (complies with path condition). This general path constraint equation is used to prevent crossing into the SEZ for L_1 transfers and to prevent any path with positions below the Earth's surface. The constraint functions that express these constraints are defined as,

$$\text{SEZ Constraint:} \quad F_{\text{p,SEZ}} = \sin\left(\alpha\left(\bar{\mathcal{X}}_{\text{j}}(t)\right) - \alpha_{\text{SEZ}}\right), \tag{5.58}$$

$$\text{Altitude Constraint:} \quad F_{\text{p,alt}} = \bar{r}_{23}\left(\bar{\mathcal{X}}_{\text{j}}(t)\right)^{T} \bar{r}_{23}\left(\bar{\mathcal{X}}_{\text{j}}(t)\right) - h_{\text{e}}^2, \tag{5.59}$$

with the surface altitude of the Earth defined as $h_{\text{e}} = 6371$ km. In Equations (5.58)-(5.59), the SEV angle, α, and the position with respect to the Earth, $\bar{r}_{23}$, are functions of the state, $\bar{\mathcal{X}}_{\text{j}}(t)$, that corresponds to the state node, $\bar{\mathcal{X}}_{\text{j}}$, propagated by time t. The path integral condition in Equation (5.57) is enforced for both the SEZ and altitude constraints. The

constraint function that corresponds to the SEZ condition, i.e., Equation (5.58), is expanded to,

$$F_{\text{p,SEZ}} = \sin\left(\alpha(t)\right)\cos\left(\alpha_{\text{SEZ}}\right) - \cos\left(\alpha(t)\right)\sin\left(\alpha_{\text{SEZ}}\right), \tag{5.60}$$

where the sine and cosine values of the ballistic transfer SEV angle, α, are defined as,

$$\cos\left(\alpha(t)\right) = \frac{\bar{r}_{23}^{T}(t)(-\hat{x})}{\|\bar{r}_{23}(t)\|}, \tag{5.61}$$

$$\sin\left(\alpha(t)\right) = \sqrt{1-\cos^2\left(\alpha\right)}, \tag{5.62}$$

where, it is recalled that, $\bar{r}_{23}(t) = \bar{r}(t) - \bar{r}_{\text{e}}$, that is, the satellite position along the ballistic transfer measured with respect to the Earth. An unconstrained ballistic transfer is constructed via a multiple-shooting strategy that implements a multidimensional Newton's method with the free-variable and constraint vectors provided by Equations (5.41) and (5.42), respectively. To construct a constrained ballistic transfer, the scalar SEZ and altitude path constraints are appended to the constraint vector in Equation (5.42), that is,

$$\bar{F}_{\text{con}} = \begin{bmatrix} \bar{F} \\ F_{\text{path,SEZ}} \\ F_{\text{path,alt}} \end{bmatrix}, \tag{5.63}$$

where,

$$F_{\text{path,SEZ}} = \sum_{\text{j}}^{N} \int_{0}^{T_{\text{j}}} F_{\text{p,SEZ}}^{2}\left(\bar{\mathcal{X}}_{\text{j}}(t)\right) - \left|F_{\text{p,SEZ}}\left(\bar{\mathcal{X}}_{\text{j}}(t)\right)\right| F_{\text{p,SEZ}}\left(\bar{\mathcal{X}}_{\text{j}}(t)\right) dt, \tag{5.64}$$

$$F_{\text{path,alt}} = \sum_{\text{j}}^{N} \int_{0}^{T_{\text{j}}} F_{\text{p,alt}}^{2}\left(\bar{\mathcal{X}}_{\text{j}}(t)\right) - \left|F_{\text{p,alt}}\left(\bar{\mathcal{X}}_{\text{j}}(t)\right)\right| F_{\text{p,alt}}\left(\bar{\mathcal{X}}_{\text{j}}(t)\right) dt, \tag{5.65}$$

with $F_{\text{p,SEZ}}$ and $F_{\text{p,alt}}$ defined in Equations (5.58)-(5.59). In this formulation, the path conditions corresponding to the SEZ and altitude are separated into two integrals, this separation offers the opportunity to enforce the constraint along different regions of the ballistic transfer. For example, the altitude constraint is only enforced during propagated

arcs near the Earth. Additionally, the path constraint requires numerical integration and the accuracy is dependent on the number of points along the transfer arc, which, near the Earth, may require higher computational effort. The separation of the SEZ and altitude path constraints mitigates increased computational time associated with propagation near the primaries, i.e., the Earth, by carefully selecting the transfer arcs to enforce the constraint conditions. The partial derivatives of the path constraint function in Equation (5.57) are denoted as,

$$\frac{\partial F_{\text{path}}}{\partial \bar{\mathcal{X}}_{\text{j}}} = \int_0^{T_{\text{j}}} 2\Big(F_p\left(\bar{\mathcal{X}}_{\text{j}}(t)\right) - \left|F_p\left(\bar{\mathcal{X}}_{\text{j}}(t)\right)\right|\Big)\frac{\partial F_p}{\partial \bar{\mathcal{X}}_{\text{j}}(t)}\frac{\partial \bar{\mathcal{X}}_{\text{j}}(t)}{\partial \bar{\mathcal{X}}_{\text{j}}(0)}\,dt, \tag{5.66}$$

$$\frac{\partial F_{\text{path}}}{\partial T_{\text{j}}} = F_p^2\left(\bar{\mathcal{X}}_{\text{j}}(T_{\text{j}})\right) - \left|F_p\left(\bar{\mathcal{X}}_{\text{j}}(T_{\text{j}})\right)\right|F_p\left(\bar{\mathcal{X}}_{\text{j}}(T_{\text{j}})\right), \tag{5.67}$$

where the STM is defined as: $\mathbf{\Phi}_{\text{j}}(t,0) = \frac{\partial \bar{\mathcal{X}}_{\text{j}}(t)}{\partial \bar{\mathcal{X}}_{\text{j}}(0)}$, i.e., the STM at the end of each propagated arc. The partial derivatives associated with the SEZ constraint function, i.e., $F_{\text{p,SEZ}}$, with respect to the current state, $\bar{\mathcal{X}}(t)$, are denoted as,

$$\frac{\partial F_{\text{p,SEZ}}}{\partial \bar{\mathcal{X}}(t)} = \frac{\partial \sin(\alpha)}{\partial \bar{\mathcal{X}}(t)}\cos\left(\alpha_{\text{SEZ}}\right) - \frac{\partial \cos(\alpha)}{\partial \bar{\mathcal{X}}(t)}\sin\left(\alpha_{\text{SEZ}}\right), \tag{5.68}$$

$$\frac{\partial \cos(\alpha)}{\partial \bar{\mathcal{X}}(t)} = \left(\frac{-\hat{x}^T}{\|\bar{r}_{23}(t)\|} + \frac{\left(\bar{r}_{23}^T(t)\hat{x}\right)\bar{r}_{23}^T(t)}{\|\bar{r}_{23}(t)\|^3}\right)\begin{bmatrix}\mathbf{I}_{3,3} & \mathbf{0}_{3,3}\end{bmatrix}, \tag{5.69}$$

$$\frac{\partial \sin(\alpha)}{\partial \bar{\mathcal{X}}(t)} = \frac{-\cos(\alpha(t))}{\sin(\alpha(t))}\frac{\partial \cos(\alpha(t))}{\partial \bar{\mathcal{X}}(t)}, \tag{5.70}$$

where, it is recalled that, all vectors are assumed to be column vectors. From Equation (5.70), when the sine value of the SEV angle is equal to zero, there is a state along the propagated transfer arc that lies on the $\hat{x}$ axis of the Sun-Earth rotating frame and the partial derivative is undefined. However, this situation is improbable during the propagation process unless it is targeted or the initial node is on the $\hat{x}$ axis. Additionally, Equations (5.68)-(5.70) form an integrand that is input into Equation (5.66), therefore, any undefined single integrand values

may be omitted in the numerical integration process without significant loss of accuracy. The partial derivative for the altitude constraint, $F_{\text{p,alt}}$, is,

$$\frac{\partial F_{\text{p,alt}}}{\partial \bar{\mathcal{X}}(t)} = 2\bar{r}_{23}^{T}(t)\begin{bmatrix}\mathbf{I}_{3,3} & \mathbf{0}_{3,3}\end{bmatrix}. \tag{5.71}$$

The integral for the general path constraint in Equation (5.57) is computed via a trapezoidal rule integration scheme, i.e., the trapz function in MATLAB, and is applicable for any path constraint for which the desired conditions are mathematically defined as $F_p \geq 0$, as defined in Equation (5.58). Constrained ballistic transfers to the vicinity of Sun-Earth L_1 are constructed by introducing the path constraint equation during the corrections process.

5.3.4 Constrained Transfers into Orbits near L_1

A guide for constrained ballistic transfers is constructed by applying the path constraints from Equations (5.57)-(5.59) to the unconstrained transfers in Figure 5.31. For example, a ballistic transfer corresponding to a departure state with $\lambda = 0°$ and $\delta = 0°$ in Figure 5.31(a) is defined as an initial guess. Then, the selected transfer, i.e., a series of nodes and propagation times described via the free-variable vector in Equation (5.41), is input into a corrections process with the constraint vector in Equation (5.63). Once a solution that enforces the path constraint is identified, the ΔV required for the single maneuver ballistic transfer is decreased via a natural parameter continuation algorithm by including Equation (5.44) in the corrections process. The SEZ cone angle, i.e., α_{SEZ}, is varied along a range of angles equal to: $\alpha_{\text{SEZ}} = \{1°, 2°, 3°, 4°, 5°\}$; note that the ACE mission initially implemented a SEZ region with a cone angle of 4.75° [11]. The constrained ballistic transfer for a range of SEZ cone angles are plotted as surfaces in Figure 5.53. Recall that the range of direct ballistic transfers for L_1 is defined in the range of $-40° \leq \lambda \leq 120$. For GTO departure state with higher inclinations, i.e., ${}^{i'}\text{i}$, the required ΔV is lower compared to states with inclinations less than 30°. Additionally, at ${}^{i'}\text{i} < 30°$, the required ΔV for the single maneuver ballistic transfer is higher when considering a larger SEZ cone, described via α_{SEZ}. Figures 5.54 -

5.58 present the geometry of selected constrained ballistic transfers from a GTO departure location of $\lambda = \delta = 0°$. The quasi-periodic orbits depicted in Figures 5.54 - 5.58 are northern quasi-halo orbits. Southern quasi-halo orbits are feasible options for a constrained ballistic transfer to Sun-Earth L_1, but, for this GTO departure location of $\lambda = 0°$, transfers into the northern quasi-halos required lower ΔV magnitudes. Additionally, for ballistic transfers from a departure location of $\lambda = 0°$, Figure 5.59 depicts the ΔV required along a range of prograde inclinations, ${}^{i'}i$. The geometries of ballistic transfers with $\lambda = \delta = 0°$ and ${}^{i'}i = 20°$ are plotted in Figure 5.59. Observe the growth of the quasi-halo, described by the increasing z-amplitude, as the SEZ cone angle, α_{SEZ}, increases. The constrained ballistic transfers presented in this analysis include a number of revolutions such that the transfer does not violate the SEZ after injecting into the quasi-halo orbits, as seen in Figures 5.54-5.59.

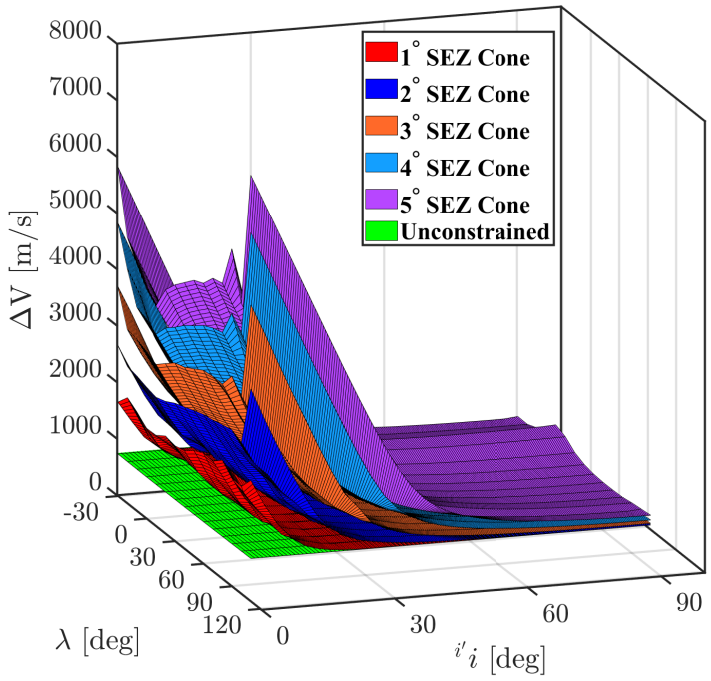

Figure 5.53. : Surfaces of constrained ballistic transfers into Sun-Earth L_1 quasi-periodic orbits that avoid crossing a variable SEZ cone size

The addition of the SEZ constraint increases the ΔV requirements at low inclinations as additional ΔV is necessary to transfer into a more out-of-plane quasi-periodic orbit that re-

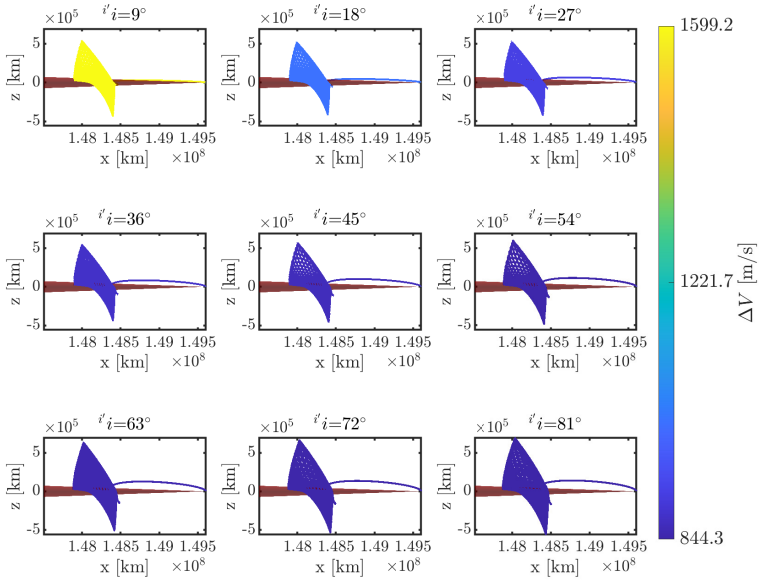

Figure 5.54. : Constrained ballistic transfers from a GTO departure location of $\lambda = \delta = 0°$ with an SEZ cone of $\alpha_{\text{SEZ}} = 1°$

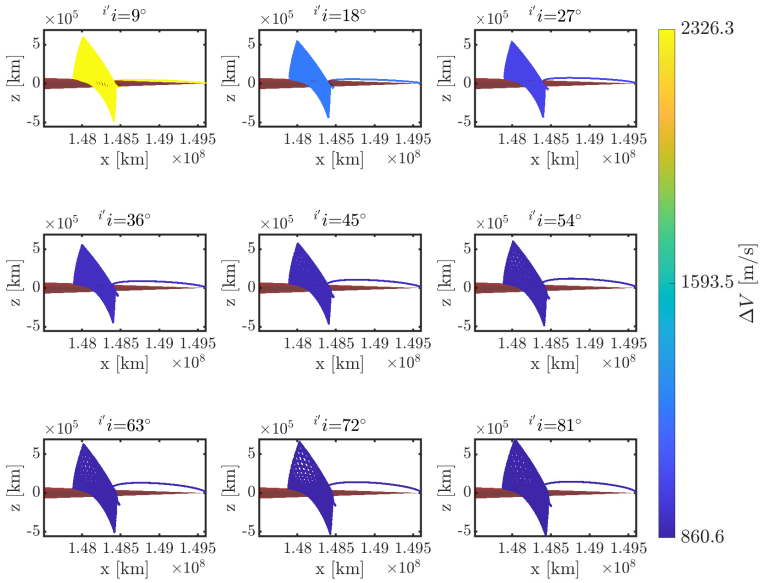

Figure 5.55. : Constrained ballistic transfers from a GTO departure location of $\lambda = \delta = 0°$ with an SEZ cone of $\alpha_{\text{SEZ}} = 2°$

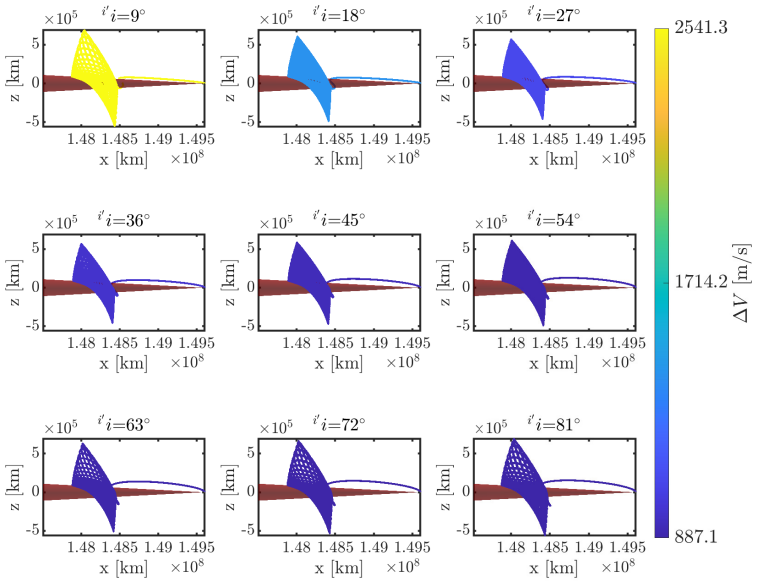

Figure 5.56. : Constrained ballistic transfers from a GTO departure location of $\lambda = \delta = 0°$ with an SEZ cone of $\alpha_{\text{SEZ}} = 3°$

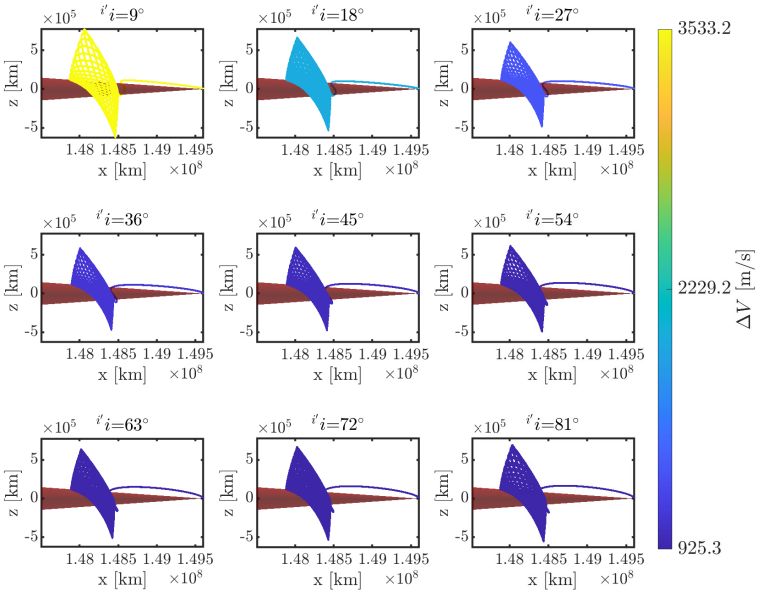

Figure 5.57. : Constrained ballistic transfers from a GTO departure location of $\lambda = \delta = 0°$ with an SEZ cone of $\alpha_{\text{SEZ}} = 4°$

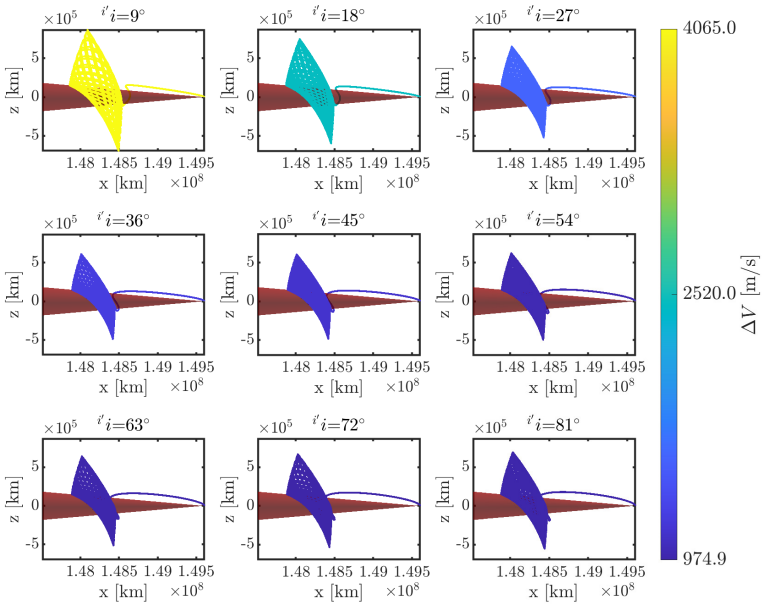

Figure 5.58. : Constrained ballistic transfers from a GTO departure location of $\lambda = \delta = 0°$ with an SEZ cone of $\alpha_{\text{SEZ}} = 5°$

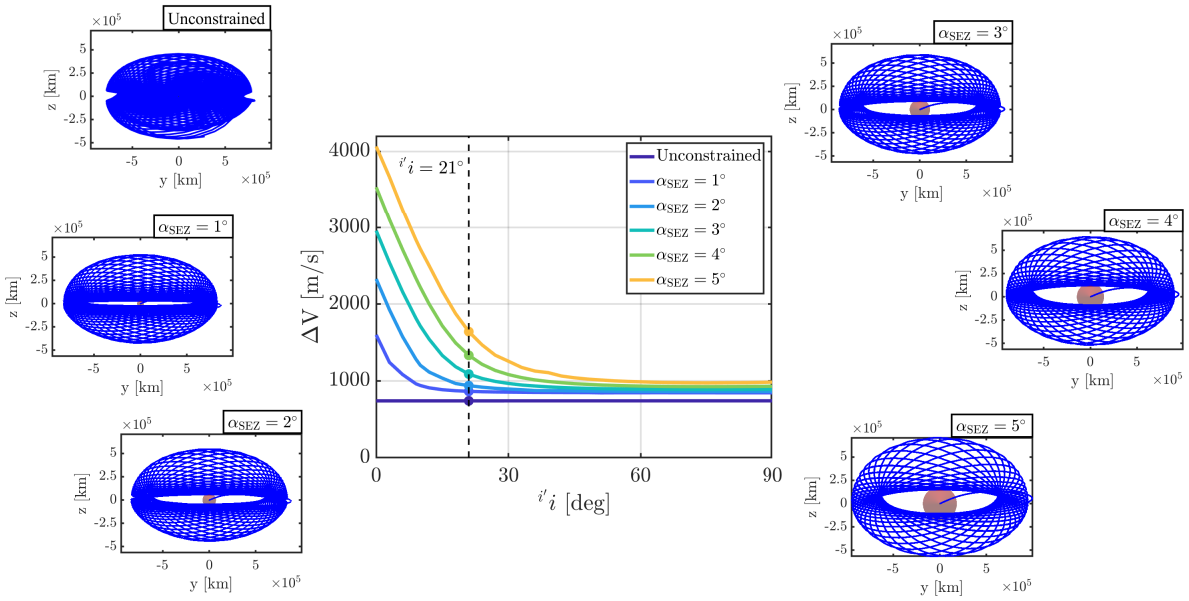

Figure 5.59. : Constrained ballistic transfer into a Sun-Earth quasi-periodic orbit considering a range of SEZ cone sizes, i.e., α_{SEZ} values. The $\hat{y}$ -$\hat{z}$ projection of ballistic transfers with an inclination, $^{i'}$i, of 20° is plotted for all SEZ cone sizes

mains outside the SEZ cone. The multiple-shooting strategy is easily adapted to investigate the SEZ constraint for ballistic transfers with GTO departure locations, i.e., location of the GTO periapsis, with $\delta \neq 0°$.

5.3.5 Path Constraint for Sun-Earth L_2 Transfers

A guide for direct constrained ballistic transfers to Sun-Earth L_2 is constructed from the unconstrained transfers to L_2 with mathematically defined Earth eclipsing conditions. Transfers and operational orbits near Sun-Earth L_2 generally avoid regions inside the Earth's shadow. The Earth's shadow, due to the Sun's light, is typically characterized by two distinct regions, the umbra and penumbra. In the Sun-Earth rotating frame, the penumbral and umbral shadow regions are labeled in Figure 5.60. In this investigation, the penumbral

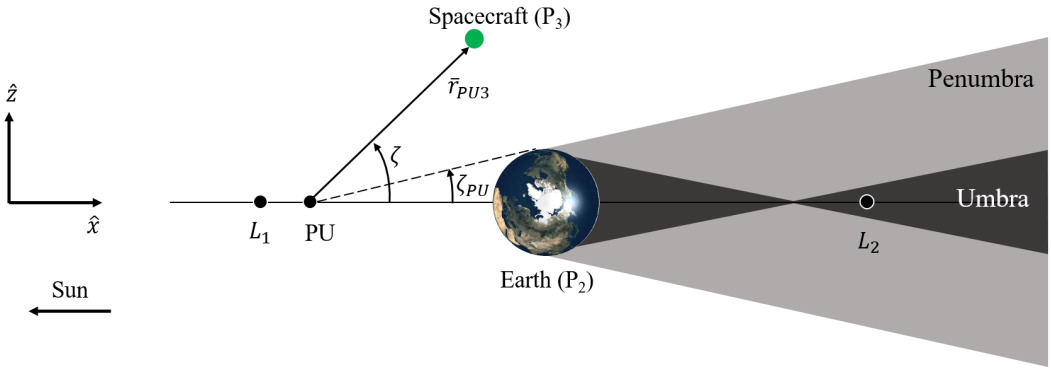

Figure 5.60. : Earth shadow cones in the rotating frame of the Sun-Earth CRTBP. The fixed angle ζ_{PU} represents the penumbral area. The vertex of the penumbral shadow cone is labeled PU

region, the larger region, is set as the constraining Earth eclipse region for the ballistic transfers to Sun-Earth L_2. The penumbral region is defined as a right circular cone, termed the shadow cone, with a vertex at the point PU, refer to Figure 5.60, and measured with a fixed shadow cone angle, ζ_{PU}. The penumbra shadow angle is measured with respect to $+\hat{x}$,

i.e., the direction from the Sun to the Earth in the Sun-Earth rotating frame. The position of the penumbral shadow cone vertex, $\bar{r}_{\mathrm{PU}}$, is defined as:

$$\bar{r}_{\mathrm{PU}} = \bar{r}_{\mathrm{e}} - l_c\hat{x}, \tag{5.72}$$

where l_c is the distance between the shadow cone vertex, PU, and the Earth and $\bar{r}_{\mathrm{e}}$ is the position of the Earth in the Sun-Earth rotating frame. In the CRTBP model, the distance between the Earth and the Sun is fixed, i.e., $l_{\mathrm{se}} = 1.496\text{x}10^8$ km. The distance l_c is dependent on the mean equatorial radius of the Earth and Sun, D_E and D_S, respectively, and is written $l_c = \frac{l_{\mathrm{se}} D_E}{D_E + D_S}$. The position of the shadow cone vertex, $\bar{r}_{PU}$, is dependent on the distance between the Earth and the Sun and remains fixed in the CRTBP model. The fixed angle, ζ_{PU}, corresponding to the penumbral shadow cone is defined as: $\zeta_{PU} = \tan^{-1}(\frac{D_E}{l_c})$. To remain outside the penumbral shadow cone, an angle ζ must remain above the fixed ζ_{PU} angle when the spacecraft is beyond the Earth and the Sun, that is when the x-component of the satellite's position vector, $\bar{r} = [x, y, z]^T$, meets the following condition: $x > 1 - \mu$. The angle ζ is then termed the shadow angle and is defined as:

$$\zeta = \cos^{-1}\left(\frac{\bar{r}_{\mathrm{PU3}} \cdot \hat{x}}{\|\bar{r}_{\mathrm{PU3}}\|}\right). \tag{5.73}$$

Note that the position of the spacecraft with respect to the penumbral shadow cone vertex, PU in Figure 5.60, is written as: $\bar{r}_{\mathrm{PU3}} = \bar{r} - \bar{r}_{\mathrm{PU}}$. The general path constraint condition from Equation (5.57) is implemented to maintain the spacecraft outside the Earth penumbral shadow cone. However, a new path function, F_p, that describes the Earth eclipsing condition is required. The Earth eclipsing condition is written as:

$$\text{Earth Eclipsing Condition:} \quad F_{\mathrm{p,PU}} = \mathrm{H}\left(\bar{r}_{23}\left(\bar{\mathcal{X}}_{\mathrm{j}}(t)\right) \cdot \hat{x}\right) \sin\left(\zeta\left(\bar{\mathcal{X}}_{\mathrm{j}}(t)\right) - \zeta_{\mathrm{PU}}\right), \tag{5.74}$$

where the shadow angle, ζ, and the position of the satellite with respect to the Earth, $\bar{r}_{23}$, is a function of the satellite state, $\bar{\mathcal{X}}_{\mathrm{j}}$, at a time along the trajectory, t, and, recall that, the penumbral shadow angle, ζ_{PU}, is a constant value. The heaviside function, $\mathrm{H}(\bar{r}_{23} \cdot \hat{x})$, in Equation (5.74) describes the positional condition for the spacecraft previously defined as:

$x > 1 - \mu$, where x is the x-component of the satellite position vector. Note that the Earth eclipsing conditions in Equations (5.72)-(5.74) are defined in the Sun-Earth rotating frame. To construct an eclipse constrained ballistic transfer to Sun-Earth L_2, the scalar eclipse and altitude path constraints are appended to the constraint vector in Equation (5.42), that is,

$$\bar{F}_{\text{con}} = \begin{bmatrix} \bar{F} \\ F_{\text{path,PU}} \\ F_{\text{path,alt}} \end{bmatrix}, \tag{5.75}$$

where,

$$F_{\text{path,PU}} = \sum_{\text{j}}^{N} \int_{0}^{T_{\text{j}}} F_{\text{p,PU}}^{2}\left(\bar{\mathcal{X}}_{\text{j}}(t)\right) - \left|F_{\text{p,PU}}\left(\bar{\mathcal{X}}_{\text{j}}(t)\right)\right| F_{\text{p,PU}}\left(\bar{\mathcal{X}}_{\text{j}}(t)\right) dt, \tag{5.76}$$

$$F_{\text{path,alt}} = \sum_{\text{j}}^{N} \int_{0}^{T_{\text{j}}} F_{\text{p,alt}}^{2}\left(\bar{\mathcal{X}}_{\text{j}}(t)\right) - \left|F_{\text{p,alt}}\left(\bar{\mathcal{X}}_{\text{j}}(t)\right)\right| F_{\text{p,alt}}\left(\bar{\mathcal{X}}_{\text{j}}(t)\right) dt, \tag{5.77}$$

with $F_{\text{p,alt}}$ and $F_{\text{p,PU}}$ defined in Equations (5.59) and (5.74). Equation (5.74) is expanded to,

$$F_{\text{p,PU}} = \text{H}\left(\bar{r}_{23}\left(\bar{\mathcal{X}}_{\text{j}}(t)\right) \cdot \hat{x}\right)\left(\sin\left(\zeta(t)\right)\cos\left(\zeta_{\text{PU}}\right) - \cos\left(\zeta(t)\right)\sin\left(\zeta_{\text{PU}}\right)\right), \tag{5.78}$$

where the sine and cosine values of the shadow angle, ζ, are defined as,

$$\cos\left(\zeta(t)\right) = \frac{\bar{r}_{\text{PU3}}^{T}(t)\ (\hat{x})}{\|\bar{r}_{\text{PU3}}(t)\|}, \tag{5.79}$$

$$\sin\left(\zeta(t)\right) = \sqrt{1 - \cos^{2}\left(\zeta\right)}, \tag{5.80}$$

where $[^T]$ is the matrix transpose. The partial derivatives associated with the eclipse constraint function, i.e., $F_{\text{p,PU}}$ in Equation (5.78), with respect to the transfer state, $\bar{\mathcal{X}}(t)$, is defined as,

$$\begin{aligned}\frac{\partial F_{\text{p,PU}}}{\partial \bar{\mathcal{X}}(t)} = \text{H}\left(\bar{r}_{23}^T\hat{x}\right)\left(\frac{\partial \sin(\zeta)}{\partial \bar{\mathcal{X}}(t)}\cos\left(\zeta_{\text{PU}}\right) - \frac{\partial \cos(\zeta)}{\partial \bar{\mathcal{X}}(t)}\sin\left(\zeta_{\text{PU}}\right)\right)+ \\ \frac{\partial \text{H}\left(\bar{r}_{23}^T\hat{x}\right)}{\partial \bar{\mathcal{X}}(t)}\Big(\sin\left(\zeta(t)\right)\cos\left(\zeta_{\text{PU}}\right) - \cos\left(\zeta(t)\right)\sin\left(\zeta_{\text{PU}}\right)\Big),\end{aligned} \tag{5.81}$$

where the partial derivatives of the sine, cosine, and heaviside functions with respect to the state, $\bar{\mathcal{X}}(t)$, are defined as,

$$\frac{\partial \cos(\zeta)}{\partial \bar{\mathcal{X}}(t)} = \left(\frac{\hat{x}^T}{\|\bar{r}_{\text{PU3}}(t)\|} - \frac{\left(\bar{r}_{\text{PU3}}^T(t)\hat{x}\right)\bar{r}_{\text{PU3}}^T(t)}{\|\bar{r}_{\text{PU3}}(t)\|^3}\right)\begin{bmatrix}\mathbf{I}_{3,3} & \mathbf{0}_{3,3}\end{bmatrix}, \tag{5.82}$$

$$\frac{\partial \sin(\zeta)}{\partial \bar{\mathcal{X}}(t)} = \frac{-\cos\left(\zeta(t)\right)}{\sin\left(\zeta(t)\right)}\frac{\partial \cos\left(\zeta(t)\right)}{\partial \bar{\mathcal{X}}(t)}, \tag{5.83}$$

$$\frac{\partial \text{H}\left(\bar{r}_{23}^T\hat{x}\right)}{\partial \bar{\mathcal{X}}(t)} = f_\delta\left(\bar{r}_{23}^T\hat{x}\right)\hat{x}^T\begin{bmatrix}\mathbf{I}_{3,3} & \mathbf{0}_{3,3}\end{bmatrix}, \tag{5.84}$$

where $\bar{r}_{23}$ is the distance of the satellite measured from the Earth, i.e., $\bar{r}_{23} = \bar{r} - \bar{r}_{\text{e}}$ and, it is recalled that, all vectors are column vectors. Additionally, the dirac-delta function in Equation (5.84) is defined as:

$$f_\delta(x) = \begin{cases}\infty, & \text{if } x = 0 \\ 0, & x \neq 0\end{cases}, \tag{5.85}$$

In Equation (5.83), the value of the partial derivative is undefined when a transfer state, $\bar{\mathcal{X}}$, lies on the $\hat{x}$ axis of the Sun-Earth rotating frame, i.e., $\sin(\zeta) = 0$. However, Equations (5.81)-(5.84) form the integrand that is input into Equation (5.66), and any undefined integrand value is omitted in the numerical integration process without significant loss of accuracy. Constrained ballistic transfers to Sun-Earth L_2 are now constructed by including the scalar path constraints for the Earth eclipse conditions.

5.3.6 Constrained Transfers into Orbits near L_2

A collection of constrained ballistic transfers to Sun-Earth L_2 is constructed by implementing the path constraint and eclipsing conditions from Equations (5.57) and (5.74). Recall that ballistic transfers to L_2 depart from a GTO periapsis altitude of 185 km and require a single maneuver at GTO periapsis to shift onto the transfer arc and the Earth eclipse condition is based on the size of the penumbral shadow cone. In this investigation, the objective is to construct direct constrained ballistic transfers to Sun-Earth L_2 which, from Figure 5.34, are contained in a range of $150^\circ \leq \lambda \leq 290^\circ$. The ballistic transfers from Figure 5.34 are collected as the initial guesses into a corrections algorithm that implements the penumbral eclipsing condition. Additionally, the ΔV required for the single maneuver ballistic transfer is decreased in a pseudo-optimization process via natural parameter continuation with a maximum ΔV magnitude. The natural parameter process is performed by including the inequality constraint in Equation (5.44) during the corrections process. A comparison between the unconstrained and the eclipse constrained transfers is plotted via two distinct surfaces in Figure 5.61. The surface in magenta, i.e., corresponding to constrained transfers, in Figure 5.61 depicts the increasing ΔV requirements as the inclination, ${}^{i'}i$, of the GTO departure state is decreased. At higher inclinations, ${}^{i'}i > 20^\circ$, the ΔV requirements of the constrained transfers approach a constant value, that is, the same ΔV magnitude is required at higher inclinations. Additionally, Figure 5.62 presents the ΔV requirements of unconstrained and constrained ballistic transfers to L_2 at a GTO departure location corresponding to $\lambda = \delta = 0^\circ$. The geometry of an unconstrained and constrained ballistic transfer with ${}^{i'}i = 20^\circ$ is plotted in Figure 5.62. The unconstrained ballistic transfer approaches a large L_2 Lissajous orbit that crosses into the penumbral cone, illustrated as a dark shaded region in Figure 5.62, while the constrained ballistic transfer remains outside the shadow region in a large quasi-halo orbit. The constrained ballistic transfers presented in Figures 5.61-5.62 includes more than 30 revolutions around the quasi-periodic orbit to verify that a trajectory never crosses into the penumbral shadow region. The direct ballistic transfer guides for L_1 and L_2 provide preliminary transfer information from a fixed GTO periapsis

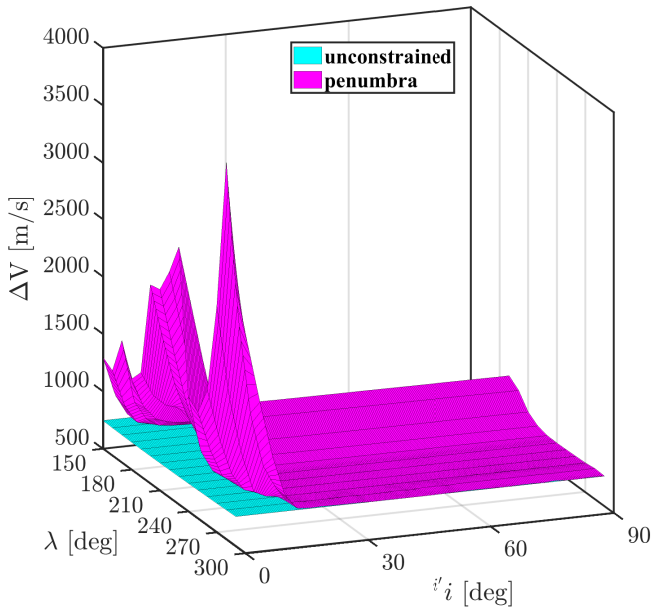

Figure 5.61. : Surfaces of unconstrained and constrained ballistic transfers into Sun-Earth L_2

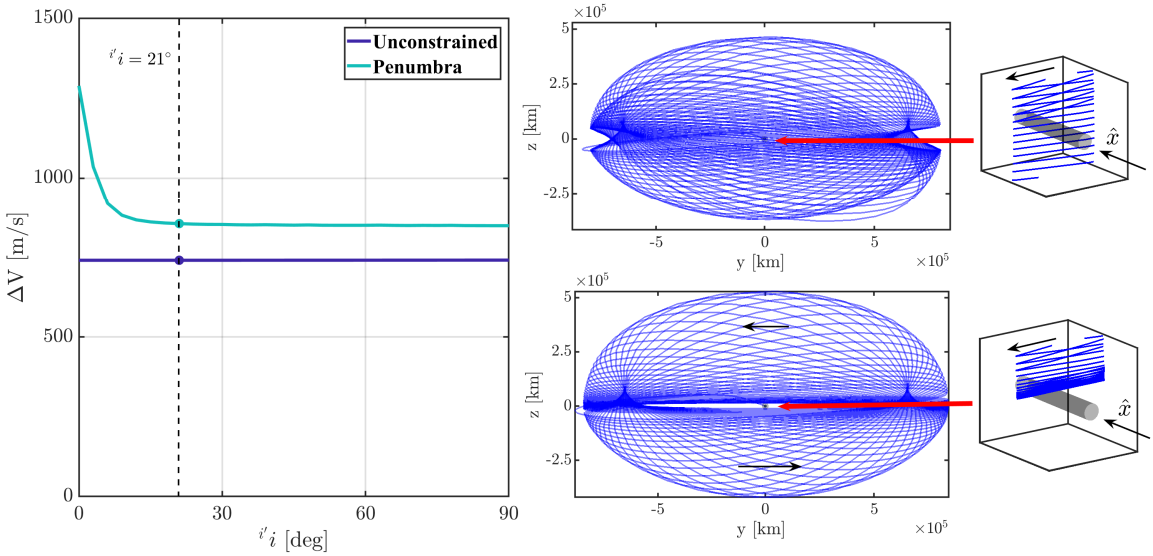

Figure 5.62. : Constrained ballistic transfers to Sun-Earth L_2 at a GTO departure location of $\lambda = 180°$. The geometry of an unconstrained and constrained ballistic transfer with $^{i'}i = 20°$ is presented

altitude. Ballistic transfers only require a single maneuver from GTO and leverage the natu-

ral dynamics of the Sun-Earth system to enter a quasi-periodic orbit. These transfers do not require any additional deterministic maneuvers, within the context of the CRTBP model, and are straightforwardly transitioned to a higher fidelity model.

5.3.7 Trajectory Injection Points into Sun-Earth Orbits

Injection points along direct ballistic transfers toward Sun-Earth L_1 and L_2 quasi-periodic orbits are summarized for the unconstrained and constrained scenarios. Identifying a point of injection into a quasi-periodic orbit is advantageous for targeting desired transfers and operational orbits. The injection points are key to ensure arrival occurs on expanding revolutions away from constraints. However, identifying an injection point, i.e., an entry point into a quasi-periodic orbit, presents challenges. One challenge is the absence of a variable with the dynamical flow information about the quasi-periodic motion, or more simply, a variable informing the injection location along a quasi-periodic orbit or on a transfer. In this investigation, the injection point onto a quasi-periodic orbit is defined to be on the $\hat{y}$ plane, which is consistent with previous mission design strategies for Sun-Earth L_1 orbiters [37]. Additionally, this definition also establishes a targeting condition, on the $\hat{y}$ plane, that can be leveraged when an initial solution in the CRTBP model is transitioned to a higher-fidelity model. The injection points for the unconstrained ballistic transfers into Sun-Earth L_1 and L_2 quasi-periodic orbits, from Figures 5.31 and 5.34, are plotted in Figures 5.63-5.64. Note that the injection points in Figures 5.63-5.64 are displayed in a x_E vs z plot, where

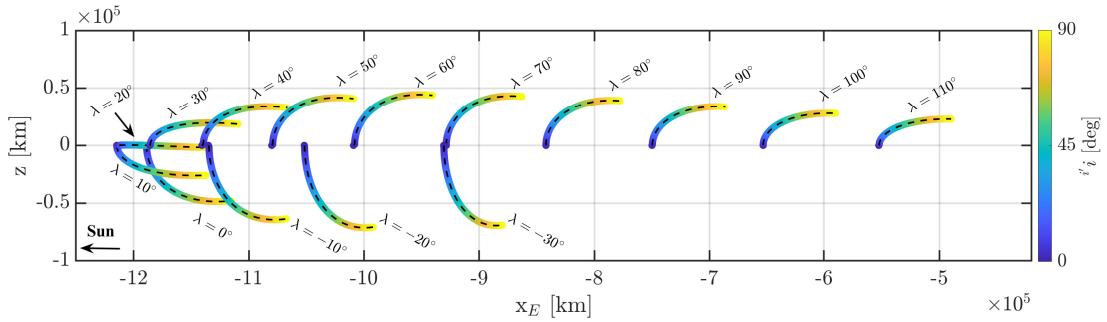

Figure 5.63. : Injection points for unconstrained direct ballistic transfer to Sun-Earth L_1

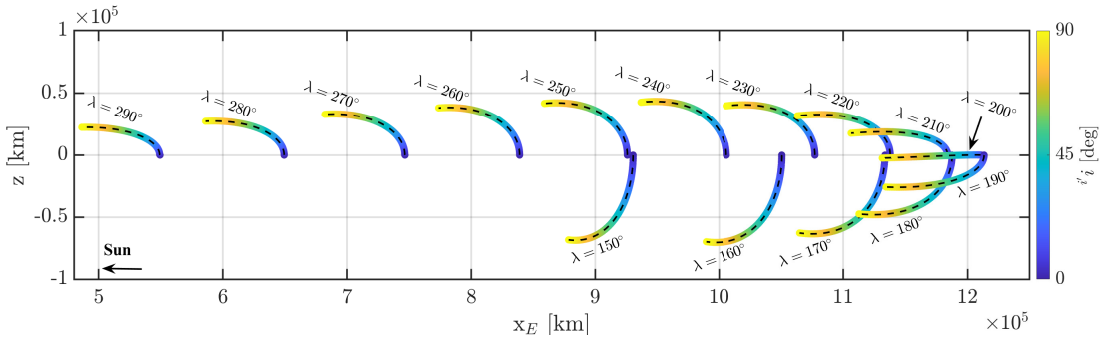

Figure 5.64. : Injection points for unconstrained direct ballistic transfer to Sun-Earth L_2

x_E is the distance measured from the Earth in the Sun-Earth rotating frame. Each injection point curve in Figures 5.63-5.64 represents a set of ballistic transfers from a single GTO periapsis location near-Earth, from a longitude angle λ in Figure 4.5(b), at a range of inclination values, given via a range of colors. Note that the injection points for a GTO at low inclinations occur near the $\hat{x}$-$\hat{y}$ plane, i.e., the Sun-Earth ecliptic. Additionally, the ballistic transfers from a GTO with ${}^{i'}i = 0°$ correspond to transfers into Lyapunov orbits, as observed in Figures 5.4 and 5.9. The injection points corresponding to direct ballistic transfers to the Sun-Earth L_1 and L_2 vicinities are located between the Earth and the Lagrange points L_1 and L_2, respectively.

The injections points for constrained direct ballistic transfers to Sun-Earth L_1 and L_2 quasi-periodic orbits are displayed in Figures 5.65-5.70. Recall that constrained ballistic transfers to L_1 orbits must remain outside the Solar Exclusion Zone, as defined in Figure 5.52, while constrained transfers to L_2 must avoid any Earth eclipsing conditions, i.e., the penumbral shadow cone in Figure 5.60. In Figures 5.65-5.69, the Solar Exclusion Zone is shaded red and all ballistic transfer injection points are outside this region. Each injection point curve in Figures 5.65-5.69 is a set of ballistic transfers at a location λ over a range of inclinations. Note that the injection points for the direct ballistic transfers are separated into groups corresponding to southern and northern quasi-halo orbits for different range of λ. Constrained ballistic transfers to the L_1 vicinity in a range $20° < \lambda < 110°$ enter a southern quasi-halo orbit while a range of $-30° < \lambda < 10°$ corresponds to northern quasi-halos. Ballistic transfers to the L_2 vicinity, see Figure 5.70, are separated into two groups of

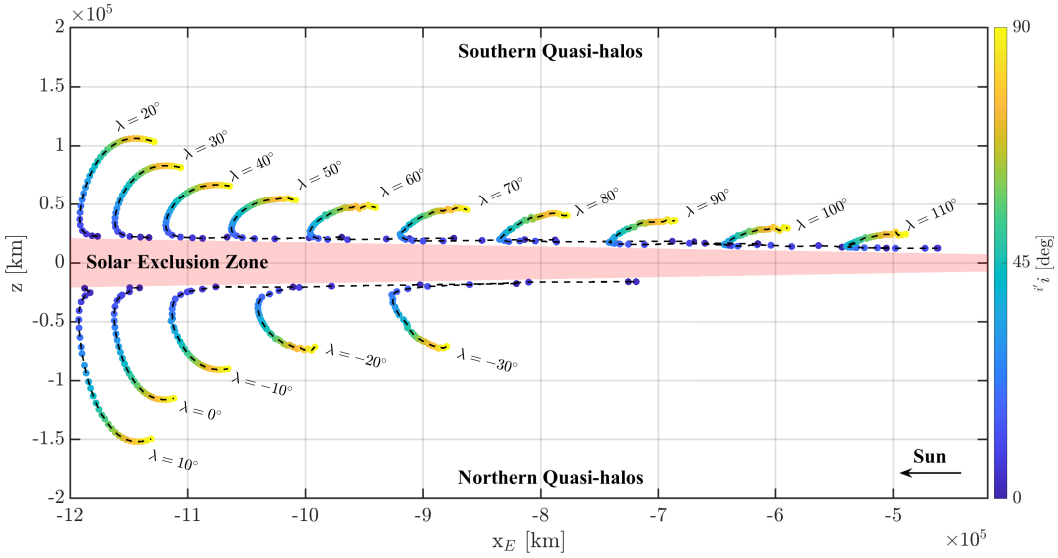

Figure 5.65. : Injection points for constrained direct ballistic transfer to Sun-Earth L_1 with $\alpha_{\text{SEZ}} = 1°$

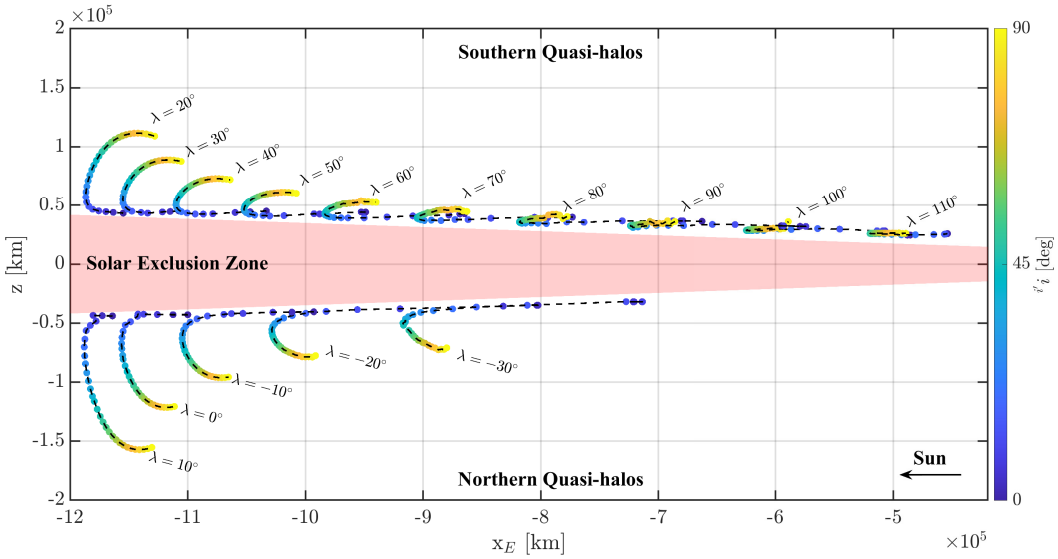

Figure 5.66. : Injection points for constrained direct ballistic transfer to Sun-Earth L_1 with $\alpha_{\text{SEZ}} = 2°$

injection point curves. The L_2 southern quasi-halo group over a range of $200° < \lambda < 290°$ and the L_2 northern quasi-halo group correspond to $150° < \lambda < 190°$. The L_1 quasi-periodic orbit for a constrained direct ballistic transfer can be a southern or northern quasi-halo orbit, that is, a constrained transfer from a GTO periapsis at a near-Earth location λ with inclination

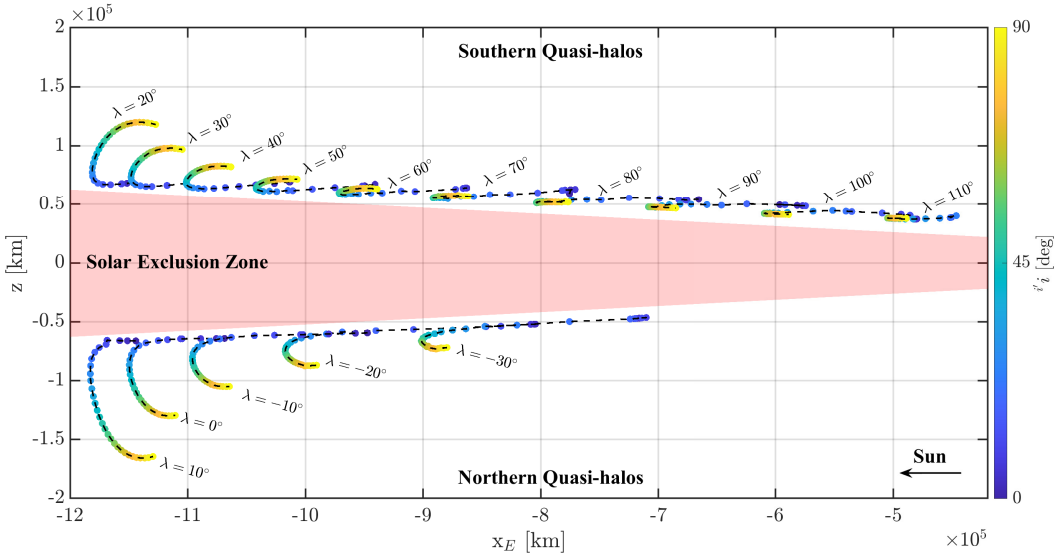

Figure 5.67. : Injection points for constrained direct ballistic transfer to Sun-Earth L_1 with $\alpha_{SEZ} = 3°$

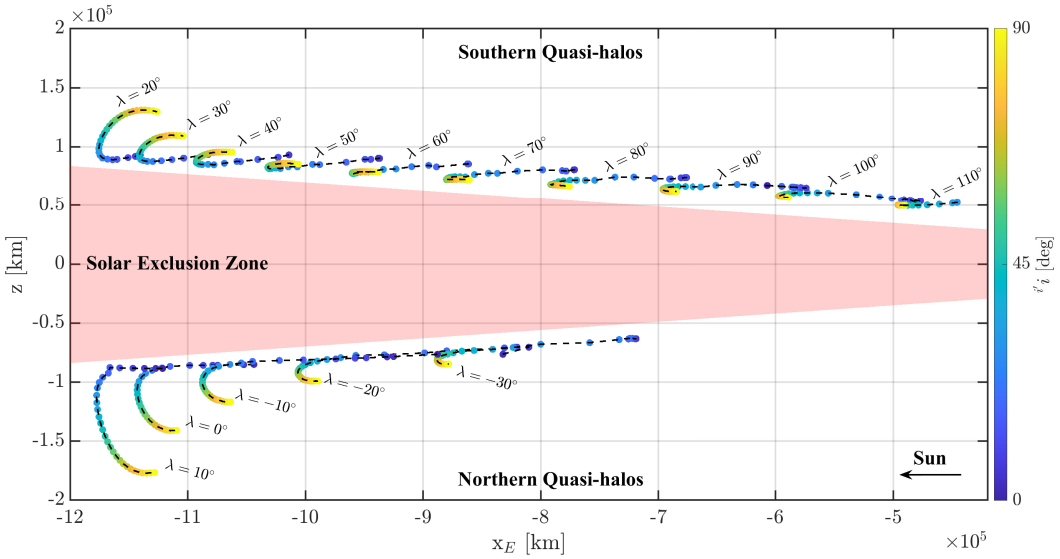

Figure 5.68. : Injection points for constrained direct ballistic transfer to Sun-Earth L_1 with $\alpha_{SEZ} = 4°$

$^{i'}$i can enter both types of quasi-halo orbits. In this investigation, the L_1 quasi-halo orbits for the constrained ballistic transfers, displayed in Figure 5.53, correspond to the most efficient ballistic transfer, i.e., the transfer with the lowest ΔV magnitude. Recall that all ballistic transfers require a single maneuver from GTO periapsis, which, in this investigation, is at

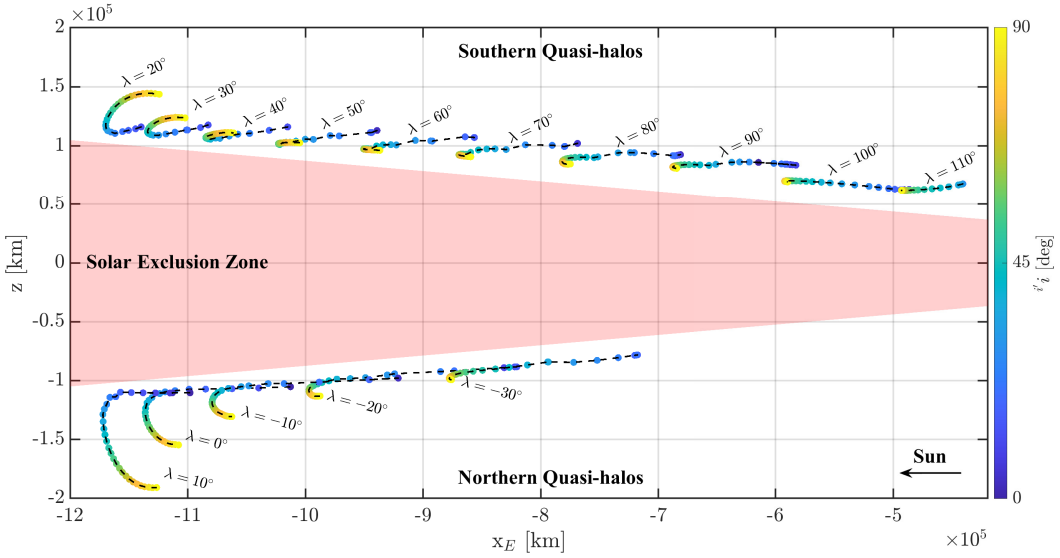

Figure 5.69. : Injection points for constrained direct ballistic transfer to Sun-Earth L_1 with $\alpha_{SEZ} = 5°$

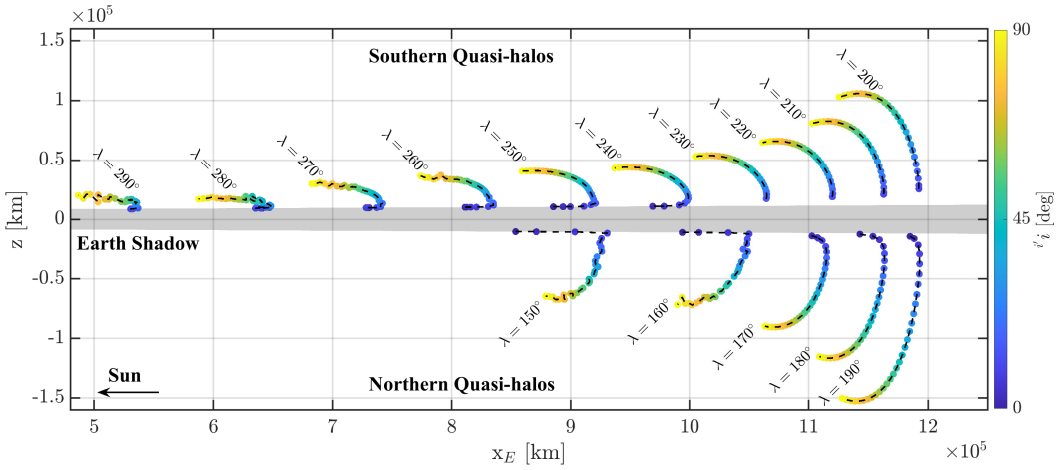

Figure 5.70. : Injection points for constrained direct ballistic transfer to Sun-Earth L_2 with penumbral Earth eclipsing condition

a 185 km altitude. Constrained ballistic transfers to the L_2 vicinity may also enter either a southern or northern quasi-halo orbit, but the most efficient transfer appears in Figures 5.61 and 5.70. The definition of the injection points in Figures 5.63-5.70 is not based on any dynamical flow information along the transfer but rather on previous mission design implementations. The geometry of the injection points from ballistic transfers to the L_1 and

L_2 regions are insightful for targeting quasi-periodic orbits near these Sun-Earth Lagrange points.

5.3.8 Altitude Study of Unconstrained Transfers to Orbits near L_1 and L_2

The construction of ballistic transfers from a range of GTO departure altitudes reveals insightful ΔV information necessary for preliminary mission design. The ΔV and amplitude information plotted in Figures 5.31 and 5.34 corresponds to a GTO departure altitude of 185 km, i.e., the baseline altitude; note that, in this investigation, the satellite departs the GTO at periapsis. Recall that the GTO size is determined via the periapsis altitude as the apoapsis altitude is the GEO altitude, i.e., $35,786$ km, and that, for a secondary payload, the GTO size is dependent on the launch vehicle performance, see to the mission scenario in Figure 4.1. In the construction of ballistic transfers from a range of GTO departure altitudes, the ΔV information reveals a possible range for the single maneuver ballistic transfers from different departure locations, i.e., λ, along the near-Earth vicinity. The required ΔV magnitudes for ballistic transfers towards Sun-Earth L_1 from locations corresponding to $\lambda = \{-20^\circ, 0^\circ, 20^\circ\}$ are plotted in Figure 5.71. The ballistic transfers in Figure 5.71 are all direct unconstrained transfers from prograde GTOs, i.e., ${}^{i'}i < 90^\circ$. The analysis reveals an increase in the required ΔV for all constrained transfers as the GTO departure altitude is increased from 185 km to 2000 km. Additionally, with a constant GTO departure location, the ΔV variation is less than 5 m/s as the inclination of the departure GTO is increased. The ΔV requirements for unconstrained transfers to Sun-Earth L_2 are plotted in Figure 5.72. The ballistic transfers to L_2 correspond to GTO departure locations of $\lambda = \{160^\circ, 180^\circ, -160^\circ\}$; note that these are unconstrained transfers, i.e., no eclipse constraints are included along the trajectory. The ΔV exposed in the departure altitude analysis for L_2 transfers exhibits the same behavior as the analysis revealed in Figure 5.71. Although only unconstrained transfers are constructed in this analysis, the ΔV patterns observed in Figures 5.71-5.72 is extended to different GTO departure locations, i.e., λ values. Note that the observations revealed in this analysis is only applicable for GTO departure locations along the ecliptic, i.e., the $\hat{x}$ -$\hat{y}$. An additional

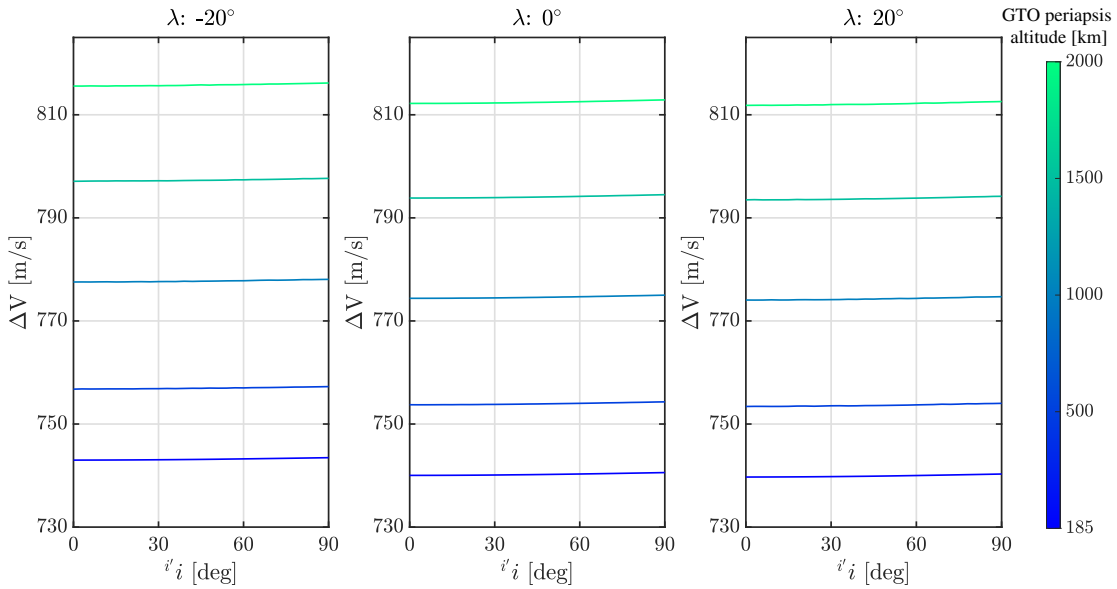

Figure 5.71. : ΔV information for unconstrained ballistic transfers to Sun-Earth L_1 from a range of GTO departure locations

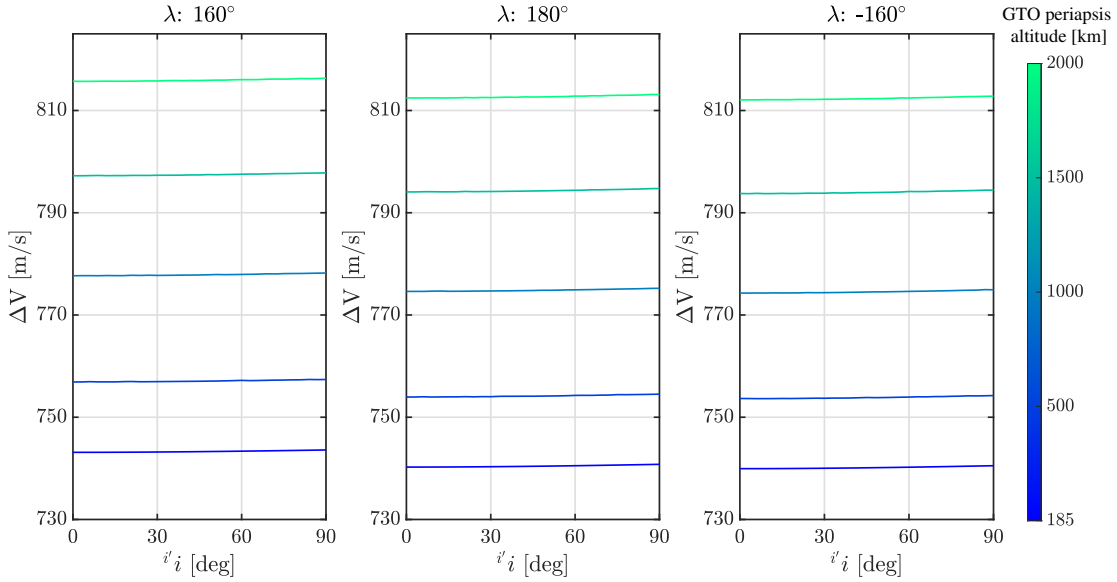

Figure 5.72. : ΔV information for unconstrained ballistic transfers to Sun-Earth L_2 from a range of GTO departure locations

analysis exploring ballistic transfers from a range of GTO departure altitudes with a location such that $\delta \neq 0°$, refer to Figure 4.5(b), will provide a global understanding of the necessary ΔV.

5.3.9 Ballistic Transfers in the Ephemeris Model

Ballistic transfers constructed in the CRTBP model are directly transitioned into a higher-fidelity ephemeris model. In the preceding sections, ballistic transfers to orbits near the Sun-Earth L_1 and L_2 points are constructed in the rotating frame of the CRTBP model. The CRTBP model serves as an adequate Three-Body appoximation of the Sun-Earth-satellite system and the existing dynamical structures in the model are leveraged to construct single maneuver ballistic transfers. Additionally, the ballistic transfers generated in the CRTBP model serve as initial guesses to identify feasible trajectories in the higher-fidelity ephemeris model. The ephemeris model implemented in this investigation includes the Sun, Earth, and Moon as primary bodies; no atmospheric or solar radiation pressure effects are included in representation of the flow. To propagate a satellite state in the ephemeris model, the Equations of Motion relative to the Earth, i.e., Equation (2.2), are implemented; note that the Sun and the Moon are the perturbing bodies. The approximate states of the perturbing bodies are retrieved from the DE430 ephemeris file available from the Jet Propulsion Laboratory. A ballistic transfer in the ephemeris model is generated via a multiple-shooting scheme and solved with a multidimensional Newton's algorithm. The free-variable and constraint vectors consistent with the multiple-shooting strategy in the ephemeris model is provided in Appendix E. Whereas the CRTBP is a time-invariant system, trajectories found in the ephemeris model are epoch-dependent. In this analysis, the objective is to observe if the geometries of the ballistic transfers constructed in the CRTBP are maintained in the higher-fidelity model. As a demonstration, a ballistic transfer corresponding to a GTO departure location of $\lambda = \delta = 0^\circ$ with an associated inclination of ${}^{i'}i = 27^\circ$ is transitioned into the inertial EME frame with an epoch of April 1, 2022 12:00:00.000. Recall that the ballistic transfer is defined as a series of nodes, consistent with a multiple-shooting algorithm, which are subsequently converted from the rotating frame into the inertial EME frame via the steps outlined in Section 2.3.2.1. The nodes are corrected via a multidimensional Newton's method with the constraint condition in Equation (E.2) with an included single maneuver at the GTO departure state, i.e, $\bar{\mathcal{X}}_{i_0}$ in Figure E.1. Once

a feasible transfer is corrected in the ephemeris model, a pseudo-optimization process that lowers the ΔV is implemented by using natural parameter continuation with a maximum ΔV, i.e., $\Delta V_{\max}$. The optimized transfer for this example is plotted in Figure 5.73. The SEZ

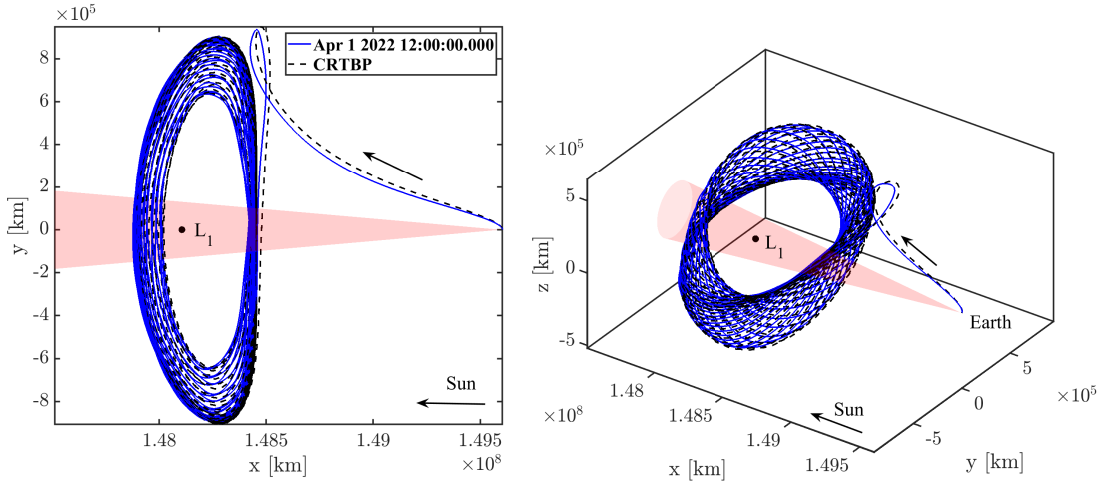

Figure 5.73. : Ballistic transfer in the ephemeris model, in blue, and the initial CRTBP model, in black. Note that the geometry is maintained in the higher fidelity ephemeris model

cone constraint, defined as $\alpha_{\text{SEZ}} = 5°$, is applied throughout the trajectory. For the initial epoch of April 1, 2022 12:00:00.000, the ballistic transfer in the ephemeris model, represented in blue in Figure 5.73, maintains a similar geometry as the initial CRTBP transfer, in black. However, the required ΔV for the ephemeris transfer is $\Delta V = 1744$ m/s compared to the CRBTP ΔV of 1334 m/s. The ephemeris corrections process is applied along different epoch throughout the year of 2022 and the ΔV information is plotted in Figure 5.74. From Figure 5.74, the ballistic transfer associated with April 1$^{\text{st}}$ has the highest corresponding ΔV, while the transfer with an epoch of October 1$^{\text{st}}$ has the lowest ΔV. Observe that the behavior of the ΔV is similar to a sine wave and the single maneuver magnitude associated with the CRTBP ballistic transfer, the red line in Figure 5.74, is an approximate average. Additionally, the transfers constructed for this range of epochs in 2022 have similar geometric features as the CRTBP transfer and remain outside the SEZ cone constraint. In this analysis, only direct transfers are considered, i.e., no Earth flybys are included along the trajectory. The

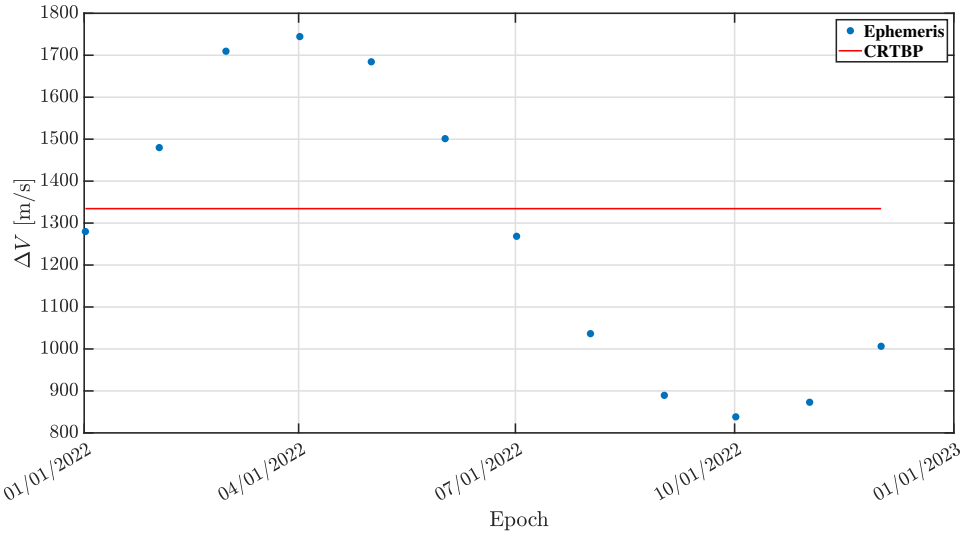

Figure 5.74. : ΔV required for optimized transfers over a range of initial epochs in the ephemeris model for a ballistic transfer to Sun-Earth L_1 . The ballistic transfer corresponds to a GTO departure state of $\lambda = \delta = 0°$ with an inclination of ${}^{i'}i = 27°$

addition of Earth or Lunar flybys introduces additional numerical challenges and may alter the geometry of the ballistic transfer.

5.4 Summary of Ballistic Transfers

In this chapter, ballistic transfers are constructed to orbits near the Sun-Earth L_1 and L_2 Lagrange points over a range of GTO departure locations. Ballistic transfers are defined as single maneuver transfers and are considered the most maneuver efficient type of transfers, that is, theoretically, the trajectories leverage the natural dynamics of the CRTBP system. In the ridesharing scenario considered for this investigation, a secondary payload is dropped off in a GTO with an unspecified orientation. Assuming that the secondary payload departs the GTO at periapsis, as such, the location of the GTO periapsis, i.e., which also corresponds to the GTO orientation, is labeled the GTO departure location. First, stable manifolds associated with periodic and quasi-periodic orbits near the Sun-Earth Lagrange points are leveraged in the construction of ballistic transfers over a range of GTO departure locations. The collection of ballistic transfer to periodic and quasi-periodic orbits exposed

the GTO departure regions that correspond to direct and indirect, i.e., the transfer includes an outbound excursion or an Earth flyby, transfers. A guide of direct transfers is created for constrained and unconstrained ballistic transfers to Sun-Earth L_1 and L_2 points. Finally, the persistence of the ballistic transfer geometry observed in Sun-Earth L_1 is confirmed in the ephemeris model over a range of GTO departure epochs. In this analysis, the quasi-periodic orbit associated with the ballistic transfer was unconstrained, that is, a specific quasi-periodic orbit is not targeted in the differential corrections process. The objective is to generate ballistic transfers from different GTO departure locations with an optimal ΔV. The collection of ballistic transfers offered in this investigation provides approximate ΔV magnitudes and quasi-periodic orbit sizes, i.e., amplitudes, that aids in identifying efficient preliminary mission design trajectories for secondary payloads.

6. MULTIPLE MANEUVER TRANSFERS IN THE SUN-EARTH SYSTEM

Transfers leveraging the trajectories along the surface of the stable manifold corresponding to periodic and quasi-periodic orbits and incorporating a single deep space maneuver (DSM) offer advantageous options over a range of GTO departure positions near the Earth. An ideal transfer scenario from GTO includes a single maneuver en route to a destination orbit near a Lagrange point. However, flow in a multi-body system is complex and multiple maneuvers are often necessary to construct efficient pathways into specific orbits near a Lagrange point. In this investigation, the specified orbits are periodic and quasi-periodic orbits near the Sun-Earth collinear Lagrange points, i.e., L_1 and L_2. Trajectories within the hyperbolic stable manifolds associated with the specified orbits are leveraged to generate transfers that asymptotically approach a destination orbit. Additionally, a bridging trajectory arc connects a GTO departure state to a stable manifold trajectory. Transfers are designed for the secondary payload transfer scenario illustrated in Figure 4.1; recalling that there is no a priori information for the GTO departure state. Optimized multiple maneuver transfers from GTO to selected periodic and quasi-periodic orbits in the CRTBP model and ephemeris model are generated through a multiple-shooting algorithm.

6.1 Formulation of Two-Maneuver Transfers

Transfers incorporating a single Deep Space Maneuver are constructed with trajectories within the stable manifolds corresponding to orbits near the Sun-Earth Lagrange points and a connecting trajectory arc. The addition of a mid-course maneuver is either for trajectory corrections, i.e., correct for any deviations due to propulsion efficiency, or to change certain orbital elements of a transfer orbit. For example, the transfer for the DSCVR mission included two mid-course correction maneuvers as well as an orbit insertion maneuver to enter a Sun-Earth L_1 Lissajous orbit. Additionally, a mid-course maneuver may also help decrease the overall ΔV required for the transfer. In this investigation, the mid-course maneuver is a

DSM used to connect a trajectory from a GTO departure state near the Earth to a trajectory along the surface of a stable manifold structure that corresponds to a specified orbit, thereby creating a two-maneuver transfer. The two-maneuver transfer consists of a Transfer Injection Maneuver (TIM) and a DSM. Figure 6.1 illustrates a transfer into a periodic orbit near the Sun-Earth L_1 point with a stable manifold trajectory arc, plotted in cyan, and a bridging arc, plotted in black. The transfer arcs in Figure 6.1 are propagated in reverse time,

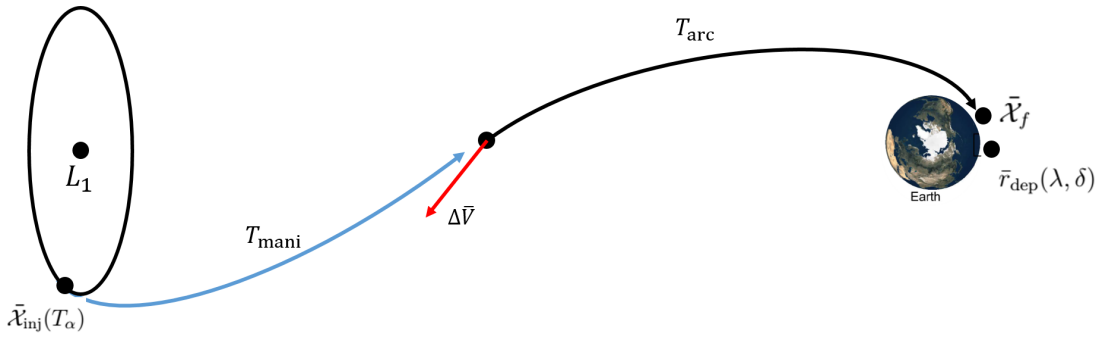

Figure 6.1. : Transfer with single Deep Space Maneuver into a general periodic orbit. Transfer arcs are propagated in reverse time

that is, the motion of the satellite is from an arrival location on the periodic orbit, i.e., an injection point, to the departure position at the GTO periapsis near Earth. Note that the injection point, $\bar{\mathcal{X}}_{\text{inj}}$, into a periodic orbit can be parameterized by the time variable: T_α. For transfers into quasi-periodic orbits, that is, orbits constructed from a two-dimensional torus, the injection point, $\bar{\mathcal{X}}_{\text{inj}}$, is parameterized by two components: T_{θ_1} and θ_2, where T_{θ_1} is a time along the orbit, analogous to the longitudinal time along the torus, and θ_2 is a location along the invariant curve, recall Figure 3.11. Two options for the DSM, the vector $\Delta\bar{V}$ in Figure 6.1, are explored in this analysis: a tangent maneuver and a general maneuver, both impulsive. Recalling that in Figure 6.1, the satellite is propagated in reverse time, the DSM is an impulsive maneuver implemented at the end of the bridging arc and the initiation of the stable manifold arc. For a tangent burn DSM, the maneuver is assumed to be directed along the velocity vector at the final state along the bridging arc and can, therefore, be defined via the scalar magnitude, ΔV_{tan}. A transfer with a general impulsive DSM possesses maneuver components defined as: $\Delta\bar{V}_{\text{gen}} = [\Delta V_x, \Delta V_y, \Delta V_z]^T$, and are also introduced at the end of the bridging arc. Observe that a state along a manifold structure, either stable or

unstable, associated with a periodic and quasi-periodic orbit can be parameterized by two and three variables, respectively. Recall that a state in the CRTBP model is defined as a six-dimensional vector. For periodic orbits, an injection point, $\bar{\mathcal{X}}_{\text{inj}}$, is evaluated by propagating an initial state, $\bar{\mathcal{X}}_0$, on the orbit by time T_α. From the periodic orbit injection point, a state on the stable manifold is constructed, via Equation (3.70), and the state is propagated in reverse time, T_{mani}. In this process, the initial state on the orbit, $\bar{\mathcal{X}}_0$, is fixed and it is assumed that a state along the global representation of the stable manifold surface can be approximated. Only two variables, T_α and T_{mani}, are required to locate a state on the stable manifold structure associated with a periodic orbit and, additionally, two variables are also necessary to parameterize states along the unstable manifold structure. For quasi-periodic orbits, an injection point, $\bar{\mathcal{X}}_{\text{inj}}$, is computed by propagating a state along the invariance curve, $\bar{\mathcal{X}}_{\text{inv}}(\theta_2)$, by time T_{θ_1}. The invariant curve state, $\bar{\mathcal{X}}_{\text{inv}}(\theta_2)$, is parameterized by the angle θ_2 and is evaluated with the truncated Fourier series utilized in the invariance condition corrections process, i.e., Equation (3.84). For states along the stable manifold structures associated with quasi-periodic orbits, the variables θ_2, T_{θ_1}, and T_{mani}, describe the state along the global representation of the manifold. In describing an end state for a transfer, i.e., $\bar{\mathcal{X}}_f$, with a tangent burn into a periodic orbit, also plotted in Figure 6.1, only four variables are required: T_α, T_{mani}, ΔV_{tan}, T_{arc}. These variables are termed the fundamental variables for a two-maneuver transfer . To address convergence issues near dynamically complex regions, the transfer arcs, i.e., the stable manifold arc and the bridging arc, are subdivided into a series of segments, i.e., reformulated into a multiple-shooting problem. However, the number of fundamental variables does not change, that is, the end state along the transfer is always described with the lowest number of fundamental variables. The fundamental variables for two-maneuver transfers into periodic and quasi-periodic orbits are summarized in Table 6.1. In this investigation, two constraints are enforced at the end state, i.e., $\bar{\mathcal{X}}_f$, of the transfer: an altitude and an apsis constraint. Note that the end state along the transfer is essentially the departure state at periapsis for a GTO with a fixed size, i.e., fixed periapsis and apoapsis altitude. Therefore, the GTO departure position is parameterized by two angles: λ and δ,

as illustrated in Figure 4.5(b). In this investigation, the constraints for the DSM transfers are written as:

$$\begin{aligned} \text{Altitude Constraint}: &\quad \bar{r}_f - \bar{r}_{\text{dep}}(\lambda, \delta) = 0, \\ \text{Apsis Constraint}: &\quad (\bar{r}_f - \bar{r}_{\text{e}}) \cdot \bar{v}_f = 0, \end{aligned} \tag{6.1}$$

where $\bar{r}_f$ and $\bar{v}_f$ are the final end state position and velocity along the transfer, $\bar{r}_{\text{e}}$ is the position of the Earth with respect to the Sun-Earth barycenter in the CRTBP rotating frame, and the desired GTO departure position, $\bar{r}_{\text{dep}}$, is defined as:

$$\bar{r}_{\text{dep}}(\lambda, \delta) = \bar{r}_{\text{e}} + h_{alt} \begin{bmatrix} \cos(\lambda)\cos(\delta) \\ \sin(\lambda)\cos(\delta) \\ \sin(\delta) \end{bmatrix}, \tag{6.2}$$

with h_{alt} as the nondimensional fixed GTO periapsis altitude corresponding to 185 km. Two additional free-variables are introduced to the transfer problem, i.e., λ and δ, with the formulation of the constraint conditions in Equation (6.1) as a four-dimensional column vector. For example, transfers into a periodic orbit with a general maneuver, i.e., scenario B from Table 6.1, requires six fundamental variables: T_α, T_{mani}, ΔV_x, ΔV_y, ΔV_z, T_{arc}. In all transfer scenarios, only the end state apsis and altitude constraints are enforced, that is, the constraint vector for the transfer problem is two-dimensional, assuming the constraints are written as scalar value functions. However, with the constraint conditions from Equation (6.1), the constraint is re-written as a four-dimensional vector and two additional free-variables, λ and δ, are included in the transfer problem, i.e., the vector of fundamental variables. The reformulation of the constraint vector and introduction of the free-variables, λ and δ, permits more control over the departure position. Additionally, the reformulation of the constraint condition does not affect the solution space for the DSM transfer problem, summarized in Table 6.1. The dimension of the solution space applicable to the DSM transfer is evaluated as the difference between the number of free-variables and the number of constraints. For example, transfers to a periodic orbit with a tangential DSM appear along a two-dimensional surface of solutions. Information regarding surface shape and terminal conditions, e.g., if the

surface is closed, is not known a priori or not known as a closed form function. The scenarios in Table 6.1 are applicable for transfers leveraging either stable and unstable manifold structures and a bridging arc. Transfers in the solution space for the scenarios in Table 6.1 offer advantageous options for mission design in the Sun-Earth system.

Table 6.1. : Fundamental variables and constraints for different DSM type transfers into periodic and quasi-periodic orbits

Scenario	Target	Fundamental Variables	DSM Type	Departure Constraints	Dimension of Solution Space
A	PO	$T_\alpha, T_{\text{mani}}, T_{\text{arc}}$	Tangent (ΔV_{tan})	Altitude Apsis	2
B	PO	$T_\alpha, T_{\text{mani}}, T_{\text{arc}}$	General ($\Delta \bar{V}_{\text{gen}}$)	Altitude Apsis	4
C	QPO	$T_{\theta_1}, \theta_2, T_{\text{mani}}, T_{\text{arc}}$	Tangent (ΔV_{tan})	Altitude Apsis	3
D	QPO	$T_{\theta_1}, \theta_2, T_{\text{mani}}, T_{\text{arc}}$	General ($\Delta \bar{V}_{\text{gen}}$)	Altitude Apsis	5

6.2 Transfers into Periodic Orbits in the Sun-Earth System

Transfers to periodic orbits near the Sun-Earth Lagrange points are constructed by connecting a trajectory from a GTO departure state to a trajectory along a stable manifold structure with a single DSM. In Figure 6.1, a two-maneuver transfer is constructed via reverse time propagation with a single trajectory arc along a stable manifold, in cyan, and a bridging arc, in black, to a GTO departure state, i.e., $\bar{r}_{\text{dep}}$. Note that in the formulation in Figure 6.1, there is an explicit maneuver, i.e., the DSM, and an implicit maneuver, the TIM performed at the GTO departure location. Each trajectory arc is computed as a single trajectory requiring a long propagation time. However, to mitigate convergence challenges due to the complex dynamical regime, the transfer illustrated in Figure 6.1 is reformulated as a multiple-shooting problem. The multiple-shooting formulation is illustrated in Figure 6.2. In Figure 6.2, the injection point into the periodic orbit, $\bar{\mathcal{X}}_{\text{inj}}(T_\alpha)$, is a state computed by propagating an initial state on the periodic orbit, $\bar{\mathcal{X}}_0$, by time T_α. The trajectory along

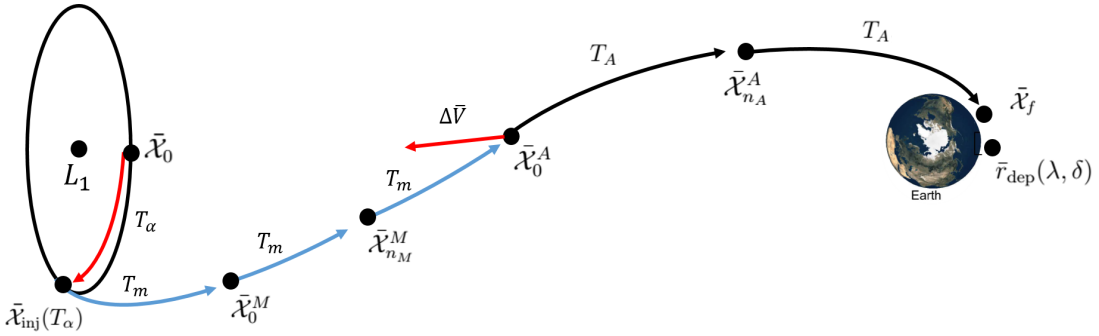

Figure 6.2. : Two-maneuver transfer into a general periodic orbit formulated as a multiple-shooting problem. Transfer arcs are propagated in reverse time. Note that a Transfer Injection Maneuver is implied at the GTO departure location

the stable manifold is described via $n_M + 2$ arcs in cyan, where each arc has a propagation time of T_m. Similarly, the bridging trajectory is created with $n_A + 1$ arcs, in black, and a propagation time of T_A. The multiple-shooting scheme in Figure 6.2 is formulated as TPBVP and solved via multidimensional Newton method. The free-variable vector consistent with the multiple-shooting formulation is,

$$\bar{\mathfrak{X}} = \begin{bmatrix} \bar{\mathcal{X}}_0^M \\ \bar{\mathcal{X}}_1^M \\ \vdots \\ \bar{\mathcal{X}}_{n_M}^M \\ \bar{\mathcal{X}}_0^A \\ \bar{\mathcal{X}}_1^A \\ \vdots \\ \bar{\mathcal{X}}_{n_A}^A \\ T_\alpha \\ T_m \\ T_A \\ \lambda \\ \delta \end{bmatrix}, \tag{6.3}$$

where T_α is the time along the periodic orbit, T_m is a time such that the total time on the stable manifold is: $T_{\text{mani}} = T_m(n_M + 2)$, and T_A is along the bridging arc defined as $T_{\text{arc}} = T_A(n_A + 1)$. Recall that the angles for λ and δ are defined in Figure 4.5(b). The constraint vector that encapsulates scenario B in Table 6.1, i.e., a transfer including a general DSM maneuver, is denoted as,

$$\bar{F} = \begin{bmatrix} \bar{F}_{\text{mani}} \\ \bar{F}_{\text{bridge}} \\ \bar{F}_{\text{DSM}} \\ F_{\text{apsis}} \\ \bar{F}_{\text{alt}} \end{bmatrix}, \tag{6.4}$$

where the constraint vectors associated with state continuity along the stable manifold trajectory, $\bar{F}_{\text{mani}}$, state continuity along the bridging arc, $\bar{F}_{\text{bridge}}$, the DSM maneuver, $\bar{F}_{\text{DSM}}$, GTO departure apsis and altitude are,

$$\bar{F}_{\text{mani}} = \begin{bmatrix} \bar{\mathcal{X}}_M(T_m, T_\alpha) - \bar{\mathcal{X}}_0^M(0) \\ \bar{\mathcal{X}}_0^M(T_m) - \bar{\mathcal{X}}_1^M(0) \\ \vdots \\ \bar{\mathcal{X}}_{n_M-1}^M(T_m) - \bar{\mathcal{X}}_{n_M}^M(0) \end{bmatrix}, \tag{6.5}$$

$$\bar{F}_{\text{bridge}} = \begin{bmatrix} \bar{\mathcal{X}}_0^A(T_A) - \bar{\mathcal{X}}_1^A(0) \\ \vdots \\ \bar{\mathcal{X}}_{n_A-1}^A(T_A) - \bar{\mathcal{X}}_{n_A}^A(0) \end{bmatrix}, \tag{6.6}$$

$$\bar{F}_{\text{DSM}} = \left[\bar{r}_{n_M}^M(T_m) - \bar{r}_0^A(0) \right], \tag{6.7}$$

$$F_{\text{apsis}} = (\bar{r}_f - \bar{r}_{\text{e}})^T \bar{v}_f, \tag{6.8}$$

$$\bar{F}_{\text{alt}} = \bar{r}_f - \bar{r}_{\text{dep}}(\lambda, \delta), \tag{6.9}$$

with the final position and velocity vectors, $\bar{r}_f$ and $\bar{v}_f$, respectively, corresponding to the final propagated state from $\bar{\mathcal{X}}^A_{n_A}$, i.e., $\bar{\mathcal{X}}^A_{n_A}(T_A)$. The formulated multiple-shooting scheme has an associated Jacobian matrix defined as,

$$\mathbf{D}\bar{\mathbf{F}} = \begin{bmatrix} \mathbf{D}_{\mathbf{x_m}}\bar{\mathbf{F}} & \mathbf{D}_{\mathbf{x_A}}\bar{\mathbf{F}} & D_{T_\alpha}\bar{F} & D_{T_m}\bar{F} & D_{T_A}\bar{F} & D_\lambda \bar{F} & D_\delta \bar{F} \end{bmatrix}, \tag{6.10}$$

where the expanded partial derivative information is provided in Appendix D. The constraint vector in Equation (6.4) is consistent with including an unconstrained DSM, that is, the direction of the maneuver is unrestricted, i.e., Scenario B in Table 6.1. The dimension of the Jacobian matrix in Equation (6.10) is $\dim(\mathbf{D}\bar{\mathbf{F}}) = 6(n_M + n_A + 1) + 7 \times 6(n_M + n_A + 2) + 5$. Note that the Jacobian has a four-dimensional null space, i.e., the solution space is four-dimensional, which is consistent with the Scenario B in Table 6.1. To formulate a scenario for a transfer to a fixed periodic orbit with a tangential maneuver, Scenario A in Table 6.1, a tangential constraint is appended to Equation (6.4). The tangential DSM condition is written as,

$$\bar{F}_{\text{DSM,tan}} = \left[\bar{v}^M_{n_M}(T_m) - \frac{\Delta V \bar{v}^A_0}{\|\bar{v}^A_0\|} - \bar{v}^A_0 \right], \tag{6.11}$$

where $\bar{v}^A_0$ is the velocity vector of the first node along the bridging arc, i.e., $\bar{\mathcal{X}}^A_0(0)$. By including the tangential constraint in Equation (6.11), the scalar DSM magnitude, i.e., ΔV, is also included in the free-variable vector, Equation (6.3). The partial derivatives for the tangential condition are,

$$\mathbf{D}_{\mathbf{x_m}}\bar{\mathbf{F}}_{\text{DSM,tan}} = \begin{bmatrix} \mathbf{0}_{3,6} & \mathbf{0}_{3,6} & \dots & \begin{bmatrix} \mathbf{0}_{3,3} & \mathbf{I}_{3,3} \end{bmatrix} \mathbf{\Phi}^M_{n_M} \end{bmatrix}, \tag{6.12}$$

$$\mathbf{D}_{\mathbf{x_A}}\bar{\mathbf{F}}_{\text{DSM,tan}} = \begin{bmatrix} \begin{bmatrix} \mathbf{0}_{3,3} & \frac{-\Delta V}{\|\bar{v}^A_0\|}\left(\mathbf{I}_{3,3} - \frac{\bar{v}^A_0 \bar{v}^{A^T}_0}{\bar{v}^{A^T}_0 \bar{v}^A_0}\right) - \mathbf{I}_{3,3} \end{bmatrix} & \mathbf{0}_{3,6} & \dots & \mathbf{0}_{3,6} \end{bmatrix}, \tag{6.13}$$

$$D_{\Delta V}\bar{F}_{\text{DSM,tan}} = -\frac{\bar{v}^A_0}{\|\bar{v}^A_0\|} \tag{6.14}$$

$$D_{T_m}\bar{F}_{\text{DSM,tan}} = \dot{\bar{v}}^M_{n_M}(T_m). \tag{6.15}$$

where $\mathbf{\Phi}^M_{n_M}$ is the STM of the final propagated arc corresponding to the state $\bar{\mathcal{X}}^M_{n_M}$ with an acceleration vector, $\dot{\bar{v}}^M_{n_M}(T_m)$, at time T_m. With the addition of the tangential constraint and the scalar ΔV magnitude, the dimension of the Jacobian $\mathbf{D}\bar{\mathbf{F}}$ becomes $\dim(\mathbf{D}\bar{\mathbf{F}}) =$

$6(n_M + n_A + 1) + 10 \times 6(n_M + n_A + 2) + 6$. The solutions space associated with the Jacobian with the tangential ΔV constraint is two-dimensional and consistent with Scenario A in Table 6.1. The DSM is a maneuver performed along the transfer from a GTO to an injection point along the periodic orbit, however an additional maneuver is required to traverse from the GTO to the transfer trajectory. The initial maneuver at the GTO departure state is the implied Transfer Injection Maneuver. Note that the multiple-shooting formulation implemented to compute the single maneuver transfers targets a specific GTO departure location and an apsis condition, and does not account for the magnitude of the required TIM. In this investigation, surface of solutions are constructed to observe transfers from a range of GTO departure locations near the Earth.

6.2.1 Transfers into L_1 Halo Orbits

Transfers into a halo orbit near the Sun-Earth L_1 Lagrange point are constructed with stable manifold trajectories and a DSM that is tangent to the path. The SOHO mission [11] leveraged a periodic halo orbit near the Sun-Earth L_1 point to avoid crossing into the Solar Exclusion Zone. The selected halo orbit for the SOHO mission employed the following orbit parameters: x-amplitude of $206,448$ km, y-amplitude of $66,672$ km, and z-amplitude of $120,000$ km [11]. Additionally, the SOHO orbit is classified as a southern halo orbit, i.e., the motion of the satellite as viewed by an observer at the Earth is counterclockwise, with a corresponding period of 180 days. Recall that the objective is the construction of efficient transfers from a GTO with a fixed periapsis altitude of 185 km with no a priori information about the GTO orientation. The secondary satellite departure state, $\bar{\mathcal{X}}_{\text{dep}}$, is at the GTO periapsis and, from Figure 4.5(b), is parameterized by angles λ and δ. Transfers with a tangential DSM, i.e., Scenario A in Table 6.1, are identified as potential transfer options into the southern halo orbit from different GTO departure positions near the Earth. Although transfers described by both scenarios A and B are applicable for the periodic halo orbit, transfer Scenario A is selected for the two-dimensional solution space. Recall that in Scenario A from Table 6.1, the end point location is also the departure position of the GTO,

$\bar{r}_{\text{dep}}$ in Figure 6.2, at different near-Earth positions. Additionally, the departure position is constrained to be on the $\hat{x}$-$\hat{y}$ plane of the Sun-Earth rotating frame, i.e., $\delta = 0°$. The additional constraint decreases the solution space for transfers with tangent DSMs by one, therefore, all transfer solutions into the periodic halo orbit with a departure state along the $\hat{x}$-$\hat{y}$ plane near Earth appear on a one-dimensional curve of solutions.

A curve of solutions that represents transfers into a southern L_1 halo orbit with a tangential DSM is constructed via a multiple-shooting corrections algorithm. The transfer scenario illustrated in Figure 6.2 is formulated as a multiple-shooting problem described via the free-variable and constraint vectors in Equations (6.3) and (6.4). Recall that, in reformulating the transfer problem into a multiple-shooting problem, the dimension of the solution space does not change and the multiple-shooting formulation only aids in the corrections process. An initial guess is generated by utilizing a Poincaré map, as plotted in Figure 6.3. The trajectories along the surface of the stable manifold that emanates from the southern L_1 halo orbit are propagated in reverse time to a surface of section defined as a plane, i.e., $x = 1.48\text{x}10^8$ km, and their crossings onto the map are plotted in blue in Figure 6.3. The

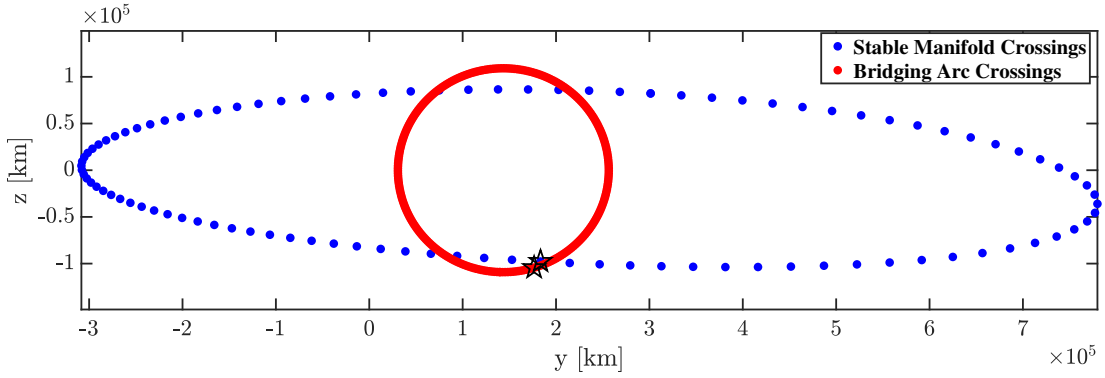

Figure 6.3. : Poincaré map of stable manifold crossings from southern halo orbit (blue) and bridging arc crossing (red) onto the cross-section. Two star points indicate the chosen stable manifold arc and bridging arc to construct an initial guess

bridging arc trajectories, i.e., the red points in Figure 6.3, are propagated forward in time from a location near the Earth, i.e., the departure position corresponding to the GTO periapsis, towards the surface of section. The bridging arc trajectories are propagated from a location near Earth that corresponds to $\lambda = 0°$ and $\delta = 0°$. In the map in Figure 6.3, only

two dimensions are displayed, y and z, and there is no information about the velocity along the trajectories. For this scenario, an initial guess is selected by identifying intersections between the stable manifold crossings and the bridging arc crossings, i.e., the black stars in Figure 6.3. Recall that the solutions space for this scenario is two-dimensional and, therefore, the transfers with a tangent maneuver are contained on a two-dimensional surface. However, for simplicity, the focus of the analysis is constructing transfers originating from different locations along the GTO near the Earth and initiated in the ecliptic plane, i.e., the $\hat{x}$-$\hat{y}$ plane of the Sun-Earth rotating frame. An additional departure constraint is included in Scenario A in Table 6.1, $\delta = 0°$, i.e., it is appended to the constraint vector in Equation (6.4). The tangent maneuver transfers are now all captured along a one-dimensional curve of solutions. Figures 6.4-6.6 display curves of transfer solutions and their respective geometries for a range of λ values, where a point along the curves corresponds to a transfer from a GTO departure point. A selected range of transfers, i.e., corresponding to the box in red in Figure 6.4(a),

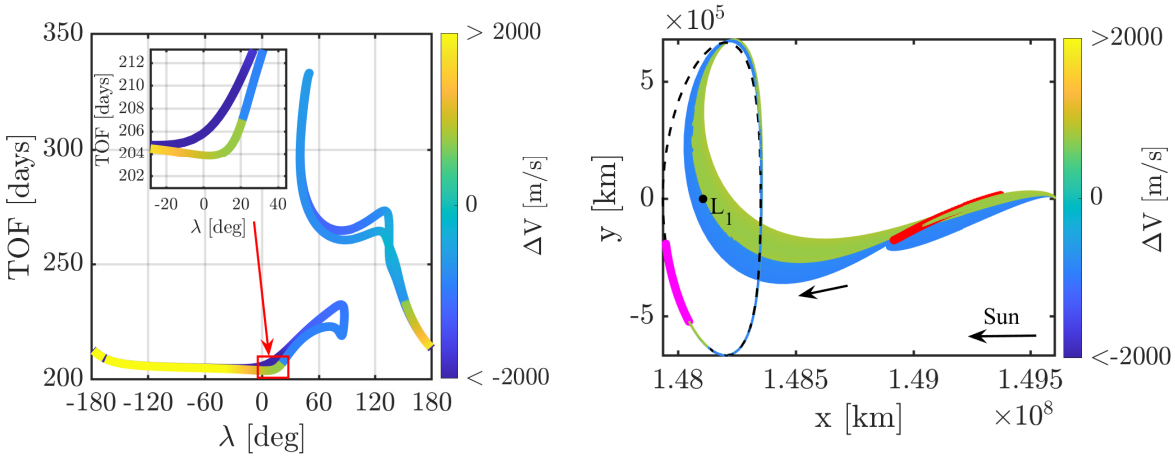

Figure 6.4. : (a) Curve of transfer solutions into a southern halo orbit with a tangent DSM. (b) Selected transfers with the location of the DSM in red and the location of the injection points into halo orbit in magenta

is plotted in Figure 6.4(b) and the transfers presented in Figure 6.5(b) correspond to the transfers in Figure 6.5(a). In Figure 6.4(b), the injection points, in magenta, are located below the y-axis, whereas the injection points in Figure 6.5(b) are situated above the y-axis.

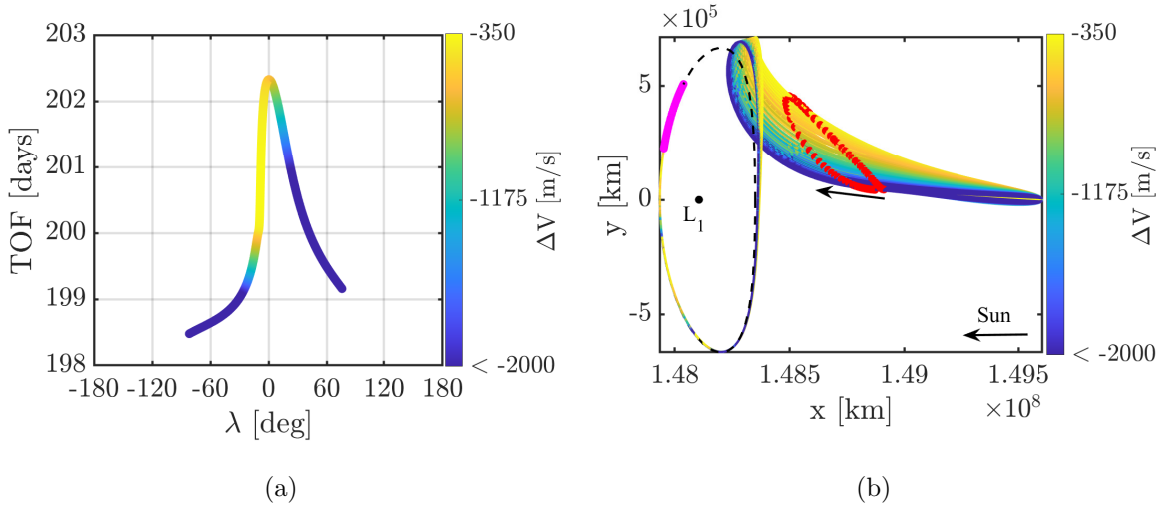

Figure 6.5. : (a) Curve of transfer solutions into southern halo orbit with a tangent DSM. (b) Selected transfers into a southern halo orbit, i.e., transfer inside the red box, with the location of DSM in red and the location of corresponding injection point in magenta

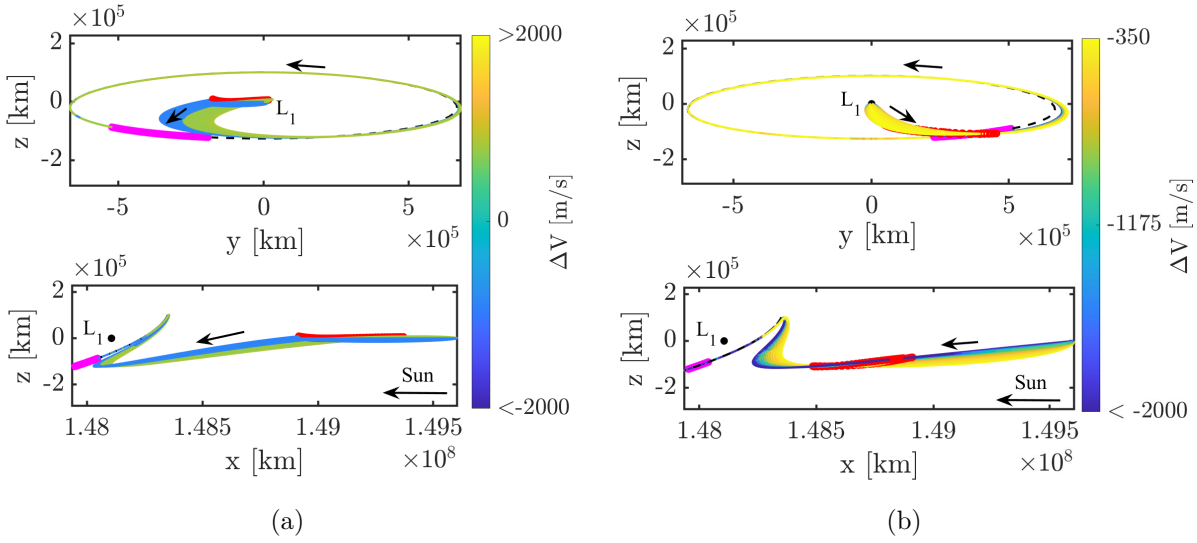

Figure 6.6. : (a) y-z and x-z projections of the two-maneuver transfers from Figure 6.4 (b) y-z and x-z projections of the two-maneuver transfers from Figure 6.5

Additionally, the location of the DSM maneuver, red points, corresponding to Figure 6.5(b) are situated closer to the southern halo orbit compared to the transfers in Figure 6.4(b). Figure 6.6 presents different projections of the transfers in Figures 6.4(b)-6.5(b). Positive ΔV magnitudes for the DSM, presented in Figures 6.4-6.5, correspond to prograde burns,

in the direction of motion, and negative ΔV values are retrograde burns, in the opposite direction of motion. Observe that the TOF in Figures 6.4-6.5 is longer than 190 days. The longer TOF values is due to the transfer asymptotically approaching the southern halo orbit before injecting into the orbit, that is, the distance between the transfer and a point on halo orbit slowly decreases, see the y-z projections in Figure 6.6. This asymptotic behavior is a direct consequence of implementing a trajectory along the stable manifold structure into the transfer design; recall that the stable and unstable manifolds asymptotically approach and depart periodic orbits. Additionally, in Figure 6.4, the region of transfers with TOF$>$ 250 days corresponds to transfers with an excursion toward L_2 before approaching L_1, i.e., indirect transfers. In this analysis, to construct multiple maneuver transfers from a range of GTO departure states, both direct and indirect transfers are considered. The curves in Figures 6.4-6.5 indicate that the departure position from the GTO towards the specific southern L_1 halo orbit can be placed along any point around the Earth.

6.2.2 Transfers into L_2 Halo Orbits

Transfers into a southern halo orbit near Sun-Earth L_2 from a range of GTO departure locations are generated in a curve of solutions. The Nancy Grace Roman Space Telescope, previously the Wide Field Infrared Survey Telescope (WFIRST), is an observatory mission developed by NASA Goddard Space Flight Center (GSFC) and intended for a launch in 2026. The telescope is equipped with instruments to study dark energy and explore distant exoplanets [75]. The Sun-Earth L_2 region provides adequate thermal requirements for the science instrument, however, the orbit of the telescope must satisfy additional geometric requirements. A communications requirement is based on the satellite-Sun-Earth angle (SSE), $\varrho < 36^\circ$, and violation of this constraint impedes ground station communications. Additionally, the orbit and transfer must remain outside the Earth eclipse region, determined to be the penumbral shadow region illustrated in Figure 5.60. An orbit along the southern halo orbit family near Sun-Earth L_2 is selected as a viable option for the Nancy Grace Roman telescope. The orbit family is plotted in Figure 6.7, with the communications cone

requirement shaded in red, and the selected southern halo orbit in green. The selected orbit has the following amplitudes: x-amplitude of $281,891$ km, y-amplitude of $721,122$ km, and z-amplitude of $244,395$ km with a period of 180 days. In this investigation, transfers for a secondary payload from a GTO periapsis are constructed for a range of departure locations, i.e., the GTO departure state is situated along different locations near the Earth.

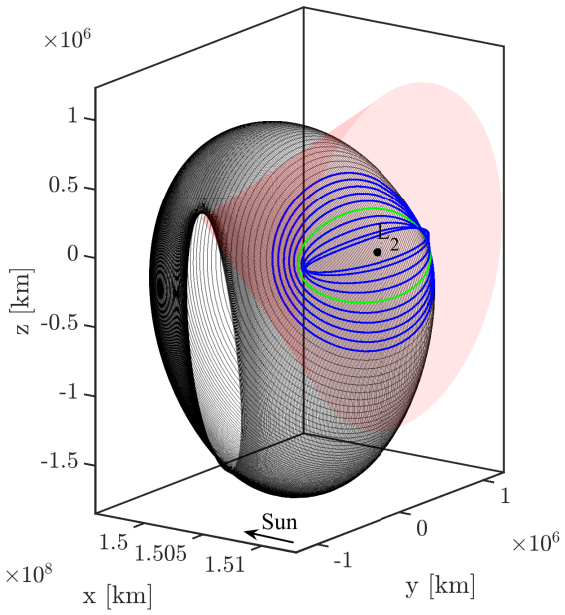

Figure 6.7. : Southern halo orbits near Sun-Earth L_2. The viable halo orbits are in blue with a communications cone of 36°. The selected orbit for the Nancy Grace Roman telescope is in green

Transfers with a single tangential DSM are constructed via a multiple-shooting strategy illustrated in Figure 6.2. The free-variable and constraint vectors corresponding to the multiple-shooting problem are defined in Equations (6.3) and (6.4), with the tangential constraint described via Equation (6.11). Transfers to periodic orbit orbits with a tangential DSM occur along a two-dimensional curve of solutions, even after the re-formulation as a multiple-shooting problem. Table 6.1 summarizes the solution space available for single DSM transfers into periodic and quasi-periodic orbits. For simplicity, transfers from a GTO departure state along the ecliptic, i.e., the $\hat{x}$ -$\hat{y}$ plane, are computed by including a constraint, $\delta = 0°$, to the constraint vector in Equation (6.4). The single maneuver transfer are now

generated along a one-dimensional curve of solutions. A Poincaré map is implemented to find feasible initial conditions for the transfer for different GTO departure locations, represented via the angle λ illustrated in Figure 4.5(b). Recall that the departure location for the secondary payload is a GTO periapsis. The curve of solutions and the transfer geometries in the CRTBP model are plotted in Figures 6.8-6.12. Positive ΔV magnitudes for the DSM,

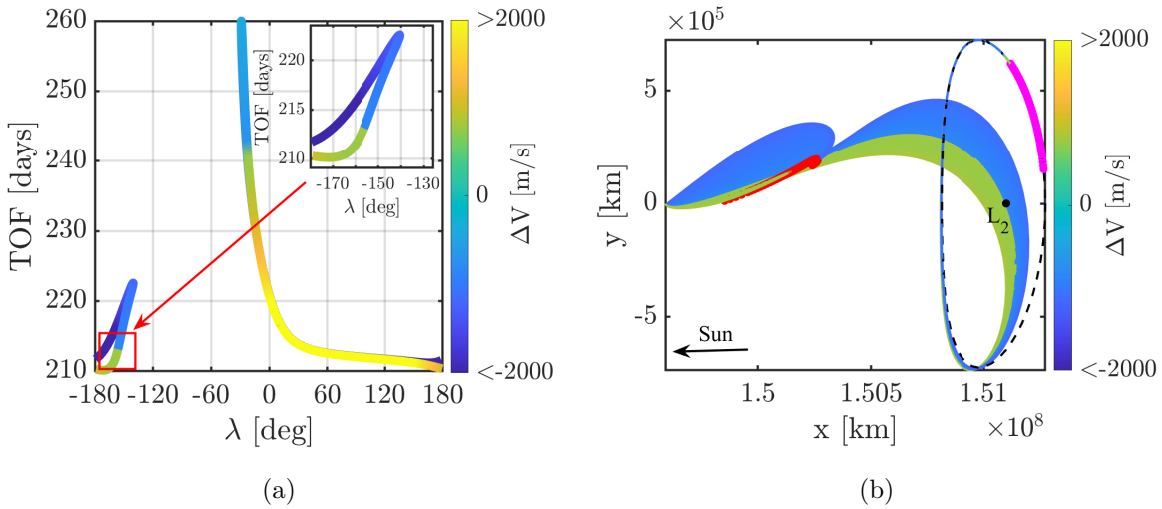

Figure 6.8. : (a) Curve of transfer solutions into southern halo orbit with a tangent DSM. (b) Transfers into a southern halo orbit with the location of DSM in red and the location of injection points into halo orbit in magenta

presented in Figures 6.8-6.10, correspond to prograde burns, i.e., in the direction of motion, and negative ΔV values are retrograde burns, or opposite to the direction of motion. Observe that the longer TOF values in Figures 6.8-6.10 is a direct consequence of implementing a trajectory along the stable manifold structure into the transfer design; recall that the stable and unstable manifolds asymptotically approach and depart periodic orbits. Additionally, different projections of the two-maneuver transfer families are plotted in Figures 6.11-6.12; note that the $\hat{y}$-$\hat{z}$ projections are from the Sun-Earth L_2 point towards the Earth. Note that the location of the injection points varies for each transfer family in Figures 6.8-6.10. For example, in Figure 6.11, the injection points, in magenta, in the $\hat{y}$-$\hat{z}$ projection are located near the bottom right, wheres the injection points corresponding to the family in Figure 6.9 are situated near the top. Additionally, the injection points of the family in Figure 6.10 are

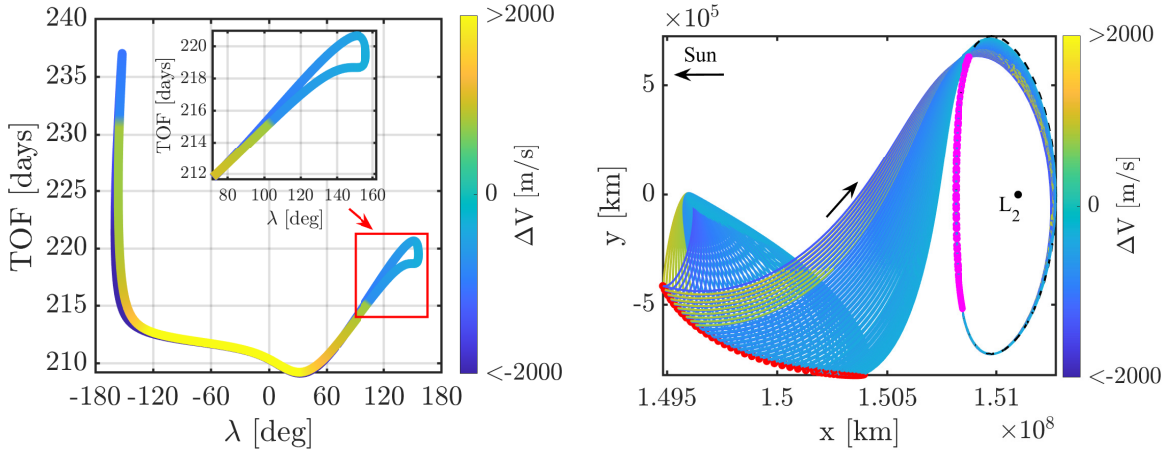

Figure 6.9. : (a) Curve of transfer solutions into southern halo orbit near L_2 with a tangent DSM. (b) Transfers into a southern halo orbit near L_2 . The location of the DSM is in red and the location of the injection points are in magenta

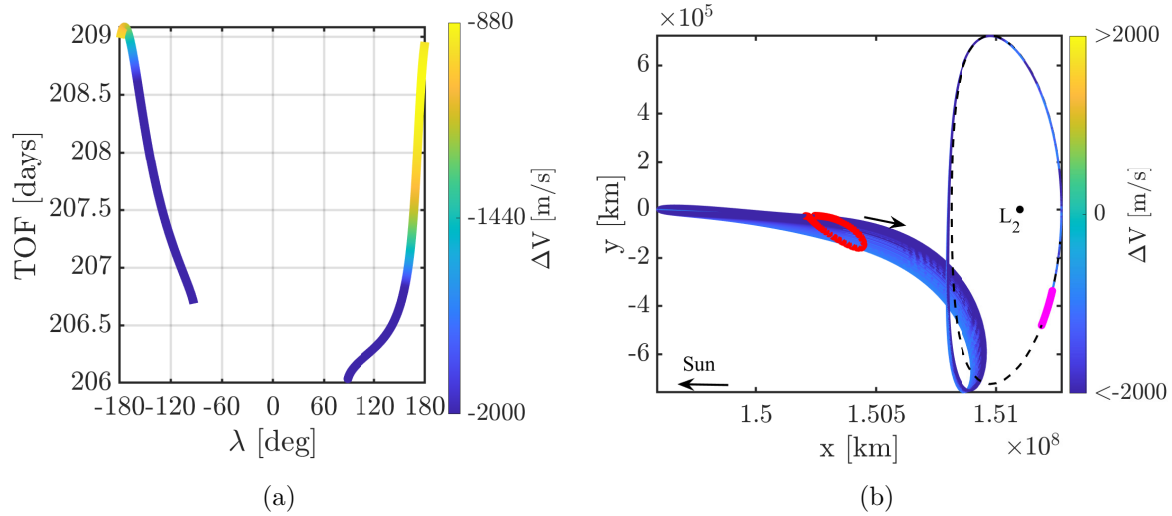

Figure 6.10. : (a) Curve of transfer solutions into southern halo orbit with a tangent DSM. (b) Geometry of select transfers into a southern halo orbit. The location of the DSM is in red and the location of the injection points are in magenta

contained near the bottom left, in the $\hat{y}$-$\hat{z}$ projection. In this analysis, to construct multiple maneuver transfers from a range of GTO departure states, both direct and indirect transfers are considered. The curves in Figures 6.8-6.10 suggest that any GTO departure position

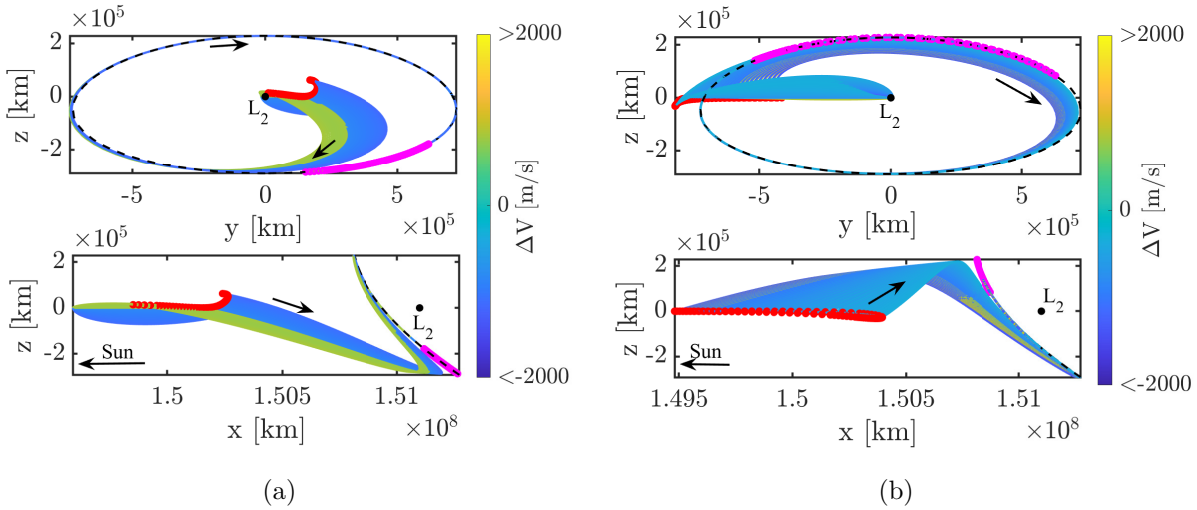

Figure 6.11. : (a) y-z and x-z projections of the two-maneuver transfers from Figure 6.8 (b) y-z and x-z projections of the two-maneuver transfers from Figure 6.9

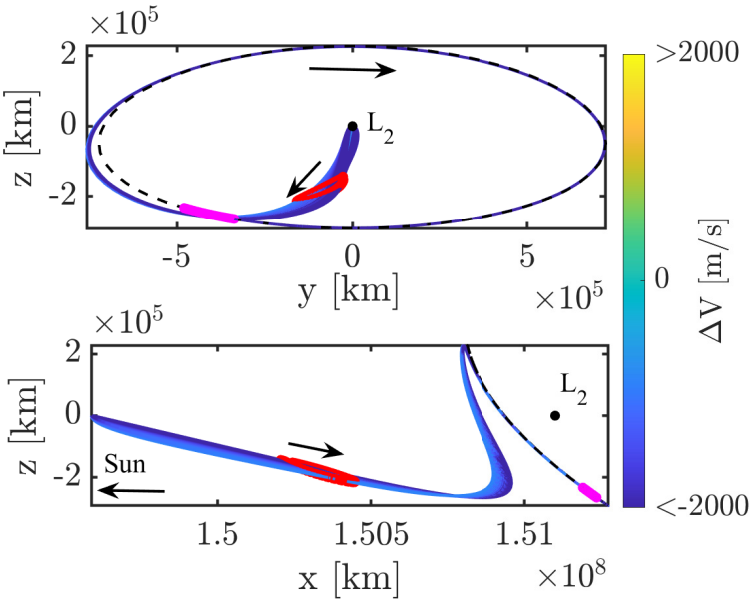

Figure 6.12. : y-z and x-z projections of the two-maneuver transfers from Figure 6.10

situated along the ecliptic has at least one two-maneuver transfer option to the specified southern L_2 halo orbit.

6.2.3 Optimized Transfers into Periodic Orbits

Optimal transfers into periodic orbits in the Sun-Earth system are constructed from a range of GTO departure positions near the Earth by leveraging insights from families of two-maneuver transfers. The families of two-maneuver transfers from Figures 6.4-6.12 offer options over the entire range of GTO departure positions, i.e., $-180^\circ \leq \lambda \leq 180^\circ$, with $\delta = 0^\circ$, i.e., on the Sun-Earth ecliptic. But these transfers are also initial guesses to compute optimal transfers. Recall that, in this analysis, there is no a priori information on the orientation of the drop-off GTO, i.e., the departure orbit for the secondary payload. To address the expected variation in orbit orientation, multiple GTO departure positions are considered as potential candidates and optimized transfers are generated from these potential departure locations to Sun-Earth periodic orbits. In the inertial EME frame, the GTO departure position and velocity vectors are constructed via Equations (4.1) and (4.2) for specific values of Ω, ${}^{\mathrm{i}}\mathrm{i}$, and ω angles in the inertial EME frame. In this investigation, the inclination and argument of periapsis angles, in the inertial EME frame, are set to ${}^{\mathrm{i}}\mathrm{i} = 27^\circ$ and $\omega = 0^\circ$, respectively; note that these are also consistent with Table 4.1. The size of the GTO, i.e., the periapsis and apoapsis altitudes are set to 185 km and $35,786$ km. The RAAN angle, Ω, is a value from the set $\{0^\circ, 20^\circ, \cdots, 340^\circ\}$, that is, the GTO periapsis is situated along the mean Earth equatorial plane at different locations; recall that the GTO departure state is at periapsis. The variation in Ω directly expresses the variation in the GTO orientation, for this analysis. In the context of the CRTBP model, a transfer from the Earth to a Sun-Earth Lagrange point is constructed in a rotating frame. The GTO departure states, $\bar{\mathcal{X}}_{\mathrm{i}_{\mathrm{dep}}}$, computed in the EME frame are rotated to the Sun-Earth rotating frame via the steps outlined in Section 2.3.2.2. In the Sun-Earth rotating frame, the position of the GTO departure state, $\bar{r}_{\mathrm{dep}}$, is parameterized via the angles λ, δ, and the rotating inclination, ${}^{\mathrm{r}}\mathrm{i}$. The two-maneuver transfer information exposed in Figures 6.4-6.12 does not explictly display the maneuver at the GTO departure state. To reduce the total ΔV necessary for the transfer, the number of maneuvers is increased to four: the TIM, two DSMs, and one Orbit Injection Maneuver (OIM). Recall that the two-maneuver transfers

from Figures 6.4-6.12 each included a TIM and a single DSM, labeled DSM1, because the transfer incorporated a stable manifold trajectory to approach the desired injection point into the periodic orbit. Now, an additional DSM, termed DSM2, and a maneuver at the injection point, denoted as OIM, are introduced to construct the optimal transfers in search of a minimal ΔV solution. The location of the DSMs along the final transfer trajectory is a free-variable in the optimization process. A direct optimization scheme is implemented via MATLAB's fmincon optimization function to compute a locally optimum transfer that minimizes the following cost function:

$$J = \min\left\{\Delta V_{\text{TIM}} + \sum_{\text{j}=1}^{b} \Delta V_{\text{j}}^{\text{DSM}} + \Delta V_{\text{OIM}}\right\}, \tag{6.16}$$

Subject to:

$$\begin{aligned}
&\text{Continuity Constraint:} && \bar{\mathcal{X}}_{m-1}(T_{m-1}) = \bar{\mathcal{X}}_{m}(0) \quad \text{where } \{m \in \{2, ..., N\} | m \notin \bar{B}\}, \\
&\text{Boundary Constraint:} && \bar{\mathcal{X}}_{0}(0) = \bar{\mathcal{X}}_{\text{dep}}\ ,\ \bar{r}_{N}(T_N) = \bar{r}_{\text{inj}},\ \ \bar{r}_{1}(0) = \bar{r}_{0}(0), \\
&\text{Path Constraint:} && \sum_{\text{j}}^{N} \int_{0}^{T_{\text{j}}} F_{\text{p}}^{2}\left(\bar{\mathcal{X}}_{\text{j}}(t)\right) - \left|F_{\text{p}}\left(\bar{\mathcal{X}}_{\text{j}}(t)\right)\right| F_{\text{p}}\left(\bar{\mathcal{X}}_{\text{j}}(t)\right) dt = 0, \\
&\text{Maneuver Conditions:} && \bar{r}_{k-1}(T_{k-1}) = \bar{r}_{k}(0) \quad \text{where } \{k \in \bar{B}\},
\end{aligned} \tag{6.17}$$

where the $\bar{B}$ vector is defined as: $\bar{B} \in \{2, \cdots, N\}$ and the dimension of the number of DSMs is equal to $b = \dim(\bar{B})$. The optimization scheme described in Equations (6.16)-(6.17) is consistent with a multiple-shooting strategy illustrated in Figure 6.13. In this investigation, two DSMs are included such that $\dim(\bar{B}) = b = 2$. As an example, in Figure 6.13, two DSM are illustrated via red points, the TIM is represented by a purple point at the GTO departure location, and the OIM is plotted as a cyan point at the injection point along the periodic orbit. The initial state along the transfer trajectory, $\bar{\mathcal{X}}_0$, is a GTO state and the position at the end of the transfer, illustrated as a cyan point in Figure 6.13, is a state on the periodic orbit. Full state continuity, position and velocity, is enforced throughout the transfer except for nodes that correspond to a maneuver, in which only position continuity is enforced. The

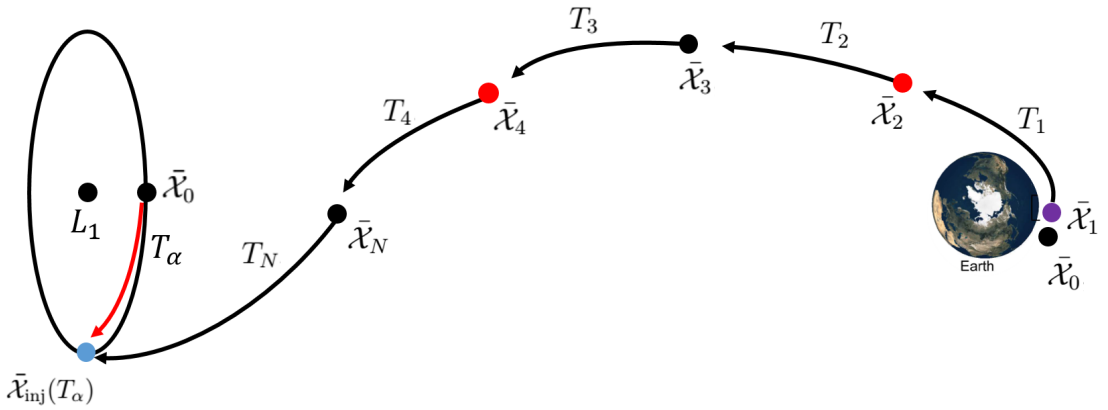

Figure 6.13. : Schematic for constructing optimized transfers. Multiple-shooting formulation with forward time propagation

steps consistent with constructing optimized transfers from different near-Earth locations, i.e., Ω angles, are summarized as follows,

- Compute GTO departure state, $\bar{\mathcal{X}}_{\underset{\text{i}}{\text{dep}}}$, in inertial EME frame from Equations (4.1) and (4.2) given Ω, ω, and $^{\text{i}}$i values. The satellite departs the GTO at periapsis at a specfied epoch.

- Rotate inertial departure state vector, $\bar{\mathcal{X}}_{\underset{\text{i}}{\text{dep}}}$, into the Sun-Earth rotating frame departure state, $\bar{\mathcal{X}}_{\text{dep}}$, via steps in Section 2.3.2.2.

- Evaluate departure λ_{dep} and δ_{dep} values associated with the departure position in the rotating frame, $\bar{r}_{\text{dep}}$. The λ_{dep} and δ_{dep} angles dictated the position of the departure state.

- Select a two-maneuver transfer from the one-dimensional curve of solutions corresponding to a periodic orbit near Sun-Earth L_1 or L_2. The selected two-maneuver transfer has an associated λ value that is close to the departure values, i.e., λ_{dep}. Recall that the two-maneuver transfer is generated via reverse time propagation.

- Construct optimization multiple-shooting problem by subdividing the selected two-maneuver transfer and propagating in forward time. Include an additional maneuver for a total of two Deep Space Maneuvers throughout the transfer. Additionally, include

a TIM at the GTO departure location and an OIM at the injection location of the periodic orbit.

- Implement direct optimization strategy, i.e., Equations (6.16) and (6.17), via fmincon function in MATLAB.

The optimization strategy is implemented for transfers to halo orbits in the Sun-Earth system. Additionally, path constraints that correspond to eclipsing constraints are included throughout the optimized transfer. In summary, optimized transfers from a range of GTO departure locations are generated by leveraging insights from families of two-maneuver transfers.

6.2.3.1 Transfers to L_1 Halo Orbit

Optimized transfers to a southern L_1 halo orbit, consistent with the SOHO spacecraft, are constructed by leveraging families of two-maneuver transfers. Select two-maneuver transfers are identified from Figures 6.4-6.5 to compute locally optimal transfers to the specified southern L_1 halo orbit. Observe that for periodic orbits, the injection point is parameterized by T_α, refer to Figure 6.2. For demonstration, in this investigation, optimized transfers are constructed from a GTO departure position at an epoch of June 2, 2022 12:00:00.000 over a range of Ω values of $\{0°, 20°, .., 340°\}$, thereby demonstrating the construction of transfers over a range GTO orientations. The geometries of the locally optimal transfers are provided in Figure 6.14.

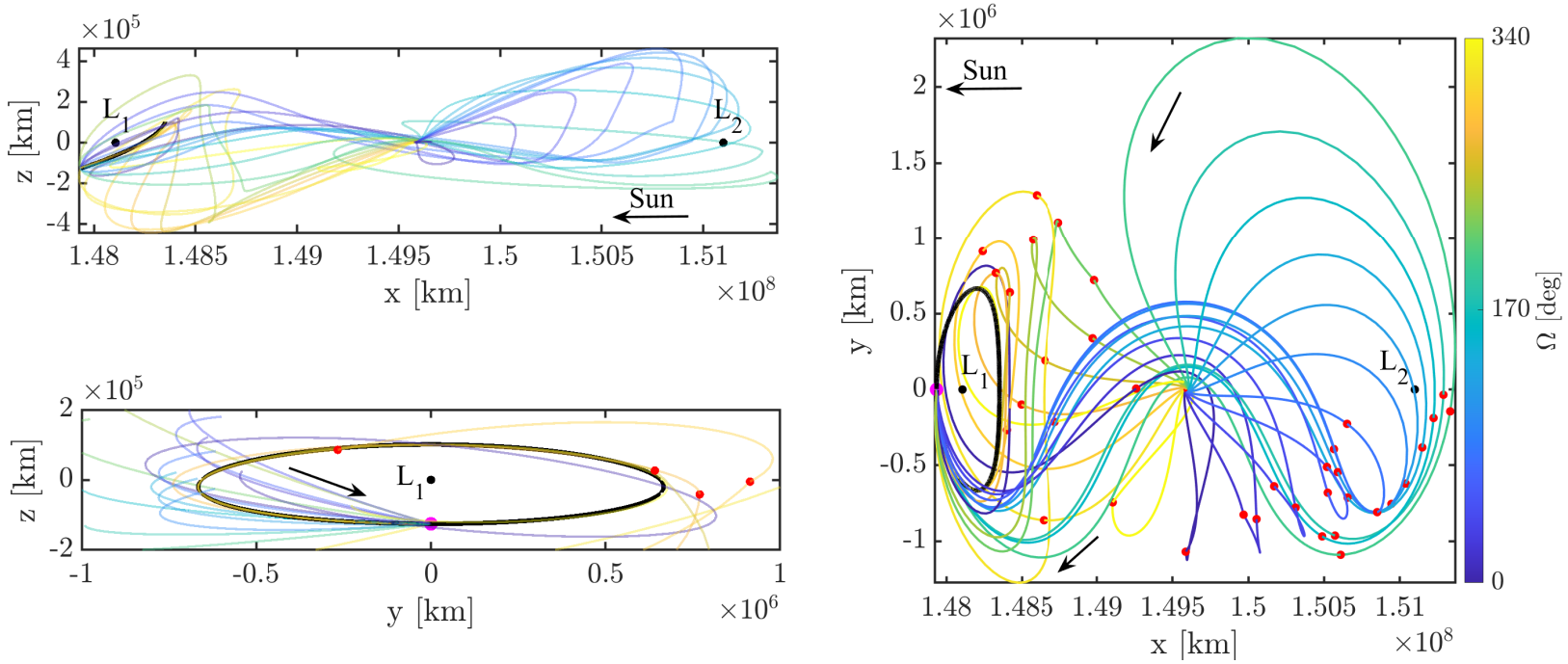

Figure 6.14. : Optimized transfers to Sun-Earth L_1 halo orbits in the CRTBP model. The desired southern halo is in black and the transfers are depicted via a range of colors. The departure epochs of the GTO correspond to a departure epoch of June 2 12:00:00.000, 2022.

For the specified epoch, optimized transfers from a range of $20° < \Omega < 200°$ include an excursion toward Sun-Earth L_2, also termed as indirect transfers. The direct transfers are contained outside the Ω value range of indirect transfers. The red points in Figure 6.14 correspond to the location of the maneuvers performed along the transfer with the OIM included at the intersection between the transfer trajectory and an injection point along the periodic orbit, i.e., the point in magenta. For the indirect transfers, the first DSM, i.e., DSM1, is performed below the $\hat{x}$-axis during the L_2 excursion while DSM2 is located between L_1 and the Earth. Additionally, the optimal injection location, i.e., the location of the OIM plotted in magenta, along the southern halo orbit occurs near to the $\hat{x}$-axis of the CRTBP rotating frame. The GTO departure positions at the specified epoch, expressed in the rotating frame, are plotted in Figure 6.15 and the total ΔV and transfer TOF are plotted in Figure 6.16. The GTO departure positions are situated along the Earth equatorial plane

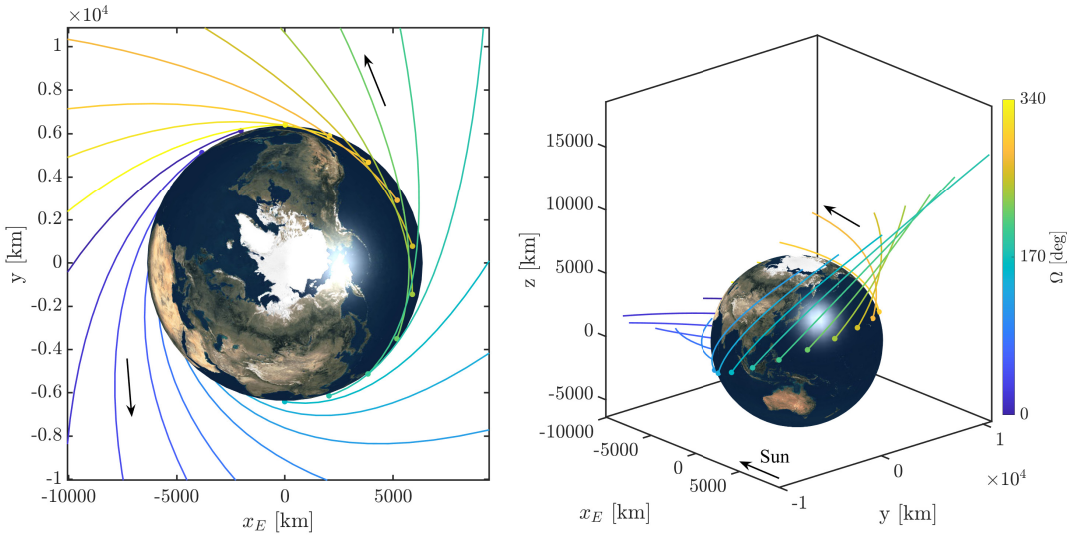

Figure 6.15. : GTO departure location corresponding to optimal transfers to Sun-Earth L_1 halo orbits at epoch of June 2 12:00:00.000, 2022. Note that x_E is with respect to the Earth

in the inertial EME frame, however, in the Sun-Earth rotating frame, the departure positions contain an out-of-plane component, i.e., $\delta \neq 0°$. This observation is a direct consequence of the inclination difference between the ecliptic plane and the Earth equatorial plane, recall that the $\hat{x}$-$\hat{y}$ plane in the Sun-Earth CRTBP model is essentially the ecliptic plane. In Figure

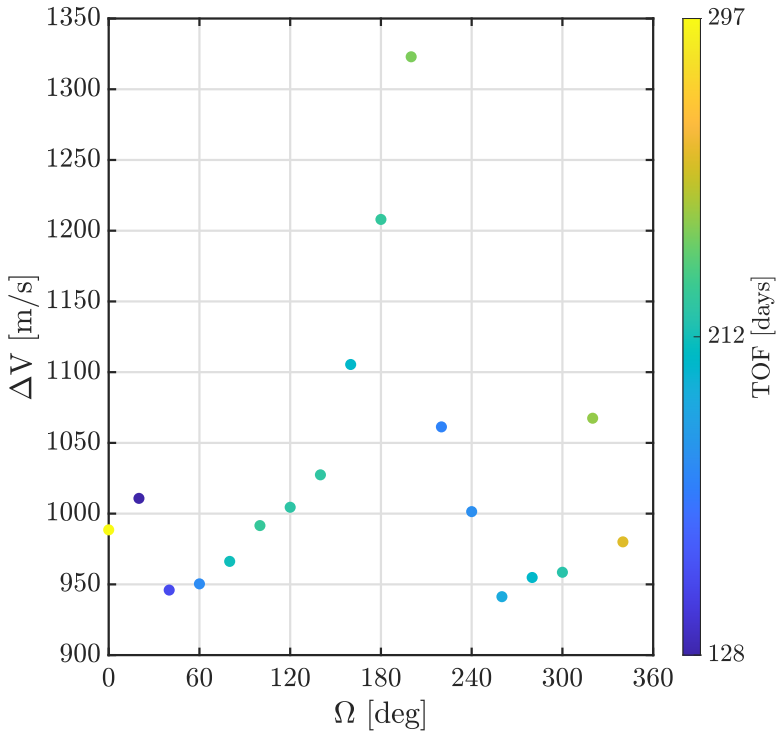

Figure 6.16. : Total maneuver ΔV for optimal transfer to Sun-Earth L_1 halo orbits at epoch of June 2 12:00:00.000, 2022

6.16, transfers with the lowest ΔV correspond to a set of indirect transfers with an Ω range, i.e., $40^\circ \leq \Omega \leq 60^\circ$ and direct transfers at a range of $260^\circ \leq \Omega \leq 280^\circ$. The ΔV values for each individual maneuver in the optimal transfers into the southern L_1 halo orbit are summarized in Table 6.2. In this scenario, there is no constraint on the OIM and no SEZ constraint. During the optimization process, the magnitude of one of the included DSMs is decreased to zero, that is, the extra maneuver is not necessary, see Table 6.2. Additionally, for the transfer corresponding to $\Omega = 340^\circ$, the OIM is zero, which suggests that after the second DSM is performed, the satellite enters a trajectory near the stable manifold structure associated with the southern halo orbit. Note that, the optimal geometries in Figure 6.14 and the ΔV plotted in Figure 6.16 are only applicable at the specified departure epoch of June 2, 2022 12:00:00.000. However, transfers into the desired southern L_1 halo orbit are easily constructed for any GTO departure epoch and Ω by leveraging the information within the curve of solutions provided in Figures 6.4-6.5.

Table 6.2. : Maneuver magnitudes for optimal transfers to Sun-Earth L_1 southern halo in m/s

Ω [deg]	TIM	DSM 1	DSM 2	OIM	Total
0	747	184	2	58	991
20	777	145	0	88	1011
40	748	91	0	107	946
60	792	0	80	79	950
80	747	0	157	62	966
100	798	131	0	63	992
120	786	153	0	65	1005
140	753	196	0	78	1027
160	758	157	0	190	1105
180	765	260	0	183	1208
200	771	304	0	248	1323
220	783	126	0	152	1061
240	804	0	40	158	1001
260	798	0	142	1	941
280	793	0	136	26	955
300	751	101	102	5	959
320	769	0	61	238	1067
340	745	226	9	0	980

6.2.3.2 Transfers to L_2 Halo Orbit

Optimized transfers with multiple maneuvers into a southern L_2 halo orbit near the Sun-Earth L_2 vicinity are constructed by implementing two-maneuver transfers. In this analysis, two-maneuver transfers to a southern L_2 halo orbit, i.e., a possible destination for the Nancy Grace Roman Space Telescope, are generated via a multiple-shooting scheme and plotted in Figures 6.8-6.10. Recall that for periodic orbits, the injection point is parameterized by T_α, refer to Figure 6.2. For transfers into the southern L_2 halo orbit, locally optimal transfers are constructed from a GTO departure position at an epoch of December 2, 2022 12:00:00.000 for a range of Ω values of $\{0°, 20°, .., 340°\}$. The position of the GTOs are plotted in Figure 6.17; observe that the GTO departure location at this epoch differ from the locations presented in Figure 6.15 which corresponds to a different epoch. For each GTO departure location corresponding to an Ω value, a locally optimal transfer is gener-

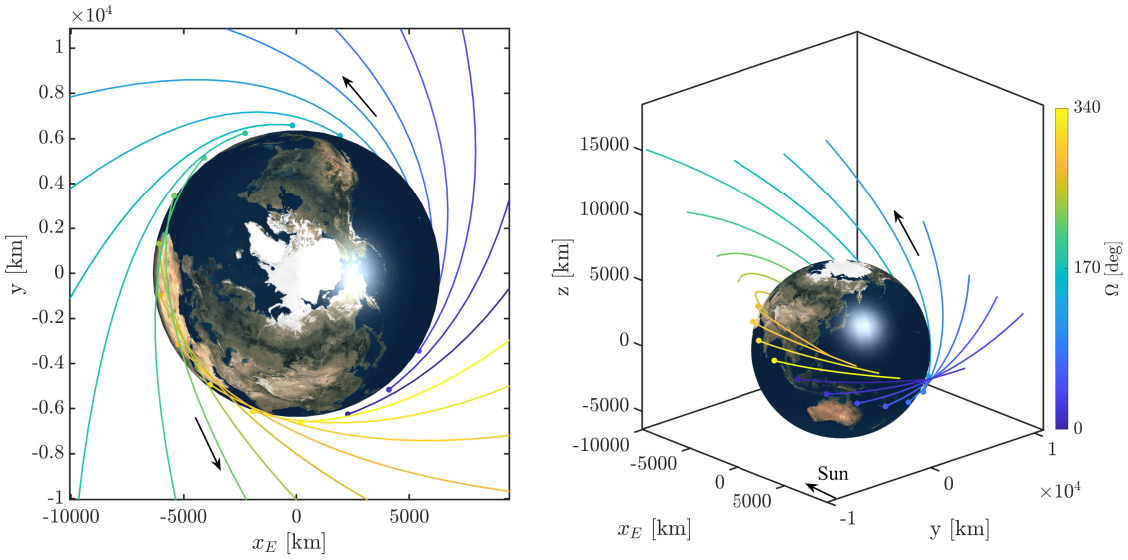

Figure 6.17. : GTO departure locations in the Sun-Earth rotating frame at epoch of Dec 2, 2022 12:00:00.000. Note that x_E is with respect to the Earth

ated via the steps outlined in Section 6.2.3. An eclipse constraint, based on the penumbral shadow cone illustrated in Figure 5.60, is included as a path constraint along the transfer to L_2. Equation (5.74) is defined as F_p in the path constraint condition in Equation (6.17). Additionally, a limit on the magnitude of the OIM is enforced such that: $\Delta V_{\text{OIM}} \leq 15$ m/s and is mathematically written as,

$$\Delta V_{\text{OIM}}^2 - (\Delta V_{\text{OIM}}^{\max})^2 + \beta_{\text{OIM}}^2, \tag{6.18}$$

where $\Delta V_{\text{OIM}}^{\max}$ is the maximum OIM limit magnitude of 15 m/s and β_{OIM} is a slack variable. The geometries of the resulting transfers are plotted in Figure 6.18 with the ΔV information presented in Figure 6.19; note that the penumbra eclipse region is shaded in black in Figure 6.18. In Figure 6.18, the indirect transfers, i.e., the trajectories with an excursion to L_1 or an Earth flyby, correspond to a range of $20° \leq \Omega \leq 180°$. Observe that the position of the injection points into the southern L_2 halo, the magenta points in Figure 6.18, appear along different locations of the desired orbit.

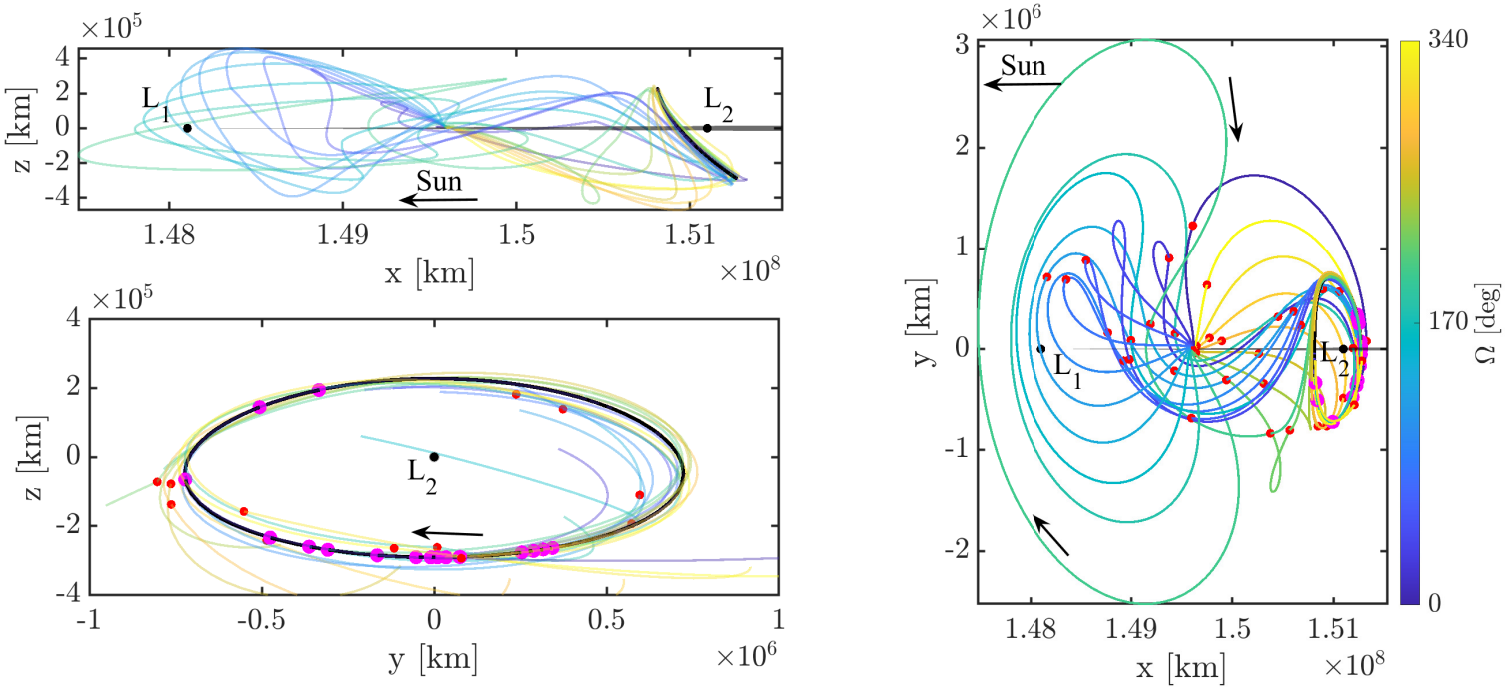

Figure 6.18. : Optimized transfers to Sun-Earth L_2 southern halo orbit at GTO departure epoch of Dec 2, 2022 12:00:00.000. The desired halo orbit is in black and the transfer are depicted via a range of colors

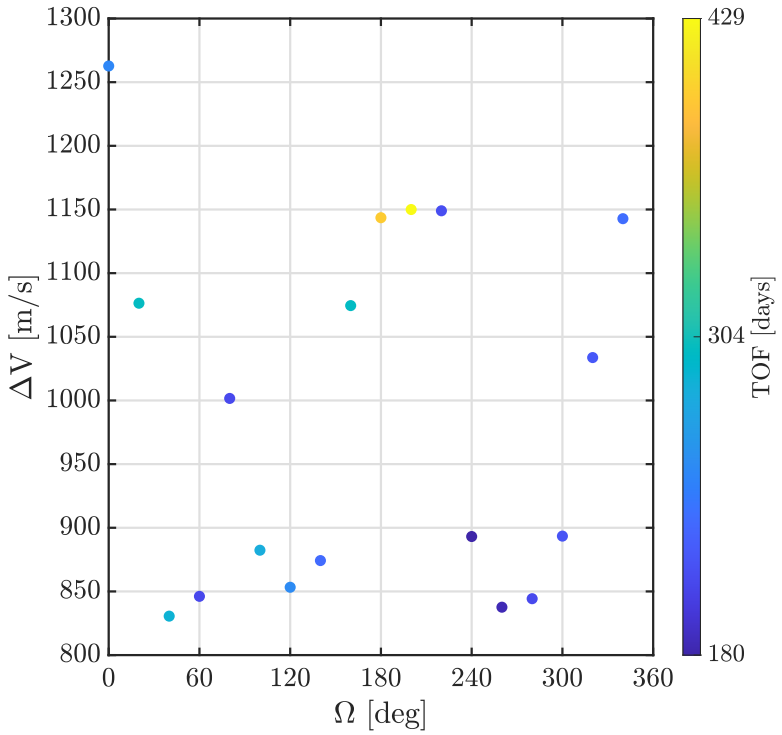

Figure 6.19. : Total ΔV required for locally optimal transfers to Sun-Earth L_2 southern halo at epoch of Dec 2, 2022 12:00:00.000

The injection location is significantly dependent on the maximum OIM magnitude desired; note that the OIM magnitude is only constrained and not the direction of the maneuver. In Figure 6.19, transfers at GTO departure locations of $\Omega = 40°$, i.e., an indirect transfer, and $\Omega = 260°$, a direct transfer, correspond to lower ΔV magnitudes. The transfers with the longer TOF have a departure location of $180° \leq \Omega \leq 200°$. Additionally, a summary of the maneuvers along the set of optimal transfer to the L_2 vicinity is provided in Table 6.3. In Table 6.3, the magnitude of the OIM is below the maximum magnitude defined in the corrections process and two transfer scenarios, with departure locations of $\Omega = 0°, 20°$, have OIM values of zero m/s. This suggests that the transfers from these two GTO departure locations, with the selected base epoch, utilize a transfer within the stable manifold structure associated with the southern L_2 halo orbit. Observe that, from Table 6.3, the average TIM magnitude is approximately 740 m/s, similar to the ΔV_{theo} magnitude corresponding to the energy, i.e., Jacobi Constant, difference between a GTO departure state and the southern halo orbit, see Table 5.1. The optimal transfer information presented in Figures 6.18-6.19 is

associated with a specified GTO departure epoch; however the curve of solutions constructed via the two-maneuver transfers is easily extended for any range of departure epochs.

Table 6.3. : Maneuver magnitude information for optimal transfers to Sun-Earth L_2 in m/s

Ω [deg]	TIM	DSM 1	DSM 2	OIM	Total
0	753	98	411	0	1263
20	735	153	188	0	1076
40	742	88	1	1	831
60	736	0	95	15	846
80	736	93	157	15	1002
100	738	20	110	14	882
120	739	62	37	15	853
140	743	53	63	15	874
160	748	215	96	15	1075
180	828	245	55	15	1144
200	761	252	122	15	1150
220	677	138	319	15	1149
240	737	0	141	15	893
260	735	39	48	15	838
280	737	0	93	14	844
300	740	0	152	2	893
320	743	0	276	15	1034
340	748	64	316	15	1143

6.3 Transfers into Quasi-Periodic Orbits in the Sun-Earth System

Trajectories into quasi-periodic orbits in the vicinity of the Sun-Earth Lagrange points are constructed by including a DSM along the transfer. In this example, transfers to quasi-periodic Lissajous orbits near Sun-Earth L_1 and L_2 are constructed with trajectories along the stable manifold structure associated with a Lissajous orbit and a bridging arc segment. This example is identified as either scenario C, with a tangent maneuver transfer, or scenario D, with a general maneuver transfer, from Table 6.1. Mission requirements, such as maximum/minimum SEV, α, constraints, may restrict a set of applicable quasi-periodic orbits for a secondary spacecraft. A multiple-shooting scheme is formulated and illustrated in Figure

6.20, to generate two-maneuver transfers into an injection point along a quasi-periodic orbit. The transfer in Figure 6.20 is propagated in reverse time such that a satellite travels on a trajectory along the stable manifold structure from an injection point on a quasi-periodic orbit. A single DSM is performed and the satellite in propagated in reverse time on a bridging arc segment towards a GTO departure position, $\bar{r}_{\text{dep}}$, near the Earth; note that there is an implied maneuver at the GTO departure location. The GTO departure location is parameterized via the angles λ and δ, see Figure 4.5(b). In Figure 6.20, the stable manifold

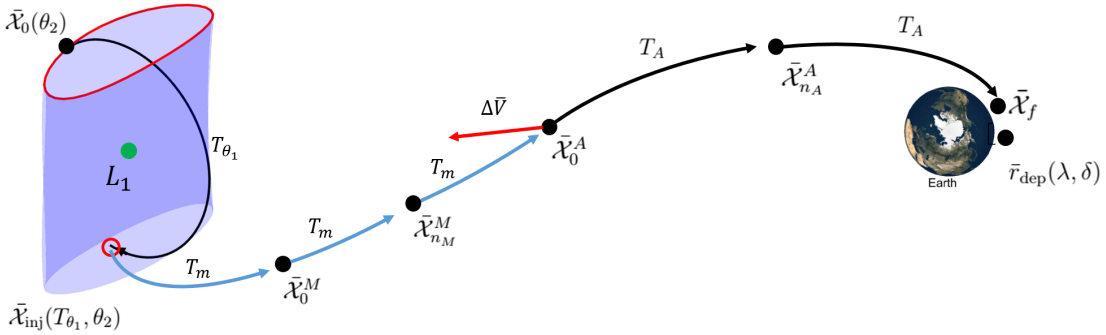

Figure 6.20. : Two-maneuver transfers to a general quasi-periodic orbit. Transfer arcs are propagated in reverse time from an injection point, the red circle, towards a GTO departure position, $\bar{r}_{\text{dep}}$

trajectory, in cyan, is divided into $n_M + 2$ trajectory arcs, and the bridging arc, in black, is divided into $n_A + 1$ arcs. An injection point along a quasi-periodic orbit is parameterized by T_{θ_1} and θ_2, where T_{θ_1} is the propagation time from a point along the invariant curve and θ_2 is an angle along the invariant curve, such that: $\bar{\mathcal{X}}_{\text{inj}}(T_{\theta_1}, \theta_2)$. Recall that an injection point is computed by propagating a state along the invariant curve, i.e., $\bar{\mathcal{X}}_{\text{inv}}(\theta_2)$, by time T_{θ_1}. The state along the invariant curve is defined as: $\bar{\mathcal{X}}_{\text{inv}}(\theta_2) = \bar{\mathcal{X}}^* + \bar{u}(0, \theta_2)$, where $\bar{\mathcal{X}}^*$ is the fixed point of a periodic orbit associated with the quasi-periodic family and $\bar{u}$ is a six-dimensional torus state. In this investigation, quasi-periodic orbits are constructed from two-dimensional tori and are initiated from a reference periodic orbit. The multiple-shooting

scheme illustrated in Figure 6.20 is formulated as a TPBVP such that a free-variable vector is written as,

$$\bar{\mathfrak{X}} = \begin{bmatrix} \bar{\mathcal{X}}_0^M \\ \bar{\mathcal{X}}_1^M \\ \vdots \\ \bar{\mathcal{X}}_{n_M}^M \\ \bar{\mathcal{X}}_0^A \\ \bar{\mathcal{X}}_1^A \\ \vdots \\ \bar{\mathcal{X}}_{n_A}^A \\ T_{\theta_1} \\ \theta_2 \\ T_m \\ T_A \\ \lambda \\ \delta \end{bmatrix}, \tag{6.19}$$

where T_m is a time such that the total time on the stable manifold is: $T_{\text{mani}} = T_m(n_M + 2)$, and T_A is along the bridging arc defined as $T_{\text{arc}} = T_A(n_A + 1)$. The constraint vector that encapsulates scenario D in Table 6.1, i.e., a transfer including a general DSM maneuver, is denoted as,

$$\bar{F} = \begin{bmatrix} \bar{F}_{\text{mani,qpo}} \\ \bar{F}_{\text{bridge}} \\ \bar{F}_{\text{DSM}} \\ F_{\text{apsis}} \\ \bar{F}_{\text{alt}} \end{bmatrix}, \tag{6.20}$$

where the constraint vectors associated with state continuity along the bridging arc, $\bar{F}_{\text{bridge}}$, the DSM maneuver, $\bar{F}_{\text{DSM}}$, GTO departure apsis and altitude are denoted in Equations

(6.5)-(6.9). The constraint vector associated with state continuity along the stable manifold trajectory from an injection point along a quasi-periodic orbit, $\bar{F}_{\text{mani,QPO}}$, is written as,

$$\bar{F}_{\text{mani,qpo}} = \begin{bmatrix} \bar{\mathcal{X}}\left(T_m, \bar{\mathcal{X}}_M(T_{\theta_1}, \theta_2)\right) - \bar{\mathcal{X}}_0^M(0) \\ \bar{\mathcal{X}}_0^M(T_m) - \bar{\mathcal{X}}_1^M(0) \\ \vdots \\ \bar{\mathcal{X}}_{n_M-1}^M(T_m) - \bar{\mathcal{X}}_{n_M}^M(0) \end{bmatrix}, \tag{6.21}$$

where the final position and velocity vectors, $\bar{r}_f$ and $\bar{v}_f$, respectively, are components of the final propagated state of $\bar{\mathcal{X}}_{n_A}^A$, i.e., $\bar{\mathcal{X}}_{n_A}^A(T_A)$. The formulated multiple shooting scheme has an associated Jacobian matrix defined as,

$$\mathbf{D}\bar{\mathbf{F}} = \begin{bmatrix} \mathbf{D_{x_m}}\bar{\mathbf{F}} & \mathbf{D_{x_A}}\bar{\mathbf{F}} & D_{T_{\theta_1}}\bar{F} & D_{\theta_2}\bar{F} & D_{T_m}\bar{F} & D_{T_A}\bar{F} & D_\lambda\bar{F} & D_\delta\bar{F} \end{bmatrix}. \tag{6.22}$$

Observe that the matrix components, $\mathbf{D_{x_m}}\bar{\mathbf{F}}$, $\mathbf{D_{x_A}}\bar{\mathbf{F}}$, $D_{T_m}\bar{F}$, $D_{T_A}\bar{F}$, $D_\lambda\bar{F}$, and $D_\delta\bar{F}$ of the Jacobian in Equation (6.22) are similar to the two-maneuver transfer scenario for periodic orbits and are presented in Appendix D. The partial derivatives of the constraint vector in Equation (6.20) with respect to T_{θ_1} and θ_2 are denoted as,

$$D_{T_{\theta_1}}\bar{F} = \begin{bmatrix} D_{T_{\theta_1}}\bar{F}_{\text{mani,qpo}} \\ \bar{0} \\ \bar{0} \\ \bar{0} \\ \bar{0} \end{bmatrix}, \tag{6.23}$$

$$D_{\theta_2}\bar{F} = \begin{bmatrix} D_{\theta_2}\bar{F}_{\text{mani,qpo}} \\ \bar{0} \\ \bar{0} \\ \bar{0} \\ \bar{0} \end{bmatrix}, \tag{6.24}$$

where the partial derivative of the state continuity of the stable manifold trajectory is expanded as,

$$D_{T_{\theta_1}} \bar{F}_{\text{mani}} = \begin{bmatrix} \frac{\partial \bar{\mathcal{X}}_M(T_m)}{\partial \bar{\mathcal{X}}_M(0)} \frac{\partial \bar{\mathcal{X}}_M(0)}{\partial T_{\theta_1}} \\ \bar{0} \\ \vdots \\ \bar{0} \end{bmatrix}. \tag{6.25}$$

The stable manifold state, $\bar{\mathcal{X}}_M$, from an injection point along a quasi-periodic orbit is defined via Equation (5.22) and the associated partials are presented in Equations (5.33)-(5.34). Additionally, the value of $D_{\theta_2} \bar{F}_{\text{mani,qpo}}$ is computed via finite difference numerical techniques. The free-variable and constraint vectors expressed in Equations (6.19) and (6.20) correspond to a general DSM, i.e., the maneuver direction is not constrained. The dimension of the Jacobian matrix for the general DSM scenario, i.e., Equation (6.22), is $\dim(\mathbf{D}\bar{\mathbf{F}}) = 6(n_M + n_A + 1) + 7 \times 6(n_M + n_A + 2) + 6$, such that the dimension of the solution space is equal to the nullity of the Jacobian, i.e., $\text{nullity}(\mathbf{D}\bar{\mathbf{F}}) = 5$. Note that the derived dimension of the solution space assumes that all columns and rows of the Jacobian matrix are linearly independent. The general two-maneuver transfer scenario is consistent with transfer Scenario D in Table 6.1. To formulate a transfer scenario into a fixed quasi-periodic orbit with a tangential maneuver, Scenario C in Table 6.1, the tangential constraint in Equation (6.11) is appended into the constraint vector in Equation (6.20). Additionally, the maneuver magnitude, ΔV, is added to the free-variable vector in Equation (6.19). The resulting Jacobian associated with a tangential maneuver has a dimension equal to: $\dim(\mathbf{D}\bar{\mathbf{F}}) = 6(n_M + n_A + 1) + 10 \times 6(n_M + n_A + 2) + 7$, with a three-dimensional solution space which is consistent with Scenario C in Table 6.1. Observe that there is no information regarding the Transfer Injection Maneuver, i.e., the transfer performed at the GTO departure location, in this multiple-shooting formulation. The end state, $\bar{\mathcal{X}}_f$, of the reversely propagated two-maneuver transfer is a specified altitude and apsis condition which allows the magnitude of the TIM to vary. In this analysis, surfaces of solutions are constructed to generated transfers into a specified quasi-periodic orbit in the Sun-Earth system over a range of GTO departure locations near the Earth.

6.3.1 Transfers into L_1 Lissajous Orbits

A surface of solutions representing two-maneuver transfers into a specified Lissajous orbit near Sun-Earth L_1 is constructed via a multiple-shooting strategy. The transfer from a GTO departure location near the Earth is composed of a bridging arc segment and a stable manifold trajectory arc as illustrated in Figure 6.20. The desired orbit is a Lissajous orbit, i.e., a quasi-periodic orbit, near Sun-Earth L_1. By implementing the numerical techniques outlined in Section 3.4, a family of Lissajous orbits, originating from a vertical orbit, is constructed with a fixed Jacobi Constant value of: $\mathcal{C} = 3.000876398$. The family of Lissajous orbits is plotted in Figure 6.21, where the initial vertical orbit is in magenta and different members of the Lissajous orbit family are in blue. Note that this family of Lissajous orbits includes members that are "taller", i.e., have higher z-amplitude compared to the y-amplitude, or "shorter", have a higher y-amplitude. To maintain the science and operational requirements imposed on previous L_1 orbiters, such as the ACE[11] spacecraft or the Deep Space Climate Observatory (DSCVR)[40] spacecraft, a "shorter" Lissajous orbit is selected and displayed in black in Figure 6.21. In this application, a quasi-periodic orbit with charac-

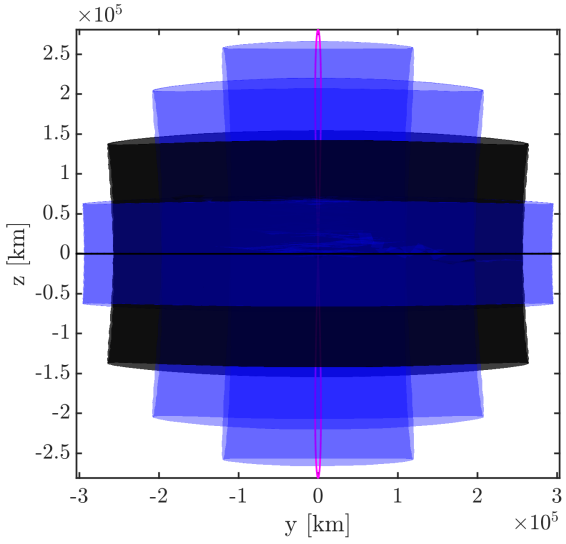

Figure 6.21. : Family of Lissajous orbits with a Jacobi Constant of $\mathcal{C} = 3.0008764$. The selected Lissajous orbit for this analysis is in black

teristics similar to that designed for the ACE spacecraft is selected as the target destination. The ACE spacecraft is in an L_1 Lissajous orbit with approximate x-, y-, and z-amplitudes of $81,755$ km, $264,071$ km, and $154,406$ km, respectively [11]. An orbit with similar amplitudes is selected, i.e., the orbit in black in Figure 6.21, from a family of Lissajous orbits constructed with a fixed Jacobi Constant value, $C = 3.000876398$, in the Sun-Earth system. A communications constraint imposed on the ACE spacecraft requires the trajectory to remain outside the Solar Exclusion Zone, defined as $\alpha_{SEZ} = 5^\circ$ and illustrated in Figure 5.52, for this investigation. Stationkeeping (STK) strategies have been developed and successfully implemented to maintain the Lissajous trajectory outside the SEZ; however, the focus of this application is the construction of a transfer into a Lissajous orbit at an ideal location, i.e., an injection point, that will maximize the time outside the SEZ before an STK maneuver is necessary.

The search for an ideal injection point that maximizes the time outside the SEZ, T_{out}, is formulated as the search for an angle, θ_2, along the invariant curve. Recall that the quasi-periodic orbits in this investigation are numerically constructed from two-dimensional tori, refer to Section 3.4 for further discussion. An injection point along a quasi-periodic orbit is parameterized by T_{θ_1} and θ_2, where T_{θ_1} is the propagation time from a point along the invariant curve and θ_2 is an angle along the invariant curve, such that: $\bar{\mathcal{X}}_{\text{inj}}(T_{\theta_1}, \theta_2)$. The state corresponding to an injection point is computed by propagating a state along the invariant curve, i.e., $\bar{\mathcal{X}}_{\text{inv}}(\theta_2)$, over time, T_{θ_1}. The state along the invariant curve is defined as: $\bar{\mathcal{X}}_{\text{inv}}(\theta_2) = \bar{\mathcal{X}}^* + \bar{u}(0, \theta_2)$, where $\bar{\mathcal{X}}^*$ is the fixed point of a periodic orbit associated with the quasi-periodic family and $\bar{u}$ is a six-dimensional torus state. In the search for an ideal injection point, the propagation time is assumed to be zero, $T_{\theta_1} = 0$, that is, the ideal injection point lies along the invariant curve and is dependent on the angle θ_2. The state along the invariant curve, $\bar{\mathcal{X}}_{\text{inv}}(\theta_2)$, is propagated along the Lissajous orbit and the SEV angle, α, is illustrated in Figure 5.52 and computed via Equation (5.56). The computation of a trajectory arc along a quasi-periodic orbit is consistent with the following steps:

1. Identify an initial angle, θ_2^0, along the invariant curve. Create the state along the invariant curve: $\bar{\mathcal{X}}_{\text{inv}}^0 = \bar{\mathcal{X}}^* + \bar{u}(0, \theta_2^0)$. Recall that $\bar{\mathcal{X}}^*$ is a fixed point associated with a periodic orbit used in the quasi-periodic orbit corrections process.

2. Propagate the current state, $\bar{\mathcal{X}}_{\text{inv}}^0$, with the mapping time, T_1, associated with the quasi-periodic orbit.

3. Identify the next state along the invariant curve. The next angle along the invariant curve is: $\theta_2^1 = \theta_2^0 + \rho$, where ρ is the rotation angle corresponding to the quasi-periodic orbit. Calculate the new state, $\bar{\mathcal{X}}_{\text{inv}}^1 = \bar{\mathcal{X}}^* + \bar{u}(0, \theta_2^1)$.

4. Propagate the new state, $\bar{\mathcal{X}}_{\text{inv}}^1$, with the mapping time T_1.

5. Connect the beginning of the trajectory from $\bar{\mathcal{X}}_{\text{inv}}^1$ to the end of the trajectory from $\bar{\mathcal{X}}_{\text{inv}}^0$.

6. Repeat steps 3-5 for any number of revolutions around the quasi-periodic orbit.

Note that this representation of the quasi-periodic trajectory utilizes the approximation of the invariant curve from a truncated Fourier series. The time above the SEZ threshold, i.e., T_{out}, for 13 revolutions on the Lissajous trajectory corresponding to a range of θ_2 values is plotted in Figure 6.22. Points A and B identified in Figure 6.22 correspond to the θ_2 angles: 152.85° and 335.35°, respectively. The trajectories that emerge from the identified injection points contain the maximum time above the SEZ threshold, $\alpha_{SEZ} = 5°$, before crossing into the SEZ cone. In Figure 6.22, several points in red, i.e., trajectories along the Lissajous orbit, are defined by longer intervals, higher T_{out} values, outside the SEZ than trajectories indicated by points A and B. However, the trajectories corresponding to the red points initially violate the SEZ cone and are plotted in Figure 6.23. The time history of the SEV angle corresponding to the trajectories from four distinct injection locations along the specified Lissajous orbits are presented in Figure 6.23. Two viable injection points are (2) and (4) from the plot in Figure 6.23, note that the SEV angle of the first revolution lies above the SEZ constraint line of $\alpha_{\text{SEZ}} = 5°$. The two non-viable options are represented by injection points (1) and (3) where the SEV angle of the initial revolution along the Lissajous

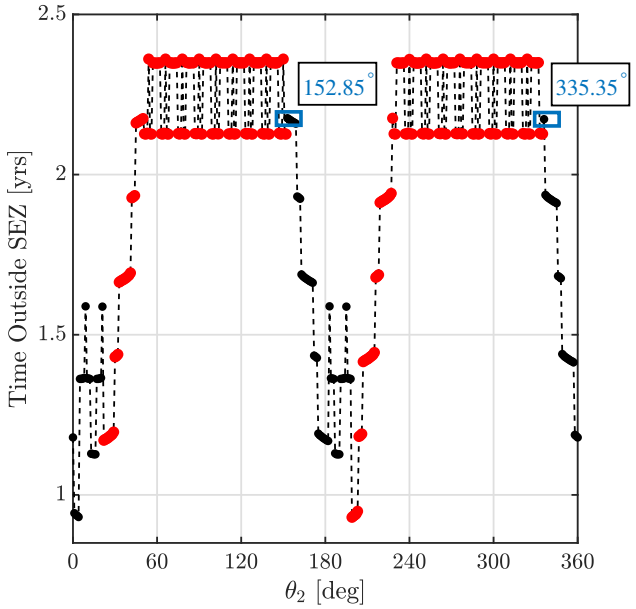

Figure 6.22. : Total time outside the SEZ for different injection points along the invariant curve corresponding to the desired Lissajous orbit. Points in red are not viable as they enter the SEZ during the first revolution. The two highlighted injection locations offer the maximum time outside the SEZ

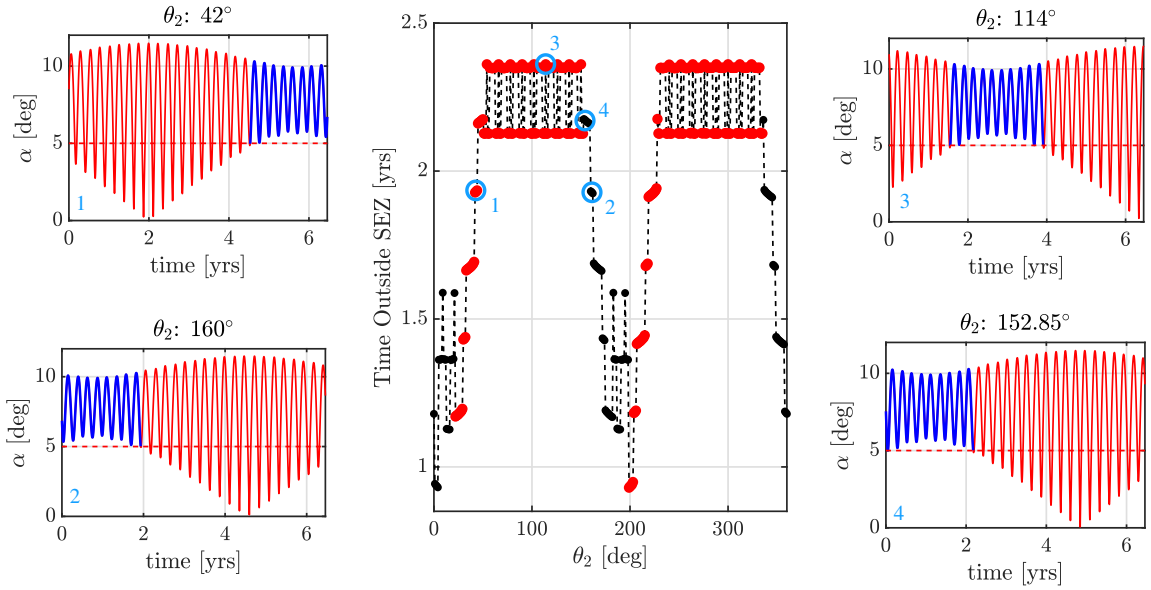

Figure 6.23. : Time histories of the SEV angle for different injection locations along a specified Lissajous orbit. Sections of the trajectories in red violate the SEZ, defined as $\alpha_{\text{SEZ}} = 5°$

orbit crosses into the SEZ region. Several injection points have similar SEV time histories to injection point (3) in Figure 6.23, and while they provide longer times outside the SEZ, these injections points are not viable for consideration due to a violation during the first revolution. The characterization of the invariant curve is not unique, therefore the θ_2 values in Figure 6.22 are dependent on the characterization of the invariant curve via the truncated Fourier series. The trajectories corresponding to points A and B, i.e., the injection location with maximum time outside the SEZ, are plotted in Figures 6.24-6.25. The $\hat{x}$-$\hat{z}$ and $\hat{y}$-$\hat{z}$ projections of the trajectory corresponding to the $\theta_2 = 152.85°$ injection point are plotted in Figure 6.24. Observe the location of the trajectory for $\theta_2 = 152.85°$ is near the "top" of the Lissajous orbit and the violation point, i.e., the point along the quasi-periodic orbit that lies on the edge of the SEZ cone, is situated near the "bottom". Additionally, the SEZ cone is a three-dimensional object, such that, information regarding when a violation occurs, i.e., a crossing into the SEZ region, and when the trajectory is outside the SEZ is unclear with only the planar projections. For example, the $\hat{y}$-$\hat{z}$ projection in Figure 6.24 shows that a section of the trajectory crosses into the SEZ region, i.e., the red shaded region, however, this is not accurate as the depth of the SEZ cone is not easily presented in this projection. To accurately observe when a violation occurs, a polar plot is generated with the angular dimension corresponding to an angle ξ defined as $\xi = \tan^{-1}\left(\frac{z}{y}\right)$, computed with the y- and z-components of a state along a Lissajous trajectory, and the radial direction is the SEV angle α, defined in Equation (5.56). The polar plot in Figure 6.24 depicts four successful revolutions along the Lissajous trajectory from the injection point with $\theta_2 = 152.85°$; note that the SEZ constraint is the dashed red line. The $\hat{x}$-$\hat{z}$ and $\hat{y}$-$\hat{z}$ projections of the trajectory corresponding to the $\theta_2 = 335.35°$ injection point are plotted in Figure 6.24. The polar plot in Figure 6.25 reveals the location of the injection point and the violation point along a trajectory with six revolutions along a Lissajous orbit. From an observer at the Earth, the direction of the trajectory with $\theta_2 = 152.85°$ is counter-clockwise and the trajectory from an injection point with $\theta_2 = 335.35°$ is clockwise. In this analysis, transfers into the injection point corresponding to $\theta_2 = 152.85°$ are termed Type A transfer, the motion is counter-clockwise, and transfers into the injection with $\theta_2 = 335.35°$ are labeled as Type B transfers, the motion is clockwise.

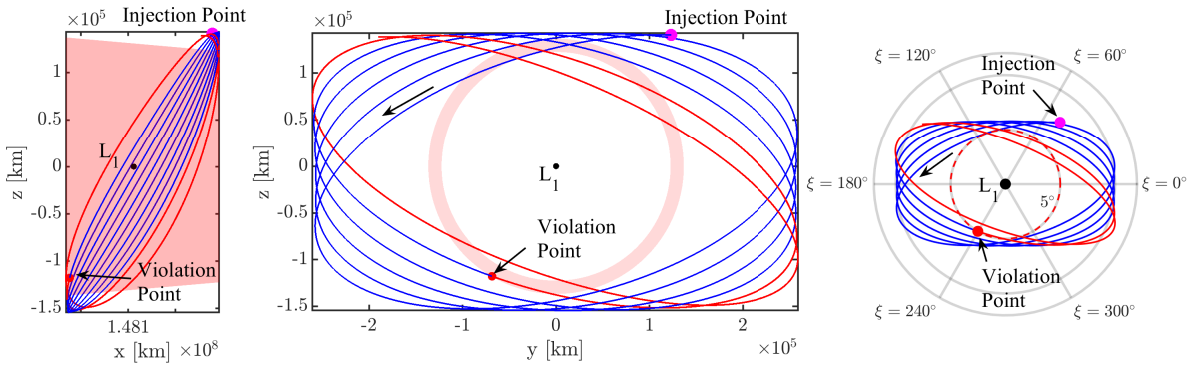

Figure 6.24. : Trajectory along Lissajous orbit from an injection point defined with $\theta_2 = 152.85°$ with six revolutions. In the $\hat{y}$-$\hat{z}$ projection, the direction of the trajectory is counter-clockwise as viewed by an observer at the Earth. The polar plot, the plot on the right, reveals the violation point of the trajectory, i.e., the red point. Transfers into this injection point are labeled as Type A

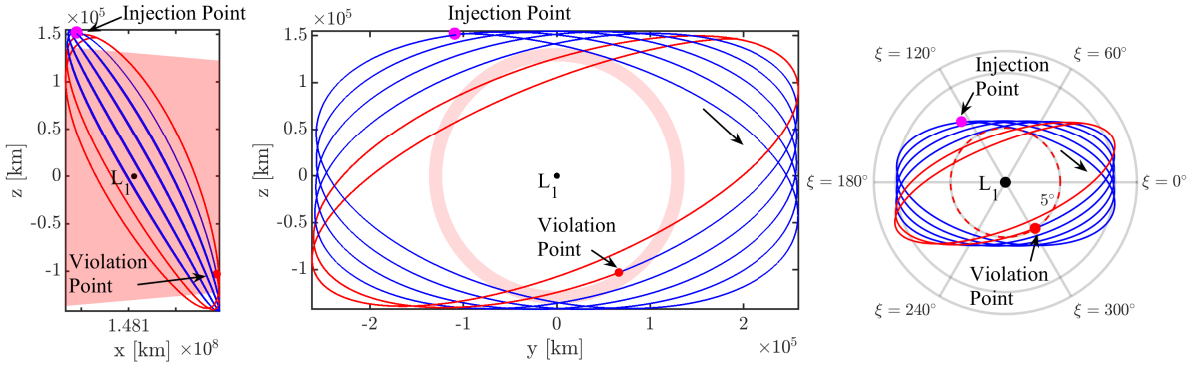

Figure 6.25. : Trajectory along Lissajous orbit from an injection point defined with $\theta_2 = 335.35°$ with six revolutions. In the $\hat{y}$-$\hat{z}$ projection, the direction of the trajectory is clockwise as viewed by an observer at the Earth. The polar plot, the plot on the right, reveals the violation point of the trajectory, i.e., the red point. Transfers into this injection point are labeled as Type B

Poincaré maps are leveraged to determine an initial guess, i.e., a two-maneuver transfer, constructed by leveraging the stable manifold structures associated with a Lissajous orbit and a bridging arc segment. The construction of a transfer into a quasi-periodic orbit, i.e., a Lissajous orbit, is essentially Scenarios C and D from Table 6.1. In this analysis, a transfer with a single general DSM originating from a GTO periapsis position near Earth is consistent with Scenario D which, from Table 6.1, has a five-dimensional solution space.

The objective of this example is to enter into an ideal injection point along a Lissajous orbit, that is, a fixed value of T_{θ_1} and θ_2; recalling that a state along the Lissajous orbit is parameterized by T_{θ_1} and θ_2. Therefore, the solution space consistent with this scenario is reduced to a three-dimensional surface. Additionally, for simplicity, the focus is the identification of transfers originating from different near-Earth positions along the ecliptic, i.e., the $\hat{x}$-$\hat{y}$ plane of the Sun-Earth rotating frame. This condition is satisfied via the introduction of the constraint $\delta = 0°$. The construction of a two-maneuver transfer is formulated as a multiple-shooting problem and defined via the free-variable and constraint vectors in Equations (6.19) and (6.20). The constraints associated with GTO departure states from the ecliptic, i.e., $\delta = 0°$, and a fixed injection location, i.e., $T_{\theta_1} = T_{\theta_1}^{\text{des}}$ and $\theta_2 = \theta_2^{\text{des}}$, are appended to the constraint vector in Equation (6.20). The solution space, i.e., the nullity of the expanded Jacobian is now two-dimensional; recall that the Jacobian corresponding to a general DSM in Equation (6.22) has nullity of nullity($\mathbf{D\bar{F}}$) = 5 and is consistent with Scenario D in Table 6.1. Finally, the solution space for two-maneuver transfers with a general DSM that insert into an ideal injection point along a Lissajous orbit from a GTO periapsis position along the Sun-Earth ecliptic is two-dimensional. To generate an initial guess for the two-maneuver transfer, the trajectories on the surface of the stable manifold corresponding to the Lissajous orbit are propagated in reverse time towards a surface of section. The position vector of the GTO departure position is a function of δ and λ as illustrated in Figure 4.5(b), with a fixed altitude, 185 km, with respect to the Earth. The GTO periapsis is situated along the Sun-Earth $\hat{x}$ line on the opposite side of the Sun and Earth; such a location corresponds to $\delta = 0°$ and $\lambda = 0°$. The initial guess for the velocity vector associated with the departure positions, i.e., the bridging arc segment, is constructed by applying a maneuver ΔV in a direction perpendicular to the radial direction of the GTO periapsis; note that the radial direction is with respect to the Earth. The direction of the departure velocity vector varies such that a set of bridging arc transfers is generated when the states are forward propagated towards a surface of section. A surface of section, defined as $y = 2.69\text{x}10^5$ km in the rotating frame, is selected to produce the initial conditions and generate a two-maneuver transfer with a general DSM. The points in red in Figure 6.26(a) are the second returns to the surface of section from a set of bridging arcs, propagated in forward time from the

GTO departure position, and the blue points correspond to the stable manifold trajectories, propagated in reverse time from the Lissajous injection points. An initial guess is produced with a pair of blue and red points that are close in position in the $\hat{x}$-$\hat{z}$ projection and is plotted in Figure 6.26(b). The solution space for a transfer into a Lissajous orbit with a

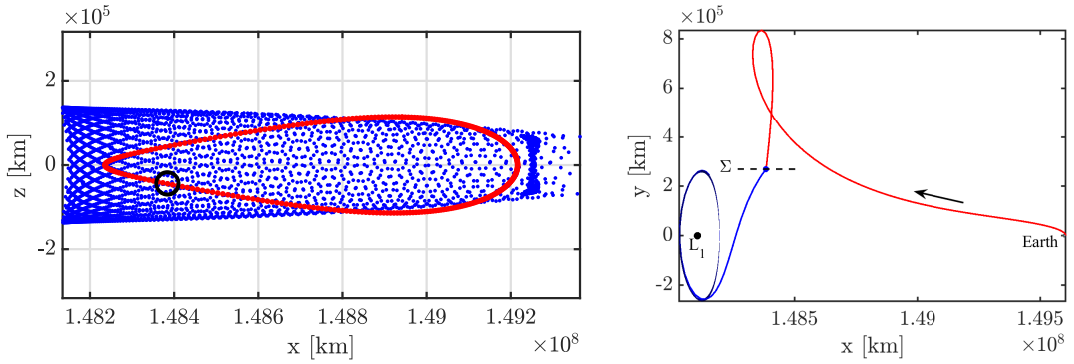

Figure 6.26. : (a) Poincaré map for trajectories along the stable manifold (blue) and connecting arcs (red). The selected initial guess is depicted by the black circle (b) Selected initial guess

single maneuver is constructed via a numerical continuation scheme. In Figure 6.22, the values of $\theta_2 = 335.35°, 152.85°$ are identified as desired injection points with $T_{\theta_1} = 0$ into the selected Lissajous orbit. The initial guess in Figure 6.26(b), from a fixed λ and δ, is divided into a series of discontinuous arcs, consistent with a multiple-shooting scheme, and a feasible solution is constructed via a multidimensional Newton's algorithm. Recall that the trajectories, consistent with scenarios in Table 6.1, are propagated in reverse time and a single general DSM is performed, as illustrated in Figure 6.20. The objective is the construction of the two-dimensional solution surface of transfers from the GTO departure positions along the Sun-Earth ecliptic. The selected initial guesses in Figure 6.26(b) do not correspond to the ideal injection locations, i.e., $\theta_2 = 335.35°, 152.85°$. The first step is a transfer into one of the two possible ideal injection locations. By reformulating the constraint conditions in Scenario D in Table 6.1 with Equation (6.1), the variables for the transfer are: T_{θ_1}, θ_2, T_m, T_A, λ, δ, and $\Delta\bar{V}_{\text{gen}}$, where $\Delta\bar{V}_{\text{gen}} = [\Delta V_x, \Delta V_y, \Delta V_z]^T$. There are nine free-variables and two departure constraints corresponding to: apsis and altitude. Note that the departure

conditions, via Equation (6.1), are defined as a four-dimensional vector and the addition of nodes along the stable manifold arc or bridging arc, consistent with a multiple-shooting technique, do not change the number of free-variables necessary. The goal is a search for a transfer into a desired injection point, defined by θ_2, therefore, four variables, T_{θ_1}, T_m, λ, and δ, remain constant so the solution space representing the transfers is a one-dimensional curve. A pseudo-arclength continuation strategy is leveraged to create a curve of transfers with varying θ_2 and T_A values. A curve can also be generated by fixing any combination of two free-variables from T_{θ_1}, T_m, and T_A with the fixed λ and δ angles. A curve of transfers is displayed in Figure 6.27(a); recalling that T_{mani} and T_{arc} are the total times along the stable manifold trajectory and the bridging arc as illustrated in Figure 6.20. This curve is not

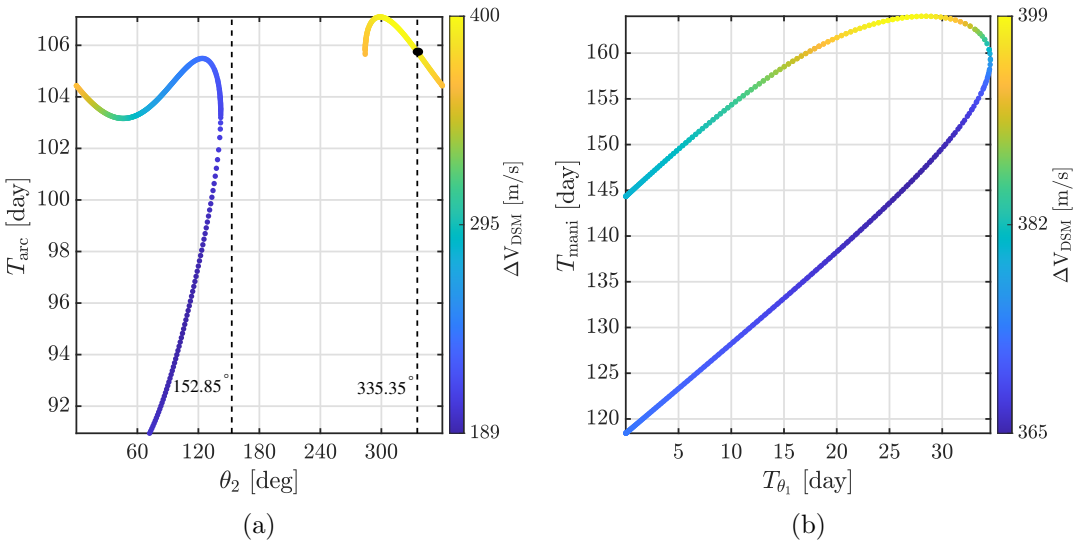

Figure 6.27. : (a) Initial guess curve - search for θ_2 (b) Solution curve for fixed $\theta_2 = 335.35°$ and T_{mani}

a complete representation of the solution space and the only point of interest is a transfer with corresponding $\theta_2 = 335.35°$ or $152.85°$; one such instance is identified in Figure 6.27(a). The time outside the SEZ reported in Figure 6.22 corresponds to a trajectory with $T_{\theta_1} = 0$, therefore the transfer from 6.27(a) is utilized as an initial point to generate a separate curve with varying T_{θ_1} and T_m. To construct the curve in Figure 6.27(b), λ, δ, and θ_2 are fixed along with one of the following variables: T_m or T_A. Two points on the solution curve in Figure 6.27(b) possess the desired $T_{\theta_1} = 0$. Finally, a surface of transfers is generated from

the sample transfer with the desired θ_2 and T_{θ_1} values, i.e., the values that correspond to the desired injection point on the Lissajous orbit. The surface, or family of transfers, is created through a pseudo-arclength continuation process by fixing θ_2 and T_{θ_1}, and one of the following variables: T_m, T_A, and λ. Recall that the objective is an exploration of the solution space for all possible GTO orientations and, in this application, only transfers such that the departure is from a GTO periapsis located along the Sun-Earth ecliptic are considered, i.e., $\delta = 0°$. The enclosed transfer solution surface for a region around the Earth, such that $-40° \leq \lambda \leq 20°$ is depicted in Figure 6.28(a). In the transfer scenarios presented in Table 6.1, there is no information about the maneuver implemented at the GTO periapsis; a Transfer Injection Maneuver, i.e., TIM, is necessary to shift from the GTO departure position to the transfers on the solution curve, e.g., Figure 6.28(b). A summary of the steps to generate the solution surface for this example follows:

1. Identify injection location, θ_2, along the invariant curve of a quasi-periodic orbit.
2. Fix the departure location from Earth, i.e., fix λ and δ. Note that the departure location is an apsis with respect to the Earth with a fixed altitude.
3. Generate transfer arcs from the fixed departure location towards a surface of section.
4. Generate stable manifold trajectories from the desired quasi-periodic orbit. These are propagated in reverse time toward a surface of section.
5. Identify an initial guess from a Poincaré map constructed via the crossings onto the surface of section.
6. Search for a solution with the desired θ_2. A continuation strategy is implemented by fixing any combination of two from the variables: T_{θ_1}, T_m, T_A along with λ and δ.
7. Search for the solution with desired $T_{\theta_1} = 0$, by fixing θ_2, λ, δ and either T_m or T_A.
8. Explore the solution space for a fixed T_{θ_1}, θ_2, δ. The surface is created from a series of curves created from a continuation strategy. The curve is created by fixing one of the variables: T_m, T_A, or λ.

These steps can be generalized to search the solution space for any single DSM transfer to a specific quasi-periodic orbit. In summary, the continuation strategy implemented to

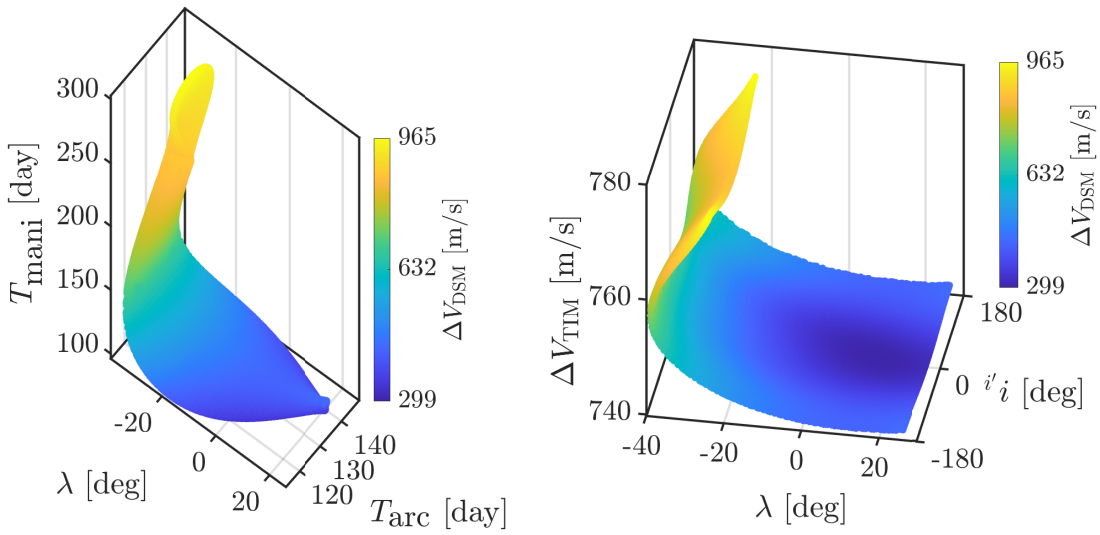

(a) (b)

Figure 6.28. : (a) surface of two-maneuver transfer solutions into a Lissajous orbit at an injection of $\theta_2 = 335.35°$, i.e., a Type B transfer, for an initial transfer at $\lambda = 0°$. (b) Transfer Injection Maneuver magnitudes for different GTO departure locations, λ, at varying inclinations. The data in both plots is represented via a range of colors corresponding to the DSM magnitude

create the surface of solutions relies on a pseudo-arclength continuation, such that a series of one-dimensional curves are stacked together to approximate the two-dimensional surface. A separate solution surface is constructed from the previous steps for a different initial departure position near the Earth, for example, given $\lambda = 90°$ and for $\delta = 0°$, see Figure 6.29(a), and $\lambda = 180°$ and $\delta = 0°$ in Figure 6.30(a). Recall that every point on this surface corresponds to a two-maneuver transfer. In Figures 6.28(b), 6.29(b), and 6.30(b), the range of the TIM magnitude is $740 \leq \Delta V_{\text{TIM}} \leq 780$ m/s, however, there is a larger variation in the magnitude of the ΔV_{DSM}. Additionally, the solution surfaces span the entire range of inclinations, $^{i'}$i, such that a single DSM transfer is computed for any GTO departure location, i.e., λ value. The surface information from Figures 6.28-6.30 fill the region of $-180° \leq \lambda \leq 180°$, therefore, it is possible to identify a feasible transfer into the selected

injection points on the Sun-Earth L_1 Lissajous trajectory from a range of GTO orientations.

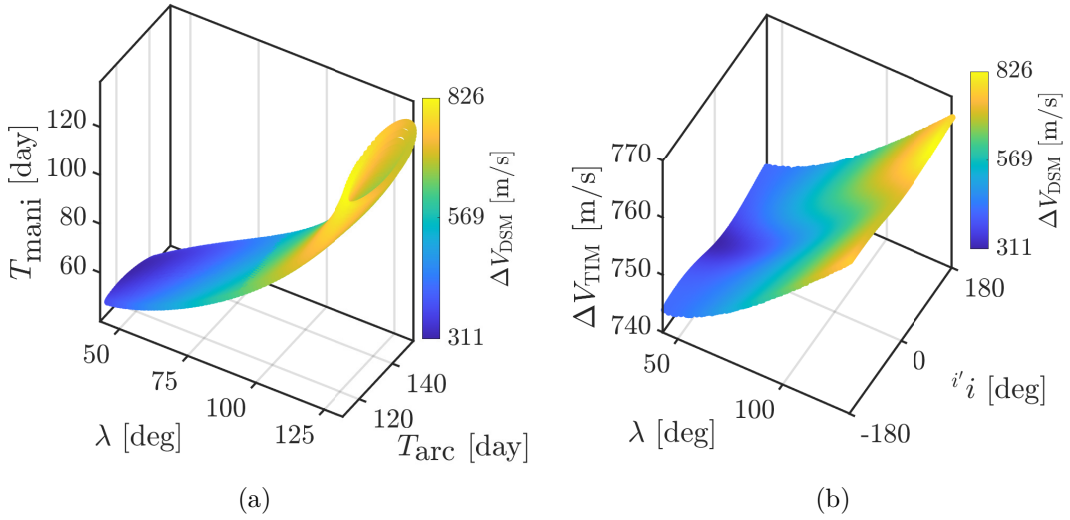

Figure 6.29. : (a) surface of two-maneuver transfer solutions into a Lissajous orbit at an injection with $\theta_2 = 335.35°$, i.e., a Type B transfer, for an initial transfer at $\lambda = 90°$. (b) Transfer Injection Maneuver magnitudes for different GTO departure locations, λ, at varying inclinations. The data in both plots is represented via a range of colors corresponding to the DSM magnitude

The surface of solutions associated with an injection point of $\theta_2 = 152.85°$, i.e., Type A transfers, for the desired Sun-Earth L_1 Lissajous orbit is constructed for a range of GTO departure locations. The surface of solutions that represent the two-maneuver transfers into the $\theta_2 = 152.85°$ injection point are plotted in Figure 6.31, 6.32, and 6.33. The objective is to create surfaces of solutions that span the entire GTO departure range of $-180° \leq \lambda \leq 180°$.

A subset of the complete surface is presented in Figure 6.31(a); note that this is also observed by inspecting the shape of the surface in Figure 6.31(b) which plots the inclination and ΔV_{TIM} information. Recall that the continuation strategy implemented to create the surface of solutions relies on a pseudo-arclength continuation, such that, essentially, a series of one-dimensional curves are stacked together to approximate the two-dimensional surface. In Figures 6.32(b) and 6.33(b), the surfaces are able to span a range of the GTO departure locations. To construct flexible transfers from a range of GTO departure locations, recalling

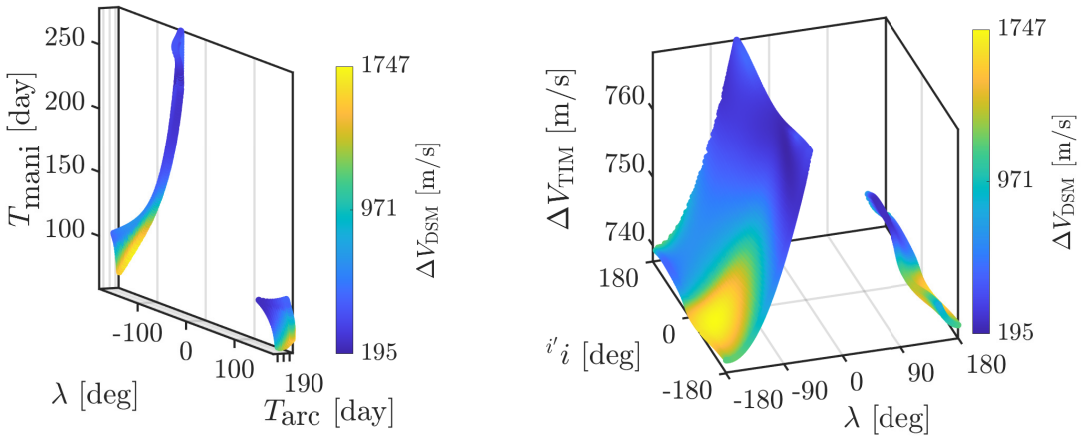

(a) (b)

Figure 6.30. : (a) surface of two-maneuver transfer solutions into a Lissajous orbit at an injection with $\theta_2 = 335.35°$, i.e., a Type B transfer, for an initial transfer at $\lambda = 180°$. (b) Transfer Injection Maneuver magnitudes for different GTO departure locations, λ, at varying inclinations. The data in both plots is represented via a range of colors corresponding to the DSM magnitude

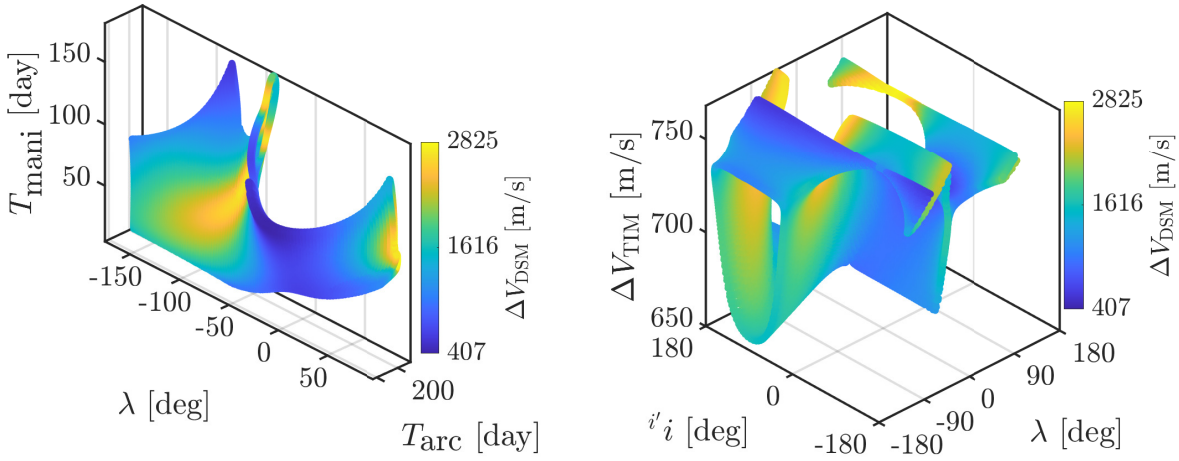

(a) (b)

Figure 6.31. : (a) surface of two-maneuver transfer solutions into a Lissajous orbit at an injection with $\theta_2 = 152.85°$, i.e., a Type A transfer, for an initial transfer at $\lambda = 90°$. (b) Transfer Injection Maneuver magnitudes for different GTO departure locations, λ, at varying inclinations

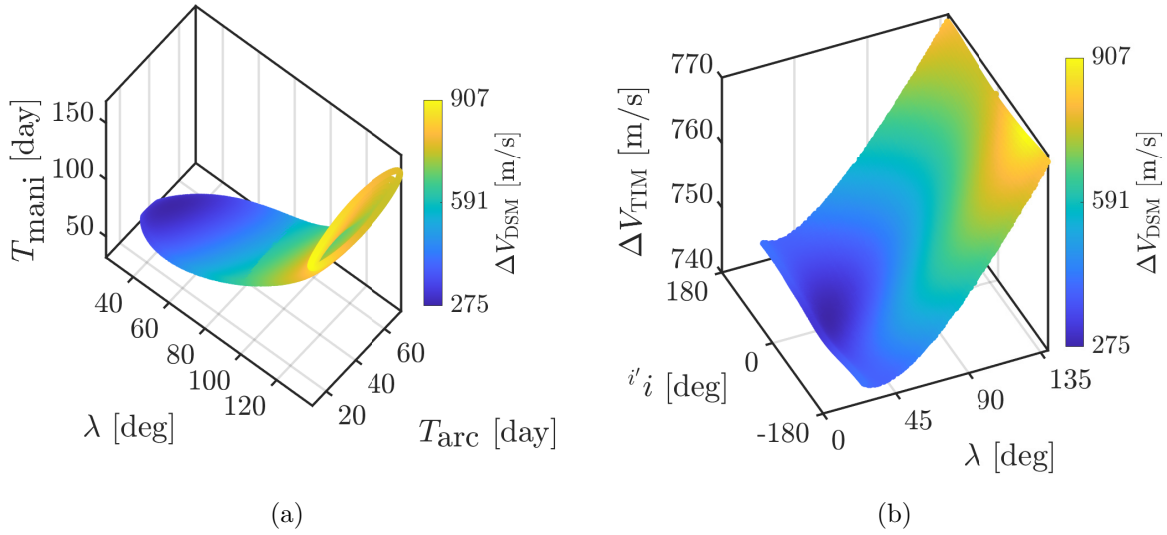

(a) (b)

Figure 6.32. : (a) surface of two-maneuver transfer solutions into a Lissajous orbit at an injection with $\theta_2 = 152.85°$, i.e., a Type A transfer, for an initial transfer at $\lambda = 90°$. (b) Transfer Injection Maneuver magnitudes for different GTO departure locations, λ, at varying inclinations

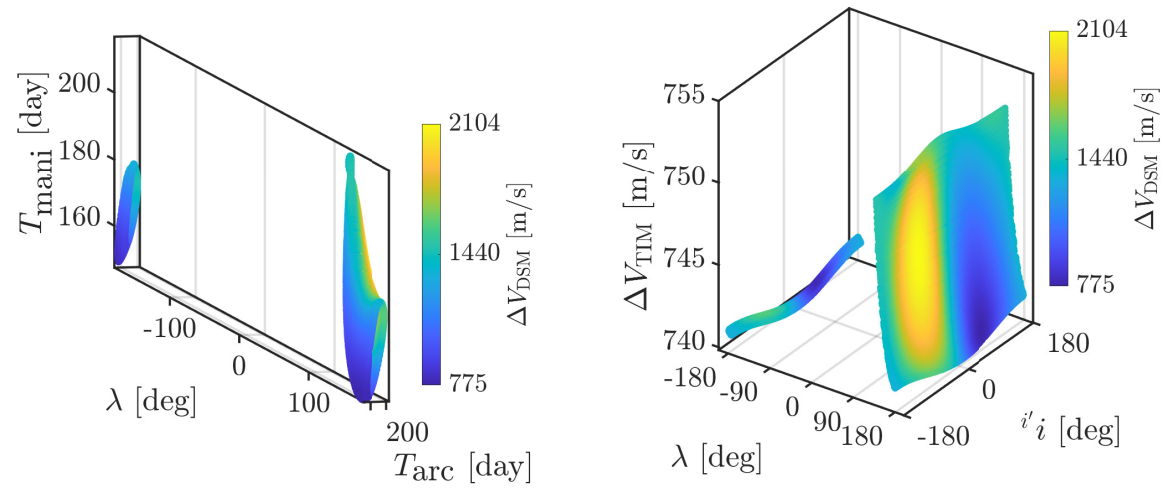

(a) (b)

Figure 6.33. : (a) surface of two-maneuver transfer solutions into a Lissajous orbit at an injection with $\theta_2 = 152.85°$, i.e., a Type A transfer, for an initial transfer at $\lambda = 90°$. (b) Transfer Injection Maneuver magnitudes for different GTO departure locations, λ, at varying inclinations

that the GTO departure is at periapsis, into specific injection locations along a specific Sun-Earth L_1 Lissajous orbit, a surface of solutions is generated via a multiple-shooting strategy. The two-maneuver transfers contained within the two-dimensional surface of solutions are generated along different GTO departure ranges, i.e., λ values, and serve as initial guesses to construct locally optimal solutions.

6.3.2 Transfers into L_2 Lissajous Orbits

Two-maneuver transfers to Lissajous orbits near the Sun-Earth L_2 point are generated for a range of GTO departure locations. In this analysis, two-maneuver transfers include a DSM, performed along the trajectory, and a TIM, performed at the GTO departure location, i.e., GTO periapsis. Additionally, transfers to a selected Lissajous orbit near L_2 are constructed via the multiple-shooting strategy illustrated in Figure 6.20. As a demonstration, transfers into a L_2 Lissajous orbit resembling the Gaia spacecraft are constructed from a reference GTO with a periapsis altitude of 185 km. The Gaia mission is a survey-type mission launched and operated by the European Space Agency [13]. The primary mission of Gaia is to observe and catalog precise mappings of the Milky Way galaxy with a secondary mission to analyze and discovery distant exoplanets. The satellite was launched in December 2013, as a primary payload, en route to the Sun-Earth L_2 vicinity; note that L_2 provides the adequate thermal, radiation, and observation requirements for Gaia to successfully meet its scientific objectives. A Lissajous orbit near L_2 is selected as the operational orbit of Gaia considering the limitations of the phased array antenna and Gaia's specific attitude strategy [76]. To satisfy these geometric constraints, the operational Lissajous orbit has a maximum Sun-satellite-Earth of 15° and approximate x-, y-, and z-amplitudes of $120,00$ km, $340,000$ km, and $180,000$ km, respectively [13]. Additionally, Gaia must avoid Earth eclipses to prevent thermal shocks to the science instruments and had an initial operation lifetime of 5 years, that is, the trajectory of the satellite was eclipse free throughout the transfer to the orbit and after injection into the Lissajous orbit. In this analysis, a Lissajous orbit similar to the Gaia mission is constructed by first generating a family of Lissajous orbits with a

fixed Jacobi Constant, i.e., $\mathcal{C} = 3.0008643$. A Lissajous orbit with similar characteristics to the Gaia mission is selected from the constructed quasi-periodic orbit family. Two-maneuver transfers are constructed to a Lissajous orbit with similar characteristics to the Gaia mission.

In constructing two-maneuver transfers for a secondary payload departing from a GTO to a desired Lissajous orbit near Sun-Earth L_2, an injection point along the quasi-periodic orbit is identified. A ideal injection location along the selected Lissajous orbit maximizes the time outside the eclipse region, i.e., the penumbra shadow cone illustrated in Figure 5.60. Recall that, in this analysis, quasi-periodic orbits are constructed from two-dimensional tori, such that any state along a quasi-periodic orbit is represented as: $\bar{\mathcal{X}}_{\text{inj}}(T_{\theta_1}, \theta_2)$. The state corresponding to an injection point is generated by propagating a state along the invariant curve, $\bar{\mathcal{X}}_{\text{inv}}(\theta_2)$, by a time T_{θ_1}; recalling that a state along the invariant curve is defined as: $\bar{\mathcal{X}}_{\text{inv}}(\theta_2) = \bar{\mathcal{X}}^* + \bar{u}(0, \theta_2)$. The vector $\bar{\mathcal{X}}^*$ is the fixed point of a periodic orbit associated with the quasi-periodic orbit and the $\bar{u}$ is the six-dimensional torus state, see Figure 3.12. In the search for an ideal injection point, the time T_{θ_1} is assumed to be zero, such that an injection point is essentially a point along the invariant curve; recall that this is approximated via the truncated Fourier Series in Equation (3.84). The steps for generating a trajectory along the Lissajous orbit from an originating injection point, $\bar{\mathcal{X}}_{\text{inv}}(\theta_2)$, are outlined in Section 6.3.1. The shadow angle, corresponding to the penumbra condition, for a trajectory along the Lissajous orbit is computed via Equation (5.73). The time outside the penumbra, T_{out}, for a range of injection points from the selected Lissajous orbit after 16 revolutions is plotted in Figure 6.34. Similar to the ACE-like Lissajous orbit in Figure 6.23, there are two possible injection points that maximize a time outside the penumbra shadow region. The injection points identified in Figure 6.34 correspond to the latitudinal angles of $\theta_2 = 93.8°, 273.95°$. Observe that there are injection points, i.e., values of θ_2, highlighted in red that correspond to longer times, however, these injection points initially cross into the Earth's penumbra region. In Figure 6.35, the time history of the shadow angle, ζ, for four selected injection points are plotted. The trajectories for (1),(2),(4) in Figure 6.35 correspond to viable injection points; recall that (4) is one of the identified ideal injection points. The trajectory for (3) is highlighted in red in Figure 6.35 and the time

history of the shadow angle in Figure 6.35 presents an initial crossing into the penumbra region immediately after injection. Several injection points have similar shadow angle time histories to injection point (3) in Figure 6.35, and while they present longer times outside the Earth penumbra, these injection points are not viable for consideration due to an initial violation during the first revolution. Recall that the characterization of the invariant curve is not unique, therefore, the θ_2 angle presented in Figures 6.34-6.35 are dependent on the characteriation of the invariant curve via the truncated Fourier series. The trajectories

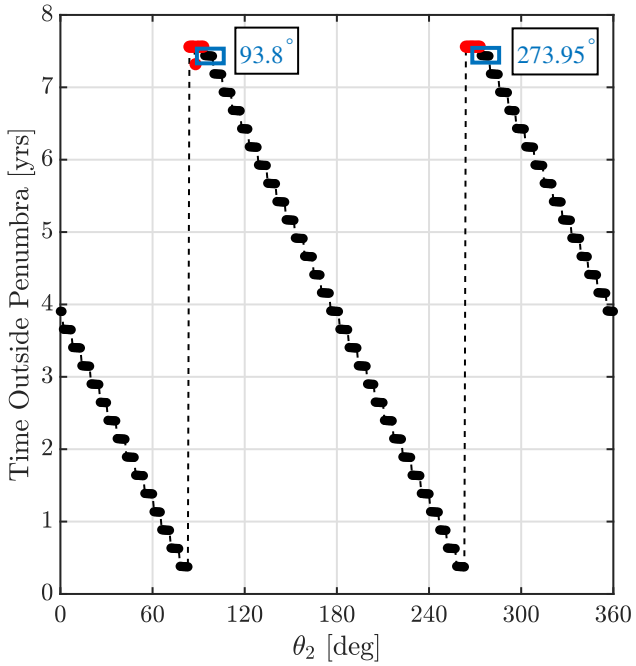

Figure 6.34. : Time outside the Earth penumbra for a series of injection points, parameterized via θ_2, along the selected Lissajous orbit

corresponding to the ideal injection points identified, i.e., $\theta_2 = 93.8°, 273.95°$, are plotted in Figures 6.36-6.37. In Figures 6.36-6.37, the $\hat{x}$-$\hat{z}$ and $\hat{y}$-$\hat{z}$ projections corresponding to the trajectories propagated from the ideal injection locations are plotted. In the $\hat{y}$-$\hat{z}$ projection corresponding to $\theta_2 = 93.8°$, i.e., Figure 6.36, the injection point states is situated near the left right and the direction of the trajectory is directed towards the top right; note that this is based on an Earth observer. Note that the penumbra eclipse condition is represented by a black cone in the $\hat{x}$-$\hat{z}$ projection and a black circle in the $\hat{y}$-$\hat{z}$ projection. The injection point state for $\theta_2 = 273.95°$ is located near the bottom right and the motion is towards the

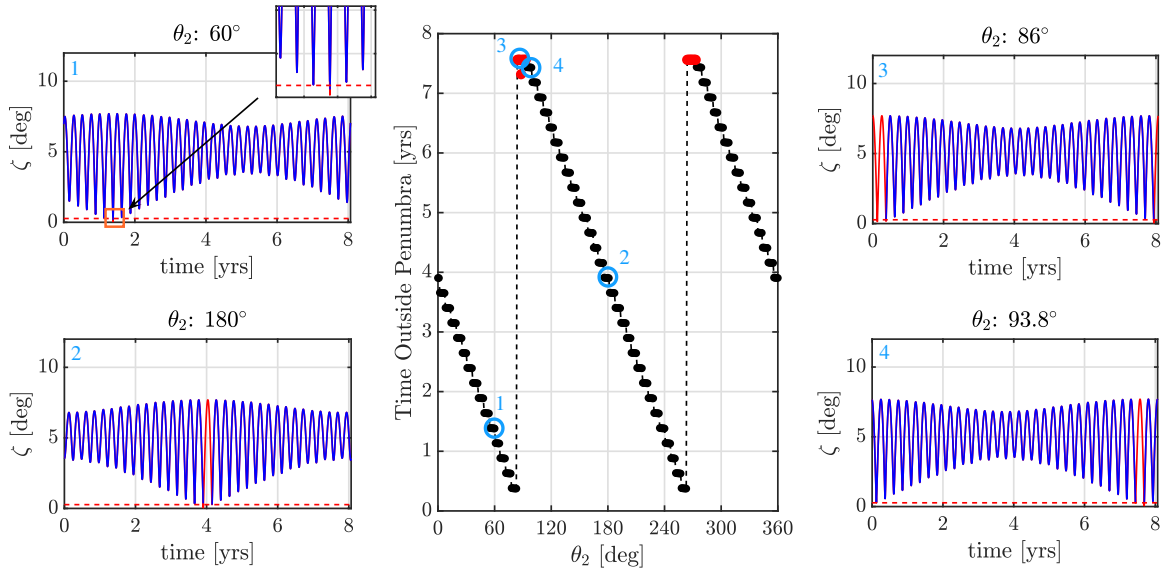

Figure 6.35. : Shadow angle, ζ, corresponding to the penumbral shadow region for selected injection points along quasi-periodic orbit. Regions highlited in red correspond periods where the trajectory crosses the penumbra region

top left corner. Recall that to accurately observe when a violation occurs for L_1 Lissajous orbits constrained by a SEZ cone, a polar plot is implemented. In the case for L_2 Lissajous orbits, the polar plot has an angular dimension defined by ξ, where $\xi = \tan^{-1} = \left(\frac{z}{y}\right)$, and the radial dimension is the shadow angle corresponding to the Earth penumbra, i.e., ζ defined in Equation (5.73). In Figures 6.36-6.37, the polar plot presents a zoomed-in view of the violation into the penumbra region. In Figure 6.36, the motion of the first couple of revolutions along the trajectory is counter-clockwise, from an Earth observer, such that, in this investigation, transfers into this injection point, i.e., $\theta_2 = 93.8°$, are termed Type A transfers. Transfers into the injection point of $\theta_2 = 273.95°$ are labeled as Type B transfers because, from Figure 6.37, the motion of trajectory post-injection is clockwise as observed from the Earth.

Poincaré maps are leveraged to determine an initial guess, i.e., a two-maneuver transfer, constructed by leveraging the stable manifold structures associated with a Lissajous orbit, a bridging arc segment, and a single DSM. Recall that the construction of a transfer with a DSM into a Lissajous orbit is essentially Scenarios C and D from Table 6.1. In this

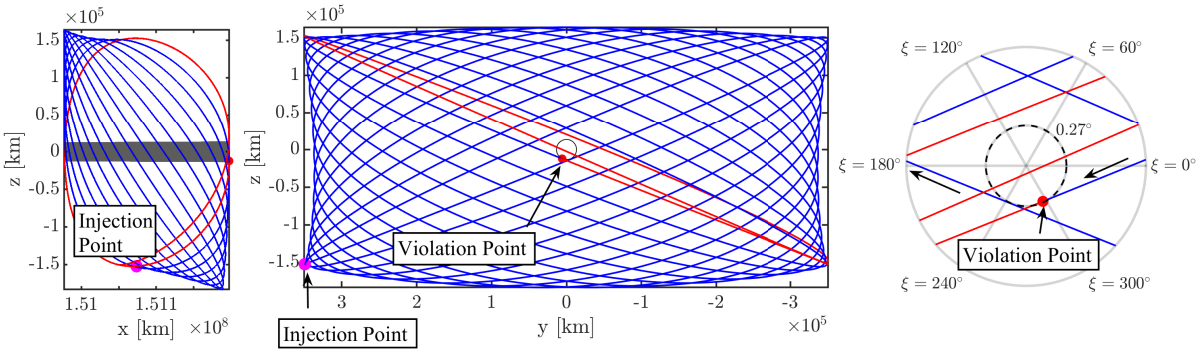

Figure 6.36. : Trajectory along Lissajous orbit from an injection point defined with $\theta_2 = 93.8°$ with 16 revolutions. In the $\hat{y}$-$\hat{z}$ projection, the direction of the trajectory is counter-clockwise as viewed by an observer at the Earth. The polar plot, the plot on the right, reveals the violation point of the trajectory, i.e., the red point. Transfers into this injection point are labeled as Type A

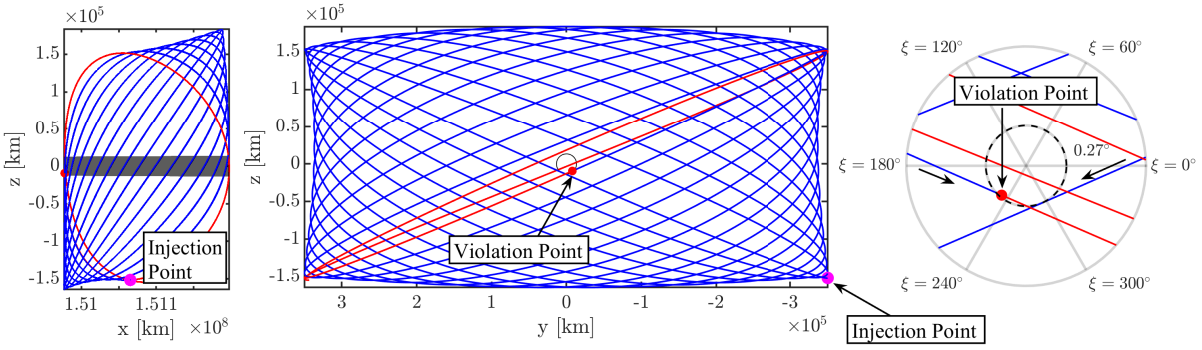

Figure 6.37. : Trajectory along Lissajous orbit from an injection point defined with $\theta_2 = 273.95°$ with 16 revolutions. In the $\hat{y}$-$\hat{z}$ projection, the direction of the trajectory is clockwise as viewed by an observer at the Earth. The polar plot, the plot on the right, reveals the violation point of the trajectory, i.e., the red point. Transfers into this injection point are labeled as Type B

analysis, a two-maneuver transfer with a single general DSM originating from a GTO periapsis position near the Earth is consistent with Scenario D which, from Table 6.1, has a five-dimensional solution space. In this demosntration, the secondary payload, i.e., a smallsat, enters the Lissajous orbit at an ideal injection point, that is, a fixed value of T_{θ_1} and θ_2; recalling that a state along the Lissajous orbit is parameterized via T_{θ_1} and θ_2. Therefore, the solution space consistent with this scenario is reduced to a three-dimensional surface. For

simplicity, the focus is to construct transfers originating from different GTO departure locations along the ecliptic, i.e., the $\hat{x}$-$\hat{y}$ plane of the Sun-Earth rotating frame. This condition is satisfied via the introduction of the constraint $\delta = 0°$. The construction of a two-maneuver transfer is formulated as a multiple-shooting problem and defined via the free-variable and constraint vectors in Equations (6.19) and (6.20). The constraints associated with GTO departure states from the ecliptic, i.e., $\delta = 0°$, and a fixed injection location, i.e., $T_{\theta_1} = T_{\theta_1}^{\text{des}}$ and $\theta_2 = \theta_2^{\text{des}}$, are appended to the constraint vector in Equation (6.20). The solution space is now two-dimensional, that is the solution space corresponding to a general DSM, i.e., Scenario D in Table 6.1, is reduced by three, Finally, the solution space for two-maneuver transfers that insert into an ideal injection point along a Lissajous orbit from a GTO periapsis position along the Sun-Earth ecliptic is two-dimensional. An initial guess for single two-maneuver transfer is generated via a Poincaré mapping using a geometric surface of section. After an initial guess is identified, the two-dimensional surface of solutions is created by pseudo-arclength continuation, the steps consistent with this methodology are outlined in Section 6.3.1. The surfaces in Figures 6.38-6.40 correspond to the injection point $\theta_2 = 93.8°$ and Figures 6.41-6.43 are associated with an injection point of $\theta_2 = 273.95°$.

The two-dimensional curve of solutions presented in Figures 6.38-6.43 span the range of GTO departure locations, i.e., λ. Observe that for both identified injection points, $\theta_2 = 93.8°, 273.95°$, the surfaces constructed cover the entire span of λ, that is, $-180° \leq \lambda \leq 180°$; recall that each point on the surface corresponds to a single two-maneuver transfer. In Figures 6.38-6.43, each point on the surface is plotted via a range of colors that represent the magnitude of a general DSM, i.e., the direction of performed DSM is unrestricted as opposed to a tangential maneuver. In Figures 6.38(b)-6.43(b), the magnitude of the TIM, the maneuver performed at the GTO departure location, is displayed for the associated surface. For the computed two-dimensional surfaces, the magnitude of the TIM is in the range of 740 m/s $\leq \Delta V_{\text{TIM}} \leq$ 780 m/s. The surfaces generated and plotted in Figures 6.38-6.43 only represent a subset of all the possible two-dimensional surfaces available. In this investigation, the information from the two-dimensional surfaces serve to construct optimal transfers into a selected Lissajous orbit.

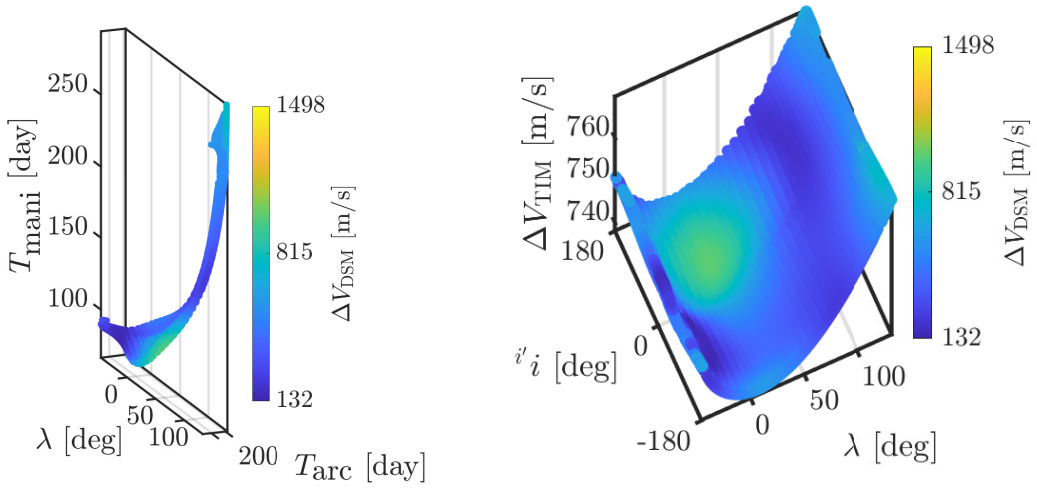

Figure 6.38. : (a) surface of two-maneuver transfer solutions into a Lissajous orbit at an injection with $\theta_2 = 93.8°$, i.e., a Type A transfer. (b) Transfer Injection Maneuver magnitudes for different GTO departure locations, λ, at varying inclinations. The initial guess corresponds to a GTO departure location of $\lambda = 0°$

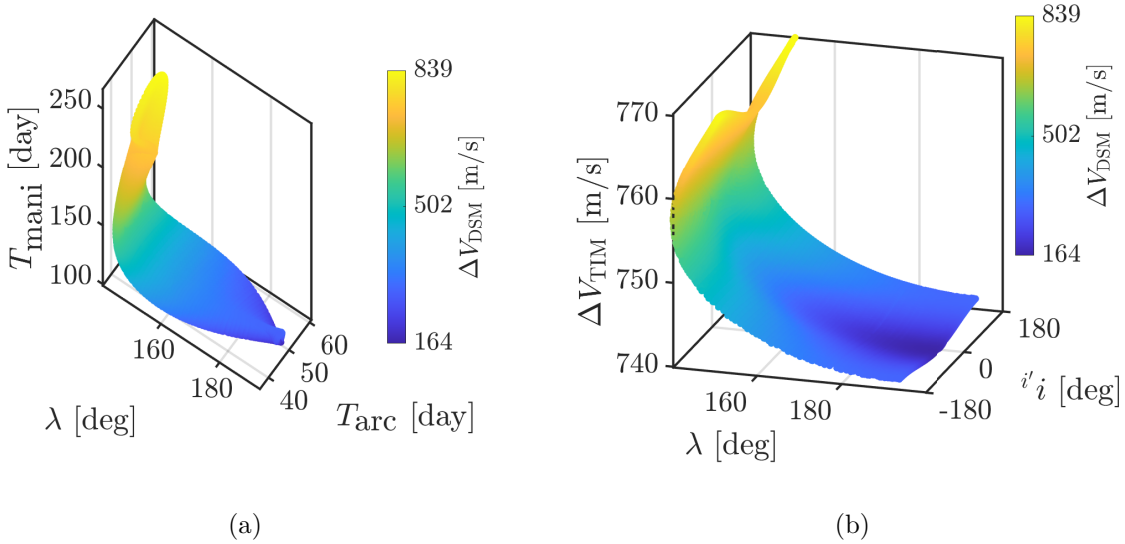

Figure 6.39. : (a) surface of two-maneuver transfer solutions into a Lissajous orbit at an injection with $\theta_2 = 93.8°$, i.e., a Type A transfer. (b) Transfer Injection Maneuver magnitudes for different GTO departure locations, λ, at varying inclinations. The initial guess corresponds to a GTO departure location of $\lambda = 180°$

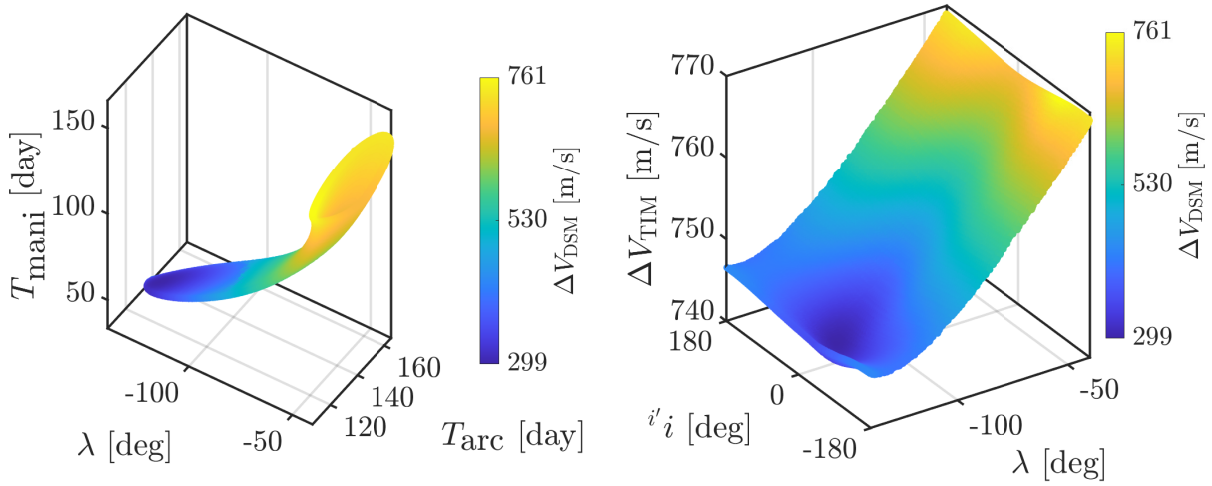

(a) (b)

Figure 6.40. : (a) surface of two-maneuver transfer solutions into a Lissajous orbit at an injection with $\theta_2 = 93.8°$, i.e., a Type A transfer. (b) Transfer Injection Maneuver magnitudes for different GTO departure locations, λ, at varying inclinations. The initial guess corresponds to a GTO departure location of $\lambda = 270°$

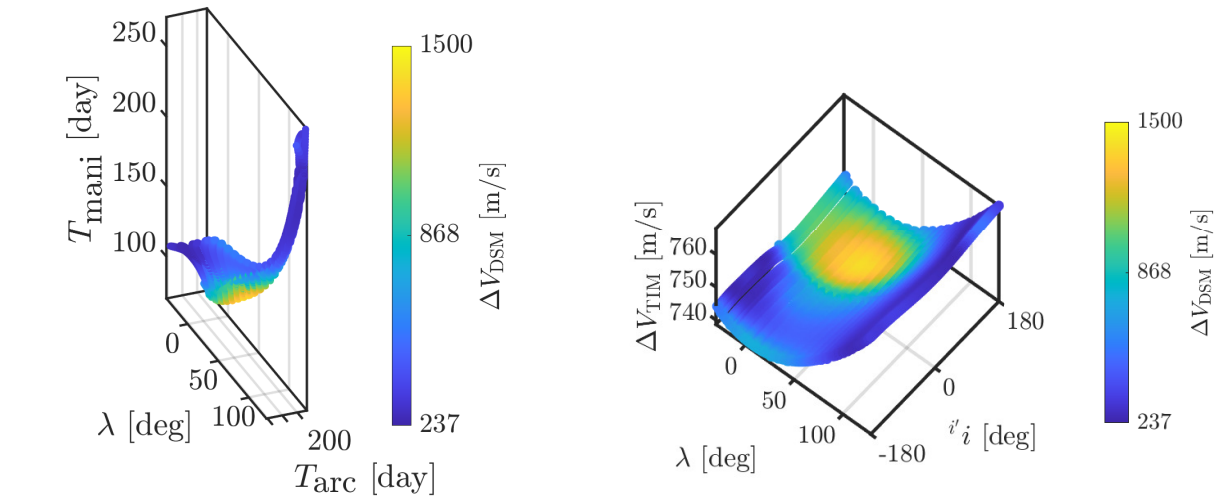

(a) (b)

Figure 6.41. : (a) surface of two-maneuver transfer solutions into a Lissajous orbit at an injection with $\theta_2 = 273.95°$, i.e., a Type B transfer. (b) Transfer Injection Maneuver magnitudes for different GTO departure locations, λ, at varying inclinations. The initial guess corresponds to a GTO departure location of $\lambda = 0°$

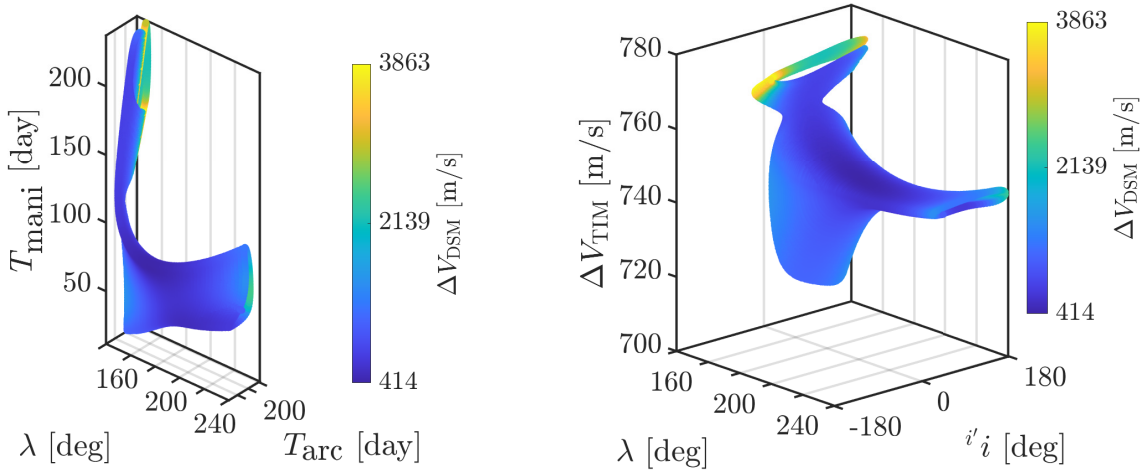

(a) (b)

Figure 6.42. : (a) surface of two-maneuver transfer solutions into a Lissajous orbit at an injection with $\theta_2 = 273.95°$, i.e., a Type B transfer. (b) Transfer Injection Maneuver magnitudes for different GTO departure locations, λ, at varying inclinations. The initial guess corresponds to a GTO departure location of $\lambda = 180°$

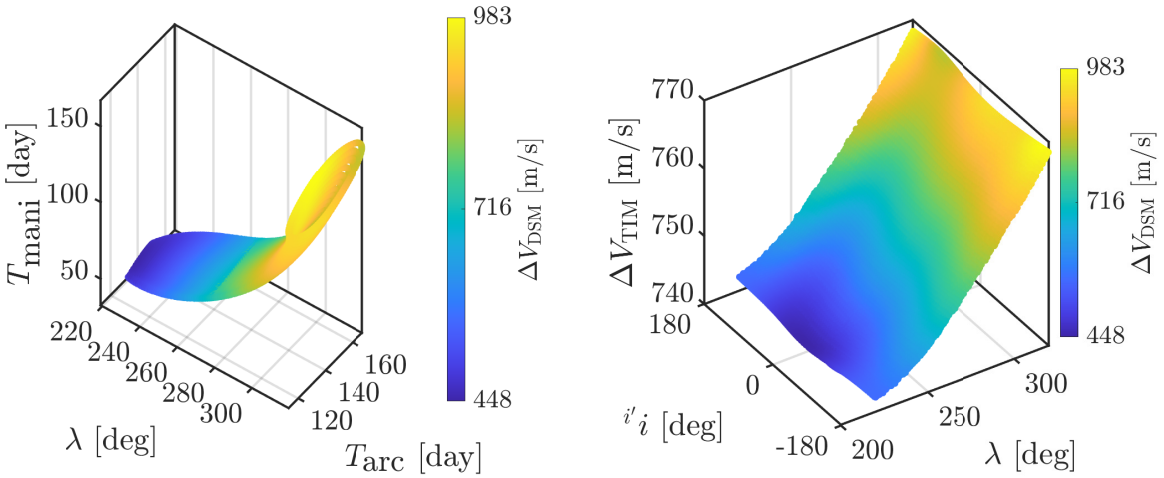

(a) (b)

Figure 6.43. : (a) surface of two-maneuver transfer solutions into a Lissajous orbit at an injection with $\theta_2 = 273.95°$, i.e., a Type B transfer. (b) Transfer Injection Maneuver magnitudes for different GTO departure locations, λ, at varying inclinations. The initial guess corresponds to a GTO departure location of $\lambda = 270°$

6.3.3 Optimized transfers into Sun-Earth Quasi-Periodic Orbits

Optimized transfers into quasi-periodic orbits in the Sun-Earth system are constructed from a range of GTO departure positions by leveraging insight from surface of solutions corresponding to two-maneuver transfers. In particular, optimal transfers into a pre-selected injection location, parameterized via θ_2, along a Lissajous orbit are explored here. The surfaces of solutions from Sections 6.3.1-6.3.2 reveal potential two-maneuver transfers from a range of GTO departure positions, i.e., the complete set of values for λ, with $\delta = 0°$, i.e., on the Sun-Earth ecliptic. But these transfers are also initial guesses to compute optimal transfers. For demonstration, in this investigation, optimized transfers are constructed from GTO departure states corresponding to a range of Ω values, as noted in Table 4.1 for a specific departure epoch. More specifically, the GTO departure state is computed via Equations (4.1)-(4.2) with the inertial Keplerian orbital elements in Table 4.1 at a specified epoch. The states are then rotated from the inertial EME frame into the Sun-Earth rotating frame through the process outlined in Section 2.3.2.2. Recall that the optimization process is performed in the Sun-Earth rotating frame, thus the GTO, as expressed in terms of the rotating frame, possesses a range of ${}^{r}\mathrm{i}$, λ, and δ values, as plotted in Figures 4.7-4.10. To reduce the total ΔV necessary for the transfer, the number of maneuvers is increased to four and include: a TIM, two DSMs, and one Orbit Injection Maneuver. Recall that the two-maneuver transfers included a TIM and a single DSM, labeled DSM1, because the transfer incorporated a stable manifold trajectory to asymptotically approach and enter the Lissajous orbit at a desired injection point. Now, an additional DSM, termed DSM2, and a maneuver at the Lissajous injection point, denoted as OIM, are introduced to construct an optimal transfer in search of a minimal ΔV solution. The transfer is described via a multiple-shooting scheme illustrated in Figure 6.44, where the TIM is in cyan, the two DSMs are in red along the transfer, and the OIM is a purple point with red edges. The location of the DSMs along the final transfer trajectory is a free variable in the optimization process with the location of the TIM and the OIM fixed at the GTO departure location and Lissajous injection location, respectively. A direct optimization scheme is implemented

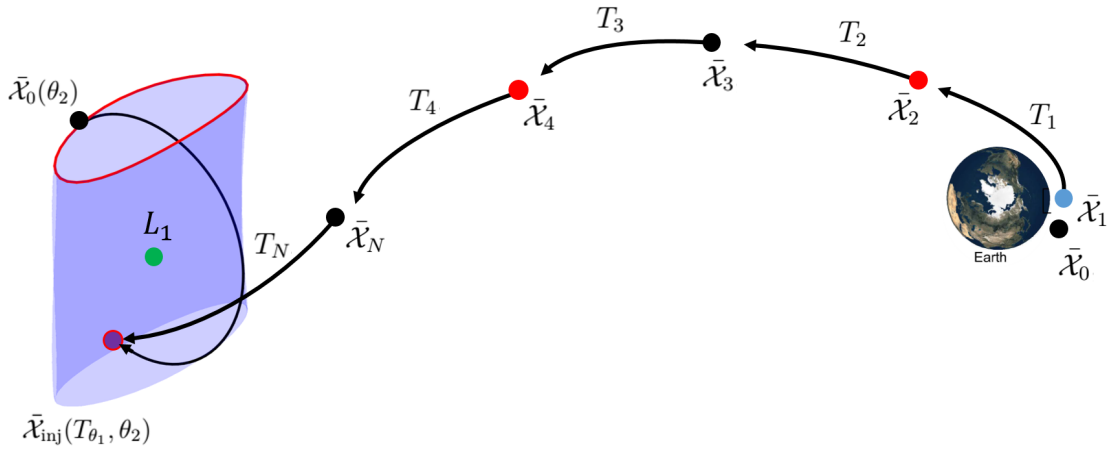

Figure 6.44. : Multiple-shooting schematic for optimization process consistent with transfers into Lissajous orbits. The optimized transfer implements four maneuvers

via MATLAB's fmincon optimization function to compute a locally optimum transfer that minimizes the following cost function:

$$J = \min\left\{\Delta V_{\text{TIM}} + \sum_{\text{j}=1}^{b} \Delta V_{\text{j}}^{\text{DSM}} + \Delta V_{\text{OIM}}\right\} \tag{6.26}$$

Subject to:

$$\begin{aligned}
&\text{Continuity Constraint:} && \bar{\mathcal{X}}_{m-1}(T_{m-1}) = \bar{\mathcal{X}}_m(0) \quad \text{where } \{m \in \{2, ..., N\} | \, m \notin \bar{B}\},\\
&\text{Boundary Constraint:} && \bar{r}_0(0) = \bar{r}_1(0) \ , \ \bar{r}_N(T_N) = \bar{r}_{\text{inj}}(T_{\theta_1}, \theta_2) \ , \ T_0 = 0 \ , \ \bar{\mathcal{X}}_0 = \bar{\mathcal{X}}^{\text{GTO}},\\
&\text{Path Constraint:} && \sum_{\text{j}}^{N} \int_0^{T_{\text{j}}} F_{\text{p}}^2\left(\bar{\mathcal{X}}_{\text{j}}(t)\right) - \left|F_{\text{p}}\left(\bar{\mathcal{X}}_{\text{j}}(t)\right)\right| F_{\text{p}}\left(\bar{\mathcal{X}}_{\text{j}}(t)\right) dt = 0,\\
&\text{Maneuver Conditions:} && \bar{r}_{k-1}(T_{k-1}) = \bar{r}_k(0) \quad \text{where } \{k \in \bar{B}\},
\end{aligned} \tag{6.27}$$

where the $\bar{B}$ vector is given as $\{\bar{B} = \{2, \cdots, N\}\}$ and contains location of applied maneuvers, i.e., the nodes corresponding to the location of a maneuver. For example, if the vector $\bar{B}$ is defined as: $\bar{B} = \{2, 3\}$, then the location of the performed maneuvers is at the beginning of the second and third nodes, i.e., the states $\bar{\mathcal{X}}_2$ and $\bar{\mathcal{X}}_3$, respectively. Additionally, a path constraint is included to implement any communications or eclipse constraints enforced

throughout the transfer. The steps consistent with computing a locally optimal transfer from a GTO departure state into a pre-selected injection location along a quasi-periodic orbit are:

- Compute GTO departure position and state in inertial EME frame from set of Keplerian orbit elements, $\{\Omega, \omega, {}^{\mathrm{i}}\mathrm{i}, a, \mathrm{e}, \nu\}$. In this analysis, the Keplerian elements are listed in Table 4.1 with a variable Ω angle.
- Select an Ω value and rotate the GTO departure state, $\bar{\mathcal{X}}_{\mathrm{i}}^{\mathrm{GTO}}$, from the inertial EME frame into the Sun-Earth rotating frame, $\bar{\mathcal{X}}^{\mathrm{GTO}}$, at the specified epoch. Note that the rotation process is described via the steps in Section 2.3.2.2.
- Evaluate λ_{dep} and δ_{dep} values associated with GTO departure state, $\bar{\mathcal{X}}^{\mathrm{GTO}}$.
- Select a two-maneuver transfer from a surface of solution that contains the λ_{dep} value of the rotated GTO departure state. Recall that the two-dimensional surface of solution is constructed from the Sun-Earth ecliptic, i.e., $\delta = 0^{\circ}$, but $\bar{\mathcal{X}}^{\mathrm{GTO}}$ may have a nonzero δ value.
- The selected two-maneuver transfer is an initial guess for the optimization process described via Equations (6.26)-(6.27) and is solved using MATLAB's fmincon function.

The optimization process described in this section is implemented to construct locally optimal transfers into Sun-Earth L_1 and L_2 Lissajous orbits, but is easily extended to compute optimized transfers for any quasi-periodic orbit generated from a two-dimensional torus.

6.3.3.1 Transfers to L_1 Lissajous Orbit

Optimal transfers into Sun-Earth L_1 Lissajous orbits are constructed by implementing an optimization process in conjunction with a multiple-shooting strategy and leveraging information from the two-maneuver analysis. Two-maneuver transfers into an ACE-like Lissajous orbit, plotted in Figure 6.21, occur along a two-dimensional surface considering

a GTO departure location along the Sun-Earth ecliptic, i.e., $\delta = 0°$ from Figure 4.5(b). The departure states are computed over a range of Ω values, i.e., $\Omega \in \{0°, 20°, \cdots, 340°\}$ with a departure epoch of June 2, 2022 12:00:00.000. Additionally, a SEZ communications constraint is enforced along the transfer to L_1 Lissajous orbits with the constraint written such that: $\alpha(t) > \alpha_{\text{SEZ}}$, where $\alpha_{\text{SEZ}} = 5°$. Recall that the SEZ is illustrated in Figure 5.52 with the SEV angle, α, defined with Equation (5.56). The steps consistent with the construction of optimal transfers to the Sun-Earth L_1 Lissajous orbit in the context of the CRTBP are outlined in Section 6.3.3. The required ΔV magnitudes corresponding to a range of GTO departure locations into the injection location defined via $\theta_2 = 152.85°$, i.e., Type A transfers, from Figure 6.24, are plotted in Figure 6.45. Additionally, the ΔV information for locally optimal transfers into an injection location of $\theta_2 = 335.35°$, i.e., Type B transfers, and recalling the trajectory in Figure 6.48, are plotted in Figure 6.45. The geometry of the optimized solutions for both transfer types are plotted in Figures 6.47-6.48. In Figure 6.45, the ΔV point corresponds to a departure location, identified by an Ω value, and displayed via a range of colors associated with the transfer TOF value. Note that the TOF value is measured from the GTO departure location to the injection point along the Lissajous orbit as the ideal location is selected such as to maximize the time outside the SEZ region. From any GTO departure location, i.e., parameterized by Ω in this example, there are two injection options available. For example, for a GTO departure location of $\Omega = 220°$, two points in the red box in Figure 6.45 represent the two transfers available, recalling that these are four-maneuver transfers. Observe that for $\Omega = 220°$, a Type A transfer requires approximately 100 m/s less compared to the Type B transfer. The geometry comparison of these two transfers are plotted in Figure 6.46, where the red points are the locations of the performed maneuvers.

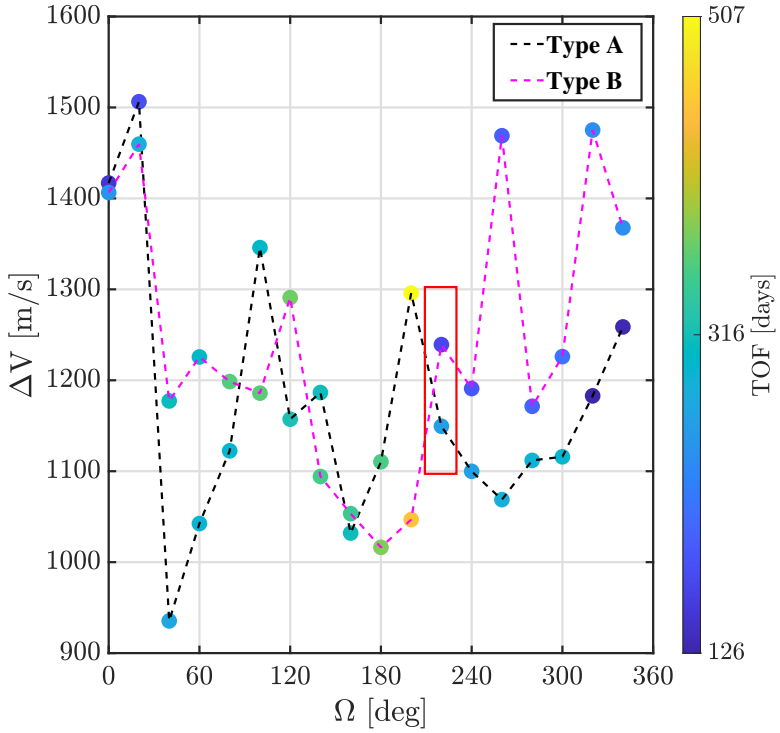

Figure 6.45. : ΔV information for optimal Type A and Type B transfers to Sun-Earth L_1 Lissajous orbit with a departure epoch of June 2, 2022 12:00:00.000. Recall that Type A and B transfers correspond to injection points of $\theta_2 = 152.85°$ and $\theta_2 = 333.35°$, respectively

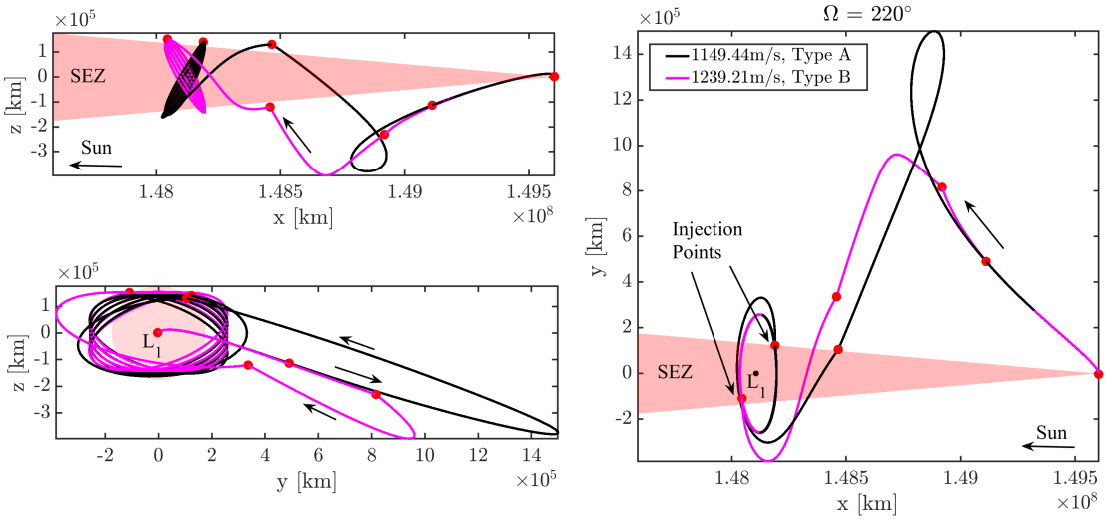

Figure 6.46. : Comparison of transfers from a GTO departure location of $\Omega = 220°$. The location of the maneuvers are displayed via red points

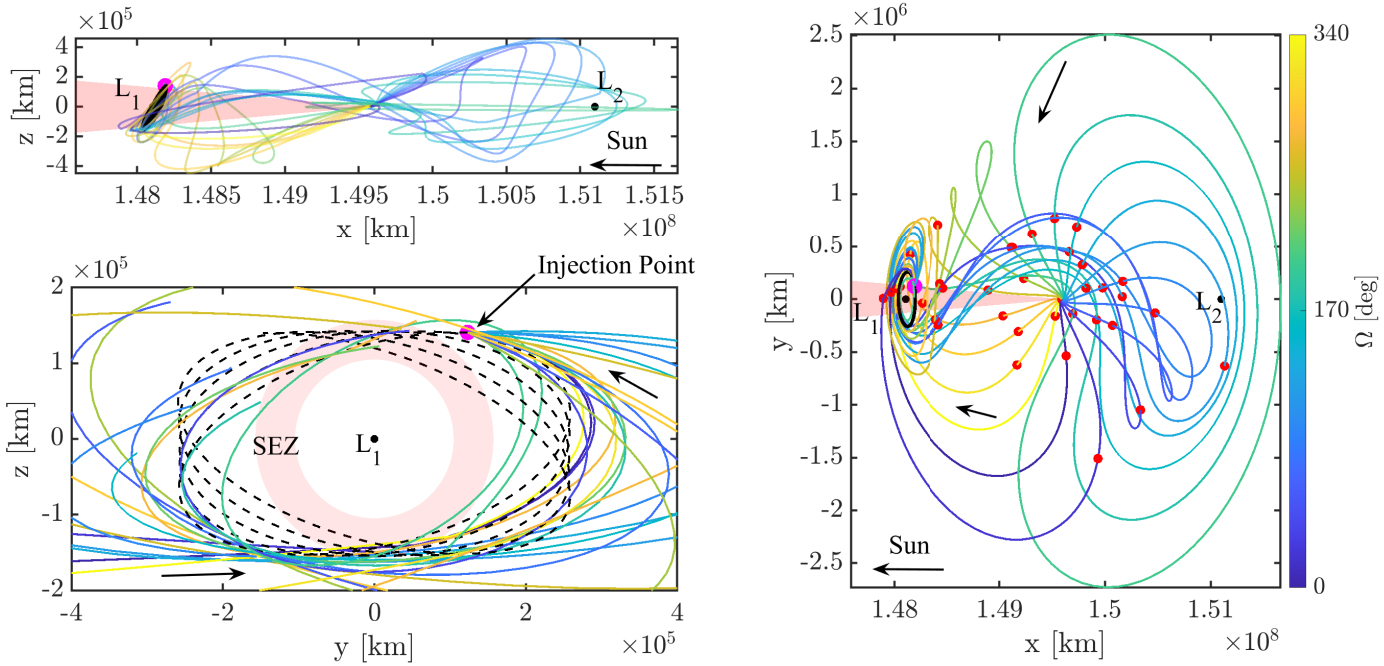

Figure 6.47. : Optimized Type A transfers to Sun-Earth Lissajous orbit with a departure epoch of June 2, 2022 12:00:00.000. The desired Lissajous orbit is plotted in a dashed black line and the SEZ cone is shaded in red. The motion of the trajectory post-injection, in the $\hat{y}$-$\hat{z}$ projection, is counter-clockwise based on an Earth observer

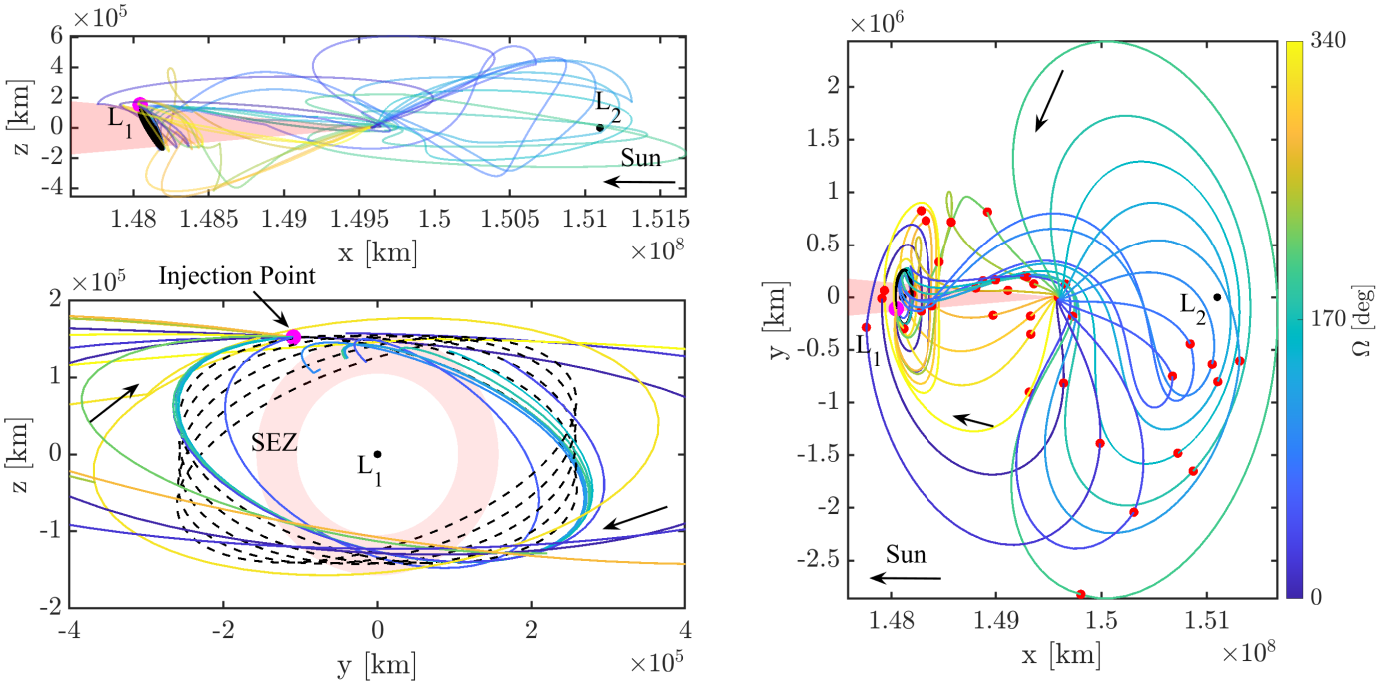

Figure 6.48. : Optimized Type B transfers to Sun-Earth Lissajous orbit with a departure epoch of June 2, 2022 12:00:00.000. The desired Lissajous orbit is plotted in a dashed black line and the SEZ cone is shaded in red. The motion of the trajectory post-injection, in the $\hat{y}$-$\hat{z}$ projection, is clockwise based on an Earth observer

Both trajectories in Figure 6.46 travel below the ecliptic, i.e., $\hat{x}$-$\hat{y}$ plane, to enter their respective injection location along the desired Lissajous orbit. For Type A optimized transfers, the trajectories approach the L_1 Lissajous orbit in a counter-clockwise direction, see the $\hat{y}$ -$\hat{z}$ projection in Figure 6.47. Alternatively, the motion approaching the injection point associated with Type B transfers is clockwise in Figure 6.48. Note that the $\hat{y}$ -$\hat{z}$ projections in Figures 6.47-6.48 are based on an Earth observer. Observe that the location of the maneuvers for the optimal transfers are the red points in Figures 6.47-6.48; recalling that four maneuvers are included in the optimization process. Additionally, the GTO departure locations that correspond to an excursion to L_2 are observed in the range of $40° \leq \Omega \leq 200°$ for both transfer types and are displayed in Figures 6.47-6.48. For transfers into Sun-Earth L_1 Lissajous orbits, a SEZ cone constraint is included and the $\alpha_{SEZ} = 5°$ cone is plotted in Figures 6.47-6.48. However, the projections of the transfers do not capture if the trajectories cross into the SEZ region along the transfer. Therefore, a polar plot is constructed, similar to the plots in Figures 6.24-6.25 , to observe any SEZ crossing conditions. In Figure 6.49, the injection point is marked in magenta and the SEZ region, corresponding to $\alpha_{SEZ} = 5°$, is the red line. Observe that the transfers in both polar plots in Figure 6.49, remain outside the SEZ region throughout their respective trajectories.

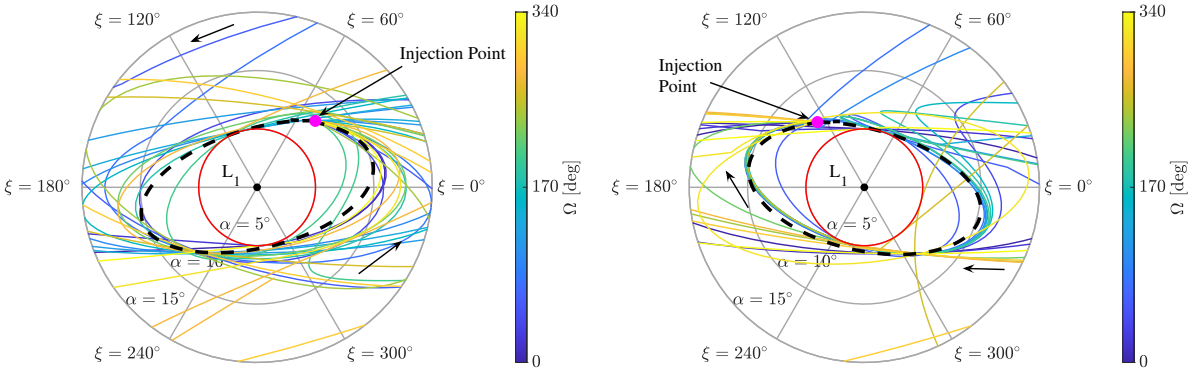

Figure 6.49. : Plot with angular dimension equal to ξ and the radial direction is the SEV angle for (a) injection point of $\theta_2 = 152.85°$, Type A transfers, and (b) $\theta_2 = 333.35°$, Type B transfers

Optimized transfer are constructed for a range of GTO departure locations for a selected departure epoch of June 2, 2022 12:00:00.000. Initial guesses for the optimization process are retrieved from the surface of solutions of two-maneuver transfers in Section 6.3.1. A summary of the maneuver magnitudes for the optimized transfers are provided in Tables 6.4-6.5. The magnitude of the TIM for each transfer is contained in the range 740 m/s $\leq \Delta V_{\text{TIM}} \leq$ 850 m/s and observe that, for most optimal transfers computed, the magnitude of DSM2 is larger than DSM1 and the OIM. In the optimization process, previous intuition is implemented to select the location of DSM2, recall that DSM1 is retrieved from the surface of solutions of the two-maneuver transfers, along the trajectory. Throughout the optimization process, the location of DSM1 and DSM2 are unconstrained, but the initial guess must be adequate. The optimized transfers in this section are computed for a desired epoch, however, the two-maneuver surfaces of solution are applicable over a range of GTO departure locations with any departure epoch.

Table 6.4. : Maneuver magnitudes (m/s) for optimal transfer to Sun-Earth L_1 Lissajous with an injection location of $\theta_2 = 152.85°$, i.e., Type A transfers

Ω [deg]	TIM	DSM 1	DSM 2	OIM	Total
0	763	76	558	20	1417
20	769	80	634	23	1506
40	755	0	148	32	935
60	748	13	171	111	1042
80	747	97	214	63	1122
100	749	0	507	90	1346
120	752	138	97	171	1157
140	791	79	166	150	1187
160	769	12	155	96	1032
180	791	38	242	39	1110
200	772	75	408	41	1296
220	757	12	345	36	1149
240	804	0	206	90	1100
260	762	7	107	193	1069
280	747	173	165	27	1112
300	750	0	229	136	1116
320	754	35	361	33	1183
340	764	11	467	17	1259

Table 6.5. : Maneuver magnitudes (m/s) for optimal transfer to Sun-Earth L_1 Lissajous with an injection location of $\theta_2 = 335.35°$, i.e., Type B transfers

Ω [deg]	TIM	DSM 1	DSM 2	OIM	Total
0	764	65	480	98	1406
20	777	6	507	170	1460
40	776	125	271	5	1177
60	781	178	237	31	1226
80	748	91	355	5	1199
100	803	75	305	3	1186
120	753	412	123	3	1291
140	755	103	233	3	1094
160	760	29	261	4	1053
180	766	4	243	3	1016
200	773	60	210	4	1047
220	748	180	259	53	1239
240	754	8	245	183	1191
260	822	435	209	3	1469
280	748	3	249	171	1171
300	758	4	250	214	1226
320	842	209	370	54	1475
340	759	112	254	242	1368

6.3.3.2 Transfers to L_2 Lissajous Orbit

Optimal transfers into a pre-selected Sun-Earth L_2 Lissajous orbit is facilitated by the two-maneuver surfaces of solution and an optimization process. Two-maneuver transfers into an L_2 Lissajous orbit, consistent with the Gaia mission[13], lie on a two-dimensional surface of solutions considering the GTO departure location is along the Sun-Earth ecliptic. Recall that two ideal injection points are identified, see Figures 6.36 and 6.37, along the selected Lissajous orbit. As a demonstration, optimized transfers from a range of GTO departure location with a fixed departure epoch of December 2, 2022 12:00:00.000 are constructed by leveraging the surface of solution information for two-maneuver transfers. The GTO departure states are computed for a range of Ω values, such that $\Omega \in \{0°, 20°, \cdots, 340°\}$. Additionally, an eclipse condition, defined as the Earth penumbra region illustrated in Figure 5.60, is included throughout the transfer. For the eclipse condition, the path constraint

for the optimization process, i.e., Equation (6.27), is written such that F_p is defined via Equation (5.78). The steps consistent with the construction of locally optimized transfers to the Sun-Earth L_2 Lissajous orbit, in the context of the CRTBP model, are outlined in Section 6.3.3. The required ΔV magnitudes for the range of GTO departure locations to the ideal injection points, i.e., parameterized via $\theta_2 = 93.8°, 273.95°$, is plotted in Figure 6.50, where the range of colors represents the TOF values. Note that the TOF values is associated with the transfer from the GTO departure to the Lissajous injection point. In this investigation, for L_2 Lissajous orbits, transfers to an injection point of $\theta_2 = 93.8°$ are termed as Type A transfer, due to the direction of motion in the $\hat{y}$-$\hat{z}$ projection based on an Earth observer, see Figure 6.36. Additionally, Type B transfers correspond to the injection point of $\theta_2 = 273.95°$, recalling Figure 6.37. For each departure location, there are two options, i.e., two injection point locations that maximize a time outside the eclipse constraint. For example, for a GTO departure state corresponding to $\Omega = 220°$, the total ΔV for a Type B transfer is lower than a Type A transfer, see the red box in Figure 6.50. The trajectories from this departure location are plotted, in configuration space, in Figure 6.51 with the location of the maneuvers marked in red; recall that each transfer presented has a total of four corresponding maneuvers. In Figure 6.51, six revolutions along the Lissajous are included to display the dynamical behavior of the initial revolutions after satellite injection. More specifically, for a Type A transfer, the satellite injects into the L_2 Lissajous orbit near the bottom left when viewed in the $\hat{y}$ -$\hat{z}$ projection in Figure 6.51, based on an Earth bserver. Alternatively, for a Type B transfer, the satellite injects near the bottom right of the $\hat{y}$ -$\hat{z}$ projection. Observe that the injection points locations, $\theta_2 = 93.8°, 273.95°$, are also plotted in Figures 6.52-6.53. Note that, while the revolutions around the L_2 Lissajous are plotted in Figure 6.51, the number of revolutions along a quasi-periodic orbit has no influence in the optimization process; recalling that the behavior of the revolutions along the Lissajous orbit serve to identify ideal injection points. The transfer geometries for the range of GTO departure location corresponding to the selected departure epoch are plotted in Figures 6.52-6.53. Transfers with an L_1 excursion, seen in Figures 6.52-6.53, are associated with GTO departure range of $20° \leq \Omega \leq 200°$. The trajectories do not cross into the Earth's penumbral shadow.

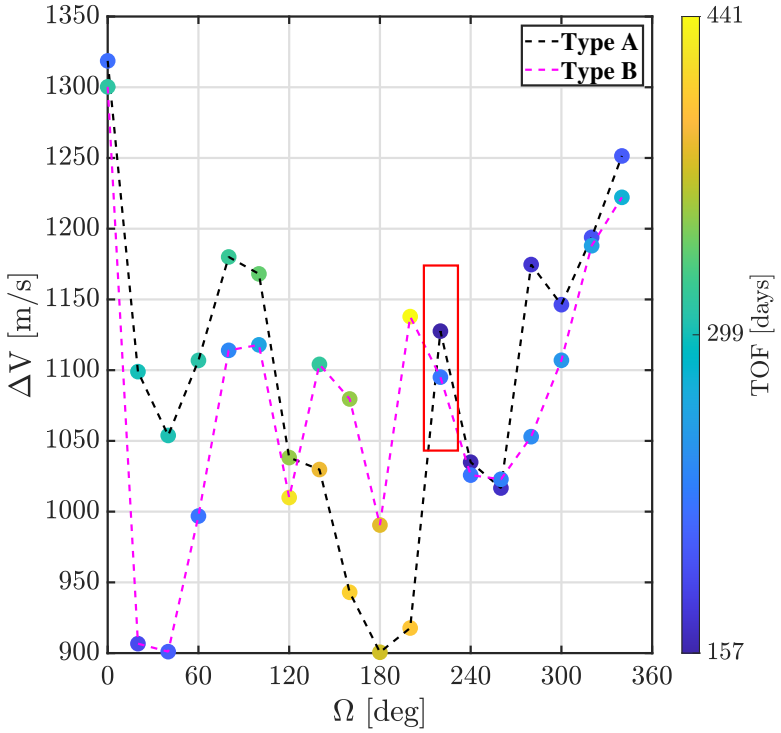

Figure 6.50. : ΔV information for optimal Type A and Type B transfers to Sun-Earth L_1 Lissajous orbit with a departure epoch of December 2, 2022 12:00:00.000. Recall that Type A and B transfers correspond to injection points of $\theta_2 = 93.8°$ and $\theta_2 = 273.95°$, respectively

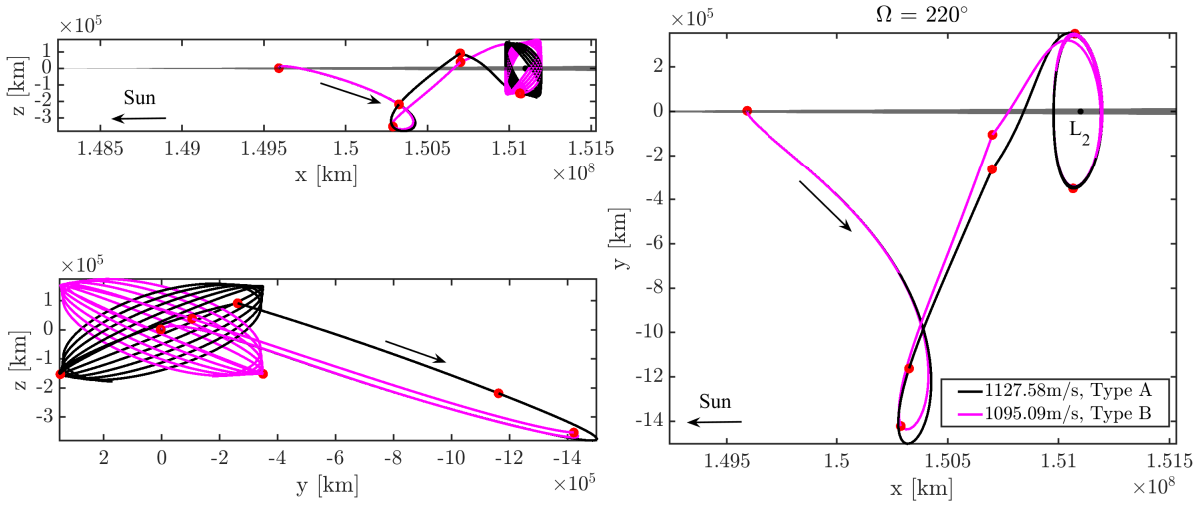

Figure 6.51. : Comparison of transfers from a GTO departure location of $\Omega = 220°$. The location of the maneuvers are displayed via red point

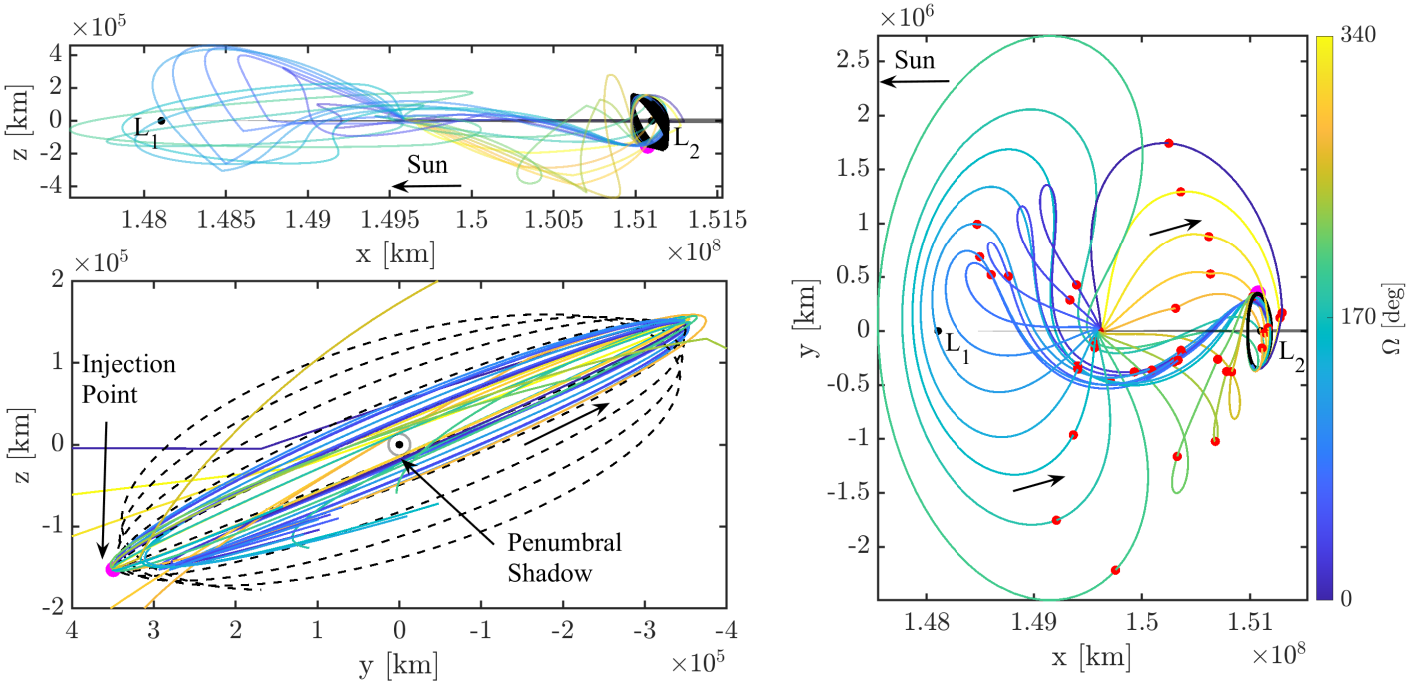

Figure 6.52. : Optimized Type A transfers to Sun-Earth Lissajous orbit with a departure epoch of December 2, 2022 12:00:00.000. The desired Lissajous orbit is plotted in a dashed black line and the Earth penumbra is in black. The motion of the trajectory post-injection, in the $\hat{y}$-$\hat{z}$ projection, is counter-clockwise based on an Earth observer

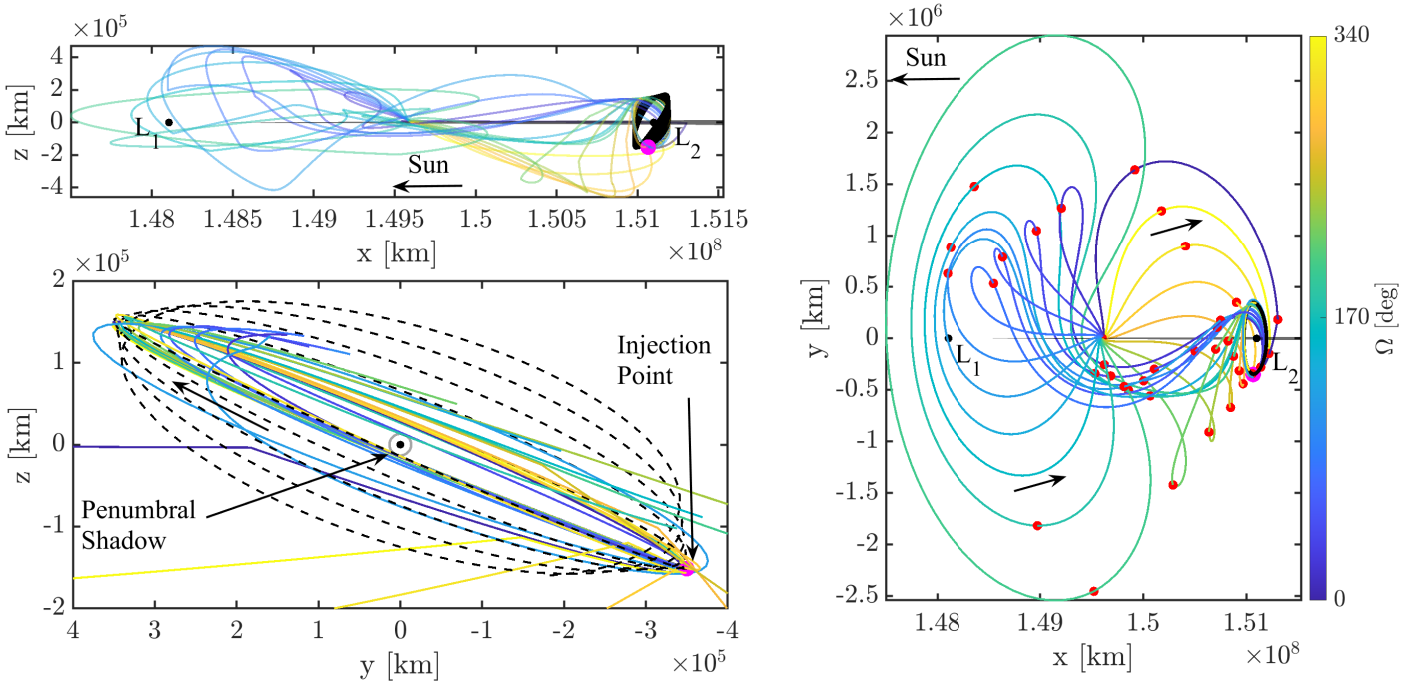

Figure 6.53. : Optimized Type B transfers to Sun-Earth Lissajous orbit with a departure epoch of December 2, 2022 12:00:00.000. The desired Lissajous orbit is plotted in a dashed black line and the Earth penumbra is in black. The motion of the trajectory post-injection, in the $\hat{y}$-$\hat{z}$ projection, is clockwise based on an Earth observer

A summary of the maneuver magnitudes for the optimized transfers are provided in Tables 6.6-6.7. The magnitude of the TIM for each transfer is contained in the range 735 m/s $\leq \Delta V_{\text{TIM}} \leq$ 770 m/s and observe that, for most optimal transfers computed, the magnitude of the OIM is less than 40 m/s. In the optimization process, previously gained intuition is leveraged to select the location of DSM2, recall that DSM1 is retrieved from the surface of solutions of the two-maneuver transfers, along the trajectory. In the construction of optimal transfers, via the process described in Section 6.3.3, the maneuver locations of DSM1 and DSM2 are unconstrained. The optimized transfers in this section are computed for a desired epoch, however, the two-maneuver surfaces of solution are applicable for any GTO departure location with any departure epoch.

Table 6.6. : Maneuver magnitudes (m/s) for optimal transfer to Sun-Earth L_2 Lissajous with an injection location of $\theta_2 = 93.8°$, i.e., Type A transfer

Ω [deg]	TIM	DSM 1	DSM 2	OIM	Total
0	754	1	543	20	1319
20	742	130	215	12	1099
40	739	0	294	21	1054
60	735	194	162	15	1107
80	734	278	146	22	1180
100	738	262	145	23	1168
120	741	150	129	19	1038
140	743	154	128	5	1030
160	749	36	153	6	943
180	754	21	119	6	901
200	763	27	119	9	918
220	744	0	358	26	1128
240	737	0	282	16	1035
260	736	191	89	0	1017
280	734	266	143	32	1175
300	739	196	207	5	1146
320	743	135	311	5	1194
340	748	50	436	17	1251

Table 6.7. : Maneuver magnitudes (m/s) for optimal transfer to Sun-Earth L_2 Lissajous with an injection location of $\theta_2 = 273.95°$, i.e., Type B transfer

Ω [deg]	TIM	DSM 1	DSM 2	OIM	Total
0	754	0	542	5	1300
20	748	65	84	10	907
40	739	38	107	17	901
60	737	131	123	6	997
80	735	161	200	18	1114
100	737	249	123	9	1118
120	740	29	209	32	1010
140	744	184	172	5	1104
160	750	104	221	5	1080
180	764	19	198	10	991
200	762	55	315	6	1138
220	743	45	303	5	1095
240	737	101	182	5	1026
260	736	151	131	5	1023
280	737	211	101	5	1053
300	739	81	282	5	1107
320	744	32	401	12	1188
340	748	2	466	6	1222

6.4 Optimized Transfers in the Ephemeris Model

Optimized transfers in the higher-fidelity ephemeris model to Sun-Earth Lagrange points are computed via a local optimization scheme. In this investigation, the local optimization scheme implemented is a built-in direct optimization process utilized within the fmincon function in MATLAB. The optimized multiple maneuver transfers, i.e., transfers that include four maneuvers, from Sections 6.2.3 and 6.3.3 are transitioned into the inertial EME frame. In the context of a multiple-shooting problem, the nodes corresponding to an optimized transfer in the CRTBP model, i.e., the states $\{\bar{\mathcal{X}}_0, \cdots, \bar{\mathcal{X}}_N\}$, are rotated to the inertial EME frame, $\{\bar{\mathcal{X}}_{\text{i}0}, \cdots, \bar{\mathcal{X}}_{\text{i}N}\}$, via the steps summarized in Section 2.3.2.1. The state transition method outlined in Section 2.3.2.1 accounts for the oscillating distance between the Sun and the Earth retrieved from planetary ephemerides; note that the planetary ephemerides are constructed from astronomical observations. However, there are alterna-

tive transition methods from the rotating frame of the CRTBP to the inertial EME frame that utilize a constant CRTBP primary distance, i.e., l^*, see Zimovan [65], Pavlak [77], and Spreen [78] for further discussion. After a trajectory is transitioned into the inertial EME frame, at a specified epoch, a feasible transfer in the ephemeris model is generated via a corrections process, refer to Appendix E for discussion about the corrections process in the ephemeris model. Note that for multiple-maneuver transfers, the maneuvers included in the corrections process are unconstrained, that is, the locations of the maneuvers are free. Several authors have successfully transitioned and corrected trajectories from the CRTBP model in the ephemeris model. In this investigation, additional path constraints are included during the corrections process and a locally optimal trajectory is implemented to construct transfers from GTO to the Sun-Earth Lagrange points.

The corrections process in the ephemeris model is formulated as an local optimization problem. The construction of optimal transfers to periodic and quasi-periodic orbits near Sun-Earth L_1 and L_2 leveraged the dynamical structure information in the CRTBP model, i.e., the trajectories within the stable manifold structures. However, no periodic or quasi-periodic motion exists in the ephemeris model. Although there is quasi-periodic like motion, no closed bounded motion has been found to exist. To generate periodic-like motion in the ephemeris model, a typical corrections process includes "stacking" a series of revolutions around a periodic orbit such that the corrected trajectory remains near the initial periodic motion. However, bounded motion, i.e., periodic or quasi-periodic, in the CRTBP model is not guaranteed to persist in the higher fidelity ephemeris model. One example is the motion of specific Near Rectilinear Halo Orbit (NRHO), which are periodic in the Earth-Moon system, but quickly deviate when transitioned and corrected in the (Sun-Earth-Moon) ephemeris model [79]. The NRHO example also highlights the epoch dependence nature of feasible ephemeris solutions. Additionally, epoch dependency may introduce numerical challenges, although, in some cases, this is often mitigated by introducing an attenuation factor during the corrections process. In this investigation, the objective is to construct multiple-maneuver transfers into specific periodic and quasi-periodic orbits in the ephemeris model. An optimization process is formulated to generate a feasible transfer in the ephemeris

model with a similar geometry as the CRTBP transfer via a multiple-shooting strategy. The cost function of the optimization process is denoted as,

$$J_{\text{path}} = \min\left\{ \sum_{\text{j}}^{N} \int_{\tau_{\text{j}}}^{\tau_{\text{j}}+T_{\text{j}}} \left(\bar{r}_{\text{i}}{}_{\text{j}}(t) - \bar{r}_{\text{i}}{}_{\text{j},d}(t)\right)^T \left(\bar{r}_{\text{i}}{}_{\text{j}}(t) - \bar{r}_{\text{i}}{}_{\text{j},d}(t)\right) dt \right\}, \tag{6.28}$$

where $\bar{r}_{\text{i}}{}_{\text{j}}(t)$ is the position of the satellite in the inertial EME frame and $\bar{r}_{\text{i}}{}_{\text{j},d}(t)$ is the position of the corrected CRTBP transfer rotated into the inertial EME frame; recall that τ is the epoch attached to the node for each transfer arc. The cost function in Equation (6.28) is derived to minimize the isochronous distance between the satellite and a defined path, i.e., the previously corrected transfer in the CRTBP model rotated into the EME frame. Additionally, the cost function in Equation (6.28) is subject to:

$$\begin{aligned}
\text{Continuity Constraint:} \quad & \bar{\mathcal{X}}_{\text{i}}{}_{m-1}(\tau_{m-1} + T_{m-1}) = \bar{\mathcal{X}}_{\text{i}}{}_{m}(\tau_m) \quad \text{where } \{m \in \{2, ..., N\} | \, m \notin \bar{B}\}, \\
\text{Epoch Continuity:} \quad & \tau_{\text{j}} + T_{\text{j}} = \tau_{\text{j}+1} \quad \text{where j} \in \{0, ..., N-1\}, \\
\text{Boundary Constraint:} \quad & \bar{\mathcal{X}}_{\text{i}}{}_{0}(0) = \bar{\mathcal{X}}_{\text{i}}^{\text{GTO}} \ , \ \bar{r}_{\text{i}}{}_{0}(\tau_0) = \bar{r}_{\text{i}}{}_{1}(\tau_1) \ , \ \tau_0 = \tau_{\text{des}} \ , \ T_0 = 0, \\
\text{Path Constraint:} \quad & \sum_{\text{j}}^{N} \int_{0}^{T_{\text{j}}} F_{\text{p}}^2 \left(\bar{\mathcal{X}}_{\text{i}}{}_{\text{j}}(t)\right) - \left| F_{\text{p}} \left(\bar{\mathcal{X}}_{\text{i}}{}_{\text{j}}(t)\right) \right| F_{\text{p}} \left(\bar{\mathcal{X}}_{\text{i}}{}_{\text{j}}(t)\right) dt = 0, \\
\text{Maneuver Conditions:} \quad & \bar{r}_{\text{i}}{}_{k-1}(\tau_{k-1} + T_{k-1}) = \bar{r}_{\text{i}}{}_{k}(\tau_k) \quad \text{where } \{k \in \bar{B}\},
\end{aligned} \tag{6.29}$$

where $\bar{B}$ is the vector the contains the maneuver locations and is defined as: $\bar{B} \in \{2, \cdots, N\}$. The optimization process presented in Equations (6.28) and (6.29) are consistent with a multiple-shooting scheme discussed in Appendix E. The partial derivatives of the cost function, J_{path}, with respect to the state, $\bar{\mathcal{X}}_{\text{i}}{}_{\text{j}}$, and transfer time, T_{j}, are written as,

$$\frac{\partial J_{\text{path}}}{\partial \bar{\mathcal{X}}_{\text{i}}{}_{\text{j}}} = \int_{\tau_{\text{j}}}^{\tau_{\text{j}}+T_{\text{j}}} 2\left(\bar{r}_{\text{i}}{}_{\text{j}}(t) - \bar{r}_{\text{i}}{}_{\text{j},d}(t)\right)^T \begin{bmatrix} \mathbf{I}_{3,3} & \mathbf{0}_{3,3} \end{bmatrix} \mathbf{\Phi}_{\text{j}}(\tau_{\text{j}} + t, \tau_{\text{j}}) \ dt, \tag{6.30}$$

$$\frac{\partial J_{\text{path}}}{\partial T_{\text{j}}} = \left(\bar{r}_{\text{i}}{}_{\text{j}}(\tau_{\text{j}} + T_{\text{j}}) - \bar{r}_{\text{i}}{}_{\text{j},d}(\tau_{\text{j}} + T_{\text{j}})\right)^T \left(\bar{r}_{\text{i}}{}_{\text{j}}(\tau_{\text{j}} + T_{\text{j}}) - \bar{r}_{\text{i}}{}_{\text{j},d}(\tau_{\text{j}} + T_{\text{j}})\right), \tag{6.31}$$

with the partial derivative with respect to the initial state epoch, τ_{j}, denoted as,

$$\begin{aligned}\frac{\partial J_{\text{path}}}{\partial \tau_{\mathrm{j}}} =& \left(\bar{r}_{\mathrm{i}}(\tau_{\mathrm{j}}+T_{\mathrm{j}}) - \bar{r}_{\mathrm{i}}{}_{\mathrm{j},d}(\tau_{\mathrm{j}}+T_{\mathrm{j}})\right)^T \left(\bar{r}_{\mathrm{i}}(\tau_{\mathrm{j}}+T_{\mathrm{j}}) - \bar{r}_{\mathrm{i}}{}_{\mathrm{j},d}(\tau_{\mathrm{j}}+T_{\mathrm{j}})\right) - \\ & \left(\bar{r}_{\mathrm{i}}(\tau_{\mathrm{j}}) - \bar{r}_{\mathrm{i}}{}_{\mathrm{j},d}(\tau_{\mathrm{j}})\right)^T \left(\bar{r}_{\mathrm{i}}(\tau_{\mathrm{j}}) - \bar{r}_{\mathrm{i}}{}_{\mathrm{j},d}(\tau_{\mathrm{j}})\right) + \\ & \int_{\tau_{\mathrm{j}}}^{\tau_{\mathrm{j}}+T_{\mathrm{j}}} 2\left(\bar{r}_{\mathrm{i}}(t) - \bar{r}_{\mathrm{i}}{}_{\mathrm{j},d}(t)\right)^T \begin{bmatrix}\mathbf{I}_{3,3} & \mathbf{0}_{3,3}\end{bmatrix} \frac{\partial \bar{\mathcal{X}}_{\mathrm{i}}{}_{\mathrm{j}}(t)}{\partial \tau_{\mathrm{j}}} \; dt.\end{aligned} \tag{6.32}$$

Observe that the constraint conditions provided in Equation (6.29) assume at least one maneuver, at the first node, $\bar{\mathcal{X}}_{\mathrm{i}}{}_0$. Additionally, the GTO departure state, i.e., $\bar{\mathcal{X}}_{\mathrm{i}}^{\mathrm{GTO}}$, is computed via Equations (4.1)-(4.2). In this analysis, the corrections process to construct locally optimal transfers in the ephemeris model is outlined as,

1. Let $\{\bar{\mathcal{X}}_0, \cdots, \bar{\mathcal{X}}_N\}$ be the nodes associated with an optimal multiple-maneuver transfer to a desired orbit near the Sun-Earth L_1 or L_2 points and w revolutions around the desired orbit. Only the transfer segment is optimized in the CRTBP model and the nodes are in the Sun-Earth rotating frame. Note that the desired orbit is either a periodic or quasi-periodic orbit.

2. Rotate the nodes from the rotating frame to the inertial EME frame via the steps outlined in Section 2.3.2.1. The nodes are written as: $\{\bar{\mathcal{X}}_{\mathrm{i}}{}_0, \cdots, \bar{\mathcal{X}}_{\mathrm{i}}{}_N\}$.

3. Compute the desired path for the optimization process, i.e., $\bar{r}_{\mathrm{i}}{}_{\mathrm{j},d}(t)$. First, a collection of position vectors, $\bar{r}_{\mathrm{j},d}(t)$, is computed from the propagated arc associated with a node, $\bar{\mathcal{X}}_{\mathrm{j}}$. Next, each vector is rotated into the inertial EME frame at a corresponding epoch.

4. Optimize the nodes, $\{\bar{\mathcal{X}}_{\mathrm{i}}{}_{\mathrm{j}}\}$, via the fmincon function in MATLAB with the cost function in Equation (6.28) subject to the conditions in Equation (6.29). During the optimization process, include any path constraints associated with the SEZ cone or the Earth eclipse. The optimization process computes a trajectory and a number of revolutions, w, around a desired orbit with a geometry near the desired position vectors, $\bar{r}_{\mathrm{i}}{}_{\mathrm{j},d}(t)$.

5. Given an optimized feasible solution in ephemeris. Use following cost function,

$$J_{\Delta V} = \min\left\{\Delta V_{\text{TIM}} + \sum_{\text{j}}^{b} \Delta V_{\text{j}}\right\}, \tag{6.33}$$

subject to the optimization conditions in Equation (6.29) to lower the total ΔV for the transfer. Recall that the TIM is a maneuver at the GTO departure location and include any path constraint throughout the transfer. The ΔV is lowered for the transfer segment and do not include the revolutions around the desired orbit.

In summary, two cost functions are implemented in the construction of optimized transfers in the ephemeris system. The cost function in Equation (6.28) attempts to compute a trajectory with similar geometry as the optimized solution in the CRTBP model. Note that both the transfer and w revolutions around the desired orbit are included in this initial process. Next, the cost function in Equation (6.33) lowers the total ΔV of the transfer segment. The construction of optimized solutions in the ephemeris model is facilitated by this process.

6.4.1 Optimized Ephemeris Transfers to L_1 Halo Orbits

Optimized transfers from a range of GTO departure states to a Sun-Earth L_1 halo are constructed via a multiple-shooting scheme in the higher-fidelity ephemeris model. In this investigation, optimal transfers into Sun-Earth L_1 periodic orbits consistent with the SOHO operational orbit are computed for a range of GTO departure states. The results of the optimization in the CRTBP model are summarized in Section 6.2.3. Note that only the transfer segment is optimized and the injection point along the periodic orbit is unconstrained. In the construction of optimized transfers to L_1 halo orbits in the ephemeris model, the optimized transfer from the CRTBP analysis and five revolutions along the periodic orbit form an initial guess for the optimization strategy. Recall that the SEZ constraint was omitted for this example. The steps consistent with the optimization scheme for this scenario are outlined in Section 6.4; note that no additional maneuvers are included during the transfer segment, that is, the transfer segment has a total of four maneuvers. Recall that the GTO

departure states correspond to a range of Ω values with the remaining Keplerian orbital parameters listed in Table 4.1. The total ΔV results for the range of optimal transfers are plotted in Figure 6.54 corresponding to a departure epoch of June 2, 2022 12:00:00.000. As

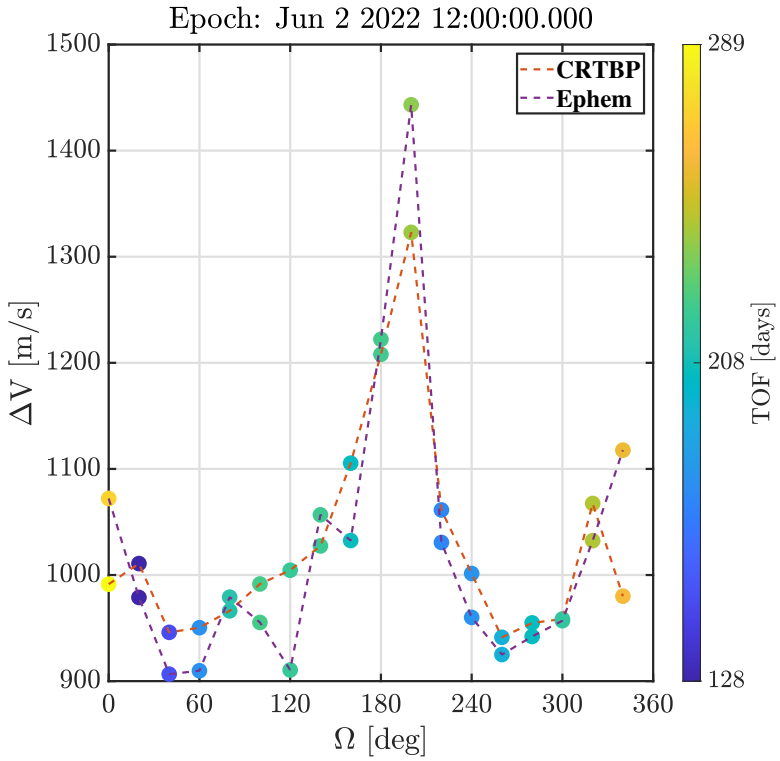

Figure 6.54. : Optimized transfers to Sun-Earth L_1 halo at epoch with June 2, 2022 12:00:00.000

a comparison, optimized results in the CRTBP and the ephemeris model are displayed in Figure 6.54 with the color representing the TOF values along the transfer segment, i.e., from the GTO departure location to the orbit injection point. The ΔV difference between the two models varies along GTO departure locations, i.e., Ω values, and ranges from 10 m/s $\leq \Delta V \leq$ 125 m/s. Observe that for most transfer, the TOF difference is small, that is, less than 5 days. In Figure 6.55, the geometry of the transfers are plotted in the rotating frame of the Sun-Earth system; note that the optimization process in ephemeris is in the inertial EME frame, but the transfer result is transitioned into the rotating frame via the steps outlined in Section 2.3.2.2.

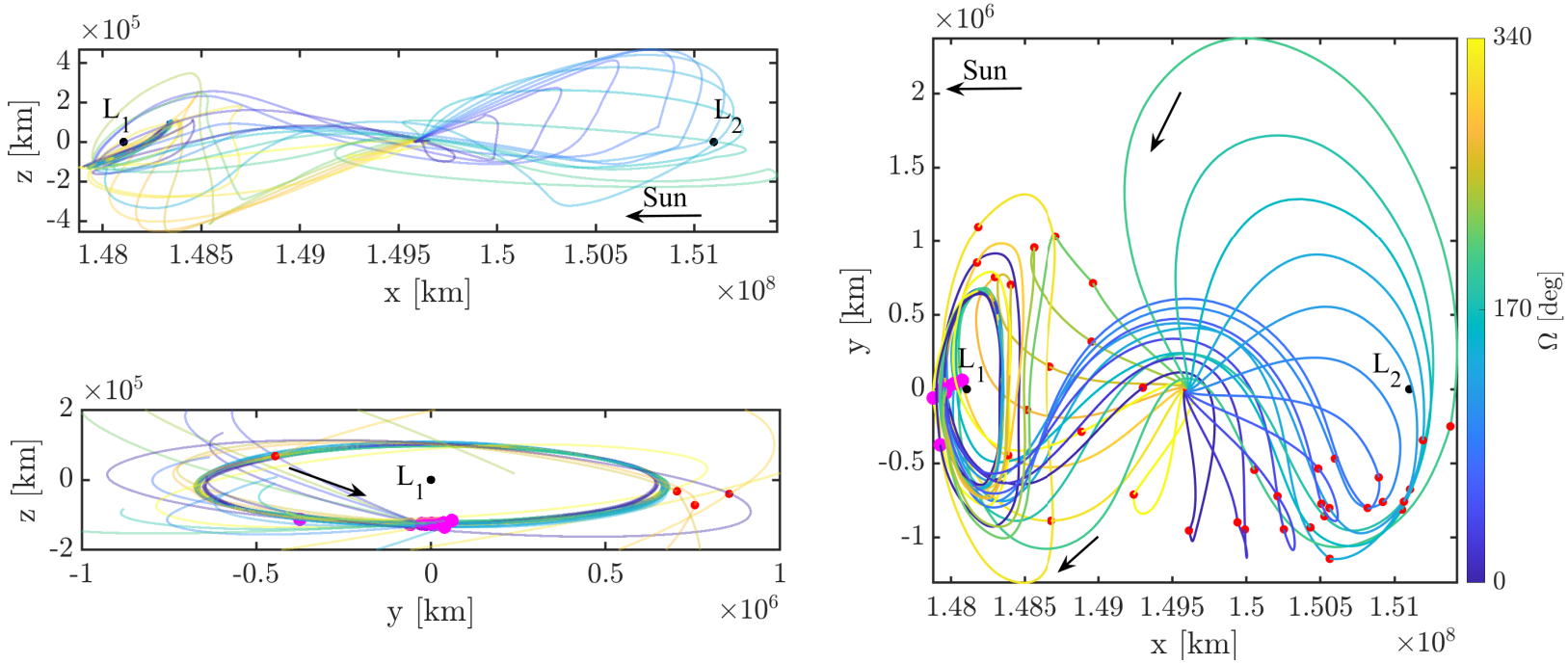

Figure 6.55. : Optimized transfers in the rotating frame to a Sun-Earth L_1 halo at epoch of June 2, 2022 12:00:00.000. The desired southern halo is in black and the transfer are depicted via a range of colors. The $\hat{y}$-$\hat{z}$ projection is based on an Earth observer

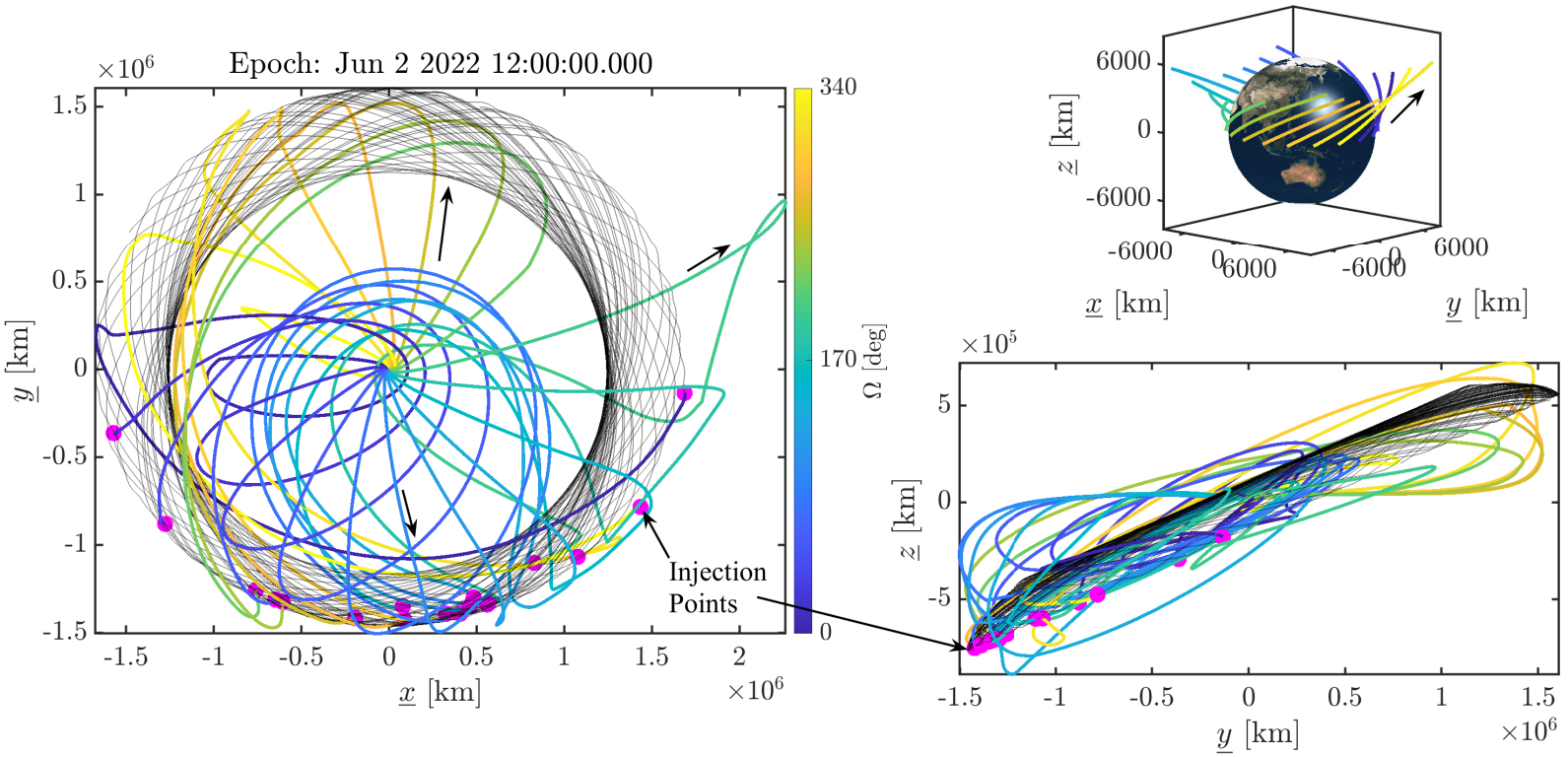

Figure 6.56. : Optimized transfers in the inertial EME frame to a Sun-Earth L_1 halo at epoch of June 2, 2022 12:00:00.000. The desired southern halo is in black and the transfer are depicted via a range of colors

Additionally, the transfers are plotted in the EME frame in Figure 6.56. In the rotating frame, the geometry of the optimal ephemeris transfers is similar to the solutions from the CRTBP optimization, a result that should be expected with the optimization strategy implemented. Recall, that in the CRTBP optimization, the injection location along the periodic orbit remains close to the $\hat{x}$ axis, however, one notable observation is the variation in the injection points, i.e., the point marked in magenta in Figure 6.55, for the optimized ephemeris solutions. In the inertial EME frame, see Figure 6.56, the location of the injection points are contained to regions below the $\underline{\hat{y}}$ axis and below the Earth equator, i.e., the $\underline{\hat{x}}$-$\underline{\hat{y}}$ plane. In Figure 6.56, the transfers are represented via range of color corresponding to an Ω value and the arrival "periodic orbit" is in black, note that the arrival orbit has periodic-like behavior for five revolutions. Due to the inclination of the ecliptic plane with respect to the mean Earth equator, i.e., ${}^{\mathrm{i}}\mathrm{i} = 27^{\circ}$ from Figure 4.5, the transfers and subsequent "periodic orbit" are inclined in the $\underline{\hat{y}}$-$\underline{\hat{z}}$ projection. Additionally, A zoomed view of the transfer near the GTO departure locations, in the inertial EME frame, is presented in Figure 6.56. A summary of the maneuver magnitudes for the optimized ephemeris transfers is provided in Appendix F. In this example, optimized transfers to a Sun-Earth L_1 halo orbit are successfully transitioned into the higher-fidelity ephemeris model for a selected departure epoch over a range of GTO orientations.

6.4.2 Optimized Ephemeris Transfers to L_2 Halo Orbits

Optimal transfers from a range of GTO departure states to a Sun-Earth L_2 halo orbits consistent with the Nancy Roman Space Telescope are constructed by leveraging an optimization strategy. Locally optimal transfers to Sun-Earth L_2 halo orbits are computed over a range of GTO departure states listed in Table 4.1 with the results in the CRTBP model summarized in Section 6.2.3. In the construction of optimized transfers to L_2 halo orbits in the ephemeris model, the optimized transfer from the CRTBP analysis and five revolutions along the periodic orbit form an initial guess for the optimization strategy. Additionally, the OIM, performed at the periodic orbit injection location, magnitude is constrained such

that $\Delta V \leq 15$ m/s. Note that the optimized CRTBP transfers include four maneuvers and no additional maneuvers are added when transitioned into the ephemeris model. Eclipsing constraints, defined as the Earth's penumbra region, are included in the optimization process and written as a path constraint along the transfer segment; note that the geometry of the selected L_2 halo orbit is eclipse free. The steps consistent with the optimization scheme for this scenario are outlined in Section 6.4. The total ΔV results for the range of optimal transfer are plotted in Figure 6.57 corresponding to a departure epoch of December 2, 2022 12:00:00.000. As a comparison, optimized results in the CRTBP and the ephemeris model

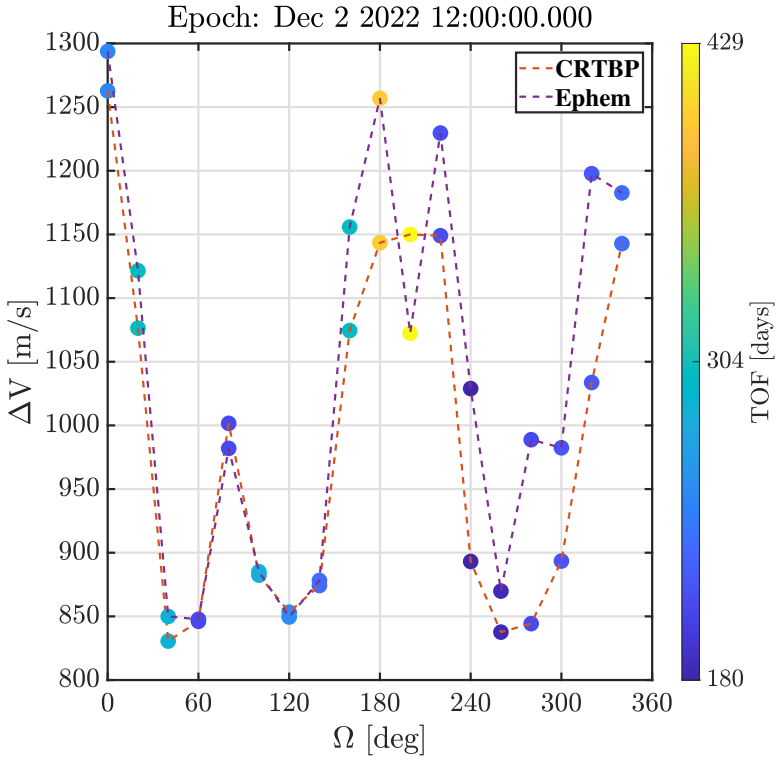

Figure 6.57. : Optimized transfers to Sun-Earth L_2 halo at epoch with Dec 2, 2022 12:00:00.000

are displayed in Figure 6.57 with the color representing the TOF values along the transfer segment, i.e., from the GTO departure location to the orbit injection point.

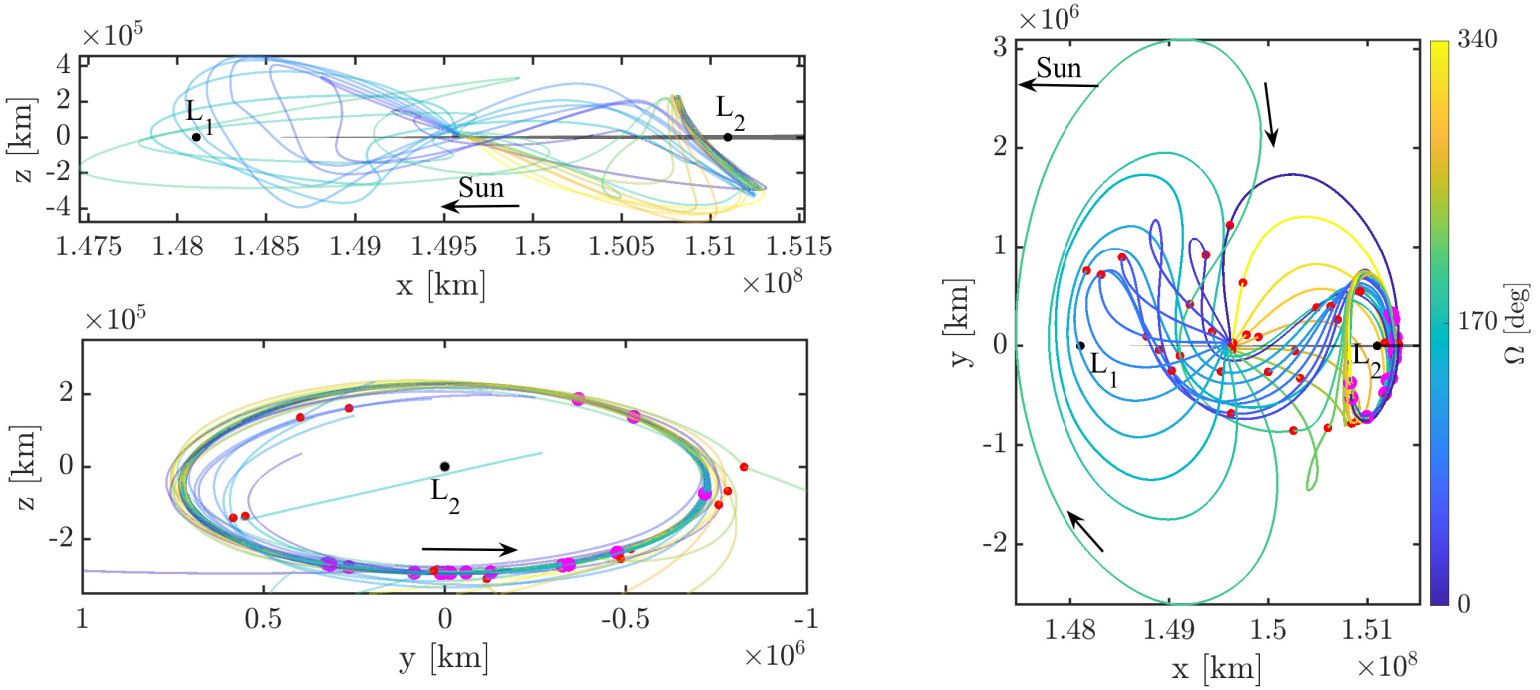

Figure 6.58. : Optimized transfers in the rotating frame to Sun-Earth L_2 halo with departure epoch of Dec 2, 2022 12:00:00.000. The desired southern halo is in black and the transfers are depicted via a range of colors. The $\hat{y}$-$\hat{z}$ projection is with respect to an Earth observer.

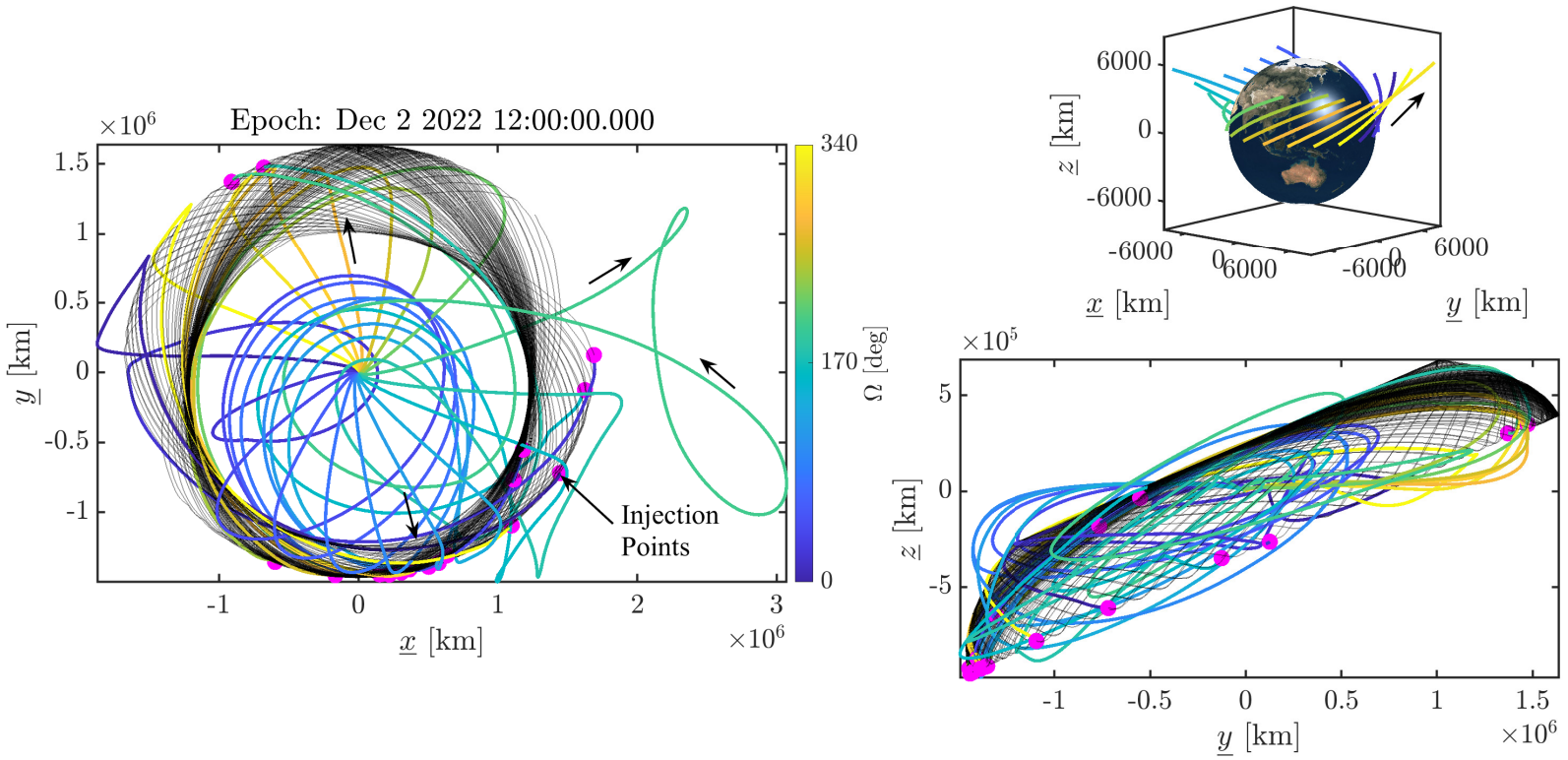

Figure 6.59. : Optimized transfers in the inertial EME frame to a Sun-Earth L_2 halo with departure epoch of Dec 2, 2022 12:00:00.000. The desired southern halo is in black and the transfers are depicted via a range of colors

The ΔV difference between the two models varies along GTO departure locations, i.e., Ω values, and ranges from 1.5 m/s $\leq \Delta V \leq$ 164 m/s with the TOF differences less than 1 day. In Figure 6.58, the geometry of the transfers are plotted in the rotating frame of the Sun-Earth system with the inertial EME frame represented in Figure 6.59. Additionally, a summary of the maneuver magnitudes is provided in Appendix F. In the rotating frame, i.e., Figure 6.58, the geometry of the optimal ephemeris transfers in configuration space is similar to the transfers from the CRTBP optimization, expected with the optimization strategy implemented. Observe that the injection points, points marked in magenta in Figure 6.58, occur at different location along the "periodic" halo orbit; note that the corrected halo orbit segment in ephemeris is not periodic, but its geometry is near-periodic for the five revolutions utilized in the optimization process. For each optimized transfer, the location of the OIM, i.e., the location of the injection point, is contingent on the constraint: $\Delta V_{\text{OIM}} \leq 15$ m/s. Each transfer in Figure 6.59 is represented via a range of color that corresponds to the GTO departure Ω value and the halo orbit segment is in black. Observe that the location of most injection points, in magenta, are situated in a region below the $\hat{\underline{y}}$ axis, except for two transfers. Additionally, the optimized transfers and their corresponding orbit segments are inclined as viewed in the $\hat{\underline{y}}$-$\hat{\underline{z}}$ plane. In the construction of optimized transfers in the ephemeris model, the optimized solutions in the CRTBP model serve as appropriate initial guesses. The optimization strategy implemented aids in the search for a transfer in the higher-fidelity ephemeris model that maintains similar geometry characteristics as the initial guess.

6.4.3 Optimized Ephemeris Transfers to L_1 Lissajous Orbits

Optimal transfers over a range of GTO departure states to ideal injection locations along a Sun-Earth ACE-like L_1 Lissajous orbit are constructed by leveraging the optimized results from the CRTBP. Locally optimal transfers into Sun-Earth L_1 Lissajous orbits are computed for the range of GTO departure states listed in Table 4.1. Recall that in Section 6.3.1, two ideal L_1 Lissajous injection locations are identified such that the time outside a

communications constraint, T_{out}, is maximized for a propagated trajectory originating from an ideal injection location. Note that the communications constraint adopted for L_1 transfers is represented via a right circular cone illustrated in Figure 5.52 with an SEV angle of $\alpha_{\text{SEZ}} = 5°$, see Equation (5.56). Additionally, optimized transfers for each ideal injection point are separated into Type A, counter-clockwise motion when viewed from earth, and Type B, the clockwise motion from an Earth observer. The locally optimized transfer results within the context of the CRTBP model are summarized in Section 6.3.3.1. In the construction of optimized transfers to L_1 Lissajous orbits in the ephemeris model, the optimized transfers from the CRTBP analysis, termed the transfer segment, and seven revolutions along the Lissajous orbit, labeled the Lissajous segment, form an initial guess for the optimization strategy. The SEZ constraint, i.e., the communications constraint, is enforced as a path constraint in Equation (6.29). The steps consistent with the optimization scheme for this scenario are outlined in Section 6.4. The total ΔV results for the range of optimal transfers are plotted in Figure 6.60 corresponding to a departure epoch of June 2, 2022 12:00:00.000. A comparison of the optimized Type A transfers is plotted in Figure 6.60(a) with Type B transfers displayed in Figure 6.60(b), note that the color represents the TOF for the transfer segment. Observe that the total ΔV difference, between the ephemeris and CRTBP results, range for Type A transfers is 4.0 m/s $\leq \Delta V \leq$ 227 m/s and for Type B transfers is 1.5 m/s $\leq \Delta V \leq$ 164 m/s. The optimized transfer geometries in the Sun-Earth rotating frames for Type A and B transfers are plotted in Figures 6.61 and 6.63 with the SEZ cone presented in red. Additionally, an inertial view of the locally optimal results are plotted in Figures 6.62 and 6.64. Observe that in Figures 6.61-6.64, the transfer segments are displayed via a range of color representing the GTO departure Ω value and the Lissajous segment is in black. The injection points are marked in magenta and any additional maneuvers are marked as red points. In the Sun-Earth rotating frame, i.e., Figures 6.61 and 6.63, the geometries of the ephemeris transfers are similar in configuration space, i.e., position space, to the optimized transfers in the CRTBP model. Next, the motion of the Lissajous segment for Type A transfers, i.e., corresponding to an ideal injection point of $\theta_2 = 152.85°$, in Figure 6.61 is counter-clockwise; note that the $\hat{y}$ -$\hat{z}$ view is directed from an Earth observer. Additionally, the motion of the Type B transfer, i.e., $\theta_2 = 335.35°$, is clockwise in the $\hat{y}$ -$\hat{z}$

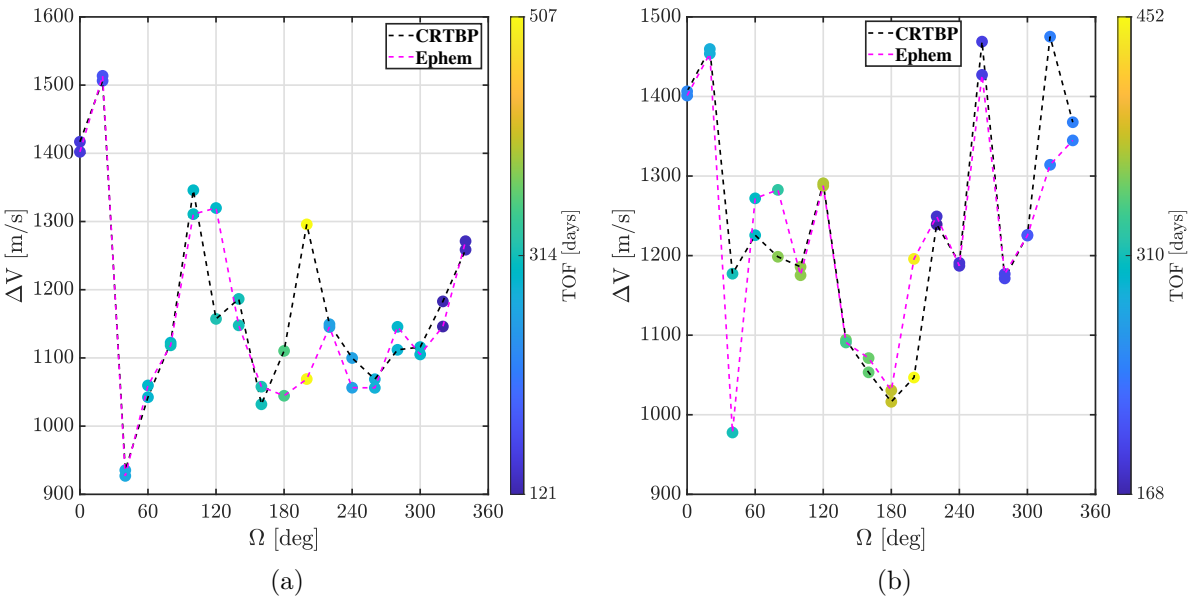

Figure 6.60. : ΔV information for the optimized transfers into an L_1 Lissajous orbit at the desired injection points corresponding to (a) Type A and (b) Type B transfers from a departure epoch of June 2, 2022 12:00:00.000. The difference between the results from the CRTBP (magenta) and ephemeris (black) vary at each departure location, i.e., Ω

projection of Figure 6.63. Finally, in the rotating frame, the location of the injections points, in magenta, for the ephemeris transfers are contained within a small region, as opposed to the fixed injection point asssociated with all optimized CRTBP transfers. Recall that in the optimization process in ephemeris, the location of the injection point is unconstrained. In the inertial EME frame, presented in Figures 6.62 and 6.64, the injection points for the ephemeris transfer are not contained within a certain region and are distributed along positions in configuration space. Recall that the Lissajous segment, i.e., the optimized transfer segment after the injection maneuver, OIM, is plotted in black. In the selection of injection points, the objective is to enter a Lissajous orbit and maximize the time outside the SEZ cone, i.e., T_{out}. For the optimized transfers in the CRTBP, T_{out} is computed by using information from the Lissajous orbit, see Figure 6.22. The T_{out} values for Type A and B ephemeris transfers are plotted in Figure 6.65.

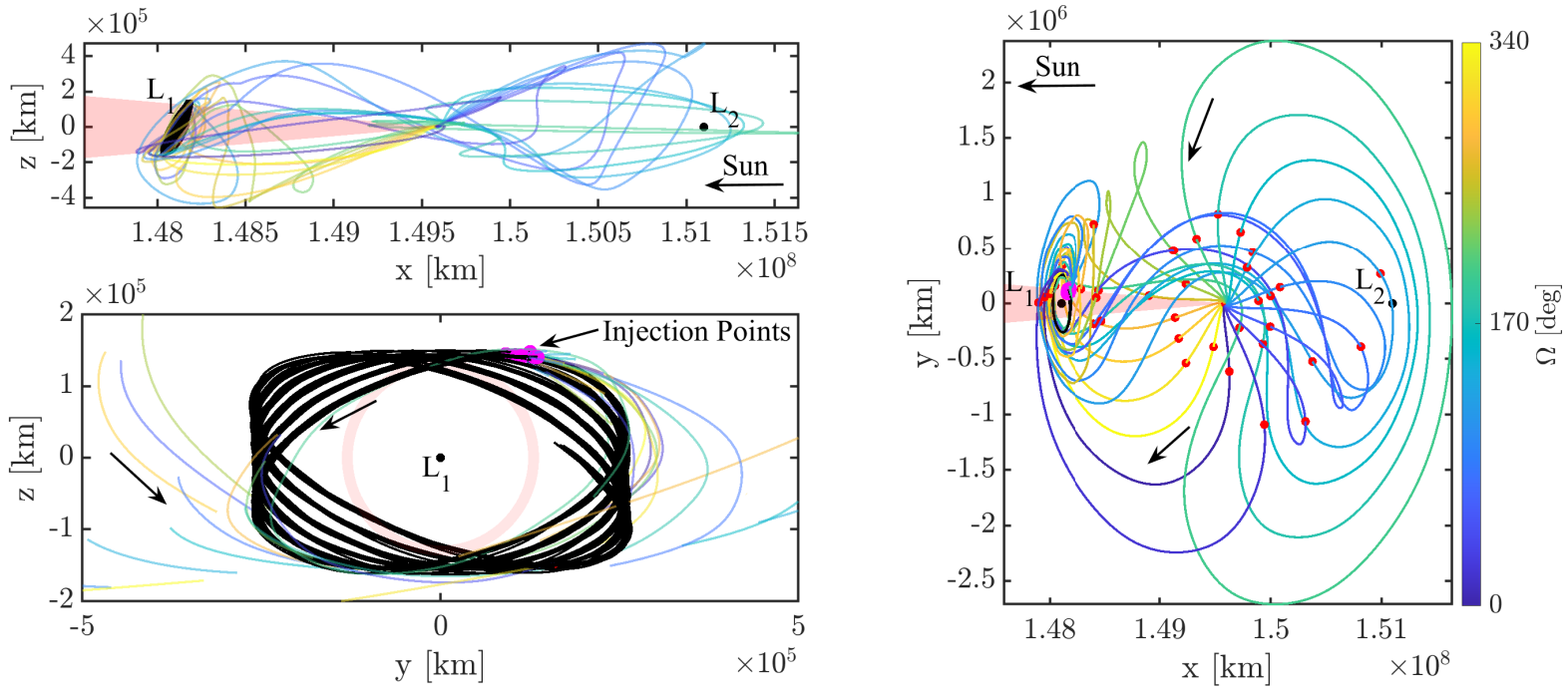

Figure 6.61. : Optimized Type A transfers in the rotating frame to Sun-Earth L_1 Lissajous orbit with a departure epoch of June 2, 2022 12:00:00.000. The motion of the Lissajous segment in the $\bar{y}$-$\hat{z}$ projection, as viewed from the Earth, is counter-clockwise

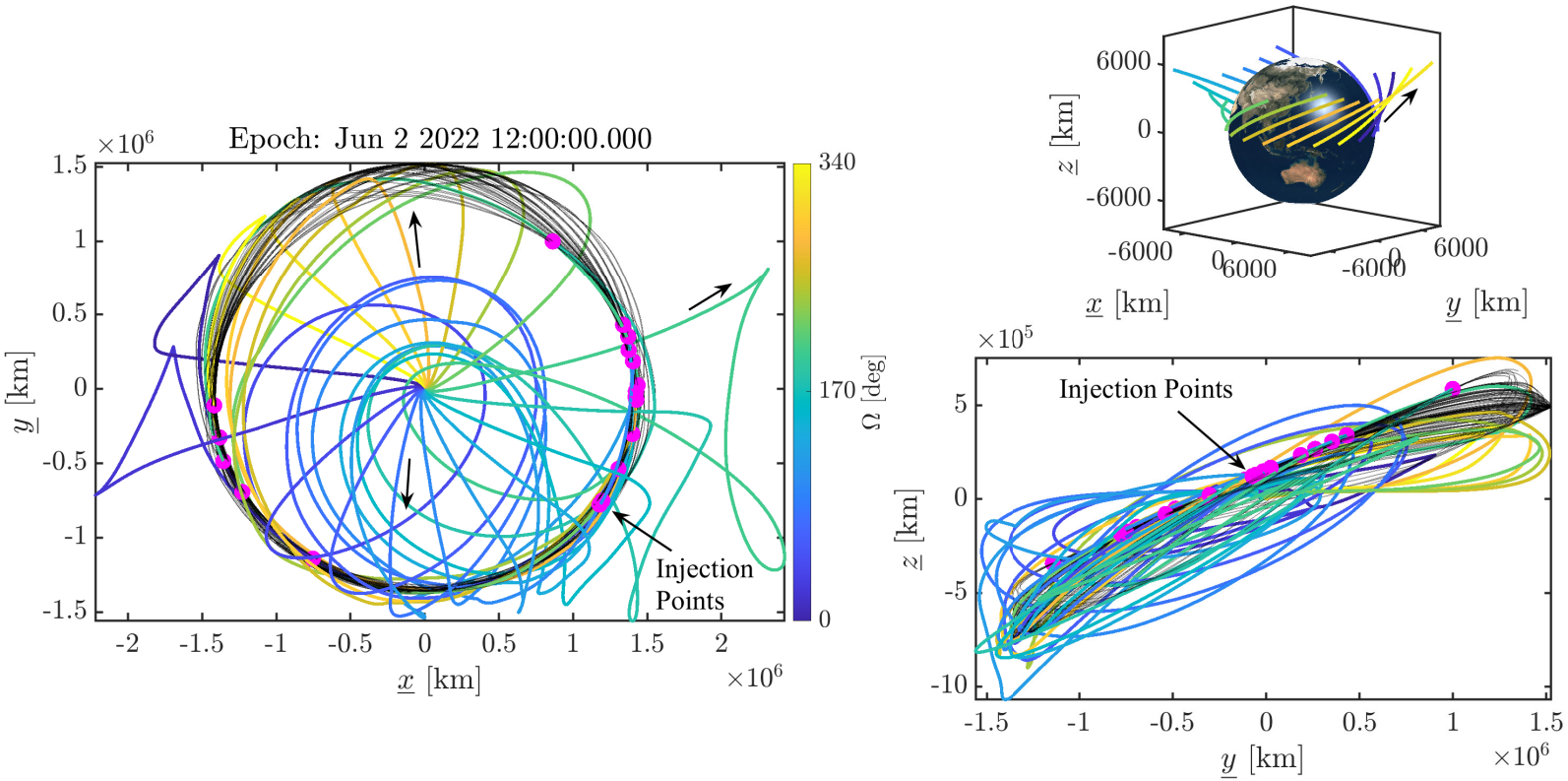

Figure 6.62. : Optimized Type A transfers in the inertial EME frame to Sun-Earth L_1 Lissajous orbit with a departure epoch of June 2, 2022 12:00:00.000. The Lissajous segment is in black and the transfers are depicted via a range of colors

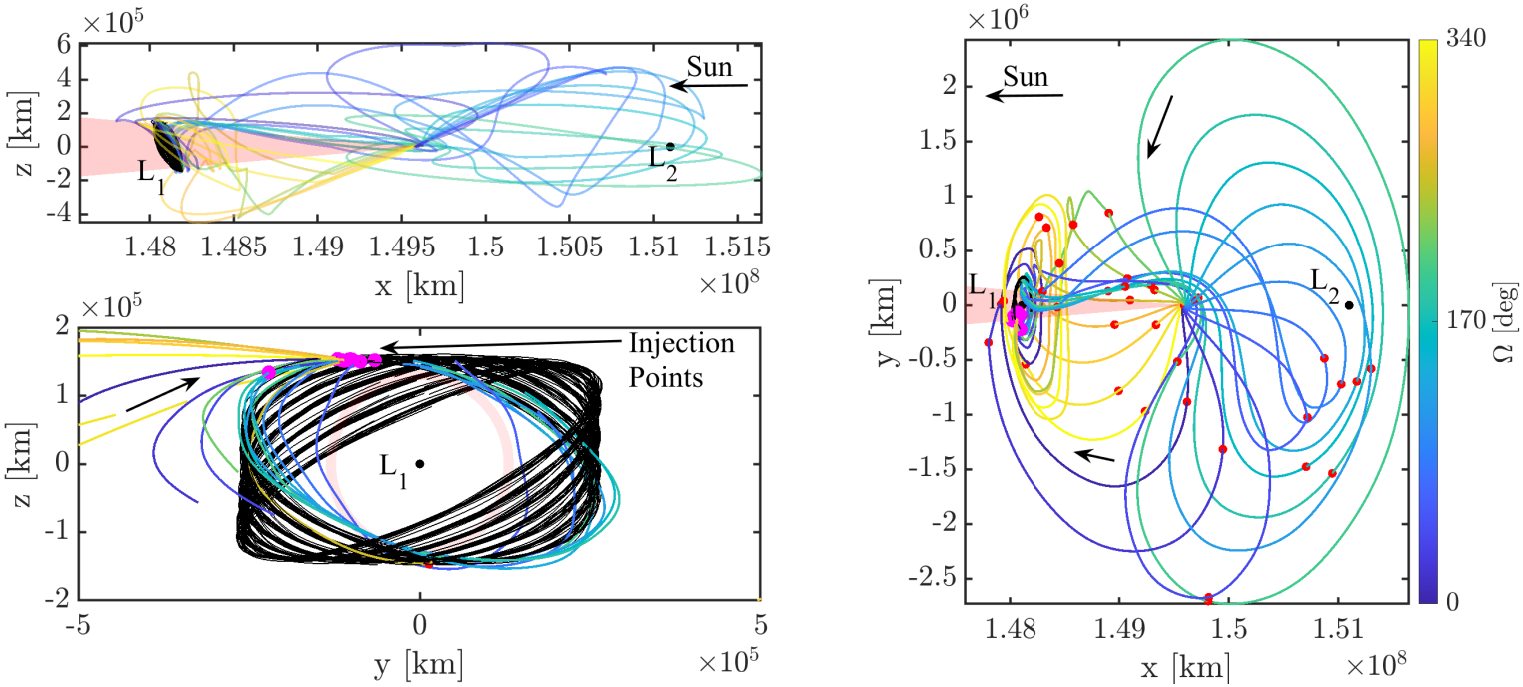

Figure 6.63. : Optimized Type B transfers in the rotating frame to Sun-Earth L_1 Lissajous orbit with a departure epoch of June 2, 2022 12:00:00.000. The motion of the Lissajous segment in the $\bar{y}$-$\hat{z}$ projection, as viewed from the Earth, is clockwise

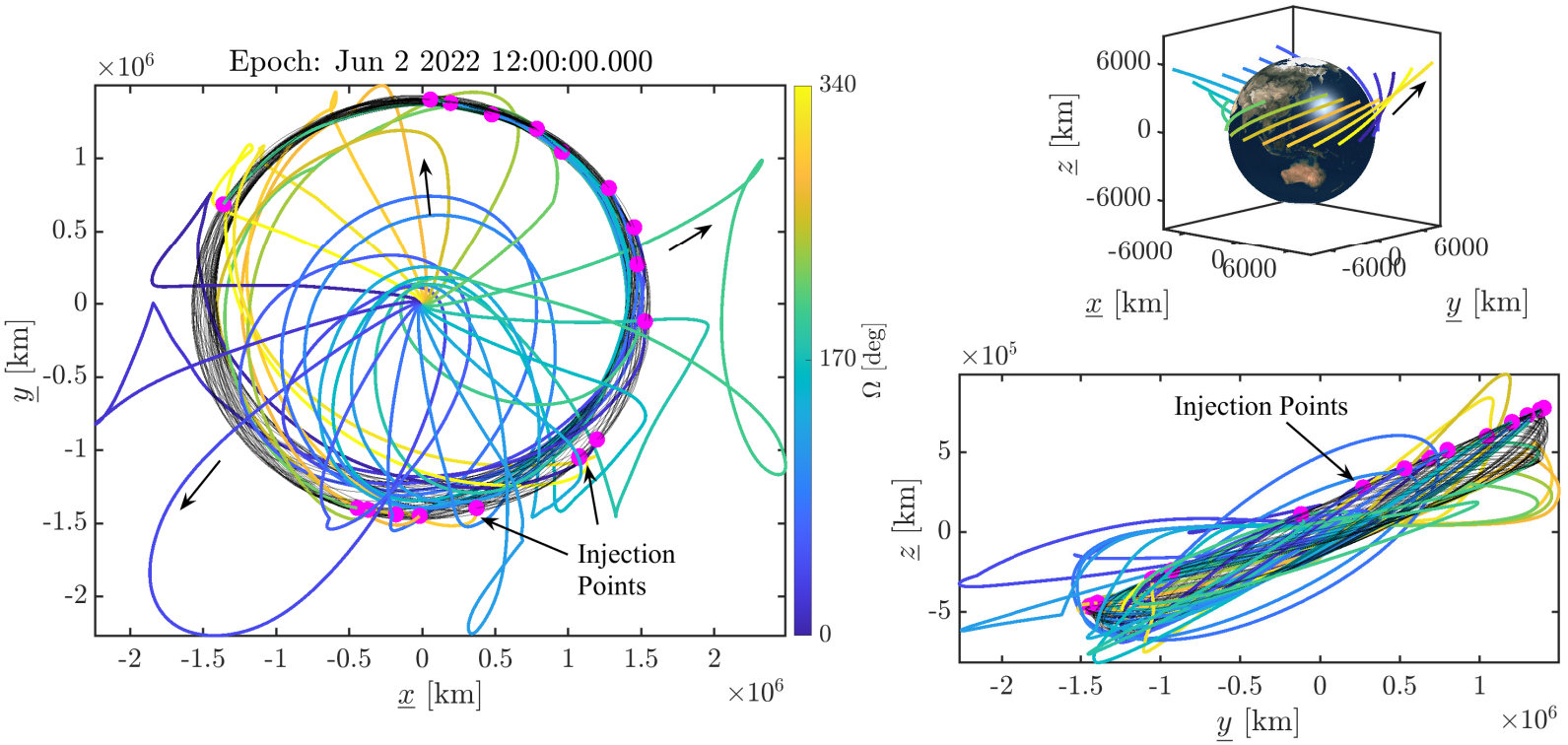

Figure 6.64. : Optimized Type B transfers in the inertial EME frame to Sun-Earth L_1 Lissajous orbit with a departure epoch of June 2, 2022 12:00:00.000. The Lissajous segment is in black and the transfers are depicted via a range of colors

For the locally optimal CRTBP transfer, the time outside the SEZ is 794 days, i.e., approx-

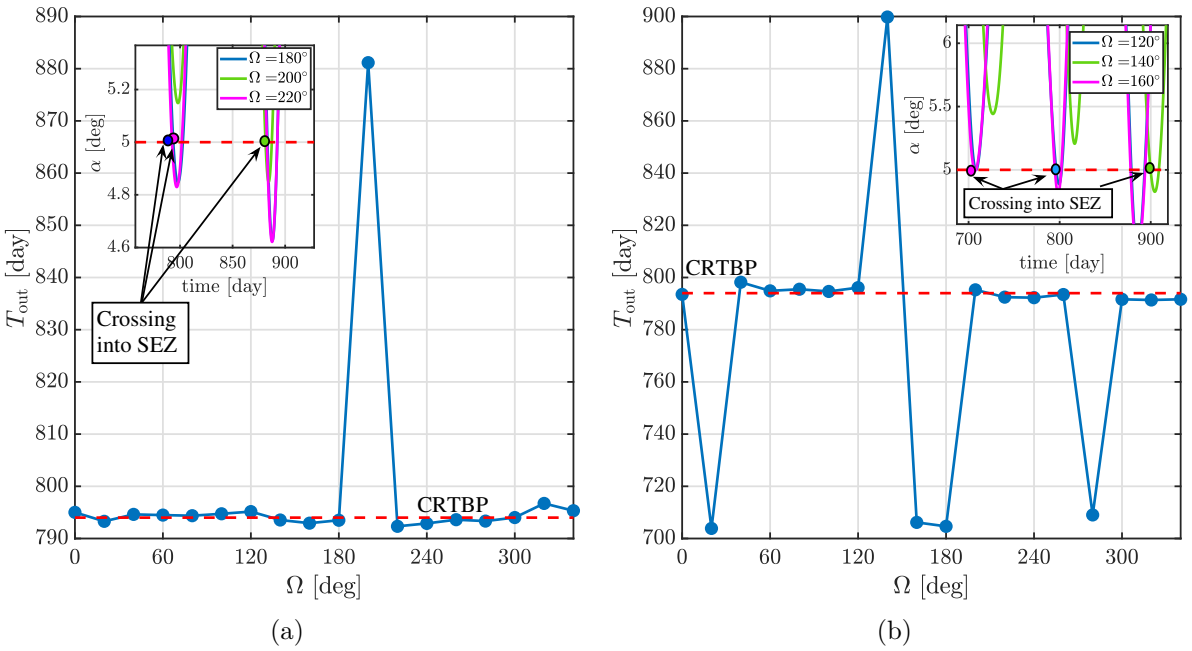

Figure 6.65. : Time outside the SEZ region, T_{out}, for the optimized transfers into an L_1 Lissajous orbit at the desired injection points corresponding to (a) Type A and (b) Type B transfers from a departure epoch of June 2, 2022 12:00:00.000. The fixed value of the CRTBP T_{out} value is presented in a red dashed line

imately over two years, displayed as a red dashed line in Figure 6.65. In Figure 6.65(a), corresponding to Type A transfers, most optimized ephemeris transfers have a T_{out} value within 10 days of the CRTBP T_{out} value. However, for the transfer corresponding to $\Omega = 200°$, the T_{out} value is significantly longer because it contains an additional revolution above the SEZ constraint, defined via an SEV angle of $\alpha_{\text{SEZ}} = 5°$. Alternatively, for Type B transfers in Figure 6.65(b), there is more variation in the T_{out} values over the different GTO departure locations. Observe that the maximum T_{out} variation is approximately 90 days, i.e., half the period of one revolution along the Lissajous orbit, note that the time between each valley in the SEV, α, plot for each transfer is approximately 90 days. In this investigation, optimized transfers in the CRTBP model into selected locations along a Lissajous orbit in the Sun-Earth L_1 point are successfully transitioned into the ephemeris model. Note that the optimized results implemented a path constraint in the ephemeris model to maintain the

trajectories outside an enforced communications region, i.e., the SEZ region. Finally, the optimization method implemented is easily extended to different departure epochs.

6.4.4 Optimized Ephemeris Transfers to L_2 Lissajous Orbits

Optimized transfers over a range of GTO departure states to a Sun-Earth L_2 Lissajous orbit are constructed in the ephemeris model. Locally optimal transfers into a Sun-Earth L_2 Lissajous orbits, with a similar geometry to the Gaia mission[13], are computed for the range of GTO departure states listed in Table 4.1. Recall that in Section 6.3.2, two ideal L_2 Lissajous injection locations are identified such that the time outside the Earth's penumbra, T_{out}, is maximized. The Earth's penumbra is illustrated in Figure 5.60 and the constraint is formulated such that the satellite shadow angle, ζ defined via Equation (5.73), is greater than the penumbra angle, ζ_{PU}. Additionally, optimized transfers for each ideal injection points are separated into Type A, the motion of trajectory is counter-clockwise when viewed from an Earth observer, and Type B, i.e., clockwise motion. From Figure 6.34, Type A transfers correspond to an invariant curve angle of $\theta_2 = 93.8°$ and Type B transfers are associated with $\theta_2 = 273.95°$, see Figures 6.36-6.37 for the corresponding trajectories. The locally optimized transfer results within the context of the CRTBP model are summarized in Section 6.3.3.2. In the construction of optimized transfers to L_2 Lissajous orbits in the ephemeris model, the optimized transfers from the CRTBP analysis, i.e., the transfer segment, and 16 revolutions along the L_2 Lissajous orbit, labeled the Lissajous segment, form an initial guess for the optimization strategy. The eclipsing constraint is enforced as a path constraint in Equation (6.29) with the steps consistent with the optimization scheme for this scenario outlined in Section 6.4. The total ΔV results for the range of optimal transfers are plotted in Figure 6.66 corresponding to a departure epoch of December 2, 2022 12:00:00.000. A comparison of optimized Type A transfers is plotted in Figure 6.66(a) with Type B transfers displayed in Figure 6.66(b), note that the color represents the TOF for the transfer segment. Observe that the ΔV difference range for Type A transfer is 1 m/s $\leq \Delta V \leq$ 141 m/s and for Type B is 1 m/s $\leq \Delta V \leq$ 82 m/s. The optimized transfer geometries in the Sun-Earth rotating

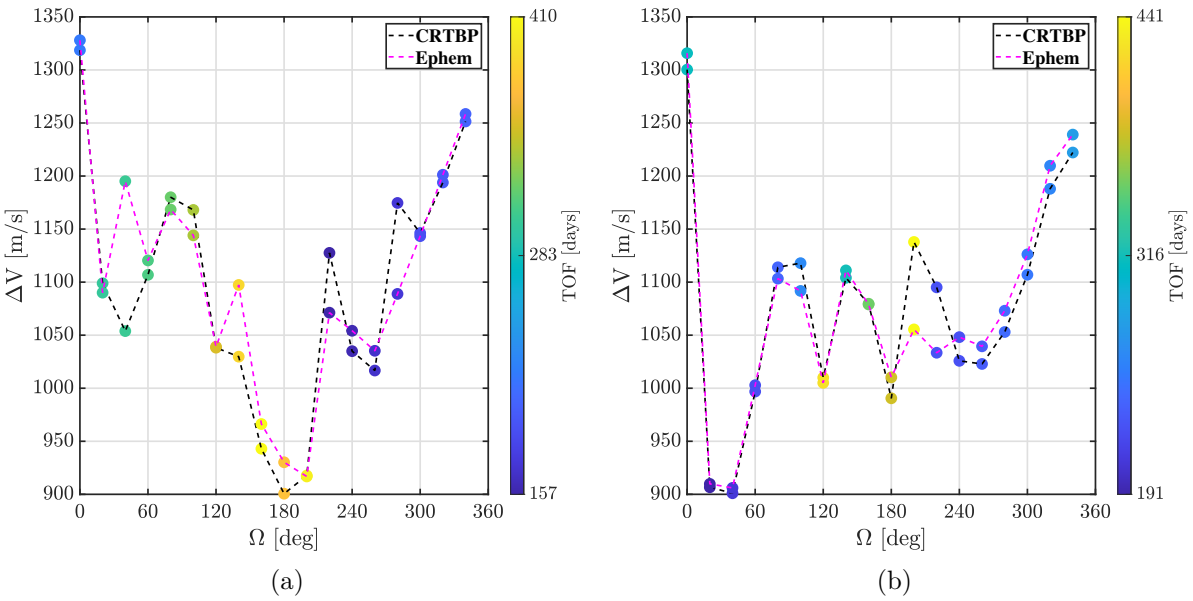

Figure 6.66. : ΔV information for the optimized transfers into an L_2 Lissajous orbit at the desired injection points corresponding to (a) Type A and (b) Type B transfers from a departure epoch of December 2, 2022 12:00:00.000. The difference between the results from the CRTBP (magenta) and ephemeris (black) vary for each departure location, i.e., Ω

frames for Type A and B transfers are plotted in Figures 6.67 and 6.69 with the SEZ cone presented in red. Additionally, the inertial view for the locally optimal results are plotted in Figures 6.68 and 6.70. Observe that in Figures 6.67 and 6.69, the transfer segments are displayed via a range of color representing the GTO departure Ω value and the Lissajous segment is in black. Additionally, the injection points are marked in magenta and the additional maneuvers are marked as red points; recalling that two DSMs are included along the transfer. In the Sun-Earth rotating frame, i.e., Figures 6.67 and 6.69, the geometries of the ephemeris transfers are similar in configuration space, i.e., position space, to the optimized results in the CRTBP model. The motion of the Lissajous segment observed for Type A transfers, in Figure 6.61, is counter-clockwise and the motion for Type B transfers is clockwise; note that the $\hat{y}$ -$\hat{z}$ view is directed from an Earth observer.

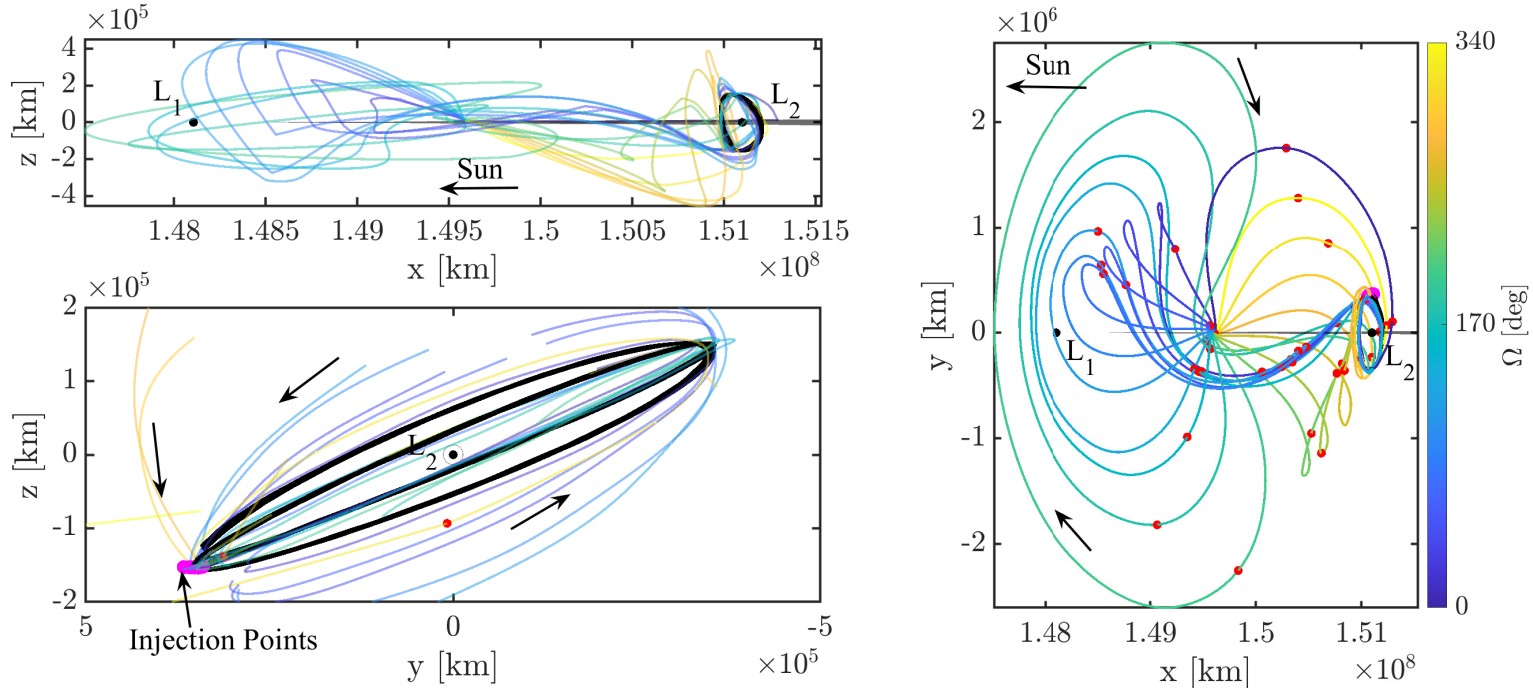

Figure 6.67. : Optimized Type A transfers in the rotating frame to Sun-Earth L_2 Lissajous orbit with a departure epoch of December 2, 2022 12:00:00.000. The motion of the Lissajous segment in the $\bar{y}$-$\hat{z}$ projection, as viewed from the Earth, is counter-clockwise. Note that only two revolutions along the Lissajous orbits are plotted

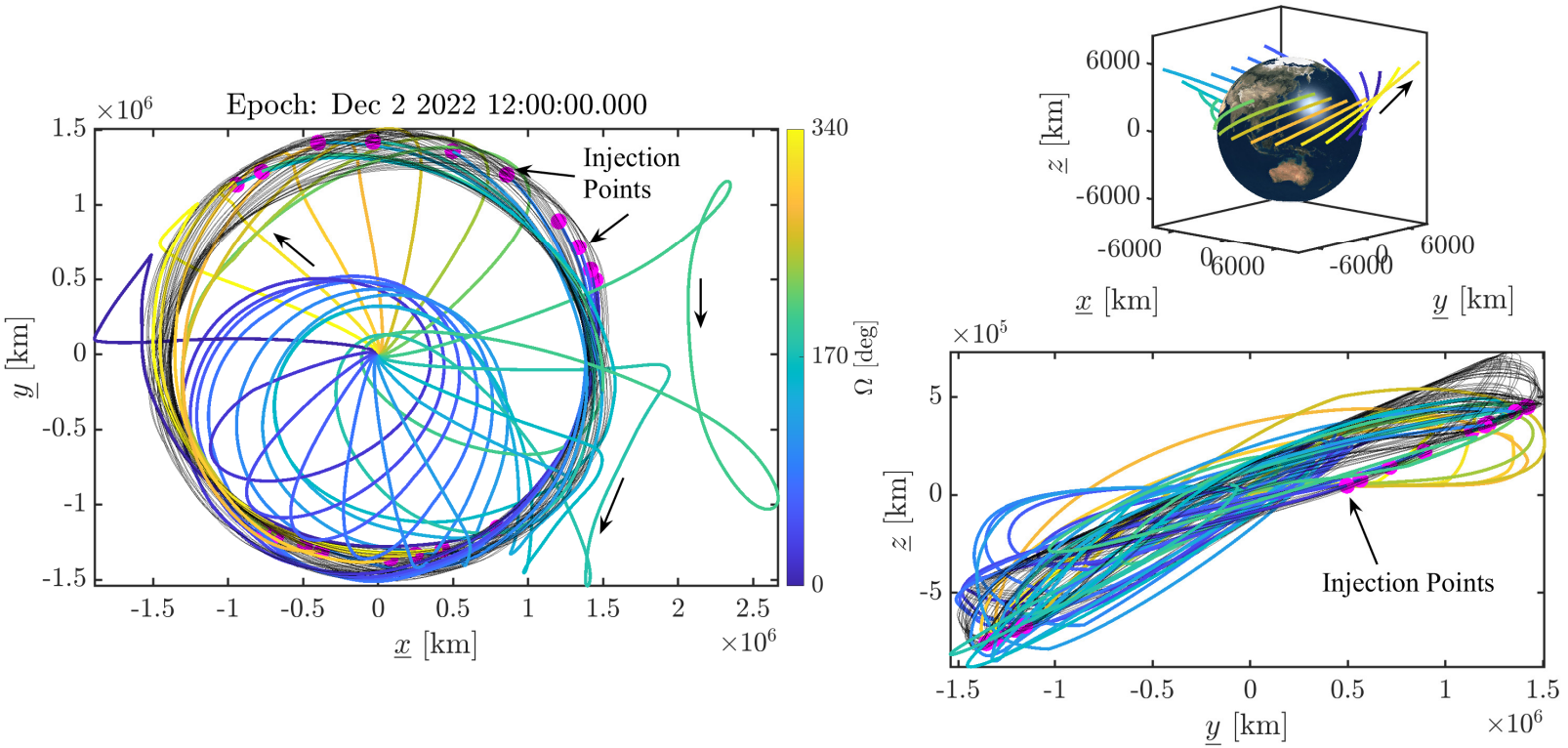

Figure 6.68. : Optimized Type A transfers in the inertial EME frame to Sun-Earth L_2 Lissajous orbit with a departure epoch of December 2, 2022 12:00:00.000. The Lissajous segment is in black and the transfers are depicted via a range of colors

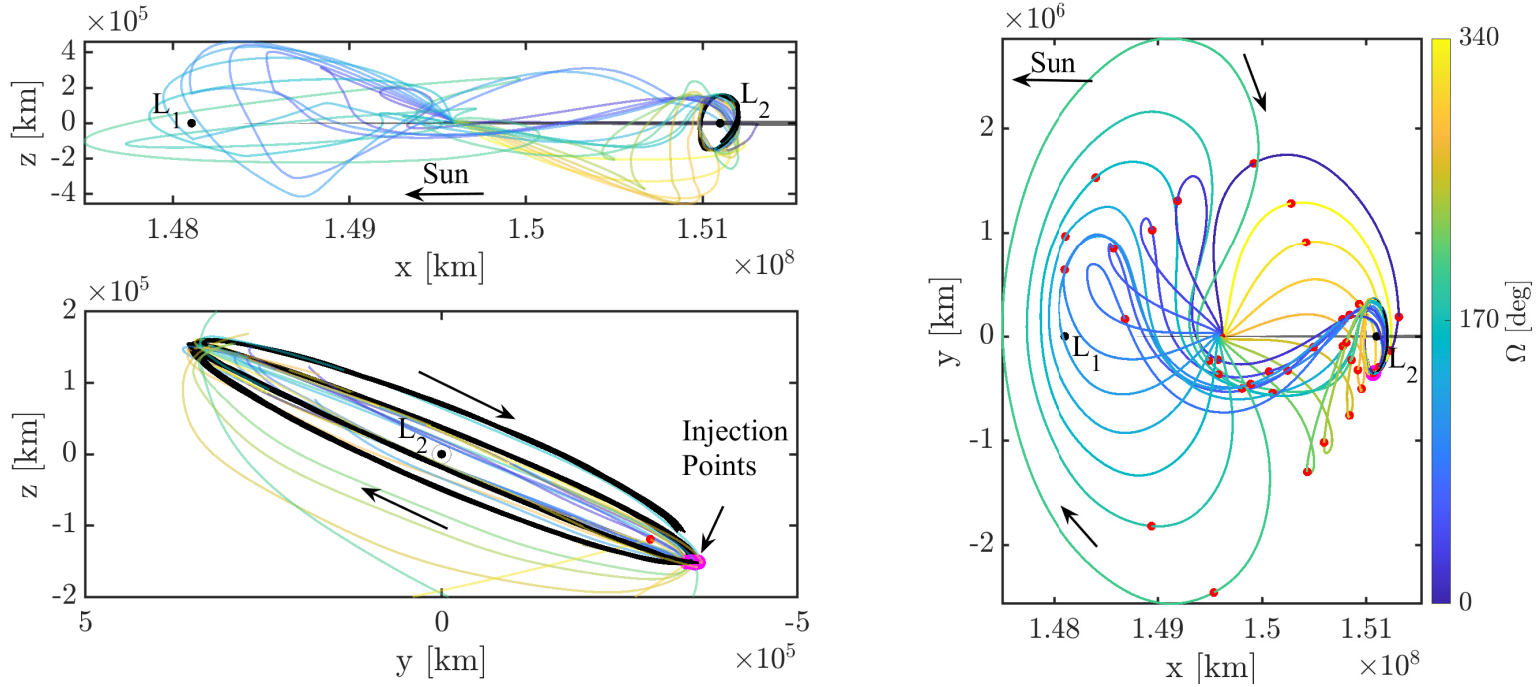

Figure 6.69. : Optimized Type B transfers in the rotating frame to Sun-Earth L_2 Lissajous orbit with a departure epoch of December 2, 2022 12:00:00.000. The motion of the Lissajous segment in the $\bar{y}$-$\hat{z}$ projection, as viewed from the Earth, is clockwise. Note that only two revolutions along the Lissajous orbits are plotted

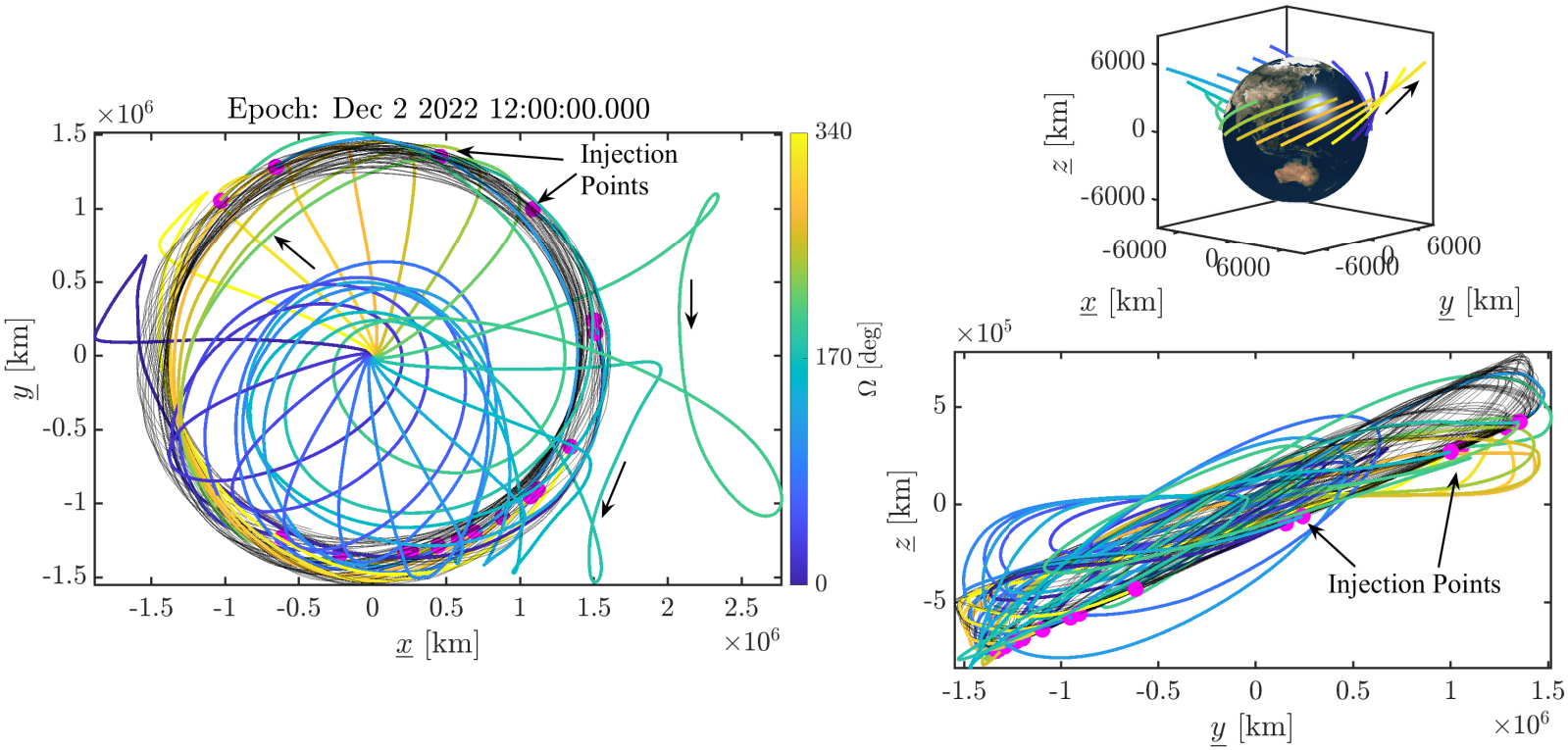

Figure 6.70. : Optimized Type B transfers in the inertial EME frame to Sun-Earth L_2 Lissajous orbit with a departure epoch of December 2, 2022 12:00:00.000. The Lissajous segment is in black and the transfers are depicted via a range of colors

Observe that, in the rotating frame, the location of the injections points, in magenta, for the ephemeris transfers are contained within a small region, as opposed to the fixed injection point asssociated with all optimized CRTBP transfers. In Figures 6.67 and 6.69, only two revolutions around the Lissajous orbit are plotted, however 16 revolutions are included in the ephemeris optimization process. In the inertial EME frame, presented in Figures 6.68 and 6.70, the injection points for the ephemeris transfer are not contained within a certain region and are distributed in configuration space. Recall that the Lissajous segment, i.e., the optimized trajectory segment after the injection maneuver, OIM, is plotted in black. In the selection of injection points, the objective is to enter a L_2 Lissajous orbit and maximize the time before the satellite crosses into the penumbra shadow region, i.e., T_{out}. For the optimized transfers in the CRTBP, T_{out} is computed by using information from the L_2 Lissajous orbit, see Figure 6.34. The T_{out} values for Type A and B ephemeris transfers are plotted in Figure 6.71. For the locally optimal CRTBP transfer, the time outside the SEZ is 2715 days,

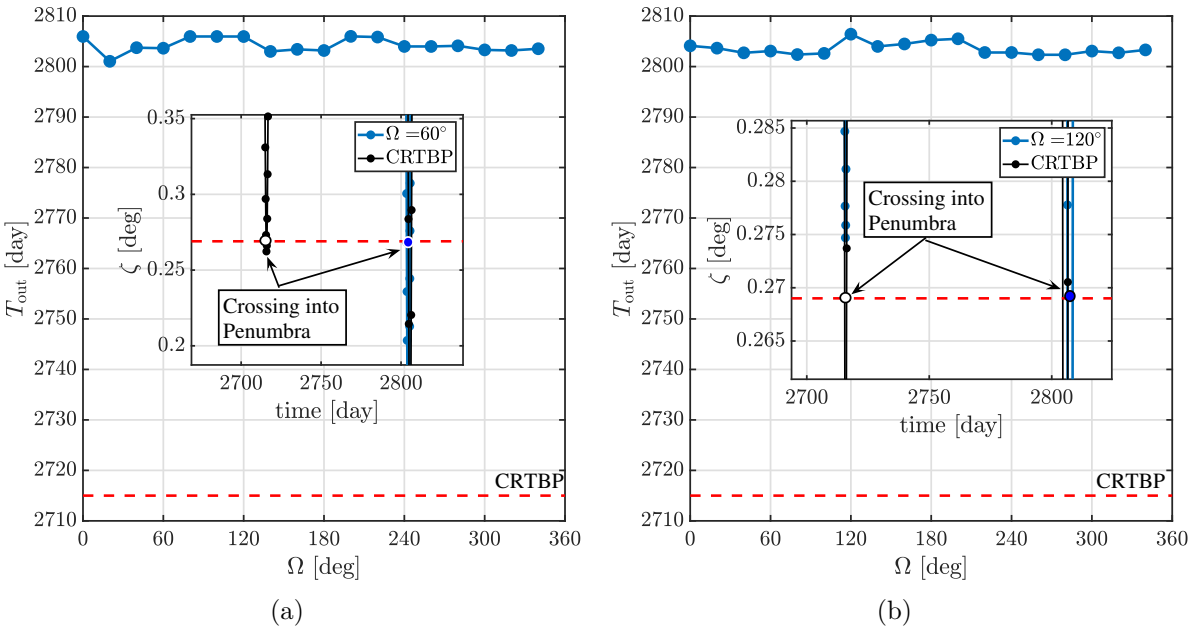

Figure 6.71. : Time outside the SEZ region, T_{out}, for (a) Type A and (b) Type B transfers from a departure epoch of December 2, 2022 12:00:00.000. The fixed value of the CRTBP T_{out} value is presented in a red dashed line

i.e., approximately over seven years, displayed as a red dashed line in Figure 6.71. For Type A and B transfer, the T_{out} values are approximately 90 days above the CRTBP time

of 2715 days; recall that the period of one revolution along the Lissajous orbit is roughly 180 days and the time between each valley in the shadow angle, ζ, plot for each transfer is approximately 90 days. In this investigation, optimized transfers in the CRTBP model into selected locations along a Lissajous orbit in the Sun-Earth L_2 point are successfully transitioned into the ephemeris model. Note that the optimized results implemented a path constraint in the ephemeris model to maintain the trajectories outside an enforced eclipsing constraint. Finally, the optimization method implemented is easily extended with different departure epochs.

7. CONCLUDING REMARKS

The construction of efficient transfers in the Sun-Earth system for ridesharing spacecraft necessitates flexible strategies that leverage the dynamical structures available in the CRTBP model. With the introduction of propulsive ESPA rings, transfers to regions beyond GEO become available for dropped-off secondary payloads in a ridesharing configuration. The propulsive ESPA ring is, essentially, an upper stage for secondary payloads and offers the opportunity to deliver multiple spacecraft, i.e., smallsats, to regions near the Sun-Earth Lagrange points. In this investigation, strategies are formulated to construct transfers for secondary payloads in a drop-off GTO to orbits near Sun-Earth L_1 and L_2 points. To address the absence of information regarding GTO orientation and departure epochs, the strategies offered in this investigation produce a families of transfers from a range GTO departure locations. The methodologies formulated in this analysis produce efficient transfer options by implementing a dynamical systems approach rather than a large and possibly computationally expensive grid search. Additionally, the transfers produced are easily transitioned into a higher-fidelity model to verify the persistence of any desired transfers properties, such as geometry or TOF. The transfer results are summarized in the following Sections.

7.1 Summary of Ballistic Transfers in the Sun-Earth System

In this investigation, the ridesharing scenario includes a secondary payload, i.e., a smallsat, delivered into a GTO with a periapsis altitude of 185 km. With no a priori information about the orientation of the drop-off GTO, i.e., Keplerian orbital elements, or the departure epochs, transfer options for secondary payloads are constructed for a range of GTO departure locations. Recall that the secondary payload departs the GTO at periapsis, such that, a GTO departure location is essentially the position of the GTO periapsis in configuration space. Ballistic transfers, i.e., single maneuver transfer, to orbits in the Sun-Earth system are constructed by leveraging the invariant stable manifold structures corresponding to periodic and quasi-periodic orbits. In the context of this investigation, ballistic transfers

represent the most theoretically efficient, not assuming maneuver errors, "one burn" transfers available to secondary payloads; note that efficiency does not correspond to low ΔV magnitudes. Two families of periodic orbits are investigated, the planar-Lyapunov orbits and out-of-plane halo orbits near Sun-Earth L_1 and L_2 . Transfers for the planar Lyapunov orbits are available from most GTO departure locations near the Earth with the Periodic Orbit Ballistic Transfer Gap classified as a region with no available ballistic transfers. Transfers from both prograde and retrograde GTOs are constructed with this methodology. Families of ballistic transfers into the spatial halo orbits near Sun-Earth L_1 and L_2 are contained in closed one-dimensional curves. The GTO departure locations corresponding to spatial halo orbits is more limited, however, the addition of ballistic transfers to quasi-halo orbits increases the region of access. By considering quasi-periodic orbits, ballistic transfers are available from a wider range of GTO departure locations. Note that both direct and indirect, i.e., containing an outbound excursion or Earth flybys, ballistic transfers are constructed.

A guide for direct ballistic transfers from prograde GTOs to quasi-periodic orbits near Sun-Earth L_1 and L_2 is constructed over a range of GTO orientations around the Earth. This guide is a reference of direct ballistic transfers from a secondary payload for a range of prograde GTO orientations to quasi-periodic orbits near the Sun-Earth Lagrange points. Additional constraints, such as communications and Earth eclipsing constraints, are enforced throughout the transfers. To incorporate additional constraints, such as the Solar Exclusion Zone and Earth penumbra condition, a path constraint function is formulated and implemented in a differential corrections process. The introduction of the SEZ and eclipsing constraints increases the ΔV magnitude from GTOs with lower inclinations. Finally, the persistence of specific properties of ballistic transfers, such as geometry, is observed when transitioned to a higher-fidelity model. The information summarized in the collection of direct ballistic transfers provide initial orbit sizes, i.e., orbit amplitudes, and approximate ΔV magnitudes over a range of GTO orientations.

7.2 Multiple-Maneuver Transfers to Sun-Earth Lagrange Point Orbits

Multiple-maneuver transfers to predetermined orbits near Sun-Earth Lagrange points are constructed by leveraging dynamical structures in the CRTBP model. In this analysis, specific periodic and quasi-periodic orbits near Sun-Earth L_1 and L_2 are selected as potential destinations for secondary payloads. To construct multiple-maneuver transfers to a pre-selected orbit, families of two-maneuver transfers are generated by leveraging trajectories within the stable manifold structures associated with the target orbit. Note that the two-maneuver magnitudes include a Transfer Injection Maneuver and a Deep Space Maneuver. For periodic orbits, families of two-maneuver transfers incorporating a tangent DSM are contained in a one-dimensional curve. Additionally, two-maneuver transfers into an ideal injection point along a Lissajous orbit occur along a two-dimensional surface. For both periodic and quasi-periodic orbit destinations, direct and indirect transfers are considered. The information retrieved from the families of two-maneuver transfers is implemented in the construction of optimized transfers in the CRTBP model and the ephemeris model for a fixed departure epoch. To address the absence of GTO orientation information, transfers over a range of GTO departure locations near the Earth are constructed in both dynamical models. Through this method, orientations corresponding to low total ΔV are identified. The methodologies formulated in this investigation are easily extended to generate optimized transfers to any periodic or quasi-periodic orbit near Sun-Earth L_1 and L_2 Lagrange points, as well as, for different CRTBP models.

7.3 Recommendations for Future Work

The methodologies proposed in this analysis serve to construct efficient transfers to periodic and quasi-periodic orbits near the collinear Lagrange points in the Sun-Earth system. An extension of this analysis is provided by the following recommendations:

1. **Investigate Alternative Departure Locations along GTO** - To construct ballistic transfers and multiple-maneuver transfers in this analysis, the departure location along the GTO is selected as the periapsis. However, an analysis from a range of GTO locations away from periapsis exposes the viable range of approximate ΔV required for ballistic transfers. This extended analysis would also reveal the variation in orbit size, i.e., orbit amplitude, associated with ballistic transfers.

2. **Transfer Applications with a Waiting Period along GTO** - In this investigation, waiting along a GTO is not considered, that is, once the primary payload is detached, consistent with the ridesharing scenario, the secondary payload departs the GTO at the next periapsis opportunity. Within the context of the rotating frame of the CRTBP, waiting along a GTO allows the line of apsides to shift and, since the secondary payload departs at the GTO periapsis, shifts the position of the GTO departure state. The addition of a waiting period will provide approximate ΔV for ballistic transfers and reveal alternative potential orbit options near Sun-Earth L_1 and L_2 points.

3. **Altitude Variation Analysis for Indirect Transfers** - A study on the variation of the GTO departure altitude is conducted for ballistic transfers to Lyapunov and spatial halo orbits to Sun-Earth Lagrange points with direct transfers. An extended analysis including indirect transfer, i.e., transfers with outbound excursions or Earth flybys, would reveal additional transfer options for a wider region of GTO departure locations. Additionally, indirect ballistic transfers to quasi-periodic orbits provides increasing opportunities for an extended range GTO orientations.

4. **Ballistic Transfers for Smallsats with Low-Thrust Capabilities** - In constructing ballistic transfers, the size of the corresponding orbit is free, that is, the orbit amplitudes are unconstrained. A future application of this research is to combine the ballistic transfers with a smallsat with low-thrust capabilities. In this scenario, a secondary payload, i.e., a smallsat with a low-thrust engine, is transported to an orbit near Sun-Earth L_1 or L_2 via a propulsive ESPA ring. Upon arrival, the low-thrust engine is utilized to achieve any potential science orbit. In this strategy, the smallsat

benefits from the "free transfer" provided by the propulsive ESPA ring and can leverage the natural dynamics near the Lagrange points and the low-thrust engine to enter more complex orbit geometries.

5. **Incorporate Lunar Flybys** - In this investigation, ballistic transfers and multiple-maneuver transfers are constructed over a range of GTO departure locations. The strategies implemented in this analysis are in the context of the Sun-Earth CRTBP model and do not include the influence of the Moon. For ballistic transfers, the addition of Lunar flybys along the transfer trajectory would reveal new feasible ΔV magnitudes and orbit geometries. By including a path constraint, such as an SEZ or eclipsing constraint, the addition of a Lunar flyby may aid in decreasing the single maneuver ΔV. Alternatively, a Lunar flyby analysis for multiple-maneuver transfers from GTO to a pre-selected orbit will also reveal important modifications to the total ΔV. To investigate transfers with Lunar flybys, the Bi-circular Four Body Problem would be the prefered dynamical model.

6. **Application of Strategy in Alternative CRTBP Systems** - The strategy for constructing two-maneuver transfers is not limited to the Sun-Earth system, but may be applied to any CRTBP model, e.g., the Earth-Moon or Sun-Mars systems. The construction of the two-maneuver transfers leverages the stable manifold information associated with periodic and quasi-periodic orbits. Additionally, the parameterization of the global analog of the stable, and unstable, manifolds may be applied to other transfer scenarios, such as transfers between L_1 and L_2 Lagrange points.

By incorporating fundamental dynamical behaviors, the proposed research offers opportunities to observe more complex pathways available for secondary payloads.

REFERENCES

[1] T. D. Chavez, M. J. Barrera, and M. H. Kanter, "Operational satellite concepts for espa rideshare," in *2007 IEEE Aerospace Conference*, IEEE, 2007, pp. 1–7.

[2] P. Tompkins, R. Hunt, M. D'Ortenzio, *et al.*, "Flight operations for the lcross lunar impactor mission," in *SpaceOps 2010 Conference Delivering on the Dream Hosted by NASA Marshall Space Flight Center and Organized by AIAA*, 2010, p. 1986.

[3] R. Pritchett, K. Howell, and D. Folta, "Low-thrust trajectory design for a cislunar cubesat leveraging structures from the bicircular restricted four-body problem," in *70th International Astronautical Congress, Washington D.C., USA*, 2019, pp. 1–18.

[4] M. Stender, C. Pearson, J. Maly, and C. Loghry, "Mission case studies using the rideshare enabling orbital maneuvering vehicle," in *2015 IEEE Aerospace Conference*, IEEE, 2015, pp. 1–9.

[5] C. Pearson, M. Stender, C. Loghry, *et al.*, "Rideshare and the orbital maneuvering vehicle: The key to low-cost lagrange-point missions," in *Proc. 29th Annu. AIAA/US Conf. Small Satellite*, 2015.

[6] SpaceX Info. "Spacex missions summary." (2021), [Online]. Available: https://spacex-info.com/launch-list/.

[7] E. Kyle. "Space launch report." (2021), [Online]. Available: https://www.spacelaunchreport.com/index.html.

[8] J. Berk, J. Straub, and D. Whalen, "The open prototype for educational nanosats: Fixing the other side of the small satellite cost equation," in *2013 IEEE Aerospace Conference*, IEEE, 2013, pp. 1–16.

[9] R. Woolley and Z. Olikara, "Optimized low-thrust missions from gto to mars," in *2019 IEEE Aerospace Conference*, IEEE, 2019, pp. 1–10.

[10] B. Foing, O. Camino, J. Schoenmakers, *et al.*, "Smart-1 mission overview from launch, lunar orbit to impact," *Lunar Planet. Sci. XXXVIII (CD-ROM)(Abstract# 1915. Lunar & Planetary Institute, Houston)*, 2007.

[11] C. Roberts, "Long term missions at the sun-earth libration point l1: Ace, soho, and wind," *Advances in the Astronautical Sciences*, vol. 142, pp. 1263–1282, Jan. 2012.

[12] R. Farquhar, "The flight of isee-3/ice-origins, mission history, and a legacy," in *AIAA/AAS Astrodynamics Specialist Conference and Exhibit*, 1998, p. 4464.

[13] T. Prusti, J. De Bruijne, A. Brown, *et al.*, "The gaia mission," *Astronomy and Astrophysics*, vol. 595, 2016.

[14] N. Bosanac, C. M. Webster, K. C. Howell, and D. C. Folta, "Trajectory design and station-keeping analysis for the wide field infrared survey telescope mission," in *AAS/AIAA Astrodynamics Specialist Conference*, 2017.

[15] M. Lo, B. Williams, W. Bollman, *et al.*, "Genesis mission design," in *AIAA/AAS Astrodynamics Specialist Conference and Exhibit*, 1998, p. 4468.

[16] G. Gómez, A. Jorba, J. Masdemont, and C. Simó, "Study of the transfer from the earth to a halo orbit around the equilibrium pointl 1," *Celestial Mechanics and Dynamical Astronomy*, vol. 56, no. 4, pp. 541–562, 1993.

[17] Z. P. Olikara, "Computation of quasi-periodic tori and heteroclinic connections in astrodynamics using collocation techniques," Ph.D. Dissertation, University of Colorado Boulder, 2016.

[18] G. Gómez, J. Masdemont, and C. Simó, "Quasihalo orbits associated with libration points," *Journal of the Astronautical Sciences*, vol. 46, no. 2, pp. 135–176, 1998.

[19] K. C. Howell and H. J. Pernicka, "Numerical determination of lissajous trajectories in the restricted three-body problem," *Celestial Mechanics*, vol. 41, no. 1-4, pp. 107–124, 1987.

[20] B. P. McCarthy and K. C. Howell, "Trajectory design using quasi-periodic orbits in the multi-body problem," in *29th AAS/AIAA Space Flight Mechanics Meeting, Hawaii, USA*, 2019.

[21] D. Scheeres, S. Van wal, Z. Olikara, and N. Baresi, "Dynamics in the phobos environment," *Advances in Space Research*, vol. 63, no. 1, pp. 476–495, 2019.

[22] N. Baresi, "Spacecraft formation flight on quasi-periodic invariant tori," Ph.D. Dissertation, University of Colorado Boulder, 2017.

[23] K. C. Howell, "Three-dimensional, periodic, 'halo' orbits," *Celestial mechanics*, vol. 32, no. 1, pp. 53–71, 1984.

[24] V. Szebehely, "Theory of orbits: The restricted problem of three bodies," Yale univ New Haven, Connecticut, Tech. Rep., 1967.

[25] D. Guzzetti, N. Bosanac, A. Haapala, K. C. Howell, and D. C. Folta, "Rapid trajectory design in the earth–moon ephemeris system via an interactive catalog of periodic and quasi-periodic orbits," *Acta Astronautica*, vol. 126, pp. 439–455, 2016.

[26] D. J. Grebow, "Generating periodic orbits in the circular restricted three-body problem with applications to lunar south pole coverage," M.S. Thesis, Purdue University, West Lafayette, Indiana, 2006.

[27] K. Howell and H. Pernicka, "Sun-earth libration point trajectories that avoid the solar exclusion zone," *Journal of the Astronautical Sciences*, vol. 38, pp. 269–288, 1990.

[28] H. Franz, P. Sharer, K. Ogilvie, and M. Desch, "Wind nominal mission performance and extended mission design," in *AIAA/AAS Astrodynamics Specialist Conference and Exhibit*, 1998, p. 4467.

[29] M. W. McElwain, L. D. Feinberg, R. A. Kimble, *et al.*, "Status of the james webb space telescope mission," in *Space Telescopes and Instrumentation 2020: Optical, Infrared, and Millimeter Wave*, International Society for Optics and Photonics, vol. 11443, 2020, 114430T.

[30] Y. Akiyama, M. Bando, H. Nemati, and S. Hokamoto, "Trajectory design using the center manifold theory in the circular restricted three-body problem," *Transactions of the Japan Society for Aeronautical and Space Sciences, Aerospace Technology Japan*, vol. 14, no. 30, pp. 151–158, 2016.

[31] E. Kolemen, N. J. Kasdin, and P. Gurfil, "Quasi-periodic orbits of the restricted three-body problem made easy," in *AIP Conference Proceedings*, American Institute of Physics, vol. 886, 2007, pp. 68–77.

[32] G. Gómez and J. M. Mondelo, "The dynamics around the collinear equilibrium points of the rtbp," *Physica D: Nonlinear Phenomena*, vol. 157, no. 4, pp. 283–321, 2001.

[33] Z. P. Olikara and D. J. Scheeres, "Numerical method for computing quasi-periodic orbits and their stability in the restricted three-body problem," *Advances in the Astronautical Sciences*, vol. 145, no. 911-930, 2012.

[34] À. Jorba, "Numerical computation of the normal behaviour of invariant curves of n-dimensional maps," *Nonlinearity*, vol. 14, no. 5, p. 943, 2001.

[35] B. P. McCarthy and H. K.C., "Quasi-periodic orbits in the sun-earth-moon bicircular restricted four-body problem," in *31st AAS/AIAA Spaceflight Mechanics Meeting, Charlotte, North Carolina (Virtual)*, 2021.

[36] N. Bosanac, "Bounded motions near resonant orbits in the earth-moon and sun-earth systems," in *AAS/AIAA Astrodynamics Specialist Conference, Snowbird, Utah*, 2018.

[37] P. Sharer and T. Harrington, "Trajectory optimization for the ace halo orbit mission," in *Astrodynamics Conference*, 1996, p. 3601.

[38] D. W. Dunham, S. Jen, C. Roberts, *et al.*, "Transfer trajectory design for the soho libration-point mission," in *Washington, DC International Astronautical Federation Congress*, 1992.

[39] J. Burt and B. Smith, "Deep space climate observatory: The dscovr mission," in *2012 IEEE Aerospace Conference*, IEEE, 2012, pp. 1–13.

[40] C. Roberts, S. Case, J. Reagoso, and C. Webster, "Early mission maneuver operations for the deep space climate observatory sun-earth l1 libration point mission," 2015.

[41] D. Eng, J. W. Hunt, S. Kubota, *et al.*, "Interstellar mapping and acceleration probe mission overview," in *2021 IEEE Aerospace Conference (50100)*, 2021, pp. 1–20.

[42] Moog Inc. "Orbital maneuvering vehicle." (2021), [Online]. Available: https://www.moog.com/markets/space/omv.html.

[43] J. M. Woytach and C. S. Loghry, "Cepus: A concept for a configurable electric propulsion utility stage to support exploration and science missions across the solar system," in *AIAA Propulsion and Energy Forum, Indianapolis, IN*, 2019.

[44] J. Andrews, "Spaceflight secondary payload system (ssps) and sherpa tug-a new business model for secondary and hosted payloads," in *26th Annual AIAA/USU Conference on Small Satellites*, 2012.

[45] Northrop Grumman. "Espastar data sheet." (2021), [Online]. Available: https://www.northropgrumman.com/wp-content/uploads/DS-23-ESPAStar.pdf.

[46] C. Pearson, M. Stender, C. Loghry, and J. Maly, "Optimal (not opportunity) orbits for rideshare paylods," in *13th Reinventing Space Conference*, 2015.

[47] A. L. Genova, F. Yang Yang, A. D. Perez, *et al.*, "Trajectory design from gto to near-equatorial lunar orbit for the dark ages radio explorer (dare) spacecraft," in *AAS/AIAA Space Flight Mechanics Meeting, Williamsburg, VA*, 2015.

[48] R. Gershman, P. Penzo, and A. Wiercigroch, "From gto to the planets," *Acta astronautica*, vol. 45, no. 4-9, pp. 517–525, 1999.

[49] J. A. Kechichian, E. T. Campbell, M. F. Werner, and E. Y. Robinson, "Solar surveillance zone population strategies with picosatellites using halo and distant retrograde orbits," *Acta Astronautica*, vol. 56, no. 5, pp. 495–506, 2005.

[50] N. Eismont, A. Sukhanov, and V. Khrapchenkov, "Technical constraints impact on mission design to the collinear sun–earth libration points," in *Libration Point Orbits And Applications*, World Scientific, 2003, pp. 75–83.

[51] A. di Salvo, "Trajectory design for space missions to libration point l2," *Annals of the New York Academy of Sciences*, vol. 1065, no. 1, pp. 311–324, 2005.

[52] I. Newton, *The Principia: Mathematical Principles of Natural Philosophy*. Berkely California: University of California Press, 1999.

[53] Jet Propulsion Laboratory. "Navigation and ancillary information facility - spice data." (2021), [Online]. Available: https://naif.jpl.nasa.gov/naif/data.html.

[54] R. Howland, *Intermediate dynamics: a linear algebraic approach*. Springer Science & Business Media, 2005.

[55] C. Ocampo, "An architecture for a generalized spacecraft trajectory design and optimization system," in *Libration Point Orbits and Applications*, World Scientific, 2003, pp. 529–571.

[56] J. Guckenheimer and P. Holmes, *Nonlinear Oscillations, Dynamical Systems, and Bifurcations of Vector Fields*. New York, USA: Springer-Verlag, 1983.

[57] W. J. Rugh, *Linear system theory*. Prentice-Hall, Inc., 1996.

[58] G. Strang, *Linear algebra and its applications*. Thomson, Brooks/Cole, 2006.

[59] E. L. Allgower and K. Georg, *Introduction to numerical continuation methods*. SIAM, 2003.

[60] T. F. Chan and H. Keller, "Arc-length continuation and multigrid techniques for nonlinear elliptic eigenvalue problems," *SIAM Journal on Scientific and Statistical Computing*, vol. 3, no. 2, pp. 173–194, 1982.

[61] H. Keller, "Numerical solution of bifurcation and nonlinear eigenvalue problems," in *Applications of Bifurcation Theory*, P.Rabinowitz, ed., Academic Press, New York, 1977, pp. 359–384.

[62] A. A. Haapala, "Trajectory design in the spatial circular restricted three-body problem exploiting higher-dimensional poincare maps," Ph.D. Dissertation, Purdue University, 2014.

[63] T. M. Vaquero Escribano, "Spacecraft transfer trajectory design exploiting resonant orbits in multi-body environments," Ph.D. Dissertation, Purdue University, 2013.

[64] E. J. Doedel, "Auto: A program for the automatic bifurcation analysis of autonomous systems," *Congr. Numer*, vol. 30, no. 265-284, pp. 25–93, 1981.

[65] E. M. Zimovan Spreen, "Trajectory design and targeting for applications to the exploration program in cislunar space," Ph.D. Dissertation, Purdue University, 2021.

[66] E. T. Campbell, "Bifurcations from families of periodic solutions in the circular restricted problem with application to trajectory design," Ph.D. Dissertation, Purdue University, 2021.

[67] N. Bosanac, "Exploring the influence of a three-body interaction added to the gravitational potential function in the circular restricted three-body problem: A numerical frequency analysis," MS Thesis, Purdue University, 2012.

[68] S. Wiggins, *Introduction to Applied Nonlinear Dynamical Systems and Chaos*. New York, USA: Springer, 2003.

[69] A. Jorba and E. Olmedo, "On the computation of reducible invariant tori on a parallel computer," *SIAM Journal on Applied Dynamical Systems*, vol. 8, no. 4, pp. 1382–1404, 2009.

[70] Y. Tsuda and D. J. Scheeres, "Numerical method of symplectic state transition matrix and application to fully perturbed earth orbit," *Transactions of the Japan Society for Aeronautical and Space Sciences*, vol. 53, no. 180, pp. 105–113, 2010.

[71] U. L. Alliance, "Atlas V Launch Services User's Guide," *Lockheed Martin Commercial Launch Services*, 2010.

[72] W. McClain and D. Vallado, *Fundamentals of Astrodynamics and Applications*, ser. Space Technology Library. Springer Netherlands, 2001, ISBN: 9780792369035.

[73] M. Kakoi, "Design of transfers from earth-moon l1/l2 libration point orbits to a destination object," Ph.D. Dissertation, Purdue University, 2015.

[74] T. A. Pavlak and K. C. Howell, "Evolution of the out-of-plane amplitude for quasi-periodic trajectories in the earth–moon system," *Acta Astronautica*, vol. 81, no. 2, pp. 456–465, 2012.

[75] C. M. Webster and D. C. Folta, "Understanding the sun-earth libration point orbit formation flying challenges for wfirst and starshade," in *9th International Workshop on Satellite Constellations and Formation Flying (IWSCFF), Boulder, CO*, 2017.

[76] F. Renk and M. Landgraf, "Gaia: Trajectory design with tightening constraints," in *Proceedings of the 24th International Symposium on Space Flight Mechanics, Laurel, MD, May 5th to 19th*, vol. 2014, 2014.

[77] T. A. Pavlak, "Trajectory design and orbit maintenance strategies in multi-body dynamical regimes," Ph.D. Dissertation, Purdue University, 2013.

[78] C. M. Spreen, "Automated patch point placement capability for hybrid trajectory targeting," Ph.D. Dissertation, Purdue University, 2017.

[79] S. Vutukuri, "Spacecraft trajectory design techniques using resonant orbits," M.S. Thesis, Purdue University, 2017.

A. DERIVATION OF NONDIMENSIONAL CRTBP EQUATIONS OF MOTION

The non-dimensional equations of motion for the CRTBP are derived with respect to a non-dimensional time, $\mathscr{T}$. The non-dimensional position, velocity, and acceleration, $\bar{r}$, $\bar{v}$, and $\bar{a}$, respectively are defined as,

$$\begin{aligned} \bar{r} &= \frac{\bar{R}}{l^*} \\ \bar{v} &= \frac{\bar{V}t^*}{l^*} \\ \bar{a} &= \frac{\bar{A}t^{*^2}}{l^*} \end{aligned} \tag{A.1}$$

Recall that $\bar{r} = [x, y, z]^T$, $\bar{v} = [\dot{x}, \dot{y}, \dot{z}]^T$, and $\bar{a} = [\ddot{x}, \ddot{y}, \ddot{z}]^T$. From Equation (2.19), the equations of motion are re-arranged so that,

$$\begin{aligned} \ddot{X} &= 2\dot{\vartheta}\dot{Y} + \dot{\vartheta}^2 X - \frac{\tilde{G}M_1\left(X - X_1\right)}{R_{13}^3} - \frac{\tilde{G}M_2\left(X - X_2\right)}{R_{23}^3} \\ \ddot{Y} &= -2\dot{\vartheta}\dot{X} + \dot{\vartheta}^2 Y - \frac{\tilde{G}M_1\left(Y - Y_1\right)}{R_{13}^3} - \frac{\tilde{G}M_2\left(Y - Y_2\right)}{R_{23}^3} \\ \ddot{Z} &= -\frac{\tilde{G}M_1\left(Z - Z_1\right)}{R_{13}^3} - \frac{\tilde{G}M_2\left(Z - Z_2\right)}{R_{23}^3} \end{aligned} \tag{A.2}$$

The following variables are re-written with nondimensional parameters,

$$\begin{aligned} M_1 &= m^*(1-\mu) \\ M_2 &= m^*\mu \\ \dot{\vartheta} &= \left(\frac{\tilde{G}m^*}{l^{*^3}}\right)^{\frac{1}{2}} \end{aligned} \tag{A.3}$$

Next, the variables in Equations (A.1) and (A.3) are substituted into Equation (A.2).

$$\begin{aligned}
\frac{\ddot{x}l^*}{t^{*^2}} &= 2\left(\frac{\tilde{G}m^*}{l^{*^3}}\right)^{\frac{1}{2}}\frac{\dot{y}l^*}{t^*} + \left(\frac{\tilde{G}m^*}{l^{*^3}}\right)xl^* - \frac{\tilde{G}m^*(1-\mu)\,(x-x_1)\,l^*}{r_{13}^3 l^{*^3}} - \frac{\tilde{G}m^*\mu\,(x-x_2)\,l^*}{r_{23}^3 l^{*^3}} \\
\frac{\ddot{y}l^*}{t^{*^2}} &= -2\left(\frac{\tilde{G}m^*}{l^{*^3}}\right)^{\frac{1}{2}}\frac{\dot{x}l^*}{t^*} + \left(\frac{\tilde{G}m^*}{l^{*^3}}\right)yl^* - \frac{\tilde{G}m^*(1-\mu)\,(y-y_1)\,l^*}{r_{13}^3 l^{*^3}} - \frac{\tilde{G}m^*\mu\,(y-y_2)\,l^*}{r_{23}^3 l^{*^3}} \\
\frac{\ddot{z}l^*}{t^{*^2}} &= -\frac{\tilde{G}m^*(1-\mu)\,(z-z_1)\,l^*}{r_{13}^3 l^{*^3}} - \frac{\tilde{G}m^*\mu\,(z-z_2)\,l^*}{r_{23}^3 l^{*^3}}
\end{aligned} \tag{A.4}$$

Then, Equation (A.4) is simplified and the definition of the characteristic time, see Equation (2.24), is substituted so that,

$$\begin{aligned}
\frac{\ddot{x}l^*}{t^{*^2}} &= 2\frac{\dot{y}l^*}{t^{*^2}} + \frac{xl^*}{t^{*^2}} - \frac{(1-\mu)\,(x-x_1)}{r_{13}^3}\left(\frac{l^*}{t^{*^2}}\right) - \frac{\mu\,(x-x_2)}{r_{23}^3}\left(\frac{l^*}{t^{*^2}}\right) \\
\frac{\ddot{y}l^*}{t^{*^2}} &= -2\frac{\dot{x}l^*}{t^{*^2}} + \frac{yl^*}{t^{*^2}} - \frac{(1-\mu)\,(y-y_1)}{r_{13}^3}\left(\frac{l^*}{t^{*^2}}\right) - \frac{\mu\,(y-y_2)}{r_{23}^3}\left(\frac{l^*}{t^{*^2}}\right) \\
\frac{\ddot{z}l^*}{t^{*^2}} &= -\frac{(1-\mu)\,(z-z_1)}{r_{13}^3}\left(\frac{l^*}{t^{*^2}}\right) - \frac{\mu\,(z-z_2)}{r_{23}^3}\left(\frac{l^*}{t^{*^2}}\right)
\end{aligned} \tag{A.5}$$

Next, the position of the barycenter of the two-body system is derived. For a system of particles, e.g., the P_1-P_2 system, the center of mass is calculated with the following equation,

$$\bar{R}_{CM} = \frac{1}{M_{tot}}\sum_{\mathrm{j}=1}^{\mathfrak{N}} M_{\mathrm{j}}\bar{R}_{\mathrm{j}} \tag{A.6}$$

Where M_{tot} is the total mass of the system, i.e., m^* from Equation (2.21), and $\bar{R}_{CM}$ is the vector distance to the center of mass for the system. The center of mass for the P_1-P_2 system is located along a line that connects P_1 and P_2, see Figure A.1. From Equation (A.6), the

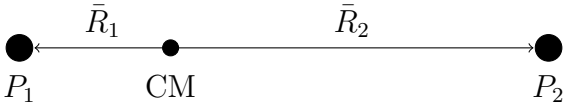

Figure A.1. : Center of mass of the P_1-P_2 system

center of mass is derived as,

$$\begin{aligned} M_1(R_1 + R_2) &= R_2(M_1 + M_2) \\ m^*(1-\mu)(l^*) &= R_2(m^*) \\ (1-\mu) &= \frac{R_2}{l^*} \end{aligned} \tag{A.7}$$

The dimensional position vectors of the primaries from the barycenter, i.e., the center of mass of the P_1-P_2 system are stated as: $\bar{R_1} = [-R_1, 0, 0]^T$ and $\bar{R_2} = [R_2, 0, 0]^T$, respectively. Recall that in the non-dimensional distances are defined by Equation (A.1) so that, $\bar{r_1} = [-\frac{R_1}{l^*}, 0, 0]^T$ and $\bar{r_2} = [\frac{R_2}{l^*}, 0, 0]^T$. From the derivation in Equation (A.7), the non-dimensional distance to P_2 is derived and the distance to P_1 is written as: $\frac{R_1}{l^*} = \mu$. The position of the primaries, i.e, $\bar{r}_1 = [x_1, y_1, z_1]^T$ and $\bar{r}_2 = [x_2, y_2, z_2]^T$ are defined as,

$$\begin{aligned} \bar{r}_1 &= [-\mu, 0, 0]^T \\ \bar{r}_2 &= [1-\mu, 0, 0]^T \end{aligned} \tag{A.8}$$

Finally, equations (A.5) is simplified to,

$$\begin{aligned} \ddot{x} &= 2\dot{y} + x - \frac{(1-\mu)(x+\mu)}{r_{13}^3} - \frac{\mu(x-1+\mu)}{r_{23}^3} \\ \ddot{y} &= -2\dot{x} + y - \frac{y(1-\mu)}{r_{13}^3} - \frac{y\mu}{r_{23}^3} \\ \ddot{z} &= -\frac{z(1-\mu)}{r_{13}^3} - \frac{z\mu}{r_{23}^3} \end{aligned} \tag{A.9}$$

B. PARTIAL DERIVATIVES FOR BALLISTIC TRANSFER TPBVP

The construction of ballistic transfers into periodic orbits in the Sun-Earth system leverage trajectories along the stable manifolds associated with the periodic orbits. The schematic for the construction of ballistic transfers is provided in Figure 5.2 with the associated constraint vector defined in Equation (5.16). The partial derivatives of the periodicity constraint is given as,

$$\mathbf{D}_{\mathbf{x_p}}\bar{\mathbf{F}}_{\text{periodic}} = \begin{bmatrix} \mathbf{\Phi_0^P} & -\mathbf{I}_{6,6} & \mathbf{0}_{6,6} & \dots & \mathbf{0}_{6,6} \\ \mathbf{0}_{6,6} & \mathbf{\Phi_1^P} & -\mathbf{I}_{6,6} & \dots & \mathbf{0}_{6,6} \\ \vdots & \vdots & \ddots & \ddots & \vdots \\ \mathbf{0}_{6,6} & \mathbf{0}_{6,6} & \mathbf{0}_{6,6} & \mathbf{\Phi_{n_p-1}^P} & -\mathbf{I}_{6,6} \\ \frac{\partial \bar{F}_1}{\partial \bar{\mathcal{X}}_0^P(0)} & \mathbf{0}_{5,6} & \mathbf{0}_{5,6} & \dots & \frac{\partial \bar{F}_1}{\partial \bar{\mathcal{X}}_{n_p}^P(0)} \\ [0,1,0,0,0,0] & \mathbf{0}_{1,6} & \mathbf{0}_{1,6} & \dots & \mathbf{0}_{1,6} \end{bmatrix}, \tag{B.1}$$

$$D_{T_a}\bar{F}_{\text{periodic}} = \begin{bmatrix} \dot{\bar{\mathcal{X}}}_0^P(T_a) \\ \dot{\bar{\mathcal{X}}}_0^P(T_a) \\ \vdots \\ \dot{\bar{\mathcal{X}}}_{n_p-1}^P(T_a) \\ \dot{x}_{n_p}^P(T_a) \\ \dot{y}_{n_p}^P(T_a) \\ \dot{z}_{n_p}^P(T_a) \\ \ddot{x}_{n_p}^P(T_a) \\ \ddot{z}_{n_p}^P(T_a) \end{bmatrix}, \tag{B.2}$$

where the STM, $\mathbf{\Phi_j^P}$, is defined as: $\mathbf{\Phi_j^P} = \frac{\partial \bar{\mathcal{X}}_{\mathrm{j}}^P(T_a)}{\partial \bar{\mathcal{X}}_{\mathrm{j}}^P(0)}$. Additionally, the function $\bar{F}_1$ corresponds to the following section of Equation (5.16),

$$\bar{F}_1 = \begin{bmatrix} x_{n_p}^P(T_a) - x_0^P(0) \\ y_{n_p}^P(T_a) - y_0^P(0) \\ z_{n_p}^P(T_a) - z_0^P(0) \\ \dot{x}_{n_p}^P(T_a) - \dot{x}_0^P(0) \\ \dot{z}_{n_p}^P(T_a) - \dot{z}_0^P(0) \end{bmatrix}, \tag{B.3}$$

where the associated partial derivatives are,

$$\frac{\partial \bar{F}_1}{\partial \bar{\mathcal{X}}_0^P(0)} = \begin{bmatrix} -1 & 0 & 0 & 0 & 0 & 0 \\ 0 & -1 & 0 & 0 & 0 & 0 \\ 0 & 0 & -1 & 0 & 0 & 0 \\ 0 & 0 & 0 & -1 & 0 & 0 \\ 0 & 0 & 0 & 0 & 0 & -1 \end{bmatrix}, \tag{B.4}$$

$$\frac{\partial \bar{F}_1}{\partial \bar{\mathcal{X}}_{n_p}^P(0)} = \begin{bmatrix} \frac{\partial x_{n_p}^P(T_a)}{\partial x_{n_p}^P(0)} & \frac{\partial x_{n_p}^P(T_a)}{\partial y_{n_p}^P(0)} & \frac{\partial x_{n_p}^P(T_a)}{\partial z_{n_p}^P(0)} & \frac{\partial x_{n_p}^P(T_a)}{\partial \dot{x}_{n_p}^P(0)} & \frac{\partial x_{n_p}^P(T_a)}{\partial \dot{y}_{n_p}^P(0)} & \frac{\partial x_{n_p}^P(T_a)}{\partial \dot{z}_{n_p}^P(0)} \\ \frac{\partial y_{n_p}^P(T_a)}{\partial x_{n_p}^P(0)} & \frac{\partial y_{n_p}^P(T_a)}{\partial y_{n_p}^P(0)} & \frac{\partial y_{n_p}^P(T_a)}{\partial z_{n_p}^P(0)} & \frac{\partial y_{n_p}^P(T_a)}{\partial \dot{x}_{n_p}^P(0)} & \frac{\partial y_{n_p}^P(T_a)}{\partial \dot{y}_{n_p}^P(0)} & \frac{\partial y_{n_p}^P(T_a)}{\partial \dot{z}_{n_p}^P(0)} \\ \frac{\partial z_{n_p}^P(T_a)}{\partial x_{n_p}^P(0)} & \frac{\partial z_{n_p}^P(T_a)}{\partial y_{n_p}^P(0)} & \frac{\partial z_{n_p}^P(T_a)}{\partial z_{n_p}^P(0)} & \frac{\partial z_{n_p}^P(T_a)}{\partial \dot{x}_{n_p}^P(0)} & \frac{\partial z_{n_p}^P(T_a)}{\partial \dot{y}_{n_p}^P(0)} & \frac{\partial z_{n_p}^P(T_a)}{\partial \dot{z}_{n_p}^P(0)} \\ \frac{\partial \dot{x}{n_p}^P(T_a)}{\partial x_{n_p}^P(0)} & \frac{\partial \dot{x}{n_p}^P(T_a)}{\partial y_{n_p}^P(0)} & \frac{\partial \dot{x}{n_p}^P(T_a)}{\partial z_{n_p}^P(0)} & \frac{\partial \dot{x}{n_p}^P(T_a)}{\partial \dot{x}_{n_p}^P(0)} & \frac{\partial \dot{x}{n_p}^P(T_a)}{\partial \dot{y}_{n_p}^P(0)} & \frac{\partial \dot{x}{n_p}^P(T_a)}{\partial \dot{z}_{n_p}^P(0)} \\ \frac{\partial \dot{z}{n_p}^P(T_a)}{\partial x_{n_p}^P(0)} & \frac{\partial \dot{z}{n_p}^P(T_a)}{\partial y_{n_p}^P(0)} & \frac{\partial \dot{z}{n_p}^P(T_a)}{\partial z_{n_p}^P(0)} & \frac{\partial \dot{z}{n_p}^P(T_a)}{\partial \dot{x}_{n_p}^P(0)} & \frac{\partial \dot{z}{n_p}^P(T_a)}{\partial \dot{y}_{n_p}^P(0)} & \frac{\partial \dot{z}{n_p}^P(T_a)}{\partial \dot{z}_{n_p}^P(0)} \end{bmatrix}, \tag{B.5}$$

The partial derivative corresponding to the continuity constraint for the stable manifold structure is,

$$\mathbf{D}_{\mathbf{x_M}}\bar{\mathbf{F}}_{\text{manifold}} = \begin{bmatrix} -\mathbf{I}_{6,6} & \mathbf{0}_{6,6} & \mathbf{0}_{6,6} & \dots & \mathbf{0}_{6,6} \\ \mathbf{\Phi}_0^M & -\mathbf{I}_{6,6} & \mathbf{0}_{6,6} & \dots & \mathbf{0}_{6,6} \\ \mathbf{0}_{6,6} & \mathbf{\Phi}_1^M & -\mathbf{I}_{6,6} & \dots & \mathbf{0}_{6,6} \\ \vdots & \vdots & \ddots & \ddots & \vdots \\ \mathbf{0}_{6,6} & \mathbf{0}_{6,6} & \mathbf{0}_{6,6} & \mathbf{\Phi}_{n_M-1}^M & -\mathbf{I}_{6,6} \end{bmatrix}. \tag{B.6}$$

with the STM for the manifold transfer arc is defined as: $\mathbf{\Phi}_{\mathrm{j}}^{M} = \frac{\partial \bar{\mathcal{X}}_{\mathrm{j}}^{M}(T_m)}{\partial \bar{\mathcal{X}}_{\mathrm{j}}^{M}(0)}$. Additionally, the rest of the partial derivatives are,

$$\mathbf{D}_{\mathbf{x_p}}\bar{\mathbf{F}}_{\text{manifold}} = \begin{bmatrix} \frac{\partial \bar{\mathcal{X}}_M(T_m)}{\partial \bar{\mathcal{X}}_M(0)}\frac{\partial \bar{\mathcal{X}}_M(0)}{\partial \bar{\mathcal{X}}_0^P(0)} & \frac{\partial \bar{\mathcal{X}}_M(T_m)}{\partial \bar{\mathcal{X}}_M(0)}\frac{\partial \bar{\mathcal{X}}_M(0)}{\partial \bar{\mathcal{X}}_1^P(0)} & \dots & \frac{\partial \bar{\mathcal{X}}_M(T_m)}{\partial \bar{\mathcal{X}}_M(0)}\frac{\partial \bar{\mathcal{X}}_M(0)}{\partial \bar{\mathcal{X}}_{n_p}^P(0)} \\ \mathbf{0} & \mathbf{0} & \dots & \mathbf{0} \\ \mathbf{0} & \mathbf{0} & \dots & \mathbf{0} \\ \vdots & \vdots & \vdots & \vdots \\ \mathbf{0} & \mathbf{0} & \dots & \mathbf{0} \end{bmatrix}. \tag{B.7}$$

$$D_{T_\alpha}\bar{F}_{\text{manifold}} = \begin{bmatrix} \frac{\partial \bar{\mathcal{X}}_M(T_m)}{\partial \bar{\mathcal{X}}_M(0)}\frac{\partial \bar{\mathcal{X}}_M(0)}{\partial T_\alpha} \\ \mathbf{0} \\ \mathbf{0} \\ \vdots \\ \mathbf{0} \end{bmatrix}. \tag{B.8}$$

$$D_{T_m}\bar{F}_{\text{manifold}} = \begin{bmatrix} \mathbf{0} \\ \dot{\bar{\mathcal{X}}}_0^M(T_m) \\ \dot{\bar{\mathcal{X}}}_1^M(T_m) \\ \vdots \\ \dot{\bar{\mathcal{X}}}_{n_M-1}^M(T_m) \end{bmatrix}. \tag{B.9}$$

The partial derivative

$$D_{T_m}\bar{F}_{\text{apsis}} = \frac{\partial \bar{F}_{\text{apsis}}}{\partial \bar{\mathcal{X}}_{n_M}^M(T_m)}\ \dot{\bar{\mathcal{X}}}_{n_M}^M(T_m), \tag{B.10}$$

$$D_{x_M}\bar{F}_{\text{apsis}} = \begin{bmatrix} \mathbf{0}_{1,6} & \mathbf{0}_{1,6} & \cdots & \frac{\partial \bar{F}_{\text{apsis}}}{\partial \bar{\mathcal{X}}_{n_M}^M(T_m)}\ \mathbf{\Phi}_{n_M}^M \end{bmatrix}, \tag{B.11}$$

$$D_{T_m}\bar{F}_{\text{alt}} = \frac{\partial \bar{F}_{\text{alt}}}{\partial \bar{\mathcal{X}}_{n_M}^M(T_m)}\ \dot{\bar{\mathcal{X}}}_{n_M}^M(T_m), \tag{B.12}$$

$$D_{x_M}\bar{F}_{\text{alt}} = \begin{bmatrix} \mathbf{0}_{1,6} & \mathbf{0}_{1,6} & \cdots & \frac{\partial \bar{F}_{\text{alt}}}{\partial \bar{\mathcal{X}}_{n_M}^M(T_m)}\ \mathbf{\Phi}_{n_M}^M \end{bmatrix}, \tag{B.13}$$

where,

$$\frac{\partial \bar{F}_{\text{apsis}}}{\partial \bar{\mathcal{X}}^M_{n_M}(T_m)} = \Big((\bar{r}_f - \bar{r}_{\text{e}})^T \begin{bmatrix} \mathbf{0}_{3,3} & \mathbf{I}_{3,3} \end{bmatrix} + \bar{v}_f^T \begin{bmatrix} \mathbf{I}_{3,3} & \mathbf{0}_{3,3} \end{bmatrix} \Big), \tag{B.14}$$

$$\frac{\partial \bar{F}_{\text{alt}}}{\partial \bar{\mathcal{X}}^M_{n_M}(T_m)} = 2\,(\bar{r}_f - \bar{r}_{\text{e}})^T \begin{bmatrix} \mathbf{I}_{3,3} & \mathbf{0}_{3,3} \end{bmatrix}, \tag{B.15}$$

C. BALLISTIC TRANSFERS TO SUN-EARTH HALO ORBITS

Ballistic transfers into the spatial halo orbits in the Sun-Earth system are constructed for a range of GTO departure locations. The access curves for for ballistic transfers into L_1 and L_2 are plotted in Figures 5.16 and 5.18. The geometry for the ballistic transfers into L_1 halo orbits in Figure 5.16 are plotted in Figures C.1-C.3. Additionally, Figures C.4-C.6 display the geometry of the ballistic transfers from Figure 5.18. In Figures C.1-C.6, the prograde transfers, i.e., transfer from a prograde GTO, are plotted in blue and the retrograde transfers are shaded in black. Note that some indirect transfer families include only prograde ballistic transfers, an example is provided in Figures C.1(e)-(h) for L_1 transfers.

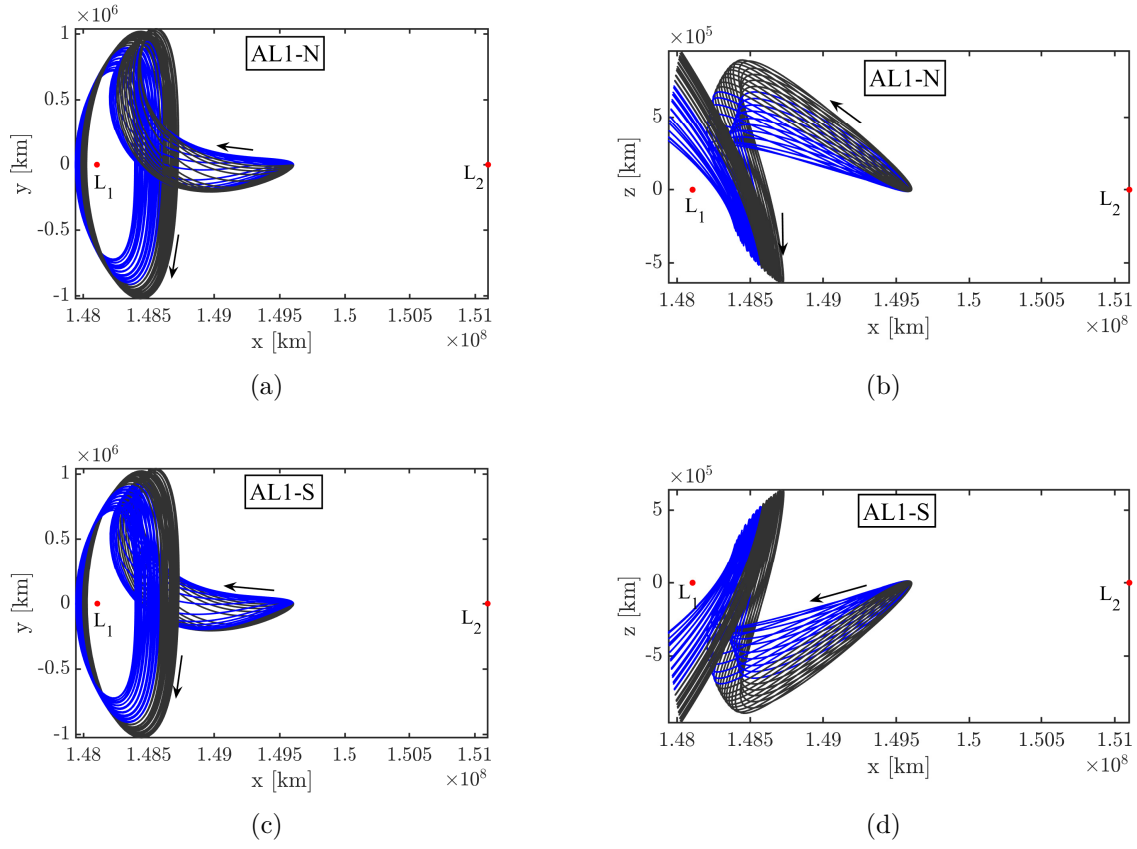

Figure C.1. : Direct ballistic transfers to L_1 halos. Retrograde ballistic transfers are shaded in black

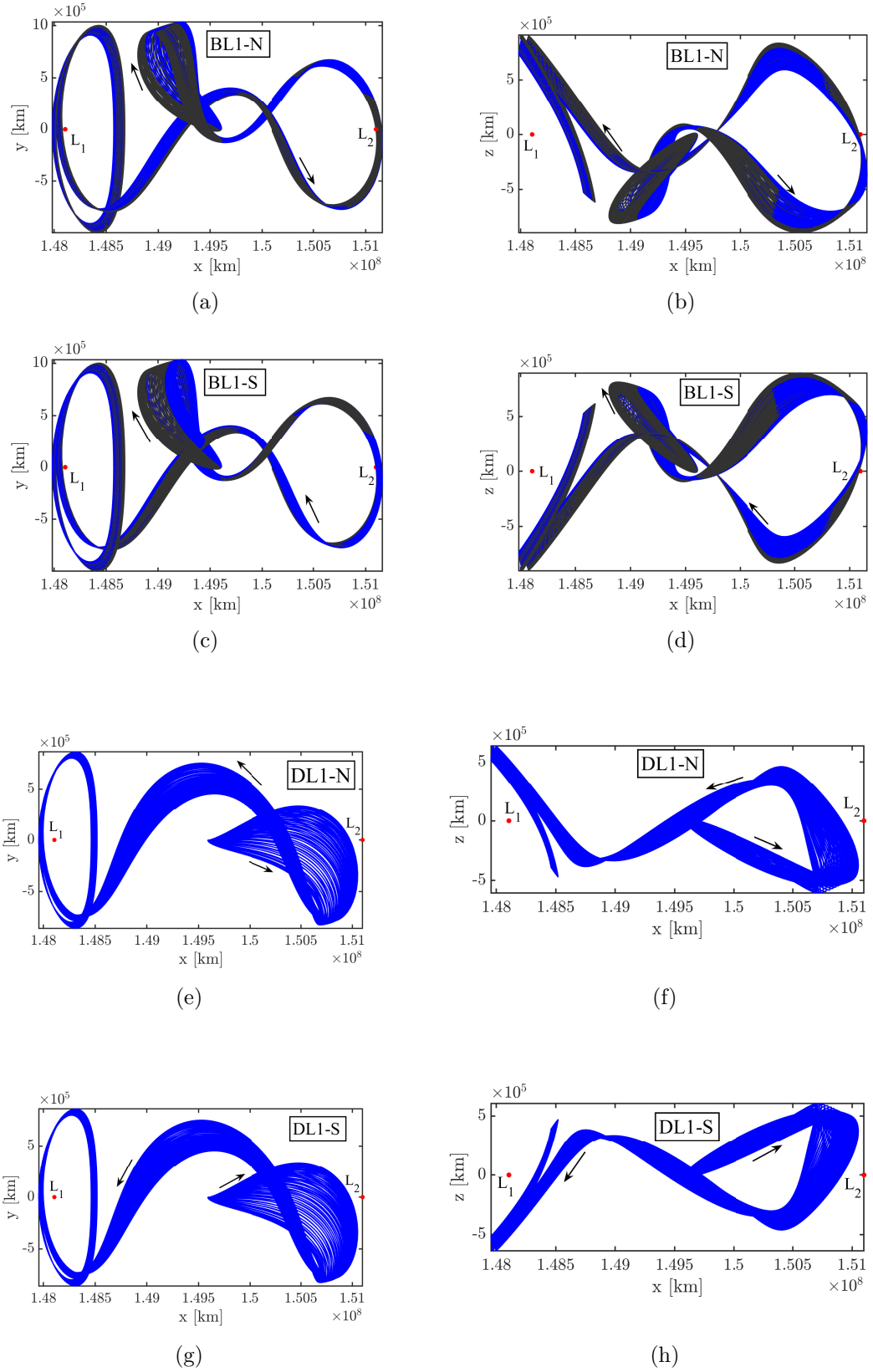

Figure C.2. : Indirect ballistic transfers to L_1 halo orbits. Retrograde ballistic transfers are shaded in black

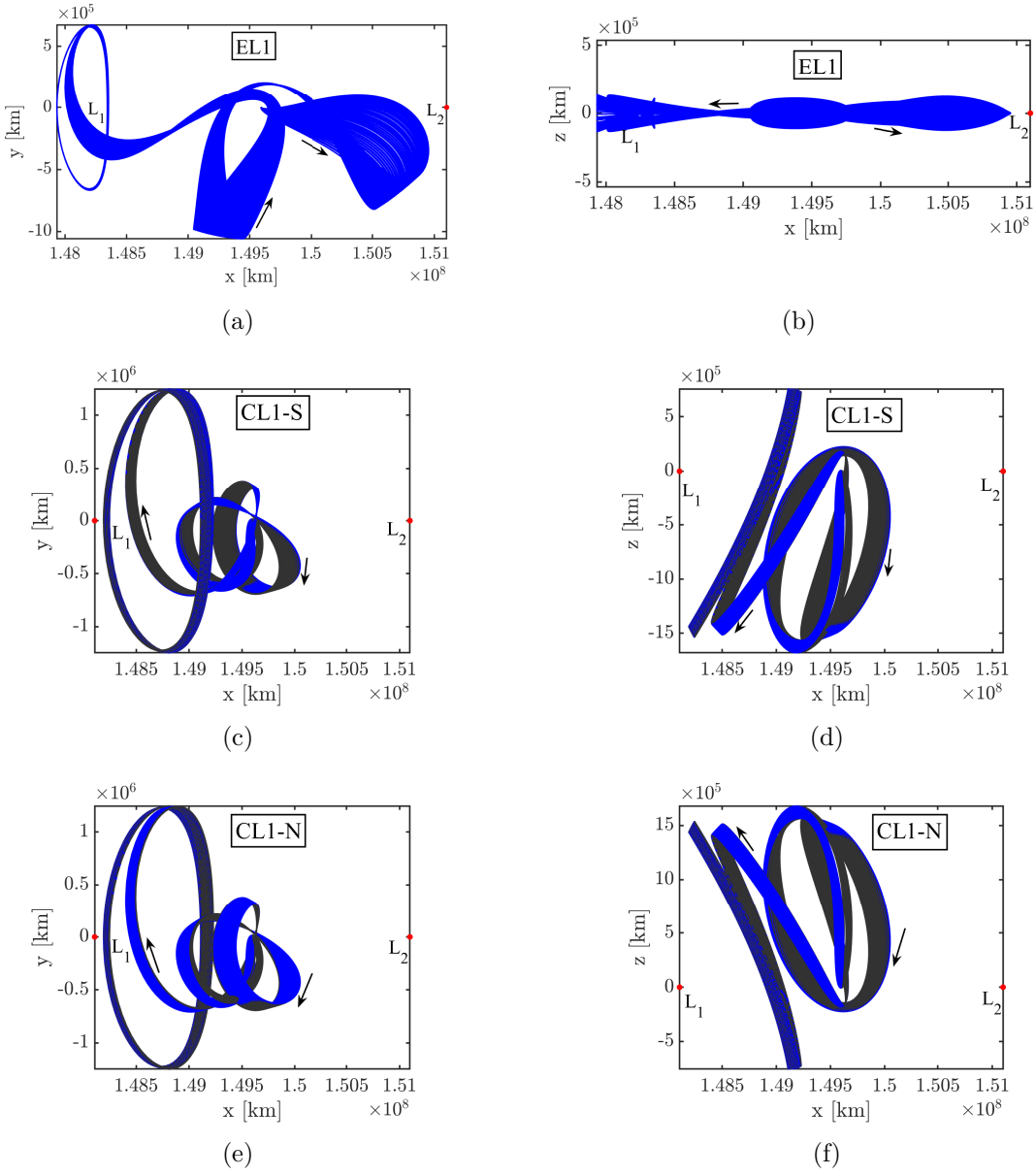

Figure C.3. : Indirect ballistic transfers to L_1 halo orbits. Retrograde ballistic transfers are shaded in black

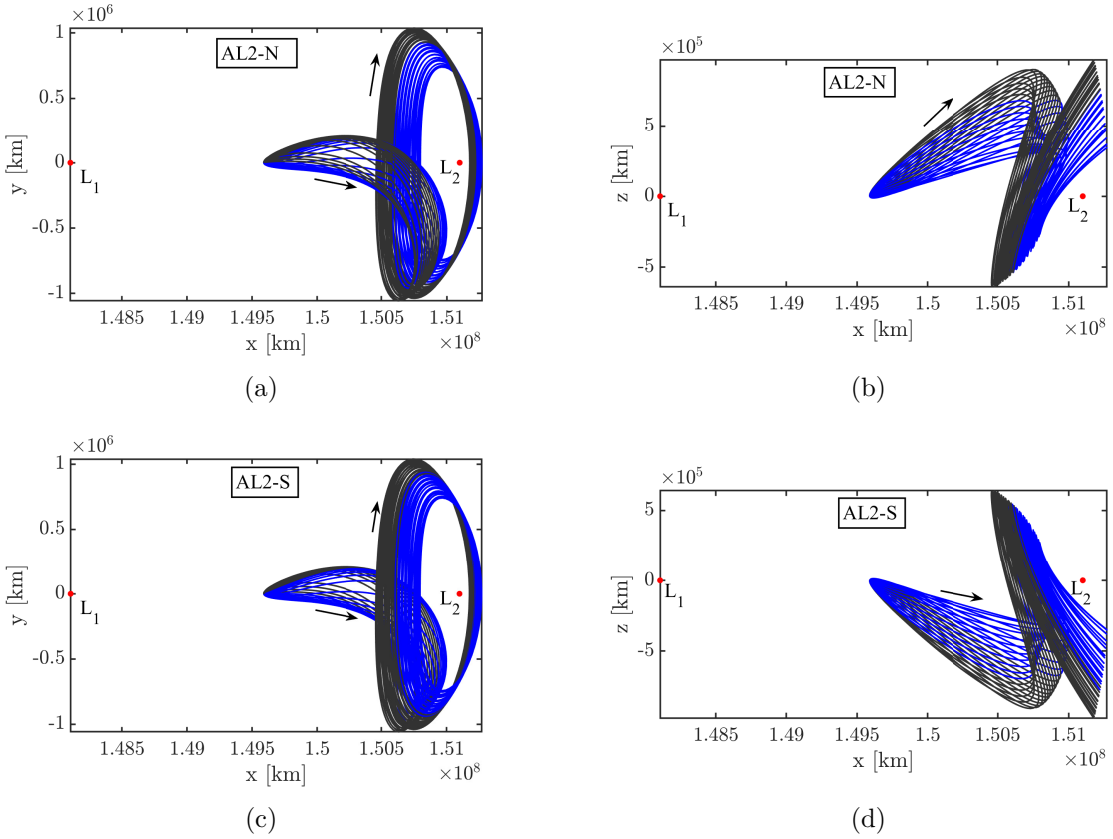

Figure C.4. : Direct ballistic transfers to L_2 halo orbits. Retrograde ballistic transfers are shaded in black

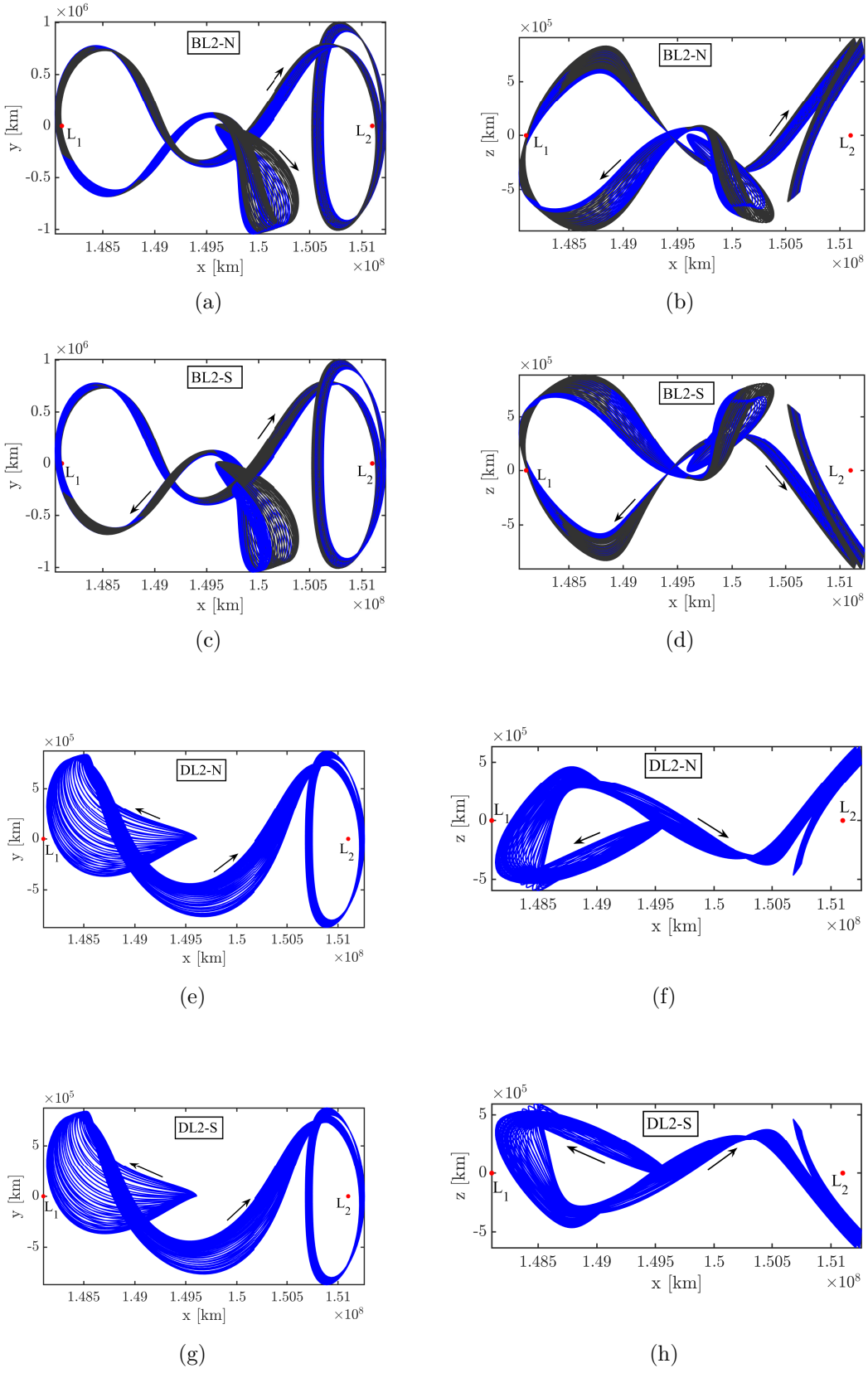

Figure C.5. : Indirect ballistic transfers to L_2 halo orbits. Retrograde ballistic transfers are shaded in black

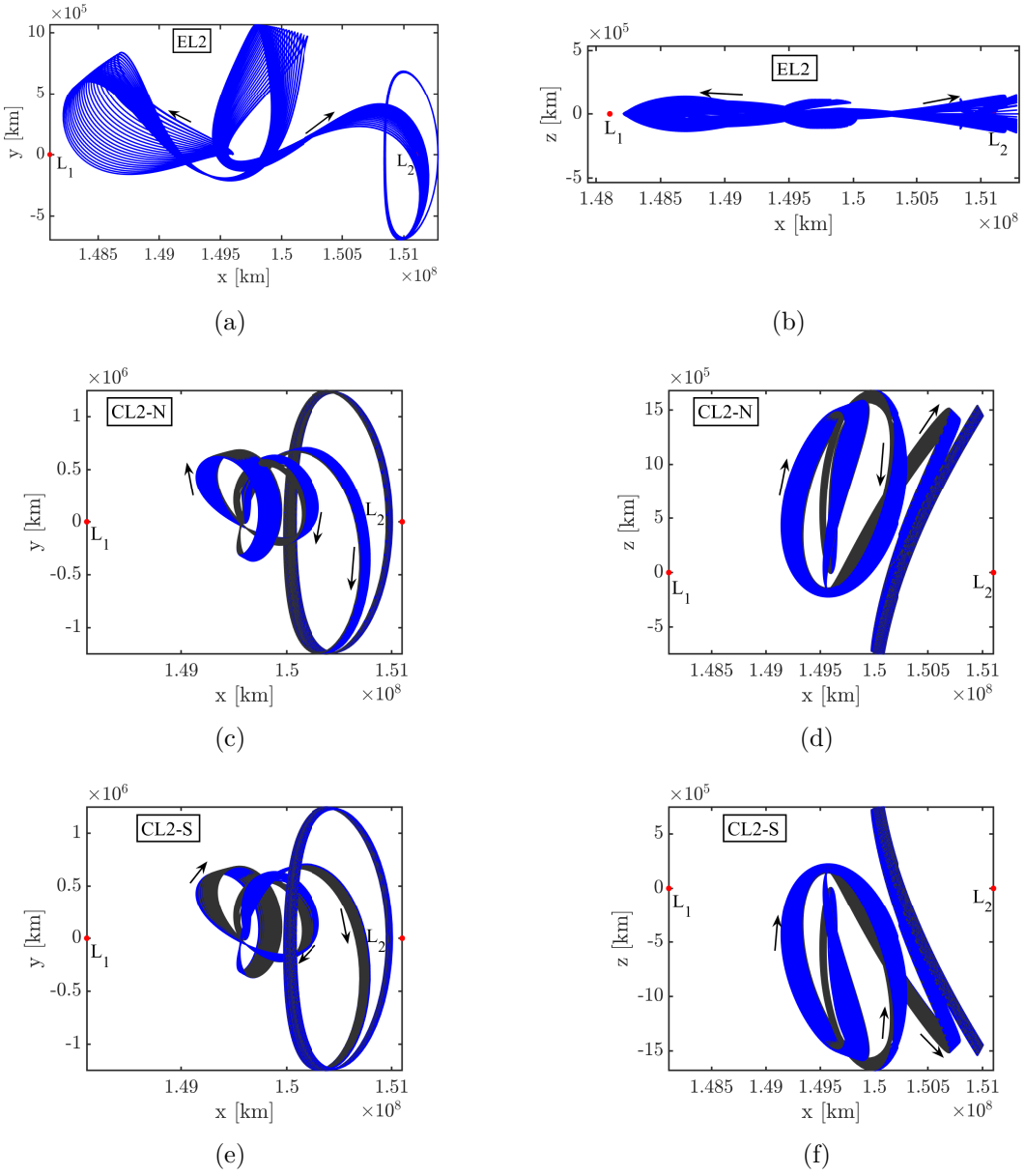

Figure C.6. : Indirect ballistic transfers to L_2 halo orbits. Retrograde ballistic transfers are shaded in black

D. PARTIAL DERIVATIVES FOR MULTIPLE MANEUVER TRANSFER TPBVP

A multiple shooting strategy is implemented to construct transfers with a deep space maneuver from a range of GTO departure locations near the Earth. A multiple shooting scheme for transfers into a fixed periodic orbit in the Sun-Earth system is illustrated in Figure 6.2. The free-variable and constraint vectors consistent with this formulation are provided in Equations (6.3) and (6.4). A multidimensional newton's method is employed to compute a feasible transfer solution. The Jacobian corresponding to the constraint vector in Equation (6.4) is given in Equation (6.4) and rewritten as,

$$\mathbf{D}\bar{\mathbf{F}} = \begin{bmatrix} \mathbf{D}_{\mathbf{x_m}}\bar{\mathbf{F}} & \mathbf{D}_{\mathbf{x_A}}\bar{\mathbf{F}} & D_{T_\alpha}\bar{F} & D_{T_m}\bar{F} & D_{T_A}\bar{F} & D_\lambda\bar{F} & D_\delta\bar{F} \end{bmatrix} \tag{D.1}$$

where $\mathbf{D}_{\mathbf{x_m}}\bar{\mathbf{F}}$ represents the partials of the constraint vector, $\bar{F}$, with respect to the states along the stable manifold trajectory, i.e., $\{\bar{\mathcal{X}}_0^M, \cdots, \bar{\mathcal{X}}_{n_M}^M\}$, and $\mathbf{D}_{\mathbf{x_A}}\bar{\mathbf{F}}$ corresponds to the partials with respect to the states along the bridging arc trajectory, $\{\bar{\mathcal{X}}_0^A, \cdots, \bar{\mathcal{X}}_{n_A}^A\}$. Recall that variables in bold represent matrices. The partial derivative associated with states the stable manifold trajectory, $\mathbf{D}_{\mathbf{x_m}}\bar{\mathbf{F}}$, in Equation (D.1) is expanded as,

$$\mathbf{D}_{\mathbf{x_m}}\bar{\mathbf{F}} = \begin{bmatrix} \mathbf{D}_{\mathbf{x_m}}\bar{\mathbf{F}}_{\text{mani}} \\ \mathbf{0} \\ \mathbf{D}_{\mathbf{x_m}}\bar{\mathbf{F}}_{\text{DSM}} \\ \bar{0} \\ \bar{0} \end{bmatrix}, \tag{D.2}$$

where the corresponding matrix components are defined as,

$$\mathbf{D}_{\mathbf{x_m}}\bar{\mathbf{F}}_{\text{mani}} = \begin{bmatrix} -\mathbf{I}_{6,6} & \mathbf{0}_{6,6} & \mathbf{0}_{6,6} & \dots & \mathbf{0}_{6,6} \\ \mathbf{\Phi}_0^M & -\mathbf{I}_{6,6} & \mathbf{0}_{6,6} & \dots & \mathbf{0}_{6,6} \\ \mathbf{0}_{6,6} & \mathbf{\Phi}_1^M & -\mathbf{I}_{6,6} & \dots & \mathbf{0}_{6,6} \\ \vdots & \vdots & \ddots & \ddots & \vdots \\ \mathbf{0}_{6,6} & \mathbf{0}_{6,6} & \mathbf{0}_{6,6} & \mathbf{\Phi}_{n_M-1}^M & -\mathbf{I}_{6,6} \end{bmatrix}. \tag{D.3}$$

$$\mathbf{D}_{\mathbf{x_m}}\bar{\mathbf{F}}_{\text{DSM}} = \begin{bmatrix} \mathbf{0}_{3,6} & \mathbf{0}_{3,6} & \dots & \begin{bmatrix} \mathbf{I}_{3,3} & \mathbf{0}_{3,3} \end{bmatrix} \mathbf{\Phi}_{n_M}^M \end{bmatrix}, \tag{D.4}$$

The STM, $\mathbf{\Phi}_{\text{j}}^M$, is evaluated from a state along the stable manifold trajectory, $\bar{\mathcal{X}}_{\text{j}}^M$, after time T_m, see illustration in Figure 6.2. The dimensions of the partials in Equations (D.3)-(D.4) is computed as,

$$\text{Dim}(\mathbf{D}_{\mathbf{x_m}}\bar{\mathbf{F}}_{\text{mani}}) = 6(n_M+1) \times 6(n_M+1), \tag{D.5}$$

$$\text{Dim}(\mathbf{D}_{\mathbf{x_m}}\bar{\mathbf{F}}_{\text{DSM}}) = 3 \times 6(n_M+1). \tag{D.6}$$

The partial derivative associated with states along the bridging arc trajectory, $\mathbf{D}_{\mathbf{x_A}}\bar{\mathbf{F}}$, in Equation (D.1) is denoted as,

$$\mathbf{D}_{\mathbf{x_A}}\bar{\mathbf{F}} = \begin{bmatrix} \mathbf{0} \\ \mathbf{D}_{\mathbf{x_A}}\bar{\mathbf{F}}_{\text{bridge}} \\ \mathbf{D}_{\mathbf{x_A}}\bar{\mathbf{F}}_{\text{DSM}} \\ D_{x_A}\bar{F}_{\text{apsis}} \\ D_{x_A}\bar{F}_{\text{alt}} \end{bmatrix}, \tag{D.7}$$

with the expanded matrix components of,

$$\mathbf{D}_{\mathbf{x_A}}\bar{\mathbf{F}}_{\text{bridge}} = \begin{bmatrix} \mathbf{\Phi}_0^A & -\mathbf{I}_{6,6} & \mathbf{0}_{6,6} & \dots & \mathbf{0}_{6,6} \\ \mathbf{0}_{6,6} & \mathbf{\Phi}_1^A & -\mathbf{I}_{6,6} & \dots & \mathbf{0}_{6,6} \\ \vdots & \vdots & \ddots & \ddots & \vdots \\ \mathbf{0}_{6,6} & \mathbf{0}_{6,6} & \mathbf{0}_{6,6} & \mathbf{\Phi}_{n_A-1}^A & -\mathbf{I}_{6,6} \end{bmatrix}. \tag{D.8}$$

$$\mathbf{D}_{\mathbf{x_A}}\bar{\mathbf{F}}_{\text{DSM}} = \begin{bmatrix} \begin{bmatrix} \mathbf{I}_{3,3} & \mathbf{0}_{3,3} \end{bmatrix} & \mathbf{0}_{3,6} & \dots & \mathbf{0}_{3,6} \end{bmatrix}, \tag{D.9}$$

$$D_{x_A}F_{\text{apsis}} = \begin{bmatrix} \mathbf{0}_{6,6} & \cdots & \left((\bar{r}_f - \bar{r}_{\text{e}})^T \begin{bmatrix} \mathbf{0}_{3,3} & \mathbf{I}_{3,3} \end{bmatrix} + \bar{v}_f^T \begin{bmatrix} \mathbf{I}_{3,3} & \mathbf{0}_{3,3} \end{bmatrix} \right) \mathbf{\Phi}_{n_A}^A \end{bmatrix}, \tag{D.10}$$

$$\mathbf{D}_{\mathbf{x_A}}\bar{\mathbf{F}}_{\text{alt}} = \begin{bmatrix} \mathbf{0}_{3,3} & \cdots & \begin{bmatrix} \mathbf{I}_{3,3} & \mathbf{0}_{3,3} \end{bmatrix} \mathbf{\Phi}_{n_A}^A \end{bmatrix}. \tag{D.11}$$

The matrix $\mathbf{\Phi}_{\text{j}}^A$ is the associated STM for a state along the bridging arc trajectory, $\bar{\mathcal{X}}_{\text{j}}^A$, after time T_A. Additionally, $\bar{r}_f$ and $\bar{v}_f$ are the position and velocity components of the final propagated state of the bridging arc trajectory, i.e., $\bar{\mathcal{X}}_{n_A}^A$, and $\bar{r}_{\text{e}}$ is the position of the Earth. The dimensions of the partial derivatives in Equations (D.8)-(D.11) are given as:

$$\text{Dim}(\mathbf{D}_{\mathbf{x_A}}\bar{\mathbf{F}}_{\text{bridge}}) = 6(n_A) \times 6(n_A + 1), \tag{D.12}$$

$$\text{Dim}(\mathbf{D}_{\mathbf{x_A}}\bar{\mathbf{F}}_{\text{DSM}}) = 3 \times 6(n_A + 1), \tag{D.13}$$

$$\text{Dim}(D_{x_A}F_{\text{apsis}}) = 1 \times 6(n_A + 1), \tag{D.14}$$

$$\text{Dim}(\mathbf{D}_{\mathbf{x_A}}\bar{\mathbf{F}}_{\text{alt}}) = 3 \times 6(n_A + 1). \tag{D.15}$$

The partial derivatives associated with T_α, T_m, T_A, λ, and δ in Equation (D.1) are written as,

$$D_{T_\alpha}\bar{F} = \begin{bmatrix} D_{T_\alpha}\bar{F}_{\text{mani}} \\ \bar{0} \\ \bar{0} \\ \bar{0} \\ \bar{0} \end{bmatrix}, \tag{D.16}$$

$$D_{T_m}\bar{F} = \begin{bmatrix} D_{T_m}\bar{F}_{\text{mani}} \\ \bar{0} \\ D_{T_m}\bar{F}_{\text{DSM}} \\ \bar{0} \\ \bar{0} \end{bmatrix}, \tag{D.17}$$

$$D_{T_A}\bar{F} = \begin{bmatrix} \bar{0} \\ D_{T_A}\bar{F}_{\text{bridge}} \\ \bar{0} \\ D_{T_A}F_{\text{apsis}} \\ D_{T_A}\bar{F}_{\text{alt}} \end{bmatrix}, \tag{D.18}$$

$$D_{\lambda}\bar{F} = \begin{bmatrix} \bar{0} \\ \bar{0} \\ \bar{0} \\ \bar{0} \\ D_{\lambda}\bar{F}_{\text{alt}} \end{bmatrix}, \tag{D.19}$$

$$D_{\delta}\bar{F} = \begin{bmatrix} \bar{0} \\ \bar{0} \\ \bar{0} \\ \bar{0} \\ D_{\delta}\bar{F}_{\text{alt}} \end{bmatrix}. \tag{D.20}$$

where the vector components of the partials are expanded as,

$$D_{T_\alpha}\bar{F}_{\text{mani}} = \begin{bmatrix} \frac{\partial \bar{\mathcal{X}}_M(T_m)}{\partial \bar{\mathcal{X}}_M(0)} \frac{\partial \bar{\mathcal{X}}_M(0)}{\partial T_\alpha} \\ \bar{0} \\ \vdots \\ \bar{0} \end{bmatrix}, \tag{D.21}$$

$$D_{T_m}\bar{F}_{\text{mani}} = \begin{bmatrix} \bar{0} \\ \dot{\bar{\mathcal{X}}}_0^M(T_m) \\ \dot{\bar{\mathcal{X}}}_1^M(T_m) \\ \vdots \\ \dot{\bar{\mathcal{X}}}_{n_M-1}^M(T_m) \end{bmatrix}, \tag{D.22}$$

$$D_{T_m}\bar{F}_{\text{DSM}} = \bar{v}_{n_M}^M(T_m), \tag{D.23}$$

$$D_{T_A}\bar{F}_{\text{bridge}} = \begin{bmatrix} \dot{\bar{\mathcal{X}}}_0^A(T_A) \\ \dot{\bar{\mathcal{X}}}_1^A(T_A) \\ \vdots \\ \dot{\bar{\mathcal{X}}}_{n_A-1}^A(T_A) \end{bmatrix}, \tag{D.24}$$

$$D_{T_A}F_{\text{apsis}} = \left((\bar{r}_f - \bar{r}_{\text{e}})^T \begin{bmatrix} \mathbf{0}_{3,3} & \mathbf{I}_{3,3} \end{bmatrix} + \bar{v}_f^T \begin{bmatrix} \mathbf{I}_{3,3} & \mathbf{0}_{3,3} \end{bmatrix} \right) \dot{\bar{\mathcal{X}}}_{n_A}^A, \tag{D.25}$$

$$D_{T_A}\bar{F}_{\text{alt}} = \begin{bmatrix} \mathbf{I}_{3,3} & \mathbf{0}_{3,3} \end{bmatrix} \dot{\bar{\mathcal{X}}}_{n_A}^A, \tag{D.26}$$

$$D_\lambda \bar{F}_{\text{alt}} = -h_{\text{alt}} \begin{bmatrix} -\sin(\lambda)\cos(\delta) \\ \cos(\lambda)\cos(\delta) \\ 0 \end{bmatrix}, \tag{D.27}$$

$$D_\delta \bar{F}_{\text{alt}} = -h_{\text{alt}} \begin{bmatrix} -\cos(\lambda)\sin(\delta) \\ -\sin(\lambda)\sin(\delta) \\ \cos(\delta) \end{bmatrix}. \tag{D.28}$$

The dimensions of the partial derivatives in Equations (D.21)-(D.28) are given as:

$$\mathrm{Dim}(D_{T_\alpha}\bar{F}_{\mathrm{mani}}) = 6(n_M+1)\times 1, \tag{D.29}$$

$$\mathrm{Dim}(D_{T_m}\bar{F}_{\mathrm{mani}}) = 6(n_M+1)\times 1, \tag{D.30}$$

$$\mathrm{Dim}(D_{T_m}\bar{F}_{\mathrm{DSM}}) = 3\times 1, \tag{D.31}$$

$$\mathrm{Dim}(D_{T_A}\bar{F}_{\mathrm{bridge}}) = 6n_A\times 1, \tag{D.32}$$

$$\mathrm{Dim}(D_{T_A}F_{\mathrm{apsis}}) = 1\times 1, \tag{D.33}$$

$$\mathrm{Dim}(D_{T_A}\bar{F}_{\mathrm{alt}}) = 3\times 1, \tag{D.34}$$

$$\mathrm{Dim}(D_{\lambda}\bar{F}_{\mathrm{alt}}) = 3\times 1, \tag{D.35}$$

$$\mathrm{Dim}(D_{\delta}\bar{F}_{\mathrm{alt}}) = 3\times 1. \tag{D.36}$$

E. PARTIAL DERIVATIVES FOR EPHEMERIS TRANSFER TPBVP

A multiple-shooting formulation for a feasible transfer in the ephemeris model is derived. The general schematic for the model is illustrated in Figure E.1; note that each state, i.e., $\bar{\mathcal{X}}_{\mathrm{j}}$, is in the inertial EME frame. Each node in the multiple-shooting scheme has an associated state and epoch time, τ. The free-variable vector consistent with the schematic in Figure

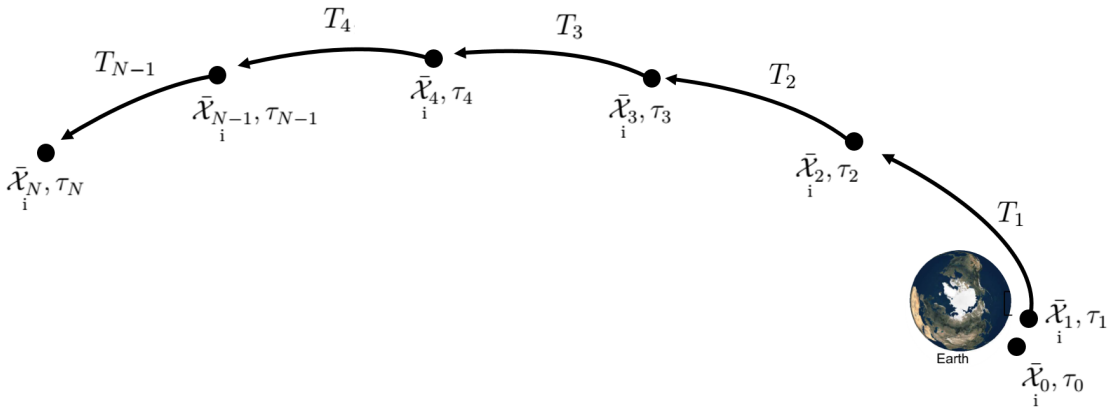

Figure E.1. : Multiple-shooting schematic for transfers in the ephemeris model. Note the each transfer node is in the inertial EME frame

E.1 is,

$$\bar{\mathfrak{X}} = \begin{bmatrix} \bar{\mathcal{X}}_{\mathrm{i}}^{0} \\ \vdots \\ \bar{\mathcal{X}}_{\mathrm{i}}^{N} \\ T_0 \\ \vdots \\ T_{N-1} \\ \tau_0 \\ \vdots \\ \tau_{N-1} \\ \tau_N \end{bmatrix}. \tag{E.1}$$

The constraint vector corresponding to a continuous transfer in the ephemeris model is,

$$\bar{F} = \begin{bmatrix} \bar{\underset{\mathrm{i}}{\mathcal{X}}}_0(T_0, \tau_0) - \bar{\underset{\mathrm{i}}{\mathcal{X}}}_1(0, \tau_1) \\ \bar{\underset{\mathrm{i}}{\mathcal{X}}}_1(T_1, \tau_1) - \bar{\underset{\mathrm{i}}{\mathcal{X}}}_2(0, \tau_2) \\ \vdots \\ \bar{\underset{\mathrm{i}}{\mathcal{X}}}_{N-1}(T_{N-1}, \tau_{N-1}) - \bar{\underset{\mathrm{i}}{\mathcal{X}}}_N(0, \tau_N) \\ T_0 - \tau_1 + \tau_0 \\ \vdots \\ T_{N-1} - \tau_N + \tau_{N-1} \end{bmatrix}, \tag{E.2}$$

note that additional constraint conditions are included to enforce time continuity on the node epochs. The formulation is corrected via a multidimensional Newton method with the associated Jacobian defined as,

$$\mathbf{D}\bar{\mathbf{F}} = \begin{bmatrix} \bar{\mathbf{F}}_{\mathbf{x}} & \bar{\mathbf{F}}_{\mathbf{T}} & \bar{\mathbf{F}}_{\tau} \end{bmatrix}, \tag{E.3}$$

With the components of the Jacobian denoted as,

$$\bar{\mathbf{F}}_{\mathbf{x}} = \begin{bmatrix} -\mathbf{I}_{6,6} & \mathbf{0}_{6,6} & \cdots & \mathbf{0}_{6,6} & \mathbf{0}_{6,6} \\ \mathbf{\Phi}_1 & -\mathbf{I}_{6,6} & \cdots & \mathbf{0}_{6,6} & \mathbf{0}_{6,6} \\ \vdots & \vdots & \ddots & \vdots & \vdots \\ \mathbf{0}_{6,6} & \mathbf{0}_{6,6} & \cdots & -\mathbf{I}_{6,6} & \mathbf{0}_{6,6} \\ \mathbf{0}_{6,6} & \mathbf{0}_{6,6} & \cdots & \mathbf{\Phi}_{N-1} & -\mathbf{I}_{6,6} \\ 0 & 0 & \cdots & 0 & 0 \\ \vdots & \vdots & \vdots & \vdots & \vdots \\ 0 & 0 & \cdots & 0 & 0 \end{bmatrix}, \tag{E.4}$$

$$\bar{\mathbf{F}}_{\mathbf{T}} = \begin{bmatrix} \dot{\bar{\mathcal{X}}}_{\mathrm{i}0} & \bar{0}_{3,1} & \cdots & \bar{0}_{3,1} & \bar{0}_{3,1} \\ \bar{0}_{6,1} & \dot{\bar{\mathcal{X}}}_{\mathrm{i}1} & \cdots & \bar{0}_{6,1} & \bar{0}_{6,1} \\ \vdots & \vdots & \ddots & \vdots & \vdots \\ \bar{0}_{6,1} & \bar{0}_{6,1} & \cdots & \dot{\bar{\mathcal{X}}}_{\mathrm{i}N-2} & \bar{0}_{6,1} \\ \bar{0}_{6,1} & \bar{0}_{6,1} & \cdots & \bar{0}_{6,1} & \dot{\bar{\mathcal{X}}}_{\mathrm{i}N-1} \\ 1 & 0 & \cdots & 0 & 0 \\ 0 & 1 & \cdots & 0 & 0 \\ \vdots & \vdots & \vdots & \vdots & \vdots \\ 0 & 0 & \cdots & 1 & 0 \\ 0 & 0 & \cdots & 0 & 1 \end{bmatrix}, \tag{E.5}$$

$$\bar{\mathbf{F}}_{\tau} = \begin{bmatrix} \frac{\partial \bar{\mathcal{X}}_{\mathrm{i}0}}{\partial \tau} & \bar{0}_{3,1} & \cdots & \bar{0}_{3,1} & \bar{0}_{3,1} \\ \bar{0}_{6,1} & \frac{\partial \bar{\mathcal{X}}_{\mathrm{i}1}}{\partial \tau} & \cdots & \bar{0}_{6,1} & \bar{0}_{6,1} \\ \vdots & \vdots & \ddots & \vdots & \vdots \\ \bar{0}_{6,1} & \bar{0}_{6,1} & \cdots & \frac{\partial \bar{\mathcal{X}}_{\mathrm{i}N-2}}{\partial \tau} & \bar{0}_{6,1} \\ \bar{0}_{6,1} & \bar{0}_{6,1} & \cdots & \bar{0}_{6,1} & \frac{\partial \bar{\mathcal{X}}_{\mathrm{i}N-1}}{\partial \tau} \\ 1 & -1 & \cdots & 0 & 0 \\ 0 & 1 & \cdots & 0 & 0 \\ \vdots & \vdots & \vdots & \vdots & \vdots \\ 0 & 0 & \cdots & -1 & 0 \\ 0 & 0 & \cdots & 1 & -1 \end{bmatrix}. \tag{E.6}$$

F. OPTIMIZED TRANSFER INFORMATION IN EPHEMERIS MODEL

F.1 Transfers to L_1 Halo Orbits

Table F.1. : Summary of maneuver magnitudes (m/s) for optimized ephemeris transfers into a Sun-Earth L_1 halo orbit. Each transfer has an originating epoch of June 2, 2022 12:00:00.000

Ω [deg]	TIM	DSM 1	DSM 2	OIM	Total
0	744	204	23	101	991
20	747	153	0	79	1011
40	746	64	0	97	946
60	744	0	71	95	950
80	743	10	148	78	966
100	744	139	0	72	992
120	745	129	0	36	1005
140	749	0	148	159	1027
160	754	193	0	86	1105
180	761	328	0	134	1208
200	766	320	65	291	1323
220	743	128	0	159	1061
240	744	0	55	162	1001
260	743	0	132	51	941
280	744	0	144	54	955
300	746	55	137	19	959
320	749	0	42	241	1067
340	741	265	56	56	980

F.2 Transfers to L_2 Halo Orbits

Table F.2. : Summary of maneuver magnitudes (m/s) for optimized ephemeris transfers into a Sun-Earth L_2 halo orbit. Each transfer has an originating epoch of December 2, 2022 12:00:00.000

Ω [deg]	TIM	DSM 1	DSM 2	OIM	Total
0	765	113	401	15	1263
20	741	141	225	15	1076
40	745	85	7	12	831
60	741	28	64	15	846
80	740	105	122	15	1002
100	741	27	103	15	882
120	744	60	31	15	853
140	748	66	49	15	874
160	766	183	192	15	1075
180	785	344	114	14	1144
200	767	170	120	15	1150
220	552	349	314	15	1149
240	679	197	138	15	893
260	741	60	54	15	838
280	730	121	123	15	844
300	761	57	150	14	893
320	752	203	234	9	1034
340	753	86	329	15	1143

F.3 Transfers to L_1 Lissajous Orbits

Table F.3. : Summary of maneuver magnitudes (m/s) for optimized ephemeris transfers into a Sun-Earth L_1 Lissajous orbit. Each transfer has an originating epoch of June 2, 2022 12:00:00.000 into an injection point consistent with $\theta_2 = 152.85°$, i.e., Type A transfer

Ω [deg]	TIM	DSM 1	DSM 2	OIM	Total
0	761	75	546	20	1417
20	767	94	628	25	1506
40	749	0	145	33	935
60	746	0	173	141	1042
80	744	78	225	71	1122
100	742	86	264	218	1346
120	748	177	28	367	1157
140	751	90	144	163	1187
160	754	22	161	122	1032
180	763	35	198	49	1110
200	775	59	218	18	1296
220	750	17	348	30	1149
240	745	0	172	139	1100
260	742	0	112	202	1069
280	743	201	177	24	1112
300	745	0	237	123	1116
320	750	0	366	31	1183
340	756	43	456	17	1259

Table F.4. : Summary of maneuver magnitudes (m/s) for optimized ephemeris transfers into a Sun-Earth L_1 Lissajous orbit. Each transfer has an originating epoch of June 2, 2022 12:00:00.000 into an injection point consistent with $\theta_2 = 335.35°$, i.e., Type B transfer

Ω [deg]	TIM	DSM 1	DSM 2	OIM	Total
0	762	59	468	113	1406
20	768	0	614	71	1460
40	794	71	78	34	1177
60	747	249	222	54	1226
80	744	122	379	38	1199
100	745	90	319	21	1186
120	748	408	127	4	1291
140	750	115	214	12	1094
160	754	35	280	2	1053
180	761	17	246	6	1016
200	766	41	379	9	1047
220	744	142	325	39	1239
240	743	0	223	221	1191
260	743	442	215	28	1469
280	743	0	253	181	1171
300	746	0	248	231	1226
320	749	129	127	309	1475
340	758	86	237	263	1368

F.4 Transfers to L_2 Lissajous Orbits

Table F.5. : Summary of maneuver magnitudes (m/s) for optimized ephemeris transfers into a Sun-Earth L_2 Lissajous orbit. Each transfer has an originating epoch of December 2, 2022 12:00:00.000 into an injection point consistent with $\theta_2 = 93.8°$, i.e., Type A transfer

Ω [deg]	TIM	DSM 1	DSM 2	OIM	Total
0	760	17	544	7	1319
20	746	134	183	27	1099
40	744	0	297	23	1054
60	740	216	138	15	1107
80	739	276	143	10	1180
100	742	220	116	66	1168
120	745	93	116	85	1038
140	753	201	114	29	1030
160	756	32	165	13	943
180	762	30	118	19	901
200	767	35	98	17	918
220	739	23	309	0	1128
240	748	0	292	14	1035
260	745	200	90	0	1017
280	745	0	166	178	1175
300	747	85	185	126	1146
320	750	99	318	34	1194
340	758	46	440	15	1251

Table F.6. : Summary of maneuver magnitudes (m/s) for optimized ephemeris transfers into a Sun-Earth L_2 Lissajous orbit. Each transfer has an originating epoch of December 2, 2022 12:00:00.000 into an injection point consistent with $\theta_2 = 273.95°$, i.e., Type B transfer

Ω [deg]	TIM	DSM 1	DSM 2	OIM	Total
0	759	0	550	7	1300
20	754	52	93	10	907
40	743	50	108	5	901
60	741	123	130	9	997
80	740	96	258	10	1114
100	742	234	109	7	1118
120	744	15	236	10	1010
140	748	188	170	4	1104
160	756	89	212	22	1080
180	769	14	216	11	991
200	767	17	186	86	1138
220	739	0	260	34	1095
240	748	51	208	41	1026
260	745	101	135	58	1023
280	745	215	98	16	1053
300	747	107	266	7	1107
320	750	46	403	11	1188
340	755	7	471	7	1222

VITA

Juan Andre Ojeda Romero graduated with his Bachelor of Science in Aerospace Engineering from Virginia Polytechnic Institute and State University (Virginia Tech) in 2013. He stayed in Virginia Tech for graduate school and completed his M.S. degree with his adviser Professor Michael Philen in 2014. His graduate work was focused on an application of Particle Swarm Optimization applied to a two satellite mission to view the Aurora. He started as a network engineer at L3 Harris Technologies in 2015, before moving to a.i. solutions, Inc. He worked as an orbit analyst for a.i. Solutions, Inc. as an on-site contractor at NASA Goddard Space Flight Center (GSFC). He joined Professor Howell's Multibody Dynamics Research Group in August of 2017, where he was awarded the National Science Foundation (NSF) Graduate Research Fellowship in 2018. Throughout his time in Graduate school, he has focused on constructing transfers for secondary payloads from Geosynchronous Transfer Orbits to orbits near the Sun-Earth system. This research was a continuation of his work with Mr. Michael Mesarch during his 2018 summer internship at NASA GSFC. During the summer of 2020, he completed a summer internship at John Hopkins Applied Physics Laboratory (APL) in Laurel M.D. with mentors Dr. Wayne Schlei and Mr. Sean Phillips. He will continue his career as a full-time employee at John Hopkins Applied Physics Laboratory.